Biological and Medical Physics, Biomedical Engineering

Rongguang Liang *Editor*

Biomedical Optical Imaging Technologies

Design and Applications

Springer

BIOLOGICAL AND MEDICAL PHYSICS, BIOMEDICAL ENGINEERING

BIOLOGICAL AND MEDICAL PHYSICS, BIOMEDICAL ENGINEERING

The fields of biological and medical physics and biomedical engineering are broad, multidisciplinary and dynamic. They lie at the crossroads of frontier research in physics, biology, chemistry, and medicine. The Biological and Medical Physics, Biomedical Engineering Series is intended to be comprehensive, covering a broad range of topics important to the study of the physical, chemical and biological sciences. Its goal is to provide scientists and engineers with textbooks, monographs, and reference works to address the growing need for information.

Books in the series emphasize established and emergent areas of science including molecular, membrane, and mathematical biophysics; photosynthetic energy harvesting and conversion; information processing; physical principles of genetics; sensory communications; automata networks, neural networks, and cellular automata. Equally important will be coverage of applied aspects of biological and medical physics and biomedical engineering such as molecular electronic components and devices, biosensors, medicine, imaging, physical principles of renewable energy production, advanced prostheses, and environmental control and engineering.

Rongguang Liang
Editor

Biomedical Optical Imaging Technologies

Design and Applications

With 153 Figures

Springer

Editor:
Rongguang Liang
College of Optical Sciences
University of Arizona
1630 E University Blvd
Tucson, AZ 85721
rliang@optics.arizona.edu

Biological and Medical Physics, Biomedical Engineering ISSN 1618-7210
ISBN 978-3-642-28390-1 ISBN 978-3-642-28391-8 (eBook)
DOI 10.1007/978-3-642-28391-8
Springer Heidelberg New York Dordrecht London

Library of Congress Control Number: 2012948781

Printed on acid-free paper

Springer is part of Springer Science+Business Media (www.springer.com)

Preface

Biomedical optics is a rapidly growing area of research that has passed the "tipping point" for technology transfer, with significant momentum toward commercialization. Designing an imaging technique to meet the specific application requirements is one of the keys in the development and commercialization of new imaging technologies. It requires a solid understanding of imaging technologies and special requirements for imaging applications; it also encompasses the selection of optical configurations, light sources, optical components, detectors, illumination and imaging system designs, and testing.

This book will provide an introduction to principles, designs, and applications of a number of imaging technologies, including spectroscopy, photoacoustic, fluorescence, hyperspectral, optical coherence tomography, confocal, multiphoton, endomicroscopy, multimodal imaging, and multimodal tomography. Each chapter covers (1) principles and limitations of optical imaging technology; (2) system design and practical implementation for one or two specific applications, including design guidelines, system configuration, optical design, component requirements and selection, system optimization, and design examples; and (3) recent advances and applications in biomedical researches and clinical imaging.

There are many books on principles and applications of biomedical optical imaging technologies; however, there is no book covering the topics of detailed design and implementation for different biomedical optical imaging modalities. This book is intended to fill this gap by giving interested readers the fundamental knowledge necessary for planning and designing successful biomedical imaging techniques for their specific application. This book can be used as a reference book for students and professionals in optics and biomedical engineering. The reader can learn the fundamentals, design principles, and implementations of biomedical optical imaging technologies.

I thank the authors for their excellent contributions. I also thank Dr. Claus E. Ascheron and the editorial staff of Springer Press for their contribution to the success of this book.

Tucson, AZ, USA *Rongguang Liang*

Contents

Contributors

Fred S. Azar Clinical Data Solutions, Office of Medical & Health Affairs, Philips Healthcare, Ramsey, NJ, USA

Jin Chen Biomedical Engineering Department, Rensselaer Polytechnic Institute, Troy, NY, USA

Yuval Garini Physics Department and Nanotechnology Institute, Bar Ilan University, Ramat Gan, Israel

Song Hu Optical Imaging Laboratory, Department of Biomedical Engineering, Washington University in St. Louis, St. Louis, MO, USA

Xavier Intes Biomedical Engineering Department, Rensselaer Polytechnic Institute, Troy, NY, USA

Rongguang Liang College of Optical Sciences, University of Arizona, Tucson, AZ, USA

Harvey Lui Laboratory for Advanced Medical Photonics, Cancer Imaging Department, British Columbia Cancer Research Center, Vancouver, BC, Canada

Department of Dermatology and Skin Science, Photomedicine Institute, University of British Columbia & Vancouver Coastal Health Research Institute, Vancouver, BC, Canada

Konstantin Maslov Optical Imaging Laboratory, Department of Biomedical Engineering, Washington University in St. Louis, St. Louis, MO, USA

Ammasi Periasamy W.M. Keck Center for Cellular Imaging, Department of Biology and Biomedical Engineering, University of Virginia, Charlottesville, VA, USA

Shakil Rehman Division of BioEngineering, National University of Singapore, Singapore, Singapore

Singapore Eye Research Institute, Third Hospital Avenue, Singapore, Singapore

Colin J. R. Sheppard Division of BioEngineering, National University of Singapore, Singapore, Singapore

Department of Biological Sciences, National University of Singapore, Singapore, Singapore

Hrebesh M. Subhash Department of Bioengineering, University of Washington, Seattle, WA, USA

Yuansheng Sun W.M. Keck Center for Cellular Imaging, Department of Biology and Biomedical Engineering, University of Virginia, Charlottesville, VA, USA

Elad Tauber Physics Department and Nanotechnology Institute, Bar Ilan University, Ramat Gan, Israel

Tomasz S. Tkaczyk Department of Bioengineering, Rice University, Houston, TX, USA

Vivek Venugopal Biomedical Engineering Department, Rensselaer Polytechnic Institute, Troy, NY, USA

Lihong V. Wang Optical Imaging Laboratory, Department of Biomedical Engineering, Washington University in St. Louis, St. Louis, MO, USA

Ruikang K. Wang Department of Bioengineering, University of Washington, Seattle, WA, USA

Haishan Zeng Laboratory for Advanced Medical Photonics, Cancer Imaging Department, British Columbia Cancer Research Center, Vancouver, BC, Canada

Department of Dermatology and Skin Science, Photomedicine Institute, University of British Columbia & Vancouver Coastal Health Research Institute, Vancouver, BC, Canada

Jianhua Zhao Laboratory for Advanced Medical Photonics, Cancer Imaging Department, British Columbia Cancer Research Center, Vancouver, BC, Canada

Department of Dermatology and Skin Science, Photomedicine Institute, University of British Columbia & Vancouver Coastal Health Research Institute, Vancouver, BC, Canada

Chapter 1
Advanced Spectroscopy Technique for Biomedicine

Jianhua Zhao and Haishan Zeng

This chapter presents an overview of the applications of optical spectroscopy in biomedicine. We focus on the optical design aspects of advanced biomedical spectroscopy systems, Raman spectroscopy system in particular. Detailed components and system integration are provided. As examples, two real-time *in vivo* Raman spectroscopy systems, one for skin cancer detection and the other for endoscopic lung cancer detection, and an *in vivo* confocal Raman spectroscopy system for skin assessment are presented. The applications of Raman spectroscopy in cancer diagnosis of the skin, lung, colon, oral cavity, gastrointestinal tract, breast, and cervix are summarized.

1.1 Introduction

Spectroscopy is a technique for studying the wavelength-dependent optical signals. A spectroscopy system or a spectrometer generally consists of five components: the illumination/excitation light source, the illumination/excitation light delivery unit, the response light collection unit, the spectrograph to separate wavelength-dependent response light, and a detection unit to convert the light signal into electrical signals and/or digital data. In a modern spectrometer, a computer is often used to control the whole system and perform spectral and intensity calibrations as well as data processing.

J. Zhao · H. Zeng (✉)
Imaging Unit - Integrative Oncology Department, British Columbia Cancer Agency Research Center, 675 West 10th Avenue, Vancouver, BC V5Z 1L3, Canada

Photomedicine Institute, Department of Dermatology and Skin Science, University of British Columbia & Vancouver Coastal Health Research Institute, 835 West 10th Avenue, Vancouver, BC V5Z 4E8, Canada
e-mail: hzeng@bccrc.ca

R. Liang (ed.), *Biomedical Optical Imaging Technologies*, Biological and Medical Physics, Biomedical Engineering, DOI 10.1007/978-3-642-28391-8_1,

Spectroscopy has been widely used in biomedicine, from photobiology to disease diagnosis [1–10]. The underlying mechanism for biomedical spectroscopy is the wavelength-dependent optical properties of many biomolecules in cells and tissues, which can be assessed by different modes of the light-matter interactions. When light is incident on a biological sample, photons are either absorbed or scattered (elastically or inelastically). The absorbed light may be reemitted at a longer wavelength, called fluorescence emission. Accordingly, spectroscopy methods to study the absorption, elastic scattering, fluorescence, and inelastic scattering properties of the sample are called absorption spectroscopy, diffuse reflectance spectroscopy, fluorescence spectroscopy, and Raman spectroscopy, respectively. Different spectroscopic techniques are not competing but complimentary with each other as each technology provides different aspects of the sample's optical properties. The absorption, elastic scattering, and fluorescence signals are relatively strong, and the spectroscopy systems for such applications are relatively easy to build. Raman spectroscopy is considered to be particularly advantageous over other techniques for *in vivo* biomedical applications because it can provide more specific and rich information about the structure and conformation of biomolecular constituents in tissues. However, Raman signal is extremely weak, and the instrumentation is more complicated and challenging. With recent technology advancement, real-time Raman spectroscopy system for *in vivo* biomedical applications is now a reality [11, 12].

In this chapter, we will focus on the designing aspects of advanced spectroscopy system, Raman spectroscopy system in particular. We will first review the main components of a standard spectroscopy system and their technical advancement. Then we will present the details of designing two real-time Raman spectroscopy systems, one for *in vivo* skin cancer detection and the other for lung cancer diagnosis, and an *in vivo* confocal Raman spectroscopy system for skin assessment, followed by the design review of other Raman spectroscopy systems. At the end, we will summarize the applications of Raman spectroscopy in different fields of medicine.

1.2 Components for Spectroscopy System

As mentioned in the introduction, a standard spectroscopy system is generally composed of five components [13]. Standard spectroscopic systems are commercially available from various manufacturers and are recommended for routine spectral measurement and analysis. For special applications, particularly in biomedicine, it may need to be custom designed by refining every aspect of the system. In this section, we will briefly discuss the basic spectroscopic components and their advancement for biomedical applications.

1.2.1 Light Sources

Sunlight is the cheapest light source. Spectroscopic system based on sunlight source has been used in remote sensing, weather forecast, and forestry monitoring. For biomedical spectroscopic system, dedicated light sources are often required. The light source must be stable, predictable, measurable, and reliable. The most often used light sources for biomedical spectroscopy include broadband lamps with wavelength spanning from ultraviolet (UV) to visible to near-infrared (NIR), light-emitting diodes (LEDs), and gas or solid-state lasers. The recent development of programmable light sources, fiber lasers, and supercontinuum light source can also be used for biomedical spectroscopy. Choice of these light sources depends on the application requirement on wavelength, intensity, beam size, and beam quality of the light source.

1.2.1.1 Broadband Light Source (High-Pressure Arc Lamp, Incandescent Lamp, Programmable Light Source, Supercontinuum Light Source)

Common broadband light sources include high-pressure arc lamp and incandescent lamp. They can be obtained from suppliers such as Newport and Ocean Optics (see Appendix for more details). High-pressure arc lamp generates intense and broadband emission from UV to NIR (200–1,000 nm). The commonly used high-pressure arc lamps include xenon (Xe) lamp, mercury (Hg) lamp, or mercury-xenon (Hg-Xe) lamp. These types of lamps consist of two tungsten electrodes in a quartz bulb filled with high-pressure gases. Example emission spectra of these types of lamps are shown in Fig. 1.1. Because there are so many spikes (peaks), these types of lamps are superior for fluorescence excitation. They are also frequently used for reflectance spectroscopy. Care must be exercised when handling these lamps because the high-pressure bulb is explosive. Xe lamp also has strong UV output; protective headgear, safety eyewear, and leather gloves are highly recommended.

Incandescent lamp is the simplest light source. The commonly used one is the quartz tungsten halogen (QTH) lamp. The spectra of QTH lamp are also shown in Fig. 1.1. The spectra are very smooth and covering the visible range and the NIR range. This type of lamp is particularly useful for transmission and absorption measurement. Calibrated QTH lamp can also be used for intensity calibration of a spectrometer (see Sect. 1.2.6).

Based on the broadband lamp, a digital programmable light source was developed recently [14]. It is not a stand-alone lamp, but a system that can modulate the intensity and spectral shape of the light source. It consists of a broadband lamp, a dispersive grating, and a digital micromirror device (DMD). The DMD is a micromirror array typically consists of 1,280 × 1,024 pixels with each pixel being 12.6 μm × 12.6 um. Each pixel is a micromirror which can be turned on and off and controlled by the computer by tilting the direction of the mirror toward or away from

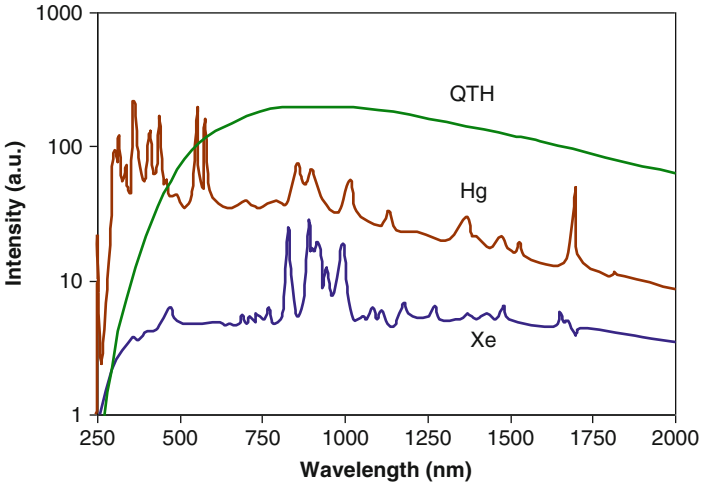

Fig. 1.1 Example emission spectra of xenon arc lamp (Xe), mercury arc lamp (Hg), and quartz tungsten halogen lamp (QTH) (Reproduced with permission from Newport)

the light source. When broadband light is dispersed by the grating and incident onto the DMD, the spectrum and the intensity of the output light beam can be selectively controlled by turning on or off the position and number of the micromirrors. Such kind of light source is versatile, rapidly programmable, and easy to use, particularly for absorption/transmission spectroscopy and spectral imaging.

Supercontinuum light source is a new type of broadband light source. It is generated by propagation of high-power pulse through nonlinear media. Although the phenomenon of supercontinuum light generation was first observed in 1970, it is only until very recently that supercontinuum light source products became commercially available that benefitted from the development of femtosecond-pulsed lasers and photonic crystal fibers (PFC) [15,16]. An example spectrum from a supercontinuum light source is shown in Fig. 1.2 [16]. The supercontinuum generation is determined by dispersion of the nonlinear media, the pumping wavelength, the pulse length, and the peak power. Newest supercontinuum light source is capable of generating several watts of total optical powers in the broad visible to NIR wavelength range [17].

1.2.1.2 Lasers (Gas, Solid State, Dye, Semiconductor, Fiber)

Broadband light sources are commonly used for absorption/transmission/reflectance spectroscopy. Lasers are often used for fluorescence and Raman spectroscopy. Laser sources can be easily monochromatic, naturally suitable for Raman excitation. Laser sources can also be highly collimated and with high intensity, thus, can be efficiently coupled into optical fibers for convenient delivery. Based on the lasing

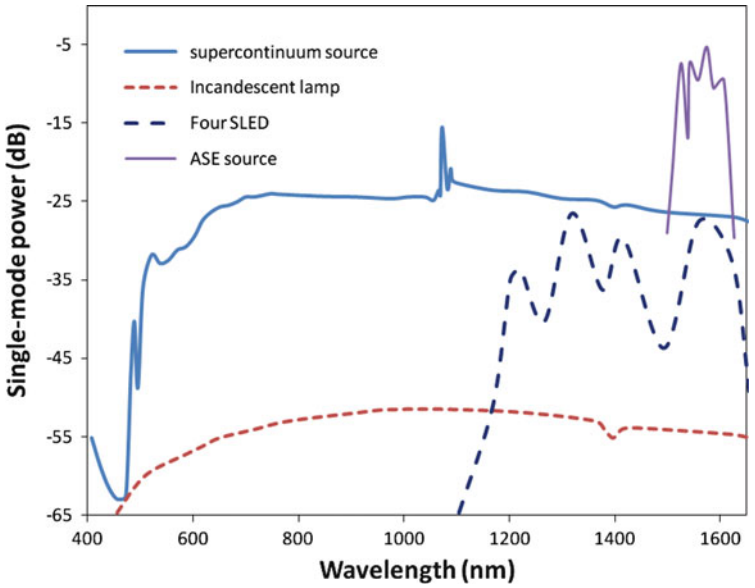

Fig. 1.2 Comparison of a PCF-based supercontinuum light source spectrum with other broadband light sources. *SLED* – superluminescent light-emitting diode. The ASE source is referred to as Thorlabs' C&L band light source (Adapted from Hansen et al. [16])

media, lasers can be divided into gas, excimer, solid state, dye, semiconductor, and fiber lasers. A summary of the lasers commercially available for biomedical spectroscopic applications is listed in Table 1.1. He–Ne, CO_2, Ar^+, and nitrogen lasers are the most used gas lasers. Excimer lasers can be used for UV-excited fluorescence spectra. Ti:sapphire, Nd:YAG, Nd:YLF, and Nd : YVO_4 are the most commonly used solid-state lasers. In recent years, the application of (semiconductor) diode laser gained popularity because of the compact size and stable output. Fiber lasers are a special type of lasers in which rare-earth ion-doped optical fibers act as gain media (such as erbium, neodymium, ytterbium, or thulium). Choice of lasers depends on the availability of the wavelength, power, system size, and cost.

1.2.1.3 LED

Light-emitting diode (LED) is a type of solid-state light source. It consists of a semiconductor chip doped with impurities to form a p-n junction. Current flows in the p-n junction from p-side (anode) to n-side (cathode) under different voltages. Once electrons meet holes, they will fall to lower energy level and release the energy in the form of light. The wavelength depends on the bandgap of the p-n junction. With the advancement in material science, now broadband LED light sources have covered the full wavelength range from UV to visible to near infrared. White LEDs

Table 1.1 A summary of lasers and their spectral characteristics

Laser type	Wavelength range (nm)	Comments
Ar+	457, 488, 514.5	Gas, CW or pulsed
He–Ne	632.8	Gas, CW
Nitrogen	337	Gas, pulsed
CO_2	10.6 μm	Gas, CW or pulsed
HeAg	224	Gas
HeCd	325, 442	Gas, CW
Nd:YAG	1,064, 532	Solid state, CW or pulsed
Nd:YVO4	914, 1,064, 1,342	Solid state
Nd:YLF	1,047, 1,053	Solid state
Ti:sapphire	690–1,000	Solid state, CW or pulsed, Q-switched
Diode laser	300–900	Semiconductor, CW
Fiber laser	514, 780, 1,025–1,600	Pulsed, doped with Er, Nd, Yb, and Tm
Kr+	406, 647, 752	Gas, CW, intermediate
KrCl	222	Excimer
KrF	248	Excimer
XeCl	308	Excimer
XeF	351	Excimer
Ruby	694.3	Solid state, pulsed

are also available, which are working in two ways. In one way, white LED is generated by mixing the primary color red, green, and blue LEDs. In the other way, white LED is generated by a second emission from a layer of phosphor material excited by a blue or UV LED. Now, high-power LEDs are available. Because LED has a very compact size and very long lifetime, it is expected that LED light source will find broad applications in biomedical spectroscopy, particularly in absorption spectroscopy, reflectance spectroscopy, and fluorescence spectroscopy.

1.2.2 Optical Fibers

Although free space light delivery is used in many optical spectroscopy systems, they are usually inconvenient for use in biomedical applications. Nowadays most biomedical spectroscopy systems use optical fiber-based light delivery. A cross section of light transmission in optical fibers is shown in Fig. 1.3.

The light transmission in fibers is based on the law of total internal reflection. The acceptance angle of an optical fiber is determined by its numerical aperture (NA), given by

$$\mathrm{NA} = n_{\mathrm{i}} \sin \theta_{\max} = \sqrt{n_{\mathrm{co}}^2 - n_{\mathrm{cl}}^2}, \tag{1.1}$$

where n_{i}, n_{co}, and n_{cl} are the refractive index of the air, core, and cladding material of the fiber and $\theta_{\max}$ is the maximum acceptance angle. When increasing

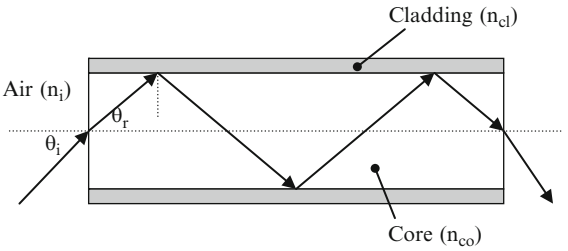

Fig. 1.3 Reflection, refraction, and light propagation in the fiber. θ_i and θ_r are the incident angle in the air and the refraction angle in the fiber. Light propagation is governed by the internal total reflection. n_{co} and n_{cl} are the refractive index of the core and cladding

the refractive index of core or decreasing the refractive index of the cladding, the numerical aperture will increase, which will increase the acceptance angle and the field of view of the optical fiber. Currently, the most commonly used silica/silica (core/cladding) fibers have an NA of 0.22. Some specialized fibers such as silica/hard polymer or silica/Teflon have an NA of 0.37 and 0.66.

To minimize light loss, the NA of the fiber needs to match the coupling optics. The light loss due to NA mismatching is given by

$$\text{Loss}_{\text{NA}} = 10\ \log\left(\frac{\text{NA}_1}{\text{NA}_2}\right)^2, \tag{1.2}$$

where NA_1 and NA_2 are the NA of the coupling optics and fiber, respectively. When $\text{NA}_1 > \text{NA}_2$, there is light loss because the coupling is overfilling the fiber. Theoretically, there is no light loss when $\text{NA}_1 \leq \text{NA}_2$ because all light from the coupling optics is accepted by the fiber. But in practice, in order to design high-throughput optical system, the ideal situation is to make the coupling optics and the fiber to be perfectly NA matched ($\text{NA}_1 = \text{NA}_2$). The choice of the fiber determines the coupling lens by $\text{NA} = \text{D}/(2\text{f}_\text{e})$, where D is the diameter of its entrance pupil, in most cases the diameter of the lens, and f_e is the effective focal length of the lens. For example, an $\text{NA} = 0.22$ fiber requires a $D = 25\,\text{mm}$ and $f_\text{e} = 56.8\,\text{mm}$ lens for perfect NA matching.

1.2.2.1 Single Mode

Single-mode fiber is a kind of fiber that there is only one mode, the primary mode, of light that can be transmitted in the fiber. The core size of single-mode fiber is usually within 4–10 μm. The mode of the light travels through the fiber with much smaller distortion compared to multimode fiber. Single-mode fiber is the choice of long-distance data and voice communication. Because the core size is small and cannot afford to high optical power, it is generally not suitable for power delivery. Single-mode fibers have been used in confocal Raman spectroscopy applications

because of its capability to maintain the single-mode quality of the transmitted laser light.

1.2.2.2 Multimode

Contrary to single-mode fiber, multimode fiber refers to the fibers that allow multimodes of light to be transmitted. The core diameter of multimode optical fiber is usually larger than about 10 μm and varies from 50 to 2,000 μm for most off-the-shelf products. Multimode fiber is the most commonly used fiber in biomedical spectroscopy. There are two types of multimode fibers: step-index multimode fiber and graded-index multimode fiber. The ways of light propagations in single-mode and multimode fibers are shown in Fig. 1.4a.

1.2.2.3 Low-OH/High-OH Fibers

For optical fibers, certain hydroxyl (–OH) absorption bands may limit the performance. The optical attenuation properties of low-OH and high-OH fibers are quite different, as shown in Fig. 1.4b. Materials with high OH (600–800 ppm) offer excellent transmission in the UV wavelength range and can transmit light from 190 to 1,064 nm. It is suitable for broadband and laser delivery in the UV range. Low-OH (<1 ppm) optical fiber, with a minor absorption peak around 1,385 nm, is suitable for longer visible and near-IR wavelength range, usually from 500 to 2,300 nm. Now, low-loss broadband optical fiber is also available for the wavelength range from 275 to 2,100 nm. These are step-index multimode fibers. The core sizes are between 50 and 1,000 μm.

1.2.2.4 Photonic Crystal Fiber

Photonic crystal fibers (PCFs) are a special kind of optical fibers [15], which contains an array of air-filled holes running along their optical axis. Comparing to conventional optical fibers, PCFs have far more complicated index profile due to the index contrast between air holes and the core materials and the capability to vary the size and position of the air holes. PCFs can be single mode, polarization maintaining, highly nonlinear, highly dispersive, and highly birefringent.

Based on the operating principles and geometry, PCFs can be divided into two distinct types: solid-core PCFs and hollow-core PCFs. The optical properties of these two types of PCFs are quite different. Solid-core PCF guides light by total internal reflection at the boundary of the high-index core and the low-index cladding, similar to the conventional optical fibers. The refractive index of the cladding is altered by the arrangement of the position, distance, and shape of the air holes. This type of PCF is highly nonlinear and dispersive and can be used for supercontinuum generation [18] and single-mode laser light delivery. Hollow-core

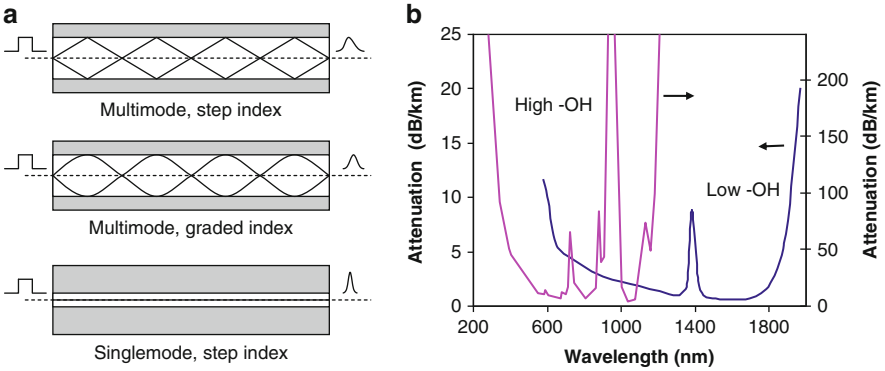

Fig. 1.4 Fiber types (**a**) and the transmission properties of high-OH and low-OH fibers (**b**). The attenuation properties of low-OH and high-OH fibers were reproduced from "The Book on the Technologies of Polymicro" with permission from Polymicro Technologies

PCF transmits light in a different mechanism. The light is confined in the hollow core by a photonic bandgap in the cladding which acts as a loss-free mirror. Because the light is transmitted in the hollow air holes, this type of PCF has extremely low dispersion and loss. It is suitable for short pulse and continuous wave laser delivery and pulse shaping.

1.2.2.5 Polarization-Maintaining Fiber

Polarization-maintaining fiber (PMF) is a special type of fiber in which the polarization of the light can be maintained throughout the light transmission in the fiber. It is based on the birefringence of the optical fiber, in which the beam is split into two orthogonal polarized beams. For the conventional fibers, because the birefringence is randomized, the polarization of the output beam is also randomized. In PMF, the birefringence is intentionally maintained by applying an external stress to the fiber cross section to make it slightly asymmetric along the length and thus prevent the cross coupling of the two orthogonal directions. There are a number of designs including Panda, Bow-Tie, Elliptical Core, or Cladding (Nufern, East Granby, CT, USA).

1.2.3 Spectrograph/Monochromator

Spectrometer refers to any spectroscopic instruments, whether it scans wavelengths individually or acquires the entire spectrum simultaneously or whether it employs a prism, grating, or other mechanisms. It is used to measure the light intensity dependence on wavelength. The commonly used configurations

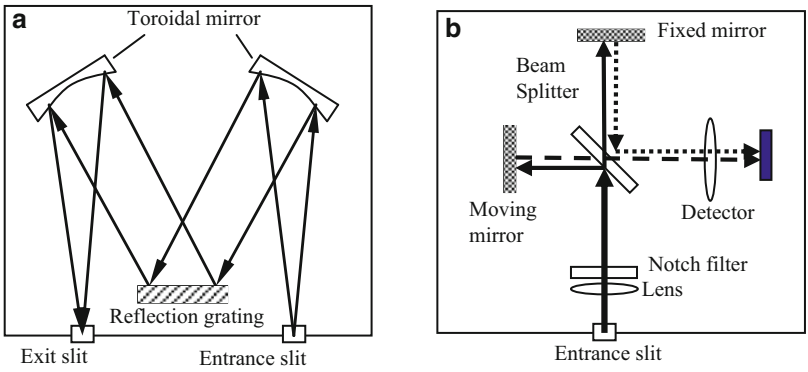

Fig. 1.5 Schematic drawings of a dispersive monochromator (**a**) and a Fourier-transformed spectrometer (**b**)

include dispersive monochromator, dispersive spectrograph, and Fourier transform spectrometer, as illustrated in Fig. 1.5. Both the dispersive spectrograph and the dispersive monochromator are based on diffraction gratings or prisms, but the Fourier transform spectrometer is based on the Michelson interferometer. The configuration of a monochromator and a spectrograph is very similar. A monochromator scans a single wavelength or wave band to its exit slit at a time by rotating its dispersive components usually a grating or prism, while a spectrograph images a range of wavelengths simultaneously onto the detector plane. In monochromator-based spectrometer, the spectral signals are captured by a single-channel detector, such as a photomultiplier tube (PMT). For spectrograph-based spectrometer, the whole spectrum is acquired simultaneously by an array detector, such as a charge-coupled device (CCD) camera.

1.2.4 Filters and Polarizers

Optical filters and polarizers are the most common components for spectroscopy. The most common filters are neutral density filters (ND), long-pass filters (LP), short-pass filters (SP), band-pass filters (BP), and notch filters (NF). Neutral density filters are used to attenuate the light for the full band in some applications where the intensity is too strong for the detectors. Long-pass filter and short-pass filter are also called edge filters that only allow the longer wavelengths for LP or shorter wavelengths for SP than the cutoff wavelength to be transmitted. Long-pass filter is usually used to transmit the signal and block the excitation light such as in fluorescence and Raman spectroscopy. Short-pass filter is used to remove the longer wavelength signal such as blocking the excitation light in the measurement of two-photon fluorescence spectra.

Band-pass filters include narrowband-pass filter and broadband-pass filter. Narrowband-pass filter is usually used to reject side bands of a laser beam for fluorescence or Raman excitation. Broadband-pass filters are usually used for detection purposes such as the fluorescence emission. Notch filter is the reverse of the band-pass filter in which a central band is blocked, allowing the signal with shorter or longer wavelength to pass. Notch filters are commonly used in fluorescence and Raman spectroscopy and imaging.

Most of the filters are based on the properties of the substrate materials and surface coatings, such as absorption, interference, or birefringence. Absorption filters include neutral density filter, short-pass filters, long-pass filters, and broadband-pass filters. Because they are based on the absorption properties of the materials, absorption filters are usually less dependent on the incident angle of the light. This is a major advantage of the absorption filters. However, because it depends on the absorption of the materials, absorption filters are usually thicker and heavier.

Interference filters are usually narrowband-pass filters made from the interference effect of thin films of dielectric or metallic layers on the substrate surface. The films are arranged such that the light within the band is transmitted through constructive interference, while the light out of the band is rejected through destructive interference. Interference filters can be made very thin and light. The rejection edge of interference filter is very steep, so it is particularly suitable for rejection of side bands for laser excitations. The main disadvantage of interference filters is its dependence on the incident angle of light beam. A few degree difference in the incident angle may change the rejection ratio by a few orders. Birefringence filters are based on the birefringence effect of the material, usually used with polarizers. Choice of the filters depends on the applications. For certain applications, the combination of absorption and interference filters shows superior advantages over only a single type of filters.

There are also two types of tunable band-pass filters commercially available for biomedical applications: liquid crystal tunable filter (LCTF) and acousto-optical tunable filter (AOTF). The mechanism of LCTF and AOTF is fundamentally different. Both tunable filters have been used for fluorescence and Raman spectroscopy [19–21].

1.2.4.1 Liquid Crystal Tunable Filters

Liquid crystal tunable filter works as a tunable band-pass filter by electrically controlling the transmission of certain wavelength and blocking of the others. The passband can be as narrow as 1 nm with a rejection ratio up to 10,000:1. The most commonly used materials for LCTF are ferroelectric liquid crystal or nematic liquid crystal wave plates. LCTF is comprised of several cascaded stages of birefringent elements based on the design of Lyot filter as shown in Fig. 1.6. A fixed retarder and liquid crystal retarder are positioned between two parallel linear polarizers. The exit polarizer for a given stage works as the input polarizer of the following stage. Because of the birefringent effect of the liquid crystal, the incident linearly

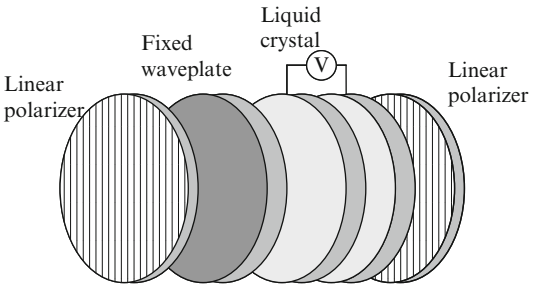

Fig. 1.6 Diagram of a single stage of an LCTF

polarized light is divided into two beams, ordinary and extraordinary. The optical path difference between these two beams is given by [19]

$$\Gamma(\lambda) = 2\pi \frac{\Delta n d}{\lambda}, \tag{1.3}$$

where Δn is the birefringence of the material and d is the thickness of the liquid crystal. The transmittance of the stage is given by

$$T(\lambda) = \cos^2\left[\frac{\Gamma(\lambda)}{2}\right]. \tag{1.4}$$

The total transmittance of a multiple-stage filter is the product of each filter in the stack. For Lyot filters, the thickness and the subsequent optical path difference increases in the powers of two for each successive stage. The spectral range of a LCTF is determined by the thinnest element, and the band pass is determined by the thickest element. The tunability of the LCTF is implemented by applying an electrical field to the liquid crystal retarder, which changes the refractive index under different electrical fields. For nematic liquid retarders, the refractive index is $n = 1.5$, and the difference in refractive index can be 0.05–0.5. The response time is approximately 50–75 ms. Liquid crystal tunable filters can cover the visible to NIR range from 420 to 1,800 nm. The bandwidth of LCTF is wavelength dependent, e.g., 10 nm at 550 nm to 16 nm at 700 nm. The main advantages of LCTFs are that they are compact and have high acceptance angle, large optical aperture, fast switching time, and relatively narrow bandwidth.

1.2.4.2 Acousto-Optical Tunable Filter

AOTF is based on the diffraction of a tunable grating which is generated by applying an acoustic wave to an acoustic optical crystal, as shown in Fig. 1.7a. The period of the acoustic grating can be tuned by changing the frequency of the radio-frequency

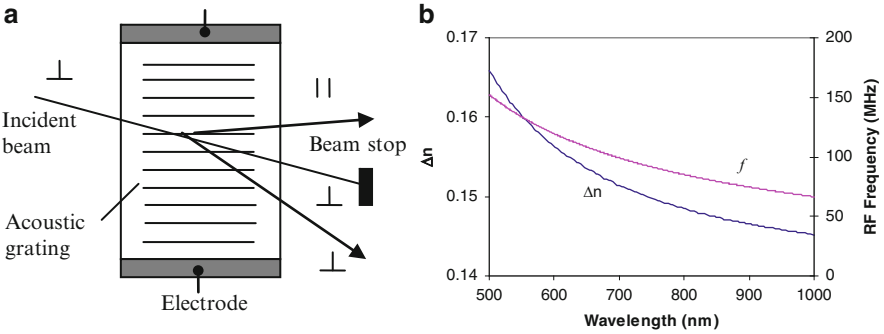

Fig. 1.7 (**a**) Operation of an AOTF filter. A grating is generated by the RF acoustic wave applied through the two electrodes. (**b**) A typical dispersion of a TeO_2 crystal and its corresponding wavelength-frequency dependence

(RF) acoustic waves. AOTF is a tunable band-pass filter. The central wavelength and the applied RF frequency are governed by

$$f = V \cdot \alpha \cdot (n_e - n_o) * \frac{1}{\lambda}, \tag{1.5}$$

where V is the velocity of the acoustic wave in the AO crystal and n_e and n_o are the birefringence of the AO crystal. α is a parameter dependent on the design. The most commonly used AO crystal is TeO_2 [22]. The dispersion of TeO_2 and the frequency and wavelength relations are shown in Fig. 1.6b. Note that the dispersion $(n_e - n_o)$ is wavelength dependent.

In general, AOTF has three outputs: one zero order and two first orders $(+1$ and $-1)$. The zero-order beam has the same polarization as the incident beam, and the two first-order beams are cross polarized. In practice, the zero order is usually blocked by a beam stop. Polarizers are also often used to block the zero-order beam and one of the first-order beams.

The main advantages of AOTF filters are their extremely fast switching time, broad spectral range, and random accessibility. The response time of the AOTF is about 100 times faster than an LCTF filter (μs vs. ms). The limitations of AOTFs are that they have relatively lower rejection ratio ($\sim 10^{-3}$) and they are sensitive to the incident angle which may cause image blurring and signal-to-noise problems.

1.2.5 Detectors

There are various types of detectors for biomedical spectroscopy systems. They can be classified as single-channel detectors and multichannel detectors. Choice of the detectors depends on the application, including the wavelength range, the signal level, the system size, and the data acquisition speed.

1.2.5.1 Single-Channel Detectors

PIN photodiode, avalanche photodiode (APD), and PMT are the most common single-channel detectors. Most PIN photodiodes are made from silicon or InGaAs. Silicon PIN has a response curve between 200 and 1,100 nm, peaked around 900 nm. InGaAs PIN has a response curve between 800 and 1,700 nm, peaked around 1,500 nm. PIN photodiode is very compact and can be made into photodiode arrays (PDAs). The main advantages of photodiode are that there is no need of high voltage and the signal is linearly dependent on the light input. However, because the overall sensitivity is low and the photoactive area is small, PIN photodiode is often used in telecommunications and light regulation applications, i.e., monitoring the excitation intensity in fluorescence spectroscopy measurement.

APD has higher sensitivity than PIN detectors due to a built-in first stage of gain through avalanche multiplication. However, it requires high reverse bias voltage. The optimal gain for APD ranges from 40–100 for silicon APDs to 10–40 for germanium or InGaAs-made APDs. Selection of APDs depends on the wavelength range, the minimum size of the detecting area, and the electrical frequency bandwidth. It can operate at the linear or breakdown mode. Because it has high sensitivity and fast response time, APD can be used in low-level signal detection, such as fluorescence spectroscopy. It has higher quantum efficiencies than PMTs at wavelengths greater than 400 nm. Now, APD is widely used in laser scanning confocal microscopy. A summary of APD types and their properties is listed in Table 1.2.

PMT is a vacuum tube consists of a photoelectron converter (photocathode) followed by an electron multiplier and an electron collector (anode). Light enters the input window and excites photoelectrons in the photocathode. Photoelectrons are accelerated and focused onto the first dynode where they are multiplied by secondary electron emission. This process is repeated until the multiplied photoelectrons hit the last dynode and collected by the anode. Because PMT has high bandwidth and high gain, it is ideal for the detection of extremely low light or short pulses of light. Most photon counting applications are based on PMTs. Choice of PMT is based on the wavelength, intensity, beam size, and detection speed.

1.2.5.2 Multichannel Detectors

Silicon-based CCD has become a popular choice over single-channel PMTs and PDAs because of its high quantum yield, low dark signal, and multichannel capability. Three types of CCD technology are widely used in scientific imaging and spectroscopy, including front-illuminated CCD, back-illuminated CCD, and back-illuminated deep-depletion CCD [23]. A cross section and the quantum efficiency of these three types of CCDs are shown in Fig. 1.8. The CCD detectors are composed of a polysilicon electrode, a silicon dioxide layer, a depletion layer (epitaxial silicon), and a substrate layer (bulk silicon). A summary of the CCD types and their applications is listed in Table 1.3. For front-illuminated CCDs, the light enters the detector from the front and is absorbed in the depletion layer after passing through

Table 1.2 APD types and their properties

APD type	Wavelength range	Gain	Dark current	Application
Silicon	300–1,100 nm	50–1,000	Low	Fluorescence, microscopy
Germanium	800–1,600 nm	10–40	High	Environment monitoring
InGaAs	900–1,700 nm	10–40	Low	Fluorescence

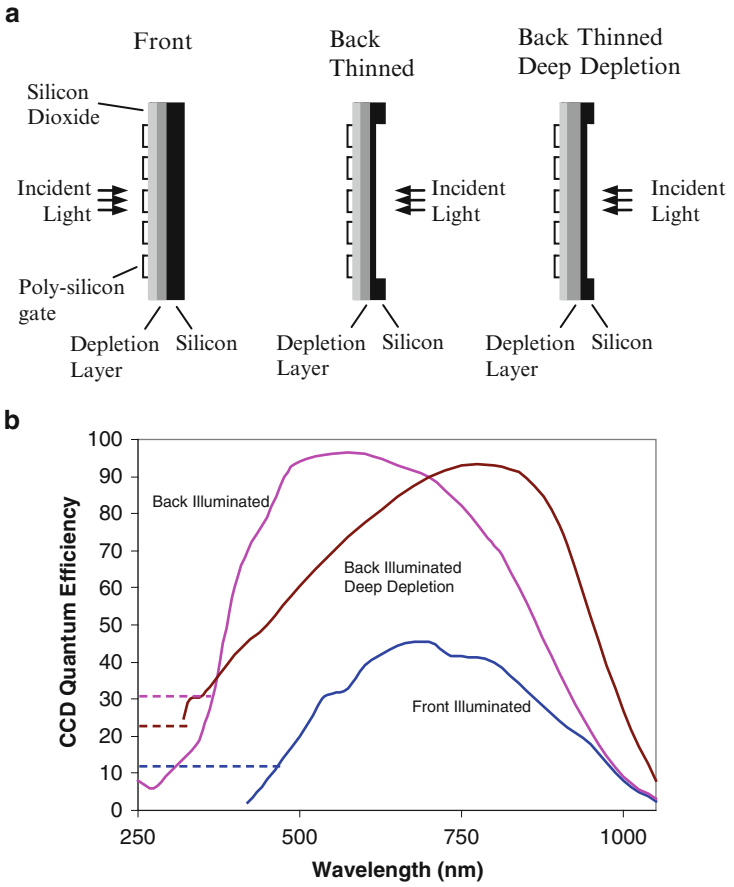

Fig. 1.8 Cross section of the three types of CCD (**a**) and their respective quantum efficiencies (**b**) (Reproduced with permission from Princeton Instruments)

a polysilicon gate, which causes significant loss. The maximum quantum efficiency of a front-illuminated CCD is around 50%. Front-illuminated CCD is used for stronger light signal detection, such as reflectance, transmission, and absorption measurement.

For back-illuminated CCDs, the light enters the detector directly from the back-thinned substrate side. As there is no light loss, the back-illuminated CCD has higher quantum efficiency, up to 90%. Such kind of CCD is particularly useful

for low signal detection, such as luminescence and fluorescence measurement. The thickness of the optical active area (depletion layer) of back-illuminated CCD is the same as the front-illuminated CCD. For near-infrared light, because the absorption of silicon is low, the light may pass through the depletion layer ($n = 4.0$) and reflected by the silicon dioxide layer ($n = 1.5$), causing an etaloning effect, a constructive and destructive interference pattern that is hard to remove in postdata processing. This is the main drawback of back-illuminated CCD. Very recently, a new type of back-illuminated CCD has been produced using a deep-depletion technique, which substantially suppresses the etaloning effect (Princeton Instruments, Trenton, NJ, USA).

Back-illuminated deep-depletion CCD has thicker depletion layer, which provides longer optical path for NIR light absorption, and thus has improved quantum efficiency for NIR imaging and at the same time prevents the etaloning effect. Back-illuminated deep-depletion CCD is suitable for extremely low signal detection, such as fluorescence and Raman measurement. But it suffers higher dark current (about 100 times higher) than the front-illuminated and back-thinned back-illuminated CCDs. Dark current arises from the thermal vibrations of the silicon lattice. Higher dark current causes higher dark noise, which is not preferable for low signal detection. Therefore, back-illuminated deep-depletion CCD requires deep cooling to suppress the dark current. Now, for most Raman spectral measurements, the back-illuminated deep-depletion CCD is usually cooled down to −90 to −130°C with either thermoelectric cooler (TEC) or liquid nitrogen. Front-illuminated and back-thinned back-illuminated CCDs do not require complicated deep cooling because of low dark current.

All types of CCDs can be UV coated to improve the detection in the UV range. For signal beyond 1,100 nm, silicon-based CCD is no longer a choice because it is transparent in this range. Indium gallium arsenide (InGaAs)-based detectors are preferred.

Further enhancement of the detection can be obtained using an electron-multiplying CCD (EMCCD), in which the signal of each pixel is amplified analogous to an avalanche photodiode. Because this amplification is proportional to the electrons in that pixel and ahead of the signal reaching the shift register, EMCCD boosts the signals above the read noise. As a result, EMCCD is suitable for ultralow light, high-frame-rate applications, such as single-molecule fluorescence spectroscopy and imaging.

For high-speed applications, intensified CCD (ICCD) is the choice. In ICCD, the CCD is coupled to a microchannel plate (MCP) image intensifier, which is essentially a multichannel photomultiplier tube. The signal hits the photocathode, and electrons are accelerated and multiplied in the MCP. The resulting electrons hit a phosphor screen and are converted to light for the CCD to detect. Therefore, the intensifier can work as a shutter, gated very rapidly by changing the potential on the photocathode in MCP. Allowing high-speed gating is the major advantage of ICCD over EMCCD. However, ICCD is expensive and has limited lifetime.

Scientific CCDs can be exposed with/without a mechanical shutter. For full-frame CCD, a shutter is usually required. The exposure is controlled by the shutter,

and the signal is read out with the shutter being closed. The scan speed is limited by the shutter opening and closing compensation time. For some applications, shutter is not needed because no light falls onto the CCD during readout. But "image smearing" may occur without a shutter for slow scientific CCD cameras, because if light keeps falling onto the CCD during readout, charge will continue to accumulate.

1.2.5.3 Software Binning and Hardware Binning

Binning is a process of combining the data of adjacent pixels to form a single output called superpixel. It is commonly used in spectroscopy, particularly for low signal detection such as fluorescence or Raman. The commonly used is hardware binning, which is performed before the signal is read out. For hardware binning, the signal-to-noise ratio (S/N) can be improved linearly with the number of pixels binned if the signal is readout noise limited. For shot noise-limited signal, the S/N ratio is improved roughly proportional to the square root of the number of pixels grouped together. However, hardware binning is limited to the rectangular groups of pixels, and the total number of pixels to be binned is limited by the well capacity of the shift register. If the total charge binned together exceeds the capacity of the shift register, the data will be invalid due to signal saturation, such as a Raman measurement with very strong fluorescence background.

An alternative way is software binning, which is performed after the signal readout. Software binning has more flexibility but is not as fast as hardware binning. It is not limited to the rectangular groups of pixels. If there is any image aberration, the pixels can be shifted before software binning. Software binning is not limited by the well capacity of the shift register either, so higher signal may be produced than hardware binning. However, the maximum improvement in S/N ratio is only the square root of the pixels binned no matter the signal is readout noise limited or shot noise limited. For some applications, a combination of hardware binning and software binning can be used for improving the S/N ratio.

Except the intensity issues, conventional spectrograph equipped with a straight slit also results in a parabolic-shaped image [24]. The parabolic shape arises from the fact that rays from different positions along the length of the slit are incident on the grating at varying degrees of obliqueness. The displacement of the image along the slit is given by [24]

$$x = f_2 \tan\left[\sin^{-1}\left(\sin\alpha - \frac{\lambda}{d}\right) - \sin^{-1}\left(\sin\alpha - \frac{\lambda}{c}\right)\right], \tag{1.6}$$

where $c = d\cos[\tan^{-1}(y/f_1)]$, f_1 and f_2 are the focal lengths of the input and output lenses, α is the incident angle, λ is the wavelength of the incident light, and d is the grating fringe spacing. x is the displacement of the image, and y is the position away from the slit center along the slit. An example of the displacement is shown in Fig. 1.9. It can be seen that the distortion is more severe for longer wavelength. This distortion is also dependent on the focal lengths of the input and output lenses.

Table 1.3 Summary of CCD types and their applications

CCD type	Peak QE/ wavelength	Applications	Light level	Dark current	Cooling type
Front illuminated	47% at 700 nm	Absorption Transmission Reflection Elastic scattering	High	1 ×	Thermoelectric (two stages)
Front illuminated open circuit	47% at 700 nm	Analytical luminescence Analytic Raman	Medium	1 ×	Thermoelectric (four stages)
Back illuminated	97% at 500 nm	Research luminescence Research Raman	Low	1–1.5 ×	Thermoelectric Liquid Nitrogen
Back illuminated, deep depletion	95% at 800 nm	Research luminescence Research Raman	Ultralow	100 ×	Thermoelectric Liquid Nitrogen

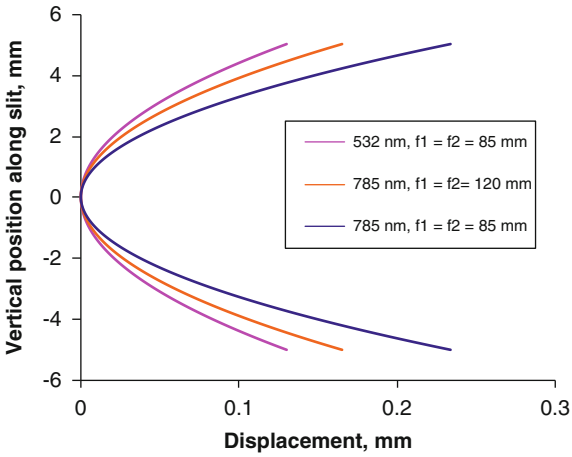

Fig. 1.9 Displacement of slit image with respect to the vertical position away from the center of the slit

For spectrographs with short focal lengths, this obliqueness causes significant distortion that can affect the performance of the detector. This image aberration causes two problems for hardware binning of CCD detectors: (1) It decreases the spectral resolution and (2) it decreases the S/N ratio. It also causes problems in wavelength calibration. The manufacturer (Kaiser) of the HoloSpec spectrograph suggested a combination of hardware and software binning in which the neighboring pixels are hardware binned, then shifted to the appropriate number of pixels and summing them up with software. Recently, we proposed a novel method for full-chip hardware binning by pretreatment of the slit [11]. Details will be discussed in Sect. 1.3.1.6.

1.2.6 Spectroscopy System Calibration

A spectrometer must be calibrated before usage. The calibration processes usually involve two distinct operations: wavelength calibration and spectral response calibration. For certain quantitative measurements, intensity calibration is also necessary.

1.2.6.1 Wavelength Calibration

The wavelength calibration of a spectrometer is to correlate the wavelength to the position of the CCD pixel or the grating position in a monochromator. Wavelength calibration is usually done with a standard lamp. The most commonly used light source for wavelength calibration is Hg(Ar) lamp or Hg(Ne) lamp. For Raman spectroscopy, standard materials, of which the Raman shifts of certain peaks are already known, can also be used for calibration, such as cyclohexane, acetone, and barium sulfate. Once the pixel and wavelength pairs are identified, the relationship can be established by a curve fitting. As the dispersion of the grating is nonuniform, a fifth-order polynomial fitting is commonly used. A rule of thumb in picking the pixel-wavelength pairs in wavelength calibration is that the peaks for calibration should be distributed as uniform as possible to cover the full spectral range.

1.2.6.2 Spectral Response Calibration

Spectral response calibration is more complicated than wavelength calibration. It is used to correct the transmission properties of the collecting optical components and the response of the detectors. It is implemented using a NIST traceable standard lamp, the output of which is assumed to be a blackbody radiator, governed by the Planck's law. The corrected sample spectrum will be

$$I(\lambda) = I'(\lambda)\frac{E_{\mathrm{L}}(\lambda)}{I_{\mathrm{L}}(\lambda)}, \tag{1.7}$$

where $E_{\mathrm{L}}(\lambda)$ is the output spectra of the calibration lamp at the specific temperature. $I_{\mathrm{L}}(\lambda)$ is the measured spectra of the calibration lamp using the current spectroscopy system; $I'(\lambda)$ is the measured sample spectrum using the current spectroscopy system. If the absolute spectral intensity is not important, the spectral correction factor $E_{\mathrm{L}}(\lambda)/I_{\mathrm{L}}(\lambda)$ may be normalized to its maximum or minimum.

1.2.6.3 Intensity Calibration

In fluorescence and Raman spectroscopy, the spectra are commonly normalized to its peak intensity or the integrated intensity (area under the curve). These

normalization procedures only keep the spectral shape information, while the absolute intensity information is ignored. The spectral shape provides the information of fluorophore species/Raman molecules and their relative concentration, while the absolute spectral intensity contains the information of the fluorophore/Raman molecule quantities. Intensity calibration is paramount in many applications, such as flow cytometry and photodynamic therapy. Quantitative fluorescence or Raman measurement enables the capability of interlaboratory comparison and evaluation. Even in the same laboratory, intensity-calibrated fluorescence or Raman measurement is still favorable because the components of the spectroscopy system such as filters, detectors, fibers, or light source may be failed or aged in the course of the study, making it necessary to calibrate the intensity before and after the system configuration change or with time.

Many researchers have proposed instrument-independent fluorescence or Raman measurement [25]. The simplest way is to divide the excitation intensity from the wavelength and spectral calibrated spectra. However, this is invalid for noncontact measurement where the collection efficiency is not taken into account. Recently, we proposed an intensity calibration procedure for fluorescence measurements, which can be written as [26]

$$I(\lambda) = \frac{I'(\lambda)}{I'_{\mathrm{R}}(\lambda_{\mathrm{m}})} \frac{E_{\mathrm{L}}(\lambda)}{E_{\mathrm{L}}(\lambda_{\mathrm{m}})} \frac{I_{\mathrm{L}}(\lambda_{\mathrm{m}})}{I_{\mathrm{L}}(\lambda)} I_{\mathrm{R}}(\lambda_{\mathrm{m}}), \tag{1.8}$$

where $E_{\mathrm{L}}(\lambda)$ and $I_{\mathrm{L}}(\lambda)$ are the emission spectra and measured spectra of current system of the standard lamp used for spectral response calibration. $I_{\mathrm{R}}(\lambda)$ is the properties of the reference standard. $I'_{\mathrm{R}}(\lambda)$ and $I'(\lambda)$ are the measured spectra of the reference standard and the sample. λ_{m} is the wavelength at the maximum of the spectra of the reference standard.

By inspection of Eq. 1.8, the physical meaning of the calibration procedure is straightforward. Intensity-calibrated spectrum is obtained by normalizing the wavelength and spectral response-calibrated sample spectra to the maximum of the wavelength and spectral calibrated spectrum of the reference standard. Although this calibration procedure is obtained from fluorescence spectrum calibration, it is also valid for Raman spectral calibration, provided the reference standard is a Raman standard. Note that this calibration procedure is valid for both contact and noncontact measurement.

1.3 Advanced Spectroscopy Systems

Advanced spectroscopic systems for biomedical applications include diffuse reflectance spectroscopy, fluorescence spectroscopy, and Raman spectroscopy. Of all the spectroscopic systems, the probes vary significantly according to the specific applications. For diffuse reflectance and fluorescence spectroscopy probes, the readers can refer to the review article of Utzinger et al. [27]. Here, we are

focusing on real-time *in vivo* Raman spectroscopy system design. First, we present the designing aspects of two real-time Raman spectroscopy systems: one for *in vivo* skin diagnosis and the other for endoscopic *in vivo* lung cancer diagnosis. Then we introduce an *in vivo* confocal Raman spectroscopy system for skin research, followed by a summary of other types of probes for different applications.

1.3.1 Real-Time Raman Spectroscopy System for Skin Diagnosis

Human skin has been the subject of numerous investigations involving noninvasive optical techniques including infrared (IR) spectroscopy and Raman spectroscopy. Because the probability of Raman scattering is exceedingly low, it has heretofore been characterized by weak signals or relatively long acquisition times on the order of several tens of seconds to minutes. These factors have limited its clinical application in medicine. It is critical to have an integrated system in the clinical setting that can provide real-time spectral acquisition and analysis. We demonstrated the feasibility of real-time *in vivo* Raman spectroscopy by reducing the integration time to less than 5 s [11]. A few other real-time *in vivo* Raman systems have also been published [28, 29].

The real-time NIR Raman system for skin disease diagnosis and evaluation is schematically shown in Fig. 1.10 [11, 12]. It consists of the typical five components of a spectroscopy system: the excitation light source, the excitation light delivery unit, the Raman signal collection unit, the spectrograph, and the detection unit, with each component specially designed for easy access to the measurement site and for real-time measurement.

1.3.1.1 Light Source

The light sources used in Raman spectroscopy are usually lasers because of their higher power output and narrower bandwidth. The choice of wavelength for Raman measurement depends on the specific application and the spectroscopy properties of the sample. For biomedical applications, a NIR laser is commonly used. NIR light has deep penetration depth (700–1,100 nm is regarded as the optical window of biological tissues) and induces lower level of tissue autofluorescence. The output of the laser source must be stable in its intensity and wavelength. Solid-state and external-cavity-stabilized diode lasers are popular choices for their portability. Our current real-time Raman system is equipped with a wavelength-stabilized diode laser (785 nm, 350 mW, model BRM-785-0.35-100-0.22-SMA, B&W Tek Inc., Newark, DE, USA).

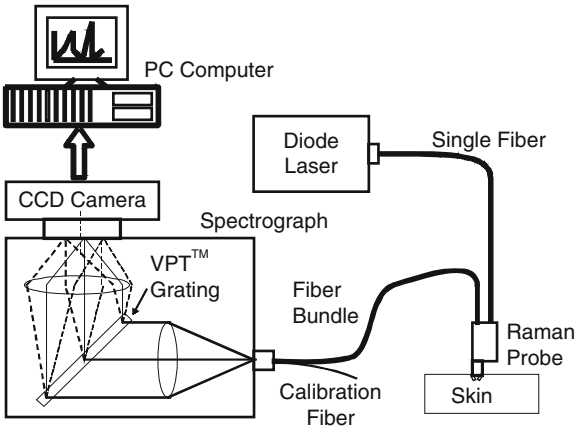

Fig. 1.10 Block diagrams of the integrated real-time Raman spectrometer system for *in vivo* skin disease diagnosis and evaluation

1.3.1.2 Excitation Light Delivery

Optical fibers are most commonly used for light delivery in medical applications. The main considerations for choosing optical fibers are numerical aperture, core diameter, core material, and its transmission properties. Multimode 100–200-μm core diameter fibers are commonly used for excitation light delivery in biological Raman measurements. The choice of the numerical apertures (0.22 or 0.37) depends on the collection capability (numerical aperture matching) of the laser system and the lens system. The transmission properties depend on the core and cladding materials. High-OH fibers have high-UV and visible wavelength transmission, while low-OH fibers are preferred for NIR and IR wavelength range (Sect. 1.2.2.3). Raman signals may arise from the fiber's core material itself and contaminate the tissue signals [30]. Choosing the right optical fiber is therefore important for *in vivo* Raman spectroscopy. Our system uses a 200-μm core-diameter low-OH single fiber for laser beam delivery because of its high NIR transmission.

1.3.1.3 Raman Probe Design

The optical layout of our skin Raman probe is schematically shown in Fig. 1.11. It is designed to maximize the collection efficiency of the tissue Raman scattering and reduce the interference of the backscattered laser light, fiber fluorescence, and silica Raman signals. It consists of two arms: a 1.27-cm (0.5-in.) diameter illumination arm and a 2.54-cm (1-in.) diameter signal collection arm. In the illumination arm, the laser beam illuminates a 3.5-mm spot on the skin surface at a 40° incident angle after having passed through a collimating lens, a band-pass filter (785 ± 2.5 nm; model HQ785/5x, Chroma, Rockingham, VT), and a focusing lens. The band-pass filter can effectively reject Raman scattering and fluorescence that may arise from within the delivery fiber. The laser intensity is controlled so that

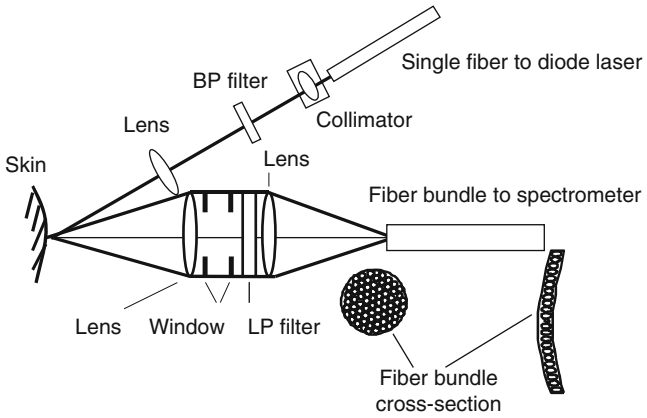

Fig. 1.11 Block diagrams of the specially designed skin Raman probe

the surface skin irradiance is $1.56\,\mathrm{W/cm^2}$, which is lower than the ANSI maximum permissible exposure (MPE) limit of $1.63\,\mathrm{W/cm^2}$ for a 785-nm laser beam with 1 s integration time [31].

The collection arm has a double-lens (FPX11685/102, JML, Rochester, NY) configuration, with the first lens for Raman signal collection and beam collimation and the second lens for focusing the Raman signal to the fiber bundle. Both lenses have a diameter of 25.4 mm with 90% of clear aperture and an effective focal length of 50 mm, which matches the numerical aperture of the fiber for high optical throughput. The focal point of the collection lens overlaps the focal point of the illumination lens on the illumination arm. The diameter of the fiber bundle determines the measurement size (1.3 mm on the skin surface). In between the two collection lenses lies a high-transmission interference 785-nm long-pass filter (LP01-785RU-25, Semrock, Rochester, NY). Because the rejection by the interference LP filter depends on the incident beam angle, two 17.7-mm aperture windows are used before the LP filter to reject stray light. This arrangement more effectively rejects the laser line and allows us to record Raman shifts down to $500\,\mathrm{cm^{-1}}$ for *in vivo* skin tissue.

1.3.1.4 Raman Signal Collection

The raw signal, which is composed of Raman scattering and the tissue autofluorescence background, is collected by the probe and transmitted to the spectrometer detection unit through a fiber bundle. The fiber bundle is composed of fifty-eight 100-μm core-diameter low-OH fibers. The number of fibers is determined by the height of the CCD detectors (6.9 mm). The end of the fiber bundle that connects the Raman probe is packed into a 1.3-mm diameter circular area, which also defines the measurement spot size at the skin surface. There is an additional single fiber

in this end that is connected to a white light source. Before each measurement, this fiber is imaged onto the skin (by turning on the white light source) to help locate the measurement position. Once the position is decided, the white light source is turned off before Raman measurement.

The end of the fiber bundle that is coupled to the spectrograph has a proprietary design that substantially improves the signal-to-noise ratio (S/N) of the Raman system and is discussed in detail in Sect. 1.3.1.6.

1.3.1.5 Raman Signal Detection

The detection unit is equipped with an NIR-optimized back-illuminated deep-depletion CCD array (LN/CCD-1024EHRB, Princeton Instruments, Trenton, NJ) and a transmissive imaging spectrograph (HoloSpec-f/2.2-NIR, Kaiser, Ann Arbor, MI) with a holographic grating (HSG-785-LF, Kaiser, Ann Arbor, MI). The CCD has a 16-bit dynamic range and is liquid nitrogen-cooled to −120°C. The f-number of the spectrograph (f/2.2) matches the numerical aperture (NA = 0.22) of the fiber, so the throughput is much better than that of a traditional f/4 Czerny-Turner spectrographs [32]. The spectral resolution of the system with 100-μm fibers is 8 cm^{-1}.

1.3.1.6 Aberration Correction and Hardware Binning

As discussed in Sect. 1.2.5.3, conventional spectrograph is equipped with a straight slit, and the image of the straight slit is parabolic through a plane grating. For spectrographs with short focal lengths, this distortion is significant that can affect the performance of spectral detection. The horizontal displacement of a spectral line of the real-time Raman system is shown graphically in Fig. 1.12, with the displacement rounded to pixels (dashed lines). The maximum horizontal displacement is 5 pixels (135 μm). The solid line is a linear-regression-fitted parabolic curve described by

$$\Delta x = 1.1904 \times 10^{-5} y^2 - 1.9455 \times 10^{-4} y - 0.98613, \tag{1.9}$$

where Δx is the horizontal displacement at a vertical position, y. Manufacturer (Kaiser) of the HoloSpec spectrograph recommended a combination of hardware and software binning in which the neighboring pixels along the dashed vertical line are hardware binned, then shifted to the appropriate number of pixels and summing them up with software. As shown in Fig. 1.12, there are 11 such hardware-binning groups. Complete software binning can also be used to correct the aberration, in which the whole image is acquired first and then all the pixels along the curve are added up together using software. However, the improvement of S/N ratio using software binning or combined hardware-software binning is limited because the binning only improves the S/N ratio by as much as the square root of the number of pixels binned together. For weak Raman signals that are readout noise limited, hardware binning is preferred because it improves the S/N ratio linearly with the

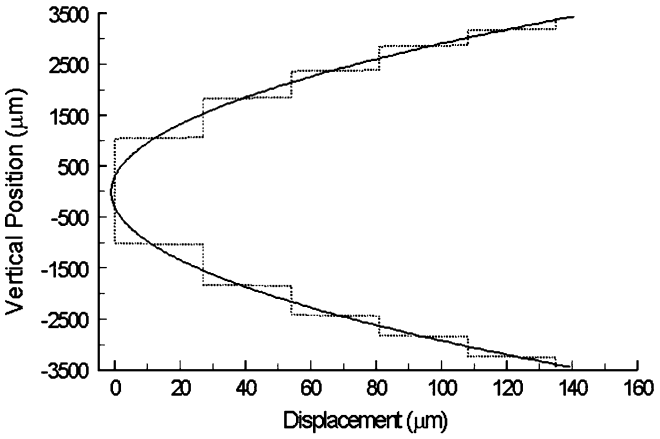

Fig. 1.12 Graphic representation of the curve observed in horizontal displacement rounded to pixels (*dashed lines*). The *solid curve* is a linear-regression-fitted parabolic line (Adapted from Huang et al. [11], with permission)

number of pixels grouped together. We proposed a simple novel solution for full-chip hardware binning by eliminating this image aberration.

As shown in Fig. 1.13, the 58 fibers of the fiber bundle are aligned at the spectrograph end along a curve (Eq. 1.9) formed by the horizontal displacement but in the reverse orientation. Figure 1.13a shows the image aberration of a 100-μm slit through the spectrograph in our uncorrected system when it is illuminated by a mercury-argon lamp. Figure 1.13b shows a CCD image of the fiber bundle illuminated by a mercury-argon lamp after image aberration correction. The center fiber (dark spot) is used for wavelength calibration. With this specific fiber arrangement, the spectral lines are substantially straight, which enables image aberration and full-chip hardware binning along the entire CCD vertical line (256 pixels) without losing resolution. The S/N ratio improvement that we achieve with our system is 3.3 times that of the combined hardware- and software-binning procedure and 16 times that of the complete software binning.

1.3.1.7 Raman Data Acquisition and Processing

The real-time Raman spectroscopic system is controlled by custom-built software implemented within Labview (National Instruments, Austin, TX drivers from R Cubed Software, Lawrenceville, NJ). There are three steps in system controlling: system initialization, real-time data acquisition, and real-time data processing. The system initialization step includes CCD dark-noise subtraction, wavelength calibration, spectral response calibration, and intensity calibration, following the procedures discussed in Sect. 1.2.6. The CCD dark noise is first measured before each measurement and sequentially subtracted immediately after the CCD readout.

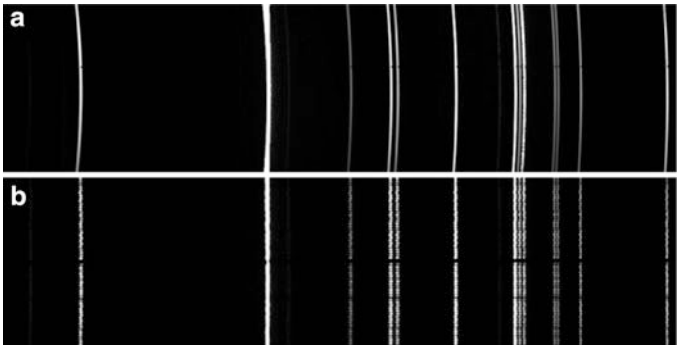

Fig. 1.13 (**a**) Mercury-argon lamp image of a 100 − μm slit on the CCD through the HoloSpec spectrograph, demonstrating the image aberration. (**b**) CCD image of 58 fibers aligned along a parabolic line at the entrance of the spectrograph, demonstrating that the image aberration has been corrected (Adapted from Huang et al. [11], with permission)

After initialization, the system is ready for real-time measurements. Measurements are started via a control signal that can be triggered from the keyboard, hand switch, foot switch, or a signal generated by the program itself. There are two shutters in the system, which essentially have identical response times. One internal shutter lies in the front of the CCD camera to prevent overexposure or exposure during the readout process. The other external shutter is used to control the laser exposure to prevent excessive illumination of the sample (*in vivo* skin). Two additional procedures are implemented in data acquisition, including saturation detection and cosmic ray rejection. Once the spectrum is obtained, it can be automatically processed by preloaded algorithms, such as for biochemical composition analysis.

The most important step in real-time Raman spectroscopy is the rejection of NIR autofluorescence background that is superimposed on the Raman signal. The most commonly used method in biomedical Raman measurement is single polynomial curve fitting. The major weakness of polynomial fitting is its dependence on the spectral range and the choice of polynomial order. Lieber et al. proposed an iterative modified polynomial method to improve the fluorescence background removal [33]. Recently, we proposed a new algorithm for fluorescence background removal (the Vancouver Raman Algorithm), which combines peak removal with a modified polynomial fitting method [34]. The algorithm is less dependent on the choice of the polynomial order and substantially improves the fluorescence background removal, particularly for spectra with high noise or intense Raman peaks. It starts from a single polynomial fitting $P(\nu)$ using the raw Raman signal $O(\nu)$, followed by calculation of its residual $R(\nu)$ and its standard deviation DEV, where ν is the Raman shift in cm^{-1}. The quantity of DEV is considered an approximation of the noise level. In order to construct data for the next round of fitting, we compared the original data with the sum of the fitted function and the value of its DEV, defined as SUM. The data set is reconstructed following the rule that if a data point is smaller than its corresponding SUM, it is kept; otherwise, it is replaced by

its corresponding SUM. Setting DEV = 0 is equivalent to Lieber's method except an additional peak removal procedure, but applying our rule provides a means for taking into account the noise effect and avoiding artificial peaks that may arise from noise and from both ends of the spectra. In order to minimize the distortion of the polynomial fitting by major Raman signals, the major peaks are identified and are removed from the following rounds of fitting. Peak removal is limited to the first few iterations to prevent unnecessary excessive data rejection. The iterative polynomial fitting procedure is terminated when further iterations cannot significantly improve the fitting, determined by $|(\mathrm{DEV}_i - \mathrm{DEV}_{i-1})/\mathrm{DEV}_i| < 5\%$. As with many iterative computation methods, the percentage can be empirically adjusted by the user according to the problem involved and computation time allowed. The final polynomial fit is regarded as the fluorescence background. The final Raman spectra are derived from the raw spectra by subtracting the final polynomial fit function. A copy of the algorithm for noncommercial use can be downloaded from http://www.bccrc.ca/dept/ic/cancer-imaging/haishan-zeng-phd.

1.3.2 Real-Time Raman Spectroscopic System for Endoscopic Lung Cancer Detection

Lung cancers have the highest mortality rate among all cancers and are second only to skin cancers in incidence. It is estimated that nearly 170,000 Americans died of lung and bronchial cancers each year. The overall 5-year survival rate of patients with lung cancers is around 15%, much lower than patients with other types of cancers. An effective way to reduce lung cancer mortality rates is early detection followed by surgery and other therapies. In the past decade, autofluorescence spectroscopy and imaging were developed for *in vivo* early detection of lung cancers [35–37]. However, the spectral features of tissue autofluorescence are broad and show less specific differences between normal and pathologic sites. In an earlier *in vitro* study [38], we found that the Raman spectra of lung cancer were greatly different from those of the normal lung tissue. This prompts us to design a real-time Raman spectroscopic system for improving *in vivo* lung cancer detection [39, 40]. A few technical difficulties must be overcome in designing spectroscopic system for endoscopic applications: (1) The size of the Raman probe is limited by the size of the instrument channel of an endoscope. Although it is desirable to have a large probe to collect as much signal as possible, it must be small enough to pass through the instrument channel. (2) The measurement time is limited by the clinical procedure. The measurement time allowed for an *in vivo* application is less than a couple of seconds. (3) Raman signal of lung tissue is very weak. Real-time *in vivo* Raman imaging of macroscopic tissue area is technologically infeasible. Therefore, Raman spectroscopy itself cannot be used as an efficient method for locating the lesion. We have to rely on autofluorescence or white light imaging to locate the sites of concern and then apply the probe for Raman spectra measurement. The real-time *in vivo* endoscopic Raman system consisted of an excitation light source,

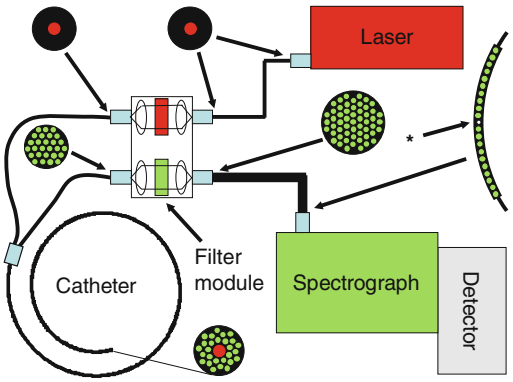

Fig. 1.14 Schematic diagram of the endoscopy Raman system with magnified views of the fiber tips. The ∗ indicates the location of a 50-μm-diameter fiber used to calibrate the spectrometer (Adapted from Short et al. [40], with permission)

an endoscopic Raman probe (including excitation light delivery and Raman signal collection), a spectrograph, and a CCD detection unit. The design of the endoscopy Raman system is schematically shown in Fig. 1.14.

1.3.2.1 Light Source

A wavelength-stabilized diode laser (785 nm, 300 mW, model: BRM-785, B&W Tek, Newark, DE) was used for Raman excitation. The laser beam was delivered through a single 200-μm core diameter fiber to a filter module, which consisted of a laser line filter (LL01-785, Semrock, Rochester, NY) and two long-pass filters (LP02-785RU, Semrock, and RG 715, 5 mm thick, Schott, Elmsford, NY). The laser beam was collimated through a lens, passed through the laser line filter to reject the side bands and background fluorescence and Raman signals generated inside the fiber, and focused into another 200-μm fiber for Raman excitation.

1.3.2.2 Endoscopy Raman Probe

The endoscopic probe was a specially designed bifurcated fiber bundle, with one branch consisting of a single fiber of 200 μm in diameter for excitation delivery and the other branch consisting of 27 fibers of 100 μm in diameter for signal delivery. The 28 fibers were bundled together into a round configuration at the distal end, approximately 1.8 mm in diameter and 0.75 m long with the excitation fiber in the center. Another stage of optical filtering was incorporated at the distal end of the catheter by evaporating interference band-pass filter coatings on the excitation fiber tip and long-pass filter on the 27 collection fibers. With this configuration of filters, the fluorescence and Raman background signal from the excitation fiber are

substantially minimized. The elastically backscattered laser light is also minimized through these two-stage filtering (long-pass filter on the fiber tips and two long-pass filters in the filter module). The filtered signal was coupled into another fiber bundle for delivery to the spectrograph. The bundle consisted of 54 fibers of 100 μm in diameter, packed in a round geometry at the filter module end and spread out into a parabolic arc at the spectrometer end, which replaced the standard entrance slit. All fibers used in this system are ultralow-OH optical fibers for high infrared transmission.

1.3.2.3 Spectrograph and Detectors

The system was equipped with a $f/2.2$ transmissive imaging spectrograph (*HoloSpec*, Kaiser Optical Systems, Ann Arbor, MI) with two interchangeable holographic gratings: one covering a low-frequency (LF) range of Raman shifts (−200 to 2,000 cm^{-1}) and the other for a higher-frequency (HF) range (1,500–3,400 cm^{-1}). Tissue Raman spectra were measured with an NIR-optimized back-illuminated, deep-depletion, liquid nitrogen-cooled CCD array ($400 \times 1{,}340$, 20×20 μm per pixel, model: Spec-10:400BR/LN, Princeton Instruments, Trenton, NJ).

Similar to earlier discussions, straight entrance slit will result in curved image on the CCD, which will lead to lower signal-to-noise ratio (S/N), the spectral resolution, and the throughput of the system. Therefore, the 54 fibers were specially aligned for hardware binning. Following the previous work, the exact shape of the parabolic image was determined by measuring the curvature of the image of the standard slit. For this system, it was found to be

$$\Delta x = 1.12824 \times 10^{-5} y^2 + 1.26767 \times 10^{-3} y + 1.80834, \qquad (1.10)$$

where Δx was the displacement along the horizontal direction and y was the distance of the slit away from the center of the slit along the vertical direction, both in μm. When such an arrangement of fibers replaced the entrance slit with orientation opposite to the image curvature, it resulted in a straight line image at the center of the CCD. Hardware binning with such an arrangement led to an S/N increase up to 20 times of the software binning.

1.3.2.4 Raman Data Acquisition and Processing

The system was wavelength calibrated using a Hg(Ne) lamp (Newport Corporation, Stratford, CT). The spectral resolution was estimated to be $\approx 9\,\mathrm{cm}^{-1}$ for both LF and HF gratings, which was in agreement with the manufacturer's specification (10 and 8.5 cm^{-1} for the LF and HF gratings, respectively, assuming a 100-μm slit width). Spectral response calibration was implemented using a standard halogen calibration lamp (RS-10, Gamma Scientific, San Diego, CA) and an integrating

sphere (Newport Corporation, Stratford, CT), following the procedure described in Sect. 1.2.6.

The system was controlled by a custom-designed program, similar to the one of the *in vivo* skin Raman system, but with a number of modifications. In order to facilitate the physician to determine the spot to be measured, a low-power focusing mode was incorporated which allowed the laser to be operated at 10% of its maximum power by fast switching (500 Hz). This enabled the physician to see the laser spot using the autofluorescence imaging system and thus direct the probe to the point of interest while not exposing the patient to long-term high laser powers.

1.3.3 In Vivo Confocal Raman Spectroscopy System

In this section, we will describe an *in vivo* confocal Raman spectroscopic system, which can perform depth-resolved Raman spectroscopy measurements [41]. The system is schematically shown in Fig. 1.15. Similar to other spectroscopic system, it consists of five components: an excitation laser light source, a microscopic probe that combines excitation delivery and Raman signal collection, a spectrograph, and a detection unit.

1.3.3.1 Light Source

A single-mode diode laser (785 nm, 100 mw, model # I0785SU0100B-TK, Innovative Photonic Solutions, Monmouth Junction, NJ) was used as the excitation source. The laser beam was directed to a lens pair to select the TEM_{00} mode and expand the beam to 6 mm in diameter to fill the aperture of the objective lens. The beam is then filtered by a 785-nm BP filter to reject noises at other wavelengths.

1.3.3.2 Confocal Raman Probe

The confocal Raman probe consists of a water immersion objective (model #: LUMPL40 × W/IR, NA 0.8, WD 3.3 mm, Olympus, Markham, Ontario, Canada) and a special attachment for reducing the effects of involuntary body movements. The 785-nm laser beam passes through a dichroic beam splitter and a mirror and is directed to the water immersion objective. The laser intensity after the objective is 27 mW, and irradiance on the skin is well below the ANSI maximum permissible exposure (MPE) level. The raw signal, composed of the Raman scattering signal and the tissue autofluorescence background, is collected by the same objective lens in the probe. The signal passes through the mirror, the dichroic beam splitter, and a 785-nm long-pass filter and is focused into a 100-μm core-diameter low-OH fiber. The fiber acts as a confocal pinhole and transmits the signal to the spectrograph. The lateral and the axial resolution of the system are 2.2 and 8.6 μm respectively.

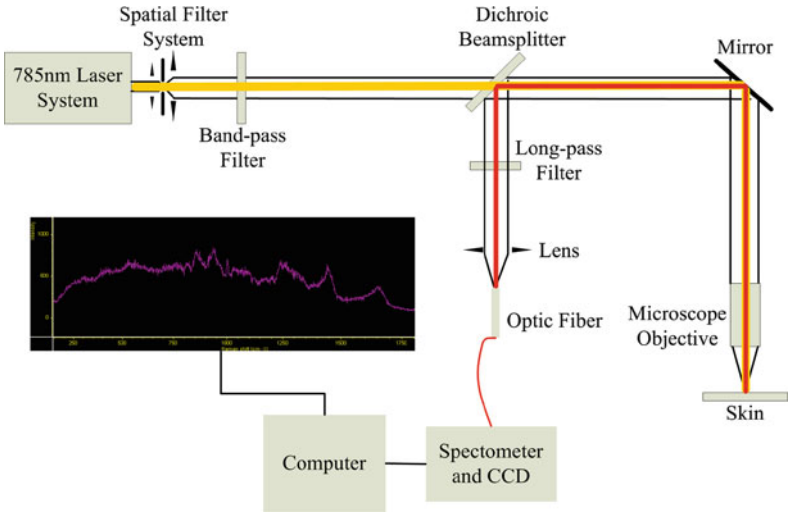

Fig. 1.15 Schematic configuration of the *in vivo* confocal Raman spectrometer system for depth-resolved skin Raman measurement (Adapted from Wang et al. [41], with permission)

1.3.3.3 Spectrograph and CCD Detection System

The spectrograph is a transmissive imaging spectrograph (HoloSpec-f/2.2-NIR, Kaiser, Ann Arbor, MI) with a holographic grating (HSG-785-LF, Kaiser, Ann Arbor, MI). The slit was replaced by the single fiber, the image of which occupied about 5 pixels. The spectral resolution of the system was around 8 cm^{-1}.

The spectrometer system is equipped with an NIR-optimized back-illuminated deep-depletion CCD array (Spec-10:100BR/LN, Princeton Instruments, Trenton, NJ). The CCD has a 16-bit dynamic range and is liquid nitrogen-cooled to −120°C. Hardware binning was used for the Raman spectra measurement, but there was no need of special treatment of the input as there was only one fiber.

1.3.3.4 Results

Raman spectra with good signal-to-noise ratio were obtained within 15 s under 27 mW of excitation light exposure to the skin surface. The mean normalized Raman spectra of normal mouse skin from 24 mice are shown in Fig. 1.16. We find that Raman spectra at different depths in mouse skin differ significantly. For example, strong peaks at 1,061, 1,128, and 1,296 cm^{-1} coming from ceramide can be found in the spectra of the epidermis, while 855 and 937 cm^{-1} are two major peaks that make up the dermal spectral pattern. Four hundred and ninety-four Raman spectra at different depths and from normal and tumor-bearing sites of 24 mice were measured. We found different spectral patterns at different depths. A peak at 899 cm^{-1} (possibly from proline or fatty acids) and one with higher intensity in

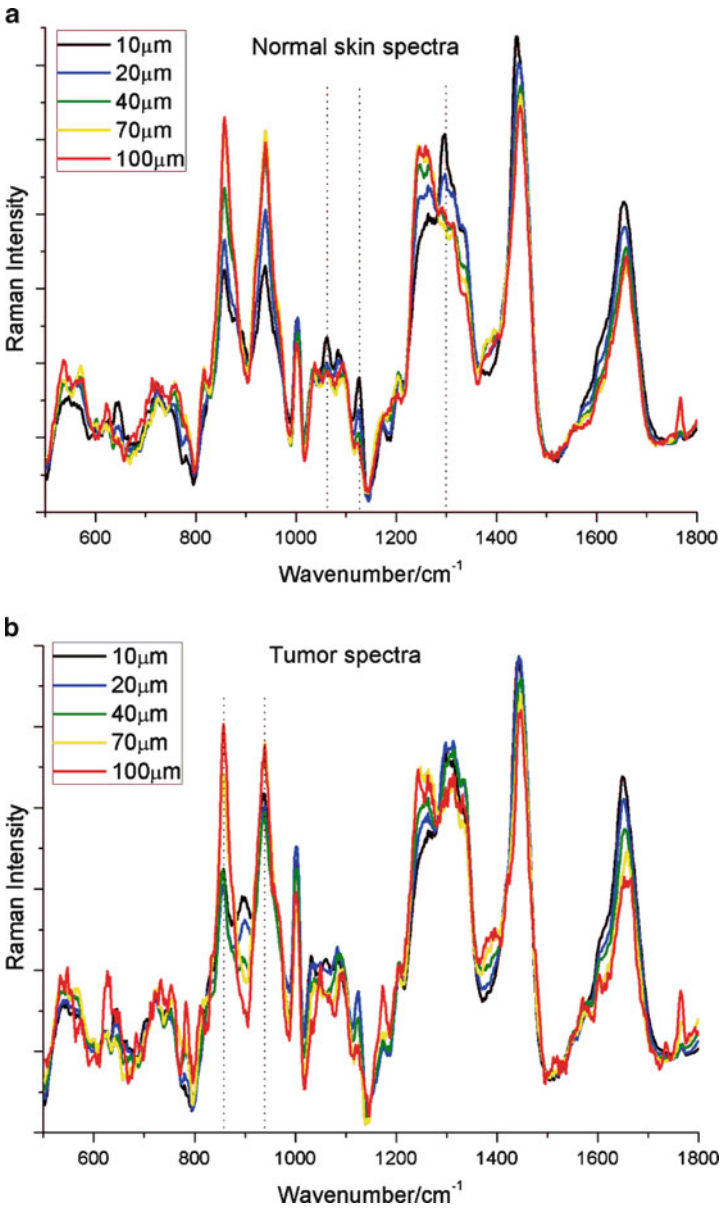

Fig. 1.16 Depth-resolved confocal Raman spectra of (**a**) normal mouse skin and (**b**) tumor-bearing skin *in vivo* (average of 24 mice) (Adapted from Wang et al. [41], with permission)

the 1,325–1,330 cm^{-1} range (assigned to nucleic acids) were correlated with the presence of tumors, which can potentially be used as biomarkers for skin cancer detection. It could also differentiate tumor from normal skin with high diagnostic sensitivity (95.8%) and specificity (93.8%). Therefore, the confocal Raman system was able to detect *in vivo* skin chemical composition variations according to depth and the presence or absence of neoplastic pathology. This work paves the way for future work of analyzing human skin *in vivo*.

1.3.4 Other Advanced Spectroscopy Systems

For biomedical spectroscopy systems, the spectrograph and CCD detection unit are usually commercial parts from a few supplies. But the probes vary significantly according to the specific applications. Except the three *in vivo* Raman systems we discussed above, a number of other designs are summarized in Fig. 1.17.

Figure 1.17a was developed by Myrick et al. [42], based on gradient-index (GRIN) lenses. A band-pass filter was placed between the two GRIN lenses to eliminate the background signals from the fibers for the excitation arm, and a long-pass filter was placed between the two GRIN lenses to reject the elastically scattered laser light. The probe in Fig. 1.17b was developed by Berger et al. [43] for glucose monitoring. It was designed to improve signal collection efficiency with a compound parabolic concentrator (CPC) at the distal end of the probe. The CPC was with an input aperture of 0.57 mm, an exit aperture of 2.1 mm, and a length of 4.1 mm, which improved the collection efficiency by sixfold. Figure 1.17c was designed by Mahadevan-Jansen et al. [44] for cervical cancer diagnosis. *A* 200-μm core diameter single fiber was used for laser delivery. The laser beam was collimated by a lens, filtered by a band-pass filter (3–4 mm in diameter, OD = 5). The signal is collected in a second arm, collimated by a biconvex lens and imaged to a fiber bundle by another biconvex lens. There was a holographic notch filter (OD = 6) between the two biconvex lenses to reject the elastically scattered laser light. The size of the probe was less than 2 cm in diameter.

Figure 1.17d was a ball-lens-based Raman probe developed by Mo et al. [45] for cervical cancer diagnosis. It consisted of two optical arms, one for laser delivery and one for signal collection, integrated with optical filtering modules. The laser beam was coupled into the excitation arm through a 200-μm core diameter fiber (NA = 0.22), collimated by an NIR lens, filtered by a narrowband-pass filter, transmitted through a dichroic mirror, and focused onto the tissue through an NIR-coated sapphire ball lens (5 mm in diameter, refractive index $n = 1.77$). The beam size was around 0.2 mm on the tissue. Signal was collected by the same ball lens and was reflected to the collection arm by a dichroic mirror and a reflection mirror. The signal was further filtered by an edge long-pass filter and focused to a fiber bundle for spectrum measurement. The total size of the probe was less than 8 mm in outer diameter.

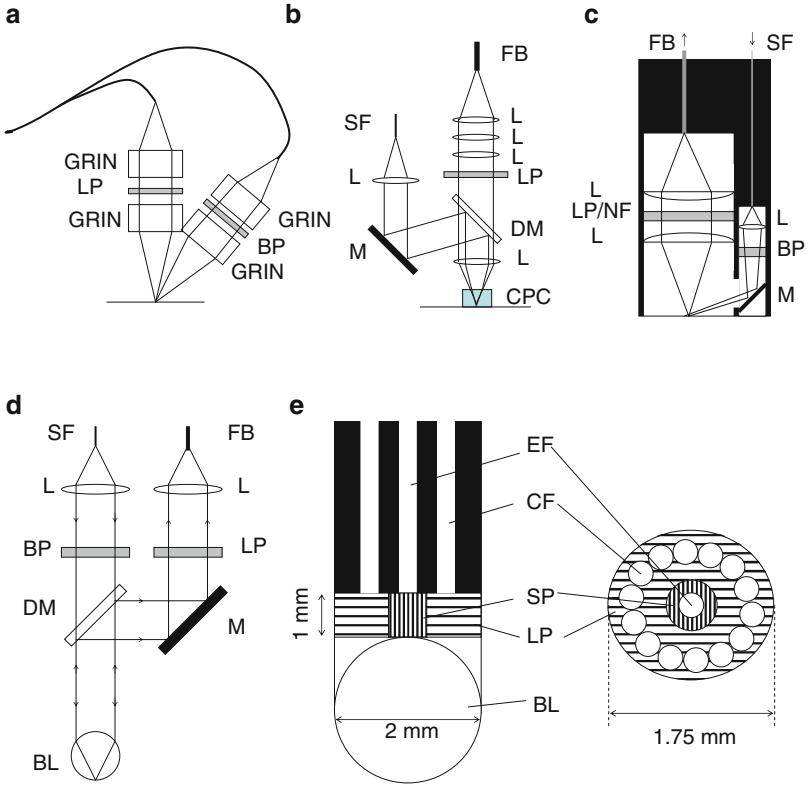

Fig. 1.17 Fiber-based Raman probes for different applications (Reproduced with permission from various sources. See text for details) (a) GRIN lens-based Raman probe for highly scattering medium, (b) Raman probe for glucose monitoring, (c) Raman probe for cervical cancer diagnosis, (d) Raman probe for cervical cancer diagnosis, (e) Raman probe for breast cancer diagnosis. *GRIN* GRIN lens, *L* lens, *LP* long-pass filter, *BP* band-pass filter, *SF* single fiber, *FB* fiber bundle, *DM* dichroic mirror, *NF* notch filter, *M* reflective mirror, *CPC* compound parabolic concentrator, *BL* ball lens, *EF* excitation fiber, *CF* collection fiber, *SP* short-pass filter

A similar ball-lens-based Raman probe was shown in Fig. 1.17e, which was developed by Motz et al. [46] for breast cancer diagnosis. The central fiber (200-μm core diameter, NA = 0.22) was used for excitation. The surrounding 15 fibers (200-μm core diameter, NA = 0.27) were used for signal collection. There were two filters between the fiber tip and the ball lens. The central rodlike short-pass filter was used to reject Raman and fluorescence signal from the fiber, and the other tubelike long-pass filter was used to reject the elastically scattered laser light. There was a metal sleeve between the two filters to prevent cross talk. The total size of the probe was 1.75 mm in outer diameter.

Shim et al. [47] developed an endoscopic probe for colon cancer diagnosis, similar to the ball-based probe (Fig. 1.17e). They were using beveled fiber rather than ball lens to improve the collection efficiency. The probe consisted of a single fiber (400-μm core diameter) for excitation, surrounded by seven single fibers

(300-μm core diameter) for signal collection. The probe had about 1-cm-long rigid tip, incorporated with long-pass filters for signal collection and a band-pass filter for the excitation fiber to reduce the fluorescence and Raman background signal generated from the optical fiber. The seven collection fibers were also cut at an angle and coated with a reflective surface to increase overlap of the excitation and collection volume.

1.4 Applications of Raman Spectroscopy in Biomedicine

Here we provide an overview, but not intended for a critical review, of the applications of Raman spectroscopy in different fields of biomedicine. We are focusing on the *in vivo* applications of the Raman system and probes described in Sect. 1.3.

1.4.1 Skin Cancer Diagnosis

Skin cancer is the most common of all cancers. Basal cell carcinoma (BCC), squamous cell carcinoma (SCC), and malignant melanoma (MM) are the major types of skin cancers. Clinical diagnosis of a skin cancer is based on a physician's visual examination followed by an invasive biopsy. Visual examination alone causes many false positives and thus large number of unnecessary invasive biopsies; moreover, many malignant lesions are undetected and not biopsied. Raman spectroscopy provides an alternative way for early noninvasive diagnosis or for guiding biopsies. *In vitro* Raman spectra of skin diseases and skin cancers have been reported [48–54]. It was found that for *in vitro* studies, a sensitivity of 85% and a specificity of 99% could be achieved for diagnosis of melanoma from normal [50]. Case studies of *in vivo* Raman spectroscopy of skin cancers are also reported [11, 55–60]. Figure 1.18 shows an example of the *in vivo* Raman spectrum of a normal light-colored skin, a normal dark-colored skin, a benign compound nevus, and a malignant melanoma. It can be seen that the biomolecular signatures of the normal skin and skin diseases are quite different. Currently, we are conducting a large-scale clinical study of skin cancers and skin diseases in order to evaluate the utility of the real-time Raman spectroscopy for noninvasive *in vivo* skin cancer detection. We have conducted an intermediate data analysis of 289 cases, of which 24 cases were basal cell carcinoma (BCC), 49 cases of squamous cell carcinoma (SCC), 37 cases of malignant melanoma (MM), 24 cases of actinic keratosis (AK), 53 cases of seborrheic keratosis (SK), 32 cases of atypical nevus (AN), 22 cases of compound nevus (CN), 25 cases of intradermal nevus (IN), and 23 cases of junctional nevus (JN) [61]. The mean of the normalized Raman spectra for different skin cancers and benign skin lesions is shown in Fig. 1.19. All of them are normalized to the strongest 1,445-cm^{-1} peak. Differences in molecular signatures for skin cancers

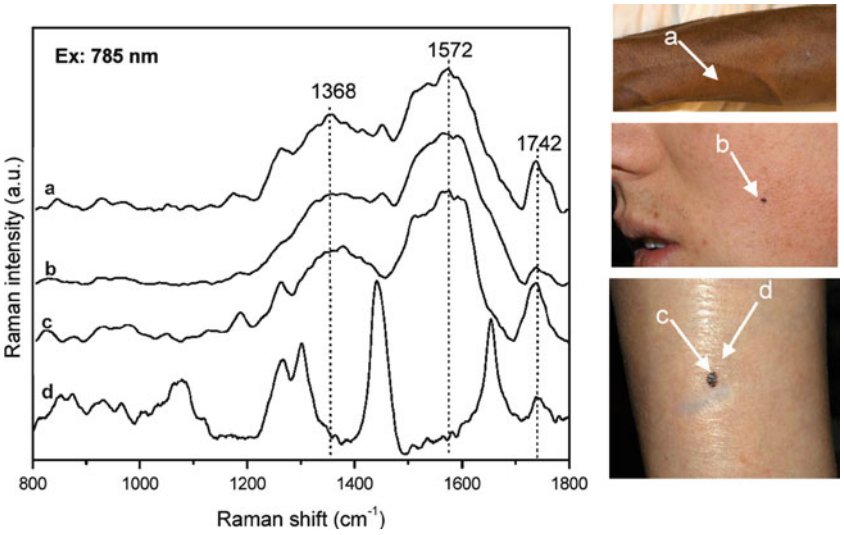

Fig. 1.18 *In vivo* Raman spectra of cutaneous melanin obtained under 785-nm laser excitation from (**a**) volar forearm skin of a volunteer of African descent, (**b**) benign compound pigmented nevus, (**c**) malignant melanoma, and (**d**) normal skin site adjacent to the malignant melanoma. Also shown at the *right* side are clinical images of the corresponding skin sites for*in vivo* Raman measurements (Adapted from Huang et al. [62], with permission)

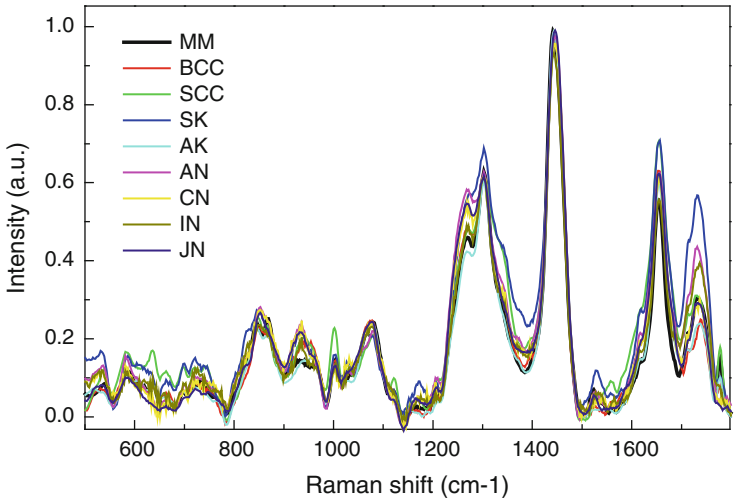

Fig. 1.19 Normalized Raman spectra of skin cancers and benign skin diseases, including melanoma (*MM*), basal cell carcinoma (*BCC*), squamous cell carcinoma (*SCC*), seborrheic keratosis (*SK*), actinic keratosis (*AK*), atypical nevus (*AN*), compound nevus (*CN*), intradermal nevus (*IN*), and junctional nevus (*JN*) (Adapted from Zhao et al. [61], with permission)

and skin diseases are apparent. We used partial least squares (PLS) regression of the measured Raman spectra to derive the biochemical constituents in each lesion and then used the linear discriminant analysis (LDA) to classify the skin diseases. Our preliminary results showed that malignant melanoma can be differentiated from other pigmented benign lesions with a diagnostic sensitivity of 91% and specificity of 75%, while precancerous and cancerous lesions can be differentiated from benign lesions with a sensitivity of 97% and a specificity of 78%, based on leave-one-out cross-validation (LOOCV) analysis.

1.4.2 Lung Cancer Diagnosis

Normal and cancerous bronchial tissue have been studied *in vitro* using the real-time skin Raman spectroscopic system [38]. Bronchial tissue specimens (12 normal, 10 squamous cell carcinoma (SCC), and 6 adenocarcinoma) were obtained from 10 patients with known or suspected malignancies of the lung. High-quality Raman spectra from human bronchial tissues could be obtained within 5 s as shown in Fig. 1.20. Raman spectra differed significantly between normal and malignant tumor tissue, with tumors showing higher percentage signals for nucleic acid, tryptophan, and phenylalanine and lower percentage signals for phospholipids, proline, and valine, compared to normal tissue. The ratio of Raman intensities at 1,445 to 1,655 cm^{-1} provided good differentiation between normal and malignant bronchial tissue ($p < 0.0001$).

In vivo lung cancer diagnosis has been evaluated using the endoscopic real-time Raman spectroscopic system (Fig. 1.14) [39, 40]. The physician identified suspect lung sites of concern using both white light and fluorescence imaging. After these sites were identified, the Raman probe was positioned with the aid of the lowered excitation intensity (10%) beam spot, and then the Raman spectra were obtained. Biopsies were then taken from the same sites and sent for histological evaluation. Based on the pathologist's reports, the lesions were classified into normal, mild dysplasia, moderate dysplasia, severe dysplasia, carcinoma *in situ* (CIS), or a specific tumor type such as squamous cell carcinoma (SCC). In addition to the normal from the pathology, Raman spectra were obtained from sites that appeared completely normal in the physician's opinion, but no biopsies were obtained. Contrary to the *in vitro* measurements [38], autofluorescence dominated the LF range, which made it difficult to discern the Raman peaks. In the high-frequency range, Raman peaks could be clearly seen from the raw spectra (Fig. 1.21a).

This was the first *in vivo* Raman spectra of lung tissue. Pure Raman spectra could be obtained after fluorescence removal for the whole range of measurement (Fig. 1.21b). The dominated Raman peaks were marked in Fig. 1.21b. The broad peaks near 1,658 cm^{-1} were due to a combination amide I (C=O) vibrations and water molecule bending motions. The intense peaks at 2,900 cm^{-1} were assigned to a combination of CH_2 antisymmetric (2,880 cm^{-1}) and CH_3 symmetric (2,935 cm^{-1}) stretching modes of phospholipids and proteins. The broad peaks near 3,300 cm^{-1} were most likely due to overlapping the symmetric and antisymmetric

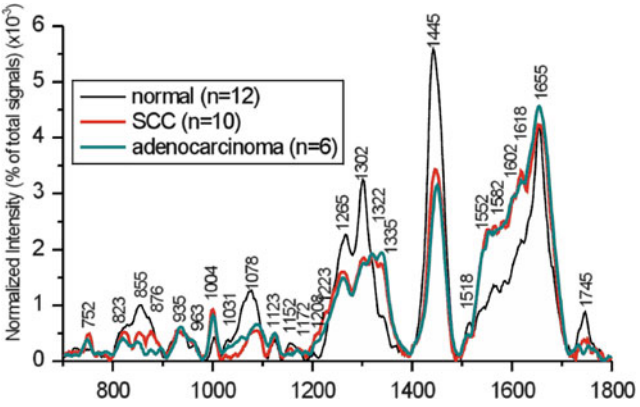

Fig. 1.20 The mean Raman spectra of normal bronchial tissue ($n = 12$) and malignant adenocarcinoma ($n = 6$) and squamous cell carcinoma (*SCC*, $n = 10$) bronchial tissue samples. Each spectrum was normalized to the area under the curve to correct the variations in absolute spectral intensity (Adapted from Huang et al. [38], with permission)

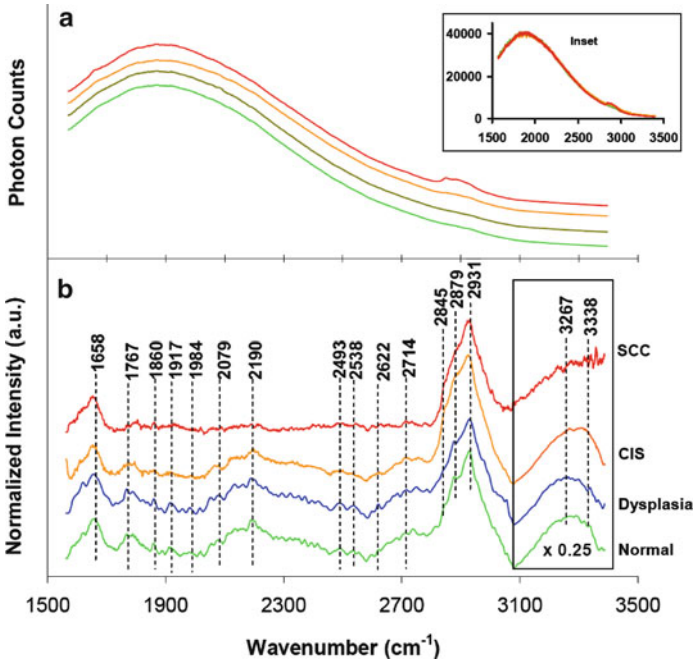

Fig. 1.21 *In vivo* NIR Raman spectra of human lung tissue with different pathologies taken with the HF grating (2-s integration). **a** (*main graph*): smoothed raw spectra. **a** (*inset*): unprocessed raw data. **b** extracted Raman spectra (spectral response calibrated and normalized). The data above $3{,}100\,\mathrm{cm}^{-1}$ have been scaled by 0.25. The spectra were shifted along y axis for clarity. Top to bottom order: *SCC*, *CIS*, moderate dysplasia, and normal tissue for both **a** and **b** (Adapted from Short et al. [39], with permission)

OH stretching motions of water. *In vivo* lung Raman spectra of different pathologies showed clear difference, particularly in the HF range. The malignant lesions (SCC and CIS) could be easily differentiated from the benign lesion (moderate dysplasia) and normal tissue. These findings indicated that there was a real possibility that *in vivo* lung tissue could be characterized at the molecular level using Raman spectroscopy. Currently, we are conducting a large-scale clinical study to test the utility of the real-time Raman spectroscopic system for *in vivo* lung cancer detection.

1.4.3 Colon Cancer Diagnosis

Colon cancer is the third most common form of cancer and the second leading cause of cancer-related deaths in the Western world. The golden standard for colon cancer diagnosis is white light endoscopy followed by invasive biopsy. However, the ability of white light endoscopy to visually detect dysplasia in precancerous conditions or reliably differentiate dysplastic from nondysplastic colon polyps is very limited. Optical spectroscopy techniques including diffuse reflectance, fluorescence, and Raman spectroscopy have been evaluated for diagnosis [63]. Shim et al. reported the measurement of colon cancer tissues *in vivo* and *ex vivo* using a fiber-based Raman probe [47, 64]. For the *ex vivo* study, a total of 33 polyps were analyzed from 8 patients. Fifty-four spectra were obtained from the 33 polyps including 20 hyperplastic and 34 adenomatous. For the *ex vivo* measurement, each spectrum was collected with an integration time of 30 s. For *in vivo* measurement, 19 spectra were collected from 9 polyps in 3 patients including 9 hyperplastic and 10 adenomatous. Each spectrum was collected with an integration time of 5 s. A PCA and LDA analysis found that adenomatous polyps could be identified with 91% sensitivity, 95% specificity, and 93% accuracy for *ex vivo* studies and 100% sensitivity, 89% specificity, and 95% accuracy for *in vivo* studies. Recently, Widjaja et al. studied the capability of support vector machines for classification of the near-infrared Raman spectra of *in vitro* colonic tissues [65]. A total of 105 colonic tissue specimens from 59 patients including 41 normal, 18 hyperplastic, and 46 adenocarcinomas were studied. A total of 817 spectra including 324 normal, 184 polyps, and 309 adenocarcinomatous were studied using the conventional support vector machine (SVM). An overall accuracy of over 99% was achieved. The Raman spectra of normal colonic tissue were also studied by FT-Raman spectroscopy [66], microconfocal Raman spectroscopy, and FTIR spectroscopy [67]. Typical Raman spectra of the normal, precancerous, and cancerous colonic tissue are shown in Fig. 1.22. The primary Raman peaks for normal, benign, and malignant tumors are around 875, 1,002, 1,090, 1,267, 1,320, 1,445, 1,605, 1,655, and 1,740 cm^{-1}. Significant difference between the tissue types including peak intensity, peak position, and spectral shapes could also be easily observed, indicating the changes of biochemical composition and structures of the tissue associated with the disease state.

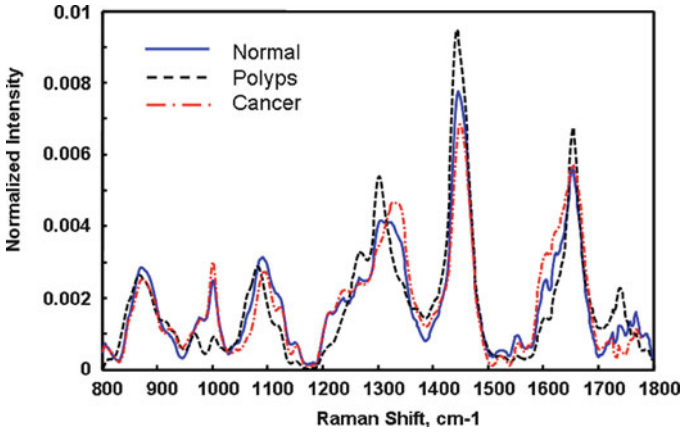

Fig. 1.22 Mean NIR Raman spectra from normal ($n = 324$), polyps ($n = 184$), and adenocarcinoma ($n = 309$) colonic tissues, respectively (Adapted from Widjaja et al. [65], with permission)

1.4.4 Oral Cancer Diagnosis

Raman spectroscopy has been used for diagnosis of oral mucosa diseases. The Raman spectra of *in vivo* oral mucosa were investigated by Schut et al. using a mouse model [68]. In their experiment, dysplasia was first induced into the mouse palate epithelium, and then the Raman spectra were assessed at various dysplastic stages. The spectra of the mouse oral mucosa were obtained from 10 to 100 s. They found a specificity of 93% and a sensitivity of 78% for detecting low-grade dysplasia and a specificity of 100% and a sensitivity of 100% for detecting high-grade dysplasia/carcinoma *in situ*. Malini et al. evaluated the ability of Raman spectroscopy to differentiate normal, inflammatory, premalignant, and malignant oral lesions of biopsied tissue [69]. A set of the Raman spectra was shown in Fig. 1.23. Each spectrum was obtained with an integration time of 600 s. Data analysis of these spectra showed that the ability to distinguish among pathologic conditions was poor. In another independent study of *ex vivo* human mucosa samples by de Veld et al. [70], similar conclusion was obtained. Very recently, Guze et al. [71] studied the Raman spectra of human normal oral mucosa among anatomic oral sites and among subjects of different races and gender. High-quality Raman spectra at the high-frequency range could be obtained within 1 second using an *in vivo* fiber-based Raman probe similar to the endoscopic lung Raman probe (Fig. 1.13). The averaged Raman spectra of oral cavity of different anatomic sites are shown in Fig. 1.24. They found that *in vivo* Raman spectra taken from the oral cavity did not show strong differences between Asian and Caucasian subgroups, but the spectra for different oral sites within the same ethnic group were different and separable. Their results demonstrated that the lack of sensitivity in the previous *ex vivo* study was due to the variability in the spectra produced by the different tissue types of the mouth and oropharynx. Further study is warranted for the potential of Raman spectroscopy for *in vivo* oral cancer diagnosis, including the low-frequency fingerprint region.

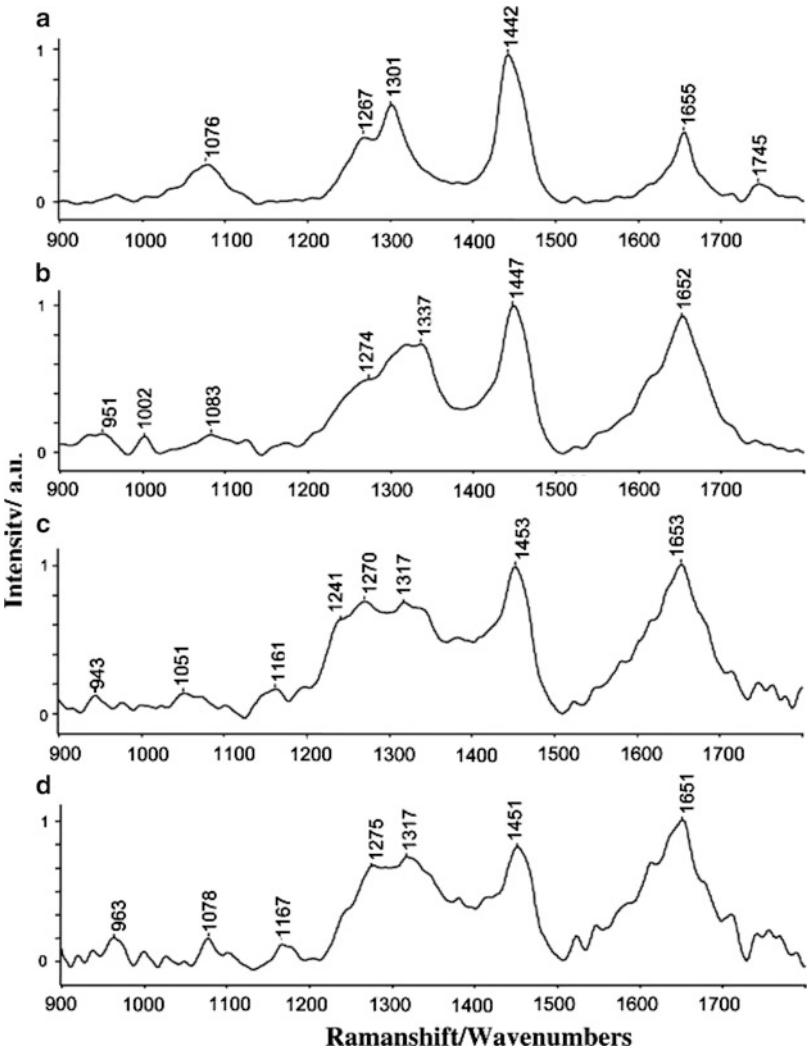

Fig. 1.23 Mean Raman spectra of biopsied oral tissues: (**a**) normal, (**b**) malignant, (**c**) inflammatory, and (**d**) premalignant (Adapted from Malini et al. [69], with permission)

1.4.5 Gastric Cancer Diagnosis

Gastric cancer is the fourth most common cancer and the second most common cause of death from cancer worldwide. Teh et al. [72–74] studied the normal and precancerous gastric tissues using near-infrared Raman spectroscopy (similar to the skin Raman probe in Fig. 1.10). The Raman spectra of normal and dysplasia gastric tissue are shown in Fig. 1.25. The main Raman peaks are 875, 1,004, 1,100,

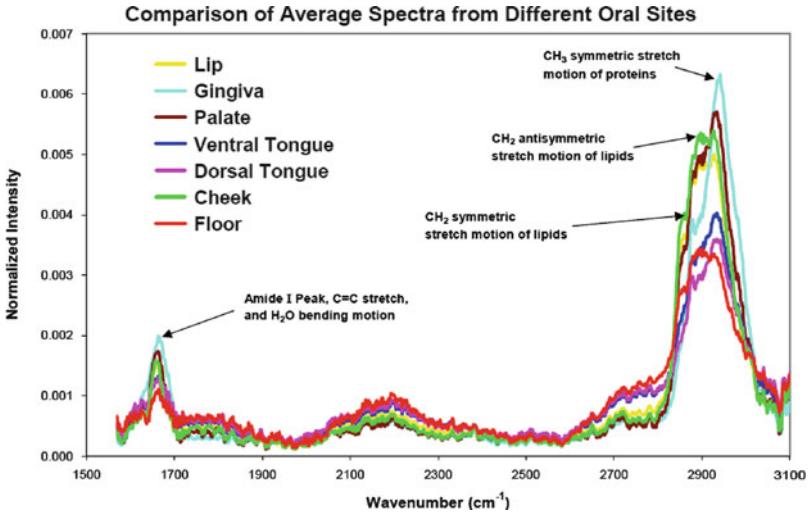

Fig. 1.24 Average Raman spectra of *in vivo* oral mucosa of different anatomic oral sites. All spectra were measured within 1 s integration time (Adapted from Guze et al. [71], with permission)

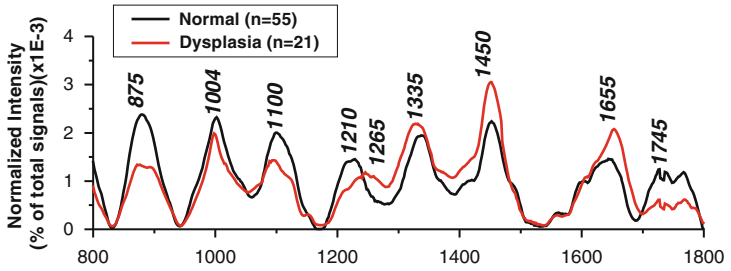

Fig. 1.25 Averaged Raman spectra of *ex vivo* normal and cancerous gastric tissue (Adapted from Teh et al. [73], with permission)

1,210, 1,265, 1,335, 1,450, 1,655, and 1,745 cm^{-1}. The authors found that the peak ratios between dysplasia and normal could be used for diagnosis. Analysis on the ratio of 875–1,450 cm^{-1} and 1,208–1,655 cm^{-1} provided a sensitivity and specificity over 90% based on leave-one-out cross validation. Diagnosis based on the intensity and spectral shape could reach 95.2% of sensitivity and 90.8% of specificity based on leave-one-out cross validation of PCA-LDA analysis. Hu et al. [75] studied the human gastric mucosa tissue using a commercial confocal Raman microspectroscopy with an argon laser at 514.5 nm. They studied 13 normal and 19 malignant tissue samples from 32 patients. Each spectrum was acquired with an integration time of 30–120 s. The fluorescence background was removed based on wavelet decomposition. The authors found that the most intense Raman peak for normal gastric mucosa is located at 1,452 cm^{-1} or 1,587 cm^{-1} and for malignant

gastric mucosa at 1,452, 1,522, or 1,660 cm^{-1}. The intensity ratio of 1,156 cm^{-1} to the maximum peak and 1,587–1,156 cm^{-1} could be used to differentiate malignant from normal tissue with an accuracy of 100%. Kalyan Kumar et al. [76] studied normal and malignant gastric tissues using a commercial Raman microspectroscopy at 785-nm excitation. A total of 111 spectra (37 normal and 74 malignant) from 10 normal and 17 malignant stomach mucosae were obtained. PCA and LDA analysis showed a 93% of sensitivity and 84% of specificity. Kawabata et al. [77] studied the gastric cancer tissues with a 1,064-nm excitation. They found that based on the 1,644 cm^{-1} peak alone, an accuracy of 70% could be realized.

In vivo gastric cancer diagnosis using endoscopic Raman spectroscopy has been implemented by Huang et al. [78, 79] for the first time. The probe is shown in Fig. 1.26. It is integrated with trimodal wide-field imaging for guiding the *in vivo* gastric tissue Raman measurements. Similar to the lung Raman probe of [39, 40], the endoscopic probe for gastric cancer diagnosis consists of 33 ultralow-OH fibers (NA = 0.22, 200-μm core diameter). The center fiber, which is coated with a narrow 785 band-pass filter, is for excitation laser delivery, and the surrounding 32 fibers, which are coated with 785-nm long-pass filter, are used for signal collection. Both the excitation and signal collection are filtered using a second stage in-line filter module. High S/N Raman spectra could be obtained within 1 s. Preliminary *in vivo* Raman results showed that the ratio at 875–1, 450 cm^{-1} could be used to differentiate dysplasia from normal gastric tissue with a sensitivity and specificity of 100% [79]. Very recently, the authors studied gastric dysplasia using narrow-band image-guided Raman spectroscopy [80]. It demonstrated the potential of the endoscopic Raman spectroscopy for *in vivo* gastric malignancy diagnosis.

1.4.6 Breast Cancer Diagnosis

Breast cancer is one of the most common cancers for women. It is estimated that there are about 216,000 new cases each year and 40,000 died of the disease. The common method is clinical examination or mammography followed by an invasive biopsy. Optical spectroscopic techniques such as fluorescence, reflectance, and Raman spectroscopy have already been used for breast cancer diagnosis [81]. Trends correlating with diseases have been identified from fluorescence spectra of *ex vivo* breast tissue samples [82,83]. Because there are only a couple of endogenous fluorophores that can be detectable and the spectra shape is relatively broad, the sensitivity and specificity are relatively low. Raman spectroscopy is found to be promising in breast cancer diagnosis. Early studies were based on small sample sets and *ex vivo* measurements [84–89]. A typical Raman spectrum of normal human breast tissue is shown in Fig. 1.27 [85]. The Raman spectrum is heavily dependent on the excitation wavelength. Spectra of formalin-fixed human tissue revealed Raman peaks for lipids and carotenoids [90]. The lipid features were better defined under 782- and 830-nm laser excitation, while the carotenoid features were strongest under 488- and 515-nm excitation due to resonance enhancement.

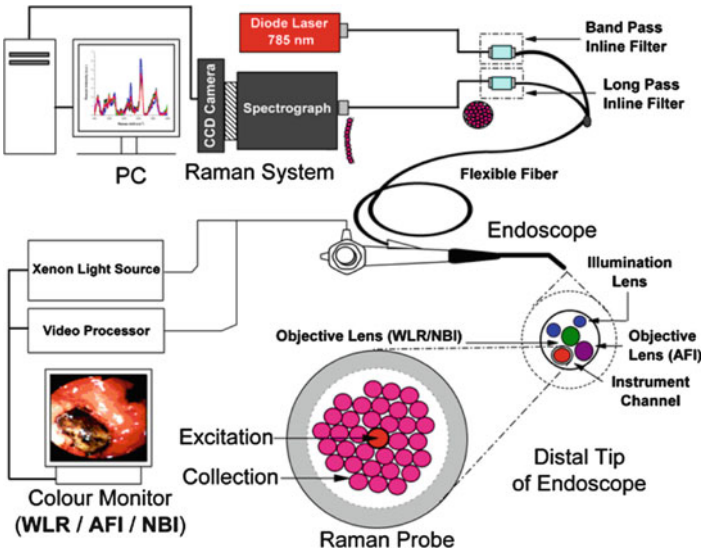

Fig. 1.26 Schematic diagram of the integrated endoscopic Raman spectroscopy and trimodal endoscopic imaging system for *in vivo* gastric cancer diagnosis (Adapted from Huang et al. [78], with permission)

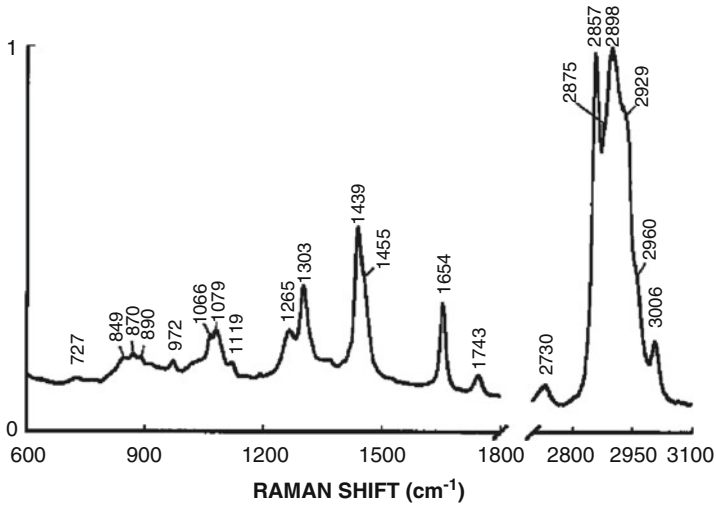

Fig. 1.27 Raman spectrum (784 nm) of normal breast tissue. Laser power was 40 mW at the sample, and integration time was 300 s (Adapted from Frank et al. [85], with permission)

Normal and diseased breast tissues could be differentiated from the contribution of carotenoids and lipids. A small contribution from a heme-type signal was detected in some samples of clinically abnormal yet histopathologically benign breast tissue, while a much stronger heme-type signal was detected in most of the breast cancers. Raman spectra of diseased breast tissue (benign and malignant) also showed diminished to absent contributions from lipids and reduced contributions from carotenoids. Haka et al. [91] did a thorough *ex vivo* study, in which 130 spectra from 58 patients were obtained. Model fitting was performed by using a linear combination of the contribution of each base spectrum with a nonnegativity constraint. Statistical analysis showed a sensitivity of 94% and specificity of 96%. Very recently, the authors also designed a ball-lens-based fiber probe for *in vivo* breast cancer diagnosis [92]. Statistical analysis showed 100% sensitivity and 100% specificity. However, this result was based on very limited samples (21 normal, 8 fibrocystic, and 1 cancer from 9 patients).

1.4.7 Cervical Cancer Diagnosis

Cervical cancer is the second most common malignancy among women worldwide. In recent years, diffuse reflectance, fluorescence, and Raman spectroscopy have been used for cervical cancer and precancer screening and diagnosis [3, 4]. Mahadevan-Jansen et al. first studied the Raman properties of *ex vivo* human cervical tissue using NIR Raman spectroscopy [93]. Thirty-six biopsies were obtained from 18 patients. The authors found that precancer tissues could be well differentiated from normal tissue with an average sensitivity of 88% and specificity of 92% and high-grade from low-grade cervical cancers with a sensitivity and specificity of 100%. Utzinger et al. studied the NIR Raman spectroscopy of cervical cancer *in vivo* using an optical fiber-based Raman probe [44, 94]. Twenty-four *in vivo* spectra were obtained from 13 patients. Spectra measured *in vivo* resemble those measured *in vitro*. The main Raman peaks for cervical tissue located in the vicinity of 1,070, 1,180, 1,195, 1,210, 1,245, 1,330, 1,400, 1,454, 1,505, 1,555, 1,656, and 1,760 cm^{-1}. The ratio of intensities at 1,454–1,656 cm^{-1} and 1,330–1,454 cm^{-1} could be used to differentiate squamous dysplasia from other tissue types. Recently, Mo et al. designed a ball-lens-based optical fiber probe for *in vivo* cervical cancer diagnosis [45]. They measured the Raman spectra of cervical tissue *in vivo* in the high wavenumber region. A total of 92 *in vivo* Raman spectra (46 normal, 46 dysplasia) were obtained from 46 patients with Pap smear abnormalities of the cervix. Significant difference was observed in the Raman intensities of the prominent Raman bands at 2,850 and 2,885 cm^{-1} (CH_2 stretching of lipids), 2,940 cm^{-1} (CH_3 stretching of proteins), and the broad Raman band of water (peaking at 3,400 cm^{-1} in the 3,100–3, 700−cm^{-1} range) between normal and dysplasia cervical tissue. The statistical analysis based on PCA and LDA together with the leave-one-out cross-validation method showed a sensitivity of 93.5% and specificity of 97.8% for dysplasia tissue identification.

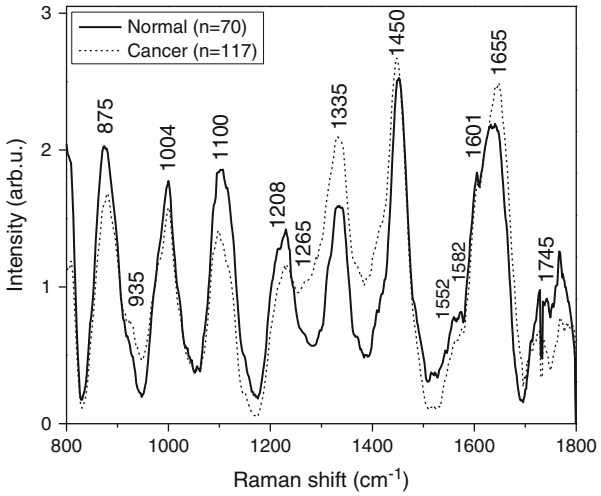

Fig. 1.28 Mean normalized Raman spectra of normal and cancerous laryngeal tissue (Adapted from Teh et al. [96] by permission of the Royal Society of Chemistry)

1.4.8 Other Applications

Raman spectroscopy has also been used for other disease diagnosis. Lau et al. studied the normal and cancerous laryngeal tissue *in vitro* using NIR Raman spectroscopy [95]. Forty-seven laryngeal specimens were measured (18 normal, 13 carcinoma, and 16 squamous papilloma) with an integration time of 1–30 s for each spectrum. The normalized Raman spectra of normal and cancerous laryngeal tissue are shown in Fig. 1.28. Based on the peak analysis, over 86% of sensitivity and specificity can be obtained to differentiate normal, carcinoma, and papilloma. In a recent study, the authors found that classification with random forest algorithm can yield 88% of sensitivity and 91.4% of specificity for laryngeal malignancy identification [96]. The authors also studied the Raman properties of normal and cancerous nasopharyngeal tissue *in vitro* [97]. Although the sample size is small ($n = 6$), consistent spectral difference was obtained in the three bands 1,290–1,320 cm^{-1}, 1,420–1,470 cm^{-1}, and 1,530–1,580 cm^{-1}. These *in vitro* studies support the potential for future *in vivo* applications in diagnosis of laryngeal and nasopharynx cancers.

Berger et al. used Raman spectroscopy to measure the concentration of constituents in serum and whole blood *in vitro* [98, 99]. They proposed a PLS model to predict the concentration of constituents from the Raman spectra of blood. Enejder et al. measured glucose noninvasively by measuring cutaneous Raman spectra *in vivo* [100]. Motz et al. designed a real-time Raman system based on fiber optic probe (Fig. 1.17e) and had successfully measured the Raman spectra of human arteries and breast tissue *in vivo* [28, 101]. Buschman et al. studied coronary

atherosclerosis using Raman spectroscopy [102, 103]. Raman spectroscopy has also been used for bone diagnosis [104], brain tumor diagnosis [105], prostate cancer diagnosis, and bladder malignancy diagnosis [106–108].

1.5 Summary

In summary, we discussed the basic components and their advancement for the standard spectroscopy system and the design of *in vivo* Raman spectroscopy systems and their biomedical applications. We have focused on the *in vivo* Raman system design. Other modalities of Raman spectroscopy such as coherent anti-Stokes Raman spectroscopy (CARS) [109], surface-enhanced Raman spectroscopy [110], and time-resolved Raman spectroscopy [111] are not discussed as those are mostly *ex vivo* diagnosis methods.

The advancement of technology provides researchers the opportunity to push the applications of biomedical spectroscopy into new horizons. Because the signal is relatively strong, diffuse reflectance and fluorescence spectroscopy or imaging will continue to find their way as diagnostic or visual aid tools in biomedicine. As an emerging *in vivo* technique, we expect *in vivo* Raman spectroscopy will become a powerful clinical tool in the years to come.

Appendix

Table 1.4 Spectroscopic component suppliers

Company	Components
Acton Research	Spectrograph
	Monochromameters
Newport Corporation	Light source
	Solid-state lasers
	Femtosecond lasers
Kaiser Optical System	Holographic gratings/filters
	Spectrograph
	Integrated spectrometers
Philip Lumileds Lightening Company	High-power LED
Brimrose Corporation of America	AOTF filters
Cambridge Research and Instrumentation	LCTF filters
Omega Optical	Filters
Semrock	Filters
Ocean Optics	Spectrometers
	Light source
	Fibers
Fiberguide Industries	Customized fiber bundles
Polymicro	High-OH, low-OH fibers
Princeton Instrument	Spectrograph
	Spectrometers
	CCD detectors
Andor Technology	Spectrograph
	Spectrometers
	CCD detectors
Hamamatsu Photonics K.K.	PMT, APD
B&W Tek	Diode lasers
Laser Components Group	Polarizers

Acknowledgements Our Raman spectroscopy work was supported by the Canadian Cancer Society, the Canadian Dermatology Foundation, the Canadian Institutes of Health Research, the BC Hydro Employees' Community Service Fund, and the VGH and UBC Foundation. The authors wish to thank Dr. Harvey Lui and Dr. David I. McLean for helpful discussions. The authors acknowledge Dr. Zhiwei Huang, Dr. Michael Short, and Ms. Tracy Wang for providing some of the figures.

References

1. N. Kollias, G. Zonios, G.N. Stamatas, Fluorescence spectroscopy of skin. Vibrational Spectrosc. **28**, 17–23 (2001)
2. H. Zeng, C. MacAulay, D.I. McLean, B. Palcic, Spectroscopic and microscopic characteristics of human skin autofluorescence emission. Photochem. Phobiol. **61**, 639–645 (1995)

3. R. Richards-Kortum, E. Sevick-Muraca, Quantitative optical spectroscopy for tissue diagnosis. Annu. Rev. Phys. Chem. **47**, 555–606 (1996)
4. A. Mahadevan-Jansen, R. Richards-Kortum, Raman spectroscopy for the detection of cancers and precancers. J. Biomed. Opt. **1**, 31–70 (1996)
5. H. Zeng, H. Lui, D.I. McLean, C. MacAulay, B. Palcic, Optical spectroscopy studies of diseased skin-preliminary results. Proc. SPIE **2628**, 281–285 (1995)
6. H. Zeng, H. Lui, D.I. McLean, C. MacAulay, B. Palcic, Update on fluorescence spectroscopy studies of diseased skin. Proc. SPIE **2671**, 196–198 (1996)
7. H. Zeng, C. MacAulay, D.I. McLean, B. Palcic, Miniature spectrometer and multispectral imager as a potential diagnostic aid in dermatology. Proc. SPIE **2387**, 57–61 (1995)
8. H. Zeng, C. MacAulay, D.I. McLean, B. Palcic, Reconstruction of in vivo skin autofluorescence spectrum from microscopic properties by Monte Carlo simulation. J. Photochem. Photobiol. B **38**, 234–240 (1997)
9. H. Zeng, D.I. McLean, C. MacAulay, H. Lui, Autofluorescence properties of skin and applications in dermatology. Proc. SPIE **4224**, 366–373 (2000)
10. H. Zeng, D.I. McLean, C. MacAulay, B. Palcic, H. Lui, Autofluorescence of basal cell carcinoma. Proc. SPIE **3245**, 5–7 (1998)
11. Z. Huang, H. Zeng, I. Hamzavi, D.I. McLean, H. Lui, Rapid near-infrared Raman spectroscopy system for real-time in vivo skin measurements. Opt. Lett. **26**, 1782–1784 (2001)
12. J. Zhao, H. Lui, D.I. McLean, H. Zeng, Integrated real-time Raman system for clinical in vivo skin analysis. Skin Res. Technol. **14**, 484–492 (2008)
13. T. Vo-Dinh, Basic instrumentation in photonics, in *Biomedical Photonics Handbook*, ed. by T. Vo-Dinh (CRC Press, New York, 2003)
14. N. MacKinnon, U. Stange, P. Lane, C. MacAulay, M. Quatrevalet, Spectrally programmable light engine for in vitro and in vivo molecular imaging and spectroscopy. Appl. Opt. **44**, 2033–2040 (2005)
15. J.C. Knight, Photonic crystal fibres. Nature **424**, 847–851 (2003)
16. K.P. Hansen, R.E. Kristiansen, Supercontinuum generation in photonic crystal fibers. http://www.thorlabs.com/ThorCat/10700/10736-A02.pdf.AccessedJune2010
17. M. Seefeldt, A. Heuer, R. Menzel, Compact white-light source with an average output power of 2.4 W and 900 nm spectral bandwidth. Opt. Commun. **216**, 199–202 (2003)
18. J.K. Ranka, R.S. Windeler, A.J. Stentz, Visible continuum generation in air-silica microstructure optical fibers with anomalous dispersion at 800 nm. Opt. Lett. **25**, 25–27 (2000)
19. H.R. Morris, C.C. Hoyt, P.J. Treado, Imaging spectrometers for fluorescence and Raman microscopy: acousto-optic and liquid crystal tunable filters. Appl. Spectrosc. **48**, 857–866 (1994)
20. C.D. Tran, R.J. Furlan, Spectrofluorometer based on acousto-optic tunable filters for rapid scanning and multicomponent sample analyses. Anal. Chem. **65**, 1675–1681 (1993)
21. E.N. Lewis, P.J. Treado, I.W. Levin, A miniaturized non-moving-parts Raman spectrometer. Appl. Spectrosc. **47**, 539–543 (193)
22. N. Uchida, Optical properties of single-crystal paratellurite (TeO2). Phys. Rev. B **4**, 3736 (1971)
23. ST-133 controller operations manual, Princeton Scientific Instruments, Monmouth Junction, N.J. 2004
24. HoloSpec Imaging Spectrograph Operations Manual, Kaiser Optical Systems Inc., Ann Arbor, MI, USA, 2002
25. N.M. Marin, N. MacKinnon, C. MacAulay, S.K. Chang, E.N. Atkinson, D. Cox, D. Serachitopol, B. Pikkula, M. Follen, R. Richards-Kortum, Calibration standard for multicenter clinical trials of fluorescence spectroscopy for in vivo diagnosis. J. Biomed. Opt. **11**, 014010 (2006)
26. J. Zhao, H. Lui, D.I. McLean, H. Zeng, Towards instrument independent quantitative measurement of fluorescence intensity in fiber optic spectrometer system. Appl. Opt. **46**, 7132–7140 (2007)

27. U. Utzinger, R. Richards-Kortum, Fiber optic probes for biomedical optical spectroscopy. J. Biomed. Opt. **8**, 121–147 (2003)
28. J.T. Motz, S.J. Gandhi, O.R. Scepanovic, A.S. Haka, J.R. Kramer, R.R. Dasari, M.S. Feld, Real-time Raman system for in vivo disease diagnosis. J. Biomed. Opt. **10**, 031113 (2005)
29. T.C.B. Schut, R. Wolthuis, P.J. Caspers, G.J. Puppels, Real-time tissue characterization on the basis of in vivo Raman spectra. J. Raman Spectrosc. **33**, 580–585 (2002)
30. L.F. Santos, R. Wolthuis, S. Koljenovic, R.M. Almeida, F.J. Puppels, Fiberoptic probes for in vivo Raman spectroscopy in the high-wavenumber region. Anal. Chem. **77**, 6747–6752 (2005)
31. American National Standard for the Safe Use of Lasers, ANSI Standard Z136.1–2007, American National Standards Institute, Washington, DC 2007
32. H. Owen, D.E. Battey, M.J. Pelletier, J.B. Slater, New spectroscopic instrument based on volume holographic optical elements. Proc. SPIE **2406**, 260–267 (1995)
33. C.A. Lieber, A. Mahadevan-Jansen, Automated method for subtraction of fluorescence from biological Raman spectra. Appl. Spectrosc. **57**, 1363–1367 (2003)
34. J. Zhao, H. Lui, D.I. McLean, H. Zeng, Automated Autofluorescence Background Subtraction Algorithm for Biomedical Raman Spectroscopy. Appl. Spectrosc. **61**, 1225–1232 (2007)
35. H. Zeng, M. Petek, M.T. Zorman, A. McWilliams, B. Palcic, S. Lam, Integrated endoscopy system for simultaneous imaging and spectroscopy for early lung cancer detection. Opt. Lett. **29**, 587–589 (2004)
36. H. Zeng, A. McWilliams, S. Lam, Optical spectroscopy and imaging for early lung cancer detection: a review. Photodiagn. Photodyn. Ther. **1**, 111–122 (2004)
37. S. Lam, C. MacAulay, J.C. Leriche, N. Ikeda, B. Palcic, Early localization of bronchogenic carcinoma. Diagnostic Therapeut. Endosc. **1**, 75–78 (1994)
38. Z. Huang, A. McWilliams, H. Lui, D.I. McLean, S. Lam, H. Zeng, Near-infrared Raman spectroscopy for optical diagnosis of lung cancer. Int. J. Cancer **107**, 1047–1052 (2003)
39. M. Short, S. Lam, A. McWilliams, J. Zhao, H. Lui, H. Zeng, Development and preliminary results of an endoscopic Raman probe for potential in-vivo diagnosis of lung cancers. Opt. Lett. **33**, 711–713 (2008)
40. M. Short, S. Lam, A. McWilliams, J. Zhao, H. Lui, H. Zeng, Development and preliminary results of an in vivo Raman probe for early lung cancer detection. Proc. SPIE **6853**, 68530J (2008)
41. H. Wang, N. Huang, J. Zhao, H. Lui, M. Korbelik, H. Zeng, Depth-resolved in vivo micro-Raman spectroscopy of a murine skin tumor model reveals cancer specific spectral biomarkers. J. Raman Spectrosc. **42**. 160–166 (2010)
42. M.L. Myrick, S.M. Angels, Elimination of background in fiber-optic Raman measurements. Appl. Spectrosc. **44**, 565–570 (1990)
43. K. Tanaka, M.T.T. Pacheco, J.F. Brennan III, I. Itzkan, A.J. Berger, R.R. Dasari, M.S. Feld, Compound parabolic concentrator probe for efficient light collection in spectroscopy of biological tissue. Appl. Opt. **35**, 758–763 (1996)
44. A. Mahadevan-Jansen, M.F. Mitchell, N. Ramanujam, U. Utzinger, R. Richards-Kortum, Development of a fiber optic probe to measure NIR Raman spectra of cervical tissue in vivo. Photochem. Phobiol. **68**, 427–431 (1998)
45. J. Mo, W. Zheng, J.J.H. Low, J. Ng, A. Ilancheran, Z. Huang, High wavenumber Raman spectroscopy for in vivo detection of cervical dysplasia. Anal. Chem. **81**, 8908–8915 (2009)
46. J.T. Motz, M. Hunter, L.H. Galindo, J.A. Gardecki, J.R. Kramer, R.R. Dasari, M.S. Feld, Optical fiber probe for biomedical Raman spectroscopy. Appl. Opt. **43**, 542–554 (2005)
47. M.G. Shim, L.M.W. Song, N.E. Marcon, B. Wilson, In vivo near-infrared Raman spectroscopy: demonstration of feasibility during clinical gastrointestinal endoscopy. Photochem. Phobiol. **72**, 146–150 (2000)
48. M. Gniadecka, O.F. Nielsen, D.H. Christensen, H.C. Wulf, Structure of water, proteins, and lipids in intact human skin, hair, and nail. J. Invest. Dermatol. **110**, 393–398 (1998)
49. M. Gniadecka, O.F. Nielsen, H.C. Wulf, Water content and structure in malignant and benign skin tumours. J. Mol. Struct. **661–662**, 405–410 (2003)

50. M. Gniadecka, P.A. Philipsen, S. Sigurdsson, S. Wessel, O.F. Nielsen, D.H. Christensen, J. Hercogova, K. Rossen, H.K. Thomsen, R. Gniadecki, L.K. Hansen, H.C. Wulf, Melanoma diagnosis by Raman spectroscopy and neural networks: structure alterations in proteins and lipids in intact cancer tissue. J. Invest. Dermatol. **122**, 443–449 (2004)
51. M. Gniadecka, H.C. Wulf, N.N. Mortensen, O.F. Nielsen, D.H. Christensen, Diagnosis of basal cell carcinoma by Raman spectroscopy. J. Raman Spectrosc. **28**, 125–129 (1997)
52. M. Short, H. Lui, D.I. McLean, H. Zeng, A, Alajlan, X.K. Chen, Changes in nuclei and peritumoral collagen within nodular basal cell carcinomas via confocal micro-Raman spectroscopy. J. Biomed. Opt. **11**, 034004 (2006)
53. H.G.M. EdwardsH, A.C. Williams, B.W. Barry, Potential applications of FT-Raman spectroscopy for dermatological diagnostics. J. Mol. Struct. **347**, 379–388 (1995)
54. B.W. Barry, H.G.M. Edwards, A.C. Williams, Fourier Transform Raman and infrared vibrational study of human skin: assignment of spectral bands. J. Raman Spectrosc. **23**, 641–645 (1992)
55. H. Zeng, J. Zhao, M. Short, D.I. McLean, S. Lam, A. McWilliams, H. Lui, Raman spectroscopy for in vivo tissue analysis and diagnosis, from instrument development to clinical applications. J. Innov. Opt. Health Sci. **1**, 95–106 (2008)
56. P.J. Caspers, G.W. Lucassen, E.A. Carter, H.A. Bruining, G.J. Puppels, In vivo confocal Raman Microspectroscopy of the skin: noninvasive determination of molecular concentration profiles. J. Invest. Dermatol. **116**, 434–442 (2001)
57. P.J. Caspers, G.W. Lucassen, G.J. Puppels, Combined in vivo confocal Raman spectroscopy and confocal microscopy of human skin. Biophys. J. **85**, 572–580 (2003)
58. P.J. Caspers, G.W. Lucassen, R. Wolthuis, H.A. Bruining, G.J. Puppels, In vitro and in vivo Raman spectroscopy of human skin. Biospectroscopy **4**, S31–S39 (1998)
59. C.A. Lieber, S.K. Majumder, D.L. Ellis, D. Billheimer, A. Mahadevan-Jansen, In vivo nonmelanoma skin cancer diagnosis using Raman microspectroscopy. Lasers Surg. Med. **40**, 461–467 (2008)
60. C.A. Lieber, S.K. Majumder, D. Billheimer, D.L. Ellis, A. Mahadevan-Jansen, Raman microspectroscopy for skin cancer detection in vitro. J. Biomed. Opt. **13**, 024013 (2008)
61. J. Zhao, H. Lui, D.I. McLean, H. Zeng, Real-time Raman spectroscopy for non-invasive skin cancer detection – preliminary results. EMBS **2008**, 3107–3109 (2008)
62. Z. Huang, H. Lui, X.K. Chen, A. Alajlan, D.I. McLean, H. Zeng, Raman spectroscopy of in vivo cutaneous melanin. J. Biomed. Opt. **9**, 1198–1205 (2004)
63. R.S. DaCosta, B.C. Wilson, N.E. Marcon, Light-induced fluorescence endoscopy of the gastrointestinal tract. Gastrointest. Endos. Clin. N. Am. **10**, 37–69 (2000)
64. A. Molckovsky, L.M.W. Song, M.G. Shim, N.E. Marcon, B. Wilson, Diagnostic potential of near-infrared Raman spectroscopy in the colon: differentiating adenomatous from hyperplastic polyps. Gastrointest. Endosc. **57**, 396–402 (2003)
65. E. Widjaja, W. Zheng, Z. Huang, Classification of colonic tissue using near-infrared Raman spectroscopy and support vector machines. Int. J. Oncol. **32**, 653–662 (2008)
66. P.O. Andrade, R.A. Bitar, K. Yassoyama, H. Martinho, A.M.E. Santo, P.M. Bruno, A.A. Martin, Study of normal colorectal tissue by FT-Raman spectroscopy. Anal. Bioanal. Chem. **387**, 1643–1648 (2007)
67. C. Krafft, D. Codrich, G. Pelizzo, V. Sergo, Raman and FTIR microscopic imaging of colon tissue: a comparative study. J. Biophoton. **1**, 154–169 (2008)
68. T.C.B. Schut, M.J.H. Witjes, H.J.C.M. Sterenborg, O.C. Speelman, J.L.N. Roodenburg, E.T. Marple, H.A. Bruining, F.J. Puppels, In vivo detection of dysplastic tissue by Raman spectroscopy. Anal. Chem. **72**, 6010–6018 (2000)
69. R. Malini, K. Venkatakrishna, J. Kurien, K.M. Pai, L. Rao, V.B. Karcha, C.M. Krishna, Discrimination of normal, inflammatory, premalignant, and malignant oral tissue: a Raman spectroscopy study. Biopolymers **81**, 179–193 (2006)
70. D.C.G. de Veld, T.C.B. Schut, M. Skurichina, M.J.H. Witjes, J.E. Van der Wal, J.L.N. Roodenburg, H.J.C. M. Sterenborg, Autofluorescence and Raman microspectroscopy of tissue sections of oral lesions. Lasers Med. Sci. **19**, 203–209 (2005)

71. K. Guze, M. Short, S. Sonis, N. Karimbux, J. Chan, H. Zeng, Parameters defining the potential applicability of Raman spectroscopy as a diagnostic tool for oral disease. J. Biomed. Opt. **14**, 014016 (2009)
72. S.K. Teh, W. Zheng, K.Y. Ho, M. Teh, K.G. Yeoh, Z. Huang, Diagnosis of gastric cancer using near-infrared Raman spectroscopy and classification and regression tree techniques. J. Biomed. Opt. **13**, 034013 (2008)
73. S.K. Teh, W. Zheng, K.Y. Ho, M. Teh, K.G. Yeoh, Z. Huang, Diagnostic potential of near infrared Raman spectroscopy in the stomach: differentiating dysplasia from normal tissue. Br. J. Cancer **98**, 457–465 (2008)
74. S.K. Teh, W. Zheng, K.Y. Ho, M. Teh, K.G. Yeoh, Z. Huang, Near-infrared Raman spectroscopy for gastric precancer diagnosis. J. Raman Spectrosc. **40**, 908–914 (2008)
75. Y. Hu, A. Shen, T. Jiang, Y. Ai, J. Hu, Classification of normal and malignant human gastric mucosa tissue with confocal Raman microspectroscopy and wavelet analysis. Spectrochim. Acta Part A: Mol. Biomol. Spectrosc. **69**, 378–382 (2008)
76. K. Kalyan, A. Anand, M.V.P. Chowdary, J. Keerthi, C.M. Krishna, S. Mathew, Discrimination of normal and malignant stomach mucosal tissues by Raman spectroscopy: a pilot study. Vibrational Spectrosc. **44**, 382–387 (2007)
77. T. Kawabata, T. Mizuno, S. Okazaki, M. Hiramatsu, T. Setoguchi, H. Kikuchi, M. Yamamoto, Y. Hiramatsu, K. Kondo, M. NBaba, M. Ohta, K. Kamiya, T. Tanaka, S. Suzuki, H. Konno, Optical diagnosis of gastric cancer using near-infrared multichannel Raman spectroscopy with a 1064-um excitation wavelength. J. Gastroenterol. **43**, 283–290 (2008)
78. Z. Huang, S.K. Teh, W. Zheng, J. Mo, K. Lin, X. Shao, K.Y. Ho, M. Teh, K.G. Yeoh, Integrated Raman spectroscopy and trimodal wide-field imaging techniques for real-time in vivo tissue Raman measurements at endoscopy. Opt. Lett. **34**, 758–760 (2009)
79. M.S. Bergholt, W. Zheng, K. Lin, K.Y. Ho, M. Teh, K.G. Yeoh, Z. Huang, In vivo Raman spectroscopy integrated with multimodal endoscopic imaging for early diagnosis of gastric dysplasia. Proc. of SPIE **7560**, 756003 (2010)
80. Z. Huang, M.S. Bergholt, W. Zheng, K. Lin, K.Y. Ho, M. The, K.G. Yeoh, In vivo early diagnosis of gastric dysplasia using narrow-band image-guide Raman endoscopy. J. Biomed. Opt. **15**, 037017 (2010)
81. S.K. Majumder, M.D. Keller, F.I. Boulos, M.C. Kelley, A. Mahadevan-Jansen, Comparison of autofluorescence, diffuse reflectance, and Raman spectroscopy for breast tissue discrimination. J. Biomed. Opt. **13**, 054009 (2008)
82. Y. Yang, A. Katz, E.J. Celmer, M. Zurawska-Szczepaniak, R.R. Alfano, Fundamental differences of excitation spectrum between malignant and benign breast tissues. Photochem. Phobiol. **66**, 518–522 (1997)
83. S.K. Majumder, P.K. Gupta, B. Jain, A. Uppal, UV excited autofluorescence spectroscopy of human breast tissues for discriminating cancerous tissue from benign tumor and normal tissue. Lasers Life Sci. **8**, 249–264 (1998)
84. R.R. Alfano, C.H. Liu, W.L. Sha, D. Zhu, L. Akins, J. Cleary, R. Prudente, E. Cellmer, Human breast tissues studied by IR Fourier transform Raman spectroscopy. Lasers Life Sci. **4**, 23–28 (1991)
85. C.J. Frank, D.C. Redd, T.S. Gansler, R.L. McCreery, Characterization of human breast specimens with near-IR Raman spectroscopy. Anal. Chem. **66**, 319–326 (1994)
86. C.J. Frank, R.L. McCreery, D.C. Redd, Raman spectroscopy of normal and diseased human breast tissues. Anal. Chem. **67**, 777–783 (1995)
87. C. Yu, E. Gestl, K. Eckert, D. Allara, J. Irudayaraj, Characterization of human breast epithelial cells by confocal Raman microspectroscopy. Cancer Detect. Prevent. **30**, 515–522 (2006)
88. R.A. Bitar, H. de Silva Martinho, C.J. Tierra-Criollo, L.N.Z. Ramalho, M.M. Netto, A.A. Martin, Biochemical analysis of human breast tissues using Fourier-transform Raman spectroscopy. J. Biomed. Opt. **11**, 054001 (2006)
89. N. Stone, P. Matousek, Advanced transmission Raman spectroscopy: a promising tool for breast disease diagnosis. Cancer Res. **68**, 4424–4430 (2008)

90. D.C. Redd, Z.C. Feng, K.T. Yue, T.S. Gansler, Raman spectroscopy characterization of human breast tissues: implications for breast cancer diagnosis. Appl. Spectrosc. **47**, 787–791 (1993)
91. A.S. Haka, K.E. Shafer, M. Fitzmaurice, P. Crowe, R.R. Dasari, M.S. Feld, Diagnosing breast cancer by using Raman spectroscopy. PNAS **102**, 12371–12376 (2005)
92. A.S. Haka, Z. Volynskaya, J.A. Gardecki, J. Nazemi, J. Lyons, D. Hicks, M. Fitzmaurice, R.R. Dasari, J.P. Crowe, M.S. Feld, In vivo margin assessment during partial mastectomy breast surgery using Raman spectroscopy. Cancer Res. **66**, 3317–3322 (2006)
93. A. Mahadevan-Jansen, M.F. Mitchell, N. Ramanujam, A. Malpica, S. Thomsen, U. Utzinger, R. Richards-Kortum, Near-infrared Raman spectroscopy for in vitro detection of cervical precancers. Photochem. Phobiol. **68**, 123–132 (1998)
94. U. Utzinger, D.L. Heintzelman, A. Mahadevan-Jansen, A. Malpica, M. Follen, R. Richards-Kortum, Near-infrared Raman spectroscopy for in vivo detection of cervical precancers. Appl. Spectrosc. **55**, 955–959 (2001)
95. D.P. Lau, Z. Huang, H. Lui, D.W. Anderson, K. Berean, M.D. Morrison, L. Shen, H. Zeng, Raman spectroscopy for optical diagnosis in the larynx: preliminary findings. Lasers Surg. Med. **37**, 192–200 (2005)
96. S.K. Teh, W. Zheng, D.P. Lau, Z. Huang, Spectroscopic diagnosis of laryngeal carcinoma using near-infrared Raman spectroscopy and random recursive partitioning ensemble techniques. Analyst **134**, 1232–1239 (2009)
97. D.P. Lau, Z. Huang, H. Lui, C.S. Man, K. Berean, M.D. Morrison, H. Zeng, Raman spectroscopy for optical diagnosis in normal and cancerous tissue of the nasopharynx - preliminary findings. Lasers Surg. Med. **32**, 210–214 (2003)
98. A.J. Berger, T.W. Koo, I. Itzkan, G.L. Horowitz, M.S. Feld, Multicomponent blood analysis by near-infrared Raman spectroscopy. Appl. Opt. **38**, 2916–2926 (1999)
99. A.J. Berger, I. Itzkan, M.S. Feld, Feasibility of measuring blood glucose concentration by near-infrared Raman spectroscopy. Spectrochim. Acta Part A **53A**, 287–292 (1997)
100. A.M.K. Enejder, T.G. Scecina, J. Oh, M. Hunter, W. Shih, S. Sasic, G.L. Horowitz, M.S. Feld, Raman spectroscopy for noninvasive glucose measurements. J. Biomed. Opt. **10**, 031114 (2005)
101. J.T. Motz, M. Fitzmaurice, A. Miller, S.J. Gandhi, A.S. Haka, L.H. Galindo, R.R. Dasari, J.R. Kramer, M.S. Feld, In vivo Raman spectral pathology of human atherosclerosis and vulnerable plaque. J. Biomed. Opt. **11**, 021003 (2006)
102. H.P. Buschman, G. Deinum, J.T. Motz, M. Fitzmaurice, J.R. Kramer, A. van der Laarse, A.V. Bruschke, M.S. Feld, Raman microspectroscopy of human coronary atherosclerosis: biochemical assessment of cellular and extracellular morphologic structures in situ. Cardiovasc. Pathol. **10**, 69–82 (2001)
103. H.P. Buschman, E.T. Marple, M.L. Wash, B. Bennett, T.C. Schut, M. Brochert, H.A. Bruining, A.V. Bruschke, A. van der Laarse, G.J. Puppels, In vivo determination of the molecular composition of artery wall by intravascular Raman spectroscopy. Anal. Chem. **72**, 3771–3775 (2000)
104. M.V. Schulmerich, W.F. Finney, V. Popescu, M.D. Morris, T.M. Vanasse, S.A. Goldstein, Transcutaneous Raman spectroscopy of bone tissue using a non-confocal fiber optic array probe. Proc. SPIE 6093, 60930O (2006)
105. C. Krafft, S.B. Sobottka, G. Schackert, R. Salzer, Near infrared Raman spectroscopic mapping of native brain tissue and intracranial tumors. Analyst **130**, 1070–1077 (2005)
106. M.C.M. Grimbergen, C.F.P. van Swol, R.J.A. van Moorselaar, J. Uff, A. Mahadevan-Jansen, N. Stone, Raman spectroscopy of bladder tissue in the presence of 5-aminolevulinic acid. J. Photochem. Photobiol. B: Biol. **95**, 170–176 (2009)
107. P. Crow, A. Molckovsky, N. Stone, J. Uff, B. Wilson, L.M. WongKeeSong, Assessment of fiber-optic near-infrared Raman spectroscopy for diagnosis of bladder and prostate cancer. Urology **65**, 1126–1130 (2005)
108. N. Stone, C. Kendall, N. Shepherd, P. Crow, H. Barr, Near-infrared Raman spectroscopy for the classification of epithelial pre-cancers and cancers. J. Raman Spectrosc. **33**, 564–573 (2002)

109. J.X. Cheng, X.S. Xie, Coherent anti-Stokes Raman scattering microscopy: instrumentation, theory and applications. J. Phys. Chem. B **108**, 827–840 (2004)
110. K. Kneipp, Y. Wang, H. Kneipp, L.T. Perelman, I. Itzkan, R.R. Dasari, M.S. Feld, Single molecule detection using surface-enhanced Raman scattering (SERS). Phys. Rev. Lett. **78**, 1667–1670 (1996)
111. J.J. Laserna, *Modern Techniques in Raman Spectroscopy* (Wiley, New York, 1996)

Chapter 2
Three-Dimensional Optical-Resolution Photoacoustic Microscopy

Song Hu, Konstantin Maslov, and Lihong V. Wang

Three-dimensional optical-resolution photoacoustic microscopy (OR-PAM), an emerging optical-acoustic hybrid technology capable of imaging optical absorption contrasts with subcellular resolution and sensitivity, has been recognized as a valuable complement to existing optical microscopy technologies. In this chapter, we provide detailed discussion on the design and operation of OR-PAM, including the principle, system design, system configuration, system alignment, experimental procedures, laser safety, functional imaging scheme, recent technical advances, and sample biomedical applications. Future directions of OR-PAM development are also discussed at the end of this chapter.

2.1 Introduction

The past two decades have witnessed a dramatic growth in biomedical applications of optical microscopy. Mainstream microscopy technologies—including, but not limited to, confocal microscopy, multiphoton microscopy, and optical coherence tomography (OCT)—have greatly benefited from advances in laser technology, fluorescent labeling, scanning mechanisms, and image acquisition; however, all these technologies rely on either optical scattering or fluorescent contrast and have difficulty in sensing optical absorption properties of biological tissues [1].

Recently, the photoacoustic effect has been utilized for biomedical imaging of tissue optical absorption, leading to a blooming technology—photoacoustic tomography (PAT). In PAT, the object absorbs short-pulsed or intensity-modulated optical irradiation, resulting in heating and further inducing high-frequency ultrasonic

S. Hu · K. Maslov · Lihong V. Wang (✉)
Optical Imaging Laboratory, Department of Biomedical Engineering, Washington University in St. Louis, St. Louis, MO 63130-4899, USA
e-mail: lhwang@wustl.edu

R. Liang (ed.), *Biomedical Optical Imaging Technologies*, Biological and Medical Physics, Biomedical Engineering, DOI 10.1007/978-3-642-28391-8_2,

waves, which can be detected to map optical absorption [2]. Thus, the photoacoustic effect provides an exquisite way to resolve the optical absorption distribution in biological tissue ultrasonically. Taking advantage of the much weaker ultrasonic scattering in tissues (1,000 times weaker than optical scattering), researchers have developed reconstruction-based photoacoustic computed tomography (PACT) [3] and focused-scanning-based photoacoustic microscopy (PAM) [4,5] for deep tissue imaging in the optical quasidiffusive or diffusive regime. When the spatial resolution in all directions is entirely determined by the photoacoustic wave, the technology is called acoustic-resolution PAT. Although having achieved great success, the acoustic-resolution PAT is inadequate for examining the anatomy and function of biological tissues at the cellular or subcellular level. To fill this gap, we have developed optical-resolution photoacoustic microscopy (OR-PAM), improving the lateral resolution of PAT to the cellular [6] or even subcellular scale [7]. As a unique optical absorption microscopy technology and a valuable complement to the existing technologies, OR-PAM has demonstrated broad biomedical applications since its invention [8–14]. Taking advantage of the strong optical absorption of endogenous hemoglobin, OR-PAM enables label-free, noninvasive, and volumetric microvascular imaging down to single capillaries, providing both anatomical (such as vessel diameter, connectivity, and tortuosity) and functional (such as hemoglobin oxygen saturation (sO_2) and blood flow velocity) information [8–11, 15]. With the aid of exogenous molecular contrast agents, OR-PAM is also capable of molecular imaging [13].

This chapter provides a detailed description of the design, operation, and application of OR-PAM, including the principle, system design, system configuration, system alignment, experimental procedures, laser safety, functional imaging scheme, recent technical advances, and sample biomedical applications. Future directions of OR-PAM development are also predicted at the conclusion of this chapter.

2.2 Principle and System Design

In PAM, volumetric imaging is realized by two-dimensional (2-D) raster scanning of the dual foci of optical excitation and ultrasonic detection, in combination with depth-resolved ultrasonic detection. The two foci are configured coaxially and confocally to maximize the imaging sensitivity. Thus, the lateral resolution of PAM is determined by the product of the two point spread functions.

In dark-field acoustic-resolution PAM (AR-PAM) [5], the maturest version of AR-PAM, a pulsed laser beam passes through a conical lens to form a ring-shaped illumination and then is weakly focused into biological tissues to overlap the tight ultrasonic focus [Fig. 2.1a]. Since the ultrasonic focus is smaller than the optical focus, the lateral resolution of AR-PAM is determined acoustically as [16]

$$\Delta r_{\mathrm{R}} = \frac{0.71\lambda_0}{\mathrm{NA}}, \tag{2.1}$$

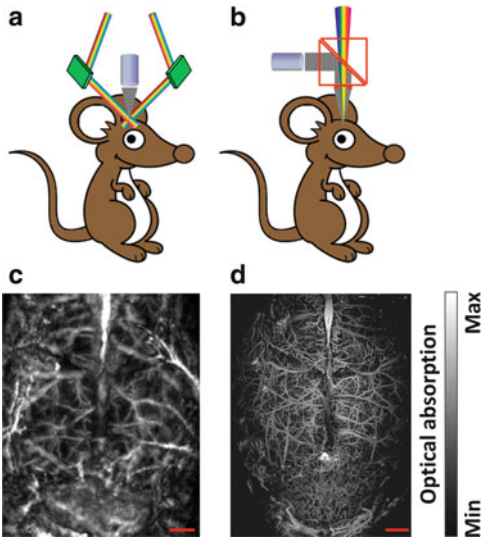

Fig. 2.1 Comparison of acoustic-resolution photoacoustic microscopy (AR-PAM) and optical-resolution photoacoustic microscopy (OR-PAM). (**a**) Schematic of AR-PAM. (**b**) Schematic of OR-PAM. (**c**) AR-PAM image of the cortical vasculature in a living adult mouse with both the scalp and the skull intact. (**d**) OR-PAM image of the cortical vasculature in a living adult mouse with the scalp removed and the skull intact. Scale bars: 1 mm

where λ_0 and NA denote the center wavelength of the photoacoustic wave and the numerical aperture of the ultrasonic detector, respectively. A lateral resolution of 45 μm has been achieved with a center frequency of 50 MHz and an NA of 0.44 [5]. This resolution, although adequate for many biomedical applications, cannot resolve fine structures such as capillaries (diameter: 4–9 μm).

To resolve single capillaries acoustically, an ultrasonic center frequency of greater than 400 MHz is required; however, at such a frequency, strong ultrasonic attenuation limits the penetration depth to less than 100 μm [6]. A more practical way to improve the lateral resolution is to use fine optical focusing. As shown in Fig. 2.1b, the optical excitation beam can be focused to a diffraction-limited spot inside the acoustic focus. Thus, the size of the optically excited region, rather than that of the ultrasonically detected region, determines the lateral resolution. Using this configuration (referred to as OR-PAM), the lateral resolution of PAM can be improved from 45 to 5 μm [6] or even better [7], at the expense of penetration depth. Figures 2.1c and d present a vivid comparison of the penetration and resolution of AR-PAM and OR-PAM [12, 17]. OR-PAM can clearly resolve as small as single capillaries in an adult mouse brain through the intact skull [Fig. 2.1d], while AR-PAM can only resolve cortical vessels thicker than 50 μm [Fig. 2.1c]. However, OR-PAM requires the scalp to be removed, while AR-PAM is able to penetrate both the scalp and the skull.

Based on the principle of OR-PAM, we list a couple of general guidelines that one may consider to follow when designing an OR-PAM system:

1. Higher optical resolution always accompanies with a smaller optical focus zone. Balance the trade-off by choosing a proper optical condenser lens or microscope objective according to the desired lateral resolution.

2. Higher-frequency ultrasonic transducer provides finer axial resolution at the expense of ultrasonic penetration. Choose a proper transducer according to the desired axial resolution and imaging depth. Generally speaking, the optimal transducer center frequency is between 50 and 150 MHz.
3. The optical and ultrasonic foci should be configured coaxially and confocally whenever possible to maximize the imaging sensitivity.

Here is an example of how to follow the guidelines. For in vivo single capillary imaging in the skin [6], a spatial resolution comparable with or smaller than the average capillary diameter (4–9 μm) is required. Thus, we choose an optical microscope objective with an NA of 0.1, which translates into a diffraction-limited focal diameter of ~3.7 μm in the operation wavelength range (500–650 nm). With such lateral resolution, OR-PAM is capable of resolving individual RBCs (average diameter: 6–8 μm) traveling along blood vessels [11]. A transducer with a center frequency of 75 MHz and a bandwidth of 80% is chosen to provide adequate axial resolution (15 μm) without encountering severe high-frequency acoustic loss in the skin [6]. Note that for transcranial imaging of cortical capillaries, the center frequency of the ultrasonic transducer should be reduced to 30–50 MHz because of the strong skull attenuation of high-frequency ultrasound [13].

2.3 System Configuration

The schematic of a representative OR-PAM system is shown in Fig. 2.2 [18]. The photoacoustic excitation source consists of a diode-pumped solid-state laser (INNOSLAB, Edgewave) and a dye laser (CBR-D, Sirah), which emits wavelength-tunable laser pulses (pulse width: 7 ns; repetition rate: <5 kHz and controlled by the external trigger signal). The pulsed laser beam is first attenuated by a neutral-density filter (NDC-50C-2M, Thorlabs) and then focused by a condenser lens (LA1131, Thorlabs), before passing through a 25-μm pinhole (P250S, Thorlabs) for spatial filtering. The pinhole is positioned slightly away from the focus of the condenser lens, where the beam size is larger than the pinhole diameter, to allow effective filtering. Then, the filtered beam is focused by a microscope objective (RMS4X, Thorlabs). The distance between the pinhole and the objective is ~400 mm, allowing sufficient beam expansion to fulfill the back aperture of the objective. This configuration gives a near-diffraction-limited optical focus (diameter: 3.7 μm). To align the optical irradiation and ultrasonic detection coaxially and confocally, we have designed an acoustic-optical beam splitter. In this beam splitter, two right-angle prisms (NT32-545, Edmund Optics) are aligned along their hypotenuses to form a cube with a thin layer (100 μm) of silicone oil (1000cSt, Clearco Products) in between. The prism glass and the silicone oil have similar optical refractive indices (1.1:1) but very different acoustic impedances (12.7:1). As a result, this beam splitter is optically transparent but acoustically reflective, thereby deflecting the

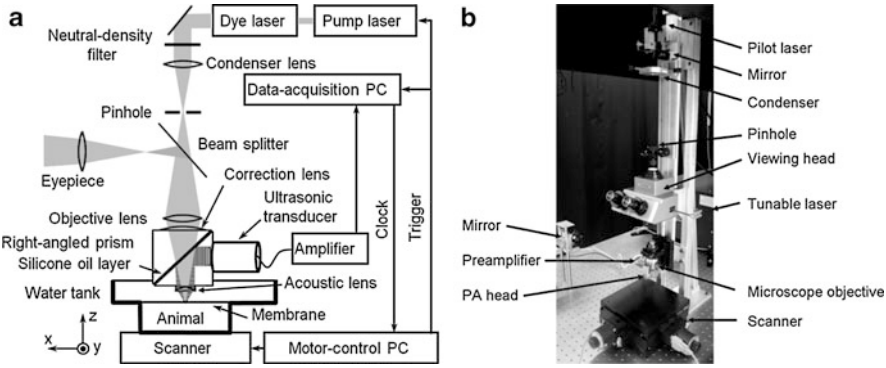

Fig. 2.2 (**a**) Schematic and (**b**) photograph of the optical-resolution photoacoustic microscopy system

acoustic axis from the optical axis by 90°. Thus, an ultrasonic transducer (V2022-BC, Olympus NDT) can be attached to the vertical side of the bottom prism for ultrasonic detection without blocking the optical irradiation, while still maintaining the coaxial alignment. An acoustic lens (geometrical radius of curvature: 5.2 mm; diameter: 6.35 mm) is attached to the bottom of the cube to be confocal with the optical irradiation. This acoustic lens has an NA of 0.46 in water and gives an acoustic focal diameter of 27 μm. To expose the imaging site, a window is opened at the bottom of the water tank and sealed with ultrasonically and optically transparent polyethylene membrane. Ultrasonic gel (Clear Image, SonoTech) is applied between the polyethylene membrane and the object for acoustic coupling. A transmission-mode optical microscope is integrated into our system by adding a white-light illumination to the object and an optical beam splitter between the pinhole and the microscope objective. Utilizing the reverse optical path of the OR-PAM, the imaging region can be viewed under the eyepiece. This addition helps quickly target the region of interest (ROI).

The photoacoustic signal detected by the ultrasonic transducer is amplified by two cascaded amplifiers (ZFL 500LN, Mini-Circuits) and then digitized by a 14-bit data acquisition (DAQ) board (CompuScope 14200, Gage Applied Sciences) at a sampling rate of 200 MS/s. Raster scanning is controlled by a separate personal computer, which triggers both the DAQ board and the pump laser. The trigger signal is synchronized with the clock-out signal from the DAQ board. The 2-D raster scanning is implemented by translating the water tank and the animal together along the horizontal (x–y) plane. The fast axis of the scanner is defined as the direction of the cross-sectional scan (B-scan). Volumetric OR-PAM image is obtained by combining a sequence of B-scan images acquired by translating the slow axis and can be viewed in direct three-dimensional (3-D) renderings or in 2-D maximum-amplitude projection (MAP) images.

2.4 System Alignment

Among the three general design guidelines, the first two are related to component selection, while the third one is about system alignment. The following acoustic-optical confocal alignment in OR-PAM is essential for high-quality imaging:

1. Use pulse-echo ultrasound and an ultrasonic reflector to determine the position of the acoustic focal plane, i.e., the time delay from the trigger signal to the maximum pulse-echo ultrasonic signal.
2. Maximize the optical power passing through the pinhole by adjusting the pinhole position within the plane perpendicular to the optical axis.
3. Check the optical diffraction pattern after the pinhole. If the beam pattern is not a clear Airy's disc surrounded by gradually fading concentric circular rings, adjust the pinhole position along the optical axis (i.e., away or towards the condenser lens) until you see the typical circular aperture diffraction pattern.
4. If the circular rings are not concentric, fine-tune the pinhole position within the plane perpendicular to the optical axis.
5. Place an optically absorbing flat target (e.g., a piece of black tape) in the acoustic focal plane.
6. Adjust the vertical position (i.e., z position) of the microscope objective to maximize the amplitude of the photoacoustic signal generated from the flat target. At the maximum, the optical focus is aligned with the acoustic focus in the vertical direction. Alternatively, users can place a 6-μm carbon fiber in the acoustic focal plane for the confocal alignment in the z direction. Repeat B-scans across the carbon fiber while adjusting the vertical position of the objective to minimize the cross-sectional diameter of the carbon fiber in the image. At the minimum, the carbon fiber is in the optical focus. Using the 6-μm carbon fiber may lead to more accurate acoustic-optical confocal alignment in the z direction.
7. With the same flat target, adjust the horizontal positions (i.e., x and y positions) of the microscope objective until the photoacoustic signal generated from the target shows a symmetric pattern as shown in Fig. 2.3. At the symmetry point, the optical focus is aligned with the acoustic focus in the horizontal direction.
8. Repeat steps 6 and 7 until the photoacoustic signal is optimized in both shape and amplitude.
9. Fix the positions of the pinhole and the microscope objective.

Note that only steps 4, 5, and 7 are required to be performed before experiments to make sure that the confocal configuration is optimized. However, if the system is found to be misaligned, users need to follow the entire procedure.

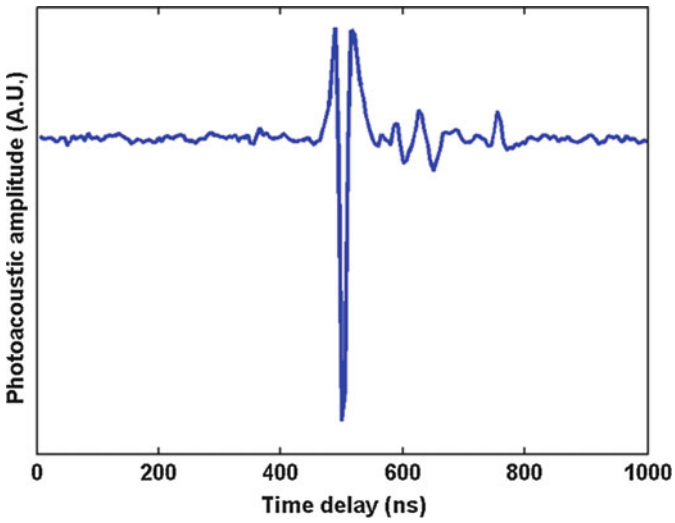

Fig. 2.3 Typical optical-resolution photoacoustic microscopy signal generated from a piece of black tape

2.5 Typical Experimental Procedures

To give readers a general idea of how to perform OR-PAM experiments, the typical procedure to image an adult mouse ear is elaborated. For other imaging applications, the procedure may be revised accordingly.

Animal depilation (if applicable):

1. Anesthetize the animal with intraperitoneal injection of a dose of 0.1 ml/10 kg cocktail (1 ml ketamine, 0.1 ml xylazine, and 8.9 ml saline).
2. Wait for 5–10 min until the animal is fully anesthetized.
3. Shave the hair in the ear.
4. Depilate the residual hair with Surgi Cream (category #: 82565, American International Industries) and clean with deionized water.

Note that the hair removal lotion may slightly irritate the animal skin, and the cocktail injection is not recommended to be used in combination with isoflurane (too much anesthesia may kill the animal). Thus, animal depilation is recommended to be performed 24 h before the planned experiment.

System preparation:

5. Turn on the photoacoustic laser system and wait for it to warm up (if applicable).
6. Seal the imaging window at the bottom of the water container with a piece of clean polyethylene membrane.
7. Fill the water container with deionized water.
8. Follow the guidelines in Sect. 2.4 to align the system.

Animal preparation:

9. Anesthetize the animal with 1% isoflurane vaporized by the inhalation gas (the typical flow rate is 1.0–1.5 l/min, depending on the animal's body weight) and maintain the anesthesia throughout the experiment. To maintain the animal under normal physiological status, the recommended inhalation gas is medical-grade air, unless other type of gas is required for specific functional studies (e.g., hypoxic challenging).
10. Fix the animal in a stereotactic stage. Set the temperature controller to the typical body temperature of mice (i.e., 37°C).
11. Flatten the mouse ear on a plastic plate and apply a layer of ultrasound gel on top of the ear. Avoid trapping air bubbles inside the gel.
12. Place the ear under the imaging window of the water tank and slowly raise the animal holder until the ultrasound gel contacts the bottom of the polyethylene membrane. Soft contact is preferred. Pressing the ear against the water tank may affect blood flow.
13. Check again to make sure no air bubble is trapped between the polyethylene membrane and the mouse ear.
14. Clamp the pulse oximeter to the animal to monitor its physiological status (recommended).
15. Apply eye ointment to the animal to prevent dryness and accidental laser damage (recommended).

Image acquisition:

16. Lower down the imaging head (i.e., the acoustic-optical beam splitter) until the acoustic lens is immersed in deionized water.
17. Remove air bubbles trapped under the acoustic lens.
18. Set the laser to the external-trigger mode and start trial scanning.
19. Adjust the z position of the imaging head until the detected photoacoustic signal is in the acoustic focal plane (judge from the acoustic delay).
20. Turn on the white-light illumination and check the imaging region under the integrated transmission-mode optical microscope. Set the scanning origin to the desired position. This is crucial for chronic monitoring, where the scanning origin should be the same position throughout the entire monitoring period.
21. Set correct scanning parameters and start image acquisition.

End experiment:

22. Turn off the laser firing once the data acquisition is completed.
23. Lift the imaging head out of water and lower down the animal holder.
24. Clean the mouse ear with deionized water, turn off the anesthesia system and the temperature controller, and unload the animal from the stereotactic stage.
25. If repetitive imaging is required, put the animal in an incubator with the temperature controlled at 37°C. Return the mouse to the animal facility after it wakes up naturally. Otherwise, follow the animal protocols to euthanatize and dispose the animal.
26. Turn off the experimental equipment and clean up the experimental area.

2.6 Functional Imaging Design

Besides the morphological information of the microvasculature that can be directly extracted from 3-D OR-PAM images, important functional and metabolic parameters, such as sO_2 and blood flow, are also measureable with specially designed imaging acquisition and data processing.

2.6.1 Spectroscopic Measurement of Oxygen Saturation of Hemoglobin

Oxyhemoglobin (HbO_2) and deoxyhemoglobin (HbR) are the two major forms of hemoglobin, the predominant endogenous photoacoustic source in the visible spectral range. HbO_2 and HbR have quite distinct optical absorption spectra and thus can be spectrally differentiated to quantify sO_2. Blood absorption imaged by label-free OR-PAM can be expressed as [19]

$$\Phi(\lambda_i) \propto \mu_a(\lambda_i) \cdot F = \ln 10 \{\varepsilon_{HbR}(\lambda_i) \cdot [HbR] + \varepsilon_{HbO_2}(\lambda_i) \cdot [HbO_2]\} \cdot F, \quad (2.2)$$

where $\mu_a(\lambda_i)$ is the blood absorption coefficient at wavelength λ_i and $\varepsilon_{HbR(HbO_2)}(\lambda_i)$ and [HbR]([HbO_2]) are the molar extinction coefficient and relative concentration of HbR (HbO_2), respectively. The detected photoacoustic signal amplitude $\Phi(\lambda_i)$ is proportional to the product of $\mu_a(\lambda_i)$ and the optical fluence F. Assuming that F is wavelength independent, we can ignore

$$\begin{bmatrix} [HbR] \\ [HbO_2] \end{bmatrix} = \begin{bmatrix} \varepsilon_{HbR}(\lambda_1) & \varepsilon_{HbO_2}(\lambda_2) \\ \varepsilon_{HbR}(\lambda_1) & \varepsilon_{HbO_2}(\lambda_2) \end{bmatrix}^{-1} \cdot \begin{bmatrix} \Phi(\lambda_1) \\ \Phi(\lambda_2) \end{bmatrix}. \quad (2.3)$$

Sequentially, sO_2 can be computed as

$$sO_2 = \frac{[HbO_2]}{[HbR] + [HbO_2]}. \quad (2.4)$$

Here are two guidelines for selecting the proper optical wavelengths to measure sO_2:

1. Wavelengths should be selected within the Q-band of hemoglobin absorption spectrum (i.e., 550–600 nm) to ensure a sufficient signal-to-noise ratio (SNR).
2. Wavelengths where ε_{HBR} and ε_{HbO_2} have a pronounced difference in their ratio (e.g., 561 nm is HbR dominant and 578 nm is HbO_2 dominant) are recommended.

Note that although a dual-wavelength measurement is adequate to calculate sO_2, using more wavelengths can potentially improve the measurement accuracy. Besides, the total hemoglobin concentration (HbT) can also be calculated in relative values, either by adding [HbR] and [HbO_2] together or by directly measuring blood

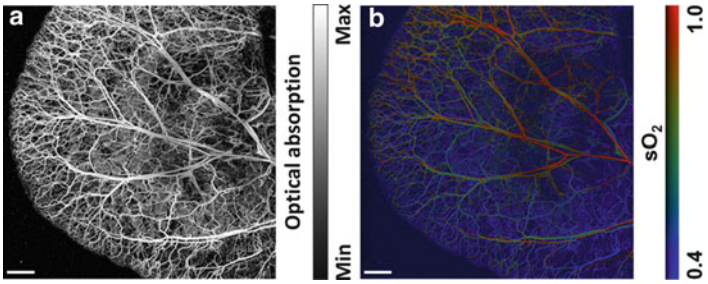

Fig. 2.4 In vivo optical-resolution photoacoustic microscopy of (**a**) vascular anatomy and (**b**) hemoglobin oxygen saturation (sO_2) in a nude mouse ear. Scale bar: 1 mm

absorption at isosbestic wavelengths (e.g., 530, 545, 570, and 584 nm) [20], where the molar extinction coefficients of HbR and HbO_2 are equal. Figure 2.4 shows the vascular anatomy and sO_2 in a nude mouse ear imaged by dual-wavelength (561 and 570 nm) OR-PAM.

2.6.2 Photoacoustic Doppler Measurement of Blood Flow Velocity

The Doppler effect, referred to the shift in wave frequency due to the relative motion between the wave source and the wave detector, has been widely used for velocity measurements. Recently, photoacoustic Doppler has been intensively studied for in vivo label-free measurement of blood flow velocity.

The prototype of photoacoustic Doppler flowmetry was invented by Fang et al. to measure the flow velocity along the acoustic axis (i.e., axial flow velocity) [21, 22]. However, within the 1 mm penetration depth of OR-PAM, biological tissues mainly form layered structures, and thus the flow component perpendicular to the acoustic axis (i.e., transverse flow) is predominant. To image transverse flow velocity, Fang et al. developed an M-mode photoacoustic particle imaging velocimetry based on OR-PAM [23]. Yao et al. further extended this technique from capillaries to all types of blood vessels with a concept called photoacoustic Doppler bandwidth broadening [15, 24].

The schematic of Doppler OR-PAM is shown in Fig. 2.5a [15]. The acoustic paths $L1$ and $L2$ subtend an obtuse angle and an acute angle with respect to the transverse flow direction, respectively. Thus, they contribute to the photoacoustic Doppler shift with opposite signs and induce bandwidth broadening. The resulting Doppler bandwidth can be computed by

$$\mathrm{PDB}_{\mathrm{OR-PAM}} = 2f_0 \cdot \frac{v_\mathrm{f}}{v_\mathrm{s}} \cdot \sin\theta \cdot \sin\varphi, \tag{2.5}$$

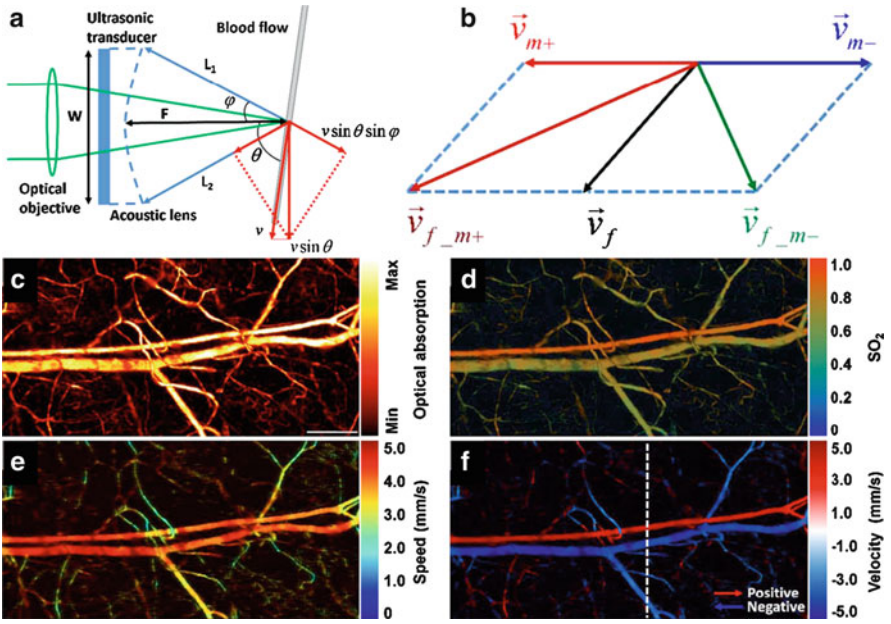

Fig. 2.5 (**a**) Schematic of the Doppler optical-resolution photoacoustic microscopy (OR-PAM). (**b**) Bidirectional scanning for flow direction sensing. OR-PAM of (**c**) vascular anatomy, (**d**) hemoglobin oxygen saturation (sO_2), (**e**) blood flow speed, and (**f**) blood flow velocity with directions in a mouse ear

where v_f is the flow speed of absorbing particles (e.g., RBCs for in vivo label-free measurement of blood flow), v_s is the speed of sound, θ is the angle subtended by the flow direction and the acoustic axis, φ is the aperture angle of the acoustic lens, and f_0 is the center frequency of the ultrasonic transducer.

Four consecutive photoacoustic A-line signals (referred to the time-resolved photoacoustic signals along the depth direction generated by individual laser pulses) are bandpass-filtered (center frequency: 75 MHz; 3-dB bandwidth: 1 MHz) and used to calculate $\mathrm{PDB}_{\mathrm{OR-PAM}}$ at each given spatial location by

$$\mathrm{PDB}_{\mathrm{OR-PAM}} = \frac{k}{T} \cdot \sqrt{1 - \frac{\left| \sum_{j=1}^{4} \tilde{p}_j \cdot \tilde{p}^*_{j+1} \right|}{\sum_{j=1}^{4} \tilde{p}_j \cdot \tilde{p}^*_j}}, \tag{2.6}$$

where T is the time interval between consecutive A-lines, k is a calibration factor, and $\tilde{p}$ is the Hilbert transform of A-line signal p. Thus, the flow speed v_f can be computed by substituting the calculated $\mathrm{PDB}_{\mathrm{OR-PAM}}$ to Eq. (2.5).

In our OR-PAM system, motor scanning also contributes to the Doppler bandwidth broadening. The measured flow speed is actually a vector combination of the flow speed and the motor-scanning speed [Fig. 2.5b]. Thus, bidirectional motor scanning can be used to determine the flow direction. The measured flow speeds under the two scanning directions are

$$v_{\mathrm{f\_m+}} = \sqrt{v_{\mathrm{f}}^2 + v_{\mathrm{m}}^2 + 2v_{\mathrm{f}} \cdot v_{\mathrm{m}} \cdot \cos\phi} \tag{2.7}$$

$$v_{\mathrm{f\_m+}} = \sqrt{v_{\mathrm{f}}^2 + v_{\mathrm{m}}^2 - 2v_{\mathrm{f}} \cdot v_{\mathrm{m}} \cdot \cos\phi}, \tag{2.8}$$

where v_{m} is the motor-scanning speed and ϕ is the angle subtended by $\vec{v}_{\mathrm{m+}}$ and $\vec{v}_{\mathrm{f}}$. Solving the simultaneous equations (2.7) and (2.8), we can get the true flow speed via

$$v_{\mathrm{f}} = \sqrt{\frac{v_{\mathrm{f\_m+}}^2 + v_{\mathrm{f\_m-}}^2 - 2v_{\mathrm{m}}^2}{2}}. \tag{2.9}$$

By comparing $v_{\mathrm{f\_m+}}$ and $v_{\mathrm{f\_m-}}$, we can further determine the flow direction.

Figure 2.5c–e shows the in vivo label-free Doppler OR-PAM imaging of a mouse ear [15]. A $1 \times 2\,\mathrm{mm}^2$ROI was bidirectionally scanned with a motor speed of 0.75 mm/s and a step size of 0.625 μm. Two optical wavelengths (560 and 570 nm) were used to image the vascular anatomy [Fig. 2.5c] and sO_2 [Fig. 2.5d]. The flow speed is pseudocolored in Fig. 2.5e, and the positive and negative flow directions are labeled red and blue in Fig. 2.5f, respectively. Determination of flow direction also helps distinguish arterioles from venules because the paired arteriole and venule are expected to have opposite flow directions [Fig. 2.5d, f].

2.7 Laser Safety

Similar to other scanning optical microscopy technologies, OR-PAM can improve SNR by increasing the pulse energy. However, for in vivo applications, laser parameters (such as optical wavelength, pulse duration, exposure duration, and exposure aperture) are regulated by laser safety standards of the American National Standards Institute (ANSI) [25].

2.7.1 Laser Safety for Ophthalmic Imaging [11, 25]

We have demonstrated OR-PAM imaging of the anterior segment of a living mouse eye [11]. The experimental parameters and ANSI-defined constants are listed as follows:

- Operation wavelengths (λ): 570 and 578 nm. Because 570 and 578 nm are close to each other and show minimal differences in terms of the safety limits, we use 570 nm throughout the calculation.
- Laser pulse repetition frequency (PRF): 600 Hz.
- Duration of a single laser pulse (t): 7 ns.
- Exposure duration of each B-scan (T_{Bscan}): 2.7 s.
- Exposure duration of a complete volumetric scan ($T_{\max}$): 7,200 s.
- Number of pulses in each B-scan (n_{Bscan}): 1,600.
- Number of pulses in the total 2-h exposure (n_{Total}): 2.56×10^6.
- Angular subtense (α): 200 mrad. The angular subtense is estimated by the NA of the microscope objective, which is 0.1 in our current system.
- Apparent angle subtended by a source above which the thermal hazard is proportional to the radiance of the source ($\alpha_{\max}$): 100 mrad.
- Apparent angle subtended by a source above which the maximum permissible exposure (MPE) for extended sources applies ($\alpha_{\min}$): 1.5 mrad.
- Extended source correction factor (C_{E}) : $C_{\text{E}} = \alpha^2/(\alpha_{\max}\alpha_{\min}) = 267$.
- Wavelength correction factor (C_{B}) : $C_{\text{B}} = 10^{0.02(\lambda-450)} = 251$.
- Exposure duration beyond which the thermal MPE for an extended source is constant in terms of irradiance (T_2) : 100 s.

Since the PRF used for OR-PAM ophthalmic imaging is less than the critical frequency defined by ANSI (55 kHz for wavelengths between 0.4 and 1.05 μm), the MPE for OR-PAM ophthalmic imaging is subject to three ANSI rules [25].

Rule 1: Single Pulse Limit

The MPE for a single laser pulse is

$$\text{MPE}_{\text{SP}} = 5.0 C_{\text{E}} \times 10^{-7} = 1.33 \times 10^{-4} \left[\text{J/cm}^2\right]. \tag{2.10}$$

Rule 2: Average Power Limit

First, consider one B-scan. During each B-scan, the OR-PAM laser sends a pulse train containing 1,600 pulses with a PRF of 600 Hz. Since the B-scan exposure time (~2.7 s) is longer than 0.7 s and the wavelength is between 400 and 600 nm, dual limits due to both photochemical and thermal effects apply here. For photochemical effects, the MPE for the B-scan pulse train is

$$\text{MPE}_{\text{Bscan}}(\text{photochemical}) = 100 C_{\text{B}} \times \left(\frac{\pi}{4}\right) \alpha^2 \times 10^{-6} = 790 \left[\text{J/cm}^2\right]. \tag{2.11}$$

For thermal effects, the MPE for the B-scan pulse train is

$$\text{MPE}_{\text{Bscan}}(\text{thermal}) = 1.8 C_{\text{E}} T_{\text{Bscan}}^{0.75} \times 10^{-3} = 1.01 \left[\text{J/cm}^2\right]. \tag{2.12}$$

Thus, the MPE/pulse for the B-scan pulse train is

$$\frac{\text{MPE}_{\text{Bscan}}(\text{thermal})}{n_{\text{Bscan}}} = 6.3 \times 10^{-4} \left[\text{J/cm}^2\right]. \tag{2.13}$$

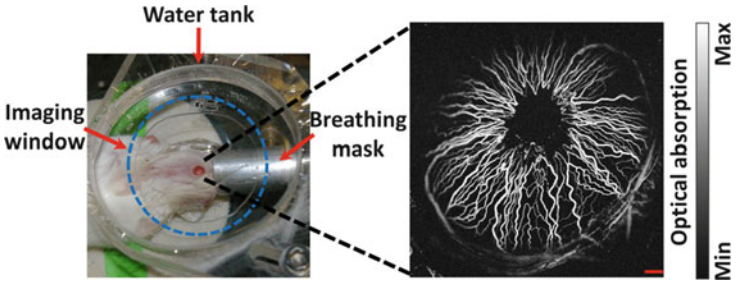

Fig. 2.6 In vivo optical-resolution photoacoustic microscopy of the anterior segment of a living mouse eye. (**a**) Photograph of the animal positioning. (**b**) Maximum-amplitude projection image acquired at 570 nm. Scale bar: 200 μm

Second, consider the total 2-h laser exposure. For photochemical effects, the MPE for the total exposure duration is the same as that for each B-scan [Eq. (2.11)]. For thermal effects, the MPE for the total exposure duration is

$$\mathrm{MPE}_{\mathrm{Total}}(\mathrm{thermal}) = 1.8 C_{\mathrm{E}} T_2^{-0.25} \times 10^{-3} \cdot T_{\max} = 1,093 \left[\mathrm{J/cm^2}\right]. \tag{2.14}$$

Thus, the MPE/pulse for the total 2-h laser exposure is

$$\frac{\mathrm{MPE}_{\mathrm{Total}}(\mathrm{photochemical})}{n_{\mathrm{Total}}} = 3.1 \times 10^{-4} \left[\mathrm{J/cm^2}\right]. \tag{2.15}$$

Rule 3: Repetitive Pulse Limit

The MPE for repetitive pulses is

$$\mathrm{MPE}_{\mathrm{RP}} = n_{\mathrm{Total}}^{-0.25} \mathrm{MPE}_{\mathrm{SP}} = 3.3 \times 10^{-6} \left[\mathrm{J/cm^2}\right]. \tag{2.16}$$

Rule 3 is the most conservative of the three. Therefore, the overall MPE for each pulse is $3.3 \times 10^{-6}\,\mathrm{J/cm^2}$. If the pupil diameter is 7 mm [25], the maximum permissible single laser pulse energy for OR-PAM ophthalmic imaging is computed to be 1.3 μJ. Thus, our experimentally used laser pulse energy (~40 nJ) is well within the ANSI limits. Figure 2.6 shows the animal positioning for ophthalmic OR-PAM imaging and a representative label-free OR-PAM image of the mouse iris microvasculature [11].

2.7.2 *Laser Safety for Skin Imaging [25]*

For skin imaging, a similar setting of experimental parameters as in the ophthalmic imaging has been used. Slightly differently, Rule 3 does not apply here. Typically, OR-PAM focuses ~200 μm beneath the skin surface with a focal diameter

of ∼5 μm. According to the geometry of a focused Gaussian beam, the beam diameter on the skin surface is ∼30 μm.

Rule 1: Single Pulse Limit

The MPE for a single laser pulse is

$$\mathrm{MPE_{SP}} = 2 \cdot C_\mathrm{A} \times 10^{-2} = 2.0 \times 10^{-2} \left[\mathrm{J/cm^2}\right], \tag{2.17}$$

where C_A, the wavelength correction factor, is unity when λ is between 400 and 700 nm.

Rule 2: Average Power Limit

Different from the anterior-eye-segment imaging, where all laser pulses overlap on the retina due to light defocusing, only ∼24 adjacent laser pulses overlap on the skin surface. With a PRF of 600 Hz, the exposure time t is 0.04 s. So, the MPE for the pulse train is

$$\mathrm{MPE_{train}} = 1.1 \cdot C_\mathrm{A} \cdot t^{0.25} = 0.5 \left[\mathrm{J/cm^2}\right]. \tag{2.18}$$

Thus, the MPE/pulse for the pulse train is

$$\frac{\mathrm{MPE_{average}} = \mathrm{MPE_{train}}}{24} = 2.1 \times 10^{-2} \left[\mathrm{J/cm^2}\right]. \tag{2.19}$$

Rule 1 is slightly more rigorous, so the overall MPE for each pulse is 2.0×10^{-2} J/cm^2. Knowing that the beam diameter on the skin surface is ∼30 μm, the maximum permissible single laser pulse energy for OR-PAM skin imaging is computed to be ∼141 nJ. Thus, our experimentally used laser pulse energy (∼40 nJ) is well within the ANSI limits.

2.8 Recent Technical Advances

Although traditional OR-PAM has demonstrated broad biomedical applications, its imaging speed is still slow compared with the mainstream optical microscopy technologies. Moreover, integration of OR-PAM with other optical microscopy for multicontrast imaging, as an original motivation for developing OR-PAM, has not been realized yet. Thus, recent technical developments of OR-PAM are focused on these two aspects.

2.8.1 New Scanning Mechanism

The integration of OR-PAM with existing optical microscopy has been hampered, mainly due to the incompatible scanning mechanisms. It is challenging to transplant the fast optical scanning widely used in optical microscopy technologies to OR-PAM, which requires scanning the ultrasonic-optical dual foci.

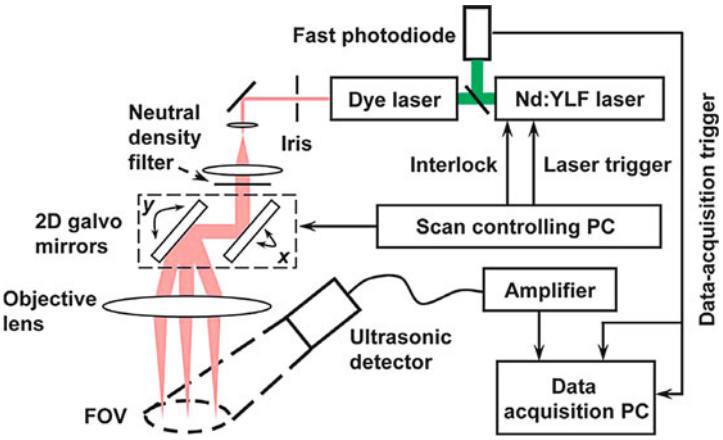

Fig. 2.7 Schematic of the laser-scanning optical-resolution photoacoustic microscopy setup

One intermediate solution is to relax the acoustic focus and keep it stationary, while the diffraction-limited optical focus is optically scanned inside the enlarged acoustic focus. This leads to the development of laser-scanning OR-PAM (LSOR-PAM) [26]. The configuration of the LSOR-PAM system is similar to that of the traditional mechanical-scanning-based OR-PAM (Fig. 2.7). The pulsed laser beam generated from the same type of wavelength-tunable laser system is spatially filtered by an iris, and the beam diameter is expanded to 8 mm by a pair of condenser lens. The expanded laser beam is then attenuated and steered by a 2-D galvanometer scanner (6230H, Cambridge Technology) before entering an objective lens (AC254-060-A1, Thorlabs) for optical focusing. An unfocused ultrasonic transducer (V312, Olympus NDT; center frequency: 10 MHz; bandwidth: 80%; active element diameter: 6 mm) is placed 30 mm away from the object with an oblique angle of ~15°, which allows to overlap the optical illumination without blockage.

LSOR-PAM enables fast scanning with designable scanning patterns, which is particularly useful when studying the behavior of a single microvessel. However, unlike traditional OR-PAM, LSOR-PAM has a limited field of view (FOV) (6 mm in diameter in this case), which is determined by the ultrasonic beam size of the unfocused transducer. Moreover, the SNR of LSOR-PAM is lower than that of traditional OR-PAM because of the reduced sensitivity of the unfocused ultrasonic transducer at the optical focus.

To improve the imaging speed of OR-PAM while maintaining a high SNR, Rao et al. developed a hybrid-scanning OR-PAM (HSOR-PAM) system [27]. In HSOR-PAM (Fig. 2.8), the pulsed laser beam is scanned along the B-scan direction by a one-dimensional (1-D) galvanometer scanner (6220H, Cambridge Technology). A glass plate is submerged in the water tank to reflect the photoacoustic waves to a cylindrically focused ultrasonic transducer (25 MHz bandwidth, focal length 15 mm,

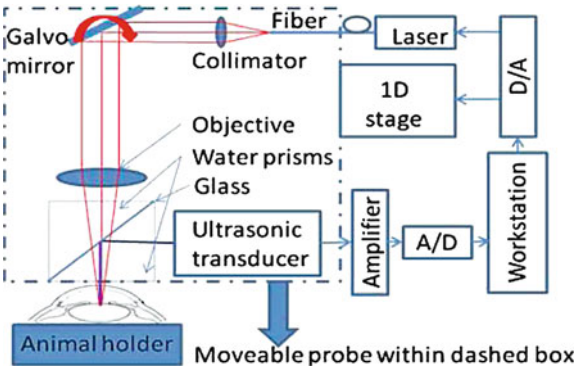

Fig. 2.8 Schematic of the hybrid-scanning optical-resolution photoacoustic microscopy system

material PZT, GE). The transducer has a line focus and thus frees acoustic scanning in the B-scan direction. The entire imaging head is mechanically scanned by a 1-D translation stage to form a volumetric image. The HSOR-PAM system operates at an imaging speed of 5,000 A-lines/s, with a slightly degraded SNR (5 dB lower) compared with traditional OR-PAM.

2.8.2 Integration with Optical Coherence Tomography

Recently, Li et al. reported the first combined system integrating transmission-mode OR-PAM with spectral-domain OCT [28]. In this combined system (Fig. 2.9), OR-PAM and OCT share the same single-mode fiber (P1-630A-FC-2, Thorlabs) for light delivery and the same microscope objective (E1, Leica) for optical illumination. Two-dimensional mechanical scanning of the object platform, in combination with the depth-resolved optical/ultrasonic detection, provides volumetric OCT/OR-PAM images.

Although the present imaging system demonstrates the feasibility of integrating OR-PAM with OCT, the relatively slow mechanical scanning limits its practical values. Taking advantage of the recently developed LSOR-PAM technology, Jiao et al. developed a combined laser-scanning-based OR-PAM and OCT system [29]. Figure 2.10 shows a schematic of the combined system. The configuration of the LSOR-PAM subsystem is the same as the one shown in Fig. 2.7. To incorporate the OCT subsystem, a dichroic mirror (NT43-955, Edmund Optics) is inserted right before the 2-D galvanometer (QS-10, Nutfield Technology). The passband of the dichroic mirror is carefully chosen to ensure a perfect reflection of the OCT beam and a maximized transmission of the OR-PAM beam. Then, the combined OCT and OR-PAM beams are focused into the object by an achromatic lens (AC254-060-A1, Thorlabs) and optically scanned by the galvanometer to form co-registered OCT and OR-PAM images.

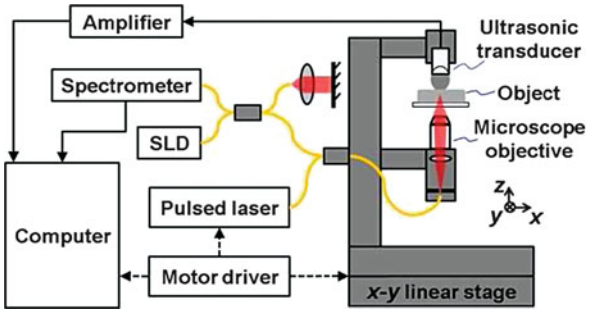

Fig. 2.9 Schematic of the combined optical-resolution photoacoustic microscopy and optical coherence tomography system

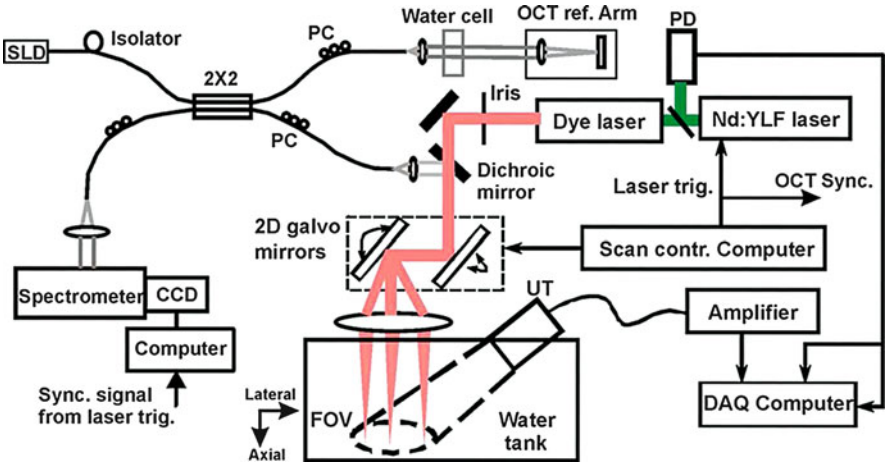

Fig. 2.10 Schematic of the integrated laser-scanning optical-resolution photoacoustic microscopy and optical coherence tomography system

Besides OCT, OR-PAM has also been integrated with confocal fluorescence microscopy to image the dual contrasts of optical absorption and molecular fluorescence simultaneously [30]. Combining OR-PAM with other optical microscopy provides fruitful anatomical, functional, and molecular information and is invaluable for both biological research and clinical diagnosis.

2.9 An Example Application: Wound Healing Monitoring

OR-PAM, capable of label-free imaging of multiple important vascular parameters (vascular morphology, HbT, sO_2, and blood flow) in a variety of in vivo anatomical sites (skin, eye, and brain), holds broad applications in circulation-related

physiological, pathophysiological, and clinical studies. Here, we only highlight the longitudinal monitoring capability of OR-PAM, which enables real-time study of disease progression and drug functioning. More biomedical applications of OR-PAM can be found in the literature [8, 10, 11, 13, 16, 31].

For technical demonstration, OR-PAM monitored the healing process of a laser-induced microvascular lesion in a mouse ear model [9]. Commercial transmission-mode optical microscopy was also used to monitor the same process, as a reference to OR-PAM. At the beginning of the chronic imaging, a $1 \times 1\,\text{mm}^2$ ROI in the mouse ear (Hsd:Athymic Nude-Foxn 1^{NU}, Harlan; body weight: $\sim$25 g) was selected and photographed by the transmission-mode optical microscope, after which the ROI was imaged by dual wavelengths (570 and 578 nm) OR-PAM [Fig. 2.11A]. Then, we switched to a continuous-wave laser (MGL-III-532, Changchun New Industries; output power: 150 mW, wavelength: 532 nm), removed the pinhole, and scanned the central part of the ROI ($0.25 \times 0.25\,\text{mm}^2$) with the focused laser beam (diameter: $\sim$30 μm) for $\sim$10 min to create a microvascular lesion. The ROI was imaged immediately after the laser destruction [Fig. 2.11B] and in the subsequent 12 days [Fig. 2.11C-1 to C-12]. Our results clearly show a four-step wound healing process that has been documented in physiology books [32]:

1. Vessel regression and hemostasis occurred right after the laser destruction [Fig. 2.11B].
2. Vasodilation was induced by inflammation 1 day after the injury and lasted for about 5 days [Figs. 2.11C-1 to C-5]. Tissue hypoxia occurred right after the laser destruction to trigger angiogenesis [Figs. 2.11B and C-1 to C-5].
3. The ingrowth of neocapillaries started to restore the microcirculation 3 days after the wound occurred [Fig. 2.11C-3].
4. The damaged arteriole-venule pair recovered morphologically and functionally after 12 days [Fig. 2.11C-12].

Note that, as an enabling technology for noninvasive label-free longitudinal monitoring of microhemodynamics, OR-PAM has potentially broader applications. In vascular physiological study, OR-PAM can help understand the signaling pathway of vascular regulation by perturbing the pathway and monitor the consequential anatomical and functional changes [31]. In cancer research, OR-PAM can monitor tumor neovascularization and evaluate cancer therapy. In vascular-related drug development, OR-PAM can trace drug functioning and evaluate drug efficacy. In laser microsurgery, surgical lasers can be readily integrated with OR-PAM to perform on-site high-precision microsurgery with presurgery diagnosis and postsurgery evaluation. In neuroscience, the minimally invasive feature of OR-PAM is ideal for chronic studies of cortical plasticity and neurovascular coupling at the capillary level.

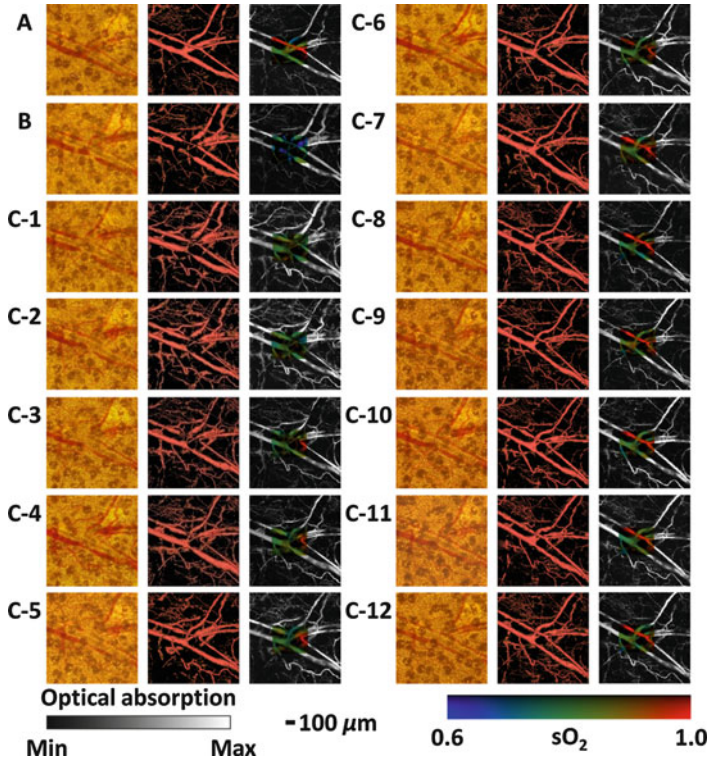

Fig. 2.11 Optical-resolution photoacoustic microscopy (OR-PAM) of the healing process of a laser-induced microvascular lesion (A) before laser destruction, (B) immediately after laser destruction, and (C) on each of the subsequent 12 days. The left image in each panel is the photograph taken by a commercial transmission-mode optical microscope; the middle image is the front view of the 3-D microvascular morphology acquired by OR-PAM at 57 nm; the right image is the maximum-amplitude projection image overlaid by the hemoglobin oxygen saturation map of the laser-damaged region

2.10 Perspectives

OR-PAM has potentially broad applications in biomedical imaging, yet much effort still needs to be invested to mature this technology. Four potential directions of future OR-PAM development are anticipated:

- Fast scanning over a large FOV. The current fast scanning strategy (i.e., optical scanning) limits the FOV to less than 6 mm, which is inadequate in many applications. One possible solution is to increase the speed of mechanical scanning by using specific scanners [33].
- Optical detection of photoacoustic waves. Current acoustic detection in OR-PAM is based on piezoelectric transducers, which require good tissue contact and

generally involve water in acoustic coupling. This configuration leads to system complexity and experimental inconvenience. Moreover, the detection sensitivity of the transducer falls off with its element size. Higher detection frequency is achieved at the expense of SNR. To overcome these limitations, noncontact optical methods for ultrasonic detection need to be explored.

- Integrating OR-PAM with AR-PAM for multiscale imaging. As shown in Fig. 2.1, OR-PAM and AR-PAM are highly complementary in terms of spatial resolution and tissue penetration. Combining them together would enable users to select an optimal trade-off between the spatial resolution and the penetration depth for different applications.
- Integrating OR-PAM with multiphoton fluorescence microscopy for neurovascular imaging. OR-PAM and multiphoton microscopy have similar penetration depths in soft brain tissues [8]. Combining them would enable direct visualization of the interaction between neuron activities and vascular dynamics.

Being one of the most actively studied optical microscopy technologies, OR-PAM has experienced a dramatic development within the last few years. We are looking forward to see OR-PAM in the mainstream.

Acknowledgements This work was sponsored by National Institutes of Health Grants R01 EB000712, EB000712A2S1, R01 EB00071207S2, R01 EB008085, R01 CA113453901, U54 CA136398, and 5P60 DK02057933. Professor Lihong V. Wang has a financial interest in Microphotoacoustics, Inc. and Endra, Inc., which, however, did not support this work.

Animal Ethics

All experimental animal procedures were carried out in conformance with the laboratory animal protocol approved by the School of Medicine Animal Studies Committee of Washington University in St. Louis.

References

1. S. Hu, L.V. Wang, Photoacoustic imaging and characterization of the microvasculature. J. Biomed. Opt. **15**, 011101(2010)
2. L.V. Wang, H. Wu, *Biomedical Optics: Principles and Imaging*. (Wiley, Hoboken, 2007)
3. X. Wang, Y. Pang, G. Ku, X. Xie, G. Stoica, L.V. Wang, Noninvasive laser-induced photoacoustic tomography for structural and functional in vivo imaging of the brain. Nat. Biotechnol. **21**, 803–806 (2003)
4. K. Maslov, G. Stoica, L.V. Wang, In vivo dark-field reflection-mode photoacoustic microscopy. Opt. Lett. **30**, 625–627 (2005)
5. H.F. Zhang, K. Maslov, G. Stoica, L.V. Wang, Functional photoacoustic microscopy for high-resolution and noninvasive in vivo imaging. Nat. Biotechnol. **24**, 848–851 (2006)
6. K. Maslov, H.F. Zhang, S. Hu, L.V. Wang, Optical-resolution photoacoustic microscopy for in vivo imaging of single capillaries. Opt. Lett. **33**, 929–931 (2008)

7. K. Maslov, G. Ku, L.V. Wang, Photoacoustic microscopy with submicron resolution. Proc. SPIE **7564**, 75640W (2010)
8. S. Hu, K. Maslov, V. Tsytsarev, L.V. Wang, Functional transcranial brain imaging by optical-resolution photoacoustic microscopy. J. Biomed. Opt. **14**, 040503 (2009)
9. S. Hu, K. Maslov, L.V. Wang, In vivo functional chronic imaging of a small animal model using optical-resolution photoacoustic microscopy. Med. Phys. **36**, 2320–2323 (2009)
10. S. Hu, K. Maslov, L.V. Wang, Noninvasive label-free imaging of microhemodynamics by optical-resolution photoacoustic microscopy. Opt. Express **17**, 7688–7693 (2009)
11. S. Hu, B. Rao, K. Maslov, L.V. Wang, Label-free photoacoustic ophthalmic angiography. Opt. Lett. **35**, 1–3 (2010)
12. S. Hu, L.V. Wang, Neurovascular photoacoustic tomography. Front. Neuroenerg. **2**, doi:10.3389/fnene.2010.00010 (2010)
13. S. Hu, P. Yan, K. Maslov, J.M. Lee, L.V. Wang, Intravital imaging of amyloid plaques in a transgenic mouse model using optical-resolution photoacoustic microscopy. Opt. Lett. **34**, 3899–3901 (2009)
14. S.L. Jiao, M.S. Jiang, J.M. Hu, A. Fawzi, Q. Zhou, K.K. Shung, C.A. Puliafito, H.F. Zhang, Photoacoustic ophthalmoscopy for in vivo retinal imaging. Opt. Express, **18**, 3967–3972 (2010)
15. J.J. Yao, K.I. Maslov, Y.F. Shi, L.A. Taber, L.V. Wang, In vivo photoacoustic imaging of transverse blood flow by using Doppler broadening of bandwidth. Opt. Lett. **35**, 1419–1421 (2010)
16. S. Hu, K. Maslov, L.V. Wang, Optical-resolution photoacoustic microscopy for in vivo imaging of microvasculature. Tuchin, V. V. (Ed.), *Handbook of Photonics for Biomedical Science* (CRC Press, 2010)
17. E.W. Stein, K. Maslov, L.V. Wang, Noninvasive mapping of the electrically stimulated mouse brain using photoacoustic microscopy. Proc. SPIE **6856**, 68561J (2008)
18. K. Maslov, H.F. Zhang, S. Hu, L.V. Wang, Optical-resolution confocal photoacoustic microscopy. Proc. SPIE **6856**, 68561I (2008)
19. H.F. Zhang, K. Maslov, M. Sivaramakrishnan, G. Stoica, L.V. Wang, Imaging of hemoglobin oxygen saturation variations in single vessels in vivo using photoacoustic microscopy. Appl. Phys. Lett. **90**, 3 (2007)
20. S.L. Jacques, S.A. Prahl, http://omlc.ogi.edu/spectra/hemoglobin/index.html
21. H. Fang, K. Maslov, L.V. Wang, Photoacoustic Doppler effect from flowing small light-absorbing particles. Phys. Rev. Lett. **99**, 184501 (2007)
22. H. Fang, K. Maslov, L.V. Wang, Photoacoustic Doppler flow measurement in optically scattering media. Appl. Phys. Lett. **91**, 3 (2007)
23. H. Fang, L.V. Wang, M-mode photoacoustic particle flow imaging. Opt. Lett. **34**, 671–673 (2009)
24. J. Yao, L.V. Wang, Transverse flow imaging based on photoacoustic Doppler bandwidth broadening. J. Biomed. Opt. **15**, 021303 (2010)
25. American National Standards Institute Inc., New York, NY (2007)
26. Z. Xie, S. Jiao, H.F. Zhang, C.A. Puliafito, Laser-scanning optical-resolution photoacoustic microscopy. Opt. Lett. **34**, 1771–1773 (2009)
27. B. Rao, L. Li, K. Maslov, L.V. Wang, Hybrid-scanning optical-resolution photoacoustic microscopy for in vivo vasculature imaging. Opt Lett, **35**, 1521–1523 (2010)
28. L. Li, K. Maslov, G. Ku, L.V. Wang, Three-dimensional combined photoacoustic and optical coherence microscopy for in vivo microcirculation studies. Opt. Express **17**, 16450–16455 (2009)
29. S. Jiao, Z. Xie, H.F. Zhang, C.A. Puliafito, Simultaneous multimodal imaging with integrated photoacoustic microscopy and optical coherence tomography. Opt. Lett. **34**, 2961–2963 (2009)
30. Y. Wang, K. Maslov, C. Kim, S. Hu, L.V. Wang, Integrated photoacoustic and fluorescence confocal microscopy. IEEE Trans. Biomed. Eng. **57**(10), 2576–2578 (2010)

31. S. Hu, J. Yao, K. Maslov, L.V. Ang, S. Oladipupo, A.C. Santeford, J. Kovalski, J.M. Arbeit, Optical-resolution photoacoustic microscopy of angiogenesis in a transgenic mouse model. Proc. SPIE **7564**, 756406 (2010)
32. A.F. Falabella, R.S. Kirsner, *Wound Healing* (Talyor & Francis, Boca Raton, 2005)
33. T. Harrison, J.C. Ranasinghesagara, H. Lu, K. Mathewson, A. Walsh, R.Z. Zemp, Combined photoacoustic and ultrasound biomicroscopy. Opt. Express **17**, 22041–22046 (2009)

Chapter 3
Fluorescence Microscopy Imaging in Biomedical Sciences

Yuansheng Sun and Ammasi Periasamy

Fluorescence microscopy is an important tool in biological sciences which provides excellent sensitivity for detecting very low concentrations of molecules over broad spatial and temporal dimensions. With fast developments of new fluorescent probes, advanced electronic and optical devices, and sophisticated data acquisition and analysis software, fluorescence microscopy resides on the central stage of life-sciences research. This chapter covers several commonly used and advanced fluorescence microscopy techniques and focuses on fluorescence lifetime imaging microscopy (FLIM). A number of FLIM systems and their applications are reviewed. As an example, we describe how we built and calibrated a two-photon excitation time-correlated single-photon counting (TPE-TCSPC) FLIM system and employed the system to investigate protein-protein interactions in living cells.

3.1 Introduction

The phenomenon of fluorescence was first reported by George G. Stokes in 1852, and the fluorescence microscope was devised in the early part of the twentieth century. The potential of the fluorescence microscopy technique was not realized until Albert Coons introduced a technique for labeling antibodies with fluorescent dye in the early 1940s [1], which has matured as the well-known immunofluorescence field. Since the early 1990s, fluorescence microscopy has been dramatically altered and advanced because of the development of the green fluorescent protein (GFP) and various fluorescent protein (FP) genetic variants [2–7] (see Sect. 3.2). Hand in hand with above, the rapid improvement in modern microscope designs

Y. Sun · A. Periasamy (✉)
W.M. Keck Center for Cellular Imaging, Department of Biology and Biomedical Engineering, University of Virginia, Charlottesville, VA 22904, USA
e-mail: ap3t@virginia.edu

R. Liang (ed.), *Biomedical Optical Imaging Technologies*, Biological and Medical Physics, Biomedical Engineering, DOI 10.1007/978-3-642-28391-8_3,

and components, including optics, electronics, detectors, light sources, etc., has greatly expanded fluorescence microscopy imaging functionalities and enabled the development of many sophisticated fluorescence microscopy techniques (see Sect. 3.3). Moreover, computer-controlled fluorescence microscopes equipped with sophisticated accessories and software have facilitated the imaging of live specimens under physiological conditions as well as expended the variety of experimental manipulations [8]. For example, motorized fluorescence microscopes equipped with devices capable of maintaining temperature, CO_2, humidity, and focus provide biologists with the capability to monitor subcellular events over a few hours to days [9–11]; the usage of optical tweezers on a motorized fluorescence microscope offers biologists the ability to manipulate subcellular structures or particles [12].

Fluorescence microscopy has become an essential tool in the life sciences due to attributes not as readily available with other optical microscopy techniques. The general advantages of fluorescence microscopy techniques include the high degree of specificity amidst nonfluorescing material, the exquisite sensitivity which is able to detect individual fluorescent molecules, and the high temporal and spatial (available in 3-D) resolution. In this chapter, basics of fluorescence and fluorescent probes are introduced (Sect. 3.2), and several commonly used and advanced fluorescence microscopy imaging techniques are briefly presented (Sect. 3.3). This chapter focuses on fluorescence lifetime imaging microscopy (FLIM) and describes the design and calibration of a two-photon excitation time-correlated single-photon counting (TPE-TCSPC) FLIM system built in our laboratory (Sect. 3.4). The combination of TPE-TCSPC FLIM system and Förster resonance energy transfer (FRET) helped to investigate protein-protein interactions in living specimens. In this chapter, we described the development of TPE-TCSPC FLIM system to investigate the homodimerization of the transcription factor CCAAT/enhancer-binding protein alpha (C/EBPα) in live mouse pituitary cell nuclei (Sect. 3.4).

3.2 Basics of Fluorescence and Fluorescent Probes

Fluorescence is one of the many different luminescence processes and is the emission of light from the excited singlet state of a substance that has absorbed light or other electromagnetic radiation of a different wavelength. The excitation of molecules by light occurs via the interaction of molecular dipole transition moments with the electric field of the light and, to a much lesser extent, interaction with the magnetic field. The fluorescence processes following light absorption and emission are usually illustrated by the Jablonski diagram (see Fig. 3.1), and the energy of the emission is typically less than that of absorption. Thus, the fluorescence emission of a fluorophore is usually red shifted (longer wavelength) compared to its excitation – a phenomenon called the Stokes shift (see Chapter 1 in [13]). Besides the absorption and emission spectra, the important photophysical parameters of a fluorophore include (1) the fluorescence lifetime (described in Sect. 3.4), (2) the quantum yield (the number of emitted photons relative to the number of absorbed photons) which represents the fluorescence emission efficiency of the fluorophore, and (3) the molar

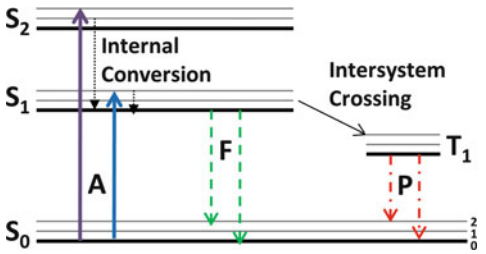

Fig. 3.1 Fluorescence illustrated by Jablonski diagram (Adapted from Fig. 1.5 in Chapter 1 of Ref. [13]). S_0, S_1, and S_2 are the singlet ground, first, and second electronic states, respectively. At each of these electronic energy levels, the fluorophores can exist in a number of vibrational energy levels, depicted by 0, 1, and 2. Following light absorption (A, *solid*), a fluorophore is usually excited to a higher vibrational level of S_1 or S_2. Through an internal conversion process (*dotted*), the excited molecule will rapidly (10^{-12} s) relax to the lowest vibrational level of S_1, where fluorescence emission (F, *dashed*) typically results from. The molecule usually returns to a higher excited vibrational ground state (S_0) level and then quickly (10^{-12} s) reaches thermal equilibrium. Thus, the energy of the emitted photon is typically less than that of the absorbed photon. The excess of the excitation energy is typically converted to the thermal energy. T_1 is the first triplet state, from which emission is termed as phosphorescence (P, *dotted dash*) and is generally shifted to longer wavelengths (lower energy) relative to fluorescence

extinction coefficient which is a direct measure of the ability of the fluorophore to absorb the light and is typically determined by measuring the absorbance at its maximum absorption wavelength for a molar concentration in a defined optical path length. It is important to recognize that the photophysical properties (e.g., fluorescence lifetime and quantum yield) of some fluorescent molecules can be influenced by their local microenvironmental factors, such as temperature, metallic ion concentration, pH, and solvent polarity.

Fluorescent probes are essential to fluorescence microscopy, and hundreds of them have been discovered or developed for scientific applications, especially in the life sciences. Many classical organic dyes, such as DAPI (4′,6-diamidino-2-phenylindole), FITC (fluorescein isothiocyanate), TRITC (tetramethylrhodamine isothiocyanate), and Texas Red, have been widely used, and the novel ones (e.g., Alexa and cyanine dyes) exhibiting improved photo- and pH-stability as well as excellent spectral characteristics provide additional choices for fluorescent labeling (see www.introgen.com, www.gelifesciences.com, www.sigmaaldrich.com). Especially, advances in immunology and molecular biology have provided insight into the molecular design of fluorescent probes targeted at specific subcellular regions, which can then be visualized by fluorescence microscopy. The greatest revolution in fluorescence microscopy is perhaps led by the discovery of GFP isolated from jellyfish, *Aequorea victoria* [2–5]. Over the past 20 years, a broad range of FP genetic variants have been developed, spanning almost the entire visible light spectrum [6, 7, 14–21]. The usage of FPs in combination with fluorescence microscopy imaging has provided scientists with the ability to visualize and track protein dynamics in living cells, tissues, and even entire organism with high spatial and temporal resolution [6, 7, 17, 22–25]. More recently, the development of

fluorescent semiconductor nanocrystals, widely known as quantum dots (QDs), has provided a new avenue for fluorescence microscopy imaging [26–33]. QDs contain a semiconductor core, e.g., Cd and Se, which is surrounded by a semiconductor shell (ZnS) to improve their optical properties. The wide range of QD fluorescence emission peaks stems from their tunable core sizes (1–10 nm). QDs show broad absorption patterns but very narrow emission spectra, making QDs very useful for fluorescence multiplexing and high-throughput screening [34]. Even though majority of biological samples visualized by fluorescence microscopy imaging are treated with extrinsic fluorescent probes, there are endogenous fluorophores in living organisms which have been utilized in life sciences and clinical applications. For example, FLIM measurements of endogenous NADH in tissues show promise for the study and diagnosis of precancer conditions and cancers because the fluorescence properties of NADH are altered by cellular metabolism [35] (see Sect. 3.4.3).

3.3 Fluorescence Microscopy Techniques

Numerous fluorescence microscopy techniques have been developed, and many of them are well described with interactive JAVA tutorials at the Molecular Expressions website: http://www.micro.magnet.fsu.edu/primer/techniques. Several commonly used and advanced fluorescence microscopy techniques are introduced below, including widefield microscopy, single-photon excitation (SPE) confocal microscopy, two-photon excitation (TPE) microscopy, total internal reflection fluorescence (TIRF) microscopy, Förster (or fluorescence) resonance energy transfer (FRET) microscopy, fluorescence recovery after photobleaching (FRAP) microscopy, fluorescence correlation spectroscopy (FCS), image correlation spectroscopy (ICS), stimulated emission depletion (STED) microscopy, photoactivated localization microscopy (PALM), and stochastic optical reconstruction microscopy (STORM). All these fluorescence microscopy techniques are now available in commercial microscope systems.

3.3.1 Widefield Epifluorescence Microscopy

Widefield microscopy is the most widely used fluorescence microscopy technique. The basic setup of an inverted widefield epifluorescence microscope is illustrated in Fig. 3.2, which also explains the basic principle of epifluorescence microscopy imaging. Any colored (from violet to red) fluorescent probe can be imaged by a widefield microscope equipped with a mercury or xenon arc lamp or X-Cite (www.ldgi-xcite.com) light source, given a correct combination of the excitation and emission filters and a dichroic mirror (see Fig. 3.2). Multicolor time-lapse imaging can be achieved in a widefield microscope equipped with software-controlled excitation and emission filter wheels and shutters, perfect for monitoring signaling

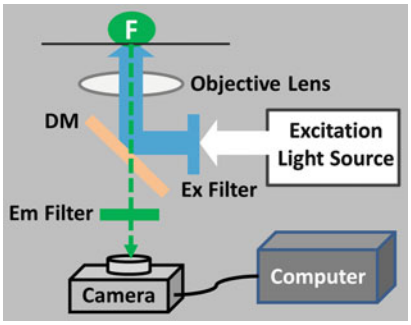

Fig. 3.2 The basic setup of an inverted widefield epifluorescence microscope. In widefield epifluorescence microscopy, imaging a fluorescent sample (F) requires a correct combination of the excitation (Ex) and emission (Em) filters and a dichroic mirror (DM), which is chosen based on the Ex and Em spectra of the fluorophore. The specific Ex wavelengths of light for the fluorophore are selected from the Ex light source (such as an arc lamp) passing through the Ex filter; the selected light is then reflected by the DM to excite the F through the objective lens (blue line trajectory); the light emitted from the excited fluorophores and collected by the same objective (*green dashed line*) will transmit through the DM and the Em filter before reaching the detector (usually a charge-coupled device (CCD) camera)

events in living cells using fluorescent reporters as long as the axial resolution is not a concern. For example, imaging genetically encoded fluorescent indicators (chameleons) for Ca^{2+} using widefield microscopy has allowed the measurements of Ca^{2+} signals in the cytosol and organelles [36–38]. An example of applying widefield microscopy to study protein-protein interactions in living cells based on FRET is shown in Fig. 3.3 (see Sect. 3.3.5). The axial resolution in widefield microscopy is poor due to the out-of-focus light contamination and can be improved by applying iterative constrained 3-D deconvolution techniques [39–42].

3.3.2 Single-Photon Excitation (SPE) Confocal Microscopy

The principle of SPE confocal microscopy or laser scanning confocal microscopy (LSCM) imaging was introduced in 1957 by Marvin Minsky. The invention of laser in the 1960s and advances in laser technologies in the past 50 years have made confocal microscopy a major imaging tool for biologists today [44–46]. For example, a new supercontinuum laser (also called white-light laser) tunable from 470 to 670 nm in 1 nm increments has been equipped in Leica TCS SP5 X confocal microscopes, giving scientists more choices of imaging with various fluorescent probes compared to a regular confocal microscope that only carries fixed laser lines [47]. Compared to conventional widefield microscopy, confocal microscopy offers much higher axial resolutions by using spatial filters to eliminate or minimize the out-of-focus light and provides the capability to collect serial optical sections (like

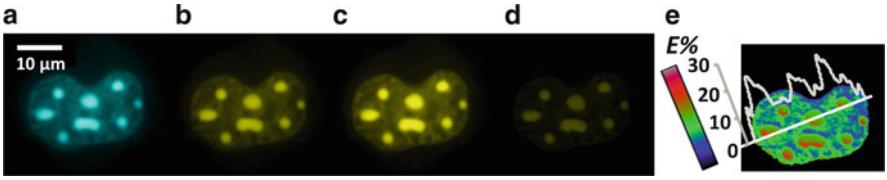

Fig. 3.3 Demonstration of the homodimerization of the CCAAT/enhancer-binding protein alpha (C/EBPα) in live mouse pituitary cell nuclei using widefield FRET microscopy. Images from the nucleus of a cell coexpressing CFP-C/EBPα (FRET donor) and YFP-C/EBPα (FRET acceptor) were acquired in the donor (a), acceptor (b), and FRET (c) imaging channels using an Olympus IX70 widefield epifluorescence microscope equipped with a ×60/1.2NA water objective lens, a Hamamatsu Orca2 CCD camera, and an X-Cite ® 120 fluorescence illumination system (www.ldgi-xcite.com). The processed FRET (PFRET, d) and apparent FRET efficiency (E%, e) images were obtained after processing the data with the PFRET algorithm in combination of the images acquired from the single-label expressing cells (see Sect. 3.3.4). The interaction between CFP- and YFP-tagged C/EBPα is demonstrated by the E% image, indicating the homodimerization of C/EBPα in regions of centromeric heterochromatin of cell nucleus. For each imaging channel, the same dichroic mirror designed for imaging both CFP (445–485 nm) and YFP (520–580 nm) was used, and the excitation and emission filters were 436/20 nm and 470/30 nm (donor channel), 500/20 nm and 535/30 nm (acceptor channel), and 436/20 nm and 535/30 nm (FRET channel). See Sect. 3.4.6 for more details about the C/EBPα biological model (Adapted from [43])

CAT scan) from a thick specimen [48, 49]. For example, a laser scanning confocal microscope (LSCM) focuses a laser beam on a single point of a specimen through an objective lens and uses a point detector – usually a photomultiplier tube (PMT) and occasionally an avalanche photodiode (APD); a pinhole is placed before the detector to reject the out-of-focus light (light signal above and below the focal plane); a 2-D image is obtained by moving the laser beam over a region of interest of the specimen through the XY raster point-scanning mechanism; a stack of 2-D images at the different depths of the specimen are acquired by moving the microscope objective lens or stage along the optical axis. Compared to LSCM, a spinning-disk confocal microscope can provide a much faster imaging speed since it employs a number of pinholes designed in a specific pattern to focus laser beams at multiple points of a specimen and uses a charge-coupled device (CCD) camera to acquire a 2-D image [49–51]. Confocal microscopy has been applied to a wide range of biological applications [46] – an example of applying an LSCM to study the receptor-ligand binding and internalization based on FRET [52–54] is shown in Fig. 3.4 (see Sect. 3.3.4). Many aspects related to confocal microscopy imaging techniques and data analysis for various applications are described in the literature [55].

3.3.3 Two-Photon Excitation (TPE) Microscopy

Two-photon absorption was theoretically predicted by Göppert-Mayer in 1931. TPE imaging experiments in a laser scanning confocal microscope were first demonstrated in 1990 [56]. In a TPE event, two photons, each of which carries

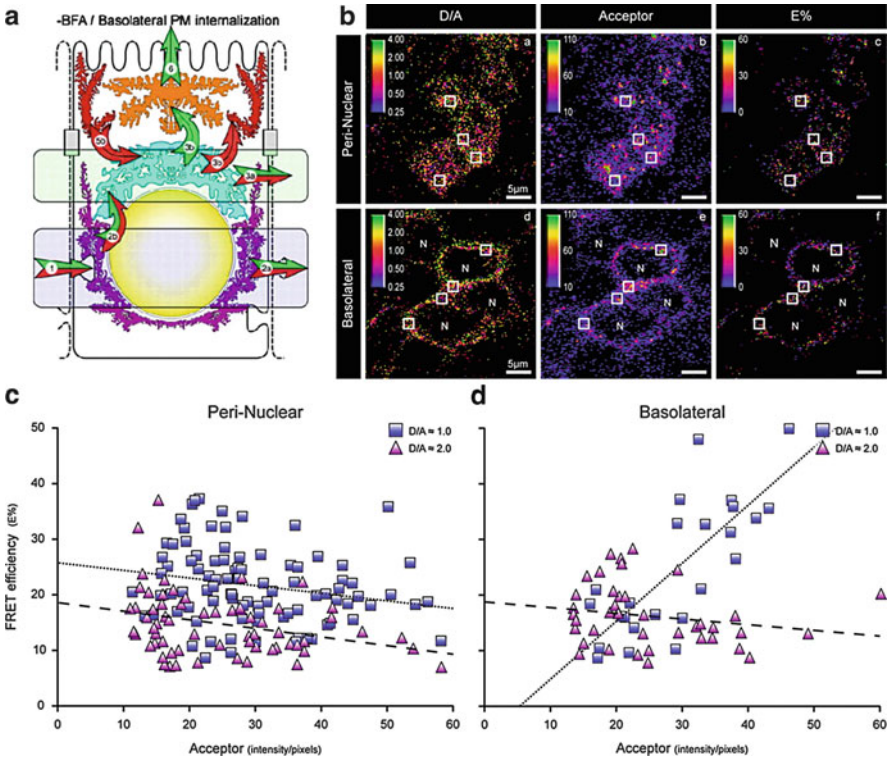

Fig. 3.4 Tracking the internalization of transferrin receptor-ligand complexes in live polarized MDCK cells using confocal FRET microscopy. (**a**) The organization and distribution of pIgA-R and TFR complexes in endosomes that are localized at the basolateral (*blue rectangle*) and perinuclear (*green rectangle*) regions was assayed using confocal FRET microscopy after co-internalization of Cy3-Tfn (FRET acceptor) and Alexa488-pIgA-R ligand (FRET donor) from the basolateral PM of live polarized MDCK-PTR cells. (**b**) Pseudocolor images, processed using the PFRET algorithm in combination of single-label images (see Sect. 3.3.4), depict the pixel-by-pixel distribution of the "donor to acceptor" ratio (D/A – a, d), acceptor (b, e), and apparent FRET efficiency (E% – c, f) levels at the perinuclear (a–c) and the basolateral (d–f) regions. Examples of selected ROIs that were selected according to the definitions of basolateral and perinuclear endocytic regions are shown as *white squares*. (**c** and **d**) The E%, D/A, and acceptor levels were calculated for a wide range of ROIs (*white squares*). E% values were plotted as a function of the acceptor levels for $D/A \approx 1$ () and for $D/A \approx 2(\Delta)$, with *trend lines* ($D/A \approx 1$, *dotted line*; $D/A \approx 2$, *dashed line*). (**c**) E% is largely independent of the acceptor levels and increases with decreasing D/A ratios, suggesting a clustered organization of TFR and pIgA-R complexes in perinuclear endosomes. (**d**) E% shows a variable dependency on the acceptor levels depending on D/A, indicating a mixed/random organization of TFR and pIgA-R complexes in basolateral endosomes. More details about this assay are described in the literature [52–54] (Adapted from [54])

approximately half of the energy to excite a molecule in a single-photon excitation event, are simultaneously absorbed by the molecule, resulting in the emission of a fluorescence photon. The probability for the two-photon absorption depends on the

colocalization of two photons within the absorption cross section of the fluorophore. The rate of excitation is proportional to the square of the instantaneous intensity. This extremely high local instantaneous intensity is produced by the combination of diffraction-limited focusing of a single laser beam in the specimen plane and the temporal concentration of a femtosecond mode-locked laser (typically of the order of 10^{-50} to 10^{-49} cm^4s/photon/molecule) [57]. Multiphoton (i.e., 3-photon or 4-photon) excitation microscopy is the extension of TPE microscopy [58]. Compared to SPE confocal microscopy (see Sect. 3.3.2), TPE microscopy offers several advantages listed in Table 3.1. TPE microscopy has been widely used in many areas of the biomedical sciences including cell biology, microbiology, molecular biology, developmental biology, neuroscience and neurology, tissue engineering, etc. [48, 59–66]. In Sect. 3.4, we describe an example of employing TPE to implement a FLIM system used for studying protein-protein interactions in living cells.

3.3.4 FRET Microscopy

FRET is the nonradiative energy transfer from an excited molecule (the donor) to another nearby molecule (the acceptor) via a long-range dipole-dipole coupling mechanism. The most basic concepts of FRET are described by Eqs. 3.1–3.2 [67–70] (also see Chapter 13 in [13]) and Fig. 3.5. More details about FRET theory and history can be read in the literature [71].

$$E = \frac{\mathrm{Ro}^6}{(\mathrm{Ro}^6 + r^6)} \quad \text{or} \quad r = \mathrm{Ro}\left[\left(\frac{1}{E}\right) - 1\right]^{\frac{1}{6}} \tag{3.1}$$

$$\mathrm{Ro} = 0.211\{\kappa^2 \cdot n^{-4} \cdot \mathrm{QY_D} \cdot J\}^{\frac{1}{6}}, \quad J = \in_{\mathrm{A}} \frac{\int_0^\infty f_{\mathrm{D}}(\lambda) f_{\mathrm{A}}(\lambda) \lambda^4 \mathrm{d}\lambda}{\int_0^\infty f_{\mathrm{D}}(\lambda) \mathrm{d}\lambda} \tag{3.2}$$

As shown in Eq. 3.1 and Fig. 3.5A, the efficiency of energy transfer (E) from the donor to the acceptor is dependent on the inverse of the sixth power of the distance (r) separating them, subject to Ro – a characteristic distance at which half of the excited-stated energy of the donor is transferred to the acceptor ($E = 50$ %). The correct calculation form of Ro (named Förster distance) was first described by Theodor Förster in the mid-1940s [67, 68]. Determination of the Ro (in angstrom) for a FRET pair is given by Eq. 3.2, where κ^2 is the dipole moment factor described in Fig. 3.5C; n is the medium refractive index; $\mathrm{QY_D}$ is the donor quantum yield; J is the degree of the overlap between the donor emission spectrum and the acceptor absorption spectrum (see Fig. 3.5B); ε_{A} is the extinction coefficient of the acceptor at its peak absorption wavelength; λ is the wavelength; $f_{\mathrm{D}}(\lambda)$ and $f_{\mathrm{A}}(\lambda)$ are the normalized donor emission and acceptor absorption spectra, respectively. Since FRET is usually limited to distances less than about 10 nm, FRET microscopy

Table 3.1 Comparison of two-photon excitation (TPE) imaging and single-photon excitation (SPE) confocal imaging

Characteristics	Two-photon	Confocal
Excitation source	Femtosecond or picosecond pulsed IR lasers with 80–100 MHz repetition rates; tunable 650–1300 nm; CW also possible	CW or pulsed UV/visible lasers; white-light or supercontinuum lasers (tunable in the visible and IR spectrum range) are available
Excitation/emission separation	Fluorescent emissions of UV and visible fluorophores can be well separated from a TPE wavelength	Usually close, depending on the Stokes shift
Detection	The detector can be a PMT (typically), an APD, or a CCD camera. No pinhole	The detector can be a PMT (typically), an APD, or a CCD camera. Pinhole(s) required
Excitation volume selectivity	Intrinsic (fraction of femtoliter)	Determined by the pinhole dimension
Imaging penetration	TPE can go deeper than 400 μm, although problems can be caused by pulse shape modifications and scattering	About 50–100 μm, depending on specimens
Spatial resolution	Diffraction limited, depending on the objective lens. Theoretically, spatial resolution in TPE is less than that in confocal because of the IR excitation wavelength. However, TPE often gives a higher signal-to-noise ratio	Diffraction limited, depending on the objective lens
Photobleaching and photo damage	TPE typically causes less photo damage and photobleaching since only the fluorophores within the small TPE volume are excited and infrared light is less toxic	Photobleaching is usually a concern for time-lapse confocal imaging. Photo damage can be an issue in confocal imaging of UV fluorophores

provides a sensitive tool for investigating a variety of phenomena that produce changes in molecular proximity. Counting the number of FRET-related publications in many diverse fields of the life sciences has shown an exponential growth in FRET applications since the early 1990s [43] – the list of publications in each category is available at http://www.kcci.virginia.edu/Literature.

FRET depopulates the excited state of the donor, resulting in a decreased probability of the photon emission from the donor and a shortening in the fluorescence lifetime of the donor; meanwhile, the probability of the photon emission from the acceptor increases (sensitizes). Measurement of each event can provide direct proof of the energy transfer. Various FRET microscopy methodologies have been developed using widefield, SPE confocal, and TPE microscopy [43, 72–76]. Acceptor photobleaching or donor dequenching FRET microscopy methods

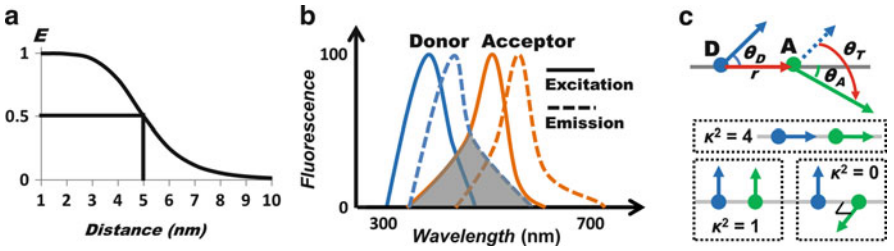

Fig. 3.5 Basic concepts of FRET. FRET is the nonradiative energy transfer from an excited-state donor (D) to an acceptor (A) at the ground state, in close proximity (1–10 nm), via a long-range dipole-dipole coupling mechanism. The energy transfer efficiency (E) from the D to the A of a FRET pair is dependent on the inverse of the sixth power of the distance between them, subject to the Förster distance of the FRET pair (see Eqs. 3.1 and 3.2 in Sect. 3.3.4). (**a**) Plotting E as a function of the D-A distance for a FRET pair with a Förster distance of 5 nm indicates that measuring E can provide sensitive indication on the change of the D-A distance within 2–8 nm. Other than a close distance between the D and the A, FRET also requires (**b**) a significant overlap between the spectra of the D emission and the A excitation (covered by the *gray area*) and (**c**) a favorable dipole moment $-\kappa^2 = (\cos\theta_T - 3\cos\theta_D \cos\theta_A)$, where θ_T is the angle between the transition dipoles of the D emission and the A absorption; θ_D and θ_A are the angles between these dipoles and the vector joining the D and the A; no FRET occurs for $\kappa^2 = 0$, and the likelihood of FRET increases with a larger κ^2 (Adapted from [43])

estimate the E by measuring the intensity change of the donor in the absence and the presence of the acceptor [77–79]. FLIM-FRET methods quantify the E from measuring the change in the donor lifetimes in the absence and the presence of the acceptor (described in Sect. 3.4). The most commonly used FRET microscopy methods are based on the detection of the sensitized emission from the acceptor – the FRET signal. For example, ratiometric FRET microscopy provides a simple way to demonstrate the change in FRET significances due to different treatments for a biological system with a fixed stoichiometry of the donor and the acceptor (e.g., FRET-based biosensors) [80–82]. However, quantitative determination of the E in sensitized emission measurements usually requires removing the spectral bleedthrough (SBT) components from the donor and the acceptor that contaminate the FRET signal, and many algorithms have been developed for this purpose [83–100].

We developed the processed FRET (PFRET) method that utilizes both donor-alone and acceptor-alone control specimens and algorithm-based software to achieve accurate SBT corrections for different donor and acceptor fluorescence levels [93, 100, 101] (also see Chapter 7 in [74]). Two examples of applying PFRET in biological studies are presented here: (1) detect dimerization of C/EBPα in live mouse pituitary cell nuclei using a widefield microscope (see Fig. 3.2) and (2) study receptor-ligand binding and internalization in polarized live MDCK cells using a confocal microscope (see Fig. 3.3). We also developed the spectral FRET (sFRET) microscopy method [97]. Spectral imaging microscopy produces λ-stacks consisting of x-, y- (spatial), and λ- (spectral) dimensions, measuring the emission signals in a series of spectral intervals equally sampled over a spectral range at each

pixel location [102–105]. This is an ideal technique to implement FRET imaging in living cells and to establish the existence of a FRET signal "on the fly." Given the reference spectra obtained from the donor-alone and acceptor-alone specimens, linear unmixing the λ-stack acquired from a specimen containing both donors and acceptors can separate the signals emitted from the donors and the acceptors. Thus, spectral imaging microscopy combined with linear unmixing provides an accurate way of removing the SBT contaminations resulting from the donor [103]. In sFRET microscopy, the acceptor SBT is removed by employing the same strategy used in the PFRET approach. Recently, we have developed a straightforward 3-color spectral FRET (3sFRET) microscopy method and demonstrated its utility for studying the interactions between three fluorescently labeled proteins in a single living cell [43,106]. The 3-color FRET microscopy approach provides the capability to simultaneously track the interactions between three fluorescently labeled cellular components that form complexes, clusters, or discrete associations during cellular signaling or trafficking events in the same region of interest over four dimensions (3-D + time).

To evaluate the accuracies of different FRET microscopy methods, the Vogel laboratory (NIH/NIAAA) developed a set of genetic constructs encoding fusion proteins containing donor and acceptor FPs separated by protein linkers of defined length [96, 107]. For each genetic construct expressed in living cells, there was consensus in the E results obtained by different FRET microscopy methods [100, 107], demonstrating that they could serve as FRET standards. The FRET-standard approach has been used by us to calibrate our FRET microscopy methods (see an example in Sect. 3.4.3) as well as to test the utilities of new FPs for FRET studies [47, 108].

3.3.5 Other Advanced Microscopy Techniques

Total internal reflection fluorescence (TIRF) microscopy provides a restricted illumination depth (typically < 100nm) into a specimen using an evanescent wave which is generated by having the excitation light totally reflected at the surface between the glass coverslip (refractive index $= \sim 1.518$) and the aqueous medium of the specimen (refractive index $= 1.33 \sim 1.37$). Thus, TIRF microscopy yields an ultrahigh signal-to-noise ratio for imaging fluorescent molecules within ~ 100 nm above the coverslip and is an ideal live-cell imaging tool for visualizing membrane proteins, studying protein-protein interactions at cell membrane surface, and investigating the mechanism and dynamics of many proteins involved in cell-cell contact [109–111]. TIRF microscopy has also been used for imaging single molecules and superresolution microscopy imaging (described below). TIRF microscopy can be purchased from any leading commercial microscope companies such as Carl Zeiss, Leica, Nikon, Olympus, etc.

Fluorescence recovery after photobleaching (FRAP) microscopy and associated techniques (e.g., fluorescence loss in photobleaching (FLIP) microscopy) are very

useful for investigating the kinetic behavior (diffusion and binding) of proteins in living cells and have been widely used by biologists to study a range of proteins (especially membrane proteins) since the emergence of GFP [112–114]. In a FRAP experiment, the fluorescent molecules in a selected region of interest of a cell are bleached using high-intensity excitation light (bleaching phase), followed by monitoring the diffusion of new fluorescent molecules into the bleached area over a period of time with low-intensity excitation light (recovery phase); fitting the recorded data into a defined kinetic model can provide quantitative estimates for the mobile fraction of the fluorescent molecules and the rate of mobility.

Fluorescence correlation spectroscopy (FCS) (also called fluorescence fluctuation spectroscopy), originally developed by Magde, Elson, and Webb [115], has become a major imaging tool for studying molecular diffusion, binding, and interactions both *in vivo* and *in vitro* [116–120]. FCS measurements are usually carried out at selected points of a sample on a confocal or 2P scanning microscope equipped with a high numerical aperture objective lens and photon-counting PMT or APD detectors. At each point, the intensity fluctuations due to number of fluorescent molecules moving into or out of the excitation volume are recorded and then analyzed to estimate the diffusion rate and concentration of the fluorescent molecules. Compared to FRAP, FCS can reveal much faster dynamics such as blinking [121]. Fluorescence cross-correlation spectroscopy (FCCS) is an extended version of FCS and allows studying the dynamic interactions between two differently colored species [117, 118, 120].

Image correlation spectroscopy (ICS) (also called image correlation microscopy) and associated techniques, including image cross-correlation spectroscopy (ICCS) [122–125], raster image correlation spectroscopy (RICS), and cross-correlation RICS [121, 126, 127], were derived from FCS and FCCS and have also been used to measure diffusion coefficients, flow rates, and concentrations of fluorescently labeled proteins in cells. Image correlation techniques can be implemented on a regular confocal or TPE scanning microscope. Using both ICS- and FCS-related techniques, quantitative characterization of the diffusion and concentration parameters based on a defined diffusion model requires calibration of the size of the excitation volume for fitting the correlation function calculated from the measured data into the model.

Superresolution microscopy refers to a collection of several new fluorescence microscopy techniques, which provide sub-diffraction-limited resolutions. Due to the diffraction limit elucidated by Ernst Abbe in the late 1800s, the fundamental resolution limit of light microscopy is approximately 200 nm. Recently, several techniques including STED microscopy, PALM, and STORM have been demonstrated to circumvent this physical barrier and to achieve lateral resolutions of less than 50 nm [128–130]. STED microscopy [131–133] uses two lasers: one for excitation of the fluorophores to induce their fluorescent state and the other for de-excitation of the fluorophores by means of stimulated emission; this achieves the sub-diffraction-limited resolution by engineering the point spread functions of the two laser beams so that only the fluorophores within a sub-diffraction-limited volume get excited. Both PALM [134–138] and STORM [139–141] utilize

photoactivatable (dark to bright) fluorescent probes and intermittently turn on individual fluorescent molecules which are imaged and then photobleached. This process allows the molecules within the same diffraction-limited volume to be temporally separated and the location of each activated molecule under a sub-diffraction-limited resolution to be determined. The final superresolution image is obtained from merging all of the single-molecule positions localized by repeated cycles of photoactivation followed by imaging and photobleaching.

3.4 FLIM and Implementation of a TPE-TCSPC FLIM System

Fluorescence lifetime is the average time a molecule spends in the excited state before returning to the ground state, typically with the emission of a photon, and it carries information about events in the probe's local microenvironment that affect the photophysical processes (see Chapter 1 in [142]). For most of the fluorescence microscopy methods, the fluorescent signal is quantified by integrating the emitted photons over a period of time which is usually much longer than the fluorescence lifetime – referred to as steady-state (or intensity-based) imaging. In contrast, FLIM measures the fluorescent signal at a very high temporal resolution (down to picoseconds (ps)) and is thus able to resolve the fluorescence lifetime information. Table 3.2 summarizes several advantages and limitations of FLIM compared to steady-state (intensity-based) imaging microscopy.

3.4.1 Overview of FLIM Techniques and Applications

The first nanosecond fluorescence lifetime measurements in optical microscopy were made in 1959 [143]. Since then, numerous FLIM methodologies have evolved for various biological and clinical applications [142]. Especially in the last 10 years, commercial FLIM systems have become available from companies, including Becker & Hickl (www.becker-hickl.de), PicoQuant (www.picoquant.com), ISS (www.iss.com), Intelligent Imaging Innovations (www.intelligent-imaging.com), and Lambert Instruments (www.lambert-instruments.com).

FLIM techniques are generally subdivided into the time-domain (TD) and the frequency-domain (FD) methods [142] (also see Chapters 4 and 5 in [55]). The basic physics that underlies the two methods is essentially identical, since both TD and FD are finite Fourier transforms of each other. The TD method uses a pulsed light source synchronized to high-speed detectors and electronics to measure the fluorescence decay profile at different time windows after each excitation pulse. The fluorescence lifetime is estimated by analyzing the recorded decay profile. Many TD FLIM techniques have been developed. For example, the TCSPC FLIM technique has been commonly implemented on single-photon confocal or multiphoton scanning microscopes using PMTs with high time resolutions (25–300 ps) [144–148]. Design

Table 3.2 The advantages and limitations of FLIM over steady-state (intensity-based) imaging microscopy

Aspects	Advantages	Limitations
General applications	The fluorescence lifetime of a fluorophore is sensitive to its environmental changes; FLIM can be a good choice for visualizing those changes that cannot be revealed by steady-state imaging methods, such as calcium binding, change in pH, etc.	FLIM is preferably applied to live specimens in life-science applications, since it can be difficult to distinguish the real fluorescence lifetime changes from those caused by the fixative in fixed specimens
FRET measurements	Since only donor signals are measured for determining the energy transfer efficiency in FLIM-FRET, the method does not usually require the corrections for spectral bleedthrough that are necessary for intensity-based measurements of sensitized emission from the acceptor (see Sect. 3.4)	In FLIM-FRET, it is important to make sure that the donor fluorophores reside in the same microenvironment in both donor-alone control specimens and specimens containing both donor and acceptor fluorophores, since the fluorescence lifetime of a fluorophore can be affected by its microenvironment
	The FLIM-FRET approach has the capability to estimate the percentage of the interacting and noninteracting donor populations, which cannot be distinguished by most of intensity-based FRET methods	The donor molecule whose intrinsic lifetime has multiple components is not suitable for FLIM-FRET, since it will complicate the data analysis
Data acquisition and analysis	FLIM can provide both lifetime and intensity information	As technology improves, the FLIM data acquisition time is expected to decrease. Currently this time varies from seconds to minutes depending on the setup of a FLIM system – particularly the detector, as well as the specimens to be imaged
	Fluorescence lifetime measurements are insensitive to the change in fluorophore concentration, excitation intensity, or light scattering and to some extent of photobleaching – all these factors commonly induce false information in intensity-based imaging	Some understanding of the physics of fluorescence lifetime is required for processing the FLIM data and interpretation of the results, particularly for a biological system
	FLIM can help to discriminate the intrinsic fluorescence of a specimen, i.e., autofluorescence	

of a TPE-TCSCP FLIM instrument is described in detail in Sect. 3.4.2. PMT arrays have also been employed in TCSPC FLIM systems to obtain spectrally resolved lifetimes [149, 150]. To achieve faster lifetime imaging speeds, the camera-based TD FLIM techniques have been developed using high-speed gated image intensifier cameras [151–154] or streak cameras [155, 156]. A gated image intensifier camera can be operated at a superfast speed to detect photons within a time (gating) window for a few hundred picoseconds to a few milliseconds relative to the excitation pulse [152]. In gating-camera FLIM, a number of images are acquired in sequential gating windows after the excitation pulse to estimate the lifetimes, and extracting single-component lifetimes requires collecting two gated images at minimal, which only takes a few seconds [152, 153]. A streak camera can be operated to transform the temporal profile of a light pulse into a spatial profile on a detector by causing a time-varying deflection of the light across the width of the detector [155]. In streak-camera FLIM, a number (y-dimension) of 2-D (x-dimension, time relative to the excitation pulse) images are acquired to estimate an XY 2-D lifetime distribution, and each line of an image consists of the time-resolved information for a pixel location [155].

The FD method uses a modulated light source to excite a fluorophore and measures the phase shift(s) and amplitude attenuation(s) of the emission signal relative to the excitation source, which are then analyzed to estimate the fluorescence lifetime. The fundamental modulation frequency of the excitation source is chosen depending upon the fluorescence lifetime to be measured – e.g., megahertz should be used for measuring nanosecond (ns) fluorescence lifetimes. The phase shift(s) and amplitude attenuation(s) can be measured by a detector modulated at the same frequency as the excitation source (homodyne methods) or a frequency slightly different (a few hundred to a few thousand hertz) from the excitation source (heterodyne methods). Similar to the TD FLIM techniques, a number of FD FLIM techniques have also been developed and implemented on both single-photon or multiphoton scanning [146] and camera-based spinning-disk or widefield microscopes [157–160]. Spectrally resolved FD FLIM system is also available [161]. In addition, a recently developed FD FLIM technique called digital FD FLIM employs a pulsed excitation source and does not modulate the detector at all, thus allowing for the acquisition of the entire fluorescence signal [162].

One of the major FLIM applications is to measure FRET (see Sect. 3.3.4) between fluorescent molecules, although the acceptor molecules need not be fluorescent. Using FLIM, FRET events can be identified by measuring the reduction in the donor lifetime that results from quenching in the presence of an acceptor, and the energy transfer efficiency (E) can be estimated from the donor lifetimes determined in the absence (τ_{D}– unquenched lifetime) and the presence (τ_{DA}– quenched lifetime) of the acceptor (Eq. 3.3) (see Chapter 13 in [13]).

$$E = 1 - \frac{\tau_{\mathrm{DA}}}{\tau_{\mathrm{D}}} \tag{3.3}$$

Since only donor signals are measured for determining E in FLIM-FRET, the method does not usually require the corrections for spectral bleedthrough that

are necessary for intensity-based measurements of sensitized emission from the acceptor (see Sect. 3.3.4). The fluorescence lifetime is not sensitive to the change in fluorophore concentration, excitation light intensity, or light scattering; these facts make FLIM-FRET an accurate method for FRET measurements. A number of FLIM-FRET methods have been developed for studying protein-protein interactions and investigation of signaling events in a variety of biological systems [142, 163, 164]. For example, we developed a fast widefield TD FLIM system using a gated intensifier camera and TPE [152] and also implemented a TPE-TCSPC FLIM system (described below). The protocols for applying both TD and FD FLIM techniques to FRET studies are available in the literature [165, 166].

Other than measuring FRET, FLIM has also been applied to in many other investigations, as seen from the following few examples. High-speed widefield FLIM was employed to measure the change in calcium concentration in live cells using calcium-sensitive probes (e.g., Oregon Green) [144, 167]. TPE-TCSPC FLIM was used to map the microenvironment (response of rigor cross-bridges to stretch) of the myosin essential light chain in skeletal muscle fibers by probing the microenvironment of the interface region of the myosin lever arm domain with coumarin [168]; FLIM was applied to characterize dental disease through imaging endogenous fluorophores in dental tissues [169]. Multiphoton FLIM tomography (3-D + lifetime) distinguished between different types of endogenous fluorophores in human skin [170], and multiphoton multispectral FLIM has shown the potential to become a valuable technique in stem cell research [171]. Nicotinamide adenine dinucleotide (NAD^+) is a coenzyme found in all living cells and carries electrons from one reaction to another through redox reactions in metabolism. When NAD^+ accepts electrons from other molecules, it forms NADH which is highly fluorescent with peak absorption and emission maxima at 340 and 460 nm (see Chapter 3 in [13]) and can be imaged with TPE microscopy [172]. Thus, NADH can serve as a convenient noninvasive fluorescent probe of the metabolic state. Since the fluorescence lifetimes of NADH usually increase upon its binding to proteins, FLIM has been applied to detect the free (shorter lifetime) and bound (longer lifetime) forms of NADH, showing promise in cancer research [173–176].

3.4.2 Design of the TPE-TCSPC FLIM System

TCSPC is a commonly used time-domain FLIM method, and the basic principle of TCSPC is described in the literature [147, 177]. The key of TCSPC FLIM is to be able to record both the spatial (x, y, z) information of each detected photon and its arrival time relative to the corresponding excitation event. In general, the major components of a TCSPC FLIM system include a microscope, a pulsed laser (one- or two-photon), a high-sensitivity detector (PMT or APD), a computer plus TCSPC devices, and a photodiode that generates the laser pulse reference fed to the TCSPC devices. The repetition rate and the pulse width of the pulsed laser should be determined depending on the lifetime values to be measured. For example, the measurement of nanosecond lifetimes requires megahertz repetition rates.

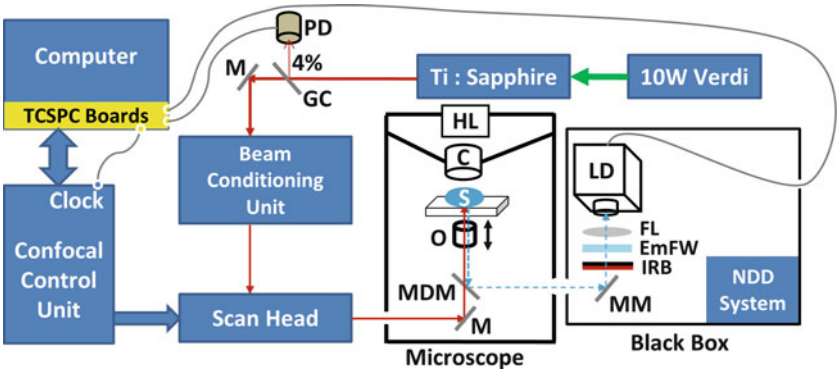

Fig. 3.6 The basic schematic of the TPE-TCSPC FLIM system. Details are described in Sect. 3.4.2. The excitation source is a 10 W Verdi pumped Ti:sapphire multiphoton (MP) laser, which is coupled to the Bio-Rad Radiance 2,100 confocal/MP control unit for scanning the specimen. The laser pulse reference is generated using a glass coverslip (GC) to reflect 4% of the laser to a photodiode (PD) connected to the TCSPC device. Microscope: HL halogen lamp; C condenser; S specimen; O objective lens; MDM movable dichroic mirror; *black box*: MM movable mirror; IRB infrared light blocker filter; EmFW emission filter wheel; FL focusing lens; LD lifetime detector; NDD system – the non-descanned detecting system for steady-state multiphoton imaging; M – mirror

Our TPE-TCSPC FLIM system was first implemented in 2002 on a Bio-Rad Radiance 2100 confocal/multiphoton (MP) microscope, using a TCSPC module and a fast PMT detector purchased from Becker & Hickl (BH) [148]. The basic schematic of the TPE-TCSPC FLIM system is illustrated in Fig. 3.6. The Bio-Rad system that is attached to a Nikon TE300 inverted epifluorescence microscope and controlled using the LaserSharp 2000 software (http://www.zeiss.com/micro) carries both single-photon (not pulsed) and MP lasers. The TCSPC FLIM system is configured using the MP laser, which is a Coherent 10W Verdi pumped tunable mode-locked ultrafast pulsed laser (Mira 900, www.coherent.com). The MP laser has a repetition rate of 78 MHz and a pulsed width of less than 150 femtoseconds (fs) with a tunable range of wavelengths (700–1,000 nm). A laser spectrum analyzer (Model E201, www.istcorp.com) is used to monitor the TPE wavelength, and the power is measured at the specimen plane using a power meter (Model SSIM-VIS & IR, www.coherent.com). The MP laser is coupled to the Bio-Rad confocal/multiphoton control unit to scan the specimen via an XY raster scanning mechanism using galvo mirrors.

A specific dichroic mirror (670UVDCLP) equipped on the microscope filter-cube slider needs to be selected for fluorescence lifetime imaging, and this dichroic mirror transmits the MP laser (670–1,000 nm) through the objective lens to excite the specimen and reflects the emission light to the external (non-descanned) detectors in a sealed black box. There are three non-descanned PMT detectors including the lifetime detector and the other two PMT detectors that are used for the TPE steady-state imaging. The emission light is routed by a movable mirror and then focused

onto the lifetime detector via a biconvex lens, before which a filter that blocks infrared light and transmits visible light (BG-36, www.chromatech.com) as well as an emission filter is placed. The lifetime detector was a BH PMH-100-0 module with a full width at half maximum (FWHM) response time of ∼150 ps, which was recently upgraded to the BH hybrid HPM-100-40 module with a FWHM response time of ∼120 ps. The hybrid lifetime detector uses a GaAsP PMT and offers higher quantum efficiencies, lower dark counts, and no after-pulsing (see the application note "HPM-100-40 Hybrid Detector" at www.becker-hickl.de/literature.htm), which are the important characteristics for choosing a lifetime detector.

The TCSPC device is controlled using the BH SPCM software v8.91 and contains PC plug-in boards (commercially available) that function as the time-to-amplitude converter, time-to-digital converter, discriminator, and multichannel analyzer [177] (also see the BH handbook available at http://www.becker-hickl.de/literature.htm#handb). The TCSPC device synchronizes the lifetime detector to the TPE pulse and the scanning clock and records both the arrival time relative to the TPE pulse and the spatial (x, y, z) information for each detected photon. The reference beam for a TPE pulse is acquired using a glass coverslip to reflect 4 % of the MP laser to be converted by a photodiode to the reference signal that is fed to the TCSPC device. Given a time period (a few seconds or minutes) of accumulating emitted photons for thousands or millions of TPE pulses, a "photon counts" histogram (often termed as a decay profile) is built for each pixel of an image. The time binning of the histogram depends on the time resolution of the TCSPC module: the SPC-730 module used before provides a resolution of ∼156 ps or 64 time windows in ∼10 ns; the SPC-150 module currently used offers a resolution of ∼39 ps or 256 time windows in ∼10 ns. The lifetime image is obtained by processing the decay data using the BH SPCImage software v2.9.2.2989 (described below).

Since the lifetime detector is extremely sensitive, it is important to place the lifetime detector in a sealed black box (see Fig. 3.6) to minimize ambient light detection. It is also suggested to cover the specimen chamber with a black cap to avoid the reflection from the condenser of an inverted microscope. A TCSPC FLIM system should be located away from any instruments which operate based on magnetic fields, since the magnetic field will damage the lifetime detector. Magnetic field interference can be avoided by putting a wire mesh around the whole system or the detector. The FLIM system should be ideally placed on an antivibration table in a room with a temperature of ∼20°C. The room temperature should be consistent, and its variance should not exceed ±2°C.

3.4.3 Measuring the Instrument Response Function (IRF) of the TPE-TCSPC FLIM System

In time-domain FLIM, a measured decay is the convolution form of the intrinsic fluorescence decay and the IRF. The distortions can be caused by the finite rise time, the width, and the decay of the excitation pulse, as well as the detector and

timing apparatus. Therefore, an iterative deconvolution routine with an input IRF is often employed to estimate the lifetime information from measured decay data based on a weighted least-squares numerical approach. Determining the IRF of a TCSPC FLIM system is essential to achieve accurate lifetime information. Although the IRF can be numerically estimated from acquired decay data, it is preferable to directly measure the IRF experimentally. The IRF should be representative of the experimental conditions and thus is ideally measured under the same conditions used for biological specimens, such as using the same objective lens and optical configurations and applying the same TCSPC and detector settings. More importantly, the IRF of a TCSPC FLIM system should be checked periodically and ideally measured before each experiment, since the IRF can change by reflections in the optical path or by poor mode locking of the MP laser.

The IRF is commonly measured by recording either the scattered excitation light or the decay of a fast reference dye such as Rose Bengal in phosphate buffer pH 7.4 (lifetime $= \sim$70 ps) [178]. For visible light excitation, a strongly scattering specimen such as nondairy coffee creamer is conventionally used for IRF measurements [151]. For infrared light excitation, the IRF can be measured using a sample that yields second-harmonic generation (SHG) signals (see the application note "Recording the Instrument Response Function of a Multiphoton FLIM System" at www.becker-hickl.de/literature.htm). SHG is an ultrafast nonlinear process that delivers a signal at one-half of the excitation wavelength. Two IRFs measured from our TPE-TCSPC FLIM system by recording the SHG signals of the urea crystal sample are shown in Fig. 3.7: (1) use the 880-nm excitation wavelength and record the SHG signals at 440 nm using a 460/50-nm emission filter, and (2) use the 940-nm excitation wavelength and record the SHG signals at 470 nm using a 480/40-nm emission filter. The IRF is not influenced by using different TPE wavelengths because the pulse width of the MP laser ($<$150 fs) is much shorter than the time response of the lifetime detector ($\sim$150 ps), which is the main determinant of the FWHM of the IRF.

3.4.4 Calibration of the TPE-TCSPC FLIM System Using Fluorescence Lifetime Standards

Prior to any scientific investigation, a FLIM system must be calibrated with standard fluorophores of known lifetimes. There are many standard fluorophores that can be used for the calibration of a FLIM system (see Appendix II in [13] and also an online source at http://www.iss.com/resources/reference/data_tables). It is preferable to choose standards whose excitation, emission, and fluorescence lifetime properties are close to those of the fluorophores in the intended samples, so that the same imaging setup used for biological samples can be applied for calibration. Very importantly, the fluorescence lifetime standard has to be carefully prepared according to the reference, such as solvent, pH, and temperature, etc., because these

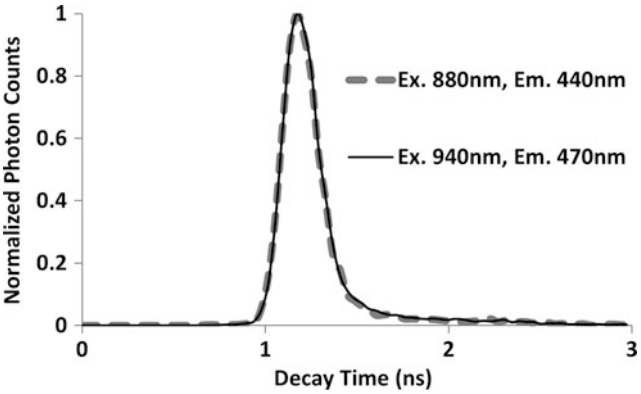

Fig. 3.7 Comparison of the two measured instrument response functions (IRFs) of the TPE-TCSPC FLIM system. Both IRFs were measured through collecting the second-harmonic generation (SHG) signals emitted from urea crystals. At the 880-nm excitation wavelength, the 440-nm SHG emission signals were collected using a 460/50-nm emission filter. Under the 940-nm excitation wavelength, the 470-nm SHG signals were collected using a 480/40-nm emission filter. The two IRFs (*solid* – the IRF measured at excitation 880 nm, emission 440 nm vs. *dashed* – the IRF measured at excitation 940 nm, emission 470 nm) are almost overlaid with each other, confirming that the IRF did not change for using the two different combinations of the TPE wavelengths and the emission filters (Adapted from [47])

factors may influence the lifetime of the standard fluorophore. Figure 3.8 shows the results of the calibrations of our TPE-TCSPC FLIM system with two fluorescence lifetime standards: (1) coumarin 6 dissolved in ethanol has a peak absorption and emission at 460 and 505 nm, and its fluorescence lifetime is ~2.5 ns; (2) fluorescein dissolved in phosphate buffer pH 7.5 has maximum absorption and emission at 495 and 517 nm, and its fluorescence lifetime is ~4.0 ns (see http://www.iss.com/resources/reference/data_tables/LifetimeDataFluorophores.html).

3.4.5 Verifying the TPE-TCSPC FLIM System for FRET Studies Using FRET Standards

As mentioned above, the FRET standard approach provides a quantitative way to evaluate a FRET method. The utility of the TPE-TCSPC FLIM system for FRET studies was assessed using four FP-based FRET-standard constructs expressed in living cells [96, 107]: C5V, C17V, C32V where C (Cerulean) and V (Venus) are tethered by either a 5, 7, or 32 amino acid linker [107], and CTV where C and V are separated by a 229 amino acid linker encoding a TRAF domain [96]. As shown in Fig. 3.9, these FRET-standard decay profiles were clearly distinguished in the TPE-TCSPC FLIM-FRET measurements, demonstrating a shorter fluorescence lifetime of Cerulean obtained from CTV to C32V to C17V to C5V cells and an increase

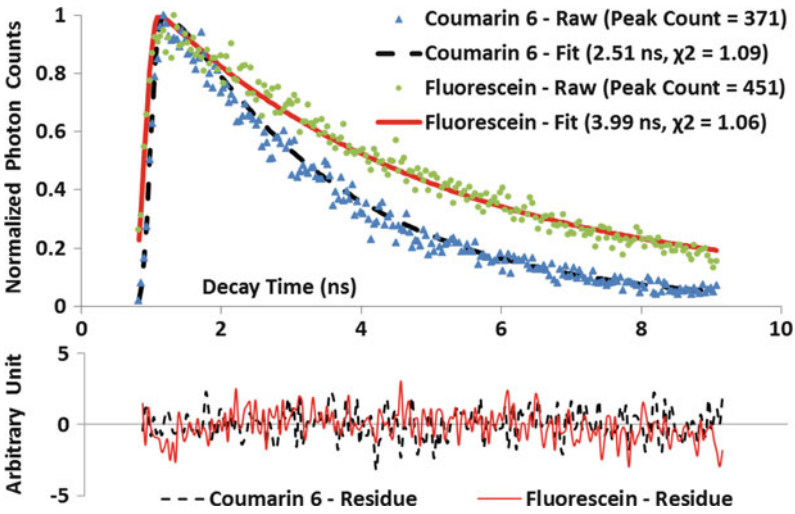

Fig. 3.8 Calibrations of the TPE-TCSPC FLIM system with two fluorescence lifetime standards – coumarin 6 dissolved in ethanol and fluorescein dissolved in phosphate buffer pH 7.5. For both coumarin 6 and fluorescein, the single exponential decay model was applied to fit the acquired data; the representative raw decay traces and corresponding fitting curves are shown together with the weighted least squares (χ^2) and residues determined by comparing the raw and fitted data, indicating good fits. The fluorescence lifetimes of coumarin 6 (2.51 ns) and fluorescein (3.99 ns) obtained through fitting closely matched their reference values (coumarin 6 – 2.5 ns and fluorescein – 4.0 ns)

in FRET efficiency (E) in the same direction. The Es of these FRET-standard constructs were determined using the TPE-TCSPC FLIM-FRET method based on Eq. 3.3, where the unquenched Cerulean lifetime (τ_D) was obtained through the single exponential fitting of the decay data acquired from cells expressing Cerulean alone; the quenched Cerulean lifetime for each FRET-standard construct (τ_{DA}) was estimated by fitting its decay data into a single or double exponential model; the resultant Es matched with those measured by other FRET methods including FD FLIM-FRET, spectral FRET, and filter-based confocal FRET [100, 179].

3.4.6 Detecting Protein-Protein Interactions in Living Cells with TPE-TCSPC FLIM-FRET

The biological model used here is the basic region-leucine zipper (bZip) domain of the C/EBPα transcription factor. The bZip family proteins form obligate dimers through their leucine-zipper domains, which positions the basic region residues for binding to specific DNA elements. Immunocytochemical staining of differentiated mouse adipocyte cells showed that the endogenous C/EBPα protein

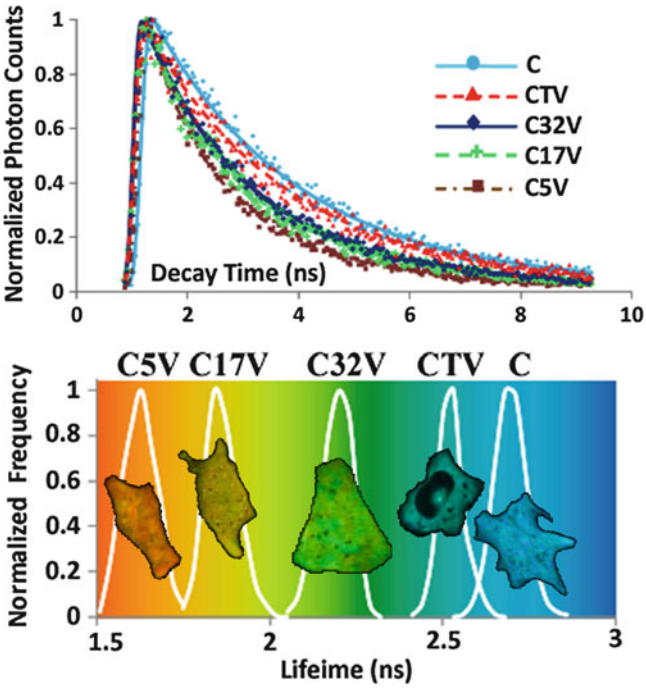

Fig. 3.9 Verification of the TPE-TCSPC FLIM-FRET approach using FRET-standard constructs – C5V, C17V, C32V, and CTV (see Sect. 3.4.5). The Cerulean fluorescence lifetimes in live cells expressing Cerulean alone (C) or a FRET-standard construct (CTV, C32V, C17V, or C5V) were measured using the TPE-TCSPC FLIM system. All acquired data were analyzed with single (for C and CTV) or double (for C32V, C17V, and C5V) exponential fittings. For each construct, the representative decay profile (at one pixel of each cell) and the lifetime distribution (in each cell) are shown, clearly demonstrating a faster decay (a shorter lifetime) from C to C5V, as expected from the designed linker systems (Adapted from [43])

was preferentially bound to satellite DNA-repeat sequences located in regions of centromeric heterochromatin [180, 181]. Standard recombinant DNA methods were used to fuse the sequences that code for either Cerulean or Venus into the reading frame of the sequence encoding the rat C/EBPα bZip domain, starting with the methionine at position 237 [182]. When the C/EBPα bZip domain is expressed as a fusion to the FPs in cells of mouse origin, such as the pituitary GHFT1 cells used here, it is localized to the well-defined regions of centromeric heterochromatin in the cell nucleus [78, 183]. As shown in Fig. 3.10, the TPE-TCSPC FLIM-FRET approach is a perfect tool to demonstrate the homodimerization of C/EBPα in live mouse pituitary cell nuclei based on the detection of FRET between Cerulean and Venus tagged to C/EBPα.

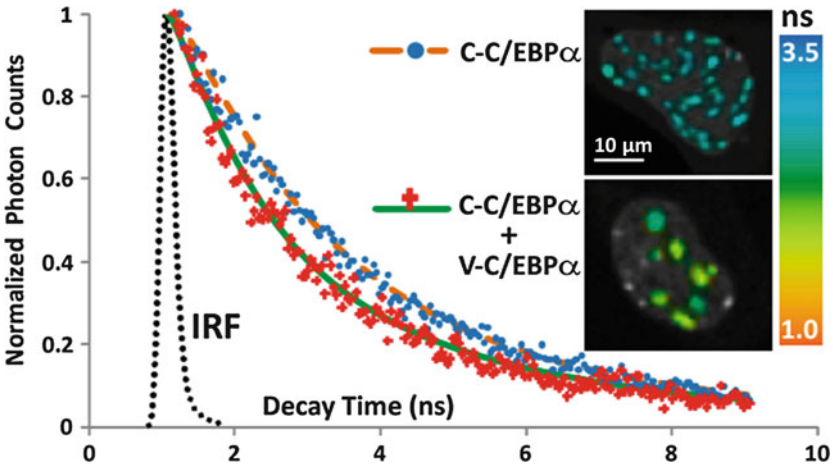

Fig. 3.10 Localization of homodimerization of CCAAT/enhancer-binding protein alpha (C/EBPα) in live mouse pituitary cell nuclei using TPE-TCSPC FLIM-FRET microscopy. C/EBPα was tagged with either Cerulean (C) or Venus (V). The fluorescent lifetime decay kinetics for the C − C/EBPα (FRET donor) in the absence and the presence of V − C/EBPα (FRET acceptor) were determined by fitting the measured decay data into a single or double exponential decay model, respectively, with the measured instrument function (IRF). By applying a suitable threshold, fittings were only applied to the pixels in regions of centromeric heterochromatin of the cell nucleus. The comparison between the representative measured decay data points, fitting curves, and lifetime images (overlaid with intensity) of the two cases clearly shows the C in cells expressing "C − C/EBPα + V − C/EBPα" decayed faster (or has a shorter lifetime) than that in cells expressing C-C/EBP*α* alone, indicating the C attached to C/EBP*α* was quenched by the V attached to C/EBPα due to FRET and further demonstrating the interaction between C- and V-tagged C/EBPα (homodimerization of C/EBPα) in regions of centromeric heterochromatin of the cell nucleus (Adapted from [166])

3.5 Conclusion and Outlook

Being the most rapidly expanding microscopy technique employed today, fluorescence microscopy will no doubt continue to remain on the central stage of the life sciences. The various applications using fluorescence microscopy technologies described in this chapter and many others not described here will continue to increase in all directions of the life sciences, driven by the growing number of biologists who routinely use these technologies. Many new advanced fluorescence microscopy techniques will continue to be developed, driven by development of new fluorescent probes, invention of new sophisticated microscope hardware and software, and the need to solve more complicated biological questions. Although some of the fluorescence microscopy techniques (e.g., FLIM described in Sect. 3.4) can be somewhat challenging for biologists without physics background, they provide an unprecedented level of information about functions, dynamics, and interactions of proteins in cells under physiological conditions at a very high temporal and spatial

resolution. The popularity of these fluorescence microscopy techniques will soon spread by the development of turn-key instruments, improvements of user-friendly data acquisition and analysis software, and demonstration of their unique usefulness to biological applications, many of which have already taken place.

Acknowledgements The authors greatly acknowledge the finance support provided by the National Center for Research Resources (NCRR) – National Institutes of Health (NIH) RR025616, RR027409, P01HL101871 and the University of Virginia. The authors would like to thank Mr. Horst Wallrabe for his critical reading of our manuscript and helpful suggestions.

References

1. A.H. Coons, H.J. Creech, R.N. Jones, E. Berliner, The demonstration of pneumococcal antigen in tissues by the use of fluorescent antibody. J. Immunol. **45**(3), 159–70 (1942)
2. O. Shimomura, F.H. Johnson, Y. Saiga, Extraction, purification and properties of aequorin, a bioluminescent protein from the luminous hydromedusan, aequorea. J. Cell Comp. Physiol. **59**, 223–39 (1962)
3. D.C. Prasher, V.K. Eckenrode, W.W. Ward, F.G. Prendergast, M.J. Cormier, Primary structure of the aequorea victoria green-fluorescent protein. Gene **111**(2), 229–33 (1992)
4. M. Chalfie, Y. Tu, G. Euskirchen, W.W. Ward, D.C. Prasher, Green fluorescent protein as a marker for gene expression. Science **263**(5148), 802–805 (1994)
5. R.Y. Tsien, The green fluorescent protein. Annu. Rev. Biochem. **67**, 509–544 (1998)
6. N.C. Shaner, P.A. Steinbach, R.Y. Tsien, A guide to choosing fluorescent proteins. Nat. Methods **2**(12), 905–909 (2005)
7. R.N. Day, M.W. Davidson, The fluorescent protein palette: Tools for cellular imaging. Chem. Soc. Rev. **38**(10), 2887–2921 (2009)
8. D.J. Stephens, V.J. Allan, Light microscopy techniques for live cell imaging. Science **300**(5616), 82–86 (2003)
9. W.A. Hing, C.A. Poole, C.G. Jensen, M. Watson, An integrated environmental perfusion chamber and heating system for long-term, high resolution imaging of living cells. J. Microsc. **199**(Pt 2), 90–95 (2000)
10. C.L. Rieder, A. Khodjakov, Mitosis through the microscope: Advances in seeing inside live dividing cells. Science **300**(5616), 91–96 (2003)
11. P.J. Davis, E.A. Kosmacek, Y. Sun, F. Ianzini, M.A. Mackey, The large-scale digital cell analysis system: An open system for nonperturbing live cell imaging. J. Microsc. **228**(Pt 3), 296–308 (2007)
12. P. Gross, G. Farge, E.J. Peterman, G.J. Wuite, Combining optical tweezers, single-molecule fluorescence microscopy, and microfluidics for studies of DNA-protein interactions. Methods Enzymol. **475**, 427–453 (2010)
13. J.R. Lakowicz, *Principles of Fluorescence Spectroscopy* (Springer, New York, 2006)
14. T. Nagai, K. Ibata, E.S. Park, M. Kubota, K. Mikoshiba, A. Miyawaki, A variant of yellow fluorescent protein with fast and efficient maturation for cell-biological applications. Nat. Biotechnol. **20**(1), 87–90 (2002)
15. G.H. Patterson, J. Lippincott-Schwartz, A photoactivatable GFP for selective photolabeling of proteins and cells. Science **297**(5588), 1873–1877 (2002)
16. J. Zhang, R.E. Campbell, A.Y. Ting, R.Y. Tsien, Creating new fluorescent probes for cell biology. Nat. Rev. Mol. Cell Biol. **3**(12), 906–918 (2002)
17. J. Lippincott-Schwartz, G.H. Patterson, Development and use of fluorescent protein markers in living cells. Science **300**(5616), 87–91 (2003)

18. N.C. Shaner, R.E. Campbell, P.A. Steinbach, B.N. Giepmans, A.E. Palmer, R.Y. Tsien, Improved monomeric red, orange and yellow fluorescent proteins derived from discosoma sp. red fluorescent protein. Nat. Biotechnol. **22**(12), 1567–1572 (2004)
19. M.A. Rizzo, G.H. Springer, B. Granada, D.W. Piston, An improved cyan fluorescent protein variant useful for FRET. Nat. Biotechnol. **22**(4), 445–449 (2004)
20. H.W. Ai, J.N. Henderson, S.J. Remington, R.E. Campbell, Directed evolution of a monomeric, bright and photostable version of clavularia cyan fluorescent protein: Structural characterization and applications in fluorescence imaging. Biochem. J. **400**(3), 531–540 (2006)
21. N.C. Shaner, M.Z. Lin, M.R. McKeown, P.A. Steinbach, K.L. Hazelwood, M.W. Davidson, R.Y. Tsien, Improving the photostability of bright monomeric orange and red fluorescent proteins. Nat. Methods **5**(6), 545–551 (2008)
22. M. Yang, E. Baranov, P. Jiang, F.X. Sun, X.M. Li, L. Li, S. Hasegawa, M. Bouvet, M. Al-Tuwaijri, T. Chishima, H. Shimada, A.R. Moossa, S. Penman, R.M. Hoffman, Whole-body optical imaging of green fluorescent protein-expressing tumors and metastases. Proc. Natl. Acad. Sci. **97**(3), 1206–1211 (2000)
23. D.M. Chudakov, S. Lukyanov, K.A. Lukyanov, Fluorescent proteins as a toolkit for in vivo imaging. Trends Biotechnol. **23**(12), 605–613 (2005)
24. B.N. Giepmans, S.R. Adams, M.H. Ellisman, R.Y. Tsien, The fluorescent toolbox for assessing protein location and function. Science **312**(5771), 217–224 (2006)
25. R.N. Day, F. Schaufele, Fluorescent protein tools for studying protein dynamics in living cells: a review. J. Biomed. Opt. **13**(3), 031202 (2008)
26. X. Gao, W.C. Chan, S. Nie, Quantum-dot nanocrystals for ultrasensitive biological labeling and multicolor optical encoding. J. Biomed. Opt. **7**(4), 532–537 (2002)
27. X. Gao, S. Nie, Molecular profiling of single cells and tissue specimens with quantum dots. Trends Biotechnol. **21**(9), 371–373 (2003)
28. T.M. Jovin, Quantum dots finally come of age. Nat. Biotechnol. **21**(1), 32–33 (2003)
29. A.P. Alivisatos, W. Gu, C. Larabell, Quantum dots as cellular probes. Annu. Rev. Biomed. Eng. **7**, 55–76 (2005)
30. F. Pinaud, X. Michalet, L.A. Bentolila, J.M. Tsay, S. Doose, J.J. Li, G. Iyer, S. Weiss, Advances in fluorescence imaging with quantum dot bio-probes. Biomaterials **27**(9), 1679–1687 (2006)
31. U. Resch-Genger, M. Grabolle, S. Cavaliere-Jaricot, R. Nitschke, T. Nann, Quantum dots versus organic dyes as fluorescent labels. Nat. Methods **5**(9), 763–775 (2008)
32. W. Zhong, Nanomaterials in fluorescence-based biosensing. Anal. Bioanal. Chem. **394**(1), 47–59 (2009)
33. I.L. Medintz, H. Mattoussi, Quantum dot-based resonance energy transfer and its growing application in biology. Phys. Chem. Chem. Phys. **11**(1), 17–45 (2009)
34. W.C. Chan, D.J. Maxwell, X. Gao, R.E. Bailey, M. Han, S. Nie, Luminescent quantum dots for multiplexed biological detection and imaging. Curr. Opin. Biotechnol. **13**(1), 40–46 (2002)
35. D.K. Bird, L. Yan, K.M. Vrotsos, K.W. Eliceiri, E.M. Vaughan, P.J. Keely, J.G. White, N. Ramanujam, Metabolic mapping of MCF10A human breast cells via multiphoton fluorescence lifetime imaging of the coenzyme NADH. Cancer Res. **65**(19), 8766–8773 (2005)
36. A. Miyawaki, O. Griesbeck, R. Heim, R.Y. Tsien, Dynamic and quantitative Ca2+ measurements using improved chameleons. Proc. Natl. Acad. Sci. USA **96**(5), 2135–2140 (1999)
37. A. Miyawaki, J. Llopis, R. Heim, J.M. McCaffery, J.A. Adams, M. Ikura, R.Y. Tsien, Fluorescent indicators for Ca2+ based on green fluorescent proteins and calmodulin. Nature **388**(6645), 882–887 (1997)
38. T. Nagai, S. Yamada, T. Tominaga, M. Ichikawa, A. Miyawaki, Expanded dynamic range of fluorescent indicators for ca(2+) by circularly permuted yellow fluorescent proteins. Proc. Natl. Acad. Sci. USA **101**(29), 10554–10559 (2004)
39. D.A. Agard, J.W. Sedat, Three-dimensional architecture of a polytene nucleus. Nature **302**(5910), 676–681 (1983)

40. J.G. McNally, T. Karpova, J. Cooper, J.A. Conchello, Three-dimensional imaging by deconvolution microscopy. Methods **19**(3), 373–385 (1999)
41. J.R. Swedlow, M. Platani, Live cell imaging using wide-field microscopy and deconvolution. Cell Struct. Funct. **27**(5), 335–341 (2002)
42. Y. Sun, P. Davis, E.A. Kosmacek, F. Ianzini, M.A. Mackey, An open-source deconvolution software package for 3-D quantitative fluorescence microscopy imaging. J. Microsc. **236**(3), 180–193 (2009)
43. Y. Sun, H. Wallrabe, S.A. Seo, A. Periasamy, FRET microscopy in 2010: The legacy of theodor forster on the 100th anniversary of his birth. Chemphyschem **12**(3), 462–474 (2011)
44. G. Cox, Biological confocal microscopy. Mater. Today **5**(3), 34–41 (2002)
45. W.B. Amos, J.G. White, How the confocal laser scanning microscope entered biological research. Biol. Cell **95**(6), 335–342 (2003)
46. S. Paddock, Over the rainbow: 25 years of confocal imaging. BioTechniques **44**(5), 643,4, 646, 648 (2008)
47. Y. Sun, C.F. Booker, S. Kumari, R.N. Day, M. Davidson, A. Periasamy, Characterization of an orange acceptor fluorescent protein for sensitized spectral fluorescence resonance energy transfer microscopy using a white-light laser. J. Biomed. Opt. **14**(5), 054009 (2009)
48. A. Periasamy, P. Skoglund, C. Noakes, R. Keller, An evaluation of two-photon excitation versus confocal and digital deconvolution fluorescence microscopy imaging in xenopus morphogenesis. Microsc. Res. Technol. **47**(3), 172–181 (1999)
49. J.A. Conchello, J.W. Lichtman, Optical sectioning microscopy. Nat. Methods **2**(12), 920–931 (2005)
50. E. Wang, C.M. Babbey, K.W. Dunn, Performance comparison between the high-speed yokogawa spinning disc confocal system and single-point scanning confocal systems. J. Microsc. **218**(Pt 2), 148–159 (2005)
51. R. Graf, J. Rietdorf, T. Zimmermann, Live cell spinning disk microscopy. Adv. Biochem. Eng. Biotechnol. **95**, 57–75 (2005)
52. H. Wallrabe, M. Elangovan, A. Burchard, A. Periasamy, M. Barroso, Confocal FRET microscopy to measure clustering of ligand-receptor complexes in endocytic membranes. Biophys. J. **85**(1), 559–571 (2003)
53. H. Wallrabe, Y. Chen, A. Periasamy, M. Barroso, Issues in confocal microscopy for quantitative FRET analysis. Microsc. Res. Technol. **69**(3), 196–206 (2006)
54. H. Wallrabe, G. Bonamy, A. Periasamy, M. Barroso, Receptor complexes cotransported via polarized endocytic pathways form clusters with distinct organizations. Mol. Biol. Cell **18**(6), 2226–2243 (2007)
55. J. Pawley, *Handbook of Biological Confocal Microscopy* (Springer, New York, 2006)
56. W. Denk, J.H. Strickler, W.W. Webb, Two-photon laser scanning fluorescence microscopy. Science **248**(4951), 73–76 (1990)
57. C. Xu, J. Guild, W. Webb, W. Denk, Determination of absolute two-photon excitation cross sections by in situ second-order autocorrelation. Opt. Lett. **20**(23), 2372 (1995)
58. H. Szmacinski, I. Gryczynski, J.R. Lakowicz, Three-photon induced fluorescence of the calcium probe indo-1. Biophys. J. **70**(1), 547–555 (1996)
59. K. Svoboda, W. Denk, D. Kleinfeld, D.W. Tank, In vivo dendritic calcium dynamics in neocortical pyramidal neurons. Nature **385**(6612), 161–165 (1997)
60. D.W. Piston, Imaging living cells and tissues by two-photon excitation microscopy. Trends Cell Biol. **9**(2), 66–69 (1999)
61. P.T. So, C.Y. Dong, B.R. Masters, K.M. Berland, Two-photon excitation fluorescence microscopy. Annu. Rev. Biomed. Eng. **2**, 399–429 (2000)
62. M. Rubart, Two-photon microscopy of cells and tissue. Circ. Res. **95**(12), 1154–1166 (2004)
63. F. Helmchen, W. Denk, Deep tissue two-photon microscopy. Nat. Methods **2**(12), 932–940 (2005)
64. A. Diaspro, G. Chirico, M. Collini, Two-photon fluorescence excitation and related techniques in biological microscopy. Q. Rev. Biophys. **38**(2), 97–166 (2005)

65. K. Svoboda, R. Yasuda, Principles of two-photon excitation microscopy and its applications to neuroscience. Neuron **50**(6), 823–839 (2006)
66. B.G. Wang, K. Konig, K.J. Halbhuber, Two-photon microscopy of deep intravital tissues and its merits in clinical research. J. Microsc. **238**(1), 1–20 (2010)
67. T. Förster, Energy transport and fluorescence [in German]. Naturwissenschafien **6**, 166–175 (1946)
68. T. Förster, Zwischenmolekulare energiewanderung und fluoreszenz. Annalen Der Physik **437**(1–2), 55–75 (1948)
69. T. Förster, Delocalized excitation and excitation transfer. In *In Modern Quantum Chemistry*, O. Sinanoglu, editor, pp. 93–137 (Academic Press Inc., 1965)
70. R.M. Clegg, Fluorescence resonance energy transfer. In *Fluorescence Imaging Spectroscopy and Microscopy*, X.F. Wang, B. Herman, editors, pp. 179–251 (Wiley, New York, 1996)
71. R.M. Clegg, The history of FRET: From conception through the labors of birth. In *Reviews in Fluorescence*, C.D. Geddes, J.R. Lakowicz, editors, pp. 1–45 (Springer, New York, 2006)
72. E.A. Jares-Erijman, T.M. Jovin, FRET imaging. Nat. Biotechnol. **21**(11), 1387–1395 (2003)
73. R.B. Sekar, A. Periasamy, Fluorescence resonance energy transfer (FRET) microscopy imaging of live cell protein localizations. J. Cell Biol. **160**(5), 629–633 (2003)
74. A. Periasamy, R.N. Day, editors, *Molecular Imaging: FRET Microscopy and Spectroscopy* (Oxford University Press, New York, 2005)
75. S.S. Vogel, C. Thaler, S.V. Koushik, Fanciful FRET. Sci. STKE **2006**(331), re2 (2006)
76. D.W. Piston, G.J. Kremers, Fluorescent protein FRET: The good, the bad and the ugly. Trends Biochem. Sci. **32**(9), 407–414 (2007)
77. A.K. Kenworthy, Imaging protein-protein interactions using fluorescence resonance energy transfer microscopy. Methods **24**(3), 289–296 (2001)
78. R.N. Day, T.C. Voss, J.F. Enwright, C.F. Booker, A. Periasamy, F. Schaufele, Imaging the localized protein interactions between pit-1 and the CCAAT/enhancer binding protein alpha in the living pituitary cell nucleus. Mol. Endocrinol. **17**(3), 333–345 (2003)
79. I.A. Demarco, A. Periasamy, C.F. Booker, R.N. Day, Monitoring dynamic protein interactions with photoquenching FRET. Nat. Methods **3**(7), 519–524 (2006)
80. M.D. Allen, L.M. DiPilato, M. Rahdar, Y.R. Ren, C. Chong, J.O. Liu, J. Zhang, Reading dynamic kinase activity in living cells for high-throughput screening. ACS Chem. Biol. **1**(6), 371–376 (2006)
81. X. Gao, J. Zhang, Spatiotemporal analysis of differential akt regulation in plasma membrane microdomains. Mol. Biol. Cell **19**(10), 4366–4373 (2008)
82. J.L. Vinkenborg, T.J. Nicolson, E.A. Bellomo, M.S. Koay, G.A. Rutter, M. Merkx, Genetically encoded FRET sensors to monitor intracellular Zn2+ homeostasis. Nat. Methods **6**(10), 737–740 (2009)
83. L. Tron, J. Szollosi, S. Damjanovich, S.H. Helliwell, D.J. Arndt-Jovin, T.M. Jovin, Flow cytometric measurement of fluorescence resonance energy transfer on cell surfaces. quantitative evaluation of the transfer efficiency on a cell-by-cell basis. Biophys. J. **45**(5), 939–946 (1984)
84. L. Matyus, Fluorescence resonance energy transfer measurements on cell surfaces. A spectroscopic tool for determining protein interactions. J. Photochem. Photobiol. B **12**(4), 323–337 (1992)
85. Z. Kam, T. Volberg, B. Geiger, Mapping of adherens junction components using microscopic resonance energy transfer imaging. J. Cell Sci. **108** (Pt 3) (Pt 3), 1051–1062 (1995)
86. D.C. Youvan, C.M. Silva, E.J. Bylina, W.J. Coleman, M.R. Dilworth, M.M. Yang, Calibration of fluorescence resonance energy transfer in microscopy using genetically engineered GFP derivatives on nickel chelating beads. Biotechnol. Et Alia(3), 1–18 (1997)
87. G.W. Gordon, G. Berry, X.H. Liang, B. Levine, B. Herman, Quantitative fluorescence resonance energy transfer measurements using fluorescence microscopy. Biophys. J. **74**(5), 2702–2713 (1998)
88. A. Sorkin, M. McClure, F. Huang, R. Carter, Interaction of EGF receptor and grb2 in living cells visualized by fluorescence resonance energy transfer (FRET) microscopy. Curr. Biol. **10**(21), 1395–1398 (2000)

89. Z. Xia, Y. Liu, Reliable and global measurement of fluorescence resonance energy transfer using fluorescence microscopes. Biophys. J. **81**(4), 2395–2402 (2001)
90. A. Hoppe, K. Christensen, J.A. Swanson, Fluorescence resonance energy transfer-based stoichiometry in living cells. Biophys. J. **83**(6), 3652–3664 (2002)
91. D.W. Hailey, T.N. Davis, E.G. Muller, Fluorescence resonance energy transfer using color variants of green fluorescent protein. Methods Enzymol. **351**, 34–49 (2002)
92. C. Berney, G. Danuser, FRET or no FRET: A quantitative comparison. Biophys. J. **84**(6), 3992–4010 (2003)
93. M. Elangovan, H. Wallrabe, Y. Chen, R.N. Day, M. Barroso, A. Periasamy, Characterization of one- and two-photon excitation fluorescence resonance energy transfer microscopy. Methods **29**(1), 58–73 (2003)
94. J. van Rheenen, M. Langeslag, K. Jalink, Correcting confocal acquisition to optimize imaging of fluorescence resonance energy transfer by sensitized emission. Biophys. J. **86**(4), 2517–2529 (2004)
95. T. Zal, N.R. Gascoigne, Photobleaching-corrected FRET efficiency imaging of live cells. Biophys. J. **86**(6), 3923–3939 (2004)
96. C. Thaler, S.V. Koushik, P.S. Blank, S.S. Vogel, Quantitative multiphoton spectral imaging and its use for measuring resonance energy transfer. Biophys. J. **89**(4), 2736–2749 (2005)
97. Y. Chen, J.P. Mauldin, R.N. Day, A. Periasamy, Characterization of spectral FRET imaging microscopy for monitoring nuclear protein interactions. J. Microsc. **228**(Pt 2), 139–152 (2007)
98. D. Megias, R. Marrero, B. Martinez Del Peso, M.A. Garcia, J.J. Bravo-Cordero, A. Garcia-Grande, A. Santos, M.C. Montoya, Novel lambda FRET spectral confocal microscopy imaging method. Microsc. Res. Technol. **72**(1), 1–11 (2009)
99. V. Raicu, M.R. Stoneman, R. Fung, M. Melnichuk, D.B. Jansma, L.F. Pisterzi, S. Rath, M. Fox, J.W. Wells, D.K. Saldin, Determination of supramolecular structure and spatial distribution of protein complexes in living cells. Nat. Photon **3**(2), 107–113 (2009)
100. Y. Sun, A. Periasamy, Additional correction for energy transfer efficiency calculation in filter-based forster resonance energy transfer microscopy for more accurate results. J. Biomed. Opt. **15**(2), 020513 (2010)
101. Y. Chen, A. Periasamy, Intensity range based quantitative FRET data analysis to localize protein molecules in live cell nuclei. J. Fluoresc. **16**(1), 95–104 (2006)
102. M.E. Dickinson, G. Bearman, S. Tille, R. Lansford, S.E. Fraser, Multi-spectral imaging and linear unmixing add a whole new dimension to laser scanning fluorescence microscopy. BioTechniques **31**(6), 1272, 1274,6, 1278 (2001)
103. T. Zimmermann, J. Rietdorf, A. Girod, V. Georget, R. Pepperkok, Spectral imaging and linear un-mixing enables improved FRET efficiency with a novel GFP2–YFP FRET pair. FEBS Lett. **531**(2), 245–249 (2002)
104. T. Zimmermann, J. Rietdorf, R. Pepperkok, Spectral imaging and its applications in live cell microscopy. FEBS Lett. **546**(1), 87–92 (2003)
105. T. Zimmermann, Spectral imaging and linear unmixing in light microscopy. Adv. Biochem. Eng. Biotechnol. **95**, 245–265 (2005)
106. Y. Sun, H. Wallrabe, C.F. Booker, R.N. Day, A. Periasamy, Three-color spectral FRET microscopy localizes three interacting proteins in living cells. Biophys. J. **99**(4), 1274–1283 (2010)
107. S.V. Koushik, H. Chen, C. Thaler, H.L. Puhl, S.S. Vogel, Cerulean, venus, and VenusY67C FRET reference standards. Biophys. J. **91**(12), L99-L101 (2006)
108. R.N. Day, C.F. Booker, A. Periasamy, Characterization of an improved donor fluorescent protein for forster resonance energy transfer microscopy. J. Biomed. Opt. **13**(3), 031203 (2008)
109. D. Toomre, D.J. Manstein, Lighting up the cell surface with evanescent wave microscopy. Trends Cell Biol. **11**(7), 298–303 (2001)
110. D. Axelrod, Total internal reflection fluorescence microscopy in cell biology. Traffic **2**(11), 764–774 (2001)

111. H. Schneckenburger, Total internal reflection fluorescence microscopy: Technical innovations and novel applications. Curr. Opin. Biotechnol. **16**(1), 13–18 (2005)
112. J. Lippincott-Schwartz, E. Snapp, A. Kenworthy, Studying protein dynamics in living cells. Nat. Rev. Mol. Cell Biol. **2**(6), 444–456 (2001)
113. E.A. Reits, J.J. Neefjes, From fixed to FRAP: measuring protein mobility and activity in living cells. Nat. Cell Biol. **3**(6), E145-7 (2001)
114. B.L. Sprague, J.G. McNally, FRAP analysis of binding: proper and fitting. Trends Cell Biol. **15**(2), 84–91 (2005)
115. D. Magde, E. Elson, W.W. Webb, Thermodynamic fluctuations in a reacting system—measurement by fluorescence correlation spectroscopy. Phys. Rev. Lett. **29**(11), 705 (1972)
116. Y. Chen, J.D. Muller, K.M. Berland, E. Gratton, Fluorescence fluctuation spectroscopy. Methods **19**(2), 234–252 (1999)
117. O. Krichevsky, G. Bonnet, Fluorescence correlation spectroscopy: The technique and its applications. Rep. Prog. Phys. **65**(2), 251–297 (2002)
118. E. Haustein, P. Schwille, Fluorescence correlation spectroscopy: Novel variations of an established technique. Annu. Rev. Biophys. Biomol. Struct. **36**, 151–169 (2007)
119. N. Altan-Bonnet, G. Altan-Bonnet, Fluorescence correlation spectroscopy in living cells: a practical approach. Curr. Protoc. Cell Biol. Chapter 4 Unit 4.24 (2009)
120. M.A. Digman, E. Gratton, Fluorescence correlation spectroscopy and fluorescence cross-correlation spectroscopy. Wiley Interdiscip. Rev. Syst. Biol. Med. **1**(2), 273–282 (2009)
121. C.M. Brown, R.B. Dalal, B. Hebert, M.A. Digman, A.R. Horwitz, E. Gratton, Raster image correlation spectroscopy (RICS) for measuring fast protein dynamics and concentrations with a commercial laser scanning confocal microscope. J. Microsc. **229**(Pt 1), 78–91 (2008)
122. N.O. Petersen, P.L. Hoddelius, P.W. Wiseman, O. Seger, K.E. Magnusson, Quantitation of membrane receptor distributions by image correlation spectroscopy: concept and application. Biophys. J. **65**(3), 1135–1146 (1993)
123. P.W. Wiseman, J.A. Squier, M.H. Ellisman, K.R. Wilson, Two-photon image correlation spectroscopy and image cross-correlation spectroscopy. J. Microsc. **200**(Pt 1), 14–25 (2000)
124. P.W. Wiseman, C.M. Brown, D.J. Webb, B. Hebert, N.L. Johnson, J.A. Squier, M.H. Ellisman, A.F. Horwitz, Spatial mapping of integrin interactions and dynamics during cell migration by image correlation microscopy. J. Cell Sci. **117**(Pt 23), 5521–5534 (2004)
125. A. Nohe, N.O. Petersen, Image correlation spectroscopy. Sci. STKE **2007**(417), l7 (2007)
126. M.A. Digman, P.W. Wiseman, A.R. Horwitz, E. Gratton, Detecting protein complexes in living cells from laser scanning confocal image sequences by the cross correlation raster image spectroscopy method. Biophys. J. **96**(2), 707–716 (2009)
127. M.J. Rossow, J.M. Sasaki, M.A. Digman, E. Gratton, Raster image correlation spectroscopy in live cells. Nat. Protoc. **5**(11), 1761–1774 (2010)
128. S.W. Hell, Far-field optical nanoscopy. Science **316**(5828), 1153–1158 (2007)
129. B. Huang, M. Bates, X. Zhuang, Super-resolution fluorescence microscopy. Annu. Rev. Biochem. **78**, 993–1016 (2009)
130. G. Patterson, M. Davidson, S. Manley, J. Lippincott-Schwartz, Superresolution imaging using single-molecule localization. Annu. Rev. Phys. Chem. **61**, 345–367 (2010)
131. T.A. Klar, S. Jakobs, M. Dyba, A. Egner, S.W. Hell, Fluorescence microscopy with diffraction resolution barrier broken by stimulated emission. Proc. Natl. Acad. Sci. USA **97**(15), 8206–8210 (2000)
132. K.I. Willig, S.O. Rizzoli, V. Westphal, R. Jahn, S.W. Hell, STED microscopy reveals that synaptotagmin remains clustered after synaptic vesicle exocytosis. Nature **440**(7086), 935–939 (2006)
133. L. Meyer, D. Wildanger, R. Medda, A. Punge, S.O. Rizzoli, G. Donnert, S.W. Hell, Dual-color STED microscopy at 30-nm focal-plane resolution. Small **4**(8), 1095–1100 (2008)
134. E. Betzig, G.H. Patterson, R. Sougrat, O.W. Lindwasser, S. Olenych, J.S. Bonifacino, M.W. Davidson, J. Lippincott-Schwartz, H.F. Hess, Imaging intracellular fluorescent proteins at nanometer resolution. Science **313**(5793), 1642–1645 (2006)

135. S.T. Hess, T.P. Girirajan, M.D. Mason, Ultra-high resolution imaging by fluorescence photoactivation localization microscopy. Biophys. J. **91**(11), 4258–4272 (2006)
136. M.F. Juette, T.J. Gould, M.D. Lessard, M.J. Mlodzianoski, B.S. Nagpure, B.T. Bennett, S.T. Hess, J. Bewersdorf, Three-dimensional sub-100 nm resolution fluorescence microscopy of thick samples. Nat. Methods **5**(6), 527–529 (2008)
137. S. Manley, J.M. Gillette, G.H. Patterson, H. Shroff, H.F. Hess, E. Betzig, J. Lippincott-Schwartz, High-density mapping of single-molecule trajectories with photoactivated localization microscopy. Nat. Methods **5**(2), 155–157 (2008)
138. T.J. Gould, V.V. Verkhusha, S.T. Hess, Imaging biological structures with fluorescence photoactivation localization microscopy. Nat. Protoc. **4**(3), 291–308 (2009)
139. M.J. Rust, M. Bates, X. Zhuang, Sub-diffraction-limit imaging by stochastic optical reconstruction microscopy (STORM). Nat. Methods **3**(10), 793–795 (2006)
140. B. Huang, S.A. Jones, B. Brandenburg, X. Zhuang, Whole-cell 3D STORM reveals interactions between cellular structures with nanometer-scale resolution. Nat. Methods **5**(12), 1047–1052 (2008)
141. X. Zhuang, Nano-imaging with storm. Nat. Photonics **3**(7), 365–367 (2009)
142. A. Periasamy, R.M. Clegg, *FLIM Microscopy in Biology and Medicine* (CRC Press, London, 2009)
143. B.D. Venetta, Microscope phase fluorometer for determining the fluorescence lifetimes of fluorochromes. Rev. Sci. Instrum. **30**(6), 450–457 (1959)
144. H.C. Gerritsen, M.A. Asselbergs, A.V. Agronskaia, W.G. Van Sark, Fluorescence lifetime imaging in scanning microscopes: Acquisition speed, photon economy and lifetime resolution. J. Microsc. **206**(Pt 3), 218–224 (2002)
145. Y. Chen, J.D. Mills, A. Periasamy, Protein localization in living cells and tissues using FRET and FLIM. Differentiation **71**(9–10), 528–541 (2003)
146. E. Gratton, S. Breusegem, J. Sutin, Q. Ruan, N. Barry, Fluorescence lifetime imaging for the two-photon microscope: time-domain and frequency-domain methods. J. Biomed. Opt. **8**(3), 381–390 (2003)
147. W. Becker, A. Bergmann, M.A. Hink, K. Konig, K. Benndorf, C. Biskup, Fluorescence lifetime imaging by time-correlated single-photon counting. Microsc. Res. Technol. **63**(1), 58–66 (2004)
148. Y. Chen, A. Periasamy, Characterization of two-photon excitation fluorescence lifetime imaging microscopy for protein localization. Microsc. Res. Technol. **63**(1), 72–80 (2004)
149. W. Becker, A. Bergmann, C. Biskup, Multispectral fluorescence lifetime imaging by TCSPC. Microsc. Res. Technol. **70**(5), 403–409 (2007)
150. C. Biskup, T. Zimmer, L. Kelbauskas, B. Hoffmann, N. Klocker, W. Becker, A. Bergmann, K. Benndorf, Multi-dimensional fluorescence lifetime and FRET measurements. Microsc. Res. Technol. **70**(5), 442–451 (2007)
151. A. Periasamy, P. Wodnicki, X.F. Wang, S. Kwon, G.W. Gordon, B. Herman, Time-resolved fluorescence lifetime imaging microscopy using a picosecond pulsed tunable dye laser system. Rev. Sci. Instrum. **67**(10), 3722–3731 (1996)
152. M. Elangovan, R.N. Day, A. Periasamy, Nanosecond fluorescence resonance energy transfer-fluorescence lifetime imaging microscopy to localize the protein interactions in a single living cell. J. Microsc. **205**(Pt 1), 3–14 (2002)
153. A.V. Agronskaia, L. Tertoolen, H.C. Gerritsen, High frame rate fluorescence lifetime imaging. J. Phys. D **36**(14), 1655–1662 (2003)
154. D.M. Grant, J. McGinty, E.J. McGhee, T.D. Bunney, D.M. Owen, C.B. Talbot, W. Zhang, S. Kumar, I. Munro, P.M. Lanigan, G.T. Kennedy, C. Dunsby, A.I. Magee, P. Courtney, M. Katan, M.A. Neil, P.M. French, High speed optically sectioned fluorescence lifetime imaging permits study of live cell signaling events. Opt. Express **15**(24), 15656–15673 (2007)
155. R.V. Krishnan, A. Masuda, V.E. Centonze, B. Herman, Quantitative imaging of protein-protein interactions by multiphoton fluorescence lifetime imaging microscopy using a streak camera. J. Biomed. Opt. **8**(3), 362–367 (2003)

156. C. Biskup, T. Zimmer, K. Benndorf, FRET between cardiac Na+ channel subunits measured with a confocal microscope and a streak camera. Nat. Biotechnol. **22**(2), 220–224 (2004)
157. J.R. Lakowicz, H. Szmacinski, K. Nowaczyk, K.W. Berndt, M. Johnson, Fluorescence lifetime imaging. Anal. Biochem. **202**(2), 316–330 (1992)
158. T.W.J. Gadella Jr., T.M. Jovin, R.M. Clegg, Fluorescence lifetime imaging microscopy (FLIM): spatial resolution of microstructures on the nanosecond time scale. Biophys. Chem. **48**(2), 221–239 (1993)
159. C. Buranachai, D. Kamiyama, A. Chiba, B.D. Williams, R.M. Clegg, Rapid frequency-domain FLIM spinning disk confocal microscope: lifetime resolution, image improvement and wavelet analysis. J. Fluoresc. **18**(5), 929–942 (2008)
160. Y.C. Chen, R.M. Clegg, Fluorescence lifetime-resolved imaging. Photosynth. Res. **102**(2–3), 143–155 (2009)
161. T.S. Forde, Q.S. Hanley, Spectrally resolved frequency domain analysis of multi-fluorophore systems undergoing energy transfer. Appl. Spectrosc. **60**(12), 1442–1452 (2006)
162. R.A. Colyer, C. Lee, E. Gratton, A novel fluorescence lifetime imaging system that optimizes photon efficiency. Microsc. Res. Technol. **71**(3), 201–213 (2008)
163. H. Wallrabe, A. Periasamy, Imaging protein molecules using FRET and FLIM microscopy. Curr. Opin. Biotechnol. **16**(1), 19–27 (2005)
164. T.W.J. Gadella, *FRET and FLIM Techniques* (Elsevier, Oxford, 2009)
165. A. Periasamy, M. Elangovan, E. Elliott, D.L. Brautigan, Fluorescence lifetime imaging (FLIM) of green fluorescent fusion proteins in living cells. Methods Mol. Biol. **183**, 89–100 (2002)
166. Y. Sun, R.N. Day, A. Periasamy, Investigating protein-protein interactions in living cells using fluorescence lifetime imaging microscopy. Nat. Protoc. (In Press)
167. A.V. Agronskaia, L. Tertoolen, H.C. Gerritsen, Fast fluorescence lifetime imaging of calcium in living cells. J. Biomed. Opt. **9**(6), 1230–1237 (2004)
168. D.S. Ushakov, V. Caorsi, D. Ibanez-Garcia, H.B. Manning, A.D. Konitsiotis, T.G. West, C. Dunsby, P.M. French, M.A. Ferenczi, Response of rigor cross-bridges to stretch detected by fluorescence lifetime imaging microscopy of myosin essential light chain in skeletal muscle fibers. J. Biol. Chem. **286**(1), 842–850 (2011)
169. K. Konig, H. Schneckenburger, R. Hibst, Time-gated in vivo autofluorescence imaging of dental caries. Cell Mol. Biol. (Noisy-Le-Grand) **45**(2), 233–239 (1999)
170. A. Ehlers, I. Riemann, M. Stark, K. Konig, Multiphoton fluorescence lifetime imaging of human hair. Microsc. Res. Technol. **70**(2), 154–161 (2007)
171. A. Uchugonova, K. Konig, Two-photon autofluorescence and second-harmonic imaging of adult stem cells. J. Biomed. Opt. **13**(5), 054068 (2008)
172. S. Huang, A.A. Heikal, W.W. Webb, Two-photon fluorescence spectroscopy and microscopy of NAD(P)H and flavoprotein. Biophys. J. **82**(5), 2811–2825 (2002)
173. V.K. Ramanujan, J.H. Zhang, E. Biener, B. Herman, Multiphoton fluorescence lifetime contrast in deep tissue imaging: prospects in redox imaging and disease diagnosis. J. Biomed. Opt. **10**(5), 051407 (2005)
174. M.C. Skala, K.M. Riching, A. Gendron-Fitzpatrick, J. Eickhoff, K.W. Eliceiri, J.G. White, N. Ramanujam, In vivo multiphoton microscopy of NADH and FAD redox states, fluorescence lifetimes, and cellular morphology in precancerous epithelia. Proc. Natl. Acad. Sci. USA **104**(49), 19494–19499 (2007)
175. H.W. Guo, C.T. Chen, Y.H. Wei, O.K. Lee, V. Gukassyan, F.J. Kao, H.W. Wang, Reduced nicotinamide adenine dinucleotide fluorescence lifetime separates human mesenchymal stem cells from differentiated progenies. J. Biomed. Opt. **13**(5), 050505 (2008)
176. N.P. Galletly, J. McGinty, C. Dunsby, F. Teixeira, J. Requejo-Isidro, I. Munro, D.S. Elson, M.A. Neil, A.C. Chu, P.M. French, G.W. Stamp, Fluorescence lifetime imaging distinguishes basal cell carcinoma from surrounding uninvolved skin. Br. J. Dermatol. **159**(1), 152–161 (2008)
177. W. Becker, *Advanced Time-Correlated Single Photon Counting Techniques* (Springer, Berlin, 2005)

178. H. Stiel, K. Teuchner, A. Paul, D. Leupold, I.E. Kochevar, Quantitative comparison of excited state properties and intensity-dependent photosensitization by rose bengal. J. Photochem. Photobiol. B **33**(3), 245–254 (1996)
179. A. Periasamy, P. So, K. Konig, Comparison of FRET microscopy imaging techniques for studying protein-protein interactions in living cells using FRET standards. Proc. SPIE **7569**, 75690Z (2010)
180. Q.Q. Tang, M.D. Lane, Activation and centromeric localization of CCAAT/enhancer-binding proteins during the mitotic clonal expansion of adipocyte differentiation. Genes Dev. **13**(17), 2231–2241 (1999)
181. Q.Q. Tang, M.D. Lane, Role of C/EBP homologous protein (CHOP-10) in the programmed activation of CCAAT/enhancer-binding protein-beta during adipogenesis. Proc. Natl. Acad. Sci. **97**(23), 12446–12450 (2000)
182. W.H. Landschulz, P.F. Johnson, E.Y. Adashi, B.J. Graves, S.L. McKnight, Isolation of a recombinant copy of the gene encoding C/EBP. Genes Dev. **2**(7), 786–800 (1988)
183. R.N. Day, A. Periasamy, F. Schaufele, Fluorescence resonance energy transfer microscopy of localized protein interactions in the living cell nucleus. Methods **25**(1), 4–18 (2001)

Chapter 4
Spectral Imaging: Methods, Design, and Applications

Yuval Garini and Elad Tauber

Spectral imaging is a relatively new field in which the advantages of optical spectroscopy as an analytical tool are combined with the power of object visualization as obtained by optical imaging; it creates a three-dimensional data set that contains many images of the same object, where each one of them is measured at a different wavelength. Biomedical applications typically require collection of complex information from tissues with minimal invasion and risk at shorter times and lower costs. This chapter will discuss the principles of spectral imaging, various optical designs, and spectral imaging analysis, while a few of the algorithms will be discussed with emphasis on the usage for different experimental modes. Different methods used for spectral imaging systems will be described as well as their advantages, limitations, and possible applications. In addition, the conceptual parts of a spectral imaging system will be described combined with brief description of the major biomedical applications.

4.1 Introduction

Almost anyone who has the pleasure to experience the marvel of light that is diffracted through a prism to a magnificent set of colors wonders what their source is. This type of experience almost perfectly defines the science of spectroscopy, the study of the interaction of light and matter through the colors, or wavelength to be more exact.

Spectroscopy is an old science being used for decades now, to understand the nature of substances, the composition of materials, and the nature of light. It can be found as part of the study of the early days of the universe, through the diagnostic

Y. Garini (✉) · E. Tauber
Physics Department and Nanotechnology Institute, Bar Ilan University, Ramat Gan 52900, Israel
e-mail: yuval.garini@biu.ac.il

R. Liang (ed.), *Biomedical Optical Imaging Technologies*, Biological and Medical Physics, Biomedical Engineering, DOI 10.1007/978-3-642-28391-8_4,

of cancer cells and all the way to atomic and nucleus structure analysis. It is a method that truly span all across the sciences. It certainly plays a major role in the biomedical field.

Interestingly, the word *spectrum* originates from Latin where it literally means appearance or image. Imaging on the other hand is a relatively new science. It is intuitive since most of the information we learn is gathered through our vision system, and imaging is just another innovative and sophisticated tool that allows us to gather better images and store them at the same time. Thanks to the digital cameras which are now common everywhere, imaging is disseminated not only to scientists but also to millions of users of phone and internet.

Spectral imaging simply combines these two widespread methodologies together, providing a lot of the benefits that each can provide onto a single technique. In biological and clinical studies, spectral imaging extends the existing capabilities by allowing the simultaneous study of multiple features such as organelles and proteins qualitatively and quantitatively.

In order to acquire a spectral image, it is required to measure a spectrum at each point of an image. For this to happen, it requires combining dispersive optics with imaging equipment, and as usually happens, it also introduces constrains.

In that light, the following chapter will discuss the principles of spectral imaging, various optical designs, and spectral imaging analysis, while a few of the algorithms will be discussed with emphasis on the usage for different experimental modes (fluorescence and bright field). Finally, spectral imaging, like any method, should be evaluated in terms of its advantages to specific applications, a selection of which will also be described.

4.2 Imaging and Spectroscopy

Spectral imaging combines spectroscopy and imaging. In principle, spectral imaging requires creating a three-dimensional data set that contains many images of the same object, where each one of them is measured at a different wavelength. It is clear that creating such a large data set costs a longer acquisition time, which stands in contrast to the requirements of many biomedical applications. Therefore, for some applications, compromises must be made for achieving high quality images in a limited amount of time. In order to understand the characteristics of spectral imaging, it is worth to introduce its two building blocks – imaging and spectroscopy.

4.2.1 Imaging Fundamentals

An image is usually referred to as a two-dimensional representation of an object. For many years, it was materialized through paintings and drawings, but for the last decades, different types of cameras evolved allowing image acquisition in a realistic way. Most common and practical today are the digital cameras, based on either

charged couple device (CCD) or the complementary metal-oxide semiconductor (CMOS) technologies. The advances in digital imaging matured the field in a short time to extremely high quality as described below, yet limitations always exist.

The amount of information that can be gathered from an image determines its quality. There are few fundamental properties that characterize the image and its quality. At this point, we refer to images that do not contain any color information, so that they can be considered as gray-level images, which means that each point of the image, or pixel, contains a value that represents the brightness of that point on the object. It may be the total integrated intensity from all the spectral range or the intensity as measured through a color filter, a polarized filter, or else.

We describe here some of the fundamental properties of the imaging detector itself, including the setting parameters that are crucial for achieving high quality of the images:

1. Spatial resolution
   Spatial resolution determines the closest distinguishable features in the acquired objects. It depends mainly on the wavelength (λ), the numerical aperture (NA) of the objective lens through which the image is acquired, the magnification, and the pixel size of the array detector, usually a CCD or CMOS camera. The latter two play a major role because they determine the sampling frequency which must be sufficiently high to achieve full resolution. Spatial resolution also depends on the signal quality [1].
2. Lowest detectable signal
   This term defines the lowest signal from the image that can be detected. It depends on the quantum efficiency of the detector (the higher the better), the noise level of the system (the lower the better), the numerical aperture of the optics (the higher the better), and the quality of the optics. It is important especially in applications where the number of photons is limited, or where the total acquisition time available for the measurement is limited (e.g., due to fluorescence quenching by oxygen or in live-cell imaging).
3. Dynamic range
   Dynamic range specifies the number of different intensity levels that can be detected in an image. For a CCD or CMOS camera, it depends on the maximal possible number of electrons at each pixel and on the lowest detectable signal (practically it is the ratio of these two values). If, however, the measured signal is low, so that the associated pixel is only partially filled, the dynamic range will be limited accordingly. As an example, if a CCD well is filled to only 10 % of its maximum capacity, the dynamic range will be reduced to 10 % of its nominal value.
4. Field of view (FOV)
   The field of view determines the size of the object that can be viewed for given conditions, such as magnification or settings of the system's fore-optics.
5. Exposure time range
   The exposure time range is usually determined by the detector and its electronic control. For applications that involve moving objects, a short exposure time is

required, while in other application, the brightness of the object is very low, requiring long exposure times. It is therefore preferable to have a wide range of exposure times that can be used according to the application.

6. Readout rate
   Readout rate is a performance factor related also to the frame rate parameter; both imply on the ability of the system to record data at high temporal frequencies. The readout rate, also referred to as the pixel rate, is dominated by the time it takes to convert an analogue signal (voltage) into a digital signal (count) and is defined as the inverse of it. Thus, the frame rate, is governed by the number of pixels acquired (or the field of view), the readout rate and also the exposure time. The frame rate (typically measured in frames per second) has immense importance in cases where recording of fast transient dynamics combined with low signals is required.

   The trade-off in high readout rates is that it also contributes to the intrinsic noise in the system. The analogue-to-digital converter contributes noise also coined as readout noise, typically growing respectively to the readout rate.
7. Binning
   The physical pixels of the array detector can be "binned" so that effectively each pixel that collects photoelectrons is bigger in size. This leads to a significantly larger dynamic range because the number of electrons that can be stored in the bigger pixel is much higher. Also, once this amount of photons is converted from an analogue value to a digital number, the readout noise is added only once to all the binned pixels, and therefore, the signal-to-noise ratio is improved. On the other hand, the binning certainly comes with a loss of spatial resolution, as the number of pixels is reduced. Some of the CCDs enable to select many different binning values.
8. Gain factor
   Photons hitting the detector are converted to electron charge which is converted to a voltage which is finally translated to a digital value. This number is stored in the computer and describes the light intensity that illuminated that pixel. The gain factor is the ratio parameter between the amount of electrons per pixel to the counts per pixel generated. In some cameras it is a fixed parameter while in others it is a variable parameter that can be determined based on the actual amount of electrons that filled the pixels of the camera. Each pixel has a full well depth that determines the maximal capacity of electrons, say 10,000. The standard gain factor converts this value to the maximal possible count number (depending on the analogue-to-digital converter – e.g., 12 bits camera consists of $2^{12} = 4{,}096$ counts). On the other hand, in a given measurement, the light intensity may be low and the wells may not be full at all.

Most of the spectral imaging systems are based on an array detector, typically a CCD combined with fore-optics, and few others on point detectors such as photomultipliers (PMTs). While excellent quality CCDs are available, the light itself has intrinsic noise due to the Poissonian nature of photon emission (Shot noise) that cannot be avoided. If n photons are counted, then shot noise, with its Poisson

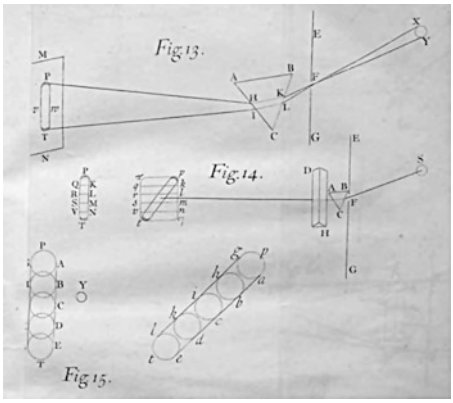

Fig. 4.1 Dispersion effect as it was described by Newton in his book Opticks in 1704 (Image is courtesy of Octavo Corp and the Warnock Library)

distribution, has a standard deviation of $\sqrt{n}$. The signal-to-noise ratio (SNR) is therefore proportional to $n/\sqrt{n}$ and can be improved only by increasing the signal in some way. At best, an imaging system is "shot-noise limited," which means that the quality of the detector is high enough so that the sensitivity of the system is limited by the shot noise.

In addition, there are other disturbances that originate from the nature of the sample and its environment, such as scattering, auto-fluorescence, and bleaching that increase the background level and decrease the real signal. The quality of the signal is therefore reduced, and these disturbances have to be taken into account in setting up the system for each specific application. Post-processing can also be used by applying various filtering methods.

4.2.2 Spectroscopy

We are all familiar with the diverse colors of a rainbow which is probably one of the most ancient examples of a spectrum. In optics, a spectrum is a collection of light intensities at different wavelengths. Spectroscopy is the science of acquiring, analyzing, and explaining the spectral characteristics of matter. It is a broad and well-established science. The dispersion of white light to its colors was initially described by Newton in his book *Opticks* published in 1704 [2, 3], and it has been used with increased interest ever since, see Fig. 4.1. Spectroscopy is an important research tool that is used in every possible science. It is interesting to note that even quantum mechanics developed by Schrödinger in 1926 was initially based on the experimental discovery of the hydrogen emission spectral lines as discovered by Balmer in 1885 and formulated to a general equation by Rydberg.

What makes the spectrum so important in different sciences is the fact that the spectrum, which is a collection of different wavelengths of electromagnetic

radiation, usually results from the interaction of light with matter, and therefore, it carries a fingerprint of the material, or structure.

The spectrum can be a result of different interactions of light with matter. Light can be described as a flux of particles, or photons, that each one carries a well-defined energy. The amount of energy depends on the wavelength of light as described by

$$E = \frac{hc}{\lambda} \tag{4.1}$$

where $h \cong 6.626 \times 10^{-34}[\mathrm{J} \cdot \mathrm{s}]$ is Planck constant and $c = 2.998 \times 10^{8}[\mathrm{m/s}]$ is the speed of light. Therefore, knowing the spectrum provides a direct access to the energy level transitions of the atoms and molecules that constitute the material being measured. A simple substitution of constants leads to a convenient form of this equation, $E = 1{,}240/\lambda$, where substituting the wavelength in nanometer units gives the energy in electronvolt units (eV).

In addition, the spectrum is affected by the geometry of the material being studied. The geometry depends on the shape and dimensions of a structure, its index of refraction, as well as the index of refraction of the boundary material. Such properties can be calculated by solving Maxwell's equations, for which there are now a handful of excellent commercial programs.

We therefore see that generally, a measured spectrum results both from the intrinsic properties of the material from which it is made and from its geometry and boundaries. This fact should be taken into account when performing a measurement. It also makes the interpretation more complex.

The most important processes that probe the energy level transition of atoms, molecules, or bulk materials are:

1. Emission
   The process of transforming energy of some sort onto electromagnetic radiation. All the light sources are emitting photons, including light bulbs, fluorescent molecules, lasers, a blackbody, and the sun. In a blackbody the spectrum is a result of the temperature, the macroscopic geometry of the body and the quantum nature of light (e.g., the Sun). In contrast, the emission of lasers, a fluorescent molecule and an atom is a result of electrons' quantized well-separated energy levels that are being excited by some sort of energy and fall back to lower-level energies, usually the ground energy state.
2. Absorption
   An electron is excited from the ground state to an empty higher-level energy band. The absorption of simple entities such as atoms and molecules is rather simple, as the number of energy bands is not large. When the structure of the absorbing material becomes more complex, such as for biological tissue, the absorption can be very complex [4].
3. Reflection
   The light is reflected from the sample according to the reflection law of light, the geometry of the material, and the index of refraction of the matter and its boundaries.

4. Scattering
   The process of re-emitting or redirecting the light that impinges on the body, so that it is scattered to directions that are different than the original trajectory of the beam of light that illuminates the object. A good example is the Rayleigh scattering of sunlight that is responsible to the blue color of the sky and the scattering of light by nano-size metal spheres also known as Mie scattering that allows to observe even small particles at high intensity [5].
5. Luminescence
   Is the emission of light from matter, originating not from the thermal emission (incandescent) of the bodies. For such a process to occur, some source energy must excite the material. There are different types of luminescent processes due to the nature of the excitation, such as electroluminescence which results from electrical excitation, photoluminescence where the matter is excited by light at a higher energy than the luminescent light, and chemiluminescence where the matter is excited by chemical reaction and others.

Spectral imaging relies mostly on the visible-light range which is relevant for the electronic transitions of atoms and molecules, but the infrared spectrum (usually 2–20 μm) is also heavily used in spectroscopy. The infrared light is much less energetic, and it is usually absorbed by molecules while exciting vibration and rotation modes, also called *vibronic* modes. These transition energies are highly specific to the interatomic bonds and molecule state, and therefore, it is an excellent fingerprint of its structure [6].

It is important to distinguish the processes of photoluminescence and absorption. In fluorescence measurement, fluorescent molecules (or other fluorescing entities such as quantum dots) are excited by an intense power source at a relatively high energy and light at lower energy emitted from the material. In many cases, there is a direct functional relationship between the concentration of fluorescent molecules and the amount of fluorescence intensity. At low concentrations, this relationship is linear and therefore quantitative analysis is possible.

Fluorescence measurements are very useful in the life sciences. Mostly due to developments in biochemistry that allow labeling almost any type of a biological entity with fluorescent molecules, so that labeled entities can be viewed on top of a dark background (to increase sensitivity). In addition, when the fluorescent material concentration is not too high, the signal intensity is a good measure of its quantity, and the method is therefore quantitative. Moreover, fluorescent proteins are available nowadays. Their genes can be inserted to a living cell that will produce the fluorescent probes by itself, a Nobel-prize award invention that revolutionized the life sciences [7]. Due to abovementioned advantages, fluorescence became one of the most abundant research and diagnostics method. In fluorescence, it is essential to distinguish the weak emitted light from the strong excitation light. This requires the use of color filters, excitation barrier filters, dichroic mirrors, and emission barrier filters that allow one to distinguish the two light sources. These filters must have adequate transmission ranges and high rejection ratios at the required wavelength, and the spectrum that is measured is, therefore, usually different from the real

Table 4.1 Typical parameters of spectral imaging systems

Category	Property	Typical
Imaging	Spatial resolution	250 nm (in plane) at $\lambda = 500$ nm
	Field of view	$\sim$50 μm (high magnification) $1,000 \times 1,000$ pixels or more
	Dynamic range	8–16 bits (256–65,536 intensity levels)
	Lowest detectable signal	Shot-noise limited
	Field of view	depends on detector area and foreoptics
	Frame rate	10–400 [fps]
Spectroscopy	Spectral resolution	1–20 nm (may depend on λ) can be a variable parameter
	Spectral range	400–900 nm
	Spectral response	60–70% at 500–600 nm 80–100% for back-illuminated chips

The *Typical* column shows the common value that is achievable but greatly depends on the specific dispersion method that is used and the quality of the system elements (e.g., high NA objective lens, high quantum efficiency *QE*)

emitted spectrum. Different effects such as saturation and bleaching may disrupt an expected linearity of the signal and should be tested for each specific case.

In bright-field microscopy, reflection and scattering microscopy, the sample is illuminated with an external light source and the detector measures that very same light after interaction with the sample. Spectral analysis of the data must take into account the light source spectrum in order to accurately extract the desired sample's spectral properties. In bright-field microscopy, the measured signal may not be directly proportional to the concentration of the observed molecules but to its logarithm.

In order to measure a spectrum, the intensity at each wavelength is measured. There are different methods to disperse the light and almost all of them are used in various spectral imaging systems, as will be described below. Some of the important characteristics of a spectrum include (see also Table 4.1):

1. Spectral resolution
   Spectral resolution determines the smallest separation of two peaks in the spectrum that can still be distinguished. Typically, spectral imaging systems can resolve down to several nanometers. In general, the spectral resolution is a function of the method in which light is dispersed, the fore-optics and other parameters, where in some systems it is a tunable parameter and in some not.
2. Spectral range
   The spectral range refers to the wavelength band in which spectra can be measured. It is governed by the same factors mentioned in the preceding term in combination with the detector's capabilities which differ in different wavelength bands.
3. Lowest detectable signal and dynamic range
   Lowest detectable signal defines the smallest measurable signal, while dynamic range dictates the number of distinguishable levels in a given measurement.

These parameters also depend on the shape of the measured spectrum. A sharp laser line has a better detectable signal because the energy is concentrated at a single wavelength when compared to a broad spectrum with equal energy which is distributed over a large spectral range.

4. Spectral response
   The spectral response of a system describes the efficiency of the detector in translating photons at a given wavelength from the sample to intensity counts by the system. It does not refer to the efficiency of the fore-optics, but to the spectral transmission and response of the detector, which usually have a large effect on the response. In addition, some of the spectral dispersion methods also affect the response, sometimes in a significant manner. Some of the methods are limited to a range where, $\lambda_{\min} \leq 2 \times \lambda_{\max}$, for example, the spectral range can only be between 400 and 800 nm. In that case, the spectral response will fall dramatically around the edges or it may lead to artifacts in the measurement.

4.3 Spectral Imaging System Configuration

Spectral imaging combines the two methodologies, spectroscopy and imaging. Whereas imaging provides the intensity at every pixel of the image, $I(x, y)$, and a typical spectrometer provides a single spectrum, $I(\lambda)$ (intensity at every given narrow wavelength), a spectral image provides a spectrum at each pixel, $I(x, y, \lambda)$. This is a three-dimensional (3D) data set and can be viewed as a cube of information. One can consider $I(x, y, \lambda)$ as either a collection of many images where each one is measured at a different wavelength or as a collection of many spectral values at each pixel (Fig. 4.2).

4.3.1 The Principles of Spectral Imaging Systems

Spectral imaging requires the combination of a dispersive element (or method) to sequentially obtain the spectral information with an imaging system that measures those spectra in an ordered manner.

The data collected at each pixel is the intensity at each wavelength, $I(x, y, \lambda)$, see Fig. 4.2. To date, there is no such three-dimensional (3D) detector that can collect the whole spectral imaging simultaneously, at least not for a spectrum with a typical resolution which is made of 10–100 separated wavelengths. Therefore, it is clear that the spectral cube of information must be collected in few measurements after dividing it somehow in a way that depends on the optical method that is being used.

The highest-rank detector available to date (except for a three-color method, as will be explained later on) is a two-dimensional (2D) array detector, either a CCD or CMOS, and with such detector, the spectral image cannot be acquired at once. If a lower-dimension detector such as a line detector or a single-point detector is used, the spectral image acquisition time will take even longer. This problem resulted

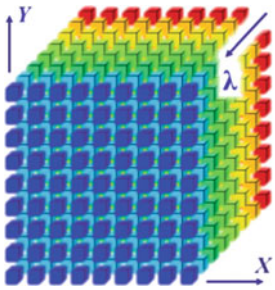

Fig. 4.2 Description of a spectral image data set. Each point in the cube represents a single number, and the spectral image is described as $I(x, y, \lambda)$. It can be viewed either as an image $I(x, y)$ at each wavelength λ or as a spectrum $I(\lambda)$ at every pixel (x, y)

in the development of many different spectral imaging techniques differing from one to another by the method in which the spectral image is collected. Each of the methods has its advantages and limitations which depend on the character of the application for which it is being used. In that sense, coming to choose a spectral imaging system is rather a matter of tailoring the most adequate spectral imaging method to the type of application.

Spectral imaging methods can be divided into the following methods:

1. Methods that capture a full spectral image at very few spectral bands simultaneously. The disadvantage is that such methods compromise on the number of points in the spectrum, the field of view, and spatial or spectral resolution. Such a measurement can be represented as $I(x, y, \lambda)$, where λ is measured at only few wavelengths, typically of the order of 3 or 4.
2. Wavelength-scan methods that measure the images one wavelength at a time. Here, each measurement i measures $I(x, y, \lambda_i)$ at a single wavelength λ_i, and the measurement is repeated n times. To span a wavelength range, typically 30–40 different acquisitions should suffice.
3. Spatial-scan methods that measure the whole spectrum of a portion of the image at a time and scan the image (e.g., line by line). In this case the measurement is $I(x, y_i, \lambda)$, where y_i represents a single point along the y axis, and the measurement repeats n times to cover the whole required range along y.
4. Time-scan methods that measure a set of images where each one of them is a superposition of spectral or spatial image information. The actual spectral information is calculated at the end of the acquisition by a mathematical transformation such as Fourier transform. Here, the measurement is of $I(x, y, f_i(\lambda))$, where $f_i(\lambda)$ is a function of the spectrum at every pixel and in the end it is transformed to give $I(x, y, \lambda)$. The method that is based on Fourier spectroscopy belongs to this category. In this method, the light coming from every pixel passes an interferometer that changes its intensity according to the time delay created in between the two arms of the interferometer. This information is then transformed to the spectrum, see Sect. 4.4.4.
5. Spectral images usually measure the emission (or transmission) from the samples, but excitation spectra can also be obtained by placing the system on the excitation optical port. For transmission measurements, such a method provides similar information, but it is different for fluorescence. Dickinson et al. [8] have

extended the excitation method to multiphoton excitation [9] and have shown how it can be used to eliminate auto-fluorescence and distinguish dyes with similar emission spectra.

4.3.2 Spectral Imaging Challenge: Information Versus Time

A spectral image contains significantly more information and data than a single-color (gray-level) image and, thus, takes longer to acquire. When comparing the total acquisition time of different methods, the common ground should be the time it takes to acquire a spectral image of the same quality (or SNR).

Theoretically, the ideal system includes many shot-noise-limited detectors that can measure simultaneously the entire spectral image. If, in addition, we could tune the spectral-range sensitivity of each one of these detectors, it would provide the ideal system. Such a detector may look like a cubical structure (Fig. 4.2) where each box is a detector.

To date, no such detector is available (unless the field of view is compromised). The total acquisition time continues to depend on the sequential number of times that data has to be collected. It is clear, however, that the larger the number of detector elements used in parallel, the shorter the measurement time will be.

As an example, assume that it is only required to measure an image with three spectral components which are in the blue, green, and red spectral ranges. If a gray-level CCD is used, it requires an acquisition of three images. There are also sensors that enable to capture three color ranges simultaneously either by having a three-layer array detector [10, 11] or with a three-chip color CCD that uses dichroic mirrors to capture the three colors simultaneously. Such devices require only a single acquisition relative to a gray-level CCD that entails three filters sequentially and will lead to an improvement of $\sqrt{3}$ in the SNR (assuming the same quality of the detector elements).

Such basic method would typically be in use only in cases where the samples' colors and associated wavelengths looked for are known a priori, so that an image would provide an answer to existence or nonexistence in the observed sample (e.g., measuring aneuploidy in cancerous cells where a specific gene is labeled with a known fluorescent tag).

A fair comparison of different acquisition methods should be based on the time it takes each method to obtain information that would suffice to satisfy the pre-requisites of the measurement. The problem can be formulated as follows: In a given amount of time, what is the optimal set of spectral-component images that enables one to interpret the data with a given level of accuracy?

Time limitation can be critical for different reasons: high throughput that is required in many biomedical applications, photobleaching in fluorescence, and phototoxicity or image motion in applications such as retinal imaging.

Methods satisfying the question formulated above have been treated before. They depend on the specificity of the spectra that have to be separated, and in the case

of fluorescence, the complexity can grow higher. In fluorescence microscopy, the observed fluorochromes have to be excited at certain spectral ranges which limit the spectral range available for detection [12]. Zimmermann et al. [13] have formulated the problem for the case of live-cell spectral imaging which introduces even stronger restrictions on the acquisition time. Neher and Neher [14] have developed a more general methodology for solving the problem for the case of multiple fluorochromes and also take into account bleaching effects.

4.4 Optical Configurations and System Design

The optical design of a spectral imaging system must ensure high image quality while the spectral dispersion method provides the required spectral selection. Figure 4.3 shows one of the simplest possible designs of a spectral imaging system. It assumes that the spectral dispersion element does not change the angle of the transmitted beam and only selects the relevant spectral band. In this case, it can be placed in the range where the optics is collimated. With such an element, in principle two lenses are required, L1 for collimating the image and L2 to focus it to the image plane.

Dispersion elements that do not maintain the angle of the incoming beam are much more complex to work with and would usually require designing further optics that can compensate the effect.

4.4.1 Methods that Compromise Spectral Performance

In some applications, the spectral resolution that is needed is limited, or there is a need for only few wavelengths that are well known. In such a case, it is possible to use a rather simple method that splits the few spectral bands of interest to different regions in space, so that the whole information can be measured simultaneously. In this approach therefore, a compromise is sought for the simultaneous measurement of spectral and spatial parameters. These methods are suitable for high-speed spectral imaging measurements which are crucial in several applications such as detecting fast metabolic processes. As a matter of fact, all of the commercially available digital cameras use one of those approaches.

One possibility is to select a smaller part of the FOV and project it multiple times on the same CCD, each one through a different filter [13], see Fig. 4.4a. As shown, a fourfold reduction of the FOV yields four spectral ranges. A related approach has been taken in flow cytometry where a dispersion element projects six emission images onto a time-delayed integration (TDI) CCD whose pixel clock rate is synchronized with the flow stream [15]. Another example of this method is ratio imaging used for calcium imaging [16]. In this application, a dual-view device is used for measuring the intensity ratio of yellow and cyan fluorescent proteins (YFP and CFP in short). These two-color proteins are tagged to a calmodulin molecule that can bind to Ca^{2+}. When doing so, the distance between the two fluorescent

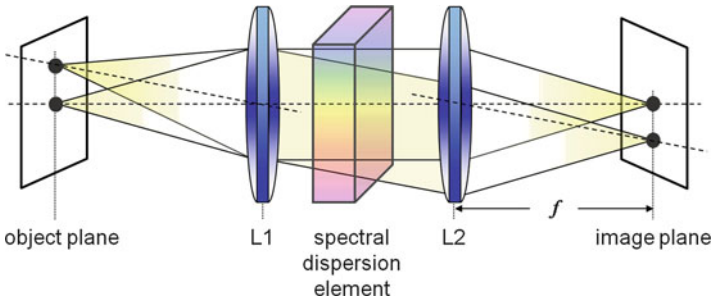

Fig. 4.3 Principle design of infinity-corrected optics for a spectral imaging system. Lens L1 transmits a collimated beam while lens L2 focuses the image on the image plane. If the spectral dispersion element is mounted in the collimated beam, and if it does not deflect the beams in a wavelength-dependent manner, it will form an adequate image. The optical axis and principal rays from two spots on the object are shown

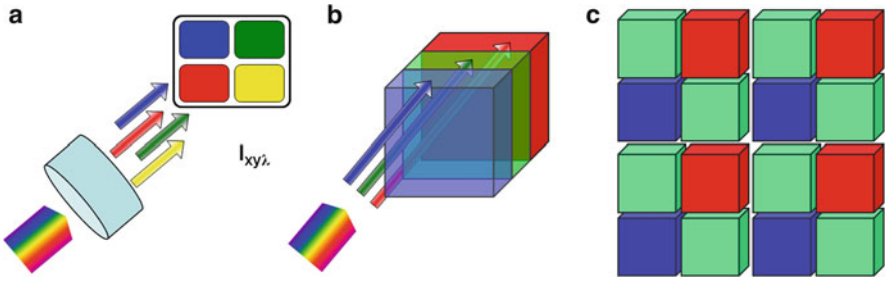

Fig. 4.4 Methods that compromise spectral or spatial resolution in favor of speed to acquire complete information simultaneously. **a** A device for splitting up to four colors on the same CCD. The spectral range of each band can be selected with adequate filters. **b** A three-layered array sensors, each measuring different basic colors. A similar technology also uses a combination of three CCD cameras and a set of dichroic filters that split each basic color to a different array sensor. **c** A typical CCD or CMOS chip of array sensors. Each unit of the array sensor is defined from four smaller pixels; two are measuring the *green* and the other two the *blue* and *red*. Here, the spatial information is compromised (50% of the *green* and 75% of the *blue* and *red*)

molecules becomes smaller, thereby leading to energy transfer from the CFP to the YFP. Therefore, when measuring the intensity of these two fluorescent molecules at each pixel, one can find the areas in the cell that are rich with Ca^{2+}. An important advantage of this method is the ability to select the exact spectral range for each of the images that are being measured. The measurement is rather fast, limited only by the frame rate of the CCD and the required exposure time that provides good-enough signal-to-noise ratio.

Other methods for measuring such a color image can be implied through a simultaneous measurement with three CCD or CMOS. Figure 4.4b shows an example of such a method using three layers of sensors array, each one measuring a different wavelength. Such a sensor was developed some time ago [11] and is available commercially (Foveon Inc., Santa Clara, CA). Another similar technique

shown in Fig. 4.4b is the 3CCD; like its name, it uses three CCD sensors with a set of dichroic filters that split the image on to them [17]. Fig. 4.4c shows the method probably most common for high-end photography and video imaging to date. It is an improvement to the typical method of a single-color array sensor (Fig. 4.4c) where each pixel of the device includes four real pixels on the array, in which each of them has a color filter that is optimized for green, red and blue. Two of the filters are green, one blue, and one red with a spectral response that imitates the human color vision. In order to construct the image, an optimized spatial interpolation filter is used to build the color image at each point.

This method, which was limited to the basic RGB colors, was lately boosted by significant improvements of patterned dichroic filters on the area of the sensor [18]. The device called *dichroic filter array* (DFA) can, in principle, have a much larger number of filters. It was demonstrated by selecting many sets of 2×3 pixels. One of the pixels is left without a filter, and the other five have, each, a dichroic filter with a desired bandwidth that can be tailored respective to the application. Such a system was demonstrated lately [19] presenting a combination of 2×2 filter to measure oxy- and deoxyhemoglobin. The filters were chosen to be at wavelengths of 750, 772, 802, and 834 nm with a full width half maximum (FWHM) of $\sim$20 nm. A CCD with $2{,}300 \times 3{,}500$ original pixels of $10 \times 10\,\mu$m was used; despite the size of the pixels, it still provided an excellent resolution and large field of view, so that a successful analysis of oxygen level in a tissue was demonstrated.

This method certainly has a potential for further improvements, especially with the new generation of high quality scientific grade CMOS cameras that have a relatively small pixel size.

4.4.1.1 Design Principles

Figure 4.5 shows two common implementation methods for simultaneous measurement of a limited number of selected spectral bands. Figure 4.5a demonstrates simultaneous two-color imaging, using a rather simple wedged dichroic mirror. Such a method was demonstrated [20] with a 3° wedged dichroic (Chroma Technology) and was used for high sensitivity fluorescence measurements. The focusing lens is mounted before the dichroic mirror, but it can also be located in between the wedged dichroic and the CCD. The wedge angle together with the lens focal length determines the spatial separation of the two images on the CCD and can be designed to provide the desired separation, based on the field of view and the spatial resolution.

Figure 4.5b shows another implementation for simultaneous imaging of up to four spectral bands. This setup is based on a set of dichroic filters combined with mirrors. Small tilting of the mirrors provides the separation of different spectral-band images on to the CCD. Although the figure shows the images one next to another, a change in the optic setup enables folding the four images to form a square. Such system, separating two spectral bands, is available from various sources, such as OptoSplit (Cairn, UK), DV^2 (Photometrics, USA), and U-SIP (Olympus).

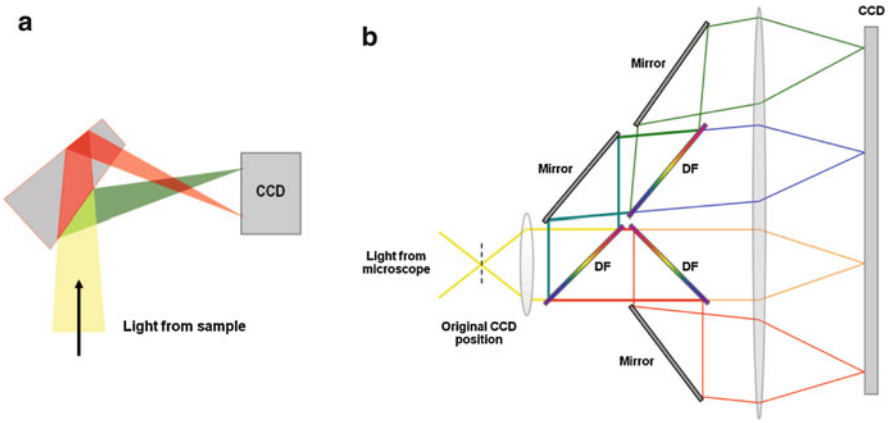

Fig. 4.5 Possible setup for achieving simultaneous imaging of (**a**) two or (**b**) four spectral channels. Both cases are based on dichroic filters. Figure **b** shows the four channels spanned along a single axis, but this is only shown for a simpler drawing. In practice, different folding of light can provide four images from a 2 × 2 matrix on the CCD

Four-channel imaging is also available commercially with QV^2 (Photometrics). The aforementioned devices provide alignment buttons to determine the optimal image separation at different spectral-band channels and also allow easy switching of different sets of dichroic filters, so that the same system can be used for multiple applications (or combination of fluorochromes).

4.4.2 Wavelength-Scan Methods

Although the previous section described a method for fast and simultaneous measurement of up to four spectral bands, it is clear that other applications require a broad and accurate spectral range. A straightforward method to obtain a spectral image is to use a set of color filters one at a time (Fig. 4.6a). If each filter is selected with a narrow bandwidth, for example, $\Delta\lambda = 10$ nm, so that altogether they cover a broad spectral range, the spectral image can be acquired by measuring the image through each of the filters so that the final image is a combination of all images (wavelengths). Appropriate design has to account for minimized pixel shift and a smooth exchange of the filters during the measurement.

Ensuring a rapid and smooth exchange of the filters requires a careful design, as these two qualities contradict each other. Rapid scan means that large accelerations and decelerations of the filter wheel have to be applied, which may also add vibrations to the optical apparatus and result in image blur. Nowadays, high quality filter wheels are available with a filter-shift time of 30–250 ms, depending on the size of the filters and the filter wheel. Although the method is also somewhat limiting the number of filters, it is a rather simple solution.

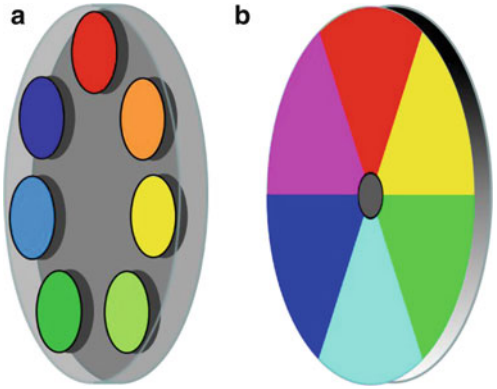

Fig. 4.6 **a** A straightforward method for spectral imaging using a set of filters mounted on a rotatable wheel. The filters' properties can be optimized for the application or standardized to have the same bandwidth and spacing all across the spectrum. **b** A filter wheel that is designed to operate at a constant rotation speed respective to each band's exposure, field of view, and acquisition time so that image acquisition become continuous and thus faster

Improved versions include the use of a circular-variable filter (CVF) [21] or the use of filters that are touching each other (Fig. 4.6b) so that the wheel can operate with a constant and fast rotation without having to stop at each filter. This way, a much faster acquisition time can be achieved. As explained above, the operation speed is mainly limited by the pixel rate of the camera and the required field of view that is projected on to the CCD. With high frame-rate CCDs, it is possible to achieve a full spectral image of 6 spectral bands at a frame rate of 60 frames per second [19] and even higher.

4.4.2.1 Variable Filters

Variable filters provide a much more advanced technique to measure one wavelength at a time. These filters are more compact and robust and they do not require moving parts. Two well-known devices are the *liquid crystal tunable filter* (LCTF) [22] shown in Fig. 4.7 and *acousto-optical tunable filter* (AOTF) [23, 24] as shown in Fig. 4.9. In the following section, we will describe their method of operation and capabilities.

LCTF

The most common LCTF system is based on the Lyot design as developed by Bernard Lyot in 1933 [25]. It transmits a narrow-band wavelength by applying a voltage on a polarizable liquid crystal mounted between two linear polarizers and a fixed retarder (Fig. 4.7a). The liquid crystal acts as a variable birefringent material

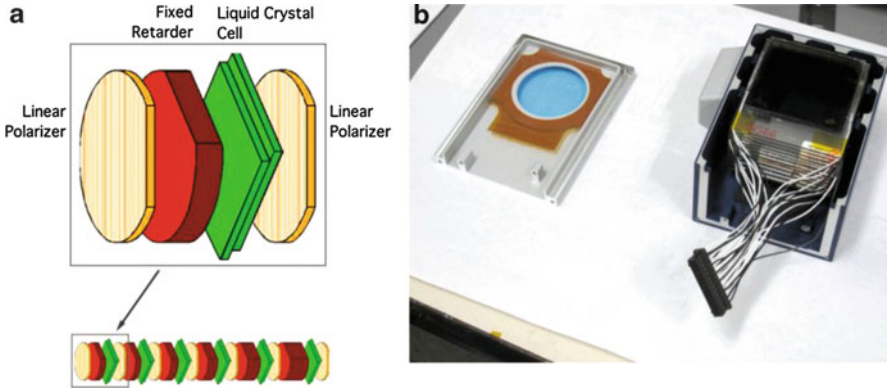

Fig. 4.7 *Liquid crystal tunable filter* (LCTF) that can be used for spectral imaging. **a** The light is transmitted through a linear polarizer and a fixed phase retarder. By rotating the polarization with the liquid crystal in a wavelength-dependent manner, only a single band is transmitted through the second linear polarizer. By using few elements in a series, the transmitted bandwidth can be narrowed as desired. **b** A 35-mm aperture LCTF with the enclosure open. Note the multiple stages of the optics "stack" and the wiring harness for the LC cells. The control circuitry normally also present in the enclosure is not shown here for reasons of clarity (Image courtesy of Cambridge Research & Instrumentation, Inc. (CRi), now part of Caliper)

that, together with the two linear polarizers around it, transmits a polarized light with a wavelength-dependent intensity that is equal to

$$I(\lambda) = I_0 \cos^2\left(\frac{2\pi\Gamma}{\lambda}\right) \tag{4.2}$$

where I_0 is the amplitude that is transmitted through the device, Γ is the phase retardation of the ordinary and extraordinary beams caused by the change in index of refraction of each of these waves, and λ is the wavelength of light [22, 26]. Such a transmission is shown in Fig. 4.8 (first stage). When few stages are used, so that each stage increases the retardation Γ by a factor of 2, each stage transmits the spectrum that entered to it multiplied by a similar cosine function with a doubled frequency (Fig. 4.8). Therefore, after few stages, the output spectrum is a narrow band given by FWHM $= \lambda/2^N$, where N is the number of stages in the system. The FWHM can be in the range of 5–20 nm and even less. By applying a different voltage on the liquid crystals, the value of Γ changes (linearly to the first order) and the transmitted wavelength is shifted. It therefore acts as a tunable filter. The out-of-band transmission can be very low, practically less than 0.01 %. The system also has a relatively large angle of acceptance that does not affect the spectral properties of the transmitted light.

The damage threshold for reasonably long-term exposure of the filters to visible (VIS) and near-infrared (NIR) energy is 500 mW/cm^2. LCTF filters absorb light that is out of the required spectral range by using hot-mirror elements to reflect unwanted

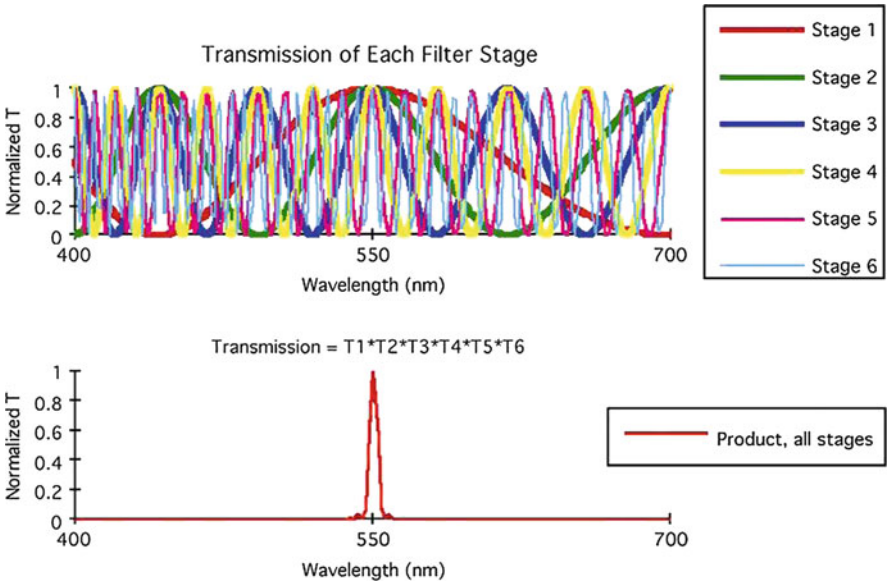

Fig. 4.8 Principle of the multiple-stage liquid crystal elements is demonstrated by showing the transmission through each stage. Each unit provides a cosine-like transmission pattern with a different frequency. Nevertheless, all the transmission curves are centered at the same selected wavelength (550 nm in this example) and the output is provided by multiplying the whole set of transmission bands. The result is shown at the *bottom*. By changing the voltage applied to the liquid crystal, the central wavelength can be changed in the whole range of $\lambda_{max} = 2 \times \lambda_{min}$ (Image courtesy of Cambridge Research & Instrumentation, Inc. (CRi), now part of Caliper)

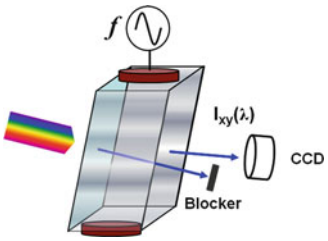

Fig. 4.9 An acousto-optical tunable filter (AOTF) used for spectral imaging. By inducing acoustic waves in a crystal that has an index of refraction that is sensitive to the material density, a grating is formed. It deflects the light according to the periodicity so that a single wavelength is transmitted. The zero-order transmitted light is blocked, so that by changing the frequency, a different wavelength can be selected

near-infrared light, but longer-wavelength light (e.g., in the form of thermal energy) can damage the filters. UV light can also cause irreparable damage. Many detectors, such as CCD or CMOS sensors, are not particularly sensitive to UV or thermal energy, so it is good practice to utilize heat-absorbing glass, a long-pass filter, or to check the temperature of the LCTF optics to make sure that the filter is not being subjected to excessive energy.

Nematic liquid crystal material is generally used in each LCTF tuning element. This material can be accurately and predictably controlled with relatively low current. Image quality is extremely high, and the field of view is relatively wide. The liquid crystal material in LCTF designs needs a few milliseconds to respond to changes in the electrical current.

AOTF

An *acousto-optical tunable filter* (AOTF) is typically constructed by an anisotropic birefringent crystal such as Tellurium dioxide (TeO_2). Piezoelectric transducers are bonded to the crystal, and by applying high-frequency voltage to the transducers, an acoustical wave is generated in the crystal (Fig. 4.9). Due to the birefringent response to the acoustic wave, the crystal forms a grating that diffracts polarized light according to the periodicity of the waves. Therefore, by selecting different frequencies, specific wavelengths can be selected one at a time. For measuring a full spectral image, each spectral bandwidth is measured one at a time. Just as with any grating, the AOTF also transmits the first-order non-diffracted beam that has to be blocked. By changing the amplitude of the voltage applied to the transducers, the transmitted intensity can also be controlled.

The AOTF can reach transmission efficiencies of 35 % and change the transmitted wavelengths in 10–100 μs. It can accept collimated beams with an acceptance angle of $\pm 5°$ and therefore can be used for imaging where each collimated beam that enters at a different angle corresponds to a different point in the image.

The system has the advantage that the spectral resolution can be tuned in a relatively large range by applying multiple frequencies to the device. In principle, adding another frequency can be used to double the spectral bandwidth (simply by selecting two frequencies that transmit two wavelengths that are close to each other so that their FWHM overlaps. Systems using up to 16 different frequencies are available, so that the resolution can be selected from the narrowest one up to a multiplication of 16 times, or practically a variable spectral resolution of 1–16 nm. It is useful in cases where several applications require each a different spectral range.

4.4.2.2 Novel Color Filter Methods

As color filters are abundant in many types of applications, new and novel filter-based methods immerge rapidly. The following method, developed recently, is based on surface plasmon nanostructures constructed of two thin metal films spaced by a subwavelength insulator [27]. The nanostructures act as surface plasmonic resonators (SPRs). SPRs are essentially charge density waves generated by the coupling of light to the collective oscillation of electrons on the metal surface. With today's nanofabrication capabilities, such arrays can be manufactured with variable density so that light traversing through them disperses respectively to its density, thus white light is dispersed to a wide wavelength range (visible and other spectra

ranges are possible). This way, color filters can be designed as well as spectral imaging systems. The advantage of this novel technique is that the SP arrays are relatively small in size (few micrometers per each color array), they do not apply high loss of energy, and also the light that is dispersed is already polarized. There is no current application based on this technique, yet this miniaturization of the dispersing element and the freedom to design variable elements on tiny arrays can become useful in future spectral imaging applications.

Another late development includes variable filters which are based on spectral selectivity that depends on the filter rotation angle (VersaChroma, Semrock, USA). These filters change the transmitted spectrum as a function of the angle of the filter. The performance of the filters is high; by changing the angle of the filter, the transmission spectral band changes, but the spectral band stays intact. The spectral range of the filter is approximately 12 % of its central wavelength, for example, 490–555 nm with a bandwidth of 25 nm. Although limited to a specific spectral range, these filters demonstrate the ever-growing number of techniques that can be combined with spectral imaging.

4.4.2.3 Advantages and Limitations of Wavelength-Scan Systems

One obvious advantage of spectral imaging systems that are based on wavelength-scan is the flexibility to select for each measurement the optimal spectral range. The downside is the low transmission rate of these devices (typically reaches only 35–50 %, depending on the type of device and model). On the other hand, systems that are based on fixed filters have very high transmission that can reach almost 100 % yet the spectral range can be tuned only by change of filter set.

The trade-off between the abovementioned spectral imaging methods can be viewed through a basic application used to determine the percentage of oxygen in the blood. Its prerequisites limit detection to the spectral range of 520–600 nm so that in principle three well-selected spectral ranges should suffice.

By using fixed filters, the spectral bandwidth of each filter is hardware dependent and cannot be changed, which means that for any other application a different set of filters is required. In contrast, both LCTF and AOTF provide variable filtering schemes with no moving parts and a higher speed with respect to the switching times of fixed filters. In addition, advanced AOTF systems provide a variable spectral resolution as well. See, for example, the review by Gat [28].

Another advantage of filter-based systems is the ability to select a different exposure time for each spectral band (filter). This can increase the overall quality of the spectral image when the measured intensity from the image is not uniform (in general) across the spectral range. One can also think about increasing the dynamic range by measuring the image with each filter at two different exposure times (or more). This can be important especially when there are varying intensity ranges along the image; normally, high intensities enforce short exposure times, thereby reducing the quality of the dimmer regions. Acquiring the same image at varying exposure times can unveil specimen varied by intensity at equal quality.

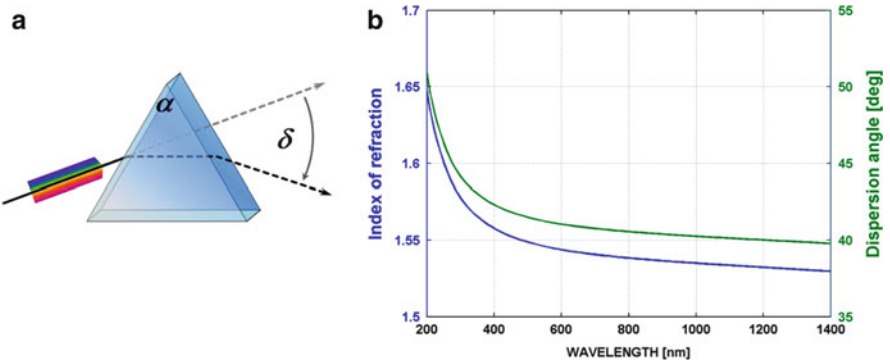

Fig. 4.10 **a** Prism dispersion depends on the wavelength of light, the prism head angle, and the dependence of the index of refraction on the wavelength. **b** The dependence of the index of refraction on wavelength (left y axis) and dispersion angle for a prism with a head angle of $\alpha = 60°$ (right y axis)

Lastly, an advantage of the AOTF lies at the fact that the AOTF acts like a grating, resulting in two diffracted beams of the orders +1 and -1 at similar angles around the non-diffracted zero-order unfiltered spectrum transmitted. The two first-order beams have orthogonal polarizations and, in principle, they can be used by either directing each order to a different CCD or by combining the two separate images to be imaged side by side on a single CCD. This will provide an advantage for different polarization-dependent applications.

4.4.3 Spatial-Scan Methods

In this method, the dispersion of light is achieved by using either a grating or a prism. The dispersion of a prism is given by

$$\frac{n_{\mathrm{p}}(\lambda)}{n_0} = \frac{\sin((\alpha+\delta)/2)}{\sin(\alpha/2)} \tag{4.3}$$

where α is the head-angle of the prism, $n_{\mathrm{p}}(\lambda)$ is the wavelength-dependent index of refraction of the prism material, and δ is the diffraction angle (Fig. 4.10). Figure 4.10b shows the index of refraction of quartz crystal (left y axis) and the resulting diffraction angle as a function of the wavelength for prism with a head angle of 60° (right y axis). As one can see, the difference is significant and provides the basis for spectroscopy.

A grating can also be used for dispersion (Fig. 4.11). The diffraction to a certain angle is strong when the following equation is fulfilled [29]:

$$\sin\alpha + \sin\beta = \frac{m\lambda}{d} \tag{4.4}$$

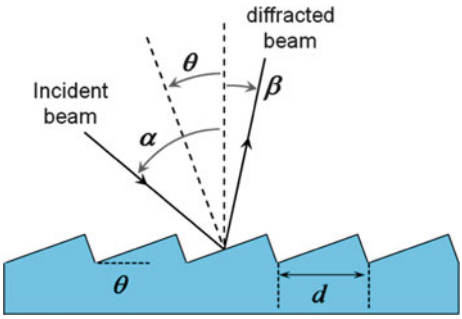

Fig. 4.11 Blazed grating. The angle of the blazes forms high reflection at the so-called Littrow condition. The *dashed lines* are perpendicular to the grating surface and to the blaze surface

where m is an integer describing the diffraction order, λ is the wavelength of light, α and β are the incident and the diffracted angles with respect to the normal to the grating surface, and d is the grating groove spacing. In addition, the blazed grating provides the highest efficiency when the so-called Littrow condition is satisfied:

$$\lambda_B = 2d \sin\theta \tag{4.5}$$

where θ is the angle of the blaze.

Both grating and prism can be used for spectroscopy. In general, the prism has a higher transmission that can reach 90 %, while the gratings usually have up to 65 % transmission. On the other hand, the gratings can provide a better spectral resolution when used in certain monochromatic configurations [30].

4.4.3.1 Spectral Imaging System Based on a Grating

Grating and prisms form the vast majority of single-point spectrometers. When used for spectral imaging with an array detector such as CCD, the inherent property of these dispersive elements, namely, the dispersion of the spectrum along one axis, forces sampling of only one line of the image at a time thus a scan along its perpendicular axis is required. In principle, a point detector such as PMT or a line detector can also be used, but these would require even more scans in order to construct a single spectral image. With an array detector, one axis is used for measuring the spectrum so that the other axis is left for measuring one line from the perpendicular axis of the image (Fig. 4.12). This requires one to scan the object line by line to collect the entire spectral image. The data is therefore collected as $I(x, y_i, \lambda)$ where y_i represents a single point along the y axis from the x–y plane, thus the scan along the vertical axis [31]. These methods have an advantage when the measured object is moving linearly and can be applied, for example, for an airborne system that can scan along its pathway or measuring substances that are moving along a conveyer. For other applications such as microscopy, a single-axis scanning mechanism must be added externally. Figure 4.12 describes only the concept of the system while the actual one looks much different due to aberrations that must be corrected, as explained below.

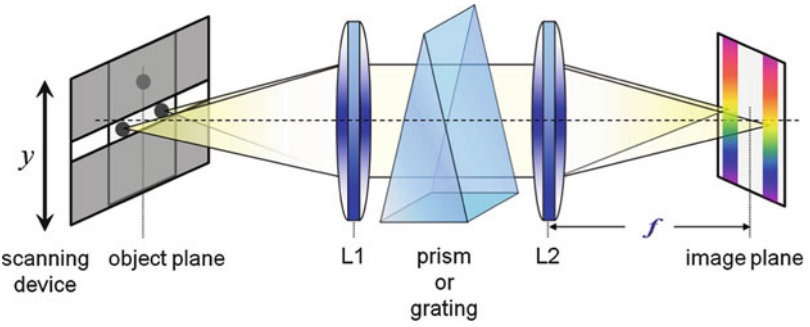

Fig. 4.12 Schematic description of a spectral imaging system with a grating or prism. One axis of the array detector measures the dispersed spectrum for only a single line from the image, in this case along x for a single point along y. Then, a scanning mechanism scans one line at a time from the object. Note however that this is a simplistic description, while the actual optical setup is different, see Fig. 4.13

The actual design of a spectral imaging system that is based on a grating or a prism requires careful attention in order to correct different aberrations that result from the nature of these elements. Two different names are used for the systems that disperse the light. *Spectrometers* are the systems that isolate a single wavelength from the whole spectrum and used either for isolated single wavelength measurement or for measuring the spectrum by scanning one wavelength at a time. A *spectrograph* on the other hand is used to disperse the whole spectrum along a single axis. When a spectrograph is combined with an appropriate detector such as a line of photomultipliers or array detectors, the full spectrum can be measured simultaneously which is certainly an advantage.

Spectrometers and spectrographs have a different optical setup, and for spectral imaging systems, it is certainly the spectrographs that should be used. Note, however, that the terminology is somewhat ambiguous because every spectrograph can be used also as a spectrometer by isolating a single wavelength from the whole dispersed spectrum. Spectrographs suffer from intrinsic aberrations. The main ones that must be corrected include field curvature, astigmatism, and anamorphism.

Field curvature causes the image of an object to be in focus on a curved surface instead of a plane. Therefore, when the center of the image is in focus, the other parts are blurred, and the further a point is away from the center, the more blurred it is. Astigmatism is an aberration that causes a change between focal length for vertical and for horizontal lines of the object. It therefore results in blurring of one of the image's dimension or the spectrum and has to be corrected. Anamorphism is another distortion that results in a nonuniform and variable size of each point that should be in focus, and it depends on its position in the object plane so that the object appears stretched in one dimension and thus must be corrected.

There are different optical designs that correct these aberrations to a satisfactory level, and only the few most common settings will be described here. More information can be found elsewhere [29, 30]. The first system is based on the

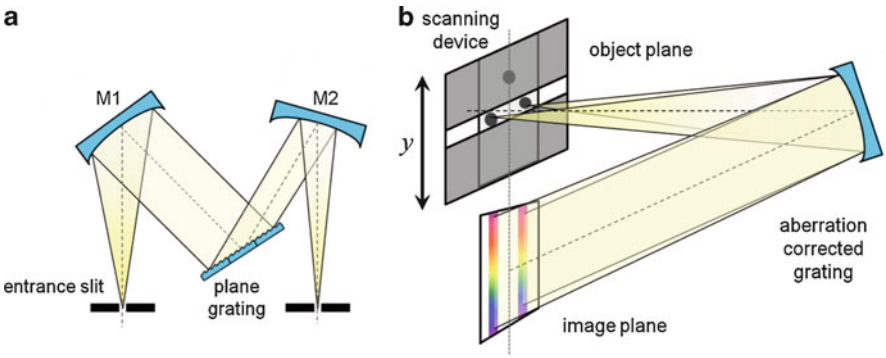

Fig. 4.13 Possible setting for spectrographs that can be used for spectral imaging. **a** Czerny-Turner setup, one of the mirrors is toroidal. **b** A Rowland-based optical setup with an aberration-corrected grating. This system does not require further optical elements for focusing the light to the array detector

Czerny-Turner design (Fig. 4.13a) or Ebert design that is not much different. In order to correct those aberrations, a toroidal mirror is placed in the set of mirrors in the spectrograph. A toroidal mirror has asymmetric vertical and horizontal radii of curvatures which can compensate for the aforementioned spherical aberrations when tuned correctly.

Another method for using a grating-based spectrograph with corrected performance is to use aberration-corrected gratings. The grooves' spacing in these gratings change in a systematic way that corrects the imaging performance of the device [32]. Sophisticated design capabilities together with optimized manufacturing techniques enable to produce such gratings on either plane or concave surfaces. Using a design that is based on Rowland mount with an aberration-corrected grating (Fig. 4.13b), a spectral imaging system with reasonable performance can be obtained.

4.4.3.2 Spectral Imaging System Based on a Prism

As described previously, prisms have higher transmission than gratings since the whole transmitted light is diffracted to a single dispersion pattern, while a grating device diffracts the light to higher dispersion orders. It therefore has the potential to act as a good dispersion element, but in order to do that, the optical aberrations should be reduced. An original design of a curved prism that corrects the aberrations to a high level of accuracy using a concave mirror was developed by Warren and Hackwell [33] (Fig. 4.14 and is available commercially with a similar instrumentation (Lightform Inc.)).

The last method for a spectrograph based on a prism that will be described is based on the development of a prism-grating-prism (PGP) device [34, 35], see Fig. 4.15. The advantage in this setup is that a very large spectral range can be handled by the system; it is also robust and has a pipelike shape that enables an

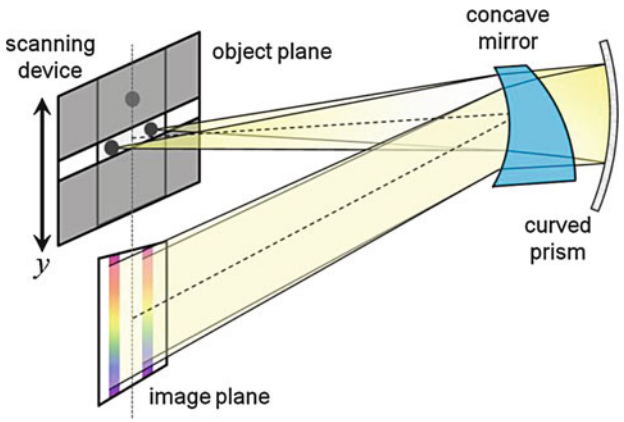

Fig. 4.14 Prism-based system. The prism is curved and a concave mirror reflects the light at the rear. It can be shown that the aberrations are significantly reduced so that a high level of imaging and spectral performance is achieved

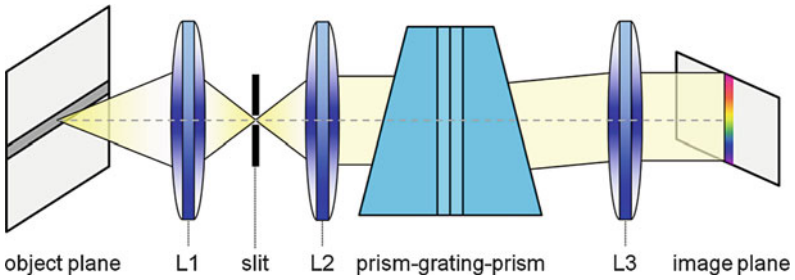

Fig. 4.15 Spectral imaging system based on a prism-grating-prism (PGP) unit. The system measures the spectrum for all points on a single line, so that a full spectral image is generated by a scan along one dimension. The front lens L1 creates an image on an entrance slit and the light is collimated again with lens L2. The PGP unit disperses the light which is focused with L3 on the array detector

easy integration with fore-optics and a detector. Lastly, due to the grating, it has high diffraction efficiency PGP systems are available commercially (e.g. Specim).

The design shown in Fig. 4.15 ensures the measurement of only a single line from the image. Construction of the full image requires scanning along the other axis of the image. Lens L1 focuses the image on an entrance slit while lens L2 collimates the light. After passing through the PGP unit, the light is focused again through lens L3. Therefore, each point along a single line from the image is imaged to a single vertical line on the array detector, while the spectrum is vertically dispersed. The design of the PGP unit has many degrees of freedom that can be optimized for the spectral performance. The head angle of the entrance prism is optimized so that the incidence angle of the refracted beam on the grating matches the Bragg condition for the first-order diffraction of the grating. This can be exact only for a

certain wavelength which is selected to be at the desired operating spectral range of the unit. It ensures the maximal transmission around that angle and results in a certain response curve of the system. The second prism does not have to be identical to the first one. Its head angle and thickness are optimized so that the required spectral range is centered on the optical axis. The grating is actually a volume grating with a thickness of few tenths of micrometers. It is commonly made of dichromated gelatine that has a very broad spectral range (∼300–3,000 nm). Because of the transmission of second harmonics at the same angles through the grating, spectrographs that are based on gratings are usually limited to one decade, i.e., from $\lambda_{\min}$ to $\lambda_{\max} \leq 2 \cdot \lambda_{\min}$. This problem, however, can be solved by using a long-pass filter in front of only part of the array detector, in such a way that long wavelengths are incident only on part of the CCD.

4.4.3.3 Advantages and Limitations of Spatial-Scan Methods

Spatial-scan methods require scanning the objects along one dimension. This is trivial for applications in which the sample is moving already, such as production line material that runs along a conveyor belt or other moving samples. For other applications, such as spectral imaging microscopy, scanning requires to implement a scanning stage or other scanning optics. This device should be synchronized with the frame acquisition rate of the array detector in order to ensure the measurement of a smooth image.

Systems that are based on either a grating or a prism have a relatively high spectral resolution [36]. The scanning may require the addition of extra mechanic and optic elements, as described previously. In addition, live view image of the sample prior to its full spectral acquisition is unavailable (at least in current offered systems). The live view enables to fine-tune parameters such as focus and exposure time or to adjust the relevant region of interest for imaging. This can be solved, as was demonstrated before, by adding another CCD that is aimed only for observing the image and performing these tasks [37]. Although it requires additional hardware, it does provide a solution to the problem.

Systems which are based on dispersion elements such as prisms and gratings are also efficient for measuring the spectral images through confocal microscopes. Actually, almost all of today's confocal microscopes attain spectral capabilities based on a dispersion element [38]. Most of the confocal microscopes use a single-point detector (photomultiplier or avalanche photodiodes), and the dispersion element is placed in front of it coupled to a slit in order to select the required spectral resolution. These systems require measuring the image once for every sampled wavelength band. Other systems use an array detector that enables to measure the full spectrum of the whole image in a single scan.

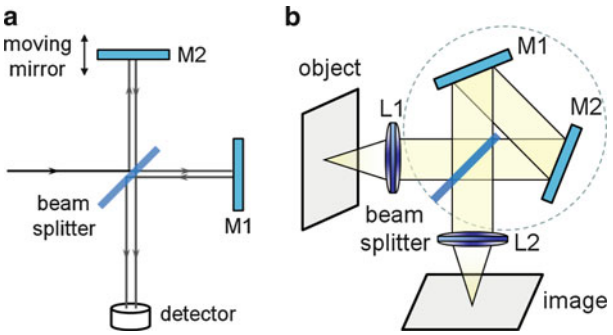

Fig. 4.16 Michelson interferometer that can be used for Fourier spectroscopy. The light is split by a beam splitter, and the two identical beams travel to two mirrors. Mirror M1 is fixed while mirror M2 can be shifted with sub-micrometer resolution. The two reflected beams combine at the detector and the resulted intensity depends on the phase difference that is created due to the optical path difference that is created. **b** Sagnac interferometer results in a similar effect, but it is a "common-path" interferometer. The beams are split by a beam splitter and reflected by mirrors M1 and M2. The optical path difference is changed by rotating the elements in the observed *gray circle*

4.4.4 Fourier-Based Spectral Imaging

Another method for measuring spectral images uses the principle of Fourier spectroscopy [39, 40]. In this technique, the dispersion is performed in the Fourier domain, unlike all other methods that directly measure the wavelength.

Fourier spectroscopy, also known as Fourier transform spectroscopy, is based on the use of an interferometer (Fig. 4.16a).

In this method, there are no filters, grating, or prism and the spectrum is measured by using the effect of interference of light. An interferometer (Fig. 4.16a) is a system that splits the light into two beams, creates an *optical path difference* (OPD) which consequently forms a time delay between the traveling beams, and joins the beams back again to interfere at the detector. The intensity at the detector is measured at many different OPDs; the output $I(\text{OPD})$ is called an *interferogram* function. The interferogram is actually a representation of the tested spectrum and by mathematical data transformation, the spectral information can be derived, as shown below.

Figure 4.16a shows a Michelson interferometer. It can certainly be used for spectral imaging, but it is very sensitive to environmental variables such as temperature changes. It results from the fact that the two splitted beams are traveling to different mirrors, and every small change in the length will affect the measured interference pattern and the interferogram.

To solve this problem, a spectral imaging that works on the Fourier spectroscopy principle was designed to work with a Sagnac interferometer as shown in Fig. 4.16b [40]. This interferometer belongs to a family of interferometers known as common-path interferometers. It has the advantage that the splitted beams are traveling through the same region of space and the same mirrors but in opposite directions. Therefore, to the first order, mechanical changes that may result from temperature expansion or other reasons are canceled out, making the interferometer very robust. The spectral imaging system is constructed of two lenses, two mirrors and a beam splitter. The lens L1 collimates the light before entering to the interferometer. The beam splitter splits the beams to a reflected one and a transmitted one. These travel in opposite directions through two reflections from mirrors M1 and M2, and the light is combined together and focused by the lens L2 to the array detector. The mirrors and beam splitter that are shown inside the gray circle (Fig. 4.16b) are mounted together on a rotating stage. Note that there are also beams that are reflected (or transmitted) backward to the light source, but the intensity of this part depends on the position of the interferometer so that on average only half of the intensity goes to the detector.

The optical geometry of such a system will keep the focusing point always at the same spot if the stage is rotated, and therefore, the object will always be imaged exactly on the same pixels without any shift or aberration. On the other hand, it can be shown by following the optical path of the transmitted and reflected beams that the OPD depends on the rotation angle. This can be formulated as

$$\mathrm{OPD}(\theta) = C\theta. \tag{4.6}$$

It means that the interferometer acts as an OPD generator without effecting the position of the image on the array detector. The effect of the OPD is to modify the intensity of each pixel while changing the angle θ.

4.4.4.1 Extracting the Spectrum from the Interferogram

In order to understand the method in which Fourier spectroscopy works, one has to follow the actual signal that is measured by the detector [41, 42].

Recall the light collected from a single pixel on the detector origin from a well-defined spot in the sample. It is better to describe this light through its electric field properties. For a single one-dimensional wavelength, this electric field can be described as $E = E_0 \cos(2\pi x/\lambda - \omega t)$ where E_0 describes the amplitude of the field, λ is the wavelength, $\omega = 2\pi c/\lambda$ is the angular frequency, c is the speed of light, x is the distance traveled by the wave from a certain reference point, and t is the time. In Fourier spectroscopy, it is common to change the wavelength to the wavenumber units simply described as $\sigma = 1/\lambda$. The light would in general contain many different wavelengths, and therefore the total electric field is

$$E = \int A(\sigma) \cos(2\pi\sigma x - \omega t)\, \mathrm{d}\sigma. \tag{4.7}$$

Here $A(\sigma)$ is the electric field amplitude per unit wavenumber. When this field enters the interferometer, it splits into two, and half of each beam goes to the detector. As mentioned above, the other half is sent back to the light source. Therefore, assuming that there are no losses at all through the optical path as a result of the reflections and transmissions, the electric field at the detector is

$$E = \frac{1}{2}\left[\int A(\sigma)\cos(2\pi\sigma\, x - \omega t)\mathrm{d}\sigma + \int A(\sigma)\cos(2\pi\sigma(x + \Delta x) - \omega t)\mathrm{d}\sigma\right] \tag{4.8}$$

where Δx is the OPD created between the two splitted beams. The intensity measured by the detector is the square of the electric field. In addition, the measured intensity is the time average of the intensity over a time interval that is long enough relative to the wave time period, which is in the range of 10^{-15} s, although it can be very short, say few nanoseconds. Therefore, it gives

$$I\,(\Delta x) = \left\langle |E|^2 \right\rangle = \left\langle \frac{1}{4}\left[\int A\,(\sigma)\cos\,(2\pi\sigma x - \omega t)\,\mathrm{d}\sigma + \int A\,(\sigma)\cos\,(2\pi\sigma\,(x + \Delta x) - \omega t)\,\mathrm{d}\sigma\right]^2\right\rangle \tag{4.9}$$

Here the triangular brackets represent averaging over time. Opening the squared parenthesis will give four terms. Two of the terms will be of the form $\left\langle \iint A^2(\sigma)\cos(2\pi\sigma x - \omega t)\cos(2\pi\sigma' x - \omega' t)\mathrm{d}\sigma\,\mathrm{d}\sigma'\right\rangle$. Because of the time dependence of each cosine, the time average will vanish for $\sigma \neq \sigma'$, or these terms will give $\left\langle \int A^2(\sigma)\cos^2(2\pi\sigma x - \omega t)\mathrm{d}\sigma\right\rangle = \int A^2(\sigma)\left\langle\cos^2(2\pi\sigma x - \omega t)\right\rangle\mathrm{d}\sigma$ where we inserted the time averaging to the only term that depends on time. The time average of $\cos^2$ is $1/2$, and therefore, each such term gives $(1/2)\int A^2(\sigma)\mathrm{d}\sigma$. This integral simply gives the total intensity of the light source. The two other terms are equal to $\left\langle \iint A^2(\sigma)\cos(2\pi\sigma(x + \Delta x) - \omega t)\cos(2\pi\sigma' x - \omega' t)\mathrm{d}\sigma\,\mathrm{d}\sigma'\right\rangle$. Using trigonometric identities, and the fact that the wavenumbers must be identical in order that the time average will not vanish, each of these terms is equal to $(1/2)\int A^2(\sigma)\cos(2\pi\sigma\Delta x)\mathrm{d}\sigma$. Substituting these to Eq. 4.9 will give

$$I(\Delta x) = \frac{1}{2}\left[\int A^2(\sigma)\mathrm{d}\sigma + \int A^2(\sigma)\cos(2\pi\sigma\Delta x)\mathrm{d}\sigma\right]. \tag{4.10}$$

The first term is a constant that is equal to the total intensity emitted from each pixel region of the image. The second term is more important, as it depends on the OPD, Δx. Actually, the second term can be identified as the real part of the Fourier transformation of $A^2(\sigma)$. Recall that Eq. 4.10 is the intensity measured by the detector when performing the measurement for many different OPDs Δx.

Having this function, the spectrum $I(\sigma)$ can be extracted by an inverse Fourier transformation. Since the intensity at the detector is sampled for discrete OPDs, the inverse FT is also a discrete operation. It is performed in the complex space

$$I(\sigma) = \sum_{i=1}^{N} I(\Delta x_i) \exp(-i 2\pi\sigma \Delta x_i) \tag{4.11}$$

Here N is the number of OPD's that were measured.

Equation 4.10 shows that the interferogram is a symmetric function with respect to the OPD. It is most common to measure a symmetric interferogram by measuring both positive and negative OPDs [41, 43]. This means moving the mirror in both directions around the zero OPD in the Michelson interferometer (Fig. 4.16a) or rotating the Sagnac interferometer in both positive and negative values around zero OPD (Fig. 4.16b).

Three additional operations are performed before or after the Fourier transformation:

1. *Phase correction*. If the interferogram given by Eq. 4.10 is symmetric, then the Fourier transformation (Eq. 4.11) will be a real function. Nevertheless, the interferogram will never be perfectly symmetric. Due to noise, as an example, there will always be a deviation from symmetry even for perfect optics. Moreover, the use of imperfect lenses can result in a π phase shift of the two splitted beams so that the intensity is an antisymmetric function. The phase correction solves that in different possible ways. The most common way is to multiply the complex measured spectrum $I(\sigma)$ by the cosine of the phase at every wavenumber σ, or simply to take into account only the normal of the complex spectrum.
2. *Apodization*. Fourier transformation (as described in Eq. 4.11) is valid given an infinite interferogram function, which is certainly impossible. The finite nature of $I(\Delta x)$ can be observed as a multiplication of the infinite function with a square window of width $2D$, where D is the maximal measured OPD. One of the known traits of Fourier transformation [41] is that a multiplication gives a convolution of the FT of the two functions. The FT of a square window is a sinc function $\sin(\sigma)/\sigma$ that has significant oscillations that will alter the spectrum, usually in an unacceptable manner. Apodization is used to eliminate this. It comes on cost of a small reduction of the spectral resolution, and different functions can give different trade-offs [44]. The apodization can be performed either as a preprocess by multiplying the interferogram with the apodization function or by deconvolution of the FT as a post-process.
3. *Zero filling*. This operation has the effect of interpolation of the calculated spectrum. It is a valuable function and it emphasizes the position of maxima as measured by the system. It is a simple operation that adds zeros to the interferogram tails. It is also common to use it in order to ensure that the interferogram has a number of points that is equal to a power of 2 (2^n). This is required in order to use fast Fourier transformation (FFT) algorithms.

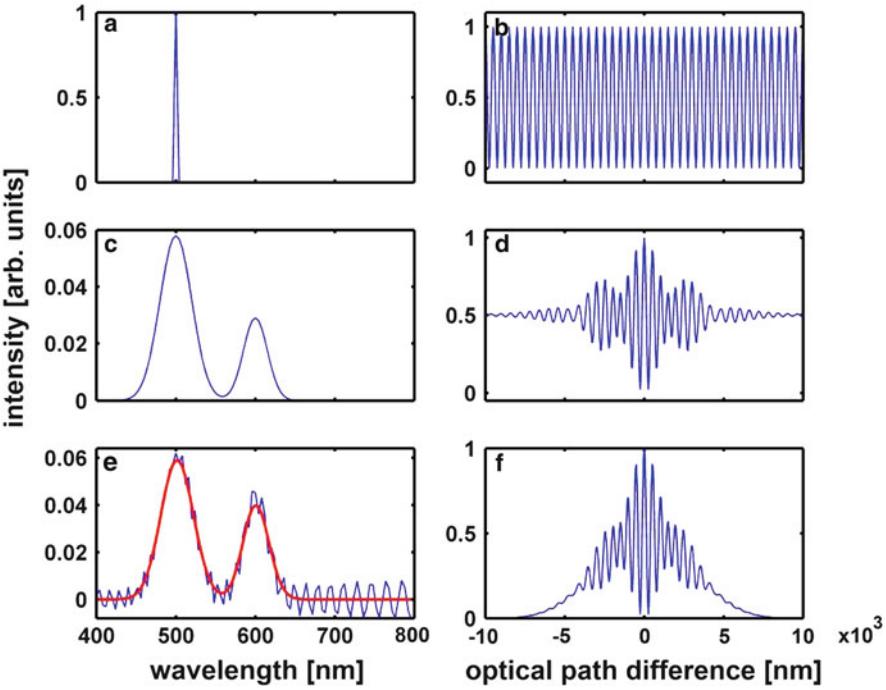

Fig. 4.17 Fourier transform analysis for Fourier spectroscopy. **a** A delta-function spectrum. **b** Its interferogram. **c** A spectrum of two Gaussian-like peaks. **d** Its measured interferogram. **e** The analyzed spectrum without apodization (*blue*) and with apodization (*red*). **f** The apodized interferogram of the spectrum shown in **c**

Figure 4.17 shows interferograms of two typical spectra and the effect of the image processing as described above. Figure 4.17a shows a delta function of quasi-monochromatic spectrum and Fig. 4.17b shows its cosine-like interferogram. Figure 4.17c shows a spectrum with two Gaussian-like peaks and Fig. 4.17d shows its interferogram. Figure 4.17f shows the apodized interferogram using a Blackman-Harris window. Figure 4.17e shows the resulted calculated spectrum by applying the inverse Fourier transformation without apodization (blue) and with the Blackman-Harris-type apodization. The dramatic effect of the apodization is clear.

Another method that is related to time-scanning methods is based on the Hadamard transform [45]. This method uses an imaging spectrometer equipped with a CCD and special optics. A spatial light modulator (SLM) compresses the whole 2D image onto the slit of the imaging spectrometer and allows blocking any set of points from the image. By measuring many 2D images, each of which contains a superposition of spatial and spectral information and performing a Hadamard transformation, the spectral imaging information can be retrieved.

4.4.4.2 Advantages and Limitations of Fourier-Based Spectral Imaging

This method has the advantage that the intensity at each wavelength is collected throughout the whole duration of the measurement. Therefore, it increases the efficiency of light collection for a typical spectrum. It also allows selecting the required spectral resolution without any changes to the hardware, simply by setting the total measured OPD. This provides an important advantage because the required spectral resolution may vary significantly from one application to another. It also has an effect on the spectral image acquisition time, which gets shorter when a lower spectral resolution is selected. The Sagnac interferometer provides another degree of freedom for the spectral resolution. As shown in Eq. 4.6, the dependence of the OPD as a function of the rotation angle depends also on the constant C. This constant depends on the optical alignment of the interferometer elements and it can be tuned for optimal measurements. Therefore, if very high spectral resolutions are required, the system can be aligned to have a relatively large C, which means that a large total OPD can be reached and therefore also a high spectral resolution. Note that the maximal rotation angle of the interferometer is limited (see Fig. 4.16) and therefore this additional degree of freedom becomes rather important.

The improvement of the spectral resolution by increasing the parameter C is limited also because of the pixel size. While increasing C, the intensity falling on a single pixel along one axis will also have an OPD that will vary along the pixel. This is physically limited to a change that is smaller than $\mathrm{OPD}_{\max} < \lambda/2$, which is the Nyquist criteria and practically even to half of that.

The advantage of collecting the intensity of all wavelengths at each OPD sets a limitation on the Fourier method, namely, it is not possible to skip unimportant parts of the spectral range. The Fourier-based system measures the whole spectrum in a given range. This limitation can partially be overcome by use of sets of single band filters. Another issue related to this limitation occurs in cases where there is a combination of spectral features that has different intensity level, as an example assume that the intensity in the range 400–500 nm is relatively high while the intensity in the range 700–800 is low. At every OPD, the intensity that is collected is a weighted sum of the whole spectrum, and because of noise, the signal from the low-intensity part of the spectrum may be affected due to the Poisson noise of the signal from the high-intensity part. This problem can be resolved, again, with the use of a filter to block the more intense parts of the spectrum.

4.4.5 Full Spectral Images in a Single Shot

When the principle of measuring a spectral image was described in Sect. 4.3.1, it stated that the ultimate spectral imaging device would be able to capture the whole spectral information $I(x, y, \lambda)$ at a single shot. It is clear, however, that this is impossible with a 2D detector, unless some compromise is done. In some cases, the compromise is not necessarily a disadvantage. As an example, consider a case where

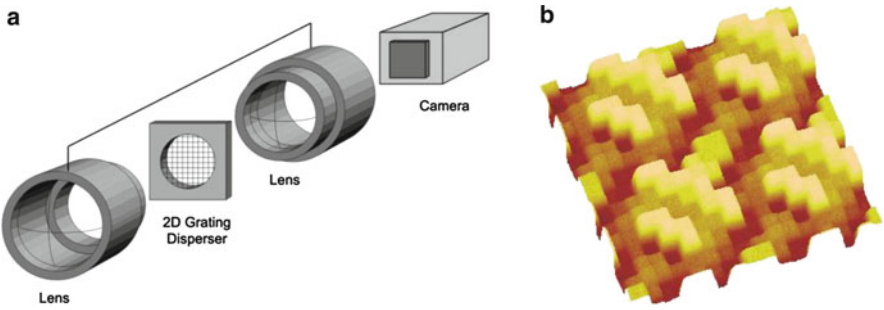

Fig. 4.18 The principle of a computed tomography imaging spectrometer (CTIS). **a** The system is constructed of a collimating lens, a two-dimensional holographic grating, (shown in **b**), a focusing lens, and an array detector (Image courtesy of Greg Bearman, Snapshot Spectra, USA)

a relatively small sample is analyzed covering a small portion of the array detector. If that is the case, there are practically a lot of extra pixels on the detector that are not being used, especially with the growing number of pixels in newer version of array detectors.

This is exactly what the method of *computed tomography imaging spectrometer* (CTIS) does, by taking advantage of a clever two-dimensional dispersion element. The method, sometimes termed as snapshot spectral imaging, should be distinguished from the methods previously described in Sect. 4.4.1 by the fact that the latter ones enable a very limited number of wavelengths to be measured while CTIS can provide a high-resolution spectral image.

CTIS allows to measure a full spectral image in a single exposure time [46, 47]. It is based on a holographic phase plate that acts as a two-dimensional dispersion element that projects the dispersed spectral-spatial information to the array detector. The spectral image is reconstructed from the raw data by using adequate algorithms, and the size of the FOV is traded off for the spectral information [48].

The schematic description of the system is shown in Fig. 4.18a. The real image is collimated with a lens and the collimated light passes through a two-dimensional dispersion element whose structure is shown in Fig. 4.18b. After passing this element, the light is imaged with another lens onto the detector.

The outcome of CTIS is a typical pattern shown in Fig. 4.19. The image is constructed of 5×5 sub-images. The central one shows the non-dispersed image and does not contain spectral information. The other images are the ± 1 and ± 2 diffraction orders of the image along the two main array axes, with a radial dispersion. By using different holographic dispersion elements, other patterns can be generated, for example, with smaller number of diffraction orders thereby increasing the size of the FOV [46]. This data is analyzed by respective types of deconvolution algorithms that take into account the transfer function of the system. The transfer function is measured during the calibration of the system and includes a series of images that each of it describes the pattern that is measured on the detector when illuminating a point at a given wavelength. This can be achieved, as an example, by

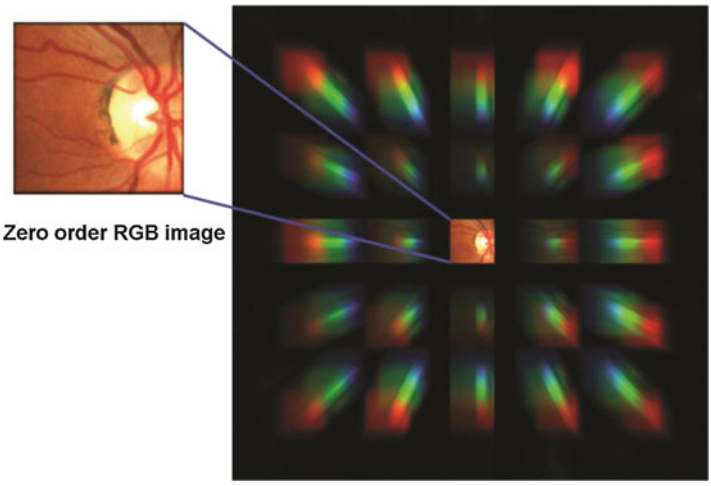

Fig. 4.19 A typical image acquired with a CTIS system. The *center* shows the zero order of the diffraction, which is the original image. The *color* is only shown for emphasizing how the dispersion looks on the camera, but it is usually a gray-level detector. The higher orders ± 1 and ± 2 around it show a dispersed image. By analyzing this information, which is clearly well organized, the spectral image can be extracted (Image courtesy of Greg Bearman, Snapshot Spectra, USA)

using a fiber connected to a monochromator and illuminating different wavelengths from different points in the image, while measuring the diffraction pattern for each illumination, $I(x, y, \lambda)$. Because the holographic dispersion element provides a linear response, a relatively small number of points can be measured. Having the series of these patterns provides the system transfer function [49].

The performance of a CTIS depends on the spectral distribution along the image. The most extreme cases would be a single point with a certain spectrum or a uniform image with the same spectrum. A single point can be analyzed with a CTIS with a relatively high spectral resolution while it gets worse with a uniform field.

Other methods that are based on a spectral-spatial projection of the spectral image onto an array detector were also developed and demonstrated based on compressed sensing [50]. In these methods, a more complex set of two dispersive elements are used together with a coding aperture. A similar method based on regular array detector and a prism was also demonstrated lately [51]. The principle is conceptually similar. Let us assume that a certain optical system with some kind of dispersion element causes the spectral information to be convolved on the image plane in a systematic manner. If we also assume that the spectral convolution function can be calculated or measured, then it means that the spectral image can be deconvolved by using the appropriate algorithm. The quality of the deconvolved spectral image depends on many parameters of the system, as well as the type of spectral image, and it is a subject that must be treated for each system separately.

4.4.5.1 Advantages and Limitations of Single-Shot Spectral Imaging

The advantages of the method are clear, as it provides the full spectral image in a time range that is limited only by the exposure time that provides a good SNR. It is an excellent solution for applications where imaging time is a major factor. One such example is the application of retinal imaging. It is well known that oxy- and deoxyhemoglobin have a somewhat different spectral absorption. By measuring the spectral image of the retina through a fundus camera, the spectral analysis can provide oxygen saturation maps that indicate on possible ischemic regions on the retina. This was demonstrated with CTIS with an exposure time of $\sim$3 ms [49].

The method has some limitations as the quality of the spectrum that is extracted depends on the spatial-frequency distributions of the image and therefore should be considered for the application. It also has a limited field of view due to the region on the array detector that collects the higher-order dispersion information.

4.4.6 Illumination-Scan Spectral Imaging

All the spectral imaging setups described thus far share in common the requirement of a single source of illumination (typically white light source), while the heart of the spectral imaging system lies in the optical path beyond the sample and contains some fore-optics.

Another possibility is to illuminate the sample with an array of light sources in different wavelengths in order to measure spectral properties. The detector in this case collects the light that is transmitted through the sample. It can also be the emitted light, if it is a fluorescence measurement, but this will be a rather uncommon setup.

The concept of such a setup was introduced recently with an application for retinal imaging using a series of narrow-band LEDs with different peak wavelength [52]. In this system only five different wavelengths were selected and coupled to the illumination optics of the fundus camera through fiber coupling, but it can certainly be extended if necessary. In this case, these five wavelengths were selected to distinguish five different chromophores that are important for retinal inspection.

Such a method is preferred over a system that illuminates with white light and disperses the colors in front of the detector, simply because much less light falls on the retina of the measured subject enabling a more comfortable examination. The LEDs that were selected are powerful enough to allow short exposure time (approximately 50 ms). For retinal imaging, this is an important factor as the retina is subjected to constant movements and short exposures reduces image smear.

In principle, all the wavelength-scan methods can be used on the illumination path before the sample while not using any filter in front of the detector. Conceptually, such a measurement for bright-field transmission or reflection will be identical to the systems that are described in Sect. 4.4.2 and with some modifications also to those that are described in Sects. 4.4.3 and 4.4.4. It can also be used for fluorescence

measurements, but then the measurement is somewhat different, as it will provide information on the excitation spectrum and would still require selecting relevant filters in front of the detector so that it will match the emission spectra of the fluorochromes.

Another approach for illumination-type spectral imaging was demonstrated by using a *digital micromirror device* or DMD [53]. A DMD is constructed of an array of mirrors, typically 10^6, each with dimensions of 10–15 square μm that can be rotated around their axis by applying electrostatic forces. A setup is constructed with light source and a diffraction element such as a grating or a prism, and the dispersed light illuminates the DMD. Each mirror is separately controlled so it will reflect the light that impinges on it onto the entrance slit to a fiber that can be connected to different optical devices such as an endoscope. The mirrors can be controlled at a rather fast speed of up to 20 kHz.

The DMD unit can also be used for constructing another type of spectral imaging system by allowing the device to illuminate a single spot at a time with a single mirror. Once the spot is illuminated, the light that is emitted by the sample can be detected with a normal spectrometer or spectrograph, and the DMD can now be used to scan each of the pixels of the image. Such a device was used for spectral imaging as well as for time-resolved measurements [54]. A somewhat similar method was developed based on a spatial light modulator (SLM). The system called programmable array microscope (PAM) enabled the measurement of the spectral image of a three-dimensional object [45].

Another interesting method that was developed using spectroscopy actually twists things up and uses the spectrum in order to gain spatial information [55]. The method called spectrally encoded endoscopy (SEE) uses diffractive optics to encode different spatial regions, each with a unique wavelength. Therefore, the spectrum is dispersed along one dimension, and the readout of each wavelength provides information on a single point in the image. In order to cover the other spatial dimension, scanning is performed. A similar method that uses an interferometer in a way that is similar to optical coherence tomography (OCT) was also used in order to measure the 3D structure of an object [56].

4.5 System Requirements

The previous section covered optical and design methods defining the core of any spectral imaging system. In order to achieve a successful measurement, the spectral imaging system must include other optical elements such as light sources, control mechanisms and software for acquisition and analysis.

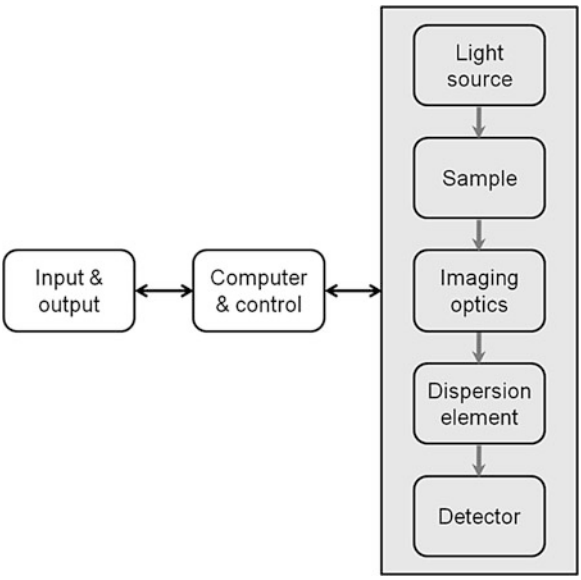

Fig. 4.20 The architecture of a typical spectral imaging system. It consists of a light source, imaging optics, a dispersion element, and a detector. The system is controlled by a computer with electronics and an input/output device

4.5.1 System Configuration

A spectral imaging system includes a certain number of elements (Fig. 4.20). It consists of a light source that matches the application, such as a Halogen, LED, or Xe lamp, an apparatus containing the dispersion device mounted to a microscope or other fore-optics and a detector, most likely an array detector. A computer controls and synchronizes all active devices and settings prior to acquisition and stores and analyzes the accumulated information with advanced analysis software. The configuration may also be somewhat different; for example, the dispersion element may be located in a different position along the optical path as described before. In addition, the actual system may not necessarily include all the elements that appear in Fig. 4.20. Commercial systems that are aimed to operate on a microscope, as an example, make use of the illumination light source and optics of the microscope and therefore may include only the dispersion element rather than simple optics and a detector.

4.5.2 Acquisition Software Requirements

Many spectral imaging applications require careful attention to the conditions under which the image is taken. In that sense, a capability of image acquisition parameter control is a prerequisite in most spectral imaging applications. In some others, control over illumination source is also necessary.

The most important acquisition settings are the detector's exposure time, the spectral range to sample, the spectral resolution, and the region of interest and spatial resolution. Observing a live view image of the sample to be measured is important and enables to review and adjust parameters of ROI and exposure time as well as to focus correctly. In some devices like the ones based on scanning (especially grating and prism based), a preview image would be time consuming as at each acquisition only a single line from the object is observed. One solution is to use another optical path for measuring the actual image that will be measured through the spectral imaging optics after scanning. Such a solution that uses an additional CCD camera for measuring the live-image is available, for example, with the PARISS system (Lightform Inc.)

A different problem arises with the systems that scan the spectral image one wavelength at a time because it may not be possible to see all the details of the object through a single wavelength band. A simple solution would be to add another extra filter that transmits the full spectrum, so that it can be used for the focusing process. Yet, the selection of the adequate exposure time per each wave band is compromised this way since a broad wavelength filter gives a bright signal at every pixel. Selection of maximal exposure time that does not saturate the pixels of the detector would not always become useful as it is most likely that the intensity will be much dimmer when measuring through each wavelength band separately. The solution therefore is the experience and knowledge of the nature of the sample or a trial and error repetitive measure.

A similar problem arises also with the Fourier-based system that scans the OPD space before transforming it to the spectrum. Here, a typical view of the image looks like a superposition of a series of fringes on top of the image and disturbs the observation of a clear image that is necessary for the settings. This was solved with the SpectraCube system (Applied Spectral Imaging, Israel) by adding a mechanism in the interferometer that effectively removes the beam splitter out of the interferometer, leaving a clear image on the detector. The exposure time can be determined after placing it back again to the interferometer.

In summation, typical spectral imaging acquisition software should have the ability to set or select the following parameters:

1. The region of interest that will be measured from the full detector area
2. The exposure time
3. The spectral resolution
4. The spectral range
5. Binning (if applicable) that can improve the SNR but decreases the spatial resolution
6. Other parameters that are relevant for the specific hardware being used, such as the zero filling in Fourier-based systems or the relative exposure time of measuring through each filter with the wavelength-scan systems

Not all applications require the whole set of the abovementioned requirements.

4.5.3 Spectral Image Analysis

The spectral image contains finer color changes than the human eye can perceive and stores that information spatially (spectrum per pixel). In light of that, the interpretation of the data cannot be assessed naively by eye observation and requires more sophisticated analysis schemes as well as methods to observe and display the results [42].

The analysis of spectral images can be performed based on both the spectral and spatial image features. All image processing methods and algorithms are adequate and relevant for spectral imaging as well, for a review, see Young et al. [57]. Spectral analysis is by itself a broad field. A few of the most basic algorithms in spectral imaging are described below. A specific application requires specific analysis methods that combine both spectral and image analysis algorithms.

Prior to the application of advanced spectral analysis algorithms, there are important software features that are essential in the everyday work for any type of application, mainly in order to get first impression of the data and examine quickly the output image:

1. Observe a spectrum of a single pixel.
2. Observe a spectrum of a defined region, (e.g., a 5×5 pixels square).
3. Select few spectra from different regions of the image and compare them.
4. Present a color image, where the red, green, and blue components are defined by the user at three different spectral ranges.
5. Setting the lookup table (LUT) for observing the color image mentioned above.
6. Scan the image along the wavelength range.
7. Save selected spectra to a library or load spectral libraries that can be compared to spectra from the image.
8. Crop the image (in the spatial plane and along the wavelength axis) and save the result.
9. Segment regions of the image by using very basic algorithms such as spectral similarity to a selected spectrum.

In the following, we describe few of the more important spectral imaging algorithms [58].

4.5.3.1 Linear Decomposition (Fluorescence)

The linear decomposition algorithm or spectral un-mixing [59, 60] assumes that the measured signal from each color is linearly proportional to the concentration of the entity that is labeled with that color in the object. This assumption holds when the absorption and fluorochrome concentrations are low and as long as energy transfer does not occur in between the fluorochromes [61]; otherwise correction terms can be used.

Assume that few fluorochromes are used so that each one labels a different entity. The entities, and therefore also the fluorochromes, may be found either separately or mixed at every pixel of the image. The purpose of the linear decomposition algorithm is to find the amount of each fluorochrome at each pixel. In its simplest form, the algorithm requires measuring and saving the emission spectra of the distinct fluorochromes prior to the actual analysis with the same experimental conditions. It also requires that the spectra of the different fluorochromes are distinguishable from one another and are linearly independent, which means that none of the spectra can be described as a linear combination of the others.

We describe the algorithm as it is performed on a spectrum at a single pixel, and it can be repeated for the whole image. The spectrum of each fluorochrome can be described as $I_i(\lambda)$ where $i = 1, 2, \ldots, N$ represents the index of the fluorochrome. The measured spectrum $I(\lambda)$ can be viewed as a vector with dimension that is equal to the number of wavelengths in the spectrum, M. We define C_i as the concentration of each fluorochrome relative to the concentration of the measured references, and the measured spectrum can be expressed as $I(\lambda) = \sum_i C_i \cdot I_i(\lambda)$. This can be written in a matrix form $\mathbf{F}$ where each column corresponds to one of the reference spectra:

$$\begin{bmatrix} I(\lambda_1) \\ I(\lambda_2) \\ \vdots \\ I(\lambda_M) \end{bmatrix} = \begin{bmatrix} I_1(\lambda_1) & I_2(\lambda_1) & \ldots & I_N(\lambda_1) \\ I_1(\lambda_2) & I_2(\lambda_2) & & \\ \vdots & & \ddots & \\ I_1(\lambda_M) & \ldots & & I_N(\lambda_M) \end{bmatrix} \times \begin{bmatrix} C_1 \\ C_2 \\ \vdots \\ C_N \end{bmatrix} = \mathbf{F} \times \begin{bmatrix} C_1 \\ C_2 \\ \vdots \\ C_N \end{bmatrix} \quad (4.12)$$

If $M \geq N$ (i.e., the number of points in the spectrum is larger than or equal to the number of fluorochromes), it is possible to find the left-inverse matrix of $\mathbf{F}$, $\mathbf{F}^{\mathrm{LI}}$, so that the multiplication $\mathbf{F}^{\mathrm{LI}} \times \mathbf{F}$ gives an identity matrix. Then, the values of C_i are found by

$$\begin{bmatrix} C_1 \\ C_2 \\ \vdots \\ C_N \end{bmatrix} = \mathbf{F}^{\mathrm{LI}} \times \begin{bmatrix} I(\lambda_1) \\ I(\lambda_2) \\ \vdots \\ I(\lambda_N) \end{bmatrix} \quad (4.13)$$

$\mathbf{F}^{\mathrm{LI}}$ depends only on the reference spectra, and therefore, it has to be calculated only once for the whole image. Because of noise, the calculation can only provide an estimated solution for the $\mathbf{C}$ values and the quality of the solution can be tested by comparing the measured spectrum with the predicted one, $I'(\lambda) = \mathbf{F} \times \mathbf{C}$. The vector $\mathbf{C}$ must have only positive values, and therefore, a constrained algorithm must be used. One method is to find the vector $\mathbf{C}$ that minimizes ε, the least square normal,

$$\varepsilon = \left| \mathrm{F}^{\mathrm{LI}} \cdot \mathbf{C} - \mathbf{I}(\lambda) \right|^2 \quad (4.14)$$

such that $C_i \geq 0$ for every i [62].

4.5.3.2 Similarity Mapping

In cases such as histological stains used with tissue section, the measured spectra may be a result of a complex interaction of the stains with the sample so that isolation of unique components that can be used as reference spectra is not doable, and therefore, the linear decomposition method that was described above cannot be used.

Still, the complex mixtures may be systematically found in the sample, and for such cases, algorithms that compare the spectra that are selected from within the image itself can be used. The similarity mapping algorithm is an example to these types of the algorithms. It is based on selecting information from the sample itself or from similar samples. The spectra can be defined by averaging the spectra in a region of the image that was defined by the user based on prior knowledge. The spectra from these regions are saved in a library as $I_i(\lambda)$ where i is the index of each of these spectra.

The similarity mapping algorithm simply tests the degree of similarity of each spectrum in the image with each one of the reference spectra. Different criteria can be used depending on the specific application and spectral features.

More commonly, a least-square algorithm is used. For every tested spectrum $\bar{I}(\lambda)$, the n-dimensional distance for each reference is calculated by

$$D_i = \sqrt{\sum_\lambda \left(I_i(\lambda) - \bar{I}(\lambda)\right)^2}. \tag{4.15}$$

The most similar reference spectrum i is the one that has the smallest distance D_i. The spectra can also be normalized to have one unit area (or peak intensity), so that only spectral shape differences are tested. Another similarity mapping algorithm is based on calculating the M-dimensional angle between each reference spectrum and the tested spectrum (M being the number of points in the spectrum). Each reference spectrum i is defined as a vector $\mathbf{I}_i = (I_{i,\lambda 1}, I_{i,\lambda 2}, \ldots, I_{i,\lambda n})$ and the angle α_i between the reference spectrum and the tested spectrum $\mathbf{I}$ is calculated by

$$\alpha_i = \cos^{-1}\left(\frac{\mathbf{I}_i \cdot \mathbf{I}}{|\mathbf{I}_i| \cdot |\mathbf{I}|}\right) = \cos^{-1}\left(\frac{\sum_\lambda I_i(\lambda) \cdot I(\lambda)}{\sqrt{\left(\sum_\lambda I_i(\lambda)\right)^2} \cdot \sqrt{\left(\sum_\lambda I(\lambda)\right)^2}}\right). \tag{4.16}$$

Here too, the reference spectrum that gives the smallest angle is the more similar one.

4.5.3.3 Spectral Un-mixing in Bright-Field Measurements

This algorithm is similar to the linear decomposition algorithm described before for fluorescence measurements but is specific for bright-field (transmission) microscopy. The method is somewhat more complex because the relevant

information in a bright-field measurement is the absorption as calculated from the transmission data.

The absorption spectrum of a dye molecule depends on the concentration of the molecules c, the light path length in the sample l, and on the extinction coefficient $\varepsilon(\lambda)$ that describes the probability of one molecule to absorb light quanta at wavelength λ. The absorption can be found by using the Beer-Lambert law:

$$I(\lambda) = I_0(\lambda) \cdot 10^{-\varepsilon(\lambda)\cdot c\cdot l}. \tag{4.17}$$

$I(\lambda)$ is the measured transmission spectrum through the sample while $I_0(\lambda)$ is the spectrum of the light source as measured with the same conditions *without* the sample. These spectra would be defined here in dimensions of flux (photons/cm^2/s/wavelength, [cm^{-2} s^{-1} nm^{-1}].

An index j is used to distinguish different absorbing molecules, $\varepsilon_j(\lambda)$ and the dimensionless term at the exponent of Eq. 4.17 is defined as

$$\text{Absorbance} = \varepsilon(\lambda) \cdot c \cdot l. \tag{4.18}$$

The absorbance is linear with the number of molecules along the optical path in the sample. For the physical units, we use the extinction coefficient in molar density [M^{-1} cm^{-1}] and the molecules concentration c in mol/l [63] (M, the molar, has units of mol/l).

An absorbance of 0.3, 1, and 2 relates to absorption values of 50, 90, and 99%, corresponding to transmission of 50, 10, and 1%. It can be measured over at least four orders of magnitude, but with imaging equipment, it is reduced due to higher noise levels. When the sample contains few absorbing stains, the transmission spectrum has a complex structure [64] and the absorbance is equal to $A(\lambda) = \sum_i \varepsilon_i(\lambda) \cdot c_i \cdot l_i$, which is similar to the case of fluorescence and it can be calculated from the measured transmission, $A(\lambda) = -\log\left(I(\lambda)/I_0(\lambda)\right)$. The division operation may insert noise wherever the background spectrum is very low, and in order to prevent it, the "tails" of the spectra where the intensity is weak are seldom excluded from the calculation. If the absorption spectra of the different stains are measured separately, it is possible to calculate the concentration of each stain in the image.

A few studies have indicated the applicability of spectral imaging for multiple-color bright-field applications such as histological sections [65], tissue sections and cervical smears [66].

4.5.3.4 Principle Components Analysis (PCA)

The spectral analysis methods described above require reference input by the user and belong to a family of algorithms called supervised classification methods. There are also algorithms called non-supervised classification methods that do not require reference spectra as an input. In these methods, the algorithm determines

a number of different spectra based on their spectral properties. This approach involves only a minimum of *a priori* information such as the number of stains that are expected to be in the image.

One of the most common non-supervised algorithms is principle component analysis (PCA). It uses statistical analysis of all the spectra in the image and finds their similarities and differences [67]. Using that, the statistical analysis finds a small set of spectra that spans the whole data set. The first spectrum in the set is the one that contributes the most to the spectra in the image; the second one contributes less, and so on. The principle spectra that are found by PCA can represent special classes of the measured objects such as cancer and normal cells.

4.6 Applications

Spectral imaging is important whenever the spectrum contains useful information on the spatial distribution of entities in an image. The spectral information enables to distinguish between different mixtures of materials or entities even if they have a similar color (or overlapping spectra). This permits one to label different entities in a sample simultaneously and to quantitatively analyze each one of them. The spectral information is also useful in differing between the spectrum of a given stain and the spectrum of artifacts that might contribute to the measured image as happens seldom due to auto-fluorescence that are physically significant in some cases but biologically irrelevant. It is also possible to study spectral changes which are indicative of a process that the sample undergoes. We will briefly describe few different possible applications.

4.6.1 Observation of Combinatorial-Labeled Entities

In many cases, there is a need to observe and analyze many entities simultaneously. They may either have natural different colors, or they may be labeled with different dyes. These entities can be a number of proteins, genes, or other biological organelles. It may be important to observe the number of each species and their spatial distribution and co-localization. Even though there are hundreds of different dyes, many of them have a similar color so that only a few can be distinguished by eye or by a simple color filtering technique. Spectral imaging enables to overcome this obstacle.

When working with fluorescence, it is necessary to excite all the dyes, and the emission spectral range cannot overlap with the excitation range. Therefore, part of the spectral range that is used for excitation cannot be used for detection, multiband filters are used, and none of the fluorochromes' excitation band can overlap with the emission of any other.

An example of such an application is spectral karyotyping or SKY [39, 68, 69]. SKY is based on fluorescence in situ hybridization (FISH) and uses five different fluorochromes (Fig. 4.21a) to label each one of the 24 human chromosomes (or other species). Each chromosome is labeled with a different combination of few out of the five fluorochromes. As an example, chromosome 2 is labeled with Cy5.5 and chromosome 3 is labeled with FITC, Rhodamine, Cy5, and Cy5.5, and with five fluorochromes, there are $2^5–1 = 31$ different possible combinations. Spectral images are usually acquired with a 63× or 100× objective lens with high NA (1.3–1.4) in the range of 450–780 nm and a spectral resolution of 10 nm at 500 nm peak. The spectral images are processed and analyzed with spectral and imaging algorithms. The spectrum at each pixel is classified based on the known spectra of the five fluorochromes by using linear decomposition algorithms as described in Sect. 4.5.3.1. The spectrum of each chromosome is rather complex, as shown in Fig. 4.21b.

The high specificity of the acquired spectral data enables a successful classification (Fig. 4.22), and it is used intensively for both diagnostics and research.

Similar approaches such as M-FISH and COBRA-FISH have been developed by using a set of matched filters instead of measuring the spectral images and provide similar information [70, 71]. Further works have shown a combination of even more colors simultaneously [72–75].

4.6.2 Observation of Mixed Stained Entities with Known Stains

The application described above is demanding, but the method enjoys a priori assumptions that simplify the procedure, the fact that there are no combinations of few species in one measurement. If, for example, few chromosomes could be co-localized, it would make the task much more complex, if solvable at all. In addition, once there are combinations of species, the quantity of each can vary, which again makes the analysis more complex.

Therefore, in cases where the mix of species is unknown, a different approach should be taken, and as a result, much fewer species can be detected simultaneously. Although complex, these applications are still based on a limited number of known stains. Therefore, their spectra can be measured, stored in a library, and be used during the analysis process.

An example of such a case appears in bright-field measurements of tissue sections or cells that are stained for different proteins that can be co-localized at different concentration ratios. In bright-field measurements, the full spectral range is available for detection, and it is not necessary to block parts of the excitation or emission ranges like in fluorescence. On the other hand, mixtures of stains may have a complex spectrum, and the more stains that are added, the more “brown” the sample gets. This is the case in histological staining when multiple features have to be detected. For such an application, spectral un-mixing algorithms can be used as described in Sect. 4.5.3.3. It allows one to separate the complex color image into a set of single-color images where each one of them shows the sample as if it

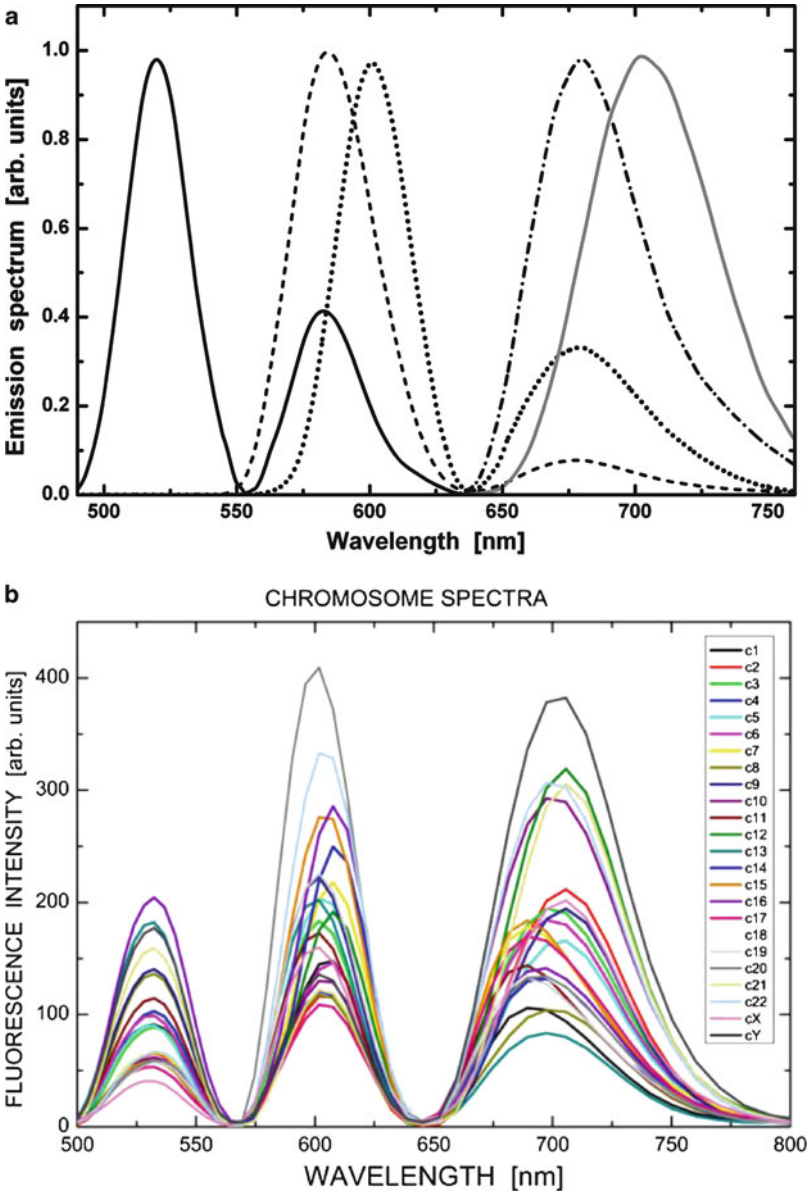

Fig. 4.21 **a** Spectra of the five fluorochromes that are used for SKY (FITC, Rhodamine, Texas Red, Cy5, and Cy5.5 or alike). **b** The spectrum measured for each one of the labeled chromosomes. Spectra are measured with the SpectraCube system through a triple dichroic SKY filter cube with a spectral resolution of ∼10 nm at 500 nm

were stained with only a single stain. By correlating the single-stain distribution, it also provides information on the co-localization of structures, proteins, and other

Fig. 4.22 SKY classification results. The human metaphase was hybridized with a SKY kit that contains the appropriate combinatorial labeling for each chromosome (Applied Spectral Imaging Inc., Migdal HaEmek, Israel). The measured spectral image is analyzed, and the results are shown in classification colors

entities. The methods require that the absorption spectra of the chromogens that are used do not change significantly as a function of the local environment, a condition that has been tested and found to be correct [66]. Other examples include the analysis of pathological samples and even whole-animal imaging [76].

Another example of such an application is the observation of oxy- and deoxyhemoglobin which appears in different biomedical applications such as tissue vitality and retinal ischemia diagnostics. The small changes in the spectrum of oxy- and deoxyhemoglobin (Fig. 4.23) allow to determine the oxygen saturation level and form a basis for these applications [19, 23, 49, 52].

Other similar applications include industrial applications such as quality control of drug manufacturing and others.

4.6.3 Observation of Spectra from Unknown Source

In some applications, the images that are measured contain spectra from an unknown source. In such cases, prior knowledge of the spectral constituents does not exist, but it is still possible to define spectral references from specific points that are identified in the image and find similar spectra from the whole image. A typical example of that kind exists in art studies as the one that was used to study the tints that were used by Leonardo da Vinci for painting the Mona Lisa [77], see Fig. 4.24.

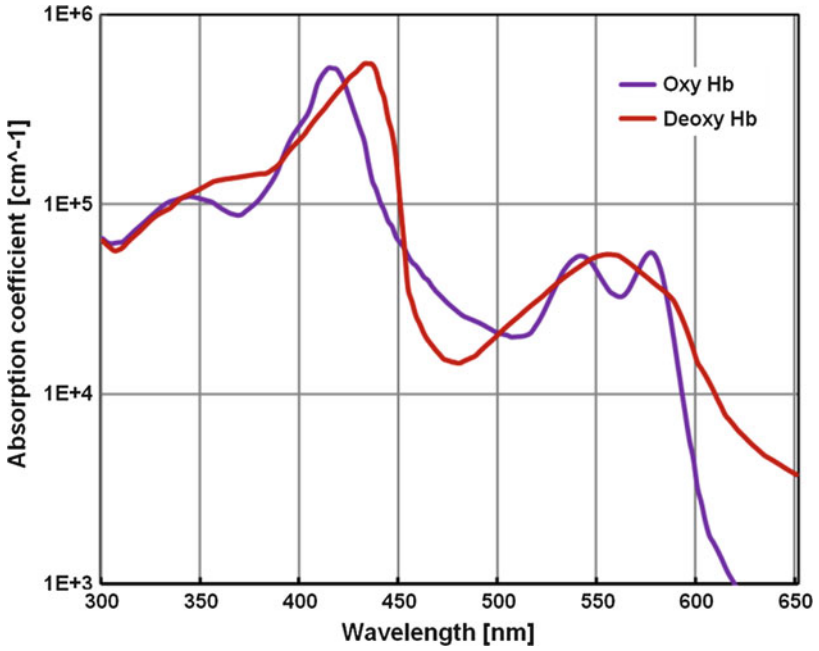

Fig. 4.23 The absorption spectrum of oxy- and deoxyhemoglobin. It is used for determination of tissue vitality, retinal ischemia diagnostics, and other applications

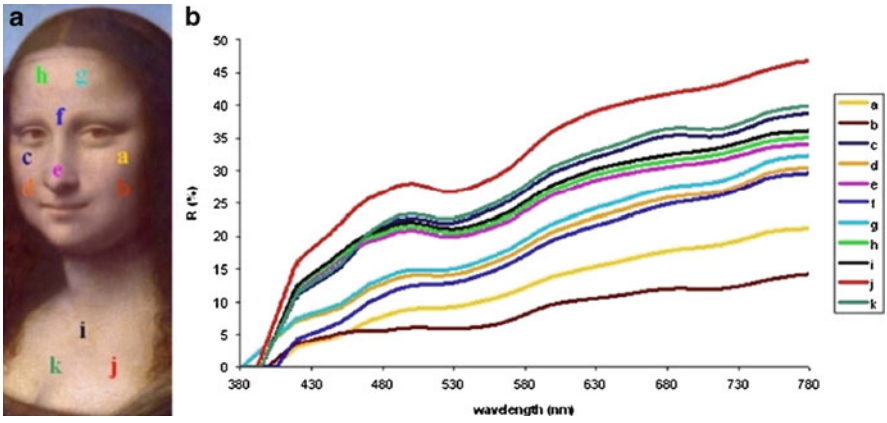

Fig. 4.24 Spectra measured from the image of the Mona Lisa. **a** Part of the image and the indication of different points. **b** Spectra measured at these points that are indicated (Image courtesy of Dr. Mady Elias, Institut des NanoSciences de Paris, Université Pierre et Marie Curie, Paris, France, adopted from [77])

4.7 Discussion and Conclusions

The field of spectral imaging grew and matured during the last three decades. The recent technological advances contributed to spectral imaging progress in almost every aspect: advances in optical elements manufacturing, detector technologies, computer speed and memory capacity, image processing algorithms and creative measurements setup.

Different methods used for spectral imaging systems were described, as well as their advantages, limitations, and possible applications. In addition, the conceptual parts of a spectral imaging system were described, combined with brief description of the major biomedical applications.

Biomedical applications typically require collection of complex information from tested samples with minimal invasion and risk at shorter times and lower costs. Spectral imaging conforms well to these demands as it provides a lot more data than typical imaging devices. Based on the significant growth and wealth of creative improvements, we believe that further technological advances will lead to the development of new architectures for detection systems that will allow significantly faster and more accurate spectral image measurements.

Acknowledgements The work was partially supported by the Israeli Science Foundation (ISF) grants numbers 985/08 and 1729/08.

References

1. E.H.K. Stelzer, Contrast, resolution, pixelation, dynamic range and signal-to-noise ratio: fundamental limits to resolution in fluorescence light microscopy. J. Microsc. **189**, 15–24 (1997)
2. I. Newton, *Opticks* (1704) (Dover Publications, Mineola, 1987)
3. F.M.A. Voltaire, Éléments de la philosophie de Newton (Etienne Ledet & Compagnie, Amsterdam, 1738)
4. A.J. Welch, M.J.C. van Gemert, W.M. Star, B.C. Wilson, In *Overview of Tissue Optics, in Optical-Thermal Response of Laser-Irradiated Tissue*, ed. by A.J. Welch and M.J.C. van Gemert (Plenum, New York, 1995)
5. J. Yguerabide, E.E. Yguerabide, Light-scattering submicroscopic particles as highly fluorescent analogs and their use as tracer labels in clinical and biological applications. Anal. Biochem. **262**, 137–156 (1998)
6. B.H. Stuart, Infrared spectroscopy: fundamentals and applications. In *Analytical Techniques in Science*, ed. by D.J. Ando (Wiley, Chichester, 2004)
7. B.N.G. Giepmans, S.R. Adams, M.H. Ellisman, R.Y. Tsien, The fluorescent toolbox for assessing protein location and function. Science, **312**, 217–224 (2006)
8. M.E. Dickinson, E. Simbuerger, C.W. Waters, S.E. Fraser, Multiphoton excitation spectra in biological samples. J. Biomed. Opt. **8**, 329–338 (2003)
9. W.R. Zipfel, R.M. Williams, W.W. Webb, Nonlinear magic: multiphoton microscopy in the biosciences. Nat. Biotechnol. **21**, 1369–1377 (2003)
10. J. Zimmer, D. Knipp, H. Stiebig, H. Wagner, Amorphous silicon-based unipolar detector for color recognition. IEEE Trans. Electron Dev. **46**, 884–891 (1999)

11. R.B. Merrill, Color separation in an active pixel cell imaging array using a triple-well structure, U.S. Patent 5,965,875 (1999)
12. Y. Garini, A. Gil, I. Bar-Am, D. Cabib, N. Katzir, Signal to noise analysis of multiple color fluorescence imaging microscopy. Cytometry, **35**, 214–226 (1999)
13. T. Zimmermann, J. Rietdorf, R. Pepperkok, Spectral imaging and its applications in live cell microscopy. FEBS Lett. **546**, 87–92 (2003)
14. R. Neher, E. Neher, Optimizing imaging parameters for the separation of multiple labels in a fluorescence image. J. Microsc. **213**, 46–62 (2004)
15. T.C. George, D.A. Basiji, B.E. Hall, D.H. Lynch, W.E. Ortyn, D.J. Perry, M.J. Seo, C.A. Zimmerman, P.J. Morrissey, Distinguishing modes of cell death using the imagestream multispectral imaging flow cytometer. Cytometry, **59A**, 237–245 (2004)
16. L. Liu, O. Yermolaieva, W.A. Johnson, F.M. Abboud, M.J. Welsh, Identification and function of thermosensory neurons in Drosophila larvae. Nat. Neurosci. **6**, 267–273 (2003)
17. H.S. Kwok, P.W. Cheng, H.C. Huang, H.F. Li, Z.R. Zheng, P.F. Gu, X. Liu, Trichroic prism assembly for separating and recombining colors in a compact projection display. Appl. Opt. **39**, 168–172 (2000)
18. J. Lane, P. Buchsbaum, J. Eichenholz, Microlithographically patterned optical thin film coatings. Proc. SPIE, **7205**, 72050G (2009)
19. J.M. Eichenholz, N. Barnett, Y. Juang, D. Fish, S. Spano, E. Lindsley, D.L. Farkas, Real time megapixel multispectral bioimaging. Proc. SPIE, **7568**, 75681L (2010)
20. L. Cognet, G.S. Harms, G.A. Blab, P.H.M. Lommerse, T. Schmidt, Simultaneous dual-color and dual-polarization imaging of single molecules. Appl. Phys. Lett. **77**, 4052–4054 (2000)
21. C.L. Wyatt, Infrared spectrometer: liquid-helium-cooled rocketborne circular-variable filter. Appl. Opt. **14**, 3086–3091 (1975)
22. P.J. Miller, Use of tunable liquid crystal filters to link radiometric and photometric standards. Metrologia, **28**, 145–149 (1991)
23. R.D. Shonat, E. Wachman, W. Niu, A. Koretsky, D. Farkas, Near-simultaneous hemoglobin saturation and oxygen tension maps in mouse brain using an AOTF microscope. Biophys. J. **73**, 1223–1231 (1997)
24. X. Gao, Y. Cui, R.M. Levenson, L.W.K. Chung, S. Nie, In vivo cancer targeting and imaging with semiconductor quantum dots. Nat. Biotechnol. **22**, 969–976 (2004)
25. B. Lyot, Optical apparatus with wide field using interference of polarized light. C.R. Acad. Sci. **197**, 1593 (1933)
26. G.D. Sharp, K.M. Johnson, D. Doroski, Continuously tunable smectic A* liquid-crystal color filter. Opt. Lett. **15**, 523–525 (1990)
27. T. Xu, Y.K. Wu, X. Luo, L.J. Guo, Plasmonic nanoresonators for high-resolution color filtering and spectral imaging. Nat. Commun. **1**, 59 (2010)
28. N. Gat, Imaging spectroscopy using tunable filters: a review. Proc. SPIE **4056**, 50–64 (2000)
29. C. Palmer, E. Loewen, *Diffraction Grating Handbook* (Newport Corporation, Rochester, 2005)
30. J.M. Lerner, Imaging spectrometer fundamentals for researchers in the biosciences - A tutorial. Cytometry **69A**, 712–734 (2006)
31. M.B. Sinclair, J.A. Timlin, D.M. Haaland, M. Werner-Washburne, Design construction characterization and application of a hyperspectral microarray scanner. Appl. Opt. **43**, 2079–2088 (2004)
32. R.S. Balaban, I. Kurtz, H.E. Cascio, P.D. Smith, Microscopic spectral imaging using a video camera. J. Microsc. **141**, 31–39 (1986)
33. D.W. Warren, A. Hackwell, Compact prism spectrograph suitable for broadband spectral surveys with array detectors. U.S. Patent No. 5,127,728 (1992)
34. M. Aikio, *Hyperspectral Prism-Grating-Prism Imaging Spectrograph* (Technical Research Center of Finland, Espoo, 2001)
35. T. Hyvärinen, E. Herrala, A. Dall'Ava, Direct sight imaging spectrograph: a unique add-on component brings spectral imaging to industrial applications. Proc. SPIE **3302**, 165–175 (1998)
36. R.M. Zucker, J.M. Lerner, Wavelength and alignment tests for confocal spectral imaging systems. Microsc. Res. Tech. **68**, 307–319 (2005)

37. H. Tsurui, J.M. Lerner, K. Takahashi, S. Hirose, K. Mitsui, K. Okumura, T. Shirai, Hyperspectral imaging of pathology samples. Proc. SPIE **3605**, 273–281 (1999)
38. M.E. Dickinson, G. Bearman, S. Tille, R. Lansford, S.E. Fraser, Multi-spectral imaging and linear unmixing add a whole new dimension to laser scanning fluorescence microscopy. BioTechniques, **31**, 1272–1278 (2001)
39. Y. Garini, M. Macville, S. du Manoir, R.A. Buckwald, M. Lavi, N. Katzir, D. Wine, I. Bar-Am, E. Schröck, D. Cabib, T. Ried, Spectral karyotyping. Bioimaging **4**, 65–72 (1996)
40. Z. Malik, D. Cabib, R.A. Buckwald, A. Talmi, Y. Garini, S.G. Lipson, Fourier transform multipixel spectroscopy for quantitative cytology. J. Microsc. **182**, 133–140 (1996)
41. R.J. Bell, *Introductory Fourier Transform Spectroscopy* (Academic Press, London, 1972)
42. Y. Garini, N. Katzir, D. Cabib, R.A. Buckwald, D.G. Soenksen, Z. Malik, Spectral bio-imaging, in *Fluorescence Imaging Spectroscopy and Microscopy*, ed. by X.F. Wang, B. Herman (Wiley, New York, 1996).
43. J.W. Goodman, *Introduction to Fourier Optics* (McGraw-Hill, New York, 1996)
44. F.J. Harris, On the use of windows for harmonic analysis with the discrete Fourier transform. Proc. IEEE, **66**, 51–83 (1978)
45. Q.S. Hanley, P.J. Verveer, D.J. Arndt-Jovin, T.M. Jovin, Three-dimensional spectral imaging by Hadamard transform spectroscopy in a programmable array microscope. J. Microsc. **197**, 5–14 (2000)
46. M.R. Descour, C.E. Volin, E.L. Dereniak, T.M. Gleeson, M.F. Hopkins, D.W. Wilson, P.D. Maker, Demonstration of a computed-tomography imaging spectrometer using a computer-generated hologram disperser. Appl. Opt. **36**, 3694–3698 (1997)
47. T. Okamoto, I. Yamaguchi, Simultaneous acquisition of spectral image information. Opt. Lett. **16**, 1277–1279 (1991)
48. C.E. Volin, B.K. Ford, M.R. Descour, J.P. Garcia, D.W. Wilson, P.D. Maker, G.H. Bearman, High-speed spectral imager for imaging transient fluorescence phenomena. Appl. Opt. **37**, 8112–8119 (1998)
49. W.R. Johnson, D.W. Wilson, W. Fink, M. Humayun, G. Bearman, Snapshot hyperspectral imaging in ophthalmology. J. Biomed. Opt. **12**, 014036–1–7 (2007)
50. M.E. Gehm, R. John, D.J. Brady, R.M. Willett, T.J. Schulz, Single-shot compressive spectral imaging with a dual-disperser architecture. Opt. Express **15**, 14013–14027 (2007)
51. M.A. Golub, M. Nathan, A. Averbuch, E. Lavi, V.A. Zheludev, A. Schclar, Spectral multiplexing method for digital snapshot spectral imaging. Appl. Opt. **48**, 1520–1526 (2009)
52. N.L. Everdell, I.B. Styles, A. Calcagni, J. Gibson, J. Hebden, E. Claridge, Multispectral imaging of the ocular fundus using light emitting diode illumination. Rev. Sci. Instrum. **81**, 093706–1–9 (2010)
53. N. MacKinnon, U. Stange, P. Lane, C. MacAulay, M. Quatrevalet, Spectrally programmable light engine for in vitro or in vivo molecular imaging and spectroscopy. Appl. Opt. **44**, 2033–2040 (2005)
54. A. Bednarkiewicz, M. Bouhifd, M.P. Whelan, Digital micromirror device as a spatial illuminator for fluorescence lifetime and hyperspectral imaging. Appl. Opt. **47**, 1193–1199 (2008)
55. A. Abramov, L. Minai, D. Yelin, Multiple-channel spectrally encoded imaging. Opt. Express **18**, 14745–14751 (2010)
56. D. Yelin, S.H. Yun, B.E. Bouma, G.J. Tearney, Three-dimensional imaging using spectral encoding heterodyne interferometry. Opt. Lett. **30**, 1794–1796 (2005)
57. I.T. Young, J.J. Gerbrands, L.J. van Vliet, Image processing fundamentals, in *The Digital Signal Processing Handbook*, ed. by D.B. Williams, V.K. Madisetti (CRC Press, Boca Raton, 1998)
58. Y. Garini, I.T. Young, G. McNamara, Spectral imaging: principles and applications. Cytometry **69A**, 735–747 (2006)
59. T. Zimmermann, Spectral imaging and linear unmixing in light microscopy. Adv. Biochem. Eng./Biotechnol. **95**, 245–265 (2005)
60. J.R. Mansfield, K.W. Gossage, C.C. Hoyt, R.M. Levenson, Autofluorescence removal multiplexing and automated analysis methods for in-vivo fluorescence imaging. J. Biomed. Opt. **10**, 041207–1–9 (2005)

61. E.A. Jares-Erijman, T.M. Jovin, FRET imaging. Nat. Biotechnol. **21**, 1387–1395 (2003)
62. C.L. Lawson, R.J. Hanson, *Solving Least Square Problems* (Prentice-Hall, Englewood Cliffs, 1974)
63. J.R. Lakowicz, *Principles of Fluorescence Spectroscopy*. 3rd edn. (Plenum Press, New York/London, 1986)
64. R. Zhou, E.H. Hammond, D.L. Parker, A multiple wavelength algorithm in color image analysis and its applications in stain decomposition in microscopy images. Med. Phys. **23**, 1977–1986 (1996)
65. R.L. Ornberg, B.M. Woerner, D.A. Edwards, Analysis of stained objects in histological sections by spectral imaging and differential absorption. J. Histochem. Cytochem. **47**, 1307–1314 (1999)
66. M.V. Macville, J.A. Van Der Laak, E.J. Speel, N. Katzir, Y. Garini, D. Soenksen, G. McNamara, P.C. de Wilde, A.G. Hanselaar, A.H. Hopman, T. Ried, Spectral imaging of multi-color chromogenic dyes in pathological specimens. Anal. Cell. Pathol. **22**, 133–142 (2001)
67. I.T. Jolliffe, *Principle Component Analysis*, 2nd edn. Springer series in statistics (Springer, New York, 2002)
68. E. Schröck, S. du Manoir, T. Veldman, B. Schoell, J. Wienberg, M.A. Ferguson-Smith, Y. Ning, D.H. Ledbetter, I. Bar-Am, D. Soenksen, Y. Garini, T. Ried, Multicolor spectral karyotyping of human chromosomes. Science **273**, 494–497 (1996)
69. E. Schröck, H. Padilla-Nash, Spectral karyotyping and multicolor fluorescence in situ hybridization reveal new tumor-specific chromosomal aberrations. Seminal Hematol. **37**, 334–347 (2000)
70. M.R. Speicher, S. Gwyn Ballard, D.C. Ward, Karyotyping human chromosomes by combinatorial multi-fluor FISH. Nat. Genet. **12**, 368–375 (1996)
71. H.J. Tanke, J. Wiegant, R.P. van Gijlswijk, V. Bezrookove, H. Pattenier, R. J. Heetebrij, E.G. Talman, A.K. Raap, J. Vrolijk, New strategy for multi-color fluorescence in situ hybridisation: COBRA: Combined Binary RAtio labeling. Eur. J. Hum. Genet. **7**, 2–11 (1999)
72. H. Tsurui, H. Nishimura, S. Hattori, S. Hirose, K. Okumura, T. Shirai, Seven-color fluorescence imaging of tissue samples based on Fourier spectroscopy and singular value decomposition. J. Histochem. Cytochem. **48**, 653–662 (2000)
73. C. Pautke, S. Vogt, T. Tischer, G. Wexel, H. Deppe, S. Milz, M. Schieker, A. Kolk, Polychrome labeling of bone with seven different fluorochromes: Enhancing fluorochrome discrimination by spectral image analysis. Bone **37**, 441–445 (2005)
74. R.C. Ecker, R.D. Martin, G.E. Steiner, J.A. Schmid, Application of spectral imaging microscopy in cytomics and fluorescence resonance energy transfer (FRET) analysis. Cytometry **59A**, 172–181 (2004)
75. A. Mittag, D. Lenz, A.O.H. Gerstner, U. Sack, M. Steinbrecher, M. Koksch, A. Raffael, J. Bocsi, A. Tárnok, Polychromatic (eight-color) slide-based cytometry for the phenotyping of leukocyte NK and NKT subsets. Cytometry **65A**, 103–115 (2005)
76. R. Levenson, J.R. Mansfield, Multispectral imaging in biology and medicine: slices of life. Cytometry **69A**, 748–758 (2006)
77. M. Elias, P. Cotte, Multispectral camera and radiative transfer equation used to depict Leonardo's sfumato in Mona Lisa. Appl. Opt. **47**, 2146–2154 (2008)

Chapter 5
Optical Coherence Tomography: Technical Aspects

Hrebesh M. Subhash and Ruikang K. Wang

Optical coherence tomography (OCT) is a high-resolution, noninvasive, 3D imaging technique with great potential in both clinical and fundamental research applications in many areas. Owing to its exceptionally high spatial resolution and velocity sensitivity, the functional extension of OCT techniques can simultaneously provide tissue structure, blood perfusion, birefringence, and other physiological information and it has great potential for basic biomedical research and clinical medicine. OCT has the far-reaching potential to be a quantitative imaging technique that could impact many, as yet unexplored, areas and should therefore be considered a vital measurement tool. In this chapter, we will first discuss the principle of operation and then the practical aspects of the OCT system; we will also provide detailed discussion on different OCT schemes and its functional extensions.

5.1 Introduction

Optical coherence tomography (OCT) is a novel, noninvasive, optical imaging modality based on low-coherence interferometry. It was first conceived in 1990 by Dr. Naohiro Tanno, a professor at Yamagata University [1, 2] and then perfected in 1991 by Massachusetts Institute of Technology team headed by Prof. James Fujimoto [3]. OCT enables the noninvasive, noncontact imaging of cross-sectional structures in biological tissues and materials with high resolution. In principle, OCT is an optical analogue to clinical ultrasound. In OCT, the temporally gated

M.S. Hrebesh (✉)
Department of Biomedical Engineering, Oregon Health & Science University, Portland, OR 97239, USA
e-mail: hrebeshms@gmail.com

R.K. Wang
Department of Bioengineering, University of Washington, Seattle, WA 98195, USA

R. Liang (ed.), *Biomedical Optical Imaging Technologies*, Biological and Medical Physics, Biomedical Engineering, DOI 10.1007/978-3-642-28391-8_5,

optical pulse remitted from scattering sites within the sample is localized by low-coherence interferometry (LCI) [4–9]. This is typically achieved with a Michelson interferometer. The sample rests in one arm of the interferometer, and a scanning reference optical delay line is in the other arm. In LCI, light interferes at the detector only when light reflected from the sample is matched in optical path length with that reflected from the scanning reference mirror. A single scan of the reference mirror thus provides a one-dimensional depth-reflectivity profile of the sample. Two-dimensional cross-sectional images are formed by laterally scanning the incident probe beam across the sample. The reconstructed OCT image is essentially a map of the changes of reflectivity that occurs at internal interfaces, similar to the discontinuities in acoustic impedance in ultrasound images.

The principal difference between ultrasound and optical imaging is that the velocity of light is approximately a million times faster than that of sound. For this reason, the distance within the materials or tissues with a resolution of 10 μm by measuring the echo time delay of backreflected or backscattered light wave corresponds to a time resolution of 30 fs (10^{-15}), which is well beyond the limits of currently available electronic detection system. But for ultrasound, the echo time delay is approximately 100 ns, which can be easily realized with modern electronic detection systems. Thus, in OCT, each time delay has to be measured indirectly, normally by correlation techniques, in which the backscattered light is compared to the reference light with known optical path length. OCT uses the low-coherence interferometric method to measure this echo time delay with high dynamic range and sensitivity.

5.1.1 Advantages of OCT over Other Imaging Technologies

Recently, OCT has attracted much attention in many clinical and basic research fields due to its high sensitivity for noninvasive high-resolution imaging at cellular level. The diagnostic capability of OCT has revolutionized many fields such as ophthalmology, dermatology, cardiology, etc. In terms of other medical imaging devices, OCT is the one best offered currently. OCT is becoming rapidly an important biomedical tool for imaging tissues and engineered tissues [10]. OCT has critical advantages over other medical imaging systems. Microscopes work well for examining small tissue samples and cells but not for examining biological tissues inside the body [11]. The ultrasound, CT, and MRI can peer inside the body; however, they do not have sufficient resolution to capture cellular detail [11]. Electron microscopy can pick up extremely fine details; however, it is not able to view living samples within the body [11]. Figure 5.1 shows the comparison of OCT with presently existing clinical imaging modalities [12]. The two major advancements which assist both scientists and medical physicians are the improvement in the depth and clarity at which they can view tissues. Current OCT systems have resolutions at 1–20 μm compared to 110 μm for high-frequency ultrasound [13]. The advancement of medical imaging systems is illustrated by the technology inherent in OCT, which allows images of living tissue to become clearer and more defined in both structure and detail. Using information inherent to the

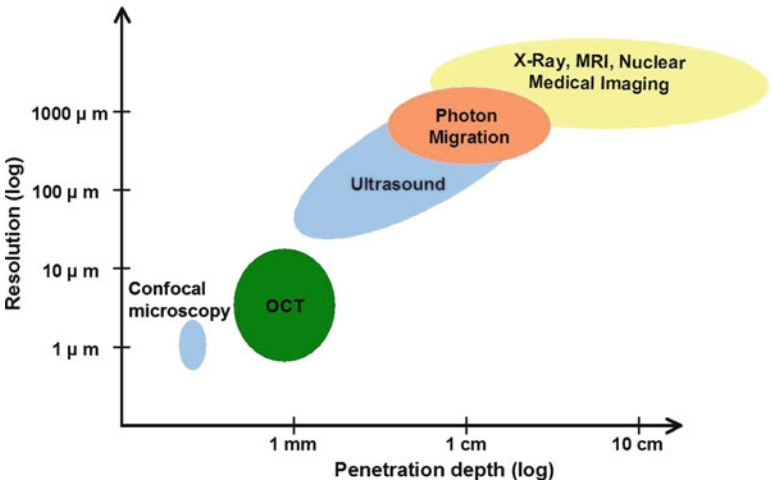

Fig. 5.1 Comparison of OCT with other clinical imaging modalities in terms of their resolution and penetration depth

returning photon signals, OCT can perform both spectroscopic and polarization imaging to better evaluate the composition of tissues and lesions. Moreover, the use of fiber optics and its ability to integrate with medical catheters, surgical guiding systems like endoscopes, and microscopes make it much easier to observe internal structures through OCT, and also widening its clinical application scope to several areas. With other technology to aid the development of OCT, doctors can actually use OCT not only on the body but within the body. Figure 5.1 shows that OCT fills the gap between the optical microscopy and the currently available clinical imaging modalities in terms of imaging depth and resolution.

There are many important advantages to OCT over other existing clinical imaging modalities, making it an important new complementary medical imaging tool. It is minimally invasive, noncontacting, and nonionizing and has very high spatial resolution and sensitivity and high speed and real-time data acquisition. The basic setup can be extended to obtain measurement based on the functional, polarization, spectroscopic, and other tissue parameters.

5.2 Low-Coherence Interferometry

As mentioned in Sect. 5.1, OCT uses the interferometric detection and correlation method to measure the echo time delay of backscattered light with high dynamic range and sensitivity. The basic building block of OCT is based on a Michelson interferometer (or its variant) with a low-coherence optical source, and this scheme is generally called low-coherence interferometry or white light interferometry. In LCI, low-coherence light reflected from the sample is used to provide information on the time-of-flight (echo time delay) from refractive boundaries and backscattered

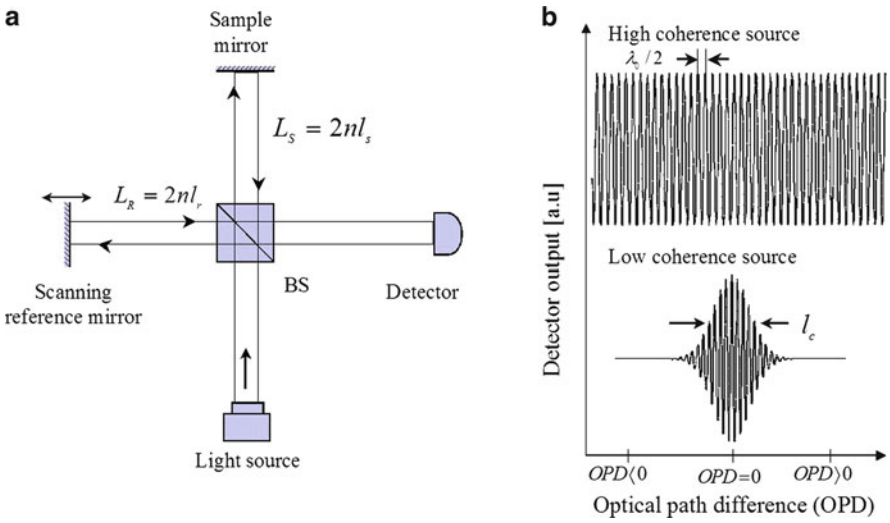

Fig. 5.2 (**a**) Free-space Michelson interferometer setup, (**b**) comparison between the photodetector outputs in cases when a high-coherence source (*top*) or a low-coherence source (*bottom*) is used

sites in the sample. LCI measures the delay and intensity of backscattered light by comparing it with the light that has traveled a known reference path length and delay through use of a Michelson interferometer. Another variant form of LCI called optical time-domain reflectometry (OTDR) is used to determine the location of defects in optical fibers and characterization of optical waveguides in the telecommunication industry [14, 15]. Figure 5.2a shows the schematic diagram of a simple free-space implementation of a Michelson-type interferometer.

The incident optical beam is directed onto a beam splitter, which splits the beam into two, from where one beam leads to a sample mirror, while the other acts as a reference beam with variable path length. The sample beam $\boldsymbol{E}_{\mathrm{S}}(t - L_{\mathrm{S}}/c)$, which reflects from the sample mirror, is interfered with the reference beam $\boldsymbol{E}_{\mathrm{R}}(t - L_{\mathrm{R}}/c)$ at the output of the interferometer, where L_{S} and L_{R} are the corresponding optical paths of the sample arm and reference arm, respectively, and c is the speed of light. According to the wave theory, interference is the superposition of two or more waves, resulting in a new wave pattern. If we consider wave as electromagnetic radiation, then the electric field can be described as [16]

$$E = E_0 \mathrm{e}^{i(\mathbf{kr}-\boldsymbol{\omega} t+\boldsymbol{\phi})}, \tag{5.1}$$

where $\boldsymbol{k}(= 2\pi/\lambda)$ is the propagation vector, $\boldsymbol{r}$ is the unit vector, $\boldsymbol{\omega}(= 2\pi \mathrm{f})$ is the angular frequency, and $\boldsymbol{\phi}$ is the phase, the resulting field of the beams at the output of the interferometer can be written as

$$E_{\mathrm{D}}(t) = E_{\mathrm{S}}(t - L_{\mathrm{S}}/c) + E_{\mathrm{R}}(t - L_{\mathrm{R}}/c), \tag{5.2}$$

using the principle of superposition. By applying Eq. 5.1 and putting $\boldsymbol{r}$ and $\boldsymbol{\phi}$ to 0 for the convenience, Eq. 5.2 can be written as

$$E_{\mathrm{D}}(t) = E_{\mathrm{S}} e^{i(t-L_{\mathrm{S}}/c)} + E_{\mathrm{R}} e^{i(t-L_{\mathrm{R}}/c)}. \tag{5.3}$$

The detector measures the intensity of the output beam, which is proportional to the square of the electromagnetic field. The irradiance (power per unit area) at the detector can be expressed in terms of the Poynting vector $S = \varepsilon_0 c^2 E_{\mathrm{D}} \times B_{\mathrm{D}}$. The irradiance measured by the detector is the time average of the rapidly varying fields ($\sim 10^{14}$ Hz for near-infrared region), that is, $I_{\mathrm{D}} = \langle |S| \rangle = \varepsilon_0 c^2 \langle |E_{\mathrm{D}} \times B_{\mathrm{D}}| \rangle$, since $|E| = c|B|$. The irradiance can be written as $I_{\mathrm{D}} = \varepsilon_0 c^2 \langle |E_D|^2 \rangle$. Using Eq. 5.3, the resultant intensity I_{D} can be expressed as

$$I_{\mathrm{D}} = \varepsilon_0 c \left\langle (E_{\mathrm{S}}(t) + E_{\mathrm{R}}(t+\tau)) \bullet (\overline{E_{\mathrm{S}}(t)} + \overline{E_{\mathrm{R}}(t+\tau)}) \right\rangle. \tag{5.4}$$

where $\tau = \Delta L/c$ is the time delay corresponding to the roundtrip optical path length difference between the reference and sample arm, that is,

$$\Delta L = L_{\mathrm{S}} - L_{\mathrm{R}} = 2n(l_{\mathrm{S}} - l_{\mathrm{R}}), \tag{5.5}$$

where l_{S} and l_{R} are the geometric lengths of the sample arm and reference arms, respectively, $n \cong 1$ corresponds to the refractive index of air, and the bar symbol denotes a complex conjugate operation. The sharp brackets denote the time average:

$$\langle f \rangle = \lim_{T \to \infty} \int_0^T f(t) \mathrm{d}t. \tag{5.6}$$

Then by omitting the constant term ε_0c, the resulting intensity can be written as follows:

$$I_{\mathrm{D}} = \left\langle |E_{\mathrm{S}}(t)|^2 + |E_{\mathrm{R}}(t+\tau)|^2 + Re\left[E_{\mathrm{S}}(t) \bullet \overline{E_{\mathrm{R}}(t+\tau)} \right] \right\rangle. \tag{5.7}$$

By assuming that the optical fields of both reference and sample beams have the same polarization states, the dot product term $\left\langle |E_{\mathrm{S}}(t) \bullet \overline{E_{\mathrm{R}}(t+\tau)}| \right\rangle = \left\langle |E_{\mathrm{S}}(t) \overline{E_{\mathrm{R}}(t+\tau)}| \right\rangle$. By introducing the correlation function (mutual coherence function) of the two fields, $\Gamma_{\mathrm{SR}}(\tau) = \left\langle E_{\mathrm{S}}(t) \overline{E_{\mathrm{R}}(t+\tau)} \right\rangle$, the interference Eq. 5.7 can be written as

$$I_{\mathrm{D}} = I_{\mathrm{S}} + I_{\mathrm{R}} + 2Re[\Gamma_{\mathrm{SR}}(\tau)], \tag{5.8}$$

where $I_{\mathrm{S}} = \langle |E_{\mathrm{S}}(t)|^2 \rangle$ and $I_{\mathrm{S}} = \langle |E_{\mathrm{S}}(t+\tau)|^2 \rangle$. For convenience, a normalized correlation function is defined, which gives the degree to which the temporal

and spatial characteristics of sample and reference beam matches, and it can be defined as

$$\gamma_{SR}(\tau) = \frac{\Gamma_{SR}(\tau)}{\sqrt{I_S I_R}}. \tag{5.9}$$

Then the irradiance equation Eq. 5.8 can be expressed as follows:

$$I_D = I_S + I_R + 2\sqrt{I_S I_R}\mathrm{Re}[\gamma_{SR}(\tau)]. \tag{5.10}$$

The normalized correction function $\gamma_{SR}(\tau)$ is a complex periodic function of τ, and the interference pattern results if $|\gamma_{SR}(\tau)|$ has a nonzero value. Depending upon the value of $|\gamma_{SR}(\tau)|$, the following type of coherence occurs:

$$\begin{aligned} |\gamma_{SR}(\tau)| &= 1, \text{ Complete coherence} \\ 0 < |\gamma_{SR}(\tau)| &< 1, \text{ Partial coherence} \\ |\gamma_{SR}(\tau)| &= 0, \text{ Complete incoherence} \end{aligned}$$

In an interference pattern, the fringe intensity varies between two limits I_{max} and I_{min}. From Eq. 5.10, this can be written as

$$I_{max} = I_S + I_R + 2\sqrt{I_S I_R}|\gamma_{SR}|, \tag{5.11}$$

$$I_{min} = I_S + I_R - 2\sqrt{I_S I_R}|\gamma_{SR}|. \tag{5.12}$$

Thus, the visibility of fringe V is defined as the ratio

$$V = \frac{I_{max} - I_{min}}{I_{max} + I_{min}} = \frac{2\sqrt{I_S I_R}|\gamma_{SR}|}{I_{max} + I_{min}}. \tag{5.13}$$

If $I_{max} = I_{min}$, then $V = |\gamma_{SR}|$, that is, the fringe visibility is equal to the modulus of degree of partial coherence. Thus, depending upon the different cases of degree of partial coherence, the interference fringe visibility varies from maximum contrast of unity (in case of complete coherence, $|\gamma_{SR}(\tau)| = 1$) to zero contrast (complete incoherence, $|\gamma_{SR}(\tau)| = 0$); there are no interference fringes at all.

Depending upon the source, the light will have frequencies within a certain frequency spectrum. According to Fourier analysis, this can be written as

$$\Delta\omega = \frac{2\pi}{\tau_0}. \tag{5.14}$$

where $\Delta\omega$ is the spectral linewidth of the source and τ_0 is the coherence time, which is the time interval in which the phase of the wave can be predictable. The coherence length, $l_c = c\tau_0$, is the propagation path difference where the beam can maintain a specified degree of coherence. Using Eq. 5.14, the coherence length can be written as

$$l_c = \frac{2\pi c}{\Delta\omega} = \frac{c}{\Delta\nu}. \tag{5.15}$$

According to the Wiener-Khintchine theorem, the complex degree of coherence $\gamma_{SR}(\tau)$ can be expressed as the Fourier transform of the power spectral density $S(\nu)$ of the source, which is fully characterized by its spectral width ($\Delta\lambda$), its central wavelength (λ_0), and its shape [17]:

$$\gamma_{SR}(\tau) = \int_0^\infty S(\nu) e^{-i2\pi\nu\tau} d\nu. \tag{5.16}$$

From the above relation, it reveals that the width of emission spectrum of light source and its shape are vital parameters which influence the sensitivity of the LCI to the optical path difference of the sample and reference arms.

The normalized power spectral density of light source $S(\nu)$ is $\int S(\nu) = 1$; then the complex coherence can be written as

$$\gamma_{SR}(\tau) = |\gamma_{SR}|(\tau) e^{-i2\pi\nu_0\tau}, \tag{5.17}$$

where ν_0 is the center frequency of the light source. Equation 5.10 can be rewritten by introducing Eq. 5.17 as follows:

$$I_D = I_S + I_R + 2\sqrt{I_S I_R}|\gamma_{SR}(\tau)| \cos(2\pi\nu_0\tau). \tag{5.18}$$

The normalized correlation function for a quasi-monochromatic source can be given by

$$|\gamma_{SR}(\tau)| = \left(1 - \frac{\tau}{\tau_0}\right), \quad \tau < \tau_0; \tag{5.19}$$

then Eq. 5.18 becomes as follows:

$$I_D = I_S + I_R + 2\sqrt{I_S I_R}\left(1 - \frac{\tau}{\tau_0}\right) \cos(2\pi\nu_0\tau). \tag{5.20}$$

If the power spectrum of the light source is approximated by a Gaussian spectrum,

$$S(\nu) = \frac{2\sqrt{\ln 2}}{\Delta\nu\sqrt{\pi}} \exp\left[-4\ln 2\left(\frac{\nu - \nu_0}{\Delta\nu}\right)^2\right], \tag{5.21}$$

substituting Eq. 5.21 into Eq. 5.16 results in

$$\gamma_{SR}(\tau) = \exp\left[-\left(\frac{\pi\Delta\nu\tau}{2\sqrt{\ln 2}}\right)^2 e^{-i2\pi\nu_0\tau}\right]. \tag{5.22}$$

From this equation, $\Delta\nu$ represents the FWHM of the normalized spectral width of the source, and then the corresponding free-space correlation length can be obtained as follows:

$$l_c = \frac{2\ln 2}{\pi}\frac{c}{\Delta\nu} = \frac{2\ln 2}{\pi}\frac{\lambda^2}{\Delta\lambda} \approx 0.44\frac{\lambda^2}{\Delta\lambda}. \tag{5.23}$$

Since the coherence length gives the practical estimation of the width of the signal envelope, it is considered as the axial resolution in low-coherence interferometry. Figure 5.2b shows the signal at the photodetector for the case of high-coherence source and low-coherence source. If the light source is highly coherent with narrow linewidth (a laser with $\Delta\lambda \approx 0.01$ nm, in which case $l_c \approx 9$ cm), then the interference will occur for a wide range of relative path length delays of the reference and sample arms. But, when the optical source is low coherent with broad linewidth laser (a tungsten with $\Delta\lambda \approx 300$ nm, in which case $l_c \approx 3\,\mu$m), then the interference occurs only when the path length in the reference and sample arms matches within the coherence length of the source of the light source. Thus, in low-coherence interferometry, the coherence length is the parameter that determines the resolving ability of backscattering or backreflecting sites in the sample.

5.3 OCT Principle of Operation

As described above, the interferometry is the core of the OCT imaging method. Different interferometric configurations can be used in OCT. One of the most common interferometric schemes used in the development of the OCT system is the Michelson interferometer, which can be implemented either with a free-space optic or fiber-optic configuration. The fiber-optic implementations of the OCT are seen as the most convenient for clinical applications because the fiber has the potential to be rugged, compact, and integrated with a wide range of medical instruments. However, there are also a few possible issues associated with the utilization of fiber. Fibers show absorption, although this will be negligible for the distances involved, but this limits the dispersion-free spectral width, resulting in degradation of longitudinal resolution. Figure 5.3 shows the schematics of a typical first-generation time-domain free-space OCT system based on heterodyne envelope detection scheme.

The beam from the low-coherence optical source splits into two parts, a reference and sample beam. The reference beam reflects from a reference mirror mounted on the scanning reference optical delay and returns to the detector. The sample beam reflects off from the different layers within the sample. And at the output of the interferometer, both the reference and sample beams recombine. Due to the broadband nature of the light source, the interference between the optical fields is only observed when the reference and sample arm optical path lengths are matched within the coherence length of the source. The light reflected from the sample and the reference mirror are mixed at a photodetector, and the resulting current signal

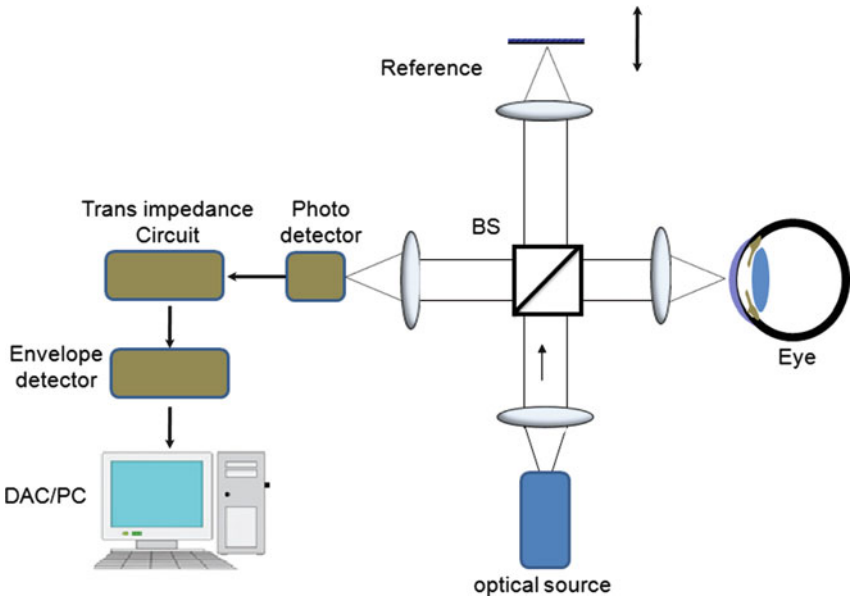

Fig. 5.3 Schematic of a typical first-generation free-space optics-based optical coherence tomography setup with balanced heterodyne detection scheme

corresponding to the interference signal is amplified and converted into a voltage signal by a transimpedance circuit. The amplified signal is demodulated by using sophisticated electronic envelope detection stages (e.g., lock in amplifier). Then the demodulated signal is fed into a data acquisition system that is interfaced with the computer. The data acquisition system is an integral part of the OCT setups that do all the timing and synchronization between different modular units of an OCT system. In OCT, the depth information can also be derived from frequency-domain measurement by taking the Fourier transform of the output spectrum of the interferogram; this alternative modality has better speed and sensitivity advantages than conventional time-domain detection scheme, which will be described later in this chapter.

In general, an OCT system can be considered from a modular viewpoint in terms of various integrated hardware and software functionalities such as imaging engine, low-coherence light source, beam delivery and probes, computer control, and image processing. Figure 5.4 shows the schematic of various modular components of a generic OCT system. Depending on the specific application, there are many variant embodiments of the interferometer and imaging engines for wide range of applications such as polarization-sensitive imaging, Doppler flow imaging, optical microangiography, spectroscopy, frequency scanning, spectral radar, and parallel detection.

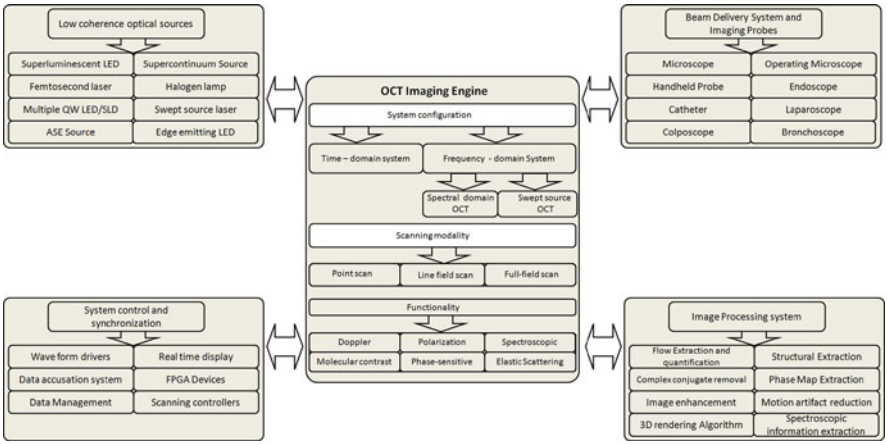

Fig. 5.4 A modular overview of OCT system with various peripheral components and schematic of a typical first-generation free-space optics-based optical coherence tomography setup with balanced heterodyne detection scheme

5.4 Practical Aspects of OCT System

5.4.1 Axial Resolution

Unlike the conventional optical microscopy, the apparent advantage of OCT is that the axial resolution is completely decoupled from the lateral resolution. The axial resolution of an OCT is an important specification of an OCT system, and in many biomedical applications, high axial resolution is often required to distinguish different cellular ultra-structures. As described in the preceding section, axial resolution is defined as the full width at half maximum of the source coherence length l_c. For a source with a Gaussian spectral distribution, the axial resolution is given by

$$\Delta z = \frac{2\ln 2}{\pi}\frac{c}{\Delta v} = \frac{2\ln 2}{\pi}\frac{\lambda^2}{\Delta\lambda} \approx 0.44\frac{\lambda^2}{\Delta\lambda}, \tag{5.24}$$

where Δz and $\Delta\lambda$ are the full width at half maximum of the autocorrelation function and spectral width and λ_0 is the source center wavelength [18]. It can be seen that broadband light sources are required to achieve high axial resolution, as the axial resolution is inversely proportional to the spectral width of the light source. The most popular light source currently used in OCT appears to be superluminescent diode (SLD). A typical SLD has a bandwidth $\Delta\lambda = 20\,\text{nm}$ centered at 830 nm, which corresponds to a coherence length of $\sim 30\,\mu\text{m}$, and since l_c is defined for a round trip, so this leads to a depth pixel size of $15\,\mu\text{m}$ in air, and in tissue, by considering the refractive index of 1.4, gives $\sim 11\,\mu\text{m}$. Modern sources for OCT use Kerr-lens mode-locked lasers and photonic crystal fibers to achieve submicron

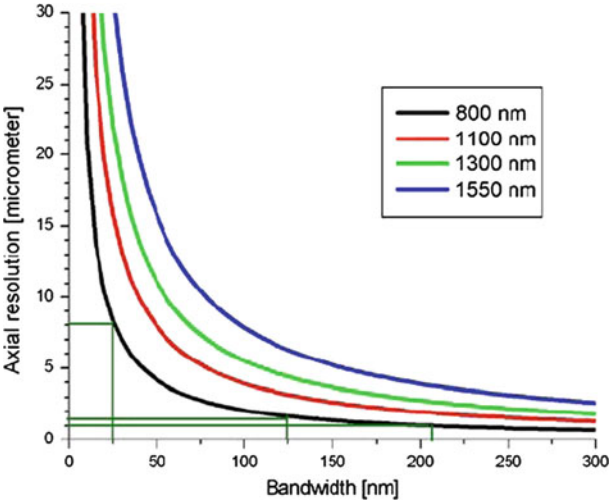

Fig. 5.5 Axial resolution vs. bandwidth of light sources for center wavelengths of 800, 1,100, 1,300, and 1,500 nm. Micrometer-scale axial resolution requires extremely broad optical bandwidths, and bandwidth requirements increase dramatically for longer wavelengths

coherence length. Apart from the wide linewidth, the sources for OCT have to exhibit a smooth Gaussian spectrum profile [19, 20]. Figure 5.5 shows a plot of axial resolution vs. bandwidth for light sources at different wavelengths. Since the axial resolution is inversely proportional to the bandwidth of the light source, broad-bandwidth light sources are required to achieve high axial resolution.

5.4.2 *Lateral Resolution*

As in conventional microscopy, the lateral resolution that may be achieved with OCT imaging is determined by the focus spot of the light beam and is completely decoupled from the axial resolution. Therefore, the optical design of the lateral scanning does not correlate with the axial resolution. The lateral resolution Δx can be written as

$$\Delta x = \frac{4\lambda}{\pi}\left(\frac{f}{d}\right), \tag{5.25}$$

where f is the focal length of the objective lens and d is the $1/e^2$ Gaussian beam waist at the objective lens. It can be seen from the above equation that high lateral resolution can be achieved by using a large numerical aperture (NA) to decrease the spot size. However, for the selection of optics, there is a trade-off between the lateral

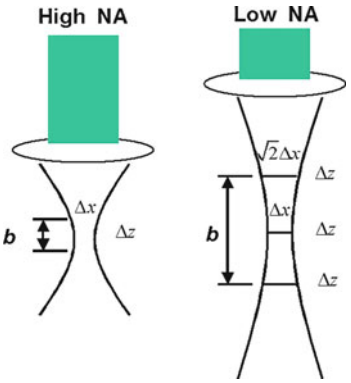

Fig. 5.6 Relationship between focus spot size and depth of field for objective lens with high and low NA

resolution and the imaging depth. A higher lateral resolution leads to a decrease in the depth of focus, or confocal parameter b, which is twice the Rayleigh range:

$$2\Delta z_{\mathrm{R}} = b = \frac{\pi \Delta x^2}{2\lambda}. \tag{5.26}$$

The Rayleigh range gives the distance from the focal point to the point where the light beam diameter has increased by a factor of $\sqrt{2}$. This effectively limits the scanning range of the OCT, quite apart from the working range of the scanning reference delay line, as it is the range over which lateral resolution is maintained. Figure 5.6 shows the relation between the depth of focus (confocal parameter) and the focused spot size for the objective lens with high and low NA.

5.4.3 Sensitivity

The sensitivity or the optical dynamic range of an OCT system can be defined as the ratio of the signal power generated by a perfectly reflecting mirror to the noise of the system and is given by the equation

$$\mathrm{SNR} = \frac{I_{\mathrm{S}}^2}{I_{\mathrm{N}}^2}, \tag{5.27}$$

where I_{S} is the photocurrent at the detector due to the interference term of Eq. 5.18 and which in the case of an ideal 50:50 beam splitter and perfectly reflecting sample is equal to the total source power P. Therefore, the signal photocurrent can be expressed as

$$I_{\mathrm{S}} = \frac{\eta q_{\mathrm{e}}}{\hbar \nu_0} P, \tag{5.28}$$

where η is the quantum efficiency of the detector, q_e is the electron charge, ω_0 is the source center angular frequency, $\hbar$ is the Planck constant divided by 2π, and P is the integral of the source power spectral density. I_N corresponds to the overall noise of the optical detection system and has three significant sources: shot noise (I_{SH}), optical intensity noise or relative intensity noise (I_{RIN}), and thermal noise (I_{TH}). Therefore, the total noise current is the sum of squares of each of the noise contributions and can be expressed as

$$I_N^2 = I_{SH}^2 + I_{RIN}^2 + I_{TH}^2. \tag{5.29}$$

However, in the OCT system, the optical detection scheme employed is heterodyne. Therefore, it can be arranged to achieve shot noise-limited optical detection, whereby the reference arm optical field is much higher than that in the sample arm. This is often the case in OCT when imaging highly scattering and absorbing biological specimens. In a shot noise-limited case, the relative intensity noise and the thermal noise become negligible. So the total noise can be expressed as

$$I_N = I_{SH} = \sqrt{2q_e I_{DC} B}, \tag{5.30}$$

where I_{SH} is the root mean square (RMS) shot noise, B is the detection bandwidth, and I_{DC} is the DC photocurrent and is assumed to be entirely due to the reference arm's optical power. In case of shot noise limit, the overall noise variance can be expressed as

$$I_N = \sqrt{\frac{\eta q_e}{h\nu_0} 2PB}. \tag{5.31}$$

Therefore, substituting Eqs. (5.28) and (5.31) into Eq. 5.27 yields

$$\text{SNR} = \frac{\eta P}{2h\nu_0 B}. \tag{5.32}$$

Generally, the SNR is quoted as a figure of merit in logarithmic unit and is related to the power SNR by

$$\text{SNR} = 10 \log_{10} \left(\frac{\eta P}{2h\nu_0 B} \right). \tag{5.33}$$

For a single detector, the measurement bandwidth $B = 1/\tau$ is a function of the acquisition time τ detector. Therefore, this expression implies that to increase either image acquisition speed or image resolution, which increases the measurement bandwidth, higher source power is required to maintain the SNR performance of the system.

5.4.4 Selection of OCT Wavelength

In OCT, the characteristics of the optical source determine the general performance of the system. For example, the shot coherence length of the optical source determines the axial resolution, and the nominal wavelength determines the achievable penetration depth of the system. The broader the linewidth $\Delta\lambda$ of the source, the smaller the coherence length l_c (Eq. 5.23) of the source is. There are four main criteria that need to be considered when choosing a light source for OCT. These parameters are wavelength, bandwidth, single transverse mode power, and stability. The depth of penetration in OCT is limited by both scattering and absorption of the sample. The absorption window for most biological tissues between 0.65 and 1.4 μm has a local minimum in the absorption of water and blood in the tissues. Absorption attenuates the light in the imaging subject and is wavelength dependent. Because more than 80% of biological tissue consists of water, the absorption of tissue is mostly attributed to the water. If we analyze the water absorption spectrum shown in Fig. 5.7, we can find a window with lower absorption, termed "therapeutic windows" for biomedical optics, existing around 600–800 nm. Absorption by melanin, as well as the scattering from structure protein such as collagen and elastin, exhibits a nearly monotonic decrease with increasing wavelength over this region. These optical properties of tissues have been investigated to some degree both experimentally and by a number of analytical and numerical models. Therefore, the selection of wavelength is a very critical parameter in OCT.

Most of the conventional OCT systems utilize the near-infrared to far-infrared region of the optical spectrum, which ranges from 700 to 1,600 nm. The exact choice of the central wavelength depends on the prospective applications and is mostly determined by the absorption and scattering properties of the medium under investigation, though the expected resolution must also be taken into account. In general, imaging at shorter wavelengths around 800 nm delivers higher axial resolutions; however, the depth of penetration is considerably degraded due to increased scattering at shorter wavelength. In the 700–1,600-nm region, scattering decreases monotonically with wavelength; in particular, the scattering behavior of light in biological specimen shows significant degradation with longer wavelength. Thus, OCT systems operating at central wavelengths around 1,300 nm show an enhanced penetration depth due to less tissue scattering and absorption of endogenous chromophores like hemoglobin and melanin [21, 22]. Recently, OCT imaging in the 1,050–1,060-nm wavelength region is getting much attention in the field of ophthalmology, where imaging the deeper layers of retina is very crucial for diagnosing retinal pathologies [23–27]. In ocular imaging, the highly scattering and absorbing retinal pigment epithelium reduces the penetration depth for wavelengths at the 800-nm region commonly used today in retinal scanning OCT system, while the application of long wavelength in retinal imaging is limited by the water absorption in the relative long path through the vitreous humor, which contains $> 95\,\%$ of water. However, in the 1,050–1,060-nm region, a suitable

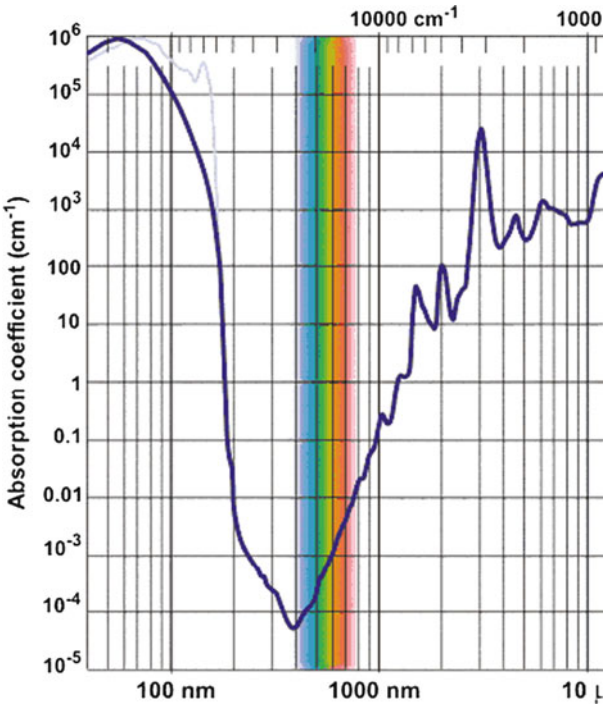

Fig. 5.7 Water absorption spectrum (The original data consult from http://omlc.ogi.edu/spectra/water/index.html)

compromise between water absorption, wavelength dispersion, and scattering loss exists, where the water absorption profile has a local minimum ($\mu a \sim 0.015\,mm^{-1}$ at $\lambda = 1{,}060\,nm$ [23], as compared to $\mu a \sim 0.0023\,mm^{-1}$ at $\lambda = 800\,nm$ [13]). This results in a reduction of the detectable light signal from the retina from $\sim 89.4\%$ at 800 nm to about 48.4% at 1,060 nm.

5.4.5 *Optical Sources for OCT*

In case of OCT, the image resolution and quality is an important factor for governing its clinical utility. The resolution of OCT images in the axial and transverse directions is determined by different mechanisms. The axial resolution is determined by the coherence length of the light source and which is decoupled from the beam focussing optics. Since the coherence length of a light source is inversely proportional to its bandwidth, broad-bandwidth optical sources are required to improve the OCT axial resolution. The axial resolution is inversely proportional to the spectral width of the used light source, and the generation of broadband

light sources has been a topic of great interest. So far, several approaches have been proposed to achieve high axial resolution, such as superluminescent diode, multiplexed superluminescent diode, femtosecond laser, continuum generation from photonic crystal fiber, amplified spontaneous emission (ASE), and xenon illuminator. In general, these solutions either have high cost or exhibit bumpy spectrum, or both. The following section briefly reviews various state-of-the-art broad-bandwidth light sources as potential light sources for the applications in OCT.

5.4.5.1 Superluminescent Diodes (SLEDs)

In principle, operations of SLEDs are very similar to the laser diode (LD), with the lasing action based on amplified simulated emission. However, in SLEDs, lasing action cannot be built up due to insufficient feedback for oscillations. The unique property of SLEDs is the combination of laser diode-like output power and brightness with broad LED-like optical spectrum. Such combination is allowed by high optical gain and wide gain spectrum in semiconductor laser materials. SLEDs are very compact, relatively cheap, and very friendly to use. Current SLEDs operate at various wavelengths, such as 0.8, 1, 1.3, and 1.55 μm, and all of these wavelengths have been used for OCT in different applications. At 830nm range, the SLEDs are based on AlGaAs emitters, and single SLEDs with up to 70-nm bandwidths and $3-15$-mW fiber pigtailed output power (corresponding to around 3.3-μm axial resolution in the tissue) are commercially available (Superlum Ltd, Russia). For ranges above 1 μm, the SLED emitters are based on InGaAs, and the typical bandwidths are around $50-60$ nm, which limits the axial resolution to $>10\mu$m in the tissue. However, using multiplexed SLED technology (synthesized optical source), SLEDs with a bandwidth more than 130 nm and optical power up to 15 mW are commercially available (Denselight Semiconductors, Singapore). While in some specific areas, like ultrahigh-resolution OCT, there are strong competitors to SLDs, namely, femtosecond lasers/supercontinuum sources, for most of practical applications, SLDs are now considered as the most attractive emitters due to their small size, easy use, and much cost-effectiveness compared to alternative light sources.

5.4.5.2 Multiple Quantum Well Semiconductor Optical Amplifiers

Multiple quantum well (MQW) optical amplifiers are another class of promising semiconductor sources widely used in OCT because of their inherently large saturation power and bandwidth. MQWs are generally considered for the use in analogue and digital communication links and are commercially available with wavelength ranging from 1,300 to 1,600 nm. Extremely broadband MQWs based on InGaAsP/InP ridge bent-waveguide semiconductor optical amplifiers with several nonidentical multiple quantum wells can be designed and fabricated on InP substrate [28–30]. However, there are few potential disadvantages for these sources, most of these QWM sources operate at the far-infrared region of the optical spectrum,

and the optical output is unpolarized, which limits its application in OCT where polarization-sensitive imaging is required.

5.4.5.3 Doped Fiber-Based Amplified Spontaneous Emission (ASE) Sources

Doped fiber-based optical sources can provide a high-power and high-brightness broadband superfluorescent optical spectrum that has many applications in many areas including evaluation of fiber optical components by low-coherence interferometry, rotation sensing, spectroscopy, and medical imaging [31]. One attractive way to generate broadband output is via the process of ASE in a rare-earth doped fiber. Over the last few years, there has been very rapid progress in developing high-efficiency output power from cladding-pumped fiber lasers and amplifiers. Rare-earth doped fluoride, telluride, and silicon fibers realize broadband spectra ranging from 1,300 to 1,600 nm. One drawback with doped fiber-based ASE is the need for high-power single-mode pump for optimal coupling into the doped single-mode core. Fiber-coupled single-mode semiconductor pump sources are commercially available; however, they are typically very expensive.

5.4.5.4 Kerr-Lens Mode-Locked (KLM) Lasers

As described earlier, SLEDs are easy to use and generate smooth and stable spectra; they can permit 20-7-μm resolution imaging at a fixed wavelength and are attractive because of their simplicity and low amplitude noise. However, achieving high-speed imaging with a high signal-to-noise ratio requires more than the mW-level power typically available from diode sources. Additionally, the limited optical bandwidth of diodes precludes cellular-level-resolution imaging. With the development of ultrafast laser, it is possible to achieve broadband spectrum. Recently, Kerr-lens mode-locked (KLM) lasers are getting more attention in the field of OCT. The titanium:sapphire laser is tunable from 0.7 μm to 1.1 μm and can produce not only broad spectral bandwidths for high-resolution imaging but also high output powers for fast image acquisition [32,33]. The $Ti:Al_2O_3$ laser is optimized for short coherence length and was demonstrated to achieve sub-2-μm resolution with a power exceeding 100 mW. Although this source provided cellular-resolution imaging, comparative studies have shown that the 800-nm center wavelength of $Ti:Al_2O_3$ is not optimal for deeply penetrating biological tissue. An optimally penetrating optical source will take advantage of the diminishing scattering cross section with wavelength while avoiding the resonant molecular absorption of common tissue constituents such as water and melanin. The chromium:forsterite laser has also been used to generate high output powers and broad spectral bandwidths (5 μm axial resolution) centered around 1,300-nm wavelength, for deeper imaging penetration in highly scattering tissue [34]. Both of these laser sources, however, are large and

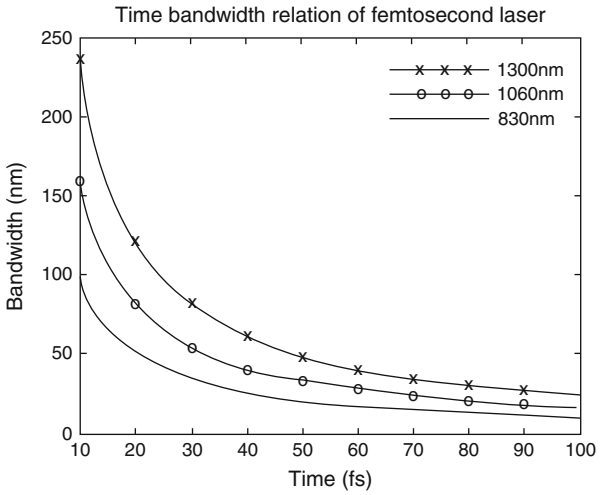

Fig. 5.8 Pulse width vs. bandwidth of femtosecond lasers

require additional pump laser sources, water cooling, and an experienced operator to align and maintain them. The ultrashort pulses from these lasers can be coupled into new tapered [35], microstructured [36], or ultrahigh-NA fiber [37] to achieve even broader bandwidths and hence higher axial resolution imaging. The bandwidth and pulse duration of a mode-locked laser can be calculated by

$$\Delta\lambda(\text{nm}) = 1.47 \times 10^{-3} \frac{\lambda_0^2(\text{nm})}{\tau(\text{fs})}. \tag{5.34}$$

Figure 5.8 plots the relation between time and bandwidth. For achieving high axial resolution, the femtosecond laser should emit less than 20 fs pulses at 800 nm. Currently, the Ti:sapphire laser, with pulses down to 7 fs, has been commercialized. With a compact design and low cost, Ti:sapphire lasers at 800 nm with axial resolution up to 1.2 μm in the tissue have been utilized for corneal and retinal imaging [38]. However, at 1 and 1.3 μm, the available lasers can emit pulses only above 50 fs. Especially for the 1.3-μm laser, bulkiness and maintenance issues continue to be problematic, particularly outside of a research laboratory.

5.4.5.5 Supercontinuum Light Source

Supercontinuum (SC) lasers are a new type of light source based on the nonlinear optical phenomenon. Supercontinuum light is generated by invoking high optical nonlinearity in a material. Typically, mode-locked pulsed laser sources are used in the near infrared (1,064 nm) in the nanosecond, picosecond, or femtosecond range, ensuring high peak powers to drive the nonlinear effect in a material, which "breaks"

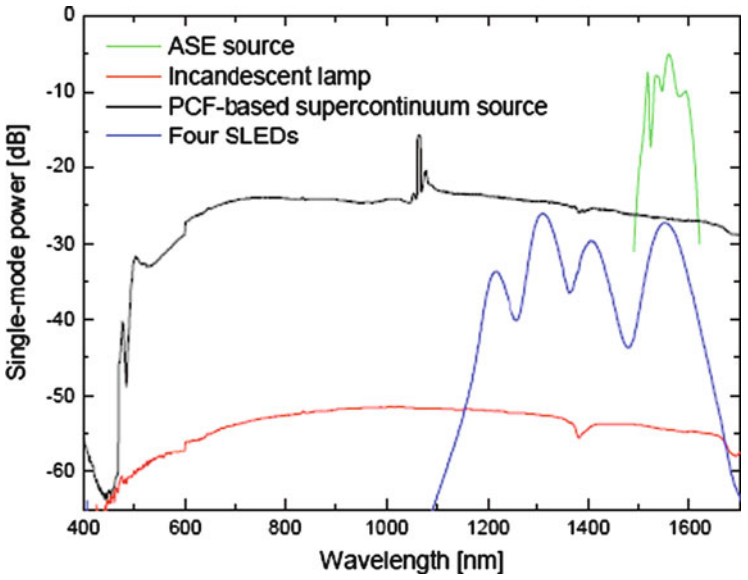

Fig. 5.9 A comparison of supercontinuum with other broadband sources

the pulse out into a SC spectrum. The supercontinuum combines high brightness with broad spectral coverage—a combination offered by no other technology. Figure 5.9 shows the comparison of supercontinuum with other broadband sources. The generation of supercontinuum is due to a plethora of nonlinear optical effects which generate new frequencies, which covers a broadband. Mathematically, the nonlinear effects can be described on the molecular scale by the following total polarization:

$$P = m + \varepsilon_0(\chi^{(1)}E + \chi^{(2)}E^2 + \chi^{(3)}E_3 + \cdots), \tag{5.35}$$

where P is the total polarization of the molecule, m is the permanent dipole moment, E represents the electric field, $\chi^{(1)}$ is the linear polarization, and $\chi^{(2)}$ and $\chi^{(3)}$ are the first and second hyperpolarizability coefficients. Here, the most noticeable terms are the second and third hyperpolarizabilities, and the related phenomena are called second harmonic generation (SHG) and third-order nonlinear effects, including self-phase modulation (SPM), four-wave mixing (FWM), stimulated Raman scattering (SRS), and others. Broadband light sources can be generated through efficient nonlinear effects. In order to enhance nonlinear effects, two conditions must be satisfied: extremely high power and long walking distance for keeping such high power. Ultrafast lasers such as femtosecond lasers can produce very high peak power. In recent years, renewed interest in supercontinuum generation has been closely related to the remarkable progress in the development of photonic crystal fibers (PCF) as well as the development of robust, well-engineered single-box ultrafast lasers. Coupling an ultrafast laser pulse directly out of an

oscillator into a few centimeters of PCF produces more than one octave broad supercontinuum. The fact that only an oscillator with a few nJ of energy is required to generate supercontinuum makes the PCF-based sources reliable, affordable, and relatively simple to operate. These sources make use of optical nonlinear effects in specially designed PCF to create light with a wide spectrum that can span the visible and near infrared, typically from around 400 to 2,000 nm. Due to their spectral properties, they are suitable for OCT imaging with submicrometer axial resolution [39]. SC light sources generating two separate spectral bands were also introduced into OCT, allowing separate scanning at 800 nm and 1,300 nm with axial resolutions of ~ 3 and $\sim 5\,\mu$m, respectively [40, 41]. Commercially, SC sources are available from Fianium and Koheras. Koheras A/S (NKT Photonics, Birkerod, Denmark) offers the SuperK Extreme, which it says is the brightest visible supercontinuum source available. The source, with the highest power the company offers, has a broad spectrum, from 460 to 2,400 nm, and provides a spectral power density of more than 3 mW nm^{-1} in the visible wavelength range. Combining the source with a tunable filter allows a user to tune up to eight simultaneous laser lines independently across the visible spectrum. The SC500-FC supercontinuum source from Fianium (Southampton, UK) is a low-cost, mode-locked fiber laser generating supercontinuum radiation in the spectral band from 500 to 1,700 nm, with an average power in excess of 250 mW. The feasibilities of the Fianium and Koheras SCs were demonstrated for both time-domain and frequency-domain OCT configurations [42–44].

5.4.5.6 Swept-Source Lasers

Swept-source lasers are a tunable light source emitting one wavelength at a time, rapidly swept over a broad spectral range. The promising capabilities of frequency-swept light sources for OCT imaging have gained intense interest in their development and enabled a quantum leap in the speed and sensitivity of OCT technology development. There are three major concepts to achieve high-speed tuning depending on the method used for wavelength selection inside the laser cavity of the wavelength-swept source: one based on a fast rotating polygonal mirror [45,46], the second based on a diffraction grating on a mechanically resonant galvo-scanner [47], and the third using a fiber Fabry-Perot tunable filter (FFP-TF) [48, 49]. For very high tuning speeds and to overcome limitations given by the buildup time of lasing in the cavity, the technique of Fourier domain mode locking (FDML) has been introduced. High repetition rate up to 370 kHz has been already demonstrated for FDML swept sources [50–54]. Recent advancements in the field of ultrahigh-speed swept-source optical source enables Fourier domain detection approach using frequency-swept lasers and provides a powerful, complementary approach for spectral/Fourier domain detection.

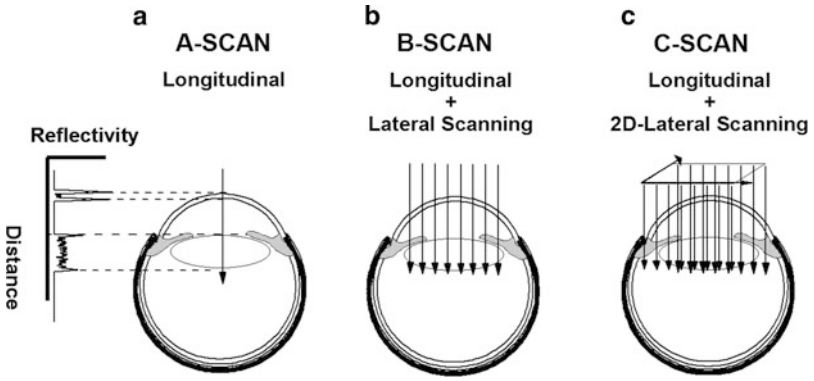

Fig. 5.10 Different scanning modalities in flying-spot optical coherence tomography. (**a**) A-scan. (**b**) B-scan. (**c**) C-scan

5.4.6 Scanning Modalities in OCT

In conventional point-scan OCT (flying-spot OCT), various types of scanning modalities have been implemented for representing the cross-sectional information about the sample. Depending upon the priority of longitudinal (depth) and transverse direction, the scanning modalities can be mainly classified into three: A-scan, B-scan, and C-scan [12]. As in ultrasound instrument, an A-scan (axial scan) typically records the two fundamental parameters of an echo: how large it is (amplitude) and where it occurs in time with respect to zero time delay (pulse transit time). As explained in Sect. 5.3, in a TD-OCT system, an A-scan is implemented by scanning the reference mirror throughout the entire depth to obtain a time-domain interference pattern, as shown in Fig. 5.10a; however, in an FD-OCT system, the total distribution of an A-scan is measured at one time without any reference scan. Similarly, a B-scan can be generated by acquiring several A-scans for different adjacent transverse positions, as shown in Fig. 5.10b. In case of C-scan, the sample is scanned along many successive x and y directions at a fixed depth, as shown in Fig. 5.10c, which can provide different transverse cross-sectional (*en face*) images of the sample at different depth.

5.5 Different OCT Schemes

In OCT, the coherence-gated information about the elementary volume of the scatters within the obscuring scattering specimen can be obtained from either the time-domain measurement principle (TD-OCT) or the frequency-domain (FD-OCT) measurement principle.

5.5.1 Time-Domain OCT Systems

The time-domain OCT operates as described in Sect 5.3; the wavenumber-dependent photodetector current I_D in Eq. 5.10 is captured using a single or multiple detectors where the reference mirror is scanned to match the optical path from reflections within the sample. Depending on the scanning modality and the signal detection scheme employed, the time-domain OCT can be further classified into three: (1) point-scan (flying-spot OCT), (2) line-field (linear OCT), and (3) full-field (wide-field) OCT.

5.5.1.1 Time-Domain Point-Scan OCT (Flying-Spot OCT)

The first generation of commercial OCT instruments has been developed for ophthalmology based on the TD-OCT configuration. However, the main drawback of TD-OCT is that the depth scanning is realized by scanning the reference arm axially. Moreover, the mechanical scanner pair for lateral scanning gives rises to motion artifacts due to mechanical jitter and limited repeatability. These effects adversely deteriorate imaging quality, especially at high speed and at high resolution for subcellular-level imaging. A single scan of the reference mirror thus provides a one-dimensional reflectivity profile of the sample. Similarly, two- or three-dimensional images are produced by scanning the beam across the sample and recording the optical backscattering vs. depth at different transverse positions. This scheme is also called point-scan OCT or flying-spot OCT.

Figure 5.11a shows the typical schematics of a time-domain flying-spot (point-scan) OCT system. As described in Sect. 5.3, in its most common version, it comprises a broadband light source emitting light of high spatial and low temporal coherence, which is coupled into a 2×2 fiber optics-based Michelson interferometer. The Michelson interferometer divides the light beam and directs it into two arms of the interferometer. The sample arm beam directs into the object to be analyzed. It usually contains collimating optics enabling formation of a narrow beam, which penetrates the object. In order to reconstruct two-dimensional cross-sectional images of the object, the beam is galvanometrically scanned across the sample surface. Light backscattered or reflected from the various structures returns to the interferometer and is brought to interference with light reflected back from the reference arm mirror (RM), which scanned back and forth through the required depth of imaging. The standard fiber-optic Michelson interferometer is not the most efficient design for practical implementation because a major disadvantage of this configuration is that the DC signal and intensity noise generated by the light from the reference arm add to the interference signal. In order to eliminate this problem, an alternative configuration called balanced heterodyne configurations, as shown in Fig. 5.11a, has been commonly used, in which these background noise components are canceled by subtracting the photocurrents generated by two photodetectors. Then the resulting interfering light is detected by a photodiode (PD).

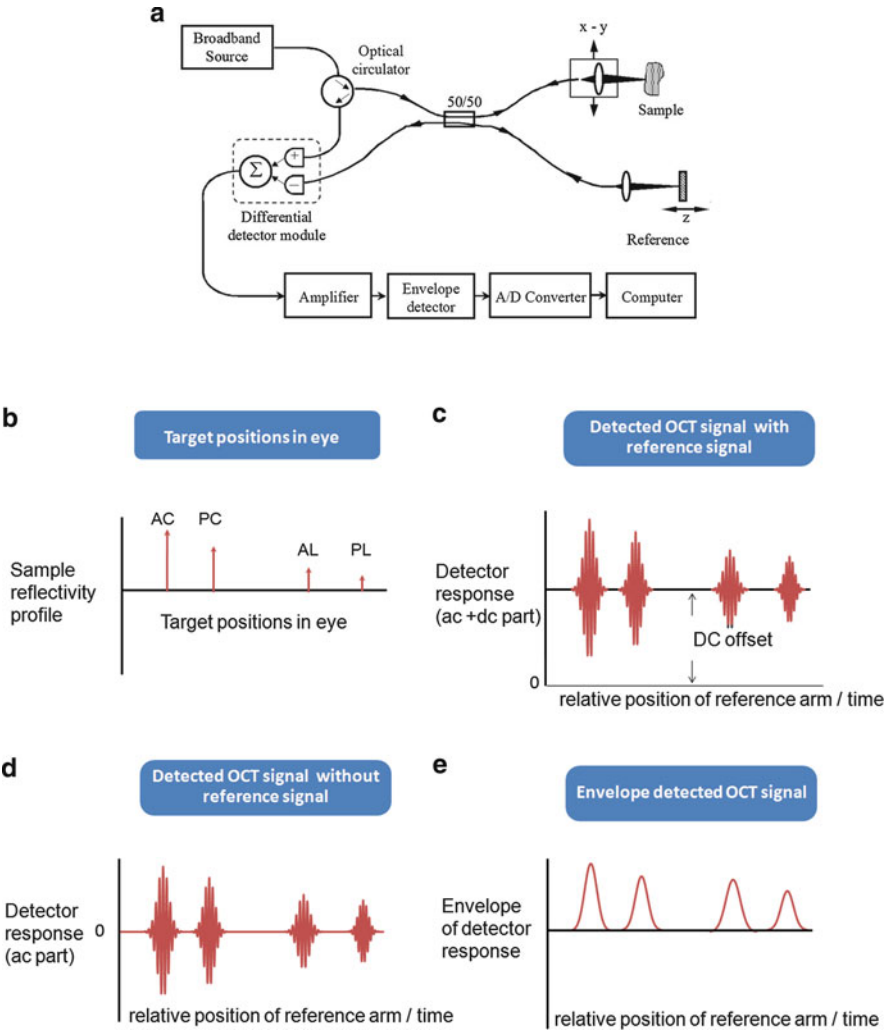

Fig. 5.11 (**a**) Schematic of a typical fiber optics-based time-domain OCT setup, (**b**) reflectivity profile of target position in the ocular medium, (**c**) detected interference signal by the photodetector, (**d**) detected signal with reference signal filtered out, and (**e**) demodulated and envelop detected OCT signal

Figure 5.11b shows the relative target positions in the eye, and Fig. 5.11c shows the raw interferograms (A-scan) which are obtained by scanning the reference arm mirror and correspond to the different structural features of the ocular medium. Figure 5.11d shows the reference arm signal-subtracted interference signal from the output of the balanced detector. In the preceding step, the interferograms are amplified and backed up with a band-pass filter tuned to the Doppler frequency,

often called the "carrier frequency," which is related to the scanning speed of the reference mirror. This procedure helps eliminate extraneous signals arising from background light. Then, for the next scan of the reference mirror, the probing beam is shifted to an adjacent position and so on, to yield a set of consecutive A-scans. These A-scans are then combined into a single picture to form a cross-sectional image of the object, the B-scan. Three-dimensional, volumetric data sets can be generated by acquiring sequential cross-sectional images by scanning the incident optical beam in a raster pattern.

5.5.1.2 Line-Field OCT (Linear OCT) and Full-Field OCT

Conventional point-scan optical coherence tomography (OCT) [55–57] can enable noninvasive, noncontact 3D cross-sectional imaging of structures in highly scattering specimens with very high resolution. However, for reconstructing the 3D image, the conventional OCT system needs a single pointer raster-scanning scheme, in which the focus of the probing beam scans across the sample surface and detects the backscattered light with a single-element photodetector. Thus, a fiber optics-based point-scan time-domain OCT scheme requires at least three scans (one depth and two lateral scans) for acquiring three-dimensional images. The lateral scans address laterally adjacent sample positions, whereas the depth scan detects longitudinal depth positions of light-reflected sites in the sample. The major limitation in point-scan OCT approach is the mechanical scanning system giving rise to motion artifacts due to mechanical jitter and limited repeatability.

Line-field [58–60] and full-field OCT (FF-OCT or wide-field (WF-OCT)) [61, 62] are alternative OCT concepts which aim to improve the image acquisition speed and to simplify the optical setup of conventional point-scan OCT by realizing direct line-field or full-field sample imaging onto an array or line detector such as CCD [61] or CMOS [63] camera. FF-OCT is based on bulk optics Linnik-type Michelson interferometer with relatively high-NA microscopic objectives, but identical, on both arms of the interferometer. Whereas WF-OCT uses imaging optics with a single lens to image a large sample area, compromising the lateral resolution, in the case of line-field OCT, the line illumination was achieved with a spherical focusing lens and a plano-concave cylindrical lens (CL). Recently, FF-OCT has been of increased interest as a nonscanning, high-resolution, en face imaging method in several medical and nonmedical applications. Moreover, en face image can provide new information, which may complement that provided by the longitudinal cross-sectional image.

The basic configuration of full-field/line-field OCT systems is based on a bulk optics low-coherence interferometer with a CCD camera placed at the output as detector. The CCD can enable the acquisition of 2D en face/1D image in a single exposure without any lateral scanning. However, the direct use of CCD cameras for heterodyne detection in time domain is limited by the relatively slow frame rate of the commercially available CCD camera (typically ≈ 100 Hz for 512×512 pixels). Therefore, the depth-scan acquisition speed has to be drastically reduced

in order to permit sufficient sampling of the interferometric signal. The temporal phase-stepping interferometric scheme is commonly used for the reconstruction of en face OCT images. Conventional FF-OCT uses a three-phase or four-phase step algorithm for the image reconstruction. Over the past decade, several FF-OCT schemes were reported based on a wide variety of optical configurations to realize the phase stepping and the type of PSI (phase-shifting interferometry) algorithm [64] used for the extraction of the interferometric signal. Typically, four images with the different phase shifts are recorded successively to reconstruct the en face OCT image. The phase-stepped interference images sequentially recorded by the CCD detector can be expressed as follows:

$$I_0 = E_{S0}^2 + E_{R0}^2 + 2E_{S0}E_{R0}\cos(\varphi_S - \varphi_R), \tag{5.36}$$

$$I_{\pi/2} = E_{S0}^2 + E_{R0}^2 + 2E_{S0}E_{R0}\cos(\varphi_S - \varphi_R + 90°), \tag{5.37}$$

$$I_{\pi} = E_{S0}^2 + E_{R0}^2 + 2E_{S0}E_{R0}\cos(\varphi_S - \varphi_R + 180°), \tag{5.38}$$

$$I_{3\pi/2} = E_{S0}^2 + E_{R0}^2 + 2E_{S0}E_{R0}\cos(\varphi_S - \varphi_R + 270°). \tag{5.39}$$

Then, for reconstructing the en face OCT image I_{OCT}, the conventional four-phase shift algorithm can be used as shown below:

$$I_{OCT} = \left[(I_0 - I_{\pi})^2 + (I_{3\pi/2} - I_{\pi/2})^2\right]^{1/2}. \tag{5.40}$$

In FF-OCT, different interferometric configurations like Michelson [61], Mirau [65], or Linnik [66, 67] configuration can be used. For wide aperture systems, the spherical aberration in the axial direction is very dominant for Michelson and Mirau configuration compared to Linnik. In case of Linnik configuration, optical path length and focusing in both arms of the interferometer can be adjusted independently [12]. Moreover, in Linnik configuration, high-NA objectives can be used to obtain high spatial resolution. In general, the axial resolution of the tomographic image in FF-OCT depends on both coherence length of the source (coherence effect) and the NA of the objective (aperture effect). A variant scheme of FF-OCT that utilizes objective with high NA (< 0.4) is called full-field optical coherence microscopy (FF-OCM) and is used for obtaining very high resolution [68, 69]. In this scheme, the aperture effect is more dominant than coherence effect. Figure 5.12 shows the basic setup of FF-OCT based on Michelson (Fig. 5.12a) and Linnik configurations (Fig. 5.12b).

The FF-OCT scheme can utilize a wide variety of optical sources, including a source with either spatially coherent illumination or spatially incoherent illumination. In FF-OCT, depending upon the nature of illumination, the multiple scattered light from the specimen can result in strong cross-talk-generated noise between parallel detection channels; thus, each detector should ideally not detect light originating from outside its conjugate volume. To avoid cross talk, one must prevent interference occurring between adjacent pixels at the detection plane [70].

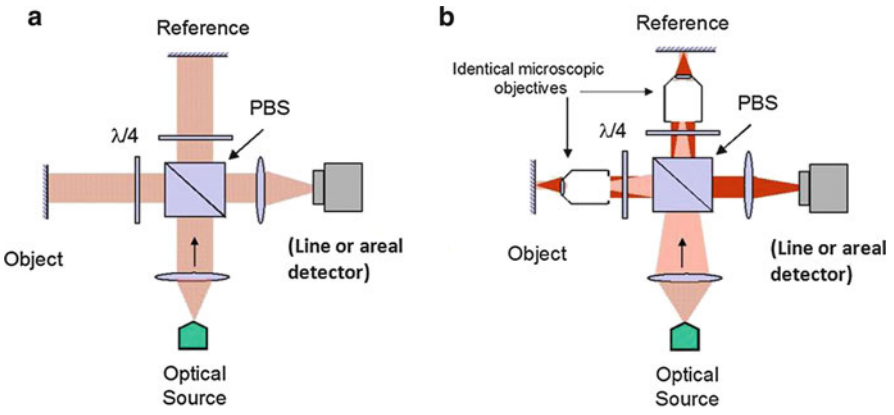

Fig. 5.12 Typical full-field OCT configurations. (**a**) Michelson geometry for wide-field OCT (WF-OCT) and (**b**) Linnik geometry for full-field OCT (FF-OCT)

This can be achieved by controlling the degree of spatial coherence of full-field illumination. FF-OCT utilizing spatially incoherent sources such as thermal sources can effectively suppress the effect of coherent cross talk [71]. Moreover, thermal sources may provide high axial resolution due to their broad spectral bandwidth. However, the brightness per spatial mode of thermal sources often remains insufficient, requiring a trade-off between sensitivity and imaging speed. The major interest of spatially coherent illumination in FF-OCT resides in the possibility to use powerful pulsed lasers such as femtosecond lasers, allowing higher sensitivity and acquisition speed than with thermal light sources. In contrast, spatially coherent source can generate considerable amount of coherent cross talk that degrades the image quality.

However, the temporal phase-stepping method employed in FF-OCT for reconstruction of en face image degrades the time resolution of the system. Over the last several years, different techniques have been reported for improving the time resolution of FF-OCT. Single-shot FF-OCT (SS FF-OCT) is a relatively new concept which aims to improve the time resolution of FF-OCT and extend the feasibility of FF-OCT for fast imaging application in biological application. The basic principle of SS FF-OCT is similar to the simultaneous phase-shifting interferometric method, which has been developed over the years for high-speed vibration-insensitive optical testing. Nevertheless, the optical configuration of the four-channel phase stepper optics is quite complex and limits this system's performance for practical implementation. Any differences caused by image projections, optical aberration, and response uniformity will directly influence the reconstruction accuracy. Recently, the feasibility of SS FF-OCT was reported for dynamic imaging of biological specimens [72] and materials [73, 74].

5.5.2 *Frequency-Domain OCT*

Frequency-domain OCT (FD-OCT) [20, 75] is a variant interferometric imaging modality. It has been widely attracted in the biomedical imaging field due to its higher sensitivity and imaging speed compared to conventional TD-OCT. The principle of FD-OCT relies on the transformation of the OCT time varying signal along the optical axis, termed the A-scan, into the frequency domain. The basic physics behind FD-OCT is based on the inverse scattering theorem. According to the Wiener-Khintchine theorem, the spectral power amplitude of the backscattered wave equals the Fourier transform of the axial distribution of the object scattering potential. FD-OCT has the advantage that the full sample depth information is obtained in a parallel manner such that no moving parts are necessary. Based on the implementation, the FD-OCT can be divided into two classes, spectral-domain OCT (SD-OCT) and swept-source OCT (SS-OCT). In SD-OCT, the optical frequency components are captured simultaneously with a dispersive element and linear detector; on the other hand, in SS-OCT, the optical frequency components are captured by a single detector in a time-encoded sequence by sweeping the frequency of the optical source. Recent studies have shown that Fourier domain OCT can provide signal-to-noise ratio that is more than 20 dB better than the conventional TD-OCT.

However, SD-OCT also has remarkable drawbacks [76–78]. One limitation in frequency domain is that the optical spectrum at the output of the interferometer consists of symmetric spectral terms, which cause same image results for positive and negative OPDs called mirroring effect. Different methods have been developed to eliminate this problem, such as phase-shifting interferometry or complex signal processing. The simple detection in the frequency domain usually introduces spatial frequency ambiguity; autocorrelation artifacts, originating from internal interferences of the sample and the system; as well as depth-dependent SNR loss, caused by finite spectral linewidth [11]. Furthermore, nonuniform FD sampling deteriorates TD signal quality, and time-consuming post-processing is a necessity for all FD-OCT techniques. It was found that some of these effects can be largely compensated by multiple, phase-shifted imaging of the same region (i.e., A-scan), followed by reconstruction of the complex phase of the FD-signal [79], resampling, and transformation into the time domain. Moreover, for getting better lateral resolution, the technique such as dynamic focusing, which is generally used in time-domain OCT, is not easily implemented in FD-OCT. In traditional FD-OCT, the imaging optics are devised with large depth of focus, to accommodate the entire range of the A-scan, usually 1–2 mm, which limits the possibility of using high-NA objectives to enhance the transverse resolution. However, recently, by employing a Bessel beam with axicon lenses, the extended-focal length FD-OCTs were demonstrated with cellular-level resolution.

5.5.2.1 Spectral-Domain OCT (SD-OCT)

A typical implementation of a fiber optics-based SD-OCT setup is shown in Fig. 5.13a. The backscattered low-coherence light is mixed with a reference beam by the 2 × 2 fiber optics-based Michelson interferometer; then the grating-based spectrometer at the output of the interferometer separates each spectral component detected using a linear array detector. The interference signal detected by the linear detector is expressed as

$$I(k) = I_{\mathrm{S}}(k) + I_{\mathrm{R}}(k) + 2\sqrt{I_{\mathrm{S}}(k) I_{\mathrm{R}}(k)} \sum_{n} \alpha_n \cos(2k z_n), \tag{5.41}$$

where $I_{\mathrm{R}}(k)$ and $I_{\mathrm{S}}(k)$ are the wavelength-dependent intensities reflected from the reference and sample arms, respectively, and k is the wavenumber. The third term on the right-hand side of Eq. 5.41 represents the interference between the backreflected lights from the sample and reference arm. α_n is the square root of the sample reflectivity at depth Z_n. In order to reconstruct the depth information, the spectrum is inverse Fourier transformed, which yields the following convolution:

$$\left|\mathrm{FT}^{-1}[I(k)]\right|^2 = \Gamma^2(z) \otimes \left[I_{\mathrm{R}}\delta(z) + \sum_{n} I_{\mathrm{S},n}\delta(z) + \sum_{n} \alpha_n^2 \delta(z - z_n) + \sum_{n} \alpha_n^2 \delta(z + z_n) \right], \tag{5.42}$$

where $\Gamma(z)$ represents the envelope of the coherence function. The first and second terms in the right-hand side of Eq. 5.42 describe the autocorrelation (or self-interference) of the reference signal and sample signal, respectively. The third and fourth terms are due to the interference of the backreflected beam from reference and sample surfaces and its complex conjugates. The SD-OCT detects the spectrally resolved interference signal with a spectrometer that consists of a high-efficiency diffraction grating and a high-speed line camera. Figure 5.13b shows the reflectivity profile of the different target positions in the ocular medium, and Fig. 5.13c shows the detected intensity spectrum by the camera. In order to suppress autocorrelation, self-cross correlation, and camera noise artifacts, first, all the spectral interferograms in each slice along the x-direction (B-scan) were ensemble-averaged at each wavelength to obtain a reference spectrum; this background spectrum is then subtracted from each A-scan. Since the Fourier transform relates the physical distance (z) with the wavenumber ($k = 2\pi/\lambda$), however, the spectra obtained with the SD-OCT spectrometer are not necessarily evenly spaced in k-space. In order to obtain a proper depth profile, the subtracted spectral interferograms are then remapped from λ-space to k-space by the use of the spline interpolation method, as shown in Fig. 5.13d. Due to the Fourier relation (Wiener-Khintchine theorem between the autocorrelation and the spectral power density), the depth-resolved information can be immediately reconstructed by a Fourier transformation from the remapped spectra, without movement of the reference arm, as shown in Fig. 5.13e.

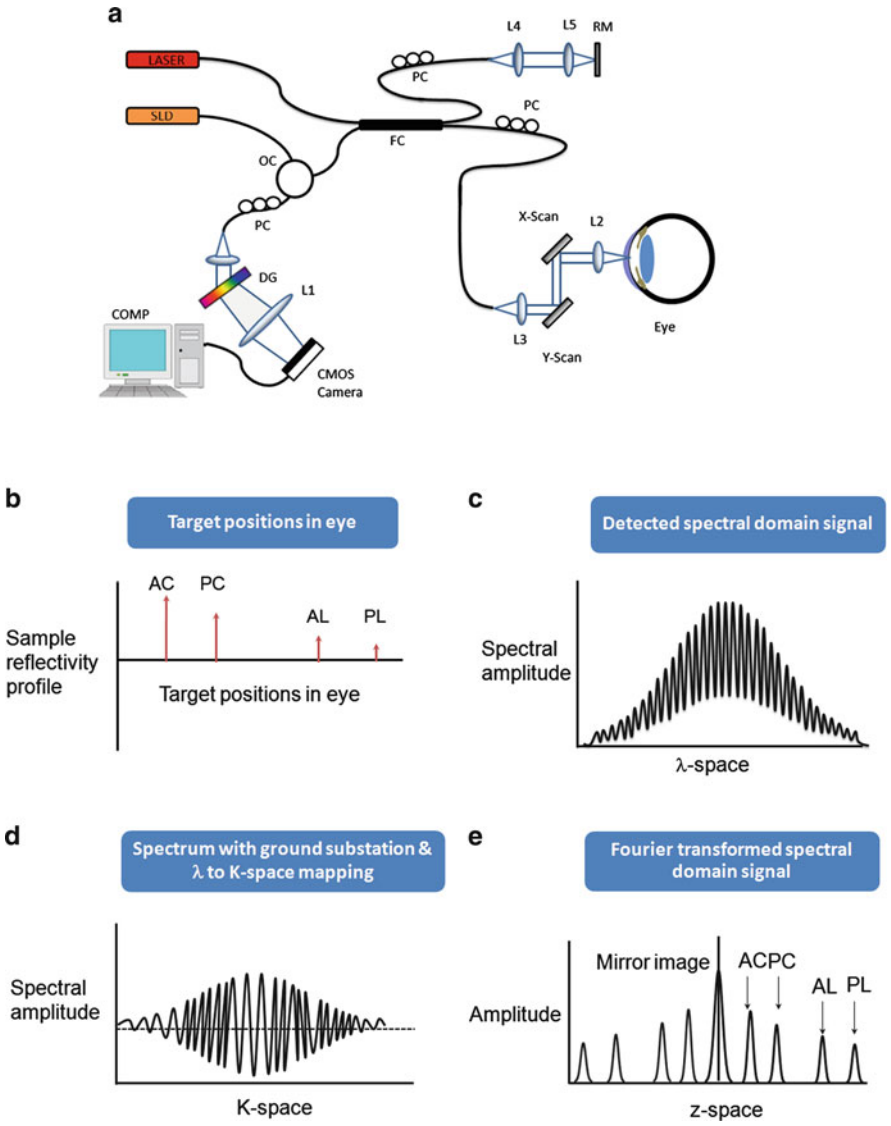

Fig. 5.13 (**a**) Experimental schematic of an FD-OCT setup, (**b**) reflectivity profile of anterior chamber of an eye, (**c**) detected spectral interferogram by the camera (A-scan), (**d**) remapped spectral interferogram in *k*-space with background subtraction, and (**e**) Fourier transformed spectrum

For a Gaussian source centered at k_0 with a full width at half maximum bandwidth Δk, the complex coherence function is described in Sect. 5.3. The depth range that can be probed with an SD-OCT is dependent on the spectrometer

resolution and the detector size (number of pixels). For a conventional SD-OCT system, the maximum imaging depth is defined as

$$l_{\max} = \frac{1}{4n} \frac{\lambda_0^2}{\Delta\lambda_S} N, \tag{5.43}$$

where n is the refractive index of the medium, λ_0 is the center wavelength of the detected spectrum, $\Delta\lambda_S$ is the spectrometer bandwidth, and N is the number of pixels of the camera. For an ambiguity-free image, this depth range should be doubled. The term $(\Delta\lambda_s/N)^{-1}$ can be seen as the inverse of the spectral resolution power $\delta\lambda^{-1}$ of the detecting spectrometer and is proportional to the coherence length of the detected spectral channel, which is responsible for one of the main drawbacks of SD-OCT, which is the signal decay observed for structures far away from the relative zero delay.

Line-Field SD-OCT

Line-field SD-OCT is an alternative implementation to improve imaging speed. To improve imaging speed, transversally multidimensional techniques have already been extensively investigated for TD-OCT imaging, as described in the above section, which profit the continued high-speed camera development with full frame acquisition in the multi-kframe/s range as well as the high stability due to the transversally static setup. Their major advantages found in almost isotropic high-resolution sampling of microscopic specimen (within the depth of field), but suffers from low imaging speed and high power requirements because of very low signal to noise ratio, limit its potential for in vivo applications. Line-field SD-OCT based on the introduction of one transversal imaging dimension and detection by a highly parallel spectrometer has been investigated by multiple groups [80–82]. These seem to have potential for high-speed acquisition of cross-sectional scans but involve a complicated mixture of geometrical imaging in one sensor axis and a spectrometer setup in the orthogonal direction, which confines area detectors to rather low pixel counts due to cross talk in the "spatial" axis. For full volume acquisition, they still need beam translation. Figure 5.14 shows the basic schematic of a line-field SD-OCT implementation.

5.5.2.2 Swept-Source OCT (SS-OCT)

The concept of FD-OCT can also be implemented using a tunable laser source over a broad spectral range in conjunction with a single detector. FD-OCT of this type has been called swept-source OCT (SS-OCT) [82]. Despite the difference in system configuration, both SD-OCT and SS-OCT have a common net result: the OCT signal is sampled in spectral domain and an SNR improvement is gained because of the Fourier reconstruction. In SS-OCT, the time required to tune the wavelength determines the time to produce an A-scan. Recently, a swept source

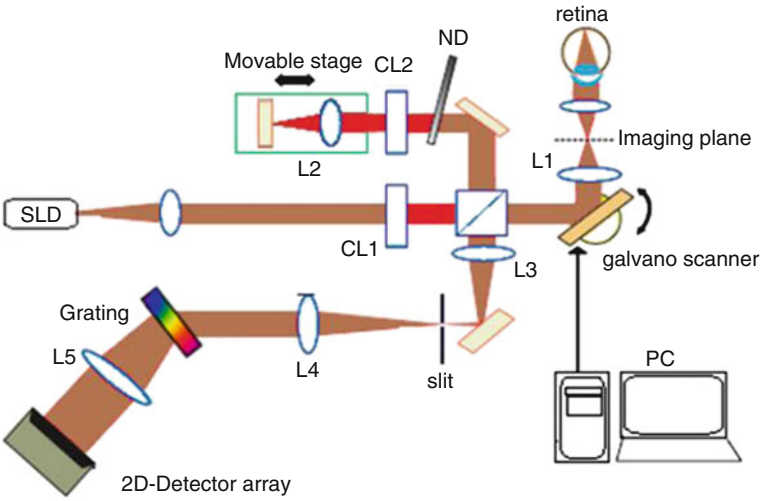

Fig. 5.14 Optical scheme of line-field spectral-domain optical coherence tomography. *CL* cylindrical lens, *ND* neutral density filter, *SLD* superluminescent diode, and *PC* personal computer

with a sweeping frequency of a few hundreds of kilohertz has been achieved, which drastically improves the imaging speed of SS-OCT to compete with SD-OCT and TD-OCT in terms of imaging speed [83].

Figure 5.15 shows the typical implementation of SS-OCT systems, which employ a broadband, rapid frequency-swept laser source and InGaAs photodetectors to perform Fourier domain OCT imaging without the use of a spectrometer [45, 50–54, 77]. With such a wavelength-swept source, interference signals at individual wavelengths can be measured sequentially with high spectral resolution. This spectrally resolved data acquisition is central to frequency-domain ranging. This method offers significantly higher sensitivity than the time-domain ranging method used in conventional OCT. Furthermore, frequency-domain ranging does not require reference delay scanning and can therefore be applied to increase imaging speed. Since SD-OCT systems typically employ silicon-based CCD detectors, they cannot operate at wavelengths longer than ~1,000 nm, since the detector efficiency degrades rapidly beyond this point. Moreover, the unavailability of relatively cheap spectrometer at 1,300 nm, which is very essential for OCT imaging of epithelial tissues and many nonbiological samples to achieve an image penetration depth of 1–3 mm. With a pressing need for high imaging speed at 1,000–1,300 nm in various applications, wavelength-swept sources, particularly rapidly tuned lasers, have developed substantially in recent years and have emerged as important and practical light sources for OCT. One particular advantage of SS-OCT over SD-OCT is worth mentioning, that is, that a balanced detection scheme can be used in SS-OCT (see Fig. 5.15) to cancel out the strong background light in the interferometer, therefore enhancing the dynamic range of the system.

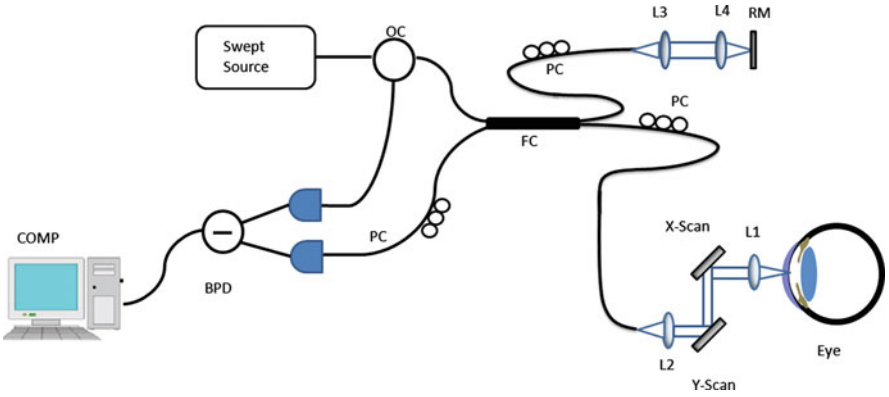

Fig. 5.15 Schematics of a fiber optics-based swept-source OCT setup. *OC* optical circulator, *PC* polarization controller, *RM* reference mirror, *BPD* balanced photodetector, *FC* fiber coupler

Line-Field/Full-Field SS-OCT

The schematics of line-field OCT system using frequency-sweeping source is similar to that of LF-SD-OCT, which is based on free-space implementation of Michelson interferometer and, instead of 2D detector array line-field SS-OCT, uses a 1D linear detector at the spectrometer side. The irradiation is done by an elliptical beam onto the imaging sample using a cylindrical lens, and then the wavelength-resolved interference signal is detected by a line CCD camera [84]. Since the system uses the line CCD camera as a detector, the exposure time can be reduced (in the microsecond range); therefore, the images are influenced to a lesser extent by motion artifacts.

Instead, the full-field SS-OCT is a full-field version of swept-source optical coherence tomography. A set of 2D Fourier holograms are recorded at discrete wavenumbers spanning the swept-source tuning range. The resultant 3D data cube contains comprehensive information on 3D morphology of the sample that can be retrieved by software via 3D discrete Fourier transform. This method of recording of the OCT signal confers signal-to-noise ratio improvement in comparison with "flying-spot" TD-OCT. The spatial resolution of the 3D reconstructed image, however, is degraded due to the presence of a phase cross-term, whose origin and effects are addressed below.

5.5.2.3 Full-Range Complex Fourier Domain OCT

As described in the preceding section, one of the major drawbacks of FD-OCT that limits its practical application is the complex conjugate ambiguity. This is because in FD-OCT the detected realvalued spectral interferogram is Fourier transformed to localize the scatter within the sample. The Fourier transform of a realvalued

function is Hermitian, so the reconstructed image is symmetric with respect to the zero-phase delay of the interferometer, leading to ambiguity in interpretation of the resulted OCT images. In order to overcome this problem, one has to place the sample entirely within the positive or negative space. Consequently, only half of the imaging depth is available for imaging in practice. By resolving the complex conjugate artifact, the imaging depth range can be doubled, which would in turn provide additional flexibility to explore the most sensible measurement range near the zero delay line [75].

To achieve the full-range complex imaging for FD-OCT, several methods have been proposed. Phase-shifting methods were among the first attempt to achieve the full-range imaging [79]; however this limits the imaging speed and complex conjugate rejection ratio due to the requirements of several phase steps at the same sampling location and its accuracy Another approach that uses a 3×3 optical coupler as phase-shifting element was proposed, which allows simultaneous detection of two quadraturely phase-shifted interferograms to obtain the complex ambiguity-free images [86]. This technique requires two separate detectors for image acquisition, which adds additional cost and complexity, thus limiting its practical application. For high-speed full-range complex imaging, an elegant, practical scheme is to introduce a constant modulation frequency into the spatial interferogram during transverse scanning of the sample [87]. In this way, the complex data can be obtained either by Fourier transform or Hilbert transform of the B-scan interferogram in transverse direction. By using this method, it is possible to achieve a full-range complex imaging with high speed. However, the original implementation requires a piezo-stage to provide modulation in the interferograms, which limits the full imaging speed due to the mechanical movement of the piezo-stage used.

Recently, the modulation of the spectral interferograms is achieved by the galvo-scanner [88], which is used for transversely (x-direction) scanning the sample. In doing so, the sample beam is offsetted from the pivot axis of the x-scanner, which causes a path length modulation during x-scanning, thus introducing a modulation frequency into the B-scan interferograms. The main advantage of this method is that it does not need any additional phase-shifting elements to realize frequency modulation and the modulation frequency is inherently given by the system itself. Another important advantage of using frequency modulation in the interferogram to achieve full-range complex FD-OCT image is that it is relatively insensitive to sample movement that is critical for in vivo application. These aspects render high-speed full-range complex SD-OCT imaging without any restriction on additional hardware component and without limitation on the imaging speed, which is critical for in vivo imaging applications.

5.6 Functional OCT

In conventional OCT, the contrast mechanism relies upon the spatial variation of the coherent backscatters within a cross-sectional plane or volume of tissue or materials. However, a number of other intrinsic properties of the tissue have been demonstrated

to provide information about the morphological changes by altering the amplitude, phase, or polarization states of the probing beam. Exploiting these properties, thus providing novel imaging contrast mechanisms, enhances the clinical and biomedical applications for OCT to achieve functional imaging that can reveal more details about the tissue dynamics and physiology. Some of the important functional modes of OCT are polarization-sensitive OCT, Doppler OCT, spectrometric OCT, and differential absorption OCT.

5.6.1 Polarization-Sensitive OCT

Most of the body tissues such as muscle, tendons, and nerve fibers contain collagen and elastin, which exhibit birefringence when they form a specific structure. Birefringence depicts a change in polarization state of light due to the refractive index difference for light polarized in two orthogonal planes. The propagation of light through such birefringence sample may alter the optical polarization state of reflected light. Therefore, polarization-sensitive measurements at the output of the interferometer can provide depth-correlated information about the birefringence nature of the material or tissue specimen. As well as providing added contrast, changes in birefringence may indicate changes in functionality or structure of the tissue. Since the first report of functional polarization-sensitive OCT (PS-OCT) system [89], a variety of PS-OCT configurations have been investigated [90–95]. They all differ in complexity, capabilities, and signal processing schemes. The most complete information about the polarization properties of a biological specimen is given by a system capable of producing depth-resolved Muller matrix elements. These configurations can account for the depolarization as well as the changes in total, linear, and circular degree of polarization of the probe beam during propagation in tissue.

The TD-OCT and FD-OCT configurations do not account for birefringence within a sample, treating the electromagnetic wave as a scalar quantity. However, light waves are transverse and, therefore, have extra degrees of freedom described by the polarization state. The PS-OCT measurement apparatus is similar to that of TD-OCT or FD-OCT, with the addition of a light polarizer after the source and a polarizing beam splitter (PBS) with an extra detector in the output arm (Fig. 5.3). Propagation of light through a sample may alter the optical polarization state of the reflected light. This can occur due to optical scattering and birefringence within the sample. Birefringence describes a change in the polarization state of light due to the refractive index difference for light polarized in two orthogonal planes. Therefore, polarization-sensitive measurement of the output interferogram can resolve depth-correlated information about the birefringence of the sample material. Mathematically, the two orthogonal polarization states can be treated separately as two electromagnetic waves propagating in separate interferometers.

The polarization state of light can be expressed in terms of Stokes vector S as

$$S = \begin{bmatrix} I \\ Q \\ U \\ V \end{bmatrix} = \begin{bmatrix} a_x^2 + a_y^2 \\ a_x^2 - a_y^2 \\ 2a_x a_y \mathrm{Cos}\varphi \\ 2a_x a_y \mathrm{Sin}\varphi \end{bmatrix}, \tag{5.44}$$

where I, Q, U, and V are Stokes parameters; a_x and a_y are amplitudes of two orthogonal components of the electric vector; and φ represents the phase difference between the two orthogonal components. By using a 4×4 Muller matrix, the effect of an optical device on the polarization of light can be expressed, and the matrix acts on the input state $S_1$to give the output state S_2:

$$S_2 = \begin{bmatrix} I_2 \\ Q_2 \\ U_2 \\ V_2 \end{bmatrix} = MS_1 = \begin{bmatrix} M_{00}\, M_{01}\, M_{02}\, M_{03} \\ M_{10}\, M_{11}\, M_{12}\, M_{13} \\ M_{20}\, M_{21}\, M_{22}\, M_{23} \\ M_{30}\, M_{31}\, M_{32}\, M_{33} \end{bmatrix} \begin{bmatrix} I_1 \\ Q_1 \\ U_1 \\ V_1 \end{bmatrix}. \tag{5.45}$$

If we consider the Poincare sphere representation, a polarization state S can be represented by a point (Q, U, V). The Poincare sphere representation provides a convenient method to evaluate changes of Stokes vector. By determining either the Stokes vector or the Muller matrix, the full quantification of birefringence properties of the biological sample can be obtained. PS-OCT imaging of the Stokes vector and Muller matrix has been demonstrated by several groups [96–99]. It is attractive for medical applications, providing an extra contrast mechanism that could potentially lead to optical diagnosis of certain pathologies [100–102].

5.6.2 *Doppler OCT*

Doppler OCT (DOCT) or optical Doppler tomography (ODT) is another functional mode, which can permit quantitative imaging of fluid flow in highly scattering specimens [103–108]. The technique is similar to Doppler velocimetry. Doppler velocimetry suffers from imprecise imaging due to the long coherence length of the light source used, which results from the interference of the static, and Doppler shifted components of light occurs over a long optical path. The low-coherence gating property of OCT overcomes this problem, permitting quantitative imaging of fluid flow in highly scattering media, such as monitoring in vivo blood flow beneath the skin. In DOCT, the velocity resolution depends upon detection electronics, scan angle, and acquisition time. Reported flow velocity resolutions are in the region 10–100 μm s^{-1}; however, recent development in Fourier domain Doppler OCT (FD-DOCT) has shown that a velocity resolution of just a few micrometers per second may be achieved [109–116]. The DOCT can provide 3D tomographic map

and velocity profile of blood flow in tissue, which attracted a number of biomedical applications, for example, determination of the depth of burns and determining tissue perfusion to ensure adequate oxygenation of the tissue after injury, wound closure, grafting, etc. Other applications include distinguishing between arterial and venous blockages in tissue after injury or monitoring the effect of pharmaceuticals on blood transport in the tissues.

The Doppler effect describes the shift in frequency of waves reflected from moving objects. This frequency shift can be used to determine object-moving velocity. For electromagnetic waves such as light, derivation of the Doppler shifted frequency from a moving object requires the application of special relativity. The result for a Doppler shifted frequency f_d is

$$f_\mathrm{d} = \sqrt{\frac{c+u}{c-u}} f_0, \tag{5.46}$$

where f_0 is the initial frequency of the electromagnetic wave, c the speed of light, and u is the speed of the moving object. Here, it is assumed that u is positive when the object is moving toward the observer. In this case, it is seen that the Doppler shifted frequency, Δf, must be greater than the initial frequency:

$$\Delta f = f_\mathrm{d} - f_0. \tag{5.47}$$

It can be shown that when u is much less than c, the velocity of the moving sample is given by

$$\Delta f = \frac{u}{c} f_\mathrm{d}. \tag{5.48}$$

In the practical DOCT system, Fig. 5.16, the interferometer sample arm is angled relative to the direction of flow by an amount θ. Detected light is scattered from a moving particle in the sample, undergoing a double Doppler shift—once from the source to the particle and once again from the particle back to the objective. These two factors are taken into account by expressing Eq. 5.48 in terms of initial source and scattered wavevectors k_0 and k_d, respectively. The Doppler shift can then be written as

$$\Delta f = \frac{1}{2\pi}(k_\mathrm{d} - k_0) \bullet u. \tag{5.49}$$

Therefore, the velocity of moving particles can be determined from the measurement of the *Doppler shift* and knowledge of the relative angle between the optical signal and the flow [112]:

$$u = \lambda_0 \frac{\Delta f}{2\cos(\theta)}. \tag{5.50}$$

Structural information about the sample is obtained by either conventional TD-OCT or more recently FD-OCT [111]. However, to retrieve data regarding the flow of particles within submerged capillary, extra measurements of the *Doppler shifted frequency* must be made. To do this in the time domain, the reference mirror of

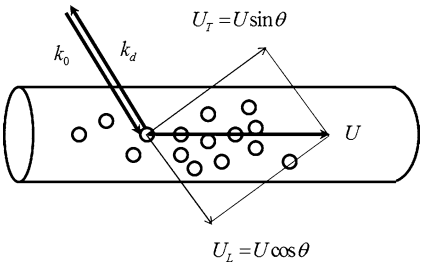

Fig. 5.16 Schematic for optical Doppler tomography. The sample arm beam is held at some angle θ to the direction of flow. Therefore, an optical signal with wavevector k_0 falls on a particle moving with velocity u. The light scattered back into the sample objective is Doppler shifted and has wavevector k_d

the interferometer is scanned to match the path length within the capillary. At each spatial point within the capillary, the detector intensity is sampled at a rate not less than two samples per time period of the source. The time varying result is then Fourier transformed to give the Doppler frequency shift due to moving particles within the capillary. By doing this at a number of points within the capillary, a profile of particle flow is determined.

The *axial resolution* of DOCT is again dependent on the source temporal coherence length and the lateral scan resolution on the beam spot size. Velocity resolution depends upon the detection electronics, scan angle, and the acquisition time. Reported flow velocity resolutions are in the region 10–100 $\mu\mathrm{ms}^{-1}$; however, recent developments in Fourier domain DOCT (FD-DOCT) have shown a velocity resolution of just a few micrometers per second. FD-DOCT has also shown greater sensitivity in the region of 90–115 dB and may, therefore, lend itself to ocular flow imaging where ANSI laser safety standards require optical powers to be below 1 mW. DOCT has been applied to a number of medical situations. Not least of these, imaging in vivo blood flow in both the skin [117] and retina [110] has been demonstrated. The capability of DOCT to measure flow within a scattering sample also has potential in new areas of research such as microfluidics [118].

5.6.3 Optical Microangiography

Optical microangiography (OMAG) is a functional extension to FD-OCT imaging modality capable of resolving 3D distribution of dynamic blood perfusion at the capillary level within microcirculatory beds in vivo. Unlike Doppler OCT to image blood flow, OMAG explores implicitly the phase information embedded in the OCT spectral interferograms. By using heterodyne technology, OMAG method effectively separates the scattering signals caused by the moving scatters, for

example, moving blood cells, from the scattering signals backscattered by the static tissue background, that is, by the tissue microstructures, to achieve imaging of blood perfusion. In essence, OMAG mathematically maps the backscattered optical signals from the moving particles into one image—that is, the blood flow image—while it simultaneously maps the backscattered optical signals from the static particles into a second image, which is the microstructural image, identical to the conventional OCT image. In OMAG, the spatial interferogram in the lateral direction (B-scan) is modulated with a Doppler frequency feasible to separate the moving and static scattering components within sample. This Doppler modulation frequency can be introduced either by mounting the reference mirror in the reference arm onto a linear piezo-translation stage, which moves the mirror at a constant velocity across the B-scan (i.e., x-direction scan), or simply by the inherent scattering fluid flow within sample. In the earlier version of OMAG system [119, 120], this is achieved by mounting the reference mirror in the reference arm onto a linear piezo-translation stage that moved the mirror at a constant velocity across the B-scan (i.e., x-direction scan). However, the latest version of OMAG utilizes the spatial modulation frequency provided by the inherent blood flow modulation rather than reference arm modulation [121]. OMAG is an emerging imaging modality with clear potential applications in many basic research and medical imaging applications. Because of its exceptionally high spatial resolution and velocity sensitivity, OMAG can provide useful information regarding microcirculation in a number of applications, both in clinical [122, 123] and basic research [124].

5.6.4 Spectroscopic OCT

Spectroscopic OCT is an alternative mode of OCT, which provides further access to the composition and functional state of the specimen. Spectroscopic OCT can be implemented in a variety of ways. One approach is based on spectral ratio imaging of OCT images using two or more spectral bands with wavelength division multiplexers, which combine lights with different wavelengths and then electronically distinguish the resulting signal by their different Doppler shifts resulting from the reference arm scan [125, 126]. By use of state-of-the-art ultrabroadband femtosecond $Ti:Al_2O_3$ lasers, spectroscopic imaging over the wavelength range from 650 to 1,000 nm has been reported by Morgner et al. [127]. Another implementation is based on estimation of depth-resolved spectral information of the source spectrum, in which the modification of the source spectrum caused by the sample can be measured directly from the Fourier domain processing of cross-correlation interferometric data [128, 129].

5.6.5 *Second Harmonic OCT*

Second harmonic OCT incorporates the use of coherence gating of second-order nonlinear optical response of biological tissues molecular contrast imaging of tissue micro-structures. [130, 131]. Optical second harmonic generation (SHG) is the lowest-order nonlinear optical process where the second-order nonlinear optical susceptibility is responsible for the generation of light at second harmonic frequency. Femtosecond laser pulses were usually used to excite second harmonic waves from biological specimens in conjunction with a reference nonlinear crystal. Second harmonic interference fringe signals were detected and used for image construction. Because of the strong dependence of second harmonic generation on molecular and tissue structures, this technique offers contrast and resolution enhancement to conventional optical coherence tomography. The second-order nonlinear optical susceptibility is sensitive to electron configurations, molecular structure and symmetry, local morphology, and ultra-structures; thus, SHG provides molecular contrast for the coherence image.

5.7 Application and New Trends in OCT

5.7.1 *Medical Applications*

OCT has recently emerged as a promising imaging technique, mainly for medical applications. It has a number of features that make it attractive for a broad range of biological, clinical, and material investigations. First, the imaging can be performed in situ and nondestructively. The image resolution of the order 10–15 μm is now routine using standard technology, and high resolution of the order of 1 μm may be achieved using state-of-the-art laser systems. High-speed, real-time imaging is possible with more than video rate frame acquisition. OCT can be interfaced with a wide range of imaging delivery systems and imaging probes. In comparison with conventional optical imaging technique, the specific features of OCT such as high resolution can be achieved independent of the beam focusing conditions and the coherence gate, that can substantially improve the probing depth in scattering medium, which make this technique a unique place in clinical imaging.

So far, the most successful medical application of OCT that has been identified and developed is in the field of ophthalmology due to the low scattering found in the optical materials of the eye [132, 133]. OCT has provided ophthalmologists with depth resolution in imaging the posterior and anterior of the eye previously only achievable with histology. OCT can detect subtle changes to the eye caused during early stage of ocular disease, such as age-related macular degeneration [134, 135], diabetic retinopathy [136, 137], macular holes [138, 139], intraocular tumors [140], and glaucoma [141–143]. Other than ophthalmology, imaging studies using OCT have been performed in a wide range of biological, medical, and surgical specialties

including developmental biology [144], cardiology [145], gastroenterology [146], urology [147], and neurosurgery [148].

Fiber-based OCT can be integrated into different imaging delivery systems including catheters and forward imaging devices to enable internal body OCT imaging [149]. More recently, the OCT catheter has been combined with endoscope-based delivery to perform in vivo imaging in animal models and human patients. Endoscopic OCT can increase the functionality, detecting the subsurface margins of lesions and quantifying tumor volumes. The feasibility of OCT to perform image-guided surgical intervention has been investigated. OCT has been used to monitor laser ablation therapy in real time and may enable more precise control of laser delivery [150].

Apart from the more immediate medical applications of OCT, it has been demonstrated in the field of developmental biology and cell research as a method to perform high-resolution, high-speed imaging of developing morphology and function [144, 151]. The ability of OCT to identify the mitotic activity, the nuclear to cytoplasmic ratio, and the migration of cell has the potential to not only impact the cell and developmental biology but also impact medical and surgical disciplines for early diagnostics of diseases such as cancer [152].

5.7.2 Nonmedical Applications

While the majority of OCT applications have been in the field of biology and medicine, OCT has also been demonstrated in the nonbiological area of materials investigation [153, 154], optical data storage [155], and microfluidic devices [156]. OCT has been used to identify subsurface defects in ceramic and polymer composites. The optical ranging capability of OCT through scattering materials has been utilized for increasing the data storage capability by assembling multiple layers of optically accessible data. The advancement of microfabrication techniques has led to increasing complex and bioMEM (biological micro-electro-mechanical) systems. Microstructures within the microfluidic systems range from 10 to $1,000\,\mu$m, which is within both imaging depth and resolution of OCT. In addition, microfluidic systems are typically fabricated from transparent or semitransparent substrates, facilitating imaging penetration to deeper 3D features [12].

5.7.3 New Trends in OCT

Although already being applied to a number of medical and nonmedical problems, the OCT technology itself is still evolving, and there have also been further developments in the refinement of OCT. Today we stand at the threshold of a new era in OCT imaging with the transformation of technology from “time-domain” OCT to the “spectral-domain” or “frequency-domain” OCT. FD-OCT will allow much

faster image capture because it does not require the reference mirror movement that is necessary in current "time-domain" systems [157]. It appears that FD-OCT can result in as many as 60,000,000 A-scans per second [158]. The major benefit of FD-OCT is that it permits point-to-point registration and can give accurate volumetric analysis. Not only has technology already improved upon OCT, but it has also made imaging scans easier and clearer than ever before. Ultrahigh-speed FD-OCT allows imaging of large areas of the retina and rapid three-dimensional volume rendering of optic nerve head and fovea [159]. Scientists and researchers have already begun refining the technique of OCT to view biological tissues as they are in the body. This represents a transition in technology from two-dimensional imaging to three-dimensional screening of large retinal volumes that is also an achievement in the efficiency of three-dimensional imaging [159]. Furthermore, OCT has been improved upon to speed up imaging scans and increase clarity of the image. This new technology is definitely a more efficient method compared to standard procedures [159]. Every photon that is emitted is detected, thus increasing efficiency by a factor of a 100 and 50. This is extremely beneficial because the imaging speed is increased without decreasing the quality of the image. This new progress made in OCT is going to make it easier for medical practitioners to perform quick and easy noninvasive procedures.

Research and development concerned with the improvement of fundamental characteristics such as imaging resolution, speed, and sensitivity are very active. Some of the technology and application areas currently having great impact on the field are ultrahigh-resolution system [160]; polarization-sensitive imaging; high-speed, high-sensitivity optical spectral-domain systems such as SS-OCT and FD-OCT; and novel approaches like full-field or wide-field OCT [161–164]. Another active area of research involved the use of external contrast agents to enhance both penetration, through reduced scattering (optical clearing), and contrast through enhanced refractive index variation, which can enable the enhanced visualization of selected features such as abnormal tissues, microvasculature, etc. [165–167]. There are numerous research applications of this technology in a broad range of fields. In addition, advances in technology are continuing. More research remains to be done, and numerous clinical studies must be performed in order to determine where OCT can play a role in clinical medicine, apart from ophthalmology. However, unique capabilities of OCT imaging suggest that it will have significant impact on fundamental research as well as on medicine.

5.8 Conclusion

OCT is a high-resolution, noninvasive, 3D imaging technique with great potential in both clinical and fundamental research application in many areas. Its wide range of current applications covers from medical diagnosis and surgical guidance to the characterization of polymer microstructures and reading of multilayered storage media, etc., which indicate that OCT will play a major role in practical

scientific innovation and research in years to come. Therefore, it is essential that OCT technologies are developed further as an enabling measurement technology. The functional extension capability of OCT technique such as spectroscopic and Doppler OCT can provide additional image contrast mechanisms to differentiate structure and assess functional activity. OCT has the far-reaching potential to be a quantitative imaging technique that could impact many, as yet unexplored, areas and should therefore be considered a vital measurement tool. Important emerging fields already impacted by OCT are those of tissue engineering and polymer composite manufacture. To realize true optical biopsy and full optical diagnosis and grading of malignant tumors by OCT will require a great number of clinical trials and solid experimental demonstration of the robustness of the technique. To enable such developments, the measurement technique must also be quantitatively validated. In particular, the clinical potential and reliability of OCT will be greatly enhanced by validated measurements of volume, structural dimensions, and flow. These stringent requirements present new and exciting challenges for optical medical metrology. Clearly, it will not be possible to fulfill all of these criteria immediately. However, as these issues are addressed, the applicability of OCT can only grow.

References

1. N. Tanno, T. Ichikawa, A. Saeki, Lightwave Reflection Measurement. Japanese Patent # 2010042. (1990) (Japanese Language)
2. S. Chiba, N. Tanno, Backscattering optical heterodyne tomography. Prepared for the 14th Laser Sensing Symposium (1991) (Japanese language)
3. D. Huang, E.A. Swanson, C.P. Lin, J.S. Shuman, W.G. Stinson, W. Chang, M.R. Hee, T. Flotte, K. Gregory, C.A. Puliafito, J.G. Fujimoto, Optical coherence tomography. Science **254**, 1178–1181 (1991)
4. A.F. Fercher, K. Mengedoht, W. Werner, Eye-length measurement by interferometry with partially coherent light. Opt. Lett. **13**, 1867–1869 (1988)
5. C.K. Hitzenberger, W. Drexler, A.F. Fercher, Measurement of corneal thickness by laser Doppler interferometry. Invest. Ophthalmol. Vis. Sci. **33**, 98–103 (1992)
6. J.A. Izatt, M.R. Hee, E.A. Swanson, C.P. Lin, D. Huang, J.S. Schuman, C.A. Puliafito, J.G. Fujimoto, Micrometer-scale resolution imaging of the anterior eye with optical coherence tomography. Arch. Ophthalmol. **112**, 1584–1589 (1994)
7. W. Clivaz, F. Marquis-Weible, R.P. Salathe, R.P. Novak, H.H. Gilgen, High-resolution reflectometry in biological tissue. Opt. Lett. **17**, 4–6 (1992)
8. J.M. Schmitt, A. Kn¨uttel, R.F. Bonner, Measurement of optical properties of biological tissues by low-coherence reflectometry. Appl. Opt. **32**, 6032–6042 (1993)
9. X. Clivaz, F. Marquis-Weible, R.P. Salathé, R.P. Novak, H.H. Gilgen, High resolution reflectometry in biological tissues. Opt. Lett. **17**, 4–6 (1992)
10. J.O. Schenk, M.E. Brezinski, Ultrasound induced improvement in optical coherence tomography (OCT) resolution. PNAS **99**(15), 9761–9764 (2002)
11. A.M Rollins, Another way to peer inside the body: optical coherence tomography combines interferometry and high-tech light sources to capture images of living tissue. Mach. Des. (2005) http://machinedesign.com/article/another-way-to-peer-inside-the-body-0106
12. B.E. Bouma, G.J. Tearney (eds.), *Handbook of Optical Coherence Tomography* (Marcel Dekker, Inc., New York, 2003)

13. P. Latkany, Retinal disease: evolving treatment approaches. Medscape Medical News (2006). [online] Available from: http://www.medscape.com/viewarticle/549001.Accessed11Jan2007.
14. R.C. Youngquist, S. Carr, D.E.N. Davies, Optical coherence-domain reflectometry – a new optical evaluation technique. Opt. Lett. **12**(3), 158–160 (1987)
15. K. Takada, I. Yokohama, K. Chida, J. Noda, New measurement system for fault location in optical waveguide devices based on an interferometric technique. Appl. Opt. **26**, 1603–1606 (1987)
16. E. Hecht, *Optics*, 3rd edn. (Addison Wesley, Reading, 1998)
17. J.W Goodman, *Statistical Optics* (Wiley, New York, 1985)
18. E.A. Swanson, D. Huang, M.R. Hee, J.G. Fujimoto, C.P. Lin, C.A. Puliafito, High-speed optical coherence domain reflectometry. Opt. Lett. **17**, 151–153 (1992)
19. W. Drexler, Ultrahigh-resolution optical coherence tomography. J. Biomed. Opt. **9**, 47–71 (2004)
20. A. Fercher, W. Drexler, C.K. Hitzenberger, T. Lasser, Optical coherence tomography – principles and applications. Rep. Progr. Phys. **66**, 239–303 (2003)
21. A.F. Fercher, C.K. Hitzenberger, G. Kamp, S.Y. Elzaiat, Measurement of Intraocular Distances by Backscattering Spectral Interferometry. Opt. Commun. **117**, 43–48 (1995)
22. J.M. Schmitt, G. Kumar, Optical scattering properties of soft tissue: a discrete particle model. Appl. Opt. **37**, 2788–2797 (1998)
23. J.M. Schmitt, A. Knuttel, M. Yadlowsky, M.A. Eckhaus, Optical-coherence tomography of a dense tissue: statistics of attenuation and backscattering. Phys. Med. Biol. **39**, 1705 (1994)
24. B. Považay, K. Bizheva, B. Hermann, A. Unterhuber, H. Sattmann, A.F. Fercher, W. Drexler, C. Schubert, P.K. Ahnelt, M. Mei, R. Holzwarth, W.J. Wadsworth, J.C. Knight, P.S. Russel, Enhanced visualization ofchoroidal vessels using ultrahigh resolution ophthalmic OCT at 1050 nm. Opt. Express **11**, 1980–1986 (2003)
25. A. Unterhuber, B. Považay, B. Hermann, H. Sattmann, A. Chavez-Pirson, W. Drexler, In vivo retinaloptical coherence tomography at 1040 nm-enhanced penetration into the choroid. Opt. Express **13**, 3252–3258 (2005)
26. B. Považay, B. Hermann, A. Unterhuber, B. Hofer, H. Sattmann, F. Zeiler, J.E. Morgan, C. Falkner-Radler, C. Glittenberg, S. Binder, W. Drexler, Three-dimensional optical coherence tomography at 1050 nm versus800 nm in retinal pathologies: enhanced performance and choroidal penetration in cataract patients. J. Biomed. Opt. **12**, 041211 (2007)
27. D.M. de Bruin, D.L. Burnes, J. Loewenstein, Y. Chen, S. Chang, T.C. Chen, D.D. Esmaili, J.F. de Boer, In vivo three-dimensional imaging of neovascular age-related macular degeneration using optical frequency domain imaging at 1050 nm. Invest. Ophthalmol. Vis. Sci. **49**, 4545–4552 (2008)
28. R. Huber, D. Adler, V. Srinivasan, J.G. Fujimoto, Fourier domain mode locking at 1050 nm for ultrahigh-speed optical coherence tomography of the human retina at 236,000 axial scans per second. Opt. Lett. **32**, 2049–2051 (2007)
29. C.F. Lin, B.L. Lee, Extremely broadband AlGaAs/GaAs super-luminescentdiodes. Appl. Phys. Lett. **71**, 1598–1600 (1997)
30. C.F. Lin, B.R. Wu, L.W. Laih, T.T. Shih, Sequence influence of nonidentical InGaAsP quantum wells on broadband characteristics of semiconductor optical amplifiers superluminescent diodes. Opt. Lett. **26**, 1099–1101 (2001)
31. P.J. Poole, M. Davies, M. Dion, Y. Feng, S. Charbonneau, R.D. Goldberg, I.V. Mitchell, The fabrication of a broad-spectrum 1215 light-emitting diode using high-energy ion implantation. IEEE Photon. Technol. Lett. 8, 1145–1147 (1996)
32. J.R. Digonnet, *Rare Earth Doped Fiber Lasers and Amplifiers* (Marcel Dekker, New York, 1993)
33. B.E. Bouma, G.J. Tearney, S.A. Boppart, M.R. Hee, M.E. Brezinski, J.G. Fujimoto, High-resolution optical coherence tomographic imaging using a mode-locked Ti: Al2O3 laser source. Opt. Lett. **20**, 1486–1489 (1995)
34. X. Clivaz, F. Marquis-Weible, R.P. Salathe, Optical low coherence reflectometry with 1.9 mm spatial resolution. Electron. Lett. **28**, 1553–1555 (1992)

35. B.E. Bouma, G.J. Tearney, I.P. Biliinski, B. Golubovic, J.G. Fujimoto, Self-phase-modulated Kerr-lens mode-locked Cr: forsterite laser source for optical coherence tomography. Opt. Lett. **21**, 1839–1842 (1996)
36. T.A. Birks, W.J. Wadsworth, P.S.J. Russell, Supercontinuum generation in tapered fibers. Opt. Lett. **25**, 1415–1417 (2000)
37. A.L. Gaeta, Nonlinear propagation and continuum generation in microstructured optical fibers. Opt. Lett. **27**, 924–926 (2002)
38. D.L. Marks, A.L. Oldenburg, J.J. Reynolds, S.A. Boppart, Digital algorithm for dispersion correction in optical coherence tomography for homogeneous and stratified media. Appl. Opt. **42**, 204–217 (2003)
39. A. Unterhuber, B. Povazay, B. Hermann, H. Sattmann, W. Drexler, V. Yakovlev, G. Tempea, C. Schubert, E.M. Anger, P.K. Ahnelt, M. Stur, J.E. Morgan, A. Cowey, G. Jung, A.S.T. Le, Compact, low-cost Ti Al_2O_3 laser for in vivo ultrahigh-resolution optical coherence tomography. Opt. Lett. **28**, 905–907 (2003)
40. B. Povazay, K. Bizheva, A. Unterhuber, B. Hermann, H. Sattmann, A.F. Fercher, W. Drexler, A. Apolonski, W.J. Wadsworth, J.C. Knight, P.St.J. Russell, M. Vetterlein, E. Scherzer, Submicrometer axial resolution optical coherence tomography. Opt. Lett. **27**(20), 1800–1802 (2002)
41. A. Aguirre, N. Nishizawa, J. Fujimoto, W. Seitz, M. Lederer, D. Kopf, Continuum generation in a novel photonic crystal fiber for ultrahigh resolution optical coherence tomography at 800 nm and 1300 nm. Opt. Express **14**(3), 1145–1160 (2006)
42. H. Wang, A.M. Rollins, Optimization of dual-band continuum light source for ultrahigh-resolution optical coherence tomography. Appl. Opt. **46**(10), 1787–1794 (2007)
43. P. Cimalla, J. Walther, M. Mehner, M. Cuevas, E. Koch, Simultaneous dual-band optical coherence tomography in the spectral domain for high resolution in vivo imaging. Opt. Express **17**, 19486–19500 (2009)
44. F. Spöler, S. Kray, P. Grychtol, B. Hermes, J. Bornemann, M. Först, H. Kurz, Simultaneous dual-band ultra-high resolution optical coherence tomography. Opt. Express **15**(17), 10832–10841 (2007)
45. S. Kray, F. Spöler, M. Först, H. Kurz, High-resolution simultaneous dual-band spectral domain optical coherence tomography. Opt. Lett. **34**(13), 1970–1972 (2009)
46. S.H. Yun, C. Boudoux, G.J. Tearney, B.E. Bouma, High-speed wavelength-swept semiconductor laser with a polygon-scanner-based wavelength filter. Opt. Lett. **28**(20), 1981–1983 (2003)
47. S. Yun, G. Tearney, J. de Boer, N. Iftimia, B. Bouma, High-speed optical frequency-domain imaging. Opt. Express **11**(22), 2953–2963 (2003)
48. R. Huber, M. Wojtkowski, J.G. Fujimoto, J.Y. Jiang, A.E. Cable, Three-dimensional and C-mode OCT imaging with a compact, frequency swept laser source at 1300 nm. Opt. Express **13**(26), 10523–10538 (2005)
49. M.A. Choma, K. Hsu, J.A. Izatt, Swept source optical coherence tomography using an all-fiber 1300-nm ring laser source. J. Biomed. Opt. **10**, 044009 (2005)
50. R. Huber, M. Wojtkowski, K. Taira, J. Fujimoto, K. Hsu, Amplified, frequency swept lasers for frequency domain reflectometry and OCT imaging: design and scaling principles. Opt. Express **13**(9), 3513–3528 (2005)
51. R. Huber, M. Wojtkowski, J.G. Fujimoto, Fourier domain mode locking (FDML): a new laser operating regime and applications for optical coherence tomography. Opt. Express **14**(8), 3225–3237 (2006)
52. R. Huber, D.C. Adler, J.G. Fujimoto, Buffered Fourier domain mode locking: unidirectional swept laser sources for optical coherence tomography imaging at 370,000 lines/s. Opt. Lett. **31**(20), 2975–2977 (2006)
53. M.Y. Jeon, J. Zhang, Z. Chen, Characterization of Fourier domain mode-locked wavelength swept laser for optical coherence tomography imaging. Opt. Express **16**(6), 3727–3737 (2008)
54. G.Y. Liu, A. Mariampillai, B.A. Standish, N.R. Munce, X. Gu, I.A. Vitkin, High power wavelength linearly swept mode locked fiber laser for OCT imaging. Opt. Express **16**(18),

14095–14105 (2008)
55. Y. Mao, C. Flueraru, S. Sherif, S. Chang, High performance wavelength-swept laser with mode-locking technique for optical coherence tomography. Opt. Commun. **282**, 88–92 (2009)
56. J.G. Fujimoto, Optical coherence tomography for ultrahigh resolution in vivo imaging. Nat. Biotechnol. **21**(11), 1361–1367 (2003)
57. M.E. Brezinski, G.J. Tearney, S.A. Boppart, B.E. Bouma, E.A. Swanson, J.F. Southern, J.G. Fujimoto, High speed catheter based OCT imaging of coronary microstructure. Circulation **94**(8), 1494–1494 (1996)
58. W. Drexler, U. Morgner, F.X. Kartner, C. Pitris, S.A. Boppart, X.D. Li, E.P. Ippen, J.G. Fujimoto, In vivo ultrahigh-resolution optical coherence tomography. Opt. Lett. **24**(17), 1221–1223 (1999)
59. Y. Chen, S. Huang, A.D. Aguirre, J.G. Fujimoto, High-resolution line-scanning optical coherence microscopy. Opt. Lett. **32**, 1971–1973 (2007)
60. Y. Watanabe, K. Yamada, M. Sato, *In vivo* nonmechanical scanning grating-generated optical coherence tomography using an InGaAs digital camera. Opt. Commun. **261**, 376–380 (2006)
61. Y. Watanabe, K. Yamada, M. Sato, Three-dimensional imaging by ultrahigh-speed axial-lateral parallel time domain optical coherence tomography. Opt. Express **14**, 5201–5209 (2006)
62. E. Beaurepaire, A.C. Boccara, M. Lebec, L. Blanchot, H. Saint-Jalmes, Full-field optical coherence tomography. Opt. Lett. **23**, 244–246 (1998)
63. E. Bordenave, E. Abraham, G. Jonusauskas, N. Tsurumachi, J. Oberl, C. Rullie‘re, P. Minot, M. Lasse‘gues, J. Bazeille, Wide-field optical coherence tomography: imaging of biological tissues. Appl. Opt. **41**, 2059 (2002)
64. S. Bourquin, V. Monterosso, P. Seitz, R.P. Salathe, Video-rate optical low-coherence reflectometry based on a linear smart detector array. Opt. Lett. **25**(2), 102–104 (2000)
65. K. Creath, Phase measurement interferometry techniques, in *Progress in Optics*, vol. 24, ed. by E. Wolf, (Elsevier Science Publishers, Amsterdam, 1988), pp. 349–393
66. G.S. Kino, S.S.C. Chim, Mirau correlation microscope. Appl. Opt. **29**, 3775–3783 (1990)
67. M. Davidson, K. Kaufman, I. Mazor, F. Cohen, An Application of Interference Microscope to Integrated Circuit Inspection and Metrology. Proc. SPIE, **775**, 233–247 (1987)
68. A. Dubois, A.C. Boccara, M. Lebec, Real-time reflectivity and topography imagery of depth-resolved microscopic surfaces. Opt. Lett. **24**, 309–311 (1999)
69. A. Dubois, L. Vabre, A.C. Boccara, E. Beaurepaire, High-resolution full-field optical coherence tomography with a Linnik microscope. Appl. Opt. **41**, 805–812 (2002)
70. W.Y. Oh, B.E. Bouma, N. Iftimia, S.H. Yun, R. Yelin, G.J. Tearney, Ultrahigh-resolution full-field optical coherence microscopy using InGaAs camera. Opt. Express **14**, 726–735 (2006)
71. A.F. Fercher, C.K. Hitzenberger, M. Sticker, E. Moreno-Barriuso, R. Leitgeb, W. Drexler, H. Sattmann, A thermal light source technique for optical coherence tomography. Opt. Commun. **185**, 57–64 (2000)
72. B. Karamata, P. Lambelet, M. Laubscher, R.P. Salathé, T. Lasser, Spatially incoherent illumination as a mechanism for cross-talk suppression in wide-field optical coherence tomography. Opt. Lett. **29**, 736–738 (2004)
73. M.S. Hrebesh, R. Dabu, M. Sato, In vivo imaging of dynamic biological specimen by real-time single-shot full-field optical coherence tomography. Opt. Commun. **282**, 674–683 (2009)
74. M.S. Hrebesh, Y. Watanabe, M. Sato, Spatial phase-shifting interferometer using paired wedge prism and combined wave plate. Jpn. J. Appl. Phys. Part 2: Lett. **46**(12–16), L369–L371 (2007)
75. M.S. Hrebesh, Y. Watanabe, M. Sato, Profilometry with compact single-shot low-coherence time-domain interferometry. Opt. Commun. **281**(18), 4566–4571 (2008)
76. G. Hausler, M.W. Lindner, Coherence radar and Spectral radar- new tools for dermatological diagnosis. J. Biomed. Opt. **3**, 21–31 (1998)
77. R. Leitgeb, C.K. Hitzenberger, A.F. Fercher, Performance of Fourier domain vs. time domain optical coherence tomography. Opt. Express **11**, 889–894 (2003)

78. M.A. Choma, M.V. Sarunic, C.H. Yang, J.A. Izatt, Sensitivity advantage of swept source and Fourier domain optical coherence tomography. Opt. Express **11**, 2183–2189 (2003)
79. J.F. de Boer, B. Cense, B.H. Park, M.C. Pierce, G.J. Tearney, B.E. Bouma, Improved signal-to-noise ratio in spectral-domain compared with time-domain optical coherence tomography. Opt. Lett. **28**, 2067–2069 (2003)
80. M. Wojtkowski, A. Kowalczyk, R. Leitgeb, A.F. Fercher, Full range complex spectral optical coherence tomography technique in eye imaging. Opt. Lett. **27**, 1415–1417 (2002)
81. B. Grajciar, M. Pircher, A.F. Fercher, R.A. Leitgeb, Parallel Fourier domain optical coherence tomography for in vivo measurement of the human eye. Opt. Express **13**, 1131–1137 (2005)
82. T. Endo, Y. Yasuno, F. Truffer, G. Aoki, S. Makita, M. Itoh, T. Yatagai, Line-field Fourier-domain optical coherence tomography. Proc. SPIE **5690**, 168–173 (2005)
83. S.R. Chinn, E.A. Swanson, J.G. Fujimoto, Optical coherence tomography using a frequency-tunable optical source. Opt. Lett. **22**, 340–342 (1997)
84. R. Huber, M. Wojtkowski, J.G. Fujimoto, Fourier Domain Mode Locking (FDML): a new laser operating regime and applications for optical coherence tomography. Opt. Express **14**, 3225–3237 (2006)
85. S.W. Lee, B.M. Kim, Line-field optical coherence tomography using frequency-sweeping source. IEEE J. Sel. Top. Quantum Electron **14**(1), 50–55 (2008)
86. M. Sarunic, M.A. Choma, C.I. Yang, J.A. Izatt, Instantaneous complex conjugate resolved spectral domain and swept-source OCT using 3x3 fiber couplers. Opt. Express **13**, 957–967 (2005)
87. R.K. Wang, In vivo full range complex Fourier domain optical coherence tomography. Appl. Phys. Lett. **90**, 054103 (2007)
88. Y. Yasuno, S. Makita, T. Endo, M. Itoh, Y. Yatagai, Simultaneous B-M-mode scanning method for real time Fourier domain optical coherence tomography. Appl. Opt. **45**, 1861–1865 (2006)
89. L. An, R.K. Wang, Use of a scanner to modulate spatial interferograms for in vivo full-range Fourier-domain optical coherence tomography. Opt. Lett. **32**, 3423–3425 (2007)
90. M.R. Hee, D. Huang, E.A. Swanson, J.G. Fujimoto, Polarization sensitive low-coherence reflectometer for birefringence characterization and ranging. J. Opt. Soc. Am. B. **9**,903–908 (1992)
91. E. Gotzinger, M. Pircher, C.K. Hitzenberger, High speed spectral domain polarization sensitive optical coherence tomography of the human retina. Opt. Express **13**, 10217–10229 (2005)
92. Y. Yasuno, S. Makita, Y. Sutoh, M. Itoh, T. Yatagai, Birefringence imaging of human skin by polarization-sensitive spectral interferometric optical coherence tomography. Opt. Lett. **27**, 1803–1805 (2002)
93. B.H. Park, M.C. Pierce, B. Cense, S.H. Yun, M. Mujat, G.J. Tearney, B.E. Bouma, J.F. de Boer, Real-time fiber-based multi-functional spectral-domain optical coherence tomography at 1.3 μm. Opt. Express **13**, 3931–3944 (2005)
94. S. Makita, Y. Yasuno, T. Endo, M. Itoh, T. Yatagai, Polarization contrast imaging of biological tissues by polarization-sensitive Fourier-domain optical coherence tomography. Appl. Opt. **45**, 1142–1147 (2006)
95. M. Yamanari, S. Makita, V.D. Madjarova, T. Yatagai, Y. Yasuno, Fiber-based polarization-sensitive Fourier domain optical coherence tomography using B-scan-oriented polarization modulation method. Opt. Express **14**, 6502–6515 (2006)
96. M. Yamanari, S. Makita, Y. Yasuno, Polarization-sensitive swept-source optical coherence tomography with continuous source polarization modulation. Opt. Express **16**, 5892–5906 (2008)
97. J.F. de Boer, S.M. Srinivas, A. Malekafzali, Z. Chen, J.S. Nelson, Imaging thermally damaged tissue by polarization sensitive optical coherence tomography. Opt. Express **3**, 212–218 (1998)
98. C.E. Saxer, J.F. de Boer, B. Hyle Park, Y. Zhao, Z. Chen, J.S. Nelson, High-speed fiber-based polarization-sensitive optical coherence tomography of in vivo human skin. Opt. Lett. **25**, 1355–1357 (2000)

99. S. Jiao, L.V. Wang, Two-dimensional depth-resolved Mueller matrix of biological tissue measured with double-beam polarization-sensitive optical coherence tomography. Opt. Lett. **27**, 101–103 (2002)
100. S. Jiao, Y. Gang, L.V. Wang, Depth-resolved two-dimensional Stokes vectors of backscattered light and Mueller matrices of biological tissue measured with optical coherence tomography. Appl. Opt. **39**, 6318–6324 (2000)
101. J.F. de Boer, T.E. Milner, M.J.C. van Gemert, J. Stuart Nelson, Two-dimensional birefringence imaging in biological tissue by polarization-sensitive optical coherence tomography. Opt. Lett. **22**, 934–936 (1997)
102. Bernhard Baumann, WooJhon Choi, Benjamin Potsaid, David Huang, Jay S. Duker, and James G. Fujimoto, "Swept source / Fourier domain polarization sensitive optical coherence tomography with a passive polarization delay unit," Opt. Express **20**, 10229–10241 (2012)
103. Z.P. Chen, T.E. Milner, D. Dave, J.S. Nelson, Optical Doppler tomographic imaging of fluid flow velocity in highly scattering media. Opt. Lett. **22**, 64–66 (1997)
104. Z.P. Chen, T.E. Milner, S. Srinivas, X.J. Wang, A. Malekafzali, M.J.C. van Gemert, J.S. Nelson, Noninvasive imaging of in vivo blood flow velocity using optical Doppler tomography. Opt. Lett. **22**, 1–3 (1997)
105. J.A. Izatt, M.D. Kulkarni, S. Yazdanfar, J.K. Barton, A.J. Welsh, In vivo color Doppler imaging of picoliter blood volumes using optical coherence tomography. Opt. Lett. **22**, 1439–1441 (1997)
106. S. Yazdanfar, M.D. Kulkarni, J.A. Izatt, High-resolution of in-vivo cardiac dynamics using color Doppler optical coherence tomography. Opt. Express **1**, 424–431 (1997)
107. M.D. Kulkarni, T.G. van Leeuwen, S. Yazdanfar, J.A. Izatt, Velocity-estimation accuracy and frame-rate limitations in color Doppler optical coherence tomography. Opt. Lett. **23**, 1057–1059 (1997)
108. Z. Ding, Y. Zhao, H. Ren, J. Nelson, Z. Chen, Real-time phase-resolved optical coherence tomography and optical Doppler tomography. Opt. Express **10**, 236–245 (2002)
109. B.R. White, M.C. Pierce, N. Nassif, B. Cense, B.H. Park, G.J. Tearney, B.E. Bouma, T.C. Chen, J.F. de Boer, In vivo dynamic human retinal blood flow imaging using ultra-high-speed spectral domain optical Doppler tomography. Opt. Express **11**, 3490–3497 (2003)
110. R.A. Leitgeb, L. Schmetterer, W. Drexler, A.F. Fercher, R.J. Zawadzki, T. Bajraszewski, Real-time assessment of retinal blood flow with ultrafast acquisition by color Doppler Fourier domain optical coherence tomography. Opt. Express **11**, 3116–3121 (2003)
111. R.A. Leitgeb, L. Schmetterer, C.K. Hitzenberger, A.F. Fercher, F. Berisha, M. Wojtkowski, T. Bajraszewski, Real-time measurement of in vitro flow by Fourier-domain color Doppler optical coherence tomography. Opt. Lett. **29**, 171–173 (2004)
112. Z. Chen, Y. Zhao, S.M. Srinivas, J.S. Nelson, N. Prakash, R.D. Frostig, Optical Doppler tomography. IEEE J. Sel. Top. Quantum Electron. **5**, 1134–1141 (1999)
113. S. Makita, Y. Hong, M. Yamanari, T. Yatagai, Y. Yasuno, Optical coherence angiography. Opt. Express**14**, 7821–7840 (2006)
114. M.A. Choma, A.K. Ellerbee, S. Yazdanfar, J.A. Izatt, Doppler flow imaging of cytoplasmic streaming using spectral domain phase microscopy. J. Biomed. Opt. **11**, 024014 (2006)
115. A. Mariampillai, B.A. Standish, N.R. Munce, C. Randall, G. Liu, J.Y. Jiang, A.E. Cable, I.A. Vitkin, V.X.D. Yang, Doppler optical cardiogram gated 2D color flow imaging at 1000 fps and 4D in vivo visualization of embryonic heart at 45 fps on a swept source OCT system. Opt. Express **15**, 1627–1638 (2007)
116. H. Wehbe, M. Ruggeri, S. Jiao, G. Gregori, C.A. Puliafito, W. Zhao, Automatic retinal blood flow calculation using spectral domain optical coherence tomography. Opt. Express **15**, 15193–15206 (2007)

117. Y. Zhao, Z. Chen, C. Saxer, S. Xiang, J.F. de Boer, J.S. Nelson, Phase-resolved optical coherence tomography and optical Doppler tomography for imaging blood flow in human skin with fast scanning speed and high velocity sensitivity. Opt. Lett. **25**, 114–116 (2000)
118. R.K. Wang, High resolution visualisation of fluid dynamics with Doppler Optical Coherence Tomography. Measure. Sci. Technol. **15**, 725–733 (2004)
119. R.K. Wang, S.L. Jacques, Z. Ma, S. Hurst, S. Hanson, A. Gruber, Three dimensional optical angiography. Opt. Express **15**, 4083–4097 (2007)
120. R.K. Wang, S. Hurst, Mapping of cerebro-vascular blood perfusion in mice with skin and skull intact by Optical Micro-AngioGraphy at 1.3 μm wavelength. Opt. Express **15**(18), 11402–11412 (2007)
121. R.K. Wang, L. An, Doppler optical micro-angiography for volumetric imaging of vascular perfusion in vivo. Opt. Express **17**, 8926–8940 (2009)
122. L. An, H.M. Subhash, D.J. Wilson, R.K. Wang, High resolution wide-field imaging of retinal and choroidal blood perfusion with optical micro-angiography. J. Biomed. Opt. **15**(2), 026011-1-9, (2010)
123. R.K. Wang, L. An, S. Saunders, D. Wilson, Optical microangiography provides depth resolved images of directional ocular blood perfusion in posterior eye segment. J. Biomed. Opt. **15** (2010)
124. Y.L. Jia, R.K. Wang, Optical micro-angiography images structural and functional cerebral blood perfusion in mice with cranium left intact. J. Biophotonics. **22**, 57–63 (2010)
125. J.M. Schmitt, S.H. Xiang, K.M. Yung, Differential absorption imaging with optical coherence tomography. J. Opt. Soc. Am. A**15**, 2288–2296 (1998)
126. Y. Pan, D. Farkas, Non-invasive imaging of living human skin with dual-wavelength optical coherence tomography in two and three dimensions. J. Biomed. Opt. **03**, 446–455 (1998)
127. U. Morgner, W. Drexler, F.X. Kärtner, X.D. Li, C. Pitris, E.P. Ippen, J.G. Fujimoto, Spectroscopic optical coherence tomography. Opt. Lett.**25**, 111–113 (2000)
128. R. Leitgeb, M. Wojtkowski, A. Kowalczyk, C.K. Hitzenberger, M. Sticker, A.F. Fercher, Spectral measurement of absorption by spectroscopic frequency-domain optical coherence tomography. Opt. Lett.**25**, 820–822 (2000)
129. R. Leitgeb, M. Wojtkowski, C. Hitzenberger, A. Fercher, H. Sattmann, Spectroscopic analysis of substances by frequency domain Optical Coherence Tomography, in *Coherence Domain Optical Methods In Biomedical Science and Clinica Applications V*, 123–127 (2001)
130. J. Su, I.V. Tomov, Y. Jiang, Z. Chen, High-resolution frequency-domain second-harmonic optical coherence tomography. Appl. Opt. **46**, 1770–1775 (2007)
131. M.V. Sarunic, B.E. Applegate, J.A. Izatt, Spectral domain second-harmonic optical coherence tomography. Opt. Lett.**30**, 2391–2393 (2005)
132. J.A. Izatt, M.R. Hee, E.A. Swanson, C.P. Lin, D. Huang, J.S. Schuman, C.A. Puliafito, J.G. Fujimoto, Micrometer-scale resolution imaging of the anterior eye *in vivo* with optical coherence tomography. Arch. Ophthalmol. **112**, 1584–1589 (1994)
133. E.A. Swanson, J.A. Izatt, M.R. Hee, D. Huang, C.P. Lin, J.S. Schuman, C.A. Puliafito, J.G. Fujimoto, *In vivo* retinal imaging by optical coherence tomography. *Opt. Lett.***18**, 1864–1866 (1993)
134. H. Ozdemir, S.A. Karacorlu, M. Karacorlu, Early optical coherence tomography changes after photodynamic therapy in patients with age-related macular degeneration. Am. J. Ophthalmol. **141**, 574–576 (2006)
135. A. Salinas-Alaman, A. Garcia-Layana, M.J. Maldonado, C. Sainz-Gomez, A. Alvarez-Vidal, Using optical coherence tomography to monitor photodynamic therapy in age related macular degeneration. Am. J. Ophthalmol. **140**, 23–28 (2005)
136. W. Goebel, R. Franke, Retinal thickness in diabetic retinopathy – comparison of optical coherence tomography, the retinal thickness analyzer, and fundus photography. Retina, **26**, 49–57 (2006)
137. A. Polito, M. Del Borrello, G. Polini, F. Furlan, M. Isola, F. Bandello, Diurnal variation in clinically significant diabetic macular edema measured by the stratus OCT. Retina, **26**, 14–20 (2006)

138. A.J. Witkin, T.H. Ko, J.G. Fujimoto, J.S. Schuman, C.R. Baumal, A.H. Rogers, E. Reichel, J.S. Duker, Redefining lamellar holes and the vitreomacular interface: an ultrahigh-resolution optical coherence tomography study. Ophthalmology **113**, 388–397 (2006)
139. M.L. Subramanian, S.N. Truong, A.H. Rogers, J.S. Duker, E. Reichel, C.R. Baumal, Vitrectomy for stage 1 macular holes identified by optical coherence tomography. Ophthalmic Surg. Lasers **37**, 42–46 (2006)
140. C.L. Shields, M.A. Materin, J.A. Shields, Review of optical coherence tomography for intraocular tumors. Curr. Opin. Ophthalmol.**16**, 141–154 (2005)
141. B. Cense, T.C. Chen, B.H. Park, M.C. Pierce, J.F. de Boer, Thickness and birefringence of healthy retinal nerve fiber layer tissue measured with polarization sensitive optical coherence tomography. Invest. Ophthalmol. Visual Sci. **45**, 2606–2612 (2004)
142. G. Wollstein, J.S. Schuman, L.L. Price, A. Aydin, P.C. Stark, E. Hertzmark, E. Lai, H. Ishikawa, C. Mattox, J.G. Fujimoto, L.A. Paunescu, Optical coherence tomography longitudinal evaluation of retinal nerve fiber layer thickness in glaucoma. Arch. Ophthalmol. **123**, 464–470 (2005)
143. F.A. Medeiros, L.M. Zangwill, C. Bowd, R.M. Vessani, R. Susanna, R.N. Weinreb, Evaluation of retinal nerve fiber layer, optic nerve head, and macular thickness measurements for glaucoma detection using optical coherence tomography. Am. J. Ophthalmol. **139**, 44–55 (2005)
144. S.A. Boppart, M.E. Brezinski, J.G. Fujimoto, Optical coherence tomography imaging in developmental biology. Methods Mol. Biol. **135**, 217–33 (1999)
145. N. Burris, K. Schwartz, C. Tang, M. Jafri, J. Schmitt, M. Kwon, O. Toshinaga, J. Gu, J. Brown, E. Brown, R. Pierson, R. Poston, Catheter-based infrared light scanner as a tool to assess conduit quality in coronary artery bypass surgery. J. Thorac. Cardiovasc. Surg. **133**(2), 419–27 (2007)
146. P. Testoni, A. Mariani, B. Mangiavillano, P. Arcidiacono, S. Pietro, E. Masci, Intraductal optical coherence tomography for investigating main pancreatic duct strictures. Am. J. Gastroenterol. **101**, 1–6 (2006)
147. G.J. Tearney, M.E. Brezinski, J.F. Southern, B.E. Bouma, S.A. Boppart, J.G. Fujimoto, Optical biopsy in human urologic tissue using optical coherence tomography. J. Urol. **157**, 1915–1919 (1997)
148. B.A. Boppart, M.E. Brezinski, C. Pitris, J.G. Fujimoto, Optical coherence tomography for neurosurgical imaging of human intracortical melanoma. Neurosurgery **43**(4), 834–841 (1998).
149. G.J. Tearney, M.E. Brezinski, B.E. Bouma, S.A. Boppart, S. Pitris, J.H. Southern, In vivo endoscopic optical biopsy with optical coherence tomography. Science **276**, 2037–2039 (1997)
150. S.A. Boppart, J.M. Herrmann, C. Pitris, D.L. Stamper, M.E. Brezinski, J.G. Fujimoto, Real-time optical coherence tomography for minimally-invasive imaging of prostate ablation. Invited Comput. Aid. Surg. **6**, 94–103 (2001)
151. C. Mason, J.F. Markusen, M.A. Town, P. Dunnill, R.K. Wang, The potential of optical coherence tomography in the engineering of living tissue. Phys. Med. Biol. **49**, 1097–1115 (2004)
152. S.A. Boppart, W. Luo, D.L. Marks, K.W. Singletary, Optical coherence tomography: feasibility for basic research and image-guided surgery of breast cancer. Breast Cancer Res. Treatment **84**, 85–97 (2004)
153. J.P. Dunkers, F.R. Phelan, C.G. Zimba, K.M. Flynn, D.P. Sanders, R.C. Peterson, R.S. Parnas, The prediction of permeability for an epoxy/E-glass composite using optical coherence tomographic images. Polym. Compos. **22**(6), 803 (2001)
154. M.D. Duncan, M. Bashkansky, J. Reintjes, Subsurface defect detection in materials using optical coherence tomography. Opt. Express**13**, 540–545 (1998)
155. Y. Shin, W. Jung, Z. Chen, J.S. Nelson, H. Kim, J. Park, Investigation of pit formation in multilayer optical storage disk using optical coherence tomography. Proc. SPIE **5604**, 38–43 (2004)

156. C. Xi, D.J. Marks, D.S. Parikh, L. Raskin, S.A. Boppart, Structural and functional imaging of three-dimensional microfluidic mixers using optical coherence tomography. Proc. Natl. Acad. Sci. **101**, 7516–7521 (2004)
157. B.E. Bouma, S. Yun, B.J. Vakoc, M.J. Suter, G.J. Tearney, Fourier-domain optical coherence tomography: recent advances toward clinical utility. Curr. Opin. Biotechnol. **20**(1), 111–118 (2009)
158. D. Choi, H. Hiro-Oka, H. Furukawa, R. Yoshimura, M. Nakanishi, K. Shimizu, K. Ohbayashi, Fourier domain optical coherence tomography using optical demultiplexers imaging at 60,000,000 lines/s. Opt. Lett.**33**, 1318–1320 (2008)
159. E. Hitt, New optical coherence tomography allows rapid three-dimensional volume rendering of the retina. Medscape Medical News [online]. Available from: http://www.medscape.com/viewarticle/474656. Accessed 9 Jan 2007.
160. W. Drexler, Ultrahigh resolution optical coherence tomography. J. Biomed. Opt. **9**, 47–74 (2004)
161. A. Dubois, K. Grieve, G. Moneron, R. Lecaque, L. Vabre, C. Boccara, Ultrahigh-resolution full-field optical coherence tomography. Appl. Opt. **43**, 2874–2883 (2004)
162. M. Akiba, N. Maeda, K. Yumikake, T. Soma, K. Nishida, Y. Tano, K.P. Chan, Ultrahigh-resolution imaging of human donor cornea using full-field optical coherence tomography. J. Biomed. Opt.**14**, 041202 (2007)
163. Y. Watanabe, Y. Takasugi, M. Sato, Quasi-single shot axial-lateral parallel time domain OCT. Opt. Express**15**, 5208–5217 (2008)
164. C. Dunsby, Y. Gu, P. French, Single-shot phase-stepped wide-field coherence gated imaging. Opt. Express**11**, 105–115 (2003)
165. T. Man, A.L. Oldenburg, S. Sitafalwalla, D.L. Marks, W. Luo, F.J. Toublan, K.S. Suslick, S.A. Boppart, Engineered microsphere contrast agents for optical coherence tomography. Opt. Lett. **28**, 1546–1548 (2003)
166. Y. He, R.K. Wang, Dynamic optical clearing effect of tissue impregnated with hyperosmotic agents and studied with optical coherence tomography. J. Biomed. Opt. **9**, 200–206 (2004)
167. D.C. Adler, S.-W. Huang, R. Huber, J.G. Fujimoto, Photothermal detection of gold nanoparticles using phase-sensitive optical coherence tomography. Opt. Express **16**, 4376–4393 (2008)

Chapter 6
Confocal Microscopy

Colin J. R. Sheppard and Shakil Rehman

Confocal microscopy is a technique for increasing the contrast of microscope images, particularly in thick specimens. It has several advantages over conventional optical microscopy, including controllable depth of field, better image quality and the ability to collect optical sections of thick specimens. In this chapter, we will first discuss the principle of confocal microscopy and then the design of confocal microscopes. We will also discuss confocal techniques and the imaging performance of the confocal microscope.

6.1 Basic Principle of Confocal Microscopy

The *confocal microscope* is a special type of scanning optical microscope, which usually uses laser illumination. In the scanning optical microscope, the laser light is focused to a small spot that is scanned relative to the sample (Fig. 6.1). The reflected, transmitted or fluorescent light is then detected and the signal stored to build up an image. Designs can be based on either an upright (Fig. 6.1a) or an inverted microscope (Fig. 6.1b). Inverted microscopes are useful for observing cell cultures through a Petri dish. Upright microscopes can be used with uncovered objects or using a sample with a cover slip. A confocal microscope is formed from

C.J.R. Sheppard
Division of BioEngineering, National University of Singapore, Singapore 117576, Singapore

Department of Biological Sciences, National University of Singapore, Singapore 117543, Singapore

S. Rehman (✉)
Department of BioEngineering, National University of Singapore, Singapore 117576, Singapore

Singapore-MIT Alliance for Research and Technology, 1 CREATE Way, #10-01 CREATE Tower, Singapore 138602
e-mail: shakil@nus.edu.sg

R. Liang (ed.), *Biomedical Optical Imaging Technologies*, Biological and Medical Physics, Biomedical Engineering, DOI 10.1007/978-3-642-28391-8_6,

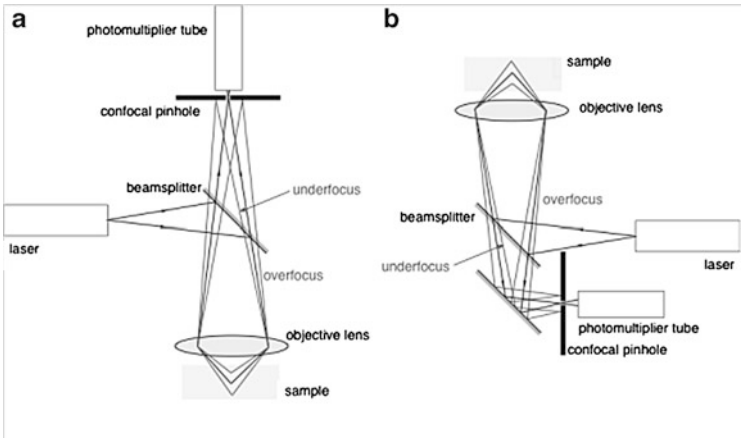

Fig. 6.1 Schematic diagram of a confocal microscope: (**a**) based on an upright microscope, (**b**) based on an inverted microscope

a scanning optical microscope by placing a pinhole in front of the detector, forming effectively a point detector. The major advantage of the confocal microscope is its optical sectioning, or depth discrimination, property. Light from different depths of the object is brought to a focus at different planes, and only the light from the in-focus region passes efficiently through the pinhole.

Figure 6.2 shows a confocal reflection microscope in which the sample is a mirror. If the mirror is in the focal plane of the system, the reflected light is brought to a focus on the pinhole, and a strong signal detected. When the mirror is moved away from focus, the light is no longer focused on to the pinhole and the detected signal drops. This optical sectioning property also occurs in confocal fluorescence microscopy. It can be used in two distinct ways. If the sample is in the form of a surface, it can be brought into the focal plane by maximizing the signal, and the surface profile hence measured.

Or if the specimen is in the form of a thick object, a series of optical sections at different focus positions can be recorded, resulting in a three-dimensional (3-D) image stack. When surface profiling, usually the intensity is sampled at only a series of discrete depth positions (Fig. 6.3). The brightest sample can be taken to give a rough estimate of the surface height, or the position of maximum intensity can be determined by curve fitting.

Figure 6.4a shows the measured surface height from a semiconductor device sample. As well as recording the axial position of the brightest intensity, the value of this intensity maximum can also be recorded to give an autofocused image where every point of the image is brought to its position of best focus Fig. 6.4b. This is sometimes called a maximum intensity projection. From the intensity and height information, an isometric view of the sample can be reconstructed in the computer (Fig. 6.4c).

Figure 6.5 shows the theoretical axial intensity recorded from a mirror for different numerical apertures (NAs) of dry objective lens. It is seen that the width

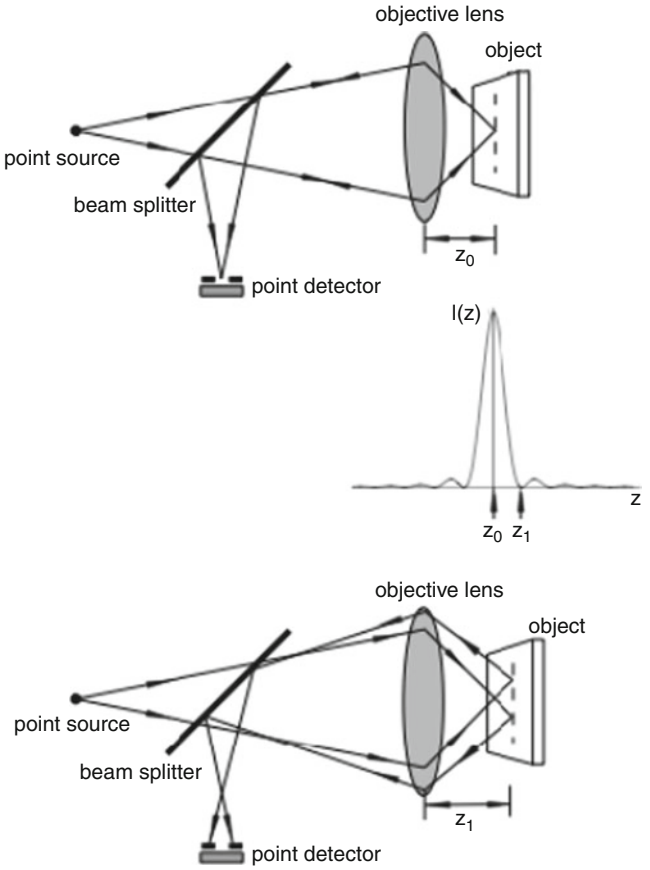

Fig. 6.2 A confocal reflection microscope in which the sample is a mirror

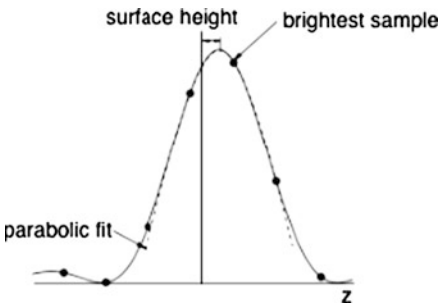

Fig. 6.3 When surface profiling, usually the intensity is sampled at only a series of discrete depth positions

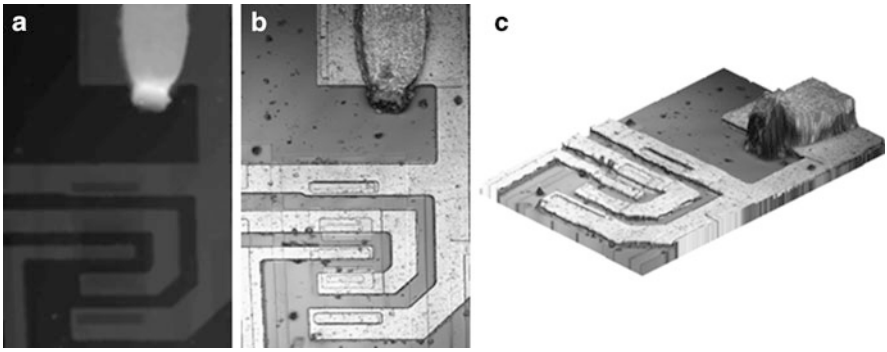

Fig. 6.4 Images of an integrated circuit sample: (**a**) the measured surface height, (**b**) an autofocused image where every point of the image is brought to its position of best focus, (**c**) an isometric view of the sample, reconstructed in the computer

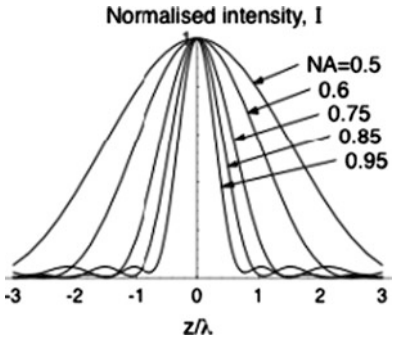

Fig. 6.5 The theoretical axial intensity recorded from a mirror for different numerical apertures (NAs) of dry objective lens

of the optical section decreases strongly as the NA is increased. This stresses that, in order to achieve good sectioning, the highest possible NA should be used, as long as system aberrations are negligible. Observation of the axial image from a mirror is in practice a useful approach to characterizing the imaging performance and aberrations of the confocal system. It is seen that the images in Fig. 6.5 are symmetrical about the focal plane: in the presence of aberrations, the axial response becomes broader with stronger side-lobes.

Figure 6.6 shows axial images of a thin film of SiO_2 on a silicon substrate, recorded using an NA of 0.8 and HeNe laser ($\lambda = 633\,\text{nm}$). Experimental results (Fig. 6.6a) and theoretical predictions (Fig. 6.6b) are shown. There are reflections from both the air/SiO_2 and SiO_2/Si interfaces. This is a dramatic demonstration of the optical sectioning property. Using some other techniques, such as digital holographic microscopy, only the optical thickness of the sample can be measured, so that the different interfaces cannot be observed. Also shown is the experimental image from a confocal interference microscope, recorded using a balanced

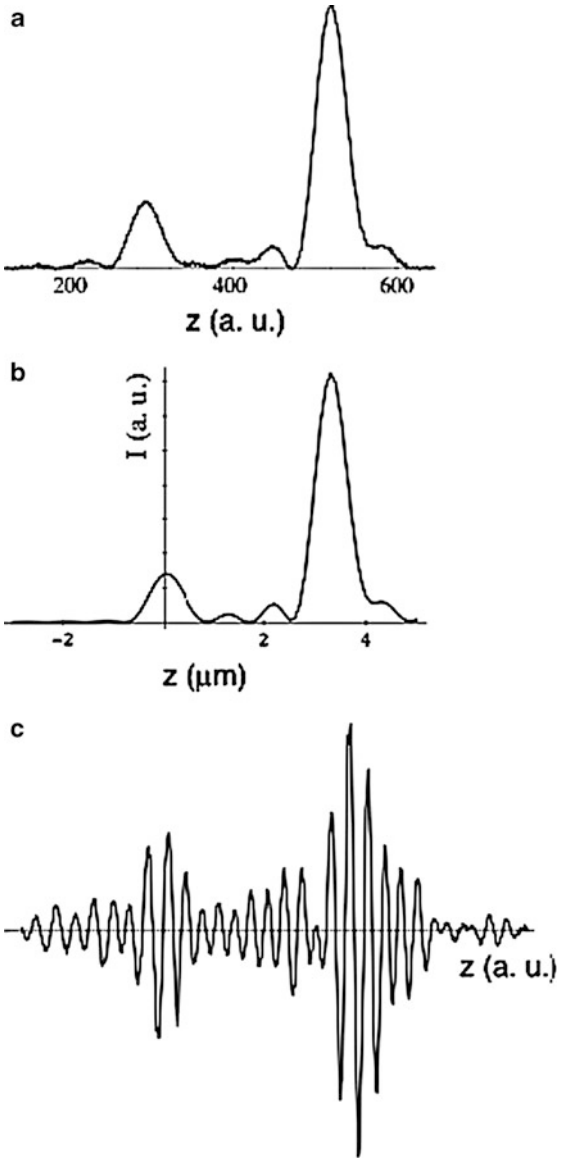

Fig. 6.6 Axial images of a thin film of SiO_2 on a silicon substrate, recorded using an NA of 0.8 and HeNe laser ($\lambda = 633$ nm): (**a**) experimental result, (**b**) theoretical prediction, (**c**) experimental confocal interference image

homodyne system, where fringe information can be used as a measure of image phase (Fig. 6.6c).

The confocal microscope also has some other advantages. The pinhole, as well as rejecting out-of-focus information, also rejects stray light, so that images have a high signal-to-noise ratio. The rejection of stray light also gets rid of scattered light, thus allowing penetration into a scattering medium such as biological tissue. In addition,

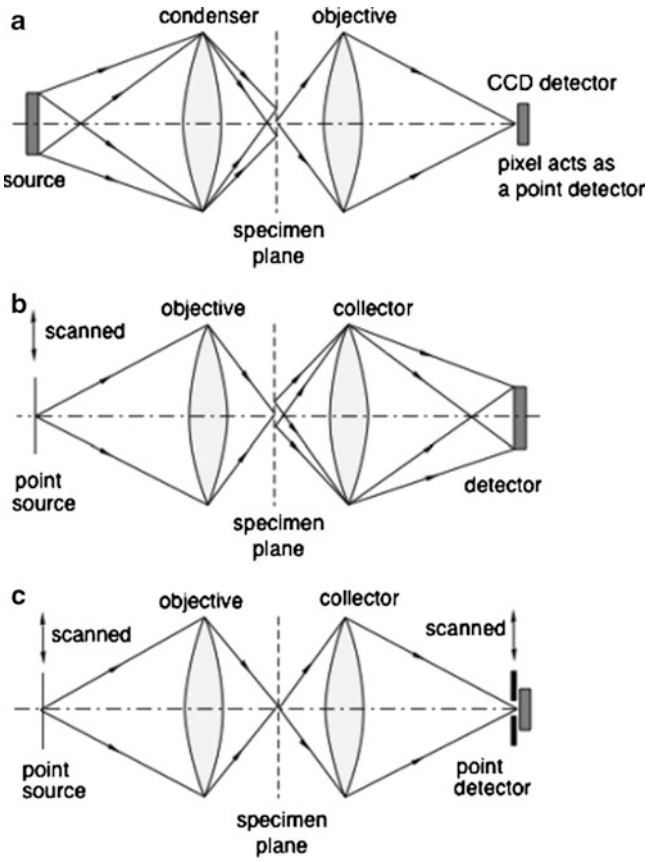

Fig. 6.7 The confocal microscope is compared with other forms of microscope: (**a**) a conventional brightfield microscope with a CCD detector, (**b**) a scanning optical microscope, (**c**) a confocal scanning optical microscope

there is also a small improvement in spatial resolution in confocal microscopy: we return to this point later.

The confocal microscope is compared with other forms of microscope in Fig. 6.7. A conventional brightfield microscope with a CCD detector is illustrated schematically in Fig. 6.7a. This simplified diagram shows a microscope with critical illumination: a large-area incoherent source is focused by a condenser lens on to the specimen such that the entire field of the specimen is illuminated. Information from each illuminated point in the specimen is simultaneously transmitted by the objective lens to form an image, which is measured point by point by the pixels of the detector. The important property to note is that it is the objective that is responsible for forming the image, with the condenser playing only a secondary role in determining the resolution of the system. In fact, the aperture of the condenser

acts to control the spatial coherence of the overall imaging process, which can vary between fully coherent (in which case field amplitudes add) and fully incoherent (when intensities add). The aberrations of the condenser are not important, so that the source and condenser together behave simply as a partially coherent effective source. For this reason, in the widely used Köhler illumination, in which the specimen plane is made conjugate with the field diaphragm rather than the light source, imaging is in principle identical to critical illumination. If the numerical aperture of the condenser is made small compared with that of the objective, imaging becomes coherent. Coherent imaging exhibits fringing on edges in the image, and phase information in the object (which results from optical thickness variations) can be imaged as intensity changes if the system is defocused. Incoherent imaging, on the other hand, is obtained if the numerical aperture of the condenser is made large compared with that of the objective, and although performance depends on the form of the specimen, generally incoherent imaging results in superior resolution. It should be noted that in practice it is impossible to obtain truly incoherent brightfield imaging when using a high-aperture objective and that in practice the condenser aperture diaphragm is adjusted to give a compromise between resolution and contrast in the image, resulting in partially coherent imaging. For the particular case, commonly adopted in practice, where the numerical apertures of condenser and objective are equal (so-called matched or full illumination), imaging, although partially coherent, has similarities to incoherent imaging.

In Fig. 6.7b, a scanning optical microscope is illustrated. A single point in the specimen is illuminated by the focused and demagnified point source, whilst a large-area detector, in conjunction with a collector lens, collects light from the full field of view of the specimen. It will be observed that the ray paths shown in Fig. 6.7a and b are identical but reversed, and, because of the optical principles of reciprocity and equivalence, the microscopes illustrated in Fig. 6.7a and b have identical imaging properties. In the scanning optical microscope, Fig. 6.7b, the resolution of the system is primarily limited by the properties of the first lens, called the objective or projector lens. The second lens, the collector, controls only the degree of spatial coherence in the imaging process, and its aberrations are unimportant. Because this optical arrangement is analogous to critical illumination, it is called critical detection. An alternative arrangement, in which the detector is placed in the back focal plane of the imaging lens, can be termed Köhler detection: it behaves identically in principle but has the advantage that sensitivity variations in the detector are not so important. Indeed, as the collector and detector together act as an effective detector, the collector may in principle be dispensed with altogether and the detector placed in that plane. Finally, in Fig. 6.7c, we combine the arrangements of Fig. 6.7a and b to give a confocal scanning optical microscope, in which a point source illuminates just a small region of the object, and a confocal point detector detects light from this illuminated region. If the point source and detector are scanned in unison, a two-dimensional image is generated. However, this system behaves very differently from the previous ones. In fact, it does not seem possible to devise a non-scanning system that behaves in the same

manner: we cannot generate a confocal image by placing a detector at any plane of a non-scanning system. From the symmetry of Fig. 6.7c, it is clear that the two lenses play an equal part in the imaging process. We might expect that this would result in an improvement in resolution, which is indeed the case. In fact, the confocal system behaves as a coherent imaging system but with a sharper effective point spread function than in a conventional coherent microscope. Although Fig. 6.7 is drawn for a transmission geometry, in practice most confocal systems operate in the reflection or epi-illumination mode, in which the same objective lens is used both for illumination and detection. For a specimen placed in the focal plane, the properties of confocal transmission and reflection systems are identical. However, once the object is moved from the focal plane, the defocus properties behave quite differently. Figure 6.7 could also equally well apply to fluorescence imaging. However, in this case, because of the incoherent nature of fluorescence emissions after excitation by coherent light, imaging is always incoherent. The Stokes shift, the increase in wavelength of emitted light relative to the excitation, means that now the scanning system of Fig. 6.7b gives better resolution than the conventional system of Fig. 6.7a. The confocal system in principle gives superior resolution to either of the other systems.

6.2 History of Confocal Microscopy

The confocal microscope arrangement is usually attributed to Minsky, who filed a patent for the confocal microscope in 1957 [1]. However, in fact, the confocal principle was described previously by others. In 1940, Goldman described a system using line illumination and a confocal slit, rather than a pinhole, and presented x–z cross-section images of human eyes [2]. Koana in 1943 and Naora in 1951 described a confocal method for reducing the strength of stray light in a photometry system [3, 4]. Laser illumination was incorporated into the confocal microscope by Davidovits and Egger in 1969 [5]. In 1972, Slomba et al. described a confocal fluorescence microscope that incorporated beam scanning [6]. The first commercial confocal microscope was launched by Oxford Optoelectronics Ltd. in 1982. This design was adopted by LaserSharp, which was subsequently taken over by BioRad.

The confocal microscope generates an image by illuminating the object point by point with a spot of light. Petran described in 1968 a system that he termed the tandem scanning microscope, in which the specimen is illuminated simultaneously by many spots of light using an array of pinholes on a rotating disk (a Nipkow disk) [7]. This arrangement allows for fast scanning and also for a confocal image to be viewed in real time through an eyepiece. A problem with the Petran system is that the Nipkow disk transmits only a small fraction of the light from the source. Recently, this disadvantage has been overcome by focusing the light on to the disk with a microlens array as in the Yokogawa system [8].

6.3 Design of Confocal Microscopes

6.3.1 Overall Layout

Confocal microscopes usually use laser illumination, from either gas lasers or semiconductor lasers. Light from the laser reflects from a beam splitter, and collected light from the sample is transmitted through the beam splitter to the detector (Fig. 6.1). For fluorescence microscopy, a dichroic mirror (chromatic beam splitter) is used to increase the efficiency of illumination and collection. An excitation filter is used to select the illumination wavelength, and a long-pass filter used to eliminate the excitation light from the detection system. Acousto-optic tunable filters (AOTFs) are now frequently used to control the intensity and wavelength of the illumination.

The radiation from the laser is expanded, using a beam-expander telescope configuration, in order to fill completely the back focal plane of the condenser or epi-illumination lens objective (Fig. 6.8). This is necessary in order to achieve optimum resolution. Usually a spatial filter pinhole (illuminating aperture) P1 is incorporated in the beam expander in order to produce a uniform illumination beam. The pinhole size should be chosen to remove the fine structure on the beam without truncating the Gaussian laser beam profile significantly. For this reason, the optimum size for the illuminating aperture is somewhat larger than that needed for the confocal aperture P2 to achieve true confocal operation. Many microscopes use a single-mode optical fibre to couple the light from the laser to the optical system, thus avoiding vibration problems emanating from the laser cooling fan, if any. A single-mode optical fibre can also be used instead of a mechanical pinhole to give the confocal effect [9, 10], as in the Optiscan microscope [11].

6.3.2 Scanning

Scanning is the vital part of a confocal/multiphoton microscope. Scanning can be achieved by scanning the stage, the beam or the objective lens. Scanning the stage has the advantage that the optical system is spatially invariant, and the optical properties can be optimized and characterized. Stage scanning can be achieved using electromechanical scanning using vibrators, stepper motors or piezoelectric scanners. Inertia limits line scanning speed to around 100 Hz. Beam scanning can be faster and avoids problems associated with moving the sample, such as difficulty in using probes or micropipettes.

The type of scanners used in a laser scanning microscope determines the image acquisition speed, field of view, beam quality, aberrations, dispersion and laser power throughput of the system. Various methods used for laser beam scanning are available depending on the speed, efficiency and price. Some of the commonly used laser beam scanning methods are galvanometric and resonant scanning, acousto-optic scanning, polygonal mirror scanning, multifocal systems, MEMS-

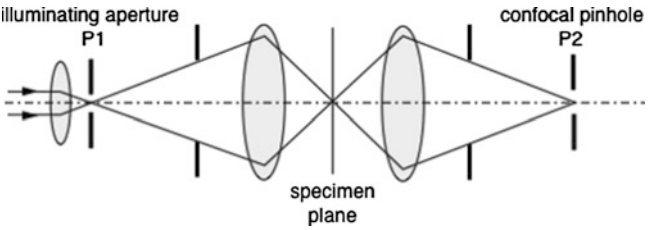

Fig. 6.8 Pinholes in the confocal microscope. P1 is a pinhole spatial filter, P2 is the confocal pinhole

based mirrors and other scanning systems. Here a brief description of these laser beam scanners is provided.

Galvanometric scanning is the most widely used scanning technology in microscopy. This is due to its flexibility and price range. The principle of operation of a galvanometer is identical to that of a motor in which the magnetic field produced by an arrangement of permanent magnets is increased or decreased by the field from a variable current electromagnet. The change in the field makes a magnet or an iron to rotate. For slow scanning rates of a few frames per second, galvanometer scanning is sufficient that has rms frequency of about 2 kHz. The scanners consist of a mirror attached to a shaft that can rotate through a given angular range. Such scanners are bandwidth limited, and therefore, it is not possible to exactly track an arbitrarily specified position within the scan range [12]. With beam scanning, the light from the sample must be descanned so that it does not move relative to the pinhole. This is usually achieved by reflecting a second time from the galvo-mirror.

For video rate imaging, faster scanning of mirrors is required that can be achieved by resonant scanners [13]. The main difference of a resonant scanner to a galvanometer scanner is that the only moving part in the resonant scanner is a single-turn coil, which reduces the damping in the scanning system and allows it to be able to vibrate at very high frequencies, close to its mechanical resonance. Since these scanners are designed to work close to resonant frequency, their angular displacement can be very large. There are 10-kHz resonant scanners capable of 60 ° scan angles. Resonant scanners also cannot provide random access of points within their scanning range. They are able to produce a sinusoidal scanning pattern at frequencies as high as 12 kHz. In such scanners, in order to take advantage of the full sinusoidal scan, data must be acquired in both the forward and backward directions.

In a polygonal scanning mirror system, very high frame rates can be obtained [14, 15]. In this scheme, the geometrical centre of a multifaceted polygonal mirror is attached to a fast rotating shaft. As the motor rotates, the facets of the mirror will scan the laser beam in a linear pattern. For slow scanning polygonal mirrors, ball bearings are used in order to keep the price reasonable. At high rotation speeds or larger mirrors, some problems might arise with precision bearings, such as lubrication and vibration. Polygon mirrors can be noisy and produce air currents.

Acousto-optic scanning devices are based on the principle that when an acoustic wave travels in an optical medium, it induces a periodic modulation in the index of refraction of the material creating a diffraction grating which is responsible for the deflection of the light beam [16]. There are two types of acousto-optic (AO) devices used for beam deflection: AO deflectors and AO modulators. Both of these devices are very similar and based on the same working principle. An AO deflector depends on the variation of the acoustic frequency in order to change the angle of deflection and hence scanning the optical beam. AO modulators are used to change the amplitude or frequency of the diffracted beam. An advantage over mechanical scanners is the possibility of direct random access to different points within the sample. If specific points of interest are identified within the sample, it is possible to use AO devices to address them individually and sequentially at high speeds. The frame rates possible with such devices can be very high up to 25 kHz. The major disadvantage of using AO devices is that they are made of highly dispersive materials; hence, propagation of ultrashort femtosecond pulses through such media causes them to disperse and change the pulse shape and duration. This results in low efficiency of the nonlinearly generated signal [17].

Faster scanning devices have a physical limit on their speed to achieve higher image acquisition rates in multiphoton microscopy. An alternative may be to parallelize the image acquisition process by using more than one focal volume at a time, thereby reducing the data acquisition time. One of the first schemes proposed to use the excitation laser more effectively in multiphoton microscopy involved using a line focus instead of point excitation [18]. The line focus is created with cylindrical optics and is scanned in a perpendicular direction relative to the line with a galvanometric scanner in order to form a 2-D image. Since only one scanner is involved in this approach, extremely high frame rates are in principle possible, but the drawback is the loss of optical section property of nonlinear excitation in the direction of long axis of the beam. A different approach to parallelize the image acquisition in nonlinear microscopy is to generate an array of focal points. A combination of lenslet array illumination and delay of a few picoseconds between individual foci can avoid the interference effects and achieve higher frame rates. A multifocal multiphoton microscope (MMM) can use the laser power efficiently and reduce the image acquisition time from 1 s to 10–50 ms [19, 20].

The basic geometry for beam scanning is shown in Fig. 6.9. The basic idea is to image the laser beam into the back aperture of the microscope objective with the help of a telecentric lens system. This ensures that the angular displacement of the scanners is translated into a tilt of the beam in the back aperture without any beam displacement. This results in a two-dimensional scan in the focal plane of the objective, as the scanners move. Usually nowadays, an infinity tube-length objective lens is used together with a tube lens. As shown, the aperture stop, which limits the numerical aperture of the system, is situated in the back focal plane of the tube lens and front focal plane of the objective. In order to fill completely the objective pupil whilst avoiding shading and vignetting problems, the scan mirror must be placed in the front focal plane of the scan lens. The light from the sample returns through the optical system and is descanned by the scan mirror. For two-

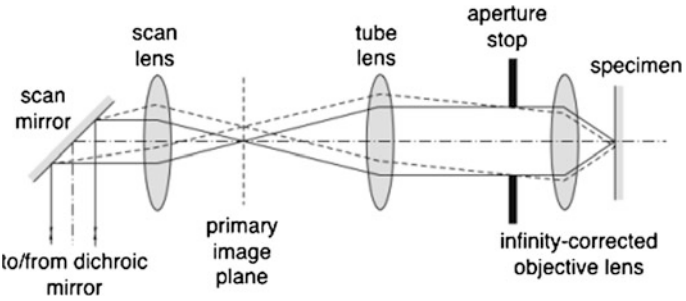

Fig. 6.9 The basic geometry for beam scanning. The aperture stop is situated in the back focal plane of the tube lens and front focal plane of the objective. The scan mirror is placed in the front focal plane of the scan lens. The light from the sample returns through the optical system and is descanned by the scan mirror

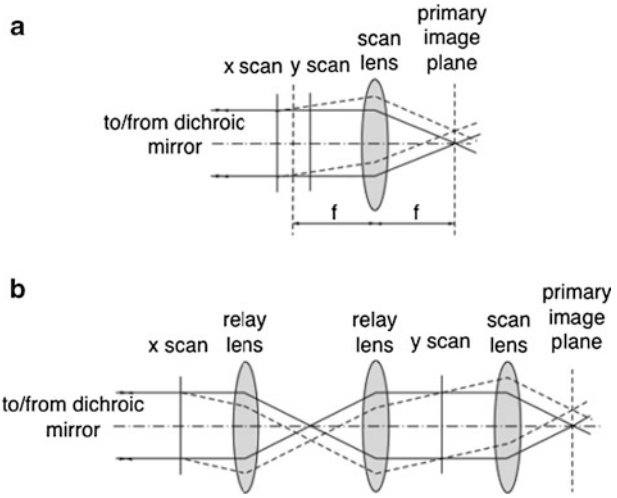

Fig. 6.10 For two-dimensional x–y scanning, the scan mirrors can be (**a**) close-coupled or (**b**) arranged using a telecentric relay system

dimensional x–y scanning, a single mirror is sometimes used, but if separate mirrors are used, they must be either close-coupled (Fig. 6.10a) or arranged using a telecentric relay system (Fig. 6.10b). In practice, the close-coupled arrangement usually works adequately and avoids the extra complication and light loss of the relay lens system.

Scan speed can be increased by using acousto-optic scanners, but as they are diffractive devices, they suffer problems when used in fluorescence imaging, as the wavelength of the fluorescent light is longer than that of the excitation, so they cannot be used to descan fluorescence signals because of the Stokes shift. Various other beam-scanning designs have been employed to improve scan speed. In Fig. 6.11a, a scanning spot is deflected over the specimen, using a TV-rate acousto-

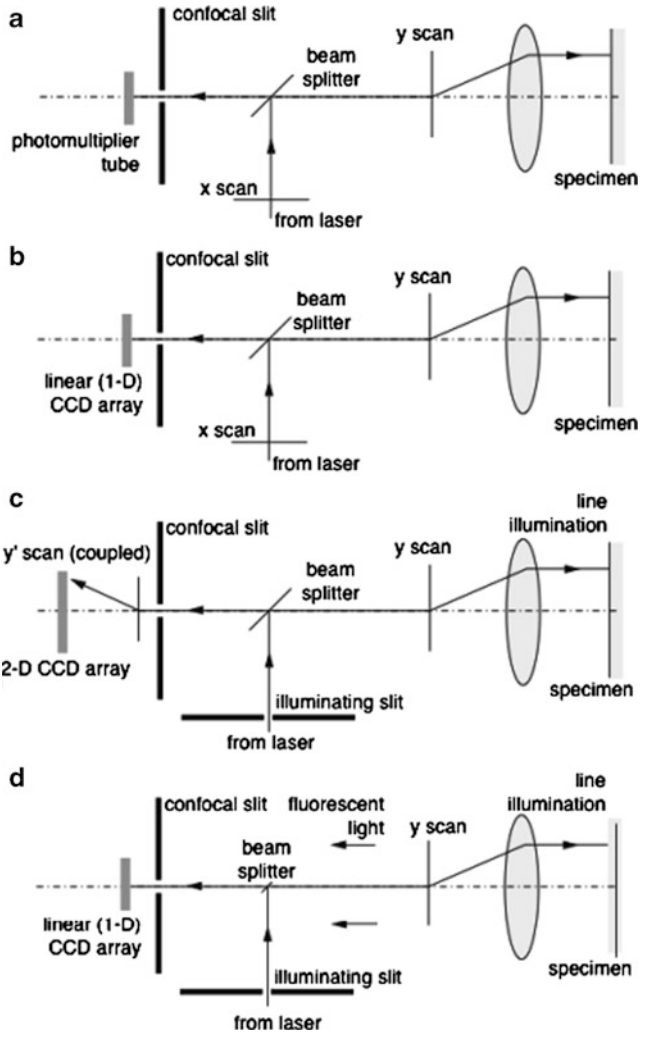

Fig. 6.11 Various beam-scanning designs to improve scan speed: (**a**) a TV-rate acousto-optic x scan and a galvo y scan, and the partially descanned spot is imaged on to a photomultiplier tube behind a confocal slit, (**b**) a TV-rate acousto-optic x scan and a galvo $y$scan, and the partially descanned spot is imaged on to a linear CCD detector, (**c**) line illumination is combined with a slit, and the confocal image written on to a CCD detector (or directly observed by eye) by a coupled $y\prime$ scan, (**d**) line illumination is combined with a confocal slit, but the normal beam splitter is replaced by a narrow strip mirror that reflects the illuminating light but allows the fluorescent light from the sample to be detected

optic x scan and a galvo $y$scan, and the partially descanned spot, still scanning along the x axis, is imaged on to a photomultiplier tube behind a confocal slit (as in the Noran Odyssey). Thus, in fluorescence imaging, the detected fluorescent light does not need to be descanned by the acousto-optic deflector. The arrangement shown

in Fig. 6.11b uses a linear CCD detector (as in the Lasertec microscope) and is useful for metrological work as geometrical distortion is absent, and calibration is determined by the dimensions of the CCD. In Fig. 6.11c, line illumination is combined with a slit (as in the former meridian system), and the confocal image written on to a CCD detector (or directly observed by eye) by a coupled y' scan [21]. The major advantage of this arrangement is that a complete line of information can be recorded simultaneously, thus greatly increasing the optical throughput of the system. Axial resolution and optical sectioning are somewhat degraded by the slit geometry, especially for very thick samples, but this is overweighed by the ability to image in the fluorescence mode at TV rates. In Fig. 6.11d, line illumination is again combined with a confocal slit, but this time the normal beam splitter is replaced by a narrow strip mirror (Achrogate, by Zeiss) that reflects the illuminating light but allows the fluorescent light from the sample to be detected [22].

6.4 Confocal Techniques

6.4.1 Basic Modes

Confocal microscopy is usually performed either in an epi-fluorescence mode or a brightfield reflection mode. Reflection microscopy can be used for imaging surface and multilayer structures, but when imaging thick biological specimens, coherent noise can result in speckle artefacts. These coherent artefacts are avoided in fluorescence microscopy. In addition to fluorescence and reflection imaging, the confocal technique can be combined with any imaging mode of conventional microscopy, including dark-field [23], polarization, Nomarski DIC [24] and interference microscopy [25]. In confocal transmission, a problem is encountered that the light spot can move relative to the confocal pinhole as a result of the refractive effects of a thick sample. This problem can be overcome using adaptive optics techniques, but confocal transmission microscopy does not allow for 3-D imaging in the same way as reflection microscopy, and the benefits of doing it are not clear.

6.4.2 Spectroscopic and Nonlinear Methods

In principle, any form of spectroscopy can be combined with scanning to form an image [26]. These include absorption spectroscopy, Raman spectroscopy, resonant Raman spectroscopy, CARS, two-photon absorption spectroscopy, two-photon fluorescence spectroscopy, photoelectron spectroscopy and photo-acoustic spectroscopy. In addition, various other nonlinear methods such as harmonic generation and parametric conversion can be used as contrast mechanisms.

6.4.3 Differential Phase Contrast

The non-confocal differential phase contrast (DPC) imaging mode is achieved by using a detector split into two halves, in place of the PMT, the DPC image being generated by displaying the difference between the signals recorded from these semicircular detectors [27]. This can be performed in either scanned-beam or scanned-stage systems. Transmission-mode DPC has been used to see single-molecular thickness variations in the sample [28]. DPC has been offered commercially by LaserSharp and Olympus. The DPC image is effectively an image of the phase gradient, modulated by the reflectivity or transmission of the object. A quadrant detector can give the phase gradient in both x and $y$directions. Further electronic processing of the DPC image and a conventional one, generated by adding the signals from the two detector halves, can be used to extract the phase gradient alone and then by integration a pure phase image produced.

6.4.4 Optical Beam-Induced Current (OBIC)

In the optical beam-induced current (OBIC) technique, the focused laser spot is used to generate electrical carriers in the specimen and the resultant current monitored. In this way, the electrical properties of the sample can be imaged. It has been used with semiconductor materials and devices, but there is the potential for other applications.

6.5 Imaging Performance of the Confocal Microscope

6.5.1 Resolution

For an ideally small confocal pinhole, the image intensity for a point object in a reflection system (or a fluorescence system neglecting the Stokes shift) is given by the square of that in a conventional system, as shown by the solid curve in Fig. 6.12. The image intensity exhibits a sharpening of the central peak of the Airy disk, narrower by a factor of about 1.4, accompanied by very weak outer rings. The curves are plotted against a normalized coordinate v, related to the true transverse displacement r by $v = krn \sin\alpha$, where n is the refractive index of the immersion fluid, α is the angular semi-aperture of the objective and $k = 2\pi/\lambda$.

The axial image of a point object is also sharpened up by a true confocal system, as shown in Fig. 6.13. Here the curves are plotted against the normalized axial coordinate $u = 4knz\sin^2(\alpha/2)$, where $z$is the true axial distance. Also shown is the axial image of a planar object, either in reflection (a) or in fluorescence (b). The image of a plane in reflection is very sharp, as a result of coherent phase effects.

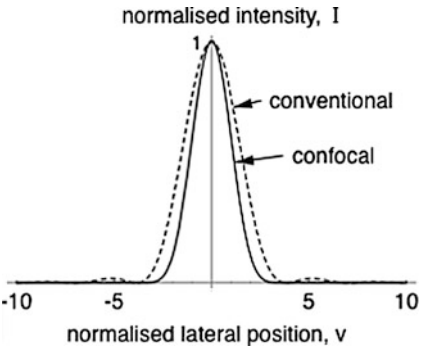

Fig. 6.12 Image intensity for a point object in a conventional microscope (*dashed line*) and in a confocal microscope with an ideally small confocal pinhole (*solid line*). The Stokes shift is neglected for a fluorescence system

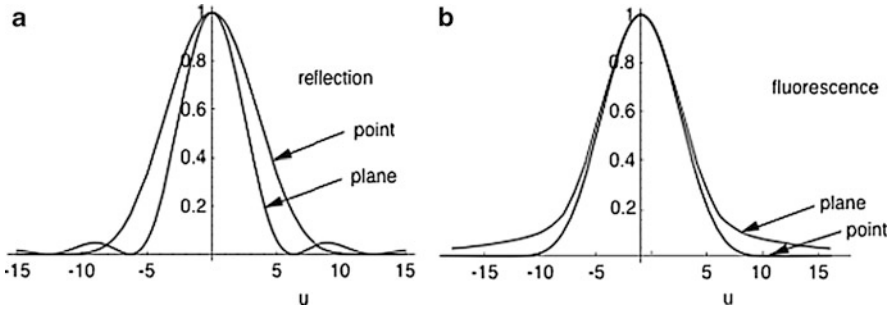

Fig. 6.13 The axial image of point and planar objects: (**a**) in reflection (**b**) in fluorescence

In practice, the confocal pinhole must have some nonzero size in order to detect enough light. The effect of changing the pinhole size, measured in normalized coordinates, is shown in Fig. 6.14. Note that what is important is the size of the pinhole compared with the spot formed on the pinhole plane, characterized in Fig. 6.14 by the first zero of the Airy disk, sometimes called 1 Airy unit. The true size of the pinhole depends on the focal length of the lens used to focus the light on to the pinhole, which may vary over a wide range for particular systems. In particular, BioRad systems used a very long focal length lens, thus giving large pinhole sizes. As the pinhole size is increased, the signal recorded from a point object increases. With a slit, rather than a pinhole, the signal increases more quickly with the cross section of the aperture. From the point of view of signal level, there is no reason to increase the size of the pinhole beyond about $v_d \approx 4$, but it is seen from Fig. 6.14 that by that size the improvement in transverse resolution (for a point object) of confocal microscopy has disappeared. Also shown in Fig. 6.14 is the axial resolution (defined so that a bigger number means higher resolution) for a planar object, either in reflection of fluorescence. The resolution for a fluorescence system with a slit is also shown. Note that although the signal is higher with a slit than a

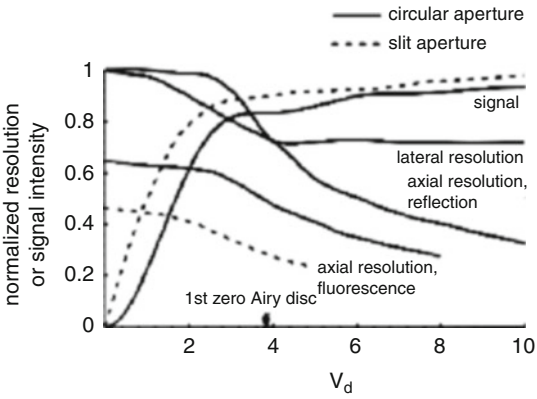

Fig. 6.14 The effect of changing confocal aperture half width, measured in normalized coordinates, on signal strength, axial resolution (for a planar object) and transverse resolution (for a point object) for circular or slit apertures

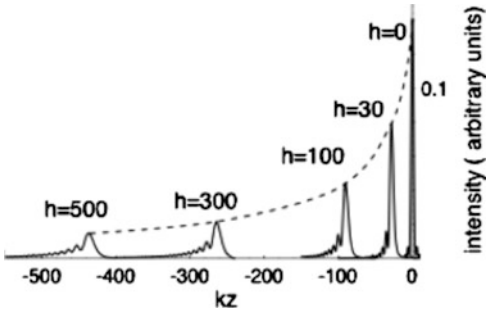

Fig. 6.15 The axial response in reflection obtained when an oil-immersion objective is used to focus a normalized distance $h = k n_s d$ inside an aqueous specimen, refractive index n_s. The value $h = 500$ corresponds to an imaging depth of 30 μm into water

pinhole, the axial resolution is worse, so there does not seem a case for using a slit from the point of view of signal level. However, it should be remembered that a line illumination system with a 1-D detector gives a multiplexed signal that images a complete line of the sample at once, thus greatly increasing detection efficiency for fast scanning, when performance is limited by saturation of the fluorophore.

6.5.2 Oil and Water Immersion

Axial imaging properties are strongly degraded by the presence of spherical aberration, which can be introduced when focusing with an oil-immersion objective into a thick object of refractive index lower than that of the oil. For example, the axial response in reflection obtained when an oil-immersion objective is used to focus a normalized distance $h = kn_S d$ inside an aqueous specimen, refractive index n_s, is illustrated in Fig. 6.15. The value $h = 500$ corresponds to an imaging depth of 30 μm into water. The response becomes broad and asymmetric, with pronounced side-lobes, and the intensity decreases substantially. For this reason, for live cell imaging, water immersion objectives are preferable, and most manufacturers now offer these. The width of the axial response (full width at half-maximum intensity)

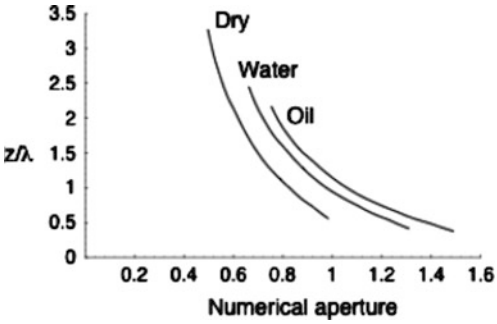

Fig. 6.16 The width of the axial response (full width at half-maximum intensity), for dry, water and oil immersion objectives

is shown in Fig. 6.16, for dry, water and oil immersion objectives. For a given numerical aperture, the dry objective results in the best resolution, as then the angular aperture is greatest.

6.6 Conclusions

A confocal microscope is often built around a commercial conventional microscope by adding a scan head with facility to scan the beam, a laser source, a detector and appropriate filters. Alternatively, the system can be constructed from optical components and laid out on an optical table. Close-coupled galvo mirrors with position feedback control are usually adequate. For fast scanning, some method of multiplexing (by illuminating with arrays of points or a line) is desirable to avoid saturation of fluorophores, but some degradation of imaging performance cannot be avoided. The confocal pinhole should be kept at a small size to optimize signal-to-noise ratio. A water immersion objective of high numerical aperture is usually the best option for biological applications.

References

1. M. Minsky, Microscopy apparatus. 3,013,467 Filed 7 Nov 1957 - Issued 19 Dec 1961
2. H. Goldman, Spaltlampenphotographie und –photometrie. Ophthalmologica **98**, 257–270 (1940)
3. Z. Koana, J. Illum. Eng. Instit. **371**, 26 (1943)
4. H. Naora, Microspectrophotometry and cytochemical analysis of nucleic acids. Science **114**, 279–280 (1951)
5. M.D. Davidovits, M.D. Egger, Scanning laser microscope. Nature **223**, 831 (1969)
6. A.F. Slomba, D.F. Wasserman, G.I. Gaufman, J.F. Nester, A laser flying spot scanner for use in automatised fluorescence antibody instrumentation. J. Assoc. Adv. Med. Instrum. **6**, 230–234 (1972)
7. M. Petrán, M. Hadravsky, M.D. Egger, R. Galambos, Tandem scanning reflected light microscope. J. Opt. Soc. Am. **58**, 661–664 (1968)

8. T. Tanaami, S. Otsuki, N. Tomosada, Y. Kosugi, M. Shimizu, H. Ishida, High-speed 1-frame/ms scanning confocal microscope with a microlens and Nipkow disks. Appl. Opt. **41**, 4704–4708 (2002)
9. L. Giniunas, R. Juskaitis, S.V. Shatalin, Scanning fiber-optic microscope. Electron. Lett. **27**, 724–726 (1991)
10. T. Dabbs, M. Glass, Single-mode fibers used as confocal microscope pinholes. Appl. Opt. **31**, 705–706 (1992)
11. P.M. Delaney, M.H. Harris, R.G. King, Fibre-optic laser scanning confocal microscopy suitable for fluorescence imaging. Appl. Opt. **33**, 573–577 (1994)
12. F. Blais, Control of galvanometers for high precision laser scanning systems. Opt. Eng. **27**(2), 104–110 (1988)
13. Q.T. Nguyen, N. Callamaras, C. Hsieh, I. Parker, Construction of a two-photon microscope for video-rate Ca(2+) imaging. Cell Calcium **30**(6), 383–393 (2001)
14. K.H. Kim, C. Buehler, P.So, High-speed, two-photon scanning microscope. Appl. Opt. **38**(28), 6004–6009 (1999)
15. C.L. Evans, E.O. Potma, M. Puoris'haag, D. Côté, C.P. Lin, X.S. Xie, Chemical imaging of tissue in vivo with video-rate coherent anti-stokes Raman scattering microscopy. Proc. Natl. Acad. Sci. USA **102**(46), 16807–16812 (2005)
16. G.D. Reddy, P. Saggau, Fast three-dimensional scanning scheme using acousto-optic deflectors. J. Biomed. Opt. **10**, 064038 (2005)
17. S. Zeng, K. Bi, S. Xue, Y. Liu, X. Lv, Q. Luo, Acousto-optic modulator system for femtosecond laser pulses. Rev. Sci. Instrum. **78**, 015103 (2007)
18. G.J. Brakenhoff, J. Squier, T. Norris, A.C. Bliton, M.H. Wade, B. Athey, Real-time two-photon confocal microscopy using a femtosecond, amplified Ti Sapphire system. J. Microsc. **181**, 253–259 (1996)
19. M. Fricke, T. Nielsen, Two-dimensional imaging without scanning by multifocal multiphoton microscopy. Appl. Opt. **44**, 2984–2988 (2005)
20. V. Andresen, A. Egner, S.W. Hell, Time-multiplexed multifocal multiphoton microscope. Opt. Lett. **26**(2), 75–77 (2001)
21. G.J. Brakenhoff, K. Visscher, Confocal imaging with bilateral scanning and array detectors. J. Microsc. **165**, 139–146 (1992)
22. R. Wolleschensky, B. Zimmermann, High-speed confocal fluorescence imaging with a novel line scanning microscope. J. Biomed. Opt. **11**, 064011 (2006)
23. P. Török, C.J.R. Sheppard, Z. Laczik, Dark-field and differential phase contrast imaging modes in confocal microscopy using a half-aperture stop. Optik **103**, 101–106 (1996)
24. C.J. Cogswell, C.J.R. Sheppard, Confocal differential interference contrast (DIC) microscopy: including a theoretical analysis of conventional and confocal (DIC) imaging. J. Microsc. **165**, 81–101 (1992)
25. D.K. Hamilton, C.J.R. Sheppard, A confocal interference microscope. Opt. Acta **29**, 1573–1577 (1982)
26. C.J.R. Sheppard, Scanning optical microscopy, in *Advances in Optical and Electron Microscopy*, ed. by R. Barer, V.E. Cosslett (Academic Press, London, 1987)
27. D.K. Hamilton, C.J.R. Sheppard, Differential phase contrast in scanning optical microscopy. J. Microsc. **133**, 27–39 (1984)
28. C.J.R. Sheppard, D.K. Hamilton, H.J. Matthews, Scanning optical microscopy of low contrast samples. Nature **334**, 572 (1988)

Chapter 7
Multiphoton Imaging

Shakil Rehman and Colin J.R. Sheppard

The nonlinear process of multiphoton imaging used in an optical microscope has inherent out-of-focus rejection of light and hence gives superior optical sectioning without a pinhole when compared with a confocal microscope. The lateral resolution remains close to the diffraction limit of the imaging optics. The flexibility of combining the various nonlinear contrast mechanisms, multiphoton microscopy is likely to become a major imaging modality in biomedical fields. With the current development of femtosecond pulsed laser technology, it is to be expected that multiphoton optical microscopes will continue to be advanced for high-resolution imaging in a variety of biomedical applications. This chapter will first discuss the principle of multiphoton process and then multiphoton imaging modes. This chapter will also provide a detailed discussion on the design of a multiphoton imaging system.

7.1 Introduction

Multiphoton imaging is fundamentally different from single photon imaging in the sense that at very high energy density of photons at the focus of an imaging system, nonlinear absorption or scattering dominates. This results in the observation

S. Rehman (✉)
Division of BioEngineering, National University of Singapore, Singapore 117576, Singapore

Singapore-MIT Alliance for Research and Technology, 1 CREATE Way,
#10-01 CREATE Tower, Singapore 138602
e-mail: shakil@nus.edu.sg

C.J.R. Sheppard
Division of BioEngineering, National University of Singapore, Singapore 117576, Singapore

Department of Biological Sciences, National University of Singapore, Singapore 117543, Singapore

R. Liang (ed.), *Biomedical Optical Imaging Technologies*, Biological and Medical Physics, Biomedical Engineering, DOI 10.1007/978-3-642-28391-8_7,

of nonlinear optical phenomena such as multiphoton fluorescence, harmonic generation, sum-frequency generation, coherent Raman scattering, and parametric oscillation. In modern imaging systems, these optical effects are frequently used to visualize the biological material from cellular to molecular level.

Multiphoton excitation process was first studied by Maria Goeppert-Mayer [1] in 1931, but multiphoton microscopy was not developed until decades later. The technology was patented by Winfried Denk, James Strickler, and Watt Webb in 1991 [2]. The first multiphoton optical process used in microscopy was second harmonic generation (SHG) [3,4] that was followed by coherent anti-Stokes Raman spectroscopy (CARS) [5]. Two-photon excitation fluorescence (TPEF) microscope for biological imaging was initially demonstrated by Denk et al. [6]. Later, third harmonic generation (THG) mode of multiphoton effect was used in a microscope by Barad et al. in 1997 [7]. Since these earlier works, multiphoton imaging has been applied in various modes of imaging in biomedical fields.

Multiphoton imaging is based on nonlinear optical response of a medium, that is, optical processes that involve more than one photon interacting simultaneously with a molecule. Such interactions of photons with a material result in either two or more photon absorption or scattering, as in two- and three-photon excited fluorescence, second and third harmonic generation effects, and coherent anti-Stokes Raman scattering. Multiphoton imaging can be divided into incoherent and coherent modes of a nonlinear optical microscope. The signal in incoherent multiphoton imaging is characterized by emission of fluorescence or phosphorescence having a random phase and whose power is proportional to the concentration of radiating molecules. The principle of incoherent imaging system is based on simultaneous absorption of two or more photons, as in, two-photon excited fluorescence microscopy [6] and three-photon excitation fluorescence microscopy [8, 9]. The coherent multiphoton imaging is characterized by the emission of light that is in phase with the excitation field and whose power is proportional to the geometrical distribution of radiating molecules. The coherent multiphoton imaging techniques are SHG microscopy [10, 11], CARS microscopy [5, 12], and THG microscopy [7, 13–15].

Two-photon excited fluorescence is the most commonly used multiphoton effect in optical microscopy and has become an invaluable tool for biological imaging. Two photons from a pulsed laser are simultaneously absorbed by a fluorophore, and a single photon is emitted in the form of fluorescence that can be used to make an image. TPEF can be used in materials with endogenous fluorophores or with labeling by exogenous dyes or quantum dots. TPEF has the advantage of multicolor labeling of various tissue elements and subcellular organelles within a single biological sample. Like all contrast methods based on fluorescence, TPEF also suffers from photobleaching and photodamage. Second harmonic generation, on the other hand, is a nonlinear optical process that is biologically compatible, noninvasive, and requires no labeling.

When excited with ultrashort laser pulses in a microscope, the amplitude of SHG is proportional to the square of the incident light intensity. The nonlinear process of SHG takes place through an interaction between the electric field and its spatial derivative. In SHG, two photons are converted into a single photon at twice the excitation energy emitted coherently in materials lacking a center of symmetry. Light emission by in this process is anisotropic and coherent, and its phase is coupled to the excitation field and hence requires phase-matching effects between the electric fields associated with the process. In biological materials, the asymmetrical structures required for efficient second harmonic generation are cellular membranes that possess such asymmetrically distributed molecular structures. Other structures within cells and tissues that can produce SHG signal are collagen and actin filaments. SHG imaging greatly reduces photobleaching and phototoxicity. Near infrared wavelength excitation allows excellent depth penetration in biological material and makes live tissue imaging possible. SHG signals have characteristic polarization, and, therefore, polarization anisotropy can also be used to determine the absolute orientation and degree of organization of proteins in a tissue.

Third harmonic generation is another multiphoton process that can be used to image materials that have some third-order nonlinearity depending on the material property, symmetry, and the incident light. At the focus of lens, if there is a discontinuity or inhomogeneity, like an interface between two media, the symmetry along the optical axis is broken, and a third harmonic signal can be obtained. Better optical sectioning can be achieved due to the nonlinear process of THG taking place only at the focal plane. Being the property of all materials, THG can be used for noninvasive imaging of biological material without the need of labeling.

All of these multiphoton imaging methods have benefited from the recent advancement in femtosecond laser technology. The state-of-the-art femtosecond lasers are available in the wavelength range of 750–1,300 nm with ultrashort pulse widths from a few 100 fs to less than 10 fs, providing a unique light source for a range of multiphoton processes to be observed and therefore making it easier than before to characterize and image intracellular and molecular features that are otherwise unobservable in a biological material.

7.2 Principle of Multiphoton Process

Nonlinear optical processes take place when the response of a material to the applied optical field depends nonlinearly on the strength of the field. The applied field changes the distribution of internal charges like electrons, ions, or nuclei within a molecular system, resulting in a field-induced electric dipole moment that, in turn, becomes a new source to emit radiation. This is the fundamental

process of light-induced polarization in a molecule that results in the emission of a secondary electromagnetic wave. The induced polarization in a medium depends on the strength of the applied field $E(t)$ and can be written as

$$P(t) = \varepsilon_o \chi^{(1)} E(t) + \varepsilon_o \chi^{(2)} E^2(t) + \varepsilon_o \chi^{(3)} E^3(t) \ldots, \tag{7.1}$$

where ε_o is the permittivity of free space; $\chi^{(1)}$, $\chi^{(2)}$, and $\chi^{(3)}$ are the linear, second-order, and third-order susceptibilities of the medium; $E(t)$ is the incident field; and P is the induced polarization. The electric susceptibility χ indicates the ability of the electric dipoles in a medium to align themselves with the incident electric field. First term in Eq. 7.1 represents the linear polarization that gives rise to linear absorption and refraction in terms of linear susceptibility $\chi^{(1)} = n^2 + 1$, where n is the refractive index. Second term in Eq. 7.1 gives the second-order nonlinear polarization $P^{(2)}(t) = \varepsilon_o \chi^{(2)} E^2(t)$ and $P^{(3)}(t) = \varepsilon_o \chi^{(3)} E^3(t)$ as third-order nonlinear polarization, and so on. Each of these polarization terms gives rise to a different physical phenomenon. For example, second-order polarization is used to produce second harmonic generation and sum/difference frequency generation, and third-order polarization is responsible for two-photon excited fluorescence, third harmonic generation, Raman scattering, Brillouin scattering, self-focusing, and optical phase conjugation. The second-order nonlinear optical interactions based on $\chi^{(2)}$ can only occur in noncentrosymmetric materials having no inversion symmetry, while third-order nonlinear phenomena can take place in any medium regardless of whether it possesses inversion symmetry or not.

The higher harmonic generation is a parametric process that is governed by a real susceptibility. On the other hand, nonparametric processes, such as multiphoton absorption, have a complex susceptibility associated with them [16]. In parametric processes, the initial and final quantum mechanical states are identical, as shown in Figs. 7.1d, e, and f. A virtual state represents the population inversion, as shown by dashed lines in Fig. 7.1, which is a superposition of one or more photon fields and an eigenstate of the molecule. The unique property of a parametric process is that photon energy is conserved, that is, no energy is deposited into the system. This property is the hallmark of multiphoton imaging using SHG/THG modes of nonlinear excitation for noninvasive and live tissue imaging in biological material without causing heating or other photodamage. In nonparametric processes, the initial and final states are different, as shown in Figs. 7.1a, b, and c, where the molecule after excitation relaxes back to a different ground state. Nonparametric interactions may cause photon absorption in the sample resulting in effects such as bleaching and thermal damage. In resonant parametric processes that are resonantly enhanced at some wavelengths, the absorption of the laser radiation also increases. Hence, there has to be a balance between the laser intensity and the wavelength used in order to obtain the strong nonlinear signal while minimizing effects like photobleaching and photodamage.

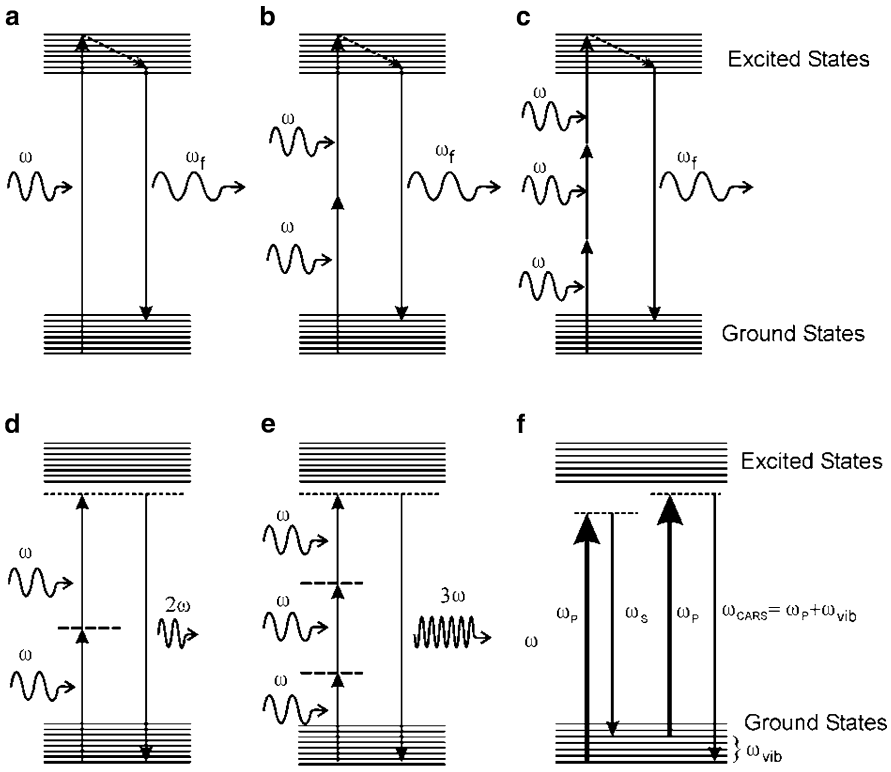

Fig. 7.1 Energy diagrams of various optical excitation methods that are used for imaging contrast in biomedical field. The incoherent (nonresonant) modes of excitation resulting in fluorescence are (**a**) 1-photon excitation, (**b**) 2-photon excitation, and (**c**) 3-photon excitation. The resonant coherent modes of multiphoton excitation are (**d**) SHG, (**e**) THG, and (**f**) CARS resulting in a coherent signal

7.3 Multiphoton Imaging Modes

SHG, THG, and TPEF have become the most widely used contrast modes of multiphoton imaging. The nonlinear contrast mechanism depends on the second- and third-order nonlinearities as described by Eq. 7.1, which can be produced by the light-matter interaction at the focus of a high numerical aperture microscope objective. As the nonlinear effects are proportional to the second or third power of the fundamental light intensity, light only at a very tiny focal volume interacts with the sample, eliminating the out-of-focus light, resulting in an inherent optical sectioning. Selecting a nonlinear contrast method of choice, a multiphoton microscope can be made by raster scanning a laser beam across the focal plane of a microscope objective and measuring the signal intensity as a function of the focal spot position. The 3-D images can be obtained by moving the sample or the objective along the laser beam axis. A typical multiphoton imaging system is shown in Fig. 7.2.

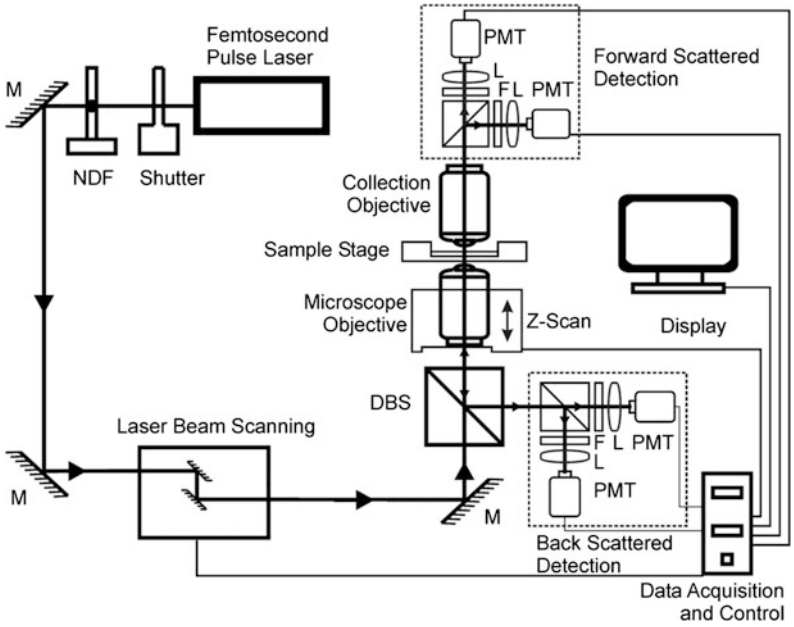

Fig. 7.2 Optical setup of a typical multiphoton imaging microscope. A femtosecond pulsed laser beam is scanned onto the sample, and signal is detected in the forward and/or backward direction in various modes of the microscope. The terms used for the optical components are *M* mirror, *NDF* neutral density filter, *DBS* dichroic beam splitter, *F* filters, *L* lens, and *PMT* photomultiplier tube

The light source is usually a femtosecond pulsed laser in the near infrared spectrum to excite most of the ultraviolet to visible light-absorbing dyes and fluorophores. The resonant processes of SHG, THG, and CARS are also excited by such a laser. The commonly used multiphoton wavelengths are in the range of 700–1,300 nm that are applicable in the biomedical field. This wavelength range is used for its long range penetration in the tissue, less scattering, and absorption by the water molecules, therefore, resulting in negligible heating of the tissue. In the following subsections, TPEF, SHG, THG, and CARS microscopy methods are described.

7.3.1 Two-Photon Excited Fluorescence (TPEF)

TPEF is by far the most commonly used multiphoton excitation process, in which a molecule simultaneously absorbs two photons in a single quantum event [6]. The combined energy of the two photons allows the use of lasers in the near infrared spectrum to excite dyes and fluorophores. The fluorescence emission induced by this

nonlinear excitation process is indistinguishable from the characteristic fluorescence in single photon excitation. TPEF microscopy has great impact in the field of laser scanning microscopy and provides a versatile tool for biological imaging. The basic principle of TPEF is shown schematically in Fig. 7.1b. Two photons from the laser source are absorbed simultaneously by an intrinsic or exogenous fluorophore molecule. A fluorescent photon is emitted after a short delay and can be collected to generate an image. TPEF also suffers from photobleaching like all other contrast mechanisms based on fluorescence and the use of very high intensities for excitation can lead to higher order 2-photon interactions in the focal volume, excitation saturation and photodamage [17].

In TPEF imaging, optical sections can be obtained at greater depths within a tissue as compared to confocal or wide-field imaging due to the use of longer wavelengths hence less scattering. The excitation light is not attenuated by a fluorophore above and below the focal plane of the lens. Since very small amount of fluorescence is generated away from the point of illumination, therefore, all the detected photons may be used for imaging regardless of whether they have been scattered or not. TPEF microscopy has wide range of applications [18–20]. TPEF has been used to image live tissue at depths of up to 1 mm [21, 22], to imaging cerebral blood flow [23] and neuronal activity [24] providing greater understanding of the function and disorders in the brain. Now, TPEF imaging is being used in compact and versatile microscopes for in vivo imaging in clinical settings. Fiber-optic-based imaging methods have also been used to build miniaturized two-photon microscopes and endoscopes [25–27].

7.3.2 Second Harmonic Generation (SHG)

In SHG process, two photons are converted into a single photon at twice the excitation energy in materials lacking a center of symmetry. Light emission in this process is anisotropic and coherent, and the phase of scattered light field is coupled to the excitation field and hence requires phase-matching effects between the electric fields associated with the process. In biological materials, the asymmetrical structures required for efficient second harmonic generation are cellular membranes that possess such asymmetrically distributed molecular structures. Other structures within cells and tissues that can produce SHG signal are collagen and actin filaments. The nonlinearity of the SHG process results in a signal that is maximum at the focus of a microscope, resulting in the intrinsic three-dimensional sectioning without the use of a confocal aperture. The SHG process greatly reduces out-of-focus plane photobleaching and phototoxicity. Near infrared wavelength excitation allows greater depth penetration in biological material, making this method well suited for studying intact tissue in biomedical field. Information about the organization of chromophores, including dyes and structural proteins, at the molecular level can be extracted from SHG imaging data in several ways. SHG signals have well-defined polarizations, and hence, SHG polarization anisotropy can also be

used to determine the absolute orientation and degree of organization of proteins in tissues.

SHG is a three-wave mixing process based on second-order polarization, as shown in Fig. 7.1d. In this picture, two photons of frequency ω are converted into one photon of twice the frequency at 2ω. The energy levels represented by solid lines are atomic or molecular levels, and dotted lines represent the virtual states. These virtual energy states are combined states of the molecular system and the photons of the incident radiation. This property of nonlinear harmonic generation via virtual states leaves no residual energy in the medium, and the emitted photon has exactly the same amount of energy as that of the absorbed photons. The conservation of energy in such a nonlinear process provides the noninvasive property of imaging in the microscopic applications of biological material.

Due to symmetry reasons, elements of the second-order susceptibility cancel out in an isotropic homogeneous medium; hence, second-order nonlinear optical effect can occur in a noncentrosymmetric crystalline structure only. The first experiment carried out to demonstrate optical second harmonic generation was performed by in 1961 [28]. Some other physical nonlinear processes based on $\chi^{(2)}$ are linear electro-optic effect (Pockels effect), optical rectification, and DC polarizability. The second-order induced polarization can be written as [29]

$$P_i^{(2)}(2\omega) = \varepsilon_o \sum_{jk} \chi_{ijk}^{(2)}(\omega, \omega) E_j(\omega) E_k(\omega), \tag{7.2}$$

where $E(\omega)$ is the incident wave at frequency ω and the induced polarization is at 2ω that produces a new radiation at double the frequency. The second-order susceptibility $\chi_{ijk}^{(2)}$ is a third rank tensor responsible for the second harmonic generation and for centrosymmetric materials, $\chi_{ijk}^{(2)}$ vanishes due to inversion symmetry. The indices ijk are summed over linear polarization directions of x, y, and z. The induced polarization $P_i^{(2)}(2\omega)$ produces an electromagnetic field $E(2\omega)$ at twice the frequency of the input field. Due to symmetry selection rules, the elements of the nonlinear susceptibility tensor $\chi_{ijk}^{(2)}$ vanish for materials with inversion symmetry. This symmetry rule also applies equally well for all even powers of nonlinear susceptibilities given by Eq. 7.1. Therefore, second harmonic effect is not observed for an isotropic and centrosymmetric material. For effective nonlinear harmonic generation effect, the specimen must be relatively transparent to the wavelength of fundamental illumination light and the generated higher harmonics.

The first application of SHG in optical microscopy was imaging the structure of nonlinearities in a crystal of ZnSe, in which a large area of the specimen was illuminated by a laser and second harmonic signal was imaged in an optical microscope [4]. The scanning mode of a SHG microscope was implemented by Sheppard et al in 1977 [30]. The first biological application of SHG microscopy was imaging a rat tail tendon [31]. The development of femtosecond mode-locked lasers provided stable sources of high-intensity excitation required for the efficient generation of nonlinear responses. Now, SHG microscopy is used in a

variety of biological applications. Optical microscopy with SHG is widely used for contrast generation in collagen [32–35] myocytes [34, 36], plants and chloroplasts, etc. [37, 38]. SHG microscopy is based on noncentrosymmetric organization of microstructures in a sample, and SHG signal can be generated due to a broken symmetry at an interface or due to a noncentrosymmetric arrangement within bulk structures. At an interface, biological membranes can produce detectable SHG signal as in the case of a lipid bilayer [39]. Molecular structures having a symmetric distribution of chirality in the membrane do not give rise to SHG signal; only an ordered asymmetric distribution of chiral molecules in the membranes is responsible for SHG. SHG can also be produced in biogenic crystal structures, for example, in calcite or starch granules [37] and biophotonic crystalline and semicrystalline structures in living cells [40].

7.3.3 Third Harmonic Generation (THG)

Third harmonic generation is a nonlinear optical process which has been intensely studied since the early days of nonlinear optics [41, 42]. This process has been applied in imaging of lipids in cells and tissues [43], subcellular structure in neurons [15], cell nuclei [44], and simultaneous SHG, THG, and TPEF imaging of live biomaterial [45]. All materials have some third-order nonlinearity depending on the material property, symmetry, and incident light. At the focus of microscope objective lens, when a discontinuity or inhomogeneity is encountered, like an interface between two media, the symmetry along the optical axis is broken, and a third harmonic signal can be obtained. High optical sectioning can be achieved because of the nonlinear process of third harmonic generation taking place only at the focal plane. Being the property of all materials, third harmonic signal can be used for noninvasive microscopy, particularly in biological materials without the need of fluorescence labeling.

THG is a four-wave mixing process based on third-order nonlinear polarization as shown in Fig. 7.1e. Unlike the second-order processes, the third-order process is possible in all media, with or without inversion symmetry. The amplitudes of nonlinear susceptibility for SHG and THG are very different: $|\chi^{(3)}| \ll |\chi^{(2)}|$, resulting in the magnitude of THG being much smaller than SHG. Third harmonic generation was first reported in1962 in a centrosymmetric calcite crystal [46]. Other physical optical processes based on third-order susceptibility $\chi^{(3)}$ are Kerr effect, DC-induced SHG, and AC Kerr effect.

The third-order induced polarization can be written as

$$P_i^{(3)}(3\omega) = \varepsilon_o \sum_{jkl} \chi_{ijkl}^{(3)}(\omega, \omega, \omega) E_j(\omega) E_k(\omega) E_l(\omega), \tag{7.3}$$

where $E(\omega)$ is the incident wave at frequency ω, third-order susceptibility $\chi_{ijkl}^{(3)}$ is a fourth rank tensor, and indices *ijkl* are summed over linear polarization directions

of x, y, and z. The induced polarization is at 3ω that produces a new radiation at three times the frequency of the incident wave. Cubic nonlinearities are responsible optical processes like self-focusing and self-defocusing of optical beams and also give rise to interesting effects, such as optical bistability, phase conjugation, and optical spatial and temporal solitons.

The phase-matching condition for THG can be written as $3\mathbf{k}_1 - \mathbf{k}_3 = 0$, where $\mathbf{k}_3$ and $\mathbf{k}_1$ are the wave vectors of the third harmonic field and the fundamental field, respectively. When a laser beam is focused, THG from a homogenous bulk medium is canceled out when the phase-matching condition is satisfied. This interesting phenomenon has been explained on the basis of Gouy phase shift (a phase change of pi within the Rayleigh range for a focused Gaussian beam), across the focus of the excitation beam [47].

Since THG is a coherent process, amplitude of the emitted optical field from all the molecules is added in contrast with the addition of intensities as in the case of an incoherent process like fluorescence. When the phases of the interacting optical fields are properly matched, a condition termed as phase-matching, the total signal intensity is proportional to the square of the number of scattering molecules [48]. When phase-matching is not right, the generated signal is significantly low in magnitude. Since the condition of phase-matching is dependent on the relative geometry of the illuminating beam, the signal and the medium, signals generated by a coherent process are typically small [47].

Third harmonic signals can be effectively generated from an interface or from an object with a size comparable to the FWHM of the axial excitation intensity profile. The signal from a bulk medium is canceled by a wave-vector mismatch associated with the Gouy phase shift of the focused excitation field. This permits THG imaging of small features with a high signal-to-background ratio. The THG radiation from a small object or an interface perpendicular to the optical axis exhibits a sharp radiation pattern along the optical axis in the forward direction. For an interface parallel to the optical axis, the role of the Gouy phase shift is to deflect the phase-matching direction, that is, the THG radiation maximum direction, off the optical axis.

Third harmonic light is produced by a laser beam tightly focused at an interface. It is possible to image both biological and nonbiological specimens with inherent optical sectioning of THG microscopy. Third harmonic light in a material is produced given that the axial focal symmetry can be broken by a change in the material properties like interfaces and boundaries due to refractive index or nonlinear susceptibility changes. This localized production of third harmonic light at material interfaces provides the inherent optical sectioning desired in a three-dimensional imaging at higher axial resolution. It is possible to produce three-dimensional images by THG from different planes perpendicular to the axis of beam propagation. Compared to other modes of single or multiphoton laser fluorescence microscopy, no exogenous fluorophores are needed in THG microscopy.

It was demonstrated by Tsang that under tight focusing conditions, THG can be generated through an interface within the focal volume of the excitation beam (Tsang 1995) [69]. Later, it was shown that whenever there is either a change

in refractive index or third-order nonlinear susceptibility, third harmonic light is produced, and as a result of this interface effect, third harmonic imaging is possible and can be applied to study transparent samples having low contrast [49]. Volumetric imaging has also been done in both biological and nonbiological specimens demonstrating the dynamical imaging properties of THG in live samples [50, 51]. Third harmonic generation near the focal point of a tightly focused laser beam can be used to probe small structures of transparent samples at the interfaces and inhomogeneities. Due to the coherent nature of third harmonic process, the axial resolution of THG microscopy is, however, equal to the confocal parameter of the fundamental beam [49]. The signal level in THG microscopy can be optimized by the influence of sample structure and beam focusing [52], where they controlled the signal level by modifying the Rayleigh range of the excitation beam and applied this method for the contrast modulation in THG images of Drosophila embryos. Besides structural and beam shape dependence, the THG is also sensitive to the local differences in the refractive index, third-order susceptibility, and dispersion. This aspect of THG was used to image lipids that are present in many biological cells and tissues [53]. In this study, a multimodal technique for microscopy was used to image lipid bodies, fluorescent compounds in tissues, and extracellular matrix by combining two-photon fluorescence, SHG, and THG microscopy. Another multimodal nonlinear microscopic technique based on a femtosecond Cr:forsterite laser was used to simultaneously generate SHG, THG, two-photon, and three-photon fluorescence images [45].

Third harmonic generation microscopy is shown to be particularly suitable for imaging biogenic crystals and polarization sensitive imaging of crystalline structure in biological samples [54, 55]. THG has been used for the characterization of saline solutions and structural changes in collagen [56]. It is shown that THG epidetection is generally possible when the sample structure is embedded in a scattering, nonabsorbing tissue with thickness greater than the reduced scattering mean free path [57]. A combination of THG, SHG, and TPEF image contrast methods on the same microscope is also being used for simultaneously imaging the biological material [58, 59].

7.3.4 Coherent Anti-Stokes Raman Scattering (CARS)

CARS microscopy is based on the use of two different laser beams, pump and the Stokes beams, that are tuned to match the energy gap between two vibrational levels in a molecule. CARS is used to probe chemical bond vibration levels and provides molecular specificity, particularly for small molecules [5, 12].

Stronger vibrational signals can be obtained with CARS microscopy that is a nonlinear Raman scattering method. CARS is a four-wave mixing process as shown in Fig. 7.1f, in which a pump beam at frequency ω_P and a Stokes beam at frequency ω_S interact with a sample to generate an anti-Stokes signal at frequency $\omega_{AS} = 2\omega_P - \omega_S$. This expression can be written as $\omega_{AS} = \omega_P + \omega_{vib}$ that

happens when the beat frequency between the pump and Stokes beams, $(\omega_P - \omega_S)$, matches the frequency of a particular Raman active molecular vibration, ω_{vib}. This results in enhanced anti-Stokes signal, providing the vibrational contrast for CARS microscopy [42]. CARS can selectively image molecules by exciting their specific vibrational mode with high sensitivity. Since its signal frequency is blue-shifted from the excitation frequencies, CARS can be used in the presence of high fluorescence background. Normally, pump and Stokes field are near infrared laser which can penetrate deeply into biological system with little absorption. This permits CARS to be noninvasive in imaging living cells. The CARS signal is generated by the induced third-order nonlinear polarization

$$P_i^{(3)}(\omega_{AS}) = \varepsilon_o \sum_{jkl} \chi_{ijkl}^{(3)}(\omega_{AS}) E_j(\omega_P) E_k(\omega_P) E_l(\omega_S), \tag{7.4}$$

where $E(\omega_P)$ is the pump beam, $E(\omega_S)$ is the Stokes beam, the 3rd-order susceptibility $\chi_{ijkl}^{(3)}$ is the fourth rank tensor, and indices $ijkl$ are summed over linear polarization directions of x, y, and z.

Raman scattering-based spectroscopy and imaging offers unique capabilities for live cell chemical contrast without using fluorescent markers. Inherent Raman signals do not photobleach, enabling long-term cellular studies. There have been new developments in CARS microscopy such as (a) F-CARS, forward-detection with parallel-polarized pump and Stokes beams; (b) E-CARS, epidetection with parallel-polarized pump and Stokes beam; (c) P-CARS, forward-detection with polarization; and (d) C-CARS, detection with counter propagating parallel-polarized pump and Stokes beams. The four kinds of the CARS microscopy can be applied under different circumstances. F-CARS microscopy produces a large signal at low excitation power. It is suitable for the vibration with a large resonant CARS signal. However, the resonant F-CARS signal is often overwhelmed by the nonresonant background from the scatterers and solvent. The E-CARS and C-CARS beam geometries introduce a phase mismatch, which acts as a size filter that effectively rejects the signal from the bulk solvent. E-CARS permits high-sensitivity imaging of small features embedded in a nonlinear medium.

CARS microscopy has advantages in imaging small molecules such as lipids and hormones. The function of these small molecules is prone to be affected when they are labeled with fluorescence tags. It has a potential to be used in fields such as membrane biology, neurobiology, and pharmacology.

7.3.5 Laser Sources in Nonlinear Microscopy

Collagen was the first biological material studied using a Q-switched ruby laser at a wavelength of 694 nm but resulted in strong absorption of the SHG signal at 347 nm [60]. Another Q-switched Nd-YAG laser at 1064 nm with nanosecond pulses was used to observe connective tissues [32]. More recently, femtosecond

pulsed lasers are being used for multiphoton microscopy due to their high peak intensities.

A femtosecond laser emits optical pulses with a duration of a few femtoseconds ($1\,\text{fs} = 10^{-15}\,\text{s}$) that are also termed as ultrashort pulses. The generation of such ultrashort pulses is achieved with a technique called mode locking, and the lasers are then termed as mode-locked lasers. The laser resonator contains either an active element (an optical modulator) or a nonlinear passive element (a saturable absorber), which causes the formation of an ultrashort pulse circulating in the laser resonator. Under the steady state operation, the various effects influencing the pulse are in a balance so that the pulse parameters are unchanged after each completed round-trip. Each time the pulse hits the output coupler mirror of the laser, a pulse is emitted. Assuming a single circulating pulse, the pulse repetition period corresponds to the resonator round-trip time (typically several nanoseconds), whereas the pulse duration is much lower, from a few femtoseconds to picoseconds range. Due to very short pulse width, the peak power of a mode-locked laser can be orders of magnitude higher than the average power.

Most widely used and current industrial standard for multiphoton microscopy is the femtosecond pulsed Ti:sapphire laser. The wavelength range is only limited by the bandwidth of the Ti:sapphire gain medium to between approximately 690 and 1,070 nm. This wavelength range is also termed as a therapeutic window, since it can penetrate deep into biological tissue without causing significant photodamage and is not absorbed by water which may result in heating. For THG microscopy, a Ti:sapphire laser seems to be ideal, but strong absorption of the signal generated in the UV region limits its application to thin biological specimens. To avoid UV absorption of the generated THG signal in thick biological samples, THG microscopy is done with wavelengths longer than 1,200 nm. Cr:forsterite laser at excitation wavelength of 1,230 nm and repetition rate of 110 MHz is widely used for THG microscopy [45,61]. Other lasers used for THG microscopy include optical parametric oscillator (OPO) working at a wavelength of 1,500 nm and repetition rate of ~80 MHz, synchronously pumped by a femtosecond Ti:sapphire laser [15,62]; an optical parametric amplifier (OPA) at 1,200-nm and 250-kHz repetition rate pumped by a Ti:sapphire laser [50,51]; and a fiber laser at 1,560 nm with a repetition rate of 50 MHz [63].

Some new laser sources being used for multiphoton microscopy are Yb:glass, Nd:glass, Cr:LiSAF, and fiber lasers. Femtosecond fiber lasers are the next generation of compact laser systems that are being used for multiphoton imaging purposes due to their small footprint as compared with their counterpart femtosecond lasers that are usually very bulky and require external cooling systems. The only drawback of a fiber laser is its lack of wavelength tuning ability that is the hallmark of a femtosecond laser like Ti:sapphire laser. Fiber lasers have a number of qualities which make them attractive for ultrashort pulse generation via active or passive mode locking. The gain bandwidth of rare-earth-doped fibers is quite large, typically tens of nanometers that allows the generation of femtosecond pulses. The high gain efficiency of active fibers makes it possible to operate such lasers with fairly low pump powers and to allow intracavity optical elements with relatively high

optical losses. For example, certain optical filters or arrangements for dispersion compensation could not be used in bulk lasers. Fiber lasers can be fabricated with low cost and can be very compact and rugged. Mode-locked fiber lasers are commonly based on telecommunication components, which have been very carefully developed for reliable long-term operation and have a moderate cost. The performance of picosecond and femtosecond mode-locked fiber lasers and amplifiers in terms of pulse energy, peak power, and pulse quality can be severely limited by the strong nonlinearities of fibers and sometimes also by the chromatic dispersion. Other problems can result from uncontrolled birefringence of fibers, if they are not polarization-maintaining.

7.4 A Multiphoton Imaging System Design

A multiphoton microscope has many common features with a confocal laser scanning microscope. Multiphoton excitation system can be developed by coupling a femtosecond laser into a confocal scanning microscope and using a nondescanned port for efficient detection of the nonlinear signal [64]. The functionality of multiphoton microscopes can be enhanced by implementing efficient detection schemes to allow different signal detection in the transmission and/or excitation direction. In this section, system design of a multiphoton laser scanning microscope is described, and various components of the system are discussed.

A customized multiphoton microscope system is described that can be used to image biological tissue in reflection mode. Such a microscope is suitable for thick tissue and in vivo imaging in biomedical applications. For simultaneous detection of second harmonic and fluorescence signal, two channels of detection are used. The emission signal is divided into different spectral ranges by appropriate dichroic mirrors and optical filters. Similarly, spectral separation can be applied for detecting second and third harmonic signals along with fluorescence. Backscattered coherently generated harmonics are usually much weaker than the forward generated signals; therefore, forward-detection of harmonics can be accomplished with lower excitation intensities. The detection in transmission requires a more extensive modification of the scanning microscope setup. The easiest way of building a transmission mode harmonic generation microscope is by using a high NA condenser that is available on some commercial microscope models [64, 65]. The design and instrumentation of nonlinear microscopes have been extensively reviewed [66–68].

7.4.1 System Design

Optical design of a multiphoton microscope capable of TPEF, SHG, and THG detection in reflection mode is shown in Fig. 7.3. A high repetition rate femtosecond

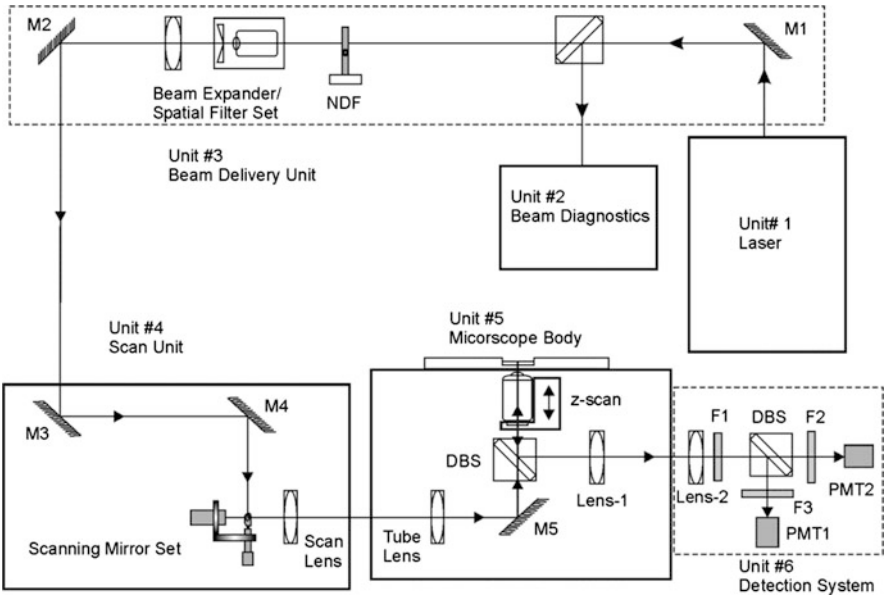

Fig. 7.3 Optical setup of the multiphoton microscope. *M* mirror, *DBS* dichroic beam splitter, *NDF* neutral density filter, *F* filter, and *PMT* photomultiplier tube

pulsed laser such as a Ti:sapphire laser is used for excitation of nonlinear signal. A neutral density filter (NDF) is used to control the intensity of the laser beam. The laser beam is then expanded using a spatial filter and beam expander optics in order to fill the entrance aperture of the microscope objective. Some part of the laser beam is directed toward an autocorrelator for beam diagnostics such as measurement of pulse width of the femtosecond laser. The beam is directed toward the scanning mirrors that are mounted in a box with their electronic drive units. A set of two lenses is used to deliver the laser beam from the scanning mirrors to the microscope objective. These two lenses form what is known as a telecentric optical system. The idea of telecentricity is to keep the scanning beam stationary at the entrance pupil of the microscope objective. One of these lenses is called the scan lens that is placed close to the scan mirrors, and the other lens, known as the tube lens, is placed before the objective. The tube lens is designed to correct for aberrations of the objective; thus, it is important to match the lens and objective from the same manufacturer. A dichroic beam splitter (DBS) is used for the collection of backscattered light from the sample. The laser beam transmits through the DBS and through the microscope objective and illuminates the sample. The backscattered light is collected with the same objective and is now reflected by the DBS that is optimized for transmission of infrared light and reflection of shorter wavelengths (that depends on the excitation wavelength). The light reflected from the DBS is passed through an infrared filter to block any scattered laser light. A set of two lenses is used to collect the signal coming from the sample and to image the pupil plane of the objective onto the

detectors. This is done so that the scanning beam remains stationary at the detector. Another dichroic beam splitter is used to separate the fluorescence and SHG signal simultaneously. The transmitted signal is passed through an arrow band pass filter to select the fluorescence, and reflected light is passed through a narrow band pass filter to select the second harmonic signal. The two signals are detected by a set of photomultiplier tubes (PMT) for their fast response and high sensitivity. The PMT signal is converted into a voltage signal using transimpedance amplifiers and fed into the data acquisition board in a computer. The pixel and line clock signals are used to synchronize the data acquisition with the scanner system. A fast data acquisition card is used to receive the pulses simultaneously from the two detectors and is synchronized with the reading of x and y positions from the scanning mirrors. This renders the two simultaneously acquired images with different nonlinear contrast mechanisms. For obtaining optical sections at different depths, the microscope objective is translated along the optical axis with a piezo scanner.

The setup of multiphoton nonlinear microscope can be divided into four main functional units: the femtosecond laser source, beam scanning unit, the optical microscope, and the detection system synchronized with the laser beam scanning. In the following sections, these units are described in detail.

7.4.2 Optical Parts

A fiber laser was used to excite the SHG signal in the samples. The IMRA fiber laser model Femtolite FX-100 is based on a passively mode-locked Er-doped fiber oscillator followed by an Er-doped fiber amplifier. The laser produces 110 fs pulses at a rate of 75 MHz and average power of 100 mW at a fixed wavelength of 800 nm. This laser is suitable in biomedical imaging systems for its compact design and turnkey solution. The laser beam was monitored with an autocorrelator (model AA-110D, Del Mar Photonics) to measure its pulse width. A neutral density filter (CSND-1-50.0M, CVI Melles Griot) was used to control the laser beam power. A Faraday isolator (ISO-04-780-MP-W, Newport Corp.) was used to block any back reflections into the laser. The mirrors used for laser beam delivery are BBDS-PM-1037-C (CVI Melles Griot).

The beam was expanded with a five axis spatial filter set (model 910A, along with a pinhole: 910PH-20 and objective lens: M10x, from Newport Corp.).The laser beam goes into a scanner consisting of a resonant scan mirror and a galvo-mirror set. The fast scanner is a resonant scanning mirror (CRS 8 KHz, General Scanning) oscillating at 8 kHz, and the slow scanning mirror is at 30 Hz (VM500PLUS, General Scanning). Combination of these two mirror sets allows to achieve a scan rate of 30 frames per second at 512×512 pixel image and 15 frames per second at $1,024 \times 1,024$ pixel image.

A scan lens, in this case, a 10× wide-field microscope eyepiece (NT36-130, Edmund Optics) and a tube lens (PLCX-50.0-77.3-UV-800, CVI Melles Griot), are used in a telecentric arrangement between the scan mirrors and the microscope

objective for illuminating the pupil plane of the microscope objective to achieve the diffraction-limited focusing. The overfilling of the back aperture of microscope objective is essential for a diffraction-limited focal spot and confocal imaging. For various magnifications, microscope objectives of 20× and 40× were used for imaging (UPlanSApo, Olympus).

The generated nonlinear signals was collected with the same microscope objective in the reflection mode, separated by the dichroic beam splitter (FF735-Di01-25x36, Semrock) which is specifically chosen to separate the fundamental and fluorescence/SHG signals. The signal is then focused on to the PMT's with lens L1 (PLCX-50.0-77.3-UV-355-532, CVI MG) and L2 (PLCX-50.0-51.5UV-355-532, CVI MG). The excitation light was filtered by a laser-blocking filter F1 (FF01-770/SP-25, Semrock). A DBS (FF580-FDi01-25x36, Semrock) was used to separate the fluorescence and SHG signals that pass through filters (FF01–06/15-25, Semrock) for SHG and (FF01-470/100-25, Semrock) for fluorescence. The signals are detected with cooled PMT's (H7422-40, Hamamatsu) in two channels and amplified by low-noise preamplifiers (59-179, Edmund Optics) before the A/D card.

The data acquisition was done with the help of a fast data acquisition card (NI PCI 6115, National Instruments), and a LabVIEW code was developed for the data acquisition and image display (LabVIEW 2010, National Instruments).

A point to be noted here is that all the optical components used have to be mounted in their proper optical mounts. The optical components and their matching mounts are easily available from respective suppliers as quoted. The optical components mentioned here are for reference purposes only; some of the mounts and components were custom designed and fabricated. The customized mounts can be easily fabricated in a mechanical workshop.

7.4.3 Application

The multiphoton microscope described in this section is capable of imaging live samples in vivo conditions. The samples need not to be prepared before imaging as is done for other fluorescence-based imaging microscopes.

In one medical application relating to ophthalmology, the microscope was used to image cornea and other ocular tissue. The cornea is the major lens of the eye for producing a focused image on the retina. There is a clinical need to image the cornea noninvasively at several levels of resolution and to monitor structural and cellular changes that interfere with the optical clarity of the cornea as a result of surgery, trauma, or infection. The current state-of-the-art clinical confocal microscope allows detection of the fibroblasts within the matrix of the cornea but not the ordered collagen matrix which is produced by these cells. The collagen is critical to clinical outcomes as it controls the strength, shape, and transparency of the cornea. The characterization of healing after the new deep corneal surgical procedures requires an instrument that allows the details of the fibroblasts and their collagen matrix for understanding the clinical outcomes. The multiphoton microscope can simultaneously image the ordered collagen matrix

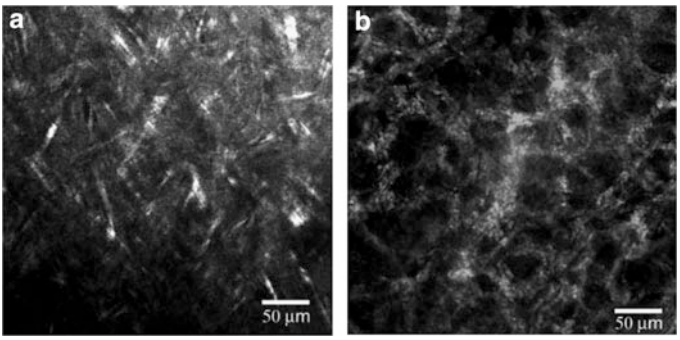

Fig. 7.4 Images of cornea (**a**) SHG showing the collagen fibrils structure and (**b**) confocal reflectance image showing the fibroblast cells

and the fibroblasts. Combination of confocal microscopy and a second harmonic generation microscopy reveals the detailed morphology of the cellular changes and the organization of the collagen matrix. Such a microscope may allow 3-D images to be rapidly constructed from noninvasive scans of the patient's cornea. Some images of collagen and cellular structure of cornea in its natural state with the backscattered second harmonic imaging method are shown in Fig. 7.4. Second harmonic signal gives a strong imaging contrast from collagen fibers lying deep in the stroma. The longer wavelength helps in deep tissue imaging, and backscattered nonlinear signal can potentially be used for in vivo imaging of cornea.

In another application of the multiphoton imaging, the microscope was used to image a vital part of the optic nerve head called lamina cribrosa. The lamina cribrosa provides metabolic and mechanical support for the retinal ganglion cell axons passing through the optic nerve and also serves as an interface between the pressurized interior of the eye and retrobulbar tissue, preventing the outflow of intraocular contents and maintaining an adequate intraocular pressure. Neuronal signals from the retinal photoreceptor layer of the eye are conveyed via retinal ganglion cell axons, through the optic nerve head and optic nerve, eventually reaching the visual cortices of the brain. The lamina cribrosa is a multilayered cribriform structure of laminar beams composed of collagen, glial cells, and capillaries. Damage to the lamina under raised intraocular pressure has been shown to be both a risk factor for and a cause of glaucoma, and there is strong evidence which suggests that lowering of the intra-ocular pressure reduces the incidence and the progression of glaucoma. Understanding the structure and function of lamina is crucial for finding the causes of blindness due to glaucoma and other ocular diseases. An image of porcine lamina cribrosa is shown Fig. 7.5, from a freshly acquired porcine eye.

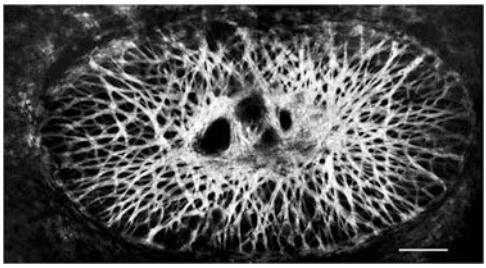

Fig. 7.5 Lamina cribrosa image with the SHG microscope showing the cribriform structure of lamina. The SHG contrast comes from the collagen fibrils only. The image is collage of six 512 × 512 pixel images taken with a 20×/0.75 microscope objective. The scale bar is 100 μm

7.5 Conclusion

The nonlinear process of multiphoton imaging used in an optical microscope has inherent out-of-focus rejection of light and hence gives superior optical sectioning without a pinhole when compared with a confocal microscope. The lateral resolution remains close to the diffraction limit of the imaging optics. In general, the interaction volume in the specimen decreases with an increasing order of the nonlinearity of the process. For multiphoton absorption processes, this effect is reduced by a relative increase in the excitation wavelength. Therefore, the real advantage of a multiphoton microscope is not in the improved resolution but in the noninvasive and in vivo imaging without any staining required. The nonlinear dependence on the intensity leads to localized excitation and is ideal for intrinsic optical sectioning in scanning laser microscopy, for example, the intensity of the SHG signal depends on square of the incident light intensity, while the intensity of THG signal depends on the third power of the incident light intensity. SHG microscopy is suitable for imaging stacked membranes and proteins with organized structures. The THG microscopy is applicable to imaging cellular or subcellular interfaces. An advantage specific to CARS microscopy is the ability to achieve chemical specificity without the addition of exogenous fluorophores. This is possible by making use of resonant energy levels in the molecules of interest to greatly enhance the desired output signal and in vivo or in vitro study of live cells without disrupting natural processes. The main advantage of a multiphoton microscope using coherent processes like SHG and THG is due to the virtual nature of higher harmonic generation, in which, no saturation or bleaching results in the signal. Long-term exposure to laser light with near infrared wavelengths at femtosecond pulses does not compromise the sample viability, while high-resolution morphological, structural, and functional information of biomedical specimens can be obtained. The flexibility of combining the various nonlinear contrast mechanisms, multiphoton microscopy is likely to become a major imaging modality in biomedical fields. With the current development of femtosecond pulsed laser technology, it is to be expected that multiphoton optical

microscopes will continue to be advanced for high-resolution imaging in a variety of biomedical applications.

References

1. M. Göppert-Mayer, Uber Elementarakte mit zwei Quantensprüngen. Ann. Phys. (Leipzig) **9**, 273–294 (1931)
2. W. Denk, H.H. Strickler, W.W. Webb, Two photon laser microscopy USA Patent 5,034,613 (1991)
3. J. Gannaway, C.J.R. Sheppard, Second harmonic imaging in the scanning optical microscope. Opt. Quantum Electron. **10**, 435–439 (1978)
4. R. Hellwarth, P. Christensen, Nonlinear optical microscopic examination of structure in polycrystalline ZnSe. Opt. Commun. **12**(3), 318–322 (1974)
5. M.D. Duncan, J. Reintjes, T.J. Manuccia, Scanning coherent anti-Stokes Raman microscope. Opt. Lett. **7**(8), 350–352 (1982)
6. Y. Denk, H.H. Strickler, W.W. Webb, Two-photon laser scanning fluorescence microscopy. Science **248**, 73–76 (1990)
7. Y. Barad, H. Eisenberg, M. Horowitz, Y. Silberberg, Nonlinear scanning laser microscopy by third-harmonic generation. Appl. Phys. Lett. **70**(8), 922–924 (1997)
8. S. Maiti, J.B. Shear, R.M. Williams, W.R. Zipfel, W.W. Webb, Measuring serotonin distribution in live cells with three-photon excitation. Science **275**, 530–532 (1997)
9. M. Schrader, K. Bahlmann, S.W. Hell, Three-photon-excitation microscopy: theory, experiment and applications. Optik **104**, 116–124 (1997)
10. P.J. Campagnola, M. Wei, A. Lewis, L.M. Loew, High-resolution nonlinear optical imaging of live cells by second harmonic generation. Biophys. J. **77**(6), 3341–3349 (1999)
11. C.J.R. Sheppard, J. Gannaway, R. Kompfner, D.A. Walsh, The scanning harmonic optical microscope. IEEE J. Quantum Electron. **13**(9), 912–912 (1977)
12. A. Zumbusch, G.R. Holtom, X.S. Xie, Three dimensional vibrational imaging by coherent anti-Stokes Raman scattering. Phys. Rev. Lett. **82**, 4142–4145 (1999)
13. M. Müller, J. Squier, K.R. Wilson, G.J. Brakenhoff, 3D-microscopy of transparent objects using third-harmonic generation. J. Microsc. **191**, 266–274 (1998)
14. J.A. Squier, M. Muller, G.J. Brakenhoff, Third harmonic generation microscopy. Opt. Express **3**, 315–324 (1998)
15. D. Yelin, Y. Silberberg, Laser scanning third-harmonic-generation microscopy in biology. Opt. Express **5**, 169–175 (1999)
16. R.W. Boyd, *Nonlinear Optics* (Academic Press, Boston, 1992)
17. G.H. Patterson, D.W. Piston, Photobleaching in two-photon excitation microscopy. Biophys. J. **78**(4), 2159–2162 (2000)
18. K. Koenig, Multiphoton microscopy in life sciences. J. Microsc. **200**(2), 83–104 (2000)
19. C. Xu, W.W. Webb, Measurement of two-photon excitation cross sections of molecular fluorophores with data from 690 to 1050 nm. JOSA B **13**(3), 481–491 (1996)
20. B. Masters, P. So, E. Gratton, Multiphoton excitation fluorescence microscopy and spectroscopy of in vivo human skin. Biophys. J. **72**(6), 2405–2412 (1997)
21. F. Helmchen, W. Denk, Deep tissue two-photon microscopy. Nat. Methods **2**(12), 932–940 (2005)
22. P. Theer, W. Denk, On the fundamental imaging-depth limit in two-photon microscopy. JOSA A **23**(12), 3139–3149 (2006)
23. N. Nishimura, C.B. Schaffer, B. Friedman, P.D. Lyden, D. Kleinfeld, Penetrating arterioles are a bottleneck in the perfusion of neocortex. PNAS **104**(1), 365–370(2007)
24. W. Gobel, B.M. Kampa, F. Helmchen, Imaging cellular network dynamics in three dimensions using fast 3D laser scanning. Nat. Methods **4**(1), 73–79 (2007)

25. F. Helmchen, W. Denk, New developments in multiphoton microscopy. Curr. Opin. Neurobiol. **12**(5), 593–601 (2002)
26. J.C. Jung, M.J. Schnitzer, Multiphoton endoscopy. Opt. Lett. **28**(11), 902–904 (2003)
27. W. Piyawattanametha, R.P.J. Barretto, T.H. Ko, B.A. Flusberg, E.D. Cocker, H. Ra, D. Lee, O. Solgaard, M.J. Schnitzer, Fast-scanning two-photon fluorescence imaging based on a microelectromechanical systems two- dimensional scanning mirror. Opt. Lett. **31**(13), 2018–2020 (2006)
28. P.A. Franken, A.E. Hill, C.W. Peters, G. Weinreich, Generation of optical harmonics. Phys. Rev. Lett. **7**, 118 (1961)
29. G. He, S.H. Liu, *Physics of Nonlinear Optics* (World Scientific Publications, Singapore, 1999)
30. C.J.R. Sheppard, J. Gannaway, R. Kompfner, D.A. Walsh, The scanning harmonic optical microscope. IEEE J. Quantum Electron. **13**(9), 912–912 (1977)
31. I. Freund, M. Deutsch, Second-harmonic microscopy of biological tissue. Opt. Lett. **11**, 94–96 (1986)
32. I. Freund, D. Deutsch, A. Sprecher, Connective tissue polarity: optical second-harmonic microscopy, crossed-beam summation, and small-angle scattering in rat-tail tendon. Biophys. J. **50**, 693–712 (1986)
33. S.J. Lin, C.Y. Hsiao, Y. Sun, W. Lo, W.C. Lin, G.J. Jan, S.H. Jee, C.Y. Dong, Monitoring the thermally induced structural transitions of collagen by use of second-harmonic generation microscopy. Opt. Lett. **30**, 622–624 (2005)
34. P.J. Campagnola, A.C. Millard, M. Terasaki, P.E. Hoppe, c.J. Malone, W.A. Mohler, Three-dimensional high-resolution second-harmonic generation imaging of endogenous structural proteins in biological tissues. Biophys. J. **82**(1), 493–508 (2002)
35. S.W. Chu, S.P. Tai, M.C. Chan, S.K. Sun, I.C. Hsiao, C.H. Lin, Y.C. Chen, B.K. Lin, Thickness dependence of optical second harmonic generation in collagen fibrils. Opt. Express **15**(19), 12005–12010 (2007)
36. V. Barzda, C. Greenhalgh, J. Ausder Au, S. Elmore, J. van Beek, J. Squier, Visualization of mitochondria in cardiomyocytes by simultaneous harmonic generation and fluorescence microscopy. Opt. Express **13**, 8263–8276 (2005)
37. G. Mizutani, Y. Sonoda, H. Sano, M. Sakamoto, T. Takahashi, S. Ushioda, Detection of starch granules in a living plant by optical second harmonic microscopy. J. Luminescence **87**, 824–826 (2000)
38. N. Prent, R. Cisek, C. Greenhalgh, R. Sparrow, N. Rohitlall, M.S. Milkereit, C. Green, V. Barzda, Application of nonlinear microscopy for studying the structure and dynamics in biological systems. Proc. SPIE **5971**, 5971061–5971068 (2005)
39. L. Moreaux, O. Sandre, M. Blanchard-Desce, J. Mertz, Membrane imaging by simultaneous second-harmonic generation and two-photon microscopy. Opt. Lett. **25**, 320–322 (2000)
40. S.W. Chu, I. Chen, T. Liu, C. Sun, S. Lee, B. Lin, P. Cheng, M. Kuo, D. Lin, H. Liu, Nonlinear bio-photonic crystal effects revealed with multimodal nonlinear microscopy. J. Microsc. **208**(3), 190–200 (2002)
41. N. Bloembergen, *Nonlinear Optics*, 4th edn. (Benjamen W. A., New York, 1965)
42. Y.R. Shen, *The Principles of Nonlinear Optics* (Wiley, New York, 1984)
43. D. Débarre, W. Suppato, A. Pena, A. Fabre, T. Tordgemann, L. Conbettes, M. Shane-Clein, E. Beaurepaire, Imaging in lipid bodies in cells and tissues using third-harmonic generation microscopy. Nat. Methods **3**(1), 47–53 (2006)
44. C. Yu, S. Tai, C. Kung, W. Lee, Y. Chan, H. Liu, J. Lyu, C. Sun, Molecular third-harmonic-generation microscopy through resonance enhancement with absorbing dye. Opt. Lett. **33**, 387–389 (2008)
45. S. Chu, I. Chen, T. Liu, P. C. Chen, C. Sun, B. Lin, Multimodal nonlinear spectral microscopy based on a femtosecond Cr:forsterite laser. Opt. Lett. **26**, 1909–1911 (2001)
46. R.W. Terhune, P.D. Maker, C.M. Savage, Optical harmonic generation in calcite. Phys. Rev. Lett. **8**(10), 404–406 (1962)
47. J. Cheng, X.S. Xie, Green's function formulation for third-harmonic generation microscopy. JOSA B **19**(7), 1604–1610 (2002)

48. R.W. Boyd, *Nonlinear Optics* (Academic Press, San Diego, 2003)
49. Y. Barad, H. Eisenberg, M. Horowitz, Y. Silberberg, Nonlinear scanning laser microscopy by third-harmonic generation. Appl. Phys. Lett. **70**(8), 922–924 (1997)
50. M. Müller, J. Squier, K.R. Wilson, G.J. Brakenhoff, 3D-microscopy of transparent objects using third-harmonic generation. J. Microsc. **191**, 266–274 (1998)
51. J.A. Squier, M. Muller, G.J. Brakenhoff, K.R. Wilson, Third harmonic generation microscopy. Opt. Express **3**(9), 315–324 (1998)
52. D. Débarr, W. Supatto, E. Beaurepaire, Structure sensitivity in third-harmonic generation microscopy. Opt. Lett. **30**, 2134–2136 (2005)
53. D. Debarre, W. Supatto, A. Pena, A. Fabre, T. Tordjmann, L. Combettes, M. Schanne-Klein, E. Beaurepaire, Imaging lipid bodies in cells and tissues using third-harmonic generation microscopy. Nat. Methods **3**(1), 47–53 (2006)
54. D. Oron, D. Yelin, E. Tal, S. Raz, R. Fachima, Y. Silberberg, Depth-resolved structural imaging by third-harmonic generation microscopy. J. Struct. Biol. **147**(1), 3–11 (2004)
55. D. Oron, E. Tal, Y. Silberberg, Depth-resolved multiphoton polarization microscopy by third-harmonic generation. Opt. Lett. **28**(23), 2315–2317 (2003)
56. V. Shcheslavskiy, G. Petrov, S. Saltiel, and V.V. Yakovlev, Quantitative characterization of aqueous solutions probed by the third-harmonic generation microscopy. J. Struct. Biol. **147**(1), 42–49 (2004)
57. D. Débarre, N. Olivier, E. Beaurepaire, Signal epidetection in third-harmonic generation microscopy of turbid media. Opt. Express **15**(15), 8913–8924 (2007)
58. E.J. Gualda, G. Filippidis, G. Voglis, M. Mari, C. Fotakis, N. Tavernarakis, In vivo imaging of cellular structures in Caenorhabditis elegans by combined TPEF, SHG and THG microscopy. J. Microsc. **229**(1), 141–150 (2008)
59. F. Aptel, N. Olivier, A. Deniset-Besseau, J. Legeais, K. Plamann, M. Schanne-Klein, E. Beaurepaire, Multimodal nonlinear imaging of the human cornea. Invest. Ophthalmol. Vis. Sci. **51**(5), 2459–2465 (2010)
60. S. Fine, W.P. Hansen, Optical second harmonic generation in biological systems. Appl. Opt. **10**, 2350–2353 (1971)
61. M. Chan, S. Chu, C. Tseng, Y. Wen, Y. Chen, G. Su, C. Sun, Cr:Forsterite-laser-based fiber-optic nonlinear endoscope with higher efficiencies. Microsc. Res. Technol. **71**(8), 559–563 (2008)
62. L. Canioni, S. Rivet, L. Sarger, R. Barille, P. Vacher, P. Voisin, Imaging of Ca2+ intracellular dynamics with a third-harmonic generation microscope. Opt. Lett. **26**(8), 515–517 (2001)
63. A.C. Millard, P.W. Wiseman, D.N. Fittinghoff, K.R. Wilson, J.A. Squier, M. Müller, Third-harmonic generation microscopy by use of a compact, femtosecond fiber laser source. Appl. Opt. **38**, 7393–7397 (1999)
64. W.R. Zipfel, R.M. Williams, W.W. Webb, Nonlinear magic: multiphoton microscopy in the biosciences. Nat. Biotechnol. **21**(11), 1369–1377 (2003)
65. G. Cox, N. Moreno, J. Feijó, Second-harmonic imaging of plant polysaccharides. J. Biomed. Opt. **10**, 0240131–0240136 (2005)
66. R. Carriles, D.N. Schafer, K.E. Sheetz, J.J. Field, R. Cisek, V. Barzda, A.W. Sylvester, J.A. Squier, Imaging techniques for harmonic and multiphoton absorption fluorescence microscopy. Rev. Sci. Instrum. **80**, 081101 (2009)
67. C. Sun, Higher harmonic generation microscopy. Adv. Biochem. Eng. Biotechnol. **95**, 17–56 (2005)
68. J.A. Squier, M. Muller, High resolution nonlinear microscopy. Rev. Sci. Instrum. **72**(7), 2855–2867 (2001)
69. T.Y.F. Tsang, Optical third-harmonic generation at interfaces. Phys. Rev. A **52**, 4116–4125 (1995)

Chapter 8
Endomicroscopy

Tomasz S. Tkaczyk

Endomicroscopy is an emerging area encompassing several imaging modalities starting from wide-field imaging, confocal imaging, nonlinear imaging, optical coherence tomography, and others; it applies several modern technologies spanning from new detectors and sources, fiber optics, integrated micromechanical systems, new fabrication technologies, and biochemical contrasts. Endomicroscopy continuously increases its presence in clinical studies and applications. This chapter will first provide a brief introduction of endomicroscopy and then focus on design requirements and system components. This chapter will also discuss its applications in animal and clinical studies.

8.1 Introduction: Context and Application Needs

Over the last two decades, endoscopic medical diagnostics have benefited from technological developments in several key components, including fiber-optic bundles, miniature lens systems, and compact high-definition image sensors. Early endoscopes used coherent fiber-optic bundles to relay an image from the distal end of the instrument to an external eyepiece for viewing by the physician. In the 1990s, systems became available with a digital camera integrated within the tip of the endoscope, allowing images to be displayed for viewing on a video monitor. Endoscopic systems evolved thanks to advances in CCD technology, including the shift to full color chips in place of sequential red/green/blue illumination with monochrome sensors, and more recently the emergence of high pixel density sensors enabling "high-definition" (HD) endoscopy.

T.S. Tkaczyk (✉)
Department of Bioengineering, Rice University, Houston, TX 77005, USA
e-mail: ttkaczyk@rice.edu

R. Liang (ed.), *Biomedical Optical Imaging Technologies*, Biological and Medical Physics, Biomedical Engineering, DOI 10.1007/978-3-642-28391-8_8,

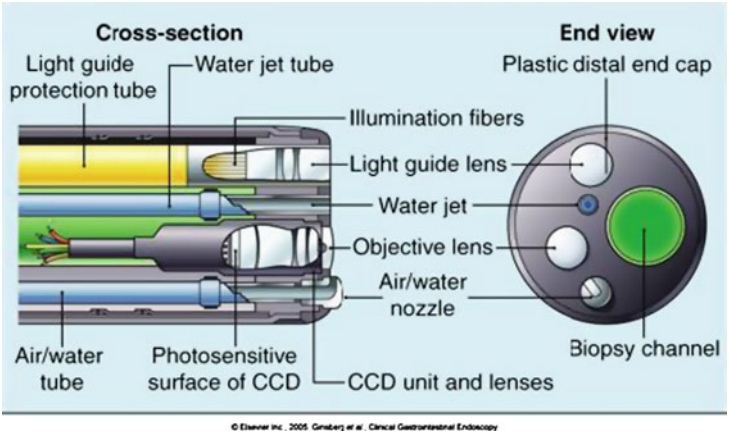

Fig. 8.1 Schematic cross section of the video endoscope tip [1]. The cross section demonstrates illumination and detection tip components as well as biopsy channel and air/water nozzle

An ongoing challenge in endoscope design involves increasing functionality and reducing endoscope diameter while including essential features such as an accessory channel for biopsy collection and air and water channels for suction and irrigation. Illumination channels are also required to deliver sufficient light intensity to obtain a clear, bright image and are separated from the imaging path to eliminate specular reflections and increase image contrast (Fig. 8.1) [1]. While current state-of-the-art endoscopes conceptually resemble their earlier counterparts, some novel forms of endoscopy have been developed, received FDA approval, and entered clinical practice. These novel techniques include for example capsule endoscopy which uses a miniature camera encased in a "pill" which is swallowed by the patient and transmits images as it passes through the gastrointestinal tract. Capsule endoscopy offers the ability to evaluate sections which conventional upper or lower GI endoscopes cannot access, such as the small intestine [2].

Endoscopic instruments are routinely used for medical diagnosis and treatment of several organs, including the upper gastrointestinal tract (esophagus, stomach, duodenum), lower gastrointestinal tract (colon, rectum), the airway, and lungs. Depending on the intended application, the endoscope may range from around 3–13 mm in diameter and provide a 90–140° field of view (FOV) with depth of field ranging from 5–50 mm. In addition to conventional white light imaging, endoscopes have also incorporated complementary modes including autofluorescence imaging (AFI) [3] and narrow band imaging (NBI) [4–6]. AFI illuminates the tissue surface with light at blue or UV wavelengths and collects only the longer wavelength fluorescent light (green) emitted by the tissue. Changes in tissue structure due to the development of cancer can alter the intensity of the fluorescent signal, assisting the endoscopist in identifying abnormal areas. NBI illuminates the tissue with red, green, and blue light within narrow wavelength bands instead of the full white light spectrum. In NBI, the reflectance of tissue at these wavelength regions is altered by the development of cancer and precancerous conditions. By digitally manipulating

the contribution of these three channels to the overall image, an improvement in contrast between abnormal and normal tissue can be achieved. In general, all of these endoscopic imaging platforms and modes provide a macroscopic or "wide-field" view of the tissue surface. This enables the endoscopist to evaluate an entire organ for abnormalities and when necessary guide the selection of sites for biopsy or endoscopic therapy.

To complement the traditional macroscopic scale view provided by endoscopy, the concept of *endomicroscopy* emerged with the goal of providing images with cellular level resolution, albeit over a small FOV. These approaches have been variously described as "optical biopsy," "*in vivo* pathology," and "endocytoscopy." Over the last 10 years, both the perception of endomicroscopy and methods for its implementation have evolved significantly. Early enthusiasm led to the belief among some communities that endomicroscopy might entirely replace traditional biopsies and pathology evaluation. Today, a more realistic role for endomicroscopy appears to lie in improving the diagnostic yield of pathology by allowing the endoscopist to target biopsy collection to the most diagnostically informative sites. By first using macroscopic methods of high-definition white light endoscopy or AFI/NBI as "red-flag" methods to highlight suspicious areas, endomicroscopy can then be used to evaluate those sites in greater detail and inform the endoscopist on whether a biopsy should be taken or whether therapy should be applied.

Endomicroscopy encompasses several imaging modalities, each of which was initially demonstrated on large-scale benchtop platforms, before undergoing the miniaturization required for endoscopic deployment. These modalities include full-field contact imaging (endocytoscopy or fiber bundle endomicroscopy), scanning confocal microscopy (in reflectance and fluorescence), and nonlinear microscopy (multiphoton, second-harmonic, and coherent scattering techniques). These approaches all generate images with subcellular level resolution, most commonly in the *en face* plane, to subsurface depths of a few hundred micrometers. Optical coherence tomography (OCT) is an approach which is considered by some to fall within the field of endomicroscopy, providing cross-sectional images of tissue to depths of around 2 mm. While OCT can delineate tissue microstructure and layered architectures, cellular level detail is generally not apparent. The related method of optical coherence *microscopy* (OCM) however does offer *en face* images with cellular level resolution, with similar operating parameters as confocal microscopy.

These endomicroscopy techniques are at various stages of clinical implementation (see Sect. 8.3 for more details), with confocal fluorescence imaging having been commercialized and under evaluation in several large-scale multicenter clinical trials. Optical coherence tomography is also being evaluated in patients at several large academic centers. Full-field contact imaging has been demonstrated in patients with small- to medium-sized studies ongoing. Nonlinear imaging techniques remain further behind in the translational pipeline largely due to the complexity of the required light sources and fiber delivery methods. Nevertheless, these implementation challenges are being addressed in laboratory settings, with data from *ex vivo*

tissues and *in vivo* animal models being reported. For more details on the current development and implementation of these endomicroscopy modes, see Sect. 8.3.

8.2 Design Requirements and System Components

8.2.1 Key Operational Parameters

8.2.1.1 Spatial Resolution and Field of View

The key distinction between conventional endoscopy and endomicroscopy is spatial resolution, the ability to provide the endoscopist with images of cellular or near-cellular level detail. With increased resolution, there is, of course, a concurrent reduction in FOV, just as one experiences when switching between different objectives on a benchtop microscope. In the field of endomicroscopy, however, systems usually require numerical aperture (NA) values above 0.4 and even up to 1.0. This requirement arises from the need to optimize the collection efficiency for weak optical signals, especially for nonlinear processes and for systems which aim to image deep beneath the tissue surface. This ability to selectively image a single subsurface tissue plane or "optical section" can extend to depths of around 200–400 μm with confocal microscopy [7] and over 500 μm for multiphoton imaging [8].

The lateral FOV should be maximized to make system more practical to use, but at high NA is usually in the range of 250–500 μm in endomicroscopy systems. This is dictated by three main reasons: (a) fundamental principle of Lagrange invariant FOV, NA, working distance, and optics diameter are strongly interrelated and have to be balanced for practical solution; (b) overall ability to fabricate and assemble miniature high-quality optics; and (c) the diameter of available coherent fiber bundles or the maximum scanning angle generated by miniaturized actuators or scanners. While simultaneously achieving high NA and FOV for small optics is challenging, the task can be somewhat mitigated by use of the shorter working distances (the distance between the imaging lens surface and the tissue). Another approach to overcome the small FOV limitation in endomicroscopy is to continuously stitch together images as the imaged field is swept across the tissue, building up a larger "macro" image for display on the monitor screen [9].

As mentioned above, optical coherence tomography generally operates in a regime where spatial resolution is lower than confocal or nonlinear microscopies, but the FOV is correspondingly larger. In most instances, the optical beam is scanned (linearly or circumferentially) to determine the lateral extent of the FOV, while the axial (depth) extent is determined by the external hardware configuration (either the physical scan range of the interferometer's reference path or the spectral resolution of the detection apparatus). The distal probe tip optics is typically configured with relatively low NA and large Rayleigh range to provide relatively uniform lateral

resolution over the depth of imaging. With spatial resolution around 10 microns, OCT systems are capable of endoscopic imaging at frame rates (10s of frames per second) which permits imaging over large areas in a relatively short time [10].

Full-field contact imaging techniques involve placing either a fiber-optic bundle or lens system directly in contact with the tissue surface, with image relayed onto a sensor. In these cases, the FOV is defined by the area of the sensor which is projected onto the tissue via the fiber bundle or lens system. For a bare fiber bundle, this area corresponds simply to the diameter of the fiber itself. The spatial resolution is on the other hand related to fiber spacing. With the addition of lenses to the fiber tip, the FOV and resolution are decreased and increased, respectively, by a factor equal to the magnification of the lens system.

A summary of typical operational parameters for currently implemented endomicroscopy systems is presented in Table 8.1. Tables 8.2 and 8.3 present examples of images obtained with these different modalities.

8.2.1.2 Optical Sectioning

High-resolution imaging within thick tissue relies on an ability to preferentially collect in-focus light over out-of-focus background. Sometimes termed "optical sectioning," both confocal microscopy and nonlinear microscopy can selectively image tissue at a single plane beneath the surface. Confocal imaging achieves this by placement of a pinhole in front of the detector at a conjugate plane to the tissue depth being imaged. Light emerging from above or below this location in the tissue is preferentially blocked by the pinhole, while light from the imaged plane passes through. Following [11], confocal microscope can provide lateral resolution defined by:

$$d_{xy} \approx \frac{0.4\lambda}{\mathrm{NA}}, \tag{8.1}$$

while axial resolution is

$$d_z \approx \frac{1.4n\lambda}{\mathrm{NA}^2}. \tag{8.2}$$

This is for pinhole diameter matching the full width at half maximum (FWHM) of the Airy disk intensity and allows 75 % of irradiance to pass through the pinhole.

Nonlinear imaging achieves optical sectioning by an alternative mechanism; due to the nonlinear dependence of emitted signal on incident light intensity, negligible signal is generated at planes above or below the focal spot in tissue. Nonlinear microscopy therefore does not require a pinhole to block out of focus light. Regardless of mechanism used to achieve optical sectioning, the working distance of the miniature endoscope objective must be sufficient to enable the focal plane to reach the desired imaging depth beneath the tissue surface. Both confocal and nonlinear techniques require miniature objective lenses with high NA

Table 8.1 Summary of operating parameters of endomicroscopes for four (contact, confocal, multiphoton, and OCT) imaging modalities

Modality	Lateral resolution[a] (μm)	NA	FOV (μm)	Working distance (μm)	Signal type	Imaging depth (μm)	Implemented in clinic
Contact imaging	6–10.0	N/A	500–1,000	0	Fluorescence	Top surface	Yes
Confocal	0.5–3.0	0.3–1.0	100–500	200–500	Reflectance and fluorescence	200 in vivo applications	Yes
Multiphoton	0.5–3.0	0.35–1.0	100–500	200–500	Multiphoton fluorescence	Usually up to 500 in the lab and 200 in tissue	Animal imaging/ex vivo
OCT	5.0–15.0	0.05–0.20	Limited by scanning range. Can be 10s of mm across	0.5–3 mm	Coherent reflectance imaging	1–2 mm	Yes

[a] While NA of optics, confocal, and multiphoton endoscopes allow high lateral resolution, the sampling might be limited by density of the fiber bundle or sampling of the scanner. The most important requirement is light collection for these two modalities

Table 8.2 Examples of images obtained with various endomicroscopic modalities (confocal fluorescence, reflectance, and two-photon)

Confocal (fluorescence): a, Image of rectal mucosa; b, Image of descending colon. Both images acquired after topical application of acriflavine. 1. Goblet cells, 2. Crypt lumen. FOV 500 by 500 μm [12]

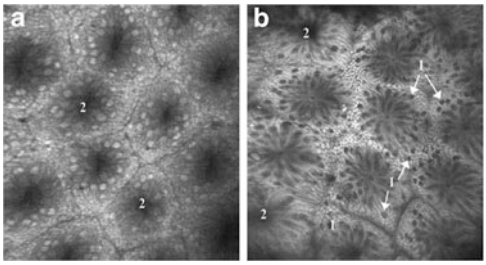

Confocal (reflectance): In vivo confocal reflectance images of ventral tongue sites. To emphasize nuclei acetic acid was topically applied. Nuclei are pointed by arrows. Scale bars: 50 μm [13]

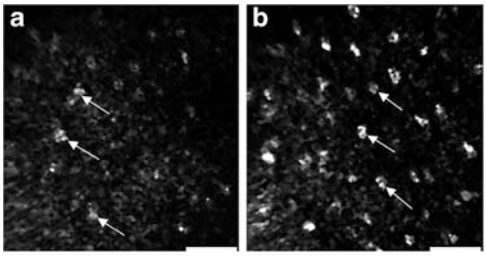

Multiphoton: Two-photon fluorescence images of a rat kidney. (a) Surface. (b)–(c) 20- and 40-μm depths. The image size is 475 μm by 475 μm. [14]

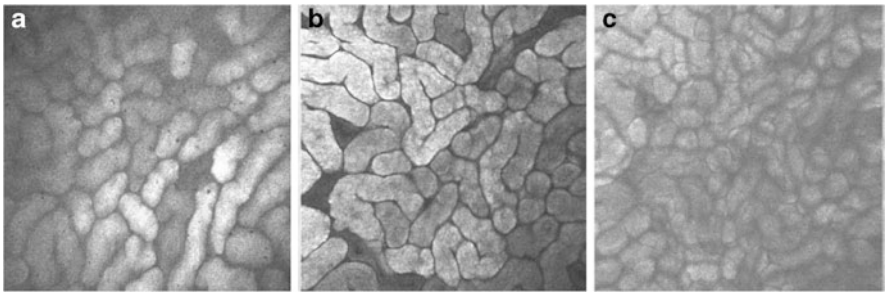

(0.4–1.0 water) for efficient light collection. In addition to light collection efficiency, the objective NA also establishes the axial resolution achieved, which can be around a few microns [15, 16]. (Factors including pinhole size in confocal microscopy as well as scattering and aberrations within tissue will degrade both axial and lateral resolution relative to the theoretical values established by wavelength and NA).

Table 8.3 Continuation of the table with examples of images obtained with various endomicroscopic modalities (contact imaging and optical coherence tomography)

Contact imaging (fluorescence): Fiber bundle contact imaging with HRME system. Top: Barrett's metaplasia and low-grade dysplasia and Bottom: esophageal adenocarcinoma. Scale bar represents 100 μm [17]

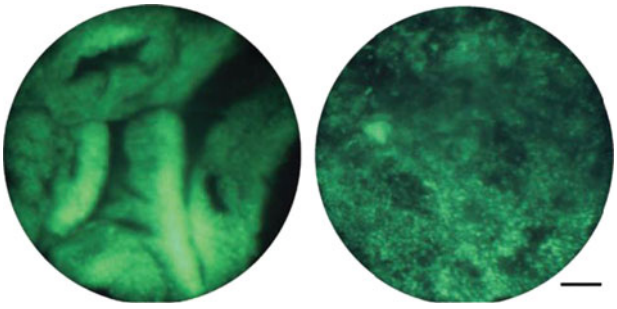

Optical coherence tomography: Top: circular transverse cross-sectional Fourier-domain OCT in vivo image of human Barrett's esophagus Bottom: expanded portion of the left figure pointing surface irregularities (black arrowheads) and glands within the epithelium (red arrowheads). Scale bar (right) and tick marks (left) represent 1 mm [10]

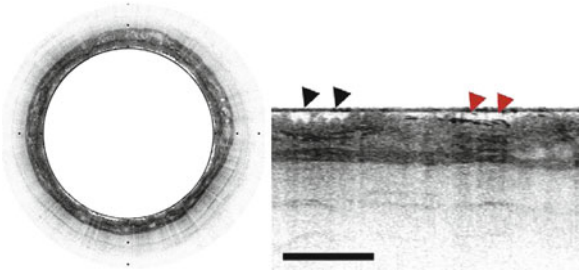

8.2.1.3 Imaging Depth

With confocal microscopy, optical sectioning can be achieved to depths ranging from 200 to 400 μm beneath the tissue surface, depending on the specific wavelengths of excitation and emission, and the optical properties of the tissue itself. Two-photon microscopy can reach greater depths due to the use of near-infrared excitation wavelengths and the ability to collect all generated fluorescence photons (no pinhole). Some recent experiments performed in the lab for 1,280-nm wavelength allowed imaging depths of 0.9 mm [18]. Typically, however, in vivo applications require lowering effective energy density and provide 200–500 μm imaging depths. Full-field contact imaging modes lack any intrinsic optical sectioning ability, imaging only the most superficial tissue layers with good contrast.

8.2.1.4 Imaging Planes

Confocal microscopy, nonlinear microscopy, and full-field contact microscopy all generate images in the plane oriented perpendicular to the optical axis (sometimes termed tangential or *en face*). This is different to the transverse cross section that is conventionally used for pathology slides. However, it is possible to acquire multiple *en face* images spanning a range of depths in tissue to create an "optical stack," amounting to an XYZ volume of data which can be manipulated to extract a single two-dimensional image in any arbitrary plane. Optical coherence tomography is distinct in that images are typically acquired in the XZ (cross-sectional) plane, analogous to histopathology. The same principle of collecting multiple 2-dimensional (XZ) images for reprocessing into a 3-D volume applies with OCT, particularly with the recent advances in imaging speed.

8.2.1.5 Imaging Speed (Frame Rate)

Endomicroscopy systems intended for clinical use require sufficient imaging speed to minimize the appearance of motion artifacts. The actual frame rate achieved by a system depends on several factors, including detection sensitivity (weaker signals require longer integration times for detection at adequate signal-to-noise ratio), speed of the scanning mechanism for point-scanning techniques, and any limitations on the illumination light intensity (which may be due to the available light source brightness or due to mandated limits for safe tissue exposure). In fluorescent techniques, light collection is the primary factor for majority of cases, and the high NA of miniature systems is highly important to sustain practical frame rates. Scanning mechanisms usually allow 15 frames per second or more for both integrated scanners [19] and external scanning systems [20–22].

Confocal fluorescence and reflectance imaging with common, clinically approved contrast agents (e.g., fluorescein, acetic acid) can reach 8–12 fps [20], although endoscopic systems with miniaturized distal scanning systems are commonly limited by the scan speed to a few or less frames per second [12, 23]. Nonlinear microscopy generates relatively weak signals, so typically requires longer integration times. Optical coherence tomography uses interferometric detection, with Fourier-domain platforms offering significantly improved detection sensitivity compared to earlier time-domain implementations. Consequently, benchtop OCT systems have surpassed 100 frames per second [24, 25], and endoscopic versions are limited by the speed of the scanning mechanism, with current state-of-the-art in the 30–60-fps range. Full-field contact imaging essentially collects light from all points within the FOV in parallel directly on an imaging detector such as a CCD or CMOS chip. With bright fluorophores (e.g., acriflavine, proflavine) these systems as well as fiber-bundle-based endoscopes can stream images to an external display at over 12 fps [26].

8.2.2 Individual Components for Endomicroscopy

8.2.2.1 Light Sources

Each of the primary modes of endomicroscopy outlined above requires light sources with specific properties. Point-scanning methods including confocal and nonlinear microscopy, as well as optical coherence tomography, require a tightly focused beam at the specimen in order to achieve high spatial resolution. This is typically achieved by using a laser source with high beam quality (M^2 close to 1, a Gaussian TEM_{00} spatial mode) to enable generation of a near-diffraction-limited spot. Full-field methods such as contact imaging can use an extended source, which can be a lamp or LED. Nonlinear techniques require an ultrafast laser source to deliver short (∼100 fs) pulses [27–30] with high peak power at high repetition rates (∼80–100 MHz). Titanium: Sapphire lasers are the most commonly used sources for two-photon and second-harmonic imaging. They usually provide a tunable output over approximately the 700–1,000-nm spectral range. Optical parametric oscillators (OPO's) are used to generate picosecond and femtosecond pulses further into the near-IR wavelength range for techniques including CARS microscopy. Endoscopic optical coherence tomography typically requires a source with high spatial coherence and low temporal coherence, the latter property being associated with a broad spectral bandwidth. Ti:S lasers are therefore commonly used for OCT imaging in the 700–1,000-nm region, but the majority of endoscopic work to enable deep tissue imaging of the 1.3-μm wavelength range uses broadband superluminescent diodes, semiconductor optical amplifiers, or rapidly swept tunable laser sources [10, 31].

8.2.2.2 Light Delivery and Collection

Endomicroscopy requires the delivery to and collection of light from confined sites within the body. This is achieved through use of fiber-optic materials which can be classified either as single optical fibers or fiber-optic bundles comprising thousands of single fibers. Use of single optical fibers for light transmission necessitates a means for laterally scanning the emerging beam at the tissue surface.

An important consideration when using both single fibers and fiber bundles is to ensure matching of the fiber NA to that of the miniature optics located at the distal tip. This allows any scattering inside the optics in the illumination path to be minimized and optical throughput to be maximized by matching the point spread function in the image with the fiber mode. Single-mode fiber has an NA typically around 0.10–0.15, while fiber-optic bundles have higher NA around 0.30–0.35. In order for any miniature optics at the fiber's distal end to match the delivery fiber's NA, the optical system needs to work at low magnification. Magnification is determined by the ratio of NA at the tissue side to NA at the fiber side. For example, using a miniature microscope objective with a relatively high NA of 1.0 (water)

Table 8.4 Comparison of selected commercially available coherent fiber bundles [32,33]

	Number of picture elements	Active diameter [μm]	Clad diameter [μm]	Coating diameter [μm]
F & T Fibers and Technology GmbH				
FTIFHR200S	3,000	180	200	250
FTIFHR350S	6,000	315	350	420
FTIFHR500S	10,000	450	500	600
FTIFHR800S	30,000	720	800	950
Fujikura				
FIGH-016–160S	1,600	140 ± 15	160 ± 20	210 ± 30
FIGH-03–215S	3,000	190 ± 20	215 ± 25	285 ± 30
FIGH-06–300S	6,000	270 ± 20	300 ± 25	400 ± 30
FIGH-10–350S	10,000	325 ± 20	350 ± 25	450 ± 30
FIGH-30–650S	30,000	600 ± 30	600 ± 30	750 ± 50
FIGH-30–850N	30,000	790 ± 50	850 ± 50	950 ± 50
FIGH-50–1100N	50,000	1,025 ± 80	1,100 ± 80	1,200 ± 100
FIGH-70–1300N	70,000	1,200 ± 100	1,300 ± 100	1,450 ± 100
FIGH-100–1500N	100,000	1,400 ± 120	1,500 ± 120	1,700 ± 150

achieves a magnification factor of 2.85 in order to match the fiber bundle NA of 0.35 [34]. In this case, while the system has good light collection efficiency due to the high object-side NA, its overall resolution is limited by the discrete sampling effect due to the fiber bundle. At its design wavelength, this objective alone can reach a theoretical 0.4 μm resolution; however, when used at the distal tip of a fiber bundle (FTIFHR800S (see Table 8.4)) with approximate fiber-to-fiber spacing of 3.9 μm, the smallest resolvable features were 2.75 μm.

8.2.2.3 Coherent Fiber Bundles

Coherent fiber-optic bundles preserve the spatial orientation of fibers throughout the length of the bundle and can therefore transmit a full-field image, or a scanned beam, from one end to the other, eliminating the need for a miniature scanner at the distal tip. However, packing of individual fibers within a bundle requires that a finite cladding volume is maintained between the light guiding cores. This results in a pixilated image with dark space between cores, limiting the achievable spatial resolution, even for the most densely packed bundle. However, the appearance of this artifact can be reduced by image processing techniques. Examples of commercially available fiber-optic bundles used for endomicroscopic applications are presented in Table 8.4. Fig. 8.2 presents typical optical fiber bundle attenuation in function of wavelength. The optimal operating range is visible wavelengths through near infrared where attenuation is the lowest.

As fiber bundles can produce autofluorescent signal, a special attention should be given for applications with short excitation wavelengths.

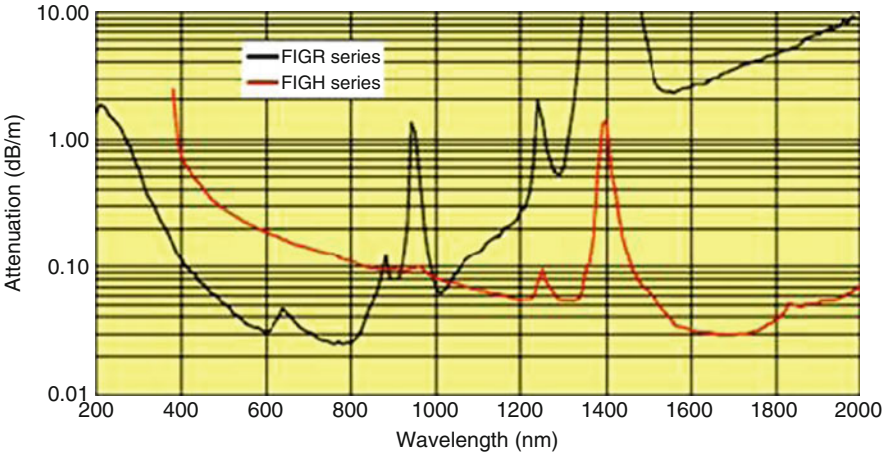

Fig. 8.2 Optical attenuation of Fujikura optical fibers [33]

Figure 8.3 presents 2-D autofluorescence plots from Fujikura, Sumitomo, (recently acquired by F & T Fibers and Technology GmbH) and Schott fiber bundles [35].

8.2.2.4 Individual Optical Fibers

Individual optical fibers include conventional or polarization-maintaining single-mode fiber, which has been used for confocal endomicroscopy in fluorescence [12] or reflectance modes [23]. Schematic view of the step-index fiber is shown in Fig. 8.4. Following [36], NA of the fiber can be described as:

$$\mathrm{NA} = \sqrt{\left(n_1^2 - n_2^2\right)}, \tag{8.3}$$

where n_1 and n_2 are refractive indices of core and cladding, respectively. The single-mode operation is met when [36, 37]:

$$\frac{2\pi a \mathrm{NA}}{\lambda} < 2.405. \tag{8.4}$$

Note that a denotes the fiber's core radius. The left side of relation is known as normalized wave number.

Nonlinear endomicroscopy requires the delivery of ultrafast laser pulses to the tissue, which is not possible with conventional fiber without excessive pulse broadening and resulting loss of intensity. Negatively prechirping the excitation laser pulses can compensate for group velocity dispersion within the fiber; however, higher order effects such as self-phase modulation (SPM) are not compensated.

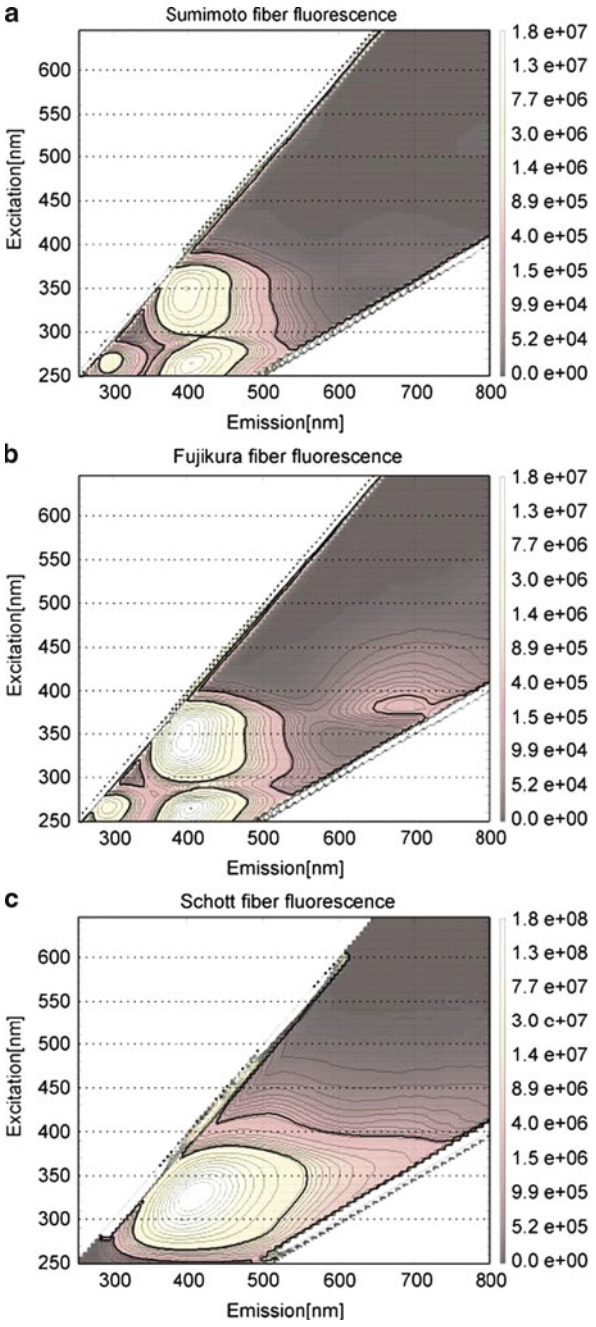

Fig. 8.3 2-D (emission/excitation) maps for Sumitomo, Fujikura, and Schott fiber bundles. Note that UV wavelengths produce the highest fluorescence signal for all fiber bundles [35]

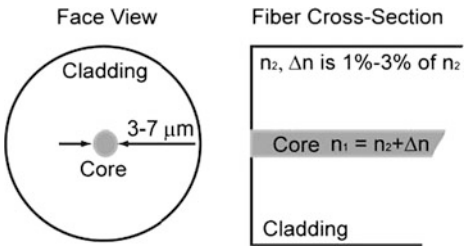

Fig. 8.4 Schematic of the single-mode index fiber

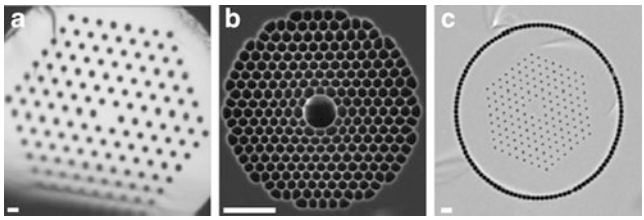

Fig. 8.5 Photographs of selected PCFs applicable to nonlinear endomicroscopy. **a** large-mode-area PCF, **b** hollow-core photonic bandgap fiber, and **c** double-clad PCFs [21]

Specialized fibers with tailored dispersion properties have been developed which can deliver the required laser pulses over the distances required for endomicroscopy with minimal dispersion or distortion. Photonic bandgap fibers and photonic crystal fibers (PCF) confine and guide light by use of periodic arrays of air holes. The core of the fiber is either made of air (which does not introduce SPM) or has a large mode area which allows delivery of light at lower intensity, reducing the generation of unwanted nonlinear effects in the delivery fiber. A third type of fiber for nonlinear endomicroscopy is the double-clad fiber, comprising a single-mode core for light delivery, surrounded by a larger multimode core for efficient light collection. Since all light generated in the tissue by nonlinear processes carries useful information, the aim is to simply collect as much light as possible, without the need for single-mode collection and descanning required by confocal imaging. Examples of selected PCF types are shown in Fig. 8.5.

Main characteristics of these fibers (Fig. 8.5) include [21]:

- Large-mode-area PCF provides a low level of self-phase modulation and allows single-mode operation over the broad pulse bandwidth. On the other hand, it has low collection NA and requires dispersion compensation.
- Hollow-core photonic bandgap fiber works within narrow wavelength range and has low effective collection NA. It is, however, very efficient and allows minimal propagation loses. It also does not require prechirping compensation.
- Double-clad PCF is characterized with low self-phase modulation, has a high collection NA (cladding), and provides dual illumination/collection functions. Similar to large-mode-area PCF, it requires dispersion compensation.

8.2.2.5 Beam Scanning Methods

Most endomicroscopy modalities require a scanning mechanism to sweep a focused spot across the tissue surface. Beam scanning is either performed at the proximal end of a fiber-optic bundle or at the distal tip of a single optical fiber. Clearly, the scanning mechanism must be miniaturized in the latter case, where its dimensions may impact the overall size of the endoscopic probe. Proximal scanning is relatively straightforward to achieve by use of galvanometric scanners, resonant scanners, DMD mirror arrays, translations stages, or other means [36]. Distal tip scanning can be performed by translation of the entire probe, either in a linear or rotational motion, with the translating force applied by a unit located external to the probe [10]. Alternatively, the probe can remain stationary and the beam exiting the delivery fiber can be scanned by a miniaturized version of the common macroscopic scanners.

While the ability to perform optical sectioning endomicroscopy without miniaturizing the scanning elements is an appealing feature of the fiber-bundle-based platform, the discrete nature of individual cores within the bundle leads to the appearance of the bundle structure within the image and can ultimately limit the spatial resolution. Two distinct approaches have been demonstrated which replace the fiber bundle with a single optical fiber and perform beam scanning through miniaturized mechanisms at the distal tip. These mechanisms can be based on use of piezoelectric actuators to sweep the fiber tip itself in a scanning pattern, which may be a linear raster or spiral motion [19, 38, 39]. These standard quad piezos have diameters ranging from 1 to 3 mm. Another option is to apply MEMS technology to create tilting mirrors for beam scanning.

Conceptual schematics and pictures of the piezo scanning and electrostatic MEMS approaches are shown in Figs. 8.6 and 8.8, respectively. The unit shown in Fig. 8.6b [38] is based on modulating a four-electrode tube piezo with a sinusoidal waveform. Each electrode pair is modulated with a 90° phase shift, generating a spiral scanning path. Therefore, following [39], the applied electrode modulation can be described with following functions:

$$+x = \sin(r)\sin(\theta), \tag{8.5a}$$

$$+y = \sin(r)\cos(\theta), \tag{8.5b}$$

where r corresponds to radial position while θ is a rotation angle.

The delivery fiber extending from the tube falls into resonance, allowing for a larger movement of the fiber tip than the piezoelectric actuator itself, with operation at low voltages (approx. 10V). The scanning range depends on the extended length of the fiber, which in turn affects the resonant frequency. The typical scan range is 100–300 μm, while the resonant frequency is usually set between 500 Hz and 10 kHz. This frequency can be obtained using numerical methods [19] or analytical models. In general [38, 40], a resonant frequency can be defined as:

$$f = \frac{\beta}{4\pi}\sqrt{\left(\frac{E}{\rho}\right)}\left(\frac{R}{L^2}\right). \tag{8.6}$$

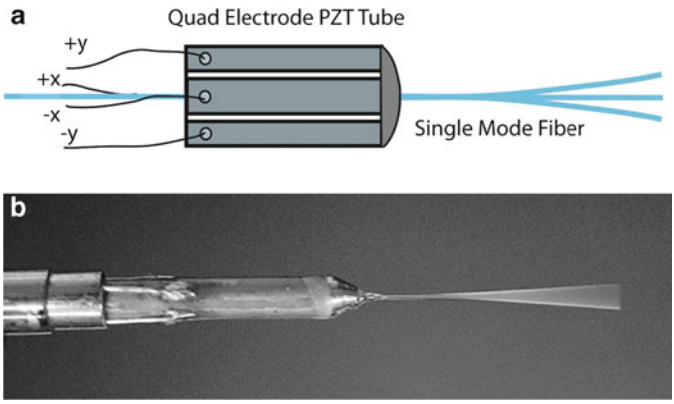

Fig. 8.6 (**a**) Conceptual drawing of a piezo-driven single-mode fiber scanner miniature endoscope. (**b**) Picture of a resonating device for endoscopic application [38]. Note that diameter of the piezo component including mounting base is 1.8 mm

L and R are respectively the length and radius of extended fiber. E and ρ denote Young's modulus and the mass density. β is a constant related to the vibration mode and boundary conditions of the fiber fixture. It is also possible to design a scanning mechanism with a short scanning range while optically relaying the change of angle of the fiber tip. In this case, a small lens is attached at the distal end of the probe. A comparison of both cases is demonstrated in Fig. 8.7. The detailed design principles are provided in [19].

The second technique is MEMS technology to fabricate miniaturized beam scanning systems [41] which can be mounted distal to a single, fixed optical fiber which both illuminates and collects light from the sample. Miniaturized optics are then located distal to the MEMS component to focus the scanning beam onto the tissue and collect remitted light. Several techniques for fabricating MEMS scanners have been reported from early work by Dickensheets and Kino [42], who fabricated a scanner comprising two separate mirrors with orthogonal scan axes by micromachining and etching in silicon. Solgaard's group at Stanford designed a scanner with a single reflecting mirror in a two-axis gimbaled arrangement which eliminated the need to incorporate a pair of discrete scanners to achieve a two-dimensional scan [43]. This design was incorporated in a benchtop prototype confocal microscope which uses a single polarization-maintaining fiber to transmit light to and from the tissue sample with a compact 5-mm-diameter 3-element objective lens positioned with its rear focal plane coincident with the MEMS scanner [23]. The system demonstrated reflectance confocal imaging of ex vivo and in vivo human oral mucosa at 8 frames per second, resolving individual cell nuclei. However, the FOV was relatively small, at only $140 \times 70\,\mu$m, due to the maximum achievable scan angles provided by the MEMS mirror. The same fabrication process involving deep reactive ion etching was used to fabricate a different MEMS scanner design, with two separate reflecting regions each to accommodate separate beams,

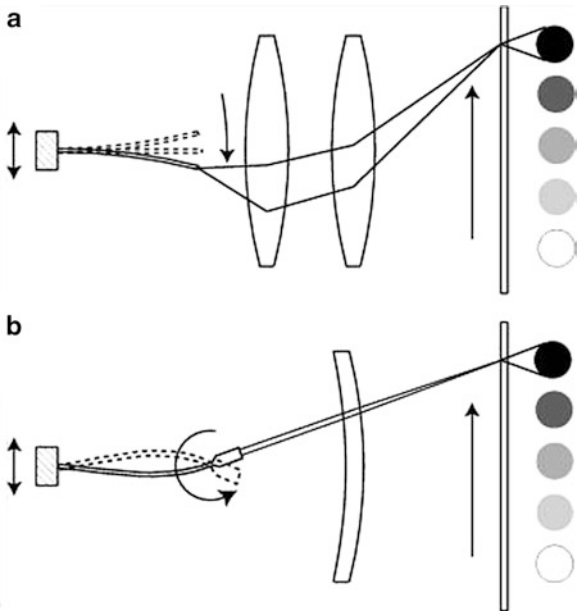

Fig. 8.7 Two general cases of the single-mode fiber scanning: (**a**) actuating a fiber at its first mode resonant frequency resulting in large tip displacement and (**b**) second mode frequency resonance causing small tip movement at large angular changes [19]

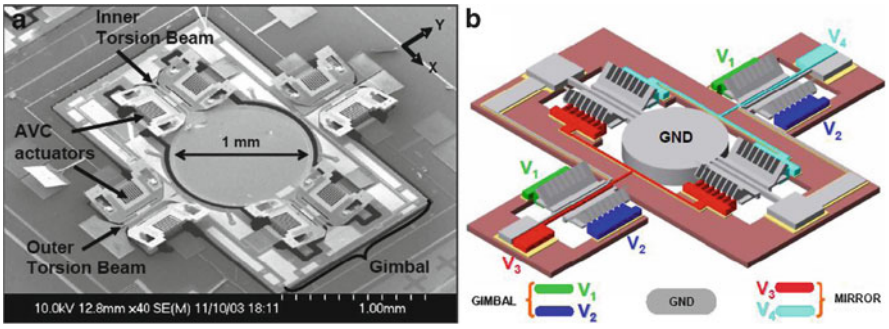

Fig. 8.8 MEMS scanner for an endoscopic applications. **a** SEM scanner image and **b** Electrical schematic of the MEMS device [44]

one delivering illumination light and one for collection, which intersect at the object plane [45]. This "dual-axes" or "theta confocal" configuration offers good optical sectioning with well-matched resolution in axial and lateral directions; however, the FOV, as determined by the available MEMS scanner range, remains limited.

MEMS mirror scanners are usually based on the application of electrostatic comb drives (see example in Fig. 8.8 [44]). A change of potential between comb electrodes can introduce both linear and angular movement of electrodes, with angles ranging

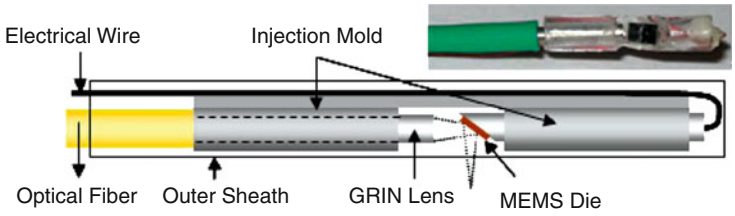

Fig. 8.9 Schematic and photo of an OCT endoscope's tip using MEMS scanner. Note that outer diameter of the encapsulated (to avoid obstruction outer layer is not shown) system is 4 mm [46]

from few to over 20° [46]. Implemented MEMS scanners have dimensions of 2–3 mm including the reflective mirror surface and actuating mechanism. An example of the MEMS implementation for OCT probe is shown in Fig. 8.9. When operating at their resonant frequencies, MEMS scanners can be run at lower power, with consumptions in the Watts range. Unfortunately these systems remain quite large, increasing the overall endoscope size and making it difficult to package the system for passage through a standard biopsy channel. MEMS scanners also usually require custom fabrication and are expensive to prototype.

In addition to the lateral (XY) scanning mechanisms described above, axial scanning methods have been developed to achieve imaging at different depths within tissue. These include translating the entire probe tip [47], using hydraulic suction to physically pull tissue toward or away from the objective lens [13], or translating the last lens of the miniature objective system [48].

8.2.2.6 Miniature Optics

Miniature objectives are one of the most important components of endomicroscopes. They need to provide high NA over a sufficiently large FOV to make endoscopic application practical. Objective systems can be divided in two groups: those that use gradient refractive index (GRIN) materials and those based on miniature multi-lens microscope objectives. Both groups have been broadly used for most imaging modalities. Note that with a lens of small outer diameter, in order to maintain high NA (and consequently efficient light collection and high resolution), either the working distance or FOV are usually reduced. However, for smaller lenses, aberrations actually scale down, allowing an improvement in the ratio between lens diameter and effective FOV compared to classical larger microscope objectives.

GRIN Lens-Based Miniature Objectives

GRIN lenses are rod-shaped components. Most commonly, the index of refraction varies radially, an effect obtained by ion exchange processes during fabrication. The index of refraction has a maximum value on axis and falls off quadratically to a

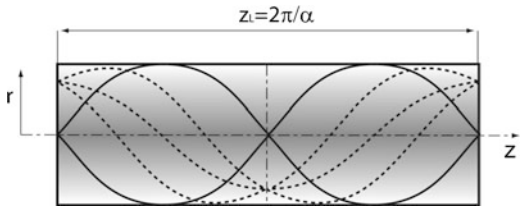

Fig. 8.10 GRIN lens operation showing on-axis (*solid lines*) and off-axis propagation (*dashed lines*)

minimum value near the edge of the rod. Following description in [49], the function describing refractive index distribution is:

$$n^2(r) = n_0^2(1 - \alpha^2 r^2), \tag{8.7}$$

where n_0 is a refractive index on axis, α is a distribution constant, and r is a radial coordinate. For small $\alpha 2r^2$ refractive index distribution is often approximated with parabolic function and takes following form [36, 49]:

$$n(r) = n_0 \left(1 - \frac{\alpha^2 r^2}{2}\right). \tag{8.8}$$

The schematic drawing demonstrating GRIN lens operation is shown in Fig. 8.10. The figure demonstrates on-axis (solid lines) and off-axis (dashed lines) propagation of optical rays. At distances of Z_L and $Z_\mathrm{L}/2$, a GRIN lens creates an upright image and inverted image, respectively. $Z_\mathrm{L}/4$ corresponds to collimated beam. Therefore, the length of the component will determine its operating properties and lengths of multiples of pitch; half and quarter pitch can be selected. A focal length of the GRIN lens depends also on the length Z of the component [49]:

$$f_\mathrm{GRIN} = \frac{1}{n_0 \alpha \sin(\alpha Z)}. \tag{8.9}$$

NA of the GRIN lens [49] will depend on the lens diameter D and is:

$$\mathrm{NA} = \frac{n_0 D \alpha}{2}. \tag{8.10}$$

Note that the original application of GRIN lenses was telecommunication applications so they are not inherently suitable for high NA and large FOV imaging, but their obvious advantage is both in simplicity and small size. They are available, for example, through NSG in Japan or GRINTECH in Germany. Several groups have used GRIN lenses to relay an image of the tissue site to a region outside the body, where conventional macroscopic optical elements and detectors record the image. Jung et al. demonstrated full-frame epifluorescence imaging within the brain of living mice and rats with GRIN relay [50]. Kim et al. [22] implemented confocal fluorescence imaging with the source, detector, and scanning system located proximal to a triple GRIN lens, 1 mm in diameter. Images were $250 \times 250\,\mu\mathrm{m}$

and acquired at 30 frames per second. Pillai et al. also showed confocal fluorescence imaging by raster scanning proximal to a GRIN lens assembly [51]. This assembly is noteworthy in that the optical design permitted a relatively large aspect ratio to be realized; 25 mm long with a diameter of only 350 μm, allowing the imaging lens to be passed through the lumen of a 22-gauge needle and advanced deep into tissue. These GRIN-lens-based systems generate a magnified image of the tissue located at the object plane, which is oriented parallel to the distal face of the GRIN lens, usually with a small working distance (10–100 μm). Kim et al. demonstrated a method, similar to that used in rotary OCT catheters, which provides a sideways-viewing probe by bonding an aluminum-coated microprism to the distal face of a GRIN lens assembly, folding the optical path by 90° [22]. When inserted into tissue, this configuration provides a cross-sectional or transverse image of tissue along the wall of the insertion hole, oriented as in conventional histopathology. A second application of this GRIN lens–prism combination is in imaging the epithelial lining within narrow lumen organs such as the mouse colon. By rotating the probe about its axis, an image of the entire wall circumference can be collected. When a spiral scan pattern is used (probe rotation combined with pullback), the lumen of an entire organ can be imaged.

While these and other studies have taken advantage of the small size and availability of GRIN lens components, a fundamental limitation is that GRIN lens objectives are still quite short and must be fixed in position relative to the scanning beam and tissue site. Imaging through flexible, narrow, fiber-optic components can permit imaging in freely moving animals and thus might be more practical for clinical application. More recently, higher-performance lenses (see Table 8.5) were added to the list of available GRIN-based components and enabled more challenging applications like nonlinear tissue imaging [52].

The three major types of GRIN or GRIN related lenses used in endomicroscopy are single element GRIN lenses (see Fig. 8.11a), two different GRIN lenses (Fig. 8.11b), and hybrid hemisphere–GRIN lens objectives (Fig. 8.11c) (versions with hemispherical lens and two GRIN lenses are also available see Table 8.5). Two-element confocal miniature objectives combine two different focal length components. For example, following [53], short focal length objective lens can be made by silver/sodium ion exchange in glass. This allows reaching refractive index gradient between 1.626 and 1.547 on axis and at the edge, respectively. Component 2 – imaging lens of a shorter focal length can use lithium/sodium exchange process. Examples of focal lengths for both components are 0.93 and 2.41, respectively, to provide 0.5 NA lens [53]. These types of lenses can be integrated with miniature scanning mechanisms or build as long rigid systems. The use of a compound GRIN lens assembly comprising a short pitch length (high NA) GRIN lens optically bonded to a one-quarter, three-quarter, five-quarter, etc., pitch lower NA relay GRIN lens, results in a GRIN assembly below 1 mm in diameter and up to several centimeters in length. The length of the assembly ultimately determines the available imaging depth on insertion into tissue. It should be noted though, that optical aberrations accumulate with increasing pitch (or multiple components), so excess length should be avoided. As with conventional wide-field epifluorescence,

Table 8.5 Comparison of selected lenses for all three GRIN lens types

Lens type	Object NA	Image NA	WD (μm)	M	Wavelength (nm)	FOV	Data source
Single GRIN lens component	0.46	0.32	900	1.42	800–900	85–150 μm imaged area	Estimates based on [39]
Two GRIN element –fluorescence	0.5	0.13 (est.)	74	Approx 4x	633	Nearly diffraction limited over entire 280 μm field	[53]
Two GRIN element –fluorescence	0.5	0.2	300	2.5	880	320 μm imaged area	[55]
2 GRIN lenses + hemisphere – fluorescence	0.8	0.18	80	4.65	488 (excitation)	NA 0.8 on axis NA 0.6 for 35 μm field position NA 0.4 for 100 μm field position	[56] GT-MO-080–018–488
2 GRIN lenses + hemisphere – two photon	0.8	0.18	200	4.8	800–900 (excitation)	NA 0.8 for 30 μm field position NA 0.6 for 60 μm field position NA 0.5 for 100 μm field position	[57] GT-MO-0 80–018–810
GRIN + hemisphere – fluorescence	0.8	0.415	80	1.92	488 (excitation)	NA 0.8 for 20 μm field position NA 0.6 for 70 μm field position NA 0.4 for 100 μm field position	[56] GT-MO-080–0415–488
GRIN + hemisphere – two photon	0.8	0.415	200	1.92	800–900 (excitation)	NA 0.8 for 70 μm field position NA 0.6 for 90 μm field position NA 0.5, +100 μm field position	[57] GT-MO-080–0415–810

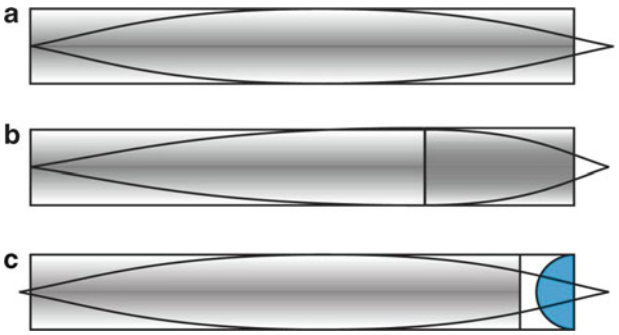

Fig. 8.11 Schematic of three types of GRIN or GRIN-related lenses used in endomicroscopy: **a** single element GRIN, **b** combination of two GRIN lenses, and **c** hybrid hemisphere-GRIN lens objective. Note that same length of systems was presented for simplicity, while in fact the length of objectives will vary between the types

out of focus light emanating from above and below the focal plane in thick tissues will degrade image contrast. Methods to reduce out-of-focus light which have been implemented on benchtop microscopes have also been adapted to endomicroscopy systems (e.g., structured illumination, confocal, or nonlinear imaging modes). To achieve optical sectioning by confocal or nonlinear methods, a focused beam can be scanned over a plane proximal to a GRIN lens assembly, which will relay this plane to the tissue surface.

A more advanced realization of GRIN-lens-based objectives combines a GRIN component with a hemispherical lens element Fig. 8.11C. Such objectives can reach 0.8–0.85 NA in water. The interesting feature of this design is that optical design software can indicate an appropriate ion exchange process to correct for some aberrations of the system [52]. Refractive index distribution of $n(r) = n_0 + n_{r2}r^2 + n_{r4}r^4$ can be considered, where n_{r2}, n_{r4} are experimentally derived coefficients to optimize it for operation with refractive first component lens.

Note that the commercially available lenses of this type allow 0.8 NA at working distances of 80 μm (fluorescence endomicroscopy design) and 200 μm (2-photon design). The lenses have a variable performance across the field and at the 50 μm field point system performs at diffraction limited performance drops so effective NA is in 0.4–0.5 range [56]. A graph showing this dependence for fluorescence design from GRINTECH is presented in Fig. 8.12. This suggests that the useful FOV for *in vivo* imaging might be limited only to 60–80 μm, for example, in 2-photon applications [52]. A brief comparison of selected lenses for all three GRIN lens types is shown in Table 8.5. The comparison includes commercially available lenses and examples of lenses reported in literature for endoscopic applications.

Miniature Compound Lenses

Another class of miniature objective lenses involves systems comprised of several individual lens elements. This approach parallels traditional microscope objective

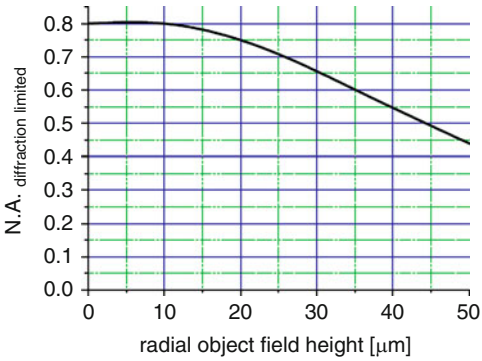

Fig. 8.12 Dependence between diffraction limited performance at different field locations for equivalent NA. Data is presented for fluorescence GRINTECH hybrid objective GT-MO-080-0415-488 [56]

design and allows the designer more degrees of freedom to satisfy criteria including FOV, NA, image quality, field flatness, and correction of chromatic aberrations. These systems are usually custom made, quite expensive to prototype, and tedious to build, with assembly usually the primary cost-driving factor. The design itself is a standard process, as are the capabilities of today's fabrication processes (grinding and polishing, diamond turning and injection molding). In addition, these modern fabrication techniques allow creation of aspherical optical surfaces that can simplify the overall optical design [58]. A comparison of selected lens implementations is presented in Fig. 8.13 and Table 8.6. Note that numbers in figure and table correspond to the same lens and that schematics of optical layouts in Fig. 8.13 are not to scale between each other.

Lenses 1 and 2 were built with traditional technologies (grinding and polishing, using glass materials). Lens 1 uses 8 spherical components, is corrected for single wavelength illumination, and can image up to 450 μm in depth. This system was designed with hydraulic suction to change the distance between the focal plane and the tissue to enable optical sectioning at different axial positions when coupled with a confocal platform. Lens 2 is particularly interesting though quite complicated and costly to manufacture. It provides a NA of 0.46 over a 450 μm FOV. This system is achromatized for significant spectral range spanning over the 480–660 nm. The aberration correction was accomplished through the use of multiple singlet, doublet, and triplet lens components and different glasses (SFL6, N-PSK53, and F2). To enable imaging at adjustable depths, the last lens can be moved, allowing the object plane to be translated from 0–200 μm.

Objectives 3, 4, and 6 were designed with the intention of simplifying the assembly process and enabling mass production techniques to be applied. The ultimate targeted fabrication technique was injection molding, while Lens 4 and 6 prototypes had elements prototyped with diamond turning in plastic. Lens 4 also incorporated a single low-tolerance spherical glass lens. For assembly, Lens 3 used kinematic mounts embedded in the lens itself. This feature increased the overall diameter to 8 mm while the clear aperture was actually 2.75 mm. Lenses 4 and 6 were assembled using self-centering springs [34] to automatically place components in the correct lateral position. Note that use of plastic materials

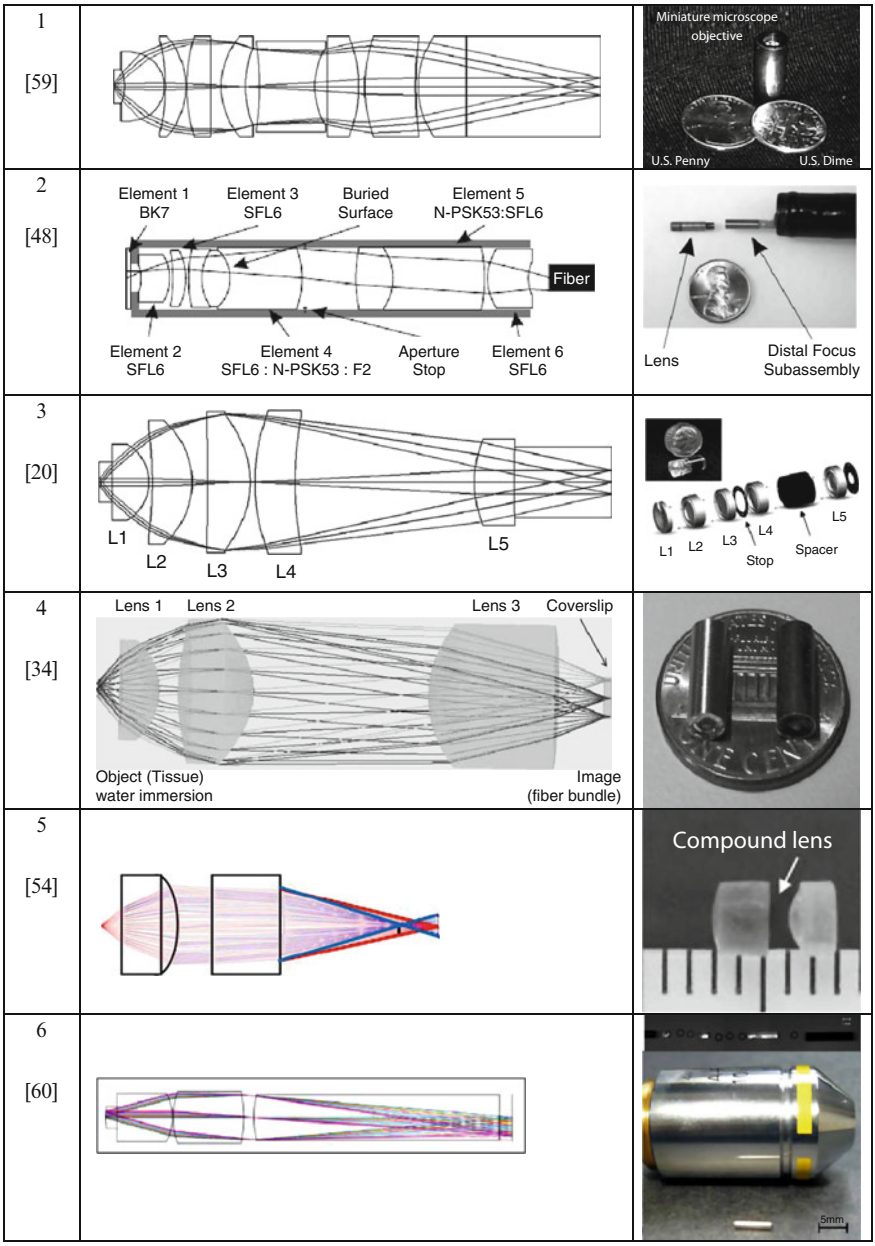

Fig. 8.13 Pictorial comparison of selected miniature microscope objectives for endomicroscopy and their implementations. Note that schematics of optical layouts are not to scale between each other. Quantitative comparison is included in Table 8.6

Table 8.6 Summary of parameters of selected miniature objectives used for endomicroscopy

	NA	FOV (μm)	WD (μm)	OD (mm)	λ (nm)	Technology	Application
1 [59]	1.0W	250	450	7	1,064	Glass spherical lenses/grinding and polishing	Confocal reflectance
2 [48]	0.46	450	0–200	3	480–660	Glass spherical lenses/grinding and polishing	Confocal fluorescence
3 [20]	1.0W	250	450	8	1,064	Plastic injection molding	Confocal reflectance
4 [34]	1.0W	250	450	3.9	810	Diamond cutting and self-assembly mounts	Confocal reflectance
5 [54]	0.5	120	650	2.2 (clear aperture)	810	–	2-Photon, second-harmonic
6 [60]	0.4	250	200	1.3	800	Plastic diamond turning or injection molding. Self-assembly mounts	2-Photon and fluorescence versions
7 [14]	0.35	475 x 475	NA imaging up to 80 μm	3.0	800	–	2-Photon

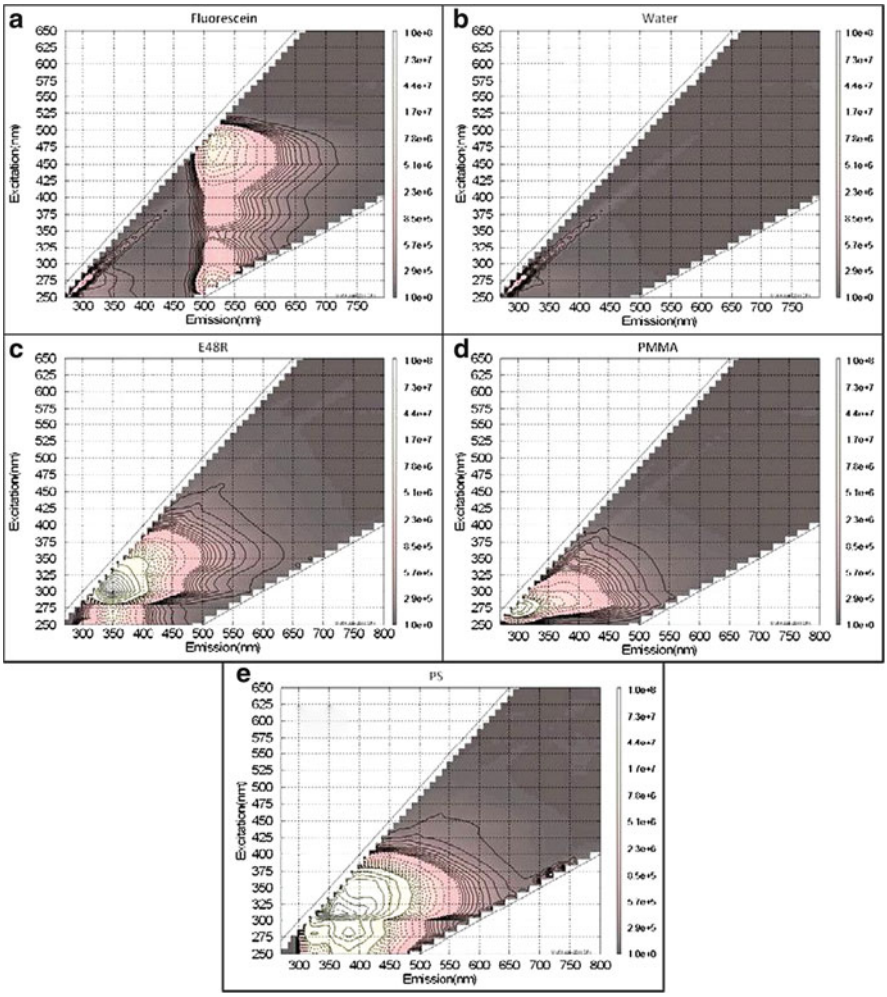

Fig. 8.14 The autofluorescence data for selected plastic, water, and fluorescein and three common optical plastic materials: PMMA, PS, and Zeonex [60]

with molding/diamond turning allowed the creation of aspheric surfaces which significantly reduced the overall system complexity. Lens 4 is simpler than Lens 3 while maintaining the same clear aperture and NA due to the fact that the glass element (far left) provides high initial power, which is later corrected with two aspheric, plastic components. Note that the use of plastic materials is more suitable for longer wavelengths as for the intrinsic autofluorescence of plastics tends to be far higher for incident light in the 400–500-nm range. The autofluorescence data for selected plastic, water, and fluorescein is presented in Fig. 8.14, and the transmission for three common plastic materials (PMMA, PS, and Zeonex) is shown in Fig. 8.15.

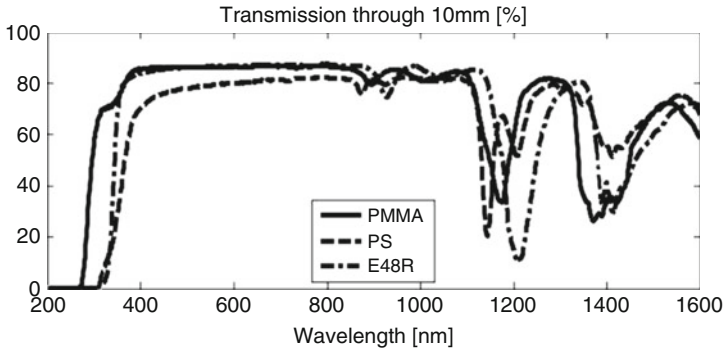

Fig. 8.15 Transmission for three common optical plastic materials: PMMA, PS, and Zeonex [60]

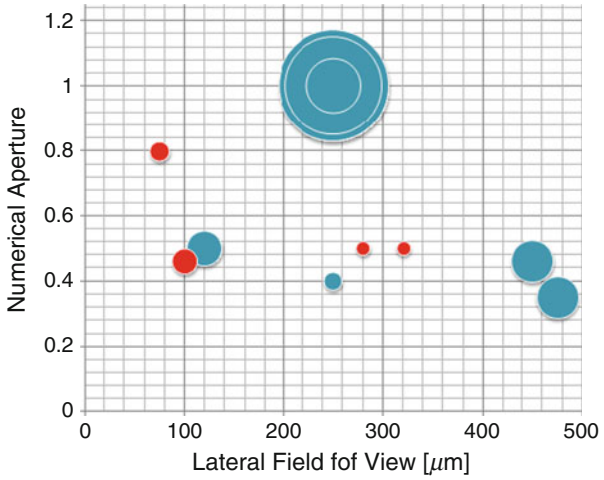

Fig. 8.16 A graphical summary of the data listed in Tables 8.5 and 8.6. field-of-view (FOV) size, NA, and the outer lens diameter are presented. The size of the *circle* represents each objective's OD. GRIN and hemispherical lens-GRIN assemblies are denoted with *red*, while compound miniature lenses are plotted in *blue*

Note that lenses 5 and 7 (Table 8.6, Fig. 8.13) were not discussed in detail due to limited design data.

A graphical summary of the data listed in Tables 8.5 and 8.6 is presented in Fig. 8.16. The graph shows a map of field-of-view size, NA, and the outer objectives diameter after assembly (the size of the circle represents each objective's OD). GRIN and hemispherical lens-GRIN assemblies are denoted with red, while compound miniature lenses are plotted in blue. An obvious trend can be noticed; GRIN lenses are significantly more compact; however, they usually provide smaller FOV for equivalent NA. In addition for higher NA they often work with shorter working distance. Multi-lens systems have larger diameters but also offer a more

practical FOV and WD. It should be noted that except some unique applications, an objective diameter of 2.5–4 mm is usually acceptable. This diameter range permits passage through the standard accessory port of video endoscopic systems.

8.3 Applications

The design principles described in Sect. 8.1 and the core components described in Sect. 8.2 have been applied and combined in many different configurations aimed at translating endomicroscopy into animal and clinical studies. This section describes how endomicroscopy systems have been applied in the laboratory, entered early stage testing on biological specimens and in animal models, and are being currently used in human subject clinical studies.

8.3.1 Endocytoscopy

Conventional endoscopes in current clinical use (including gastroscopes, colonoscopes, bronchoscopes, etc.) are typically characterized as standard definition (SD) or high-definition (HD) instruments, depending on the number of pixels used for imaging [61]. Recent advances in the pixel size and density of CCD and CMOS image sensors have led to instruments with up to 1.25 megapixel chips reaching the commercial market. These HD scopes are used in the conventional fashion to examine the mucosal surface for abnormalities under white light illumination. While clinically relevant features such as the microvasculature can be seen in exquisite detail, even HD scopes cannot resolve the individual cells of the mucosa. A relatively recent development toward this goal is endocytoscopy, which is essentially a very high-resolution/small FOV form of endoscopy [4, 62]. Through the use of probe-based systems which are passed within the accessory channel of a standard endoscope, or integrated systems which are built into a standard endoscope, endocytoscopy refers to the direct imaging of the tissue surface onto a digital image sensor, with sufficient resolution and magnification to observe individual cells. The technique requires the mucosa to be stained with a topical contrast agent, typically 0.5–1 % methylene blue or 0.25 % toluidine blue, immediately prior to imaging. Images are acquired with a very short working distance, with the tip of the probe (or a slightly protruding cap) placed in direct contact with the mucosal surface. This results in a typical FOV of $400 \times 400\,\mu$m and lateral resolution around $4\,\mu$m. Olympus (Tokyo, Japan) manufactures a selection of both probe- and endoscope-based platforms with parameters in this range and also with higher resolution at the expense of FOV. The depth of field for these systems is typically 30–50 μm, but this does not imply optical sectioning or rejection of out-of-focus light in as provided by confocal and nonlinear endomicroscopy platforms.

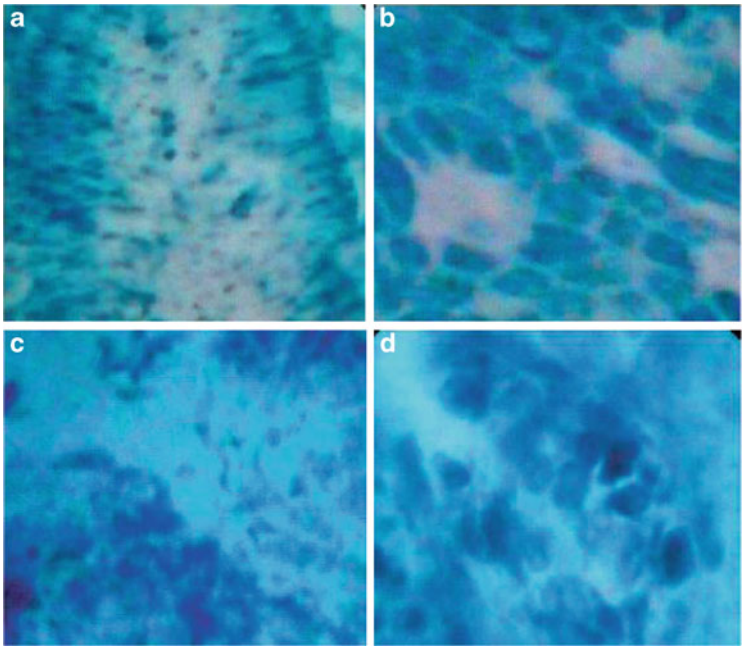

Fig. 8.17 Image produced by endocytoscopy in the human esophagus, in vivo, illustrating cellular level features in normal tissue (**a** and **b**) and in squamous cell carcinoma (**c** and **d**). **a**, **c** and **b**, **d** correspond to 450 and 1,125 magnifications, respectively. Normal tissue demonstrates uniform glandular structure, while abnormal tissue orientation of cells is random and irregular [63]

The use of endocytoscopy with chromoscopic dyes such as toluidine blue primarily allows individual cell nuclei to be seen, with criteria such as nuclear density, pleomorphism, and nuclear-to-cytoplasm area ratio used to differentiate neoplastic from nonneoplastic mucosa. Figure 8.17 illustrates the type of image produced by endocytoscopy in the human esophagus, in vivo, illustrating these cellular level features in normal tissue and in squamous cell carcinoma. Endocytoscopy has been used to evaluate Barrett's esophagus, a recognized risk factor for neoplastic transformation to adenocarcinoma, as well as cancers of the colon, stomach, and lung. In terms of imaging parameters (FOV and resolution, working distance), endocytoscopy is very similar to confocal endomicroscopy; however, the images with the former technique tend to exhibit lower contrast, likely due to the lack of optical sectioning. While the use of established dyes that are also used in chromoendoscopy is appealing, the resulting range of tissue features that can be observed (nuclear morphology) may be limited, with consequences for the ability to identify neoplasia. Several pilot clinical studies have begun to evaluate the diagnostic performance of endocytoscopy against histopathology [63]. A clear advantage of endocytoscopy is its ability to provide cellular level information in real time, enabling the endoscopist to inspect suspicious regions that are identified

on conventional endoscopy. Current limitations include the inability to see beyond the most superficial tissue layer (a few 10s of micrometers of tissue) and a lack of established criteria with which to make a diagnosis.

8.3.2 Fiber-Optic Endomicroscopy

The simplest implementation of fiber-optic-based endomicroscopy uses a length of image guide fiber (also known as a coherent fiber bundle) to relay an image of the tissue located in contact with the distal tip to an image sensor (CCD, CMOS, film, or the human eye). This approach has been demonstrated in wide-field epifluorescence and reflectance modes. Epifluorescent imaging has used exogenous contrast agents to generate contrast; Dromard et al. used topical fluorescein to enable contact imaging of the skin [64]. Muldoon et al. carried out pilot clinical studies which established the relevant image features observable in this configuration which can be used to distinguish normal from neoplastic tissue in the oral cavity and esophagus [65, 66]. A portable, battery-powered version of this system was described by Pierce et al. [67], which was subsequently used during screening endoscopy in the esophagus and colon of patients [68]. Zhong et al. reported a quantitative study of tumor detection and photodynamic therapy treatment with a similar system configured for imaging indocyanine green in the near infrared [69]. This simplicity and relatively low cost of this platform has led to its use in several applications, including imaging of tuberculosis bacilli [70] and for detecting lymph node metastases in breast cancer patients [71]. A fiber bundle can be combined with a GRIN lens to effectively improve the spatial resolution of the system by directly bonding the low NA side of the GRIN assembly to the distal face of the bundle. The spatial resolution of the system will be increased beyond that dictated by the core spacing of the bundle alone by a factor equal to the GRIN lens magnification; however, the FOV is reduced by the same factor. Flusberg et al. demonstrated an elegant miniaturized epifluorescence imaging setup with a fiber bundle and GRIN lens assembly, weighing only 1.1 g, sufficiently light to attach directly to a living mouse to study cellular processes (blood flow and calcium dynamics) as the animal was free to move [72].

8.3.3 Scanning Fiber-Optic Endomicroscopy

While conventional epifluorescence imaging can be performed through a fiber bundle, wide-field imaging remains vulnerable to image contrast degradation due to generation and collection of out-of-focus light. As with the approaches described previously using only a GRIN lens assembly, optical sectioning can be achieved by either performing beam scanning proximal to a coherent fiber bundle. Gmitro and Aziz described a commercial scanning fluorescence confocal microscope coupled to

a fiber-optic bundle in 1993, demonstrating its optical sectioning capabilities with conventional microscope objectives used for focusing at the distal (tissue) end of the fiber [73]. Later, Richards-Kortum et al. developed a fiber-bundle-based confocal microscope which imaged reflected (backscattered) light. This system used a fiber bundle with 7-μm spacing between neighboring cores, with a custom designed 8-element, 7-mm-diameter, and miniature 3×/NA 1.0 objective lens at the distal tip (see Sect. 8.2 for more details). The lateral resolution was approximately 2 microns with a 250-μm diameter FOV [59, 74]. This fiber-optic scanning confocal reflectance system was evaluated in pilot clinical studies for the cervix [75] and oral cavity [13], where in both cases, alterations in nuclear morphology were apparent under confocal imaging which correlated with the grade of neoplasia on pathology.

A similar confocal system operating in fluorescence mode was commercialized by Mauna Kea Technologies, with early systems focused on 488-nm excitation for fluorescein-stained tissue [26] and later versions using multiple excitation sources [76]. The Mauna Kea system is designed to be compatible with a range of fiber-optic probes, each offering different imaging parameters including FOV, resolution, and working distance, depending on the properties of the fiber bundle and the optical element(s) at the distal tip. For example, one probe designed for gastrointestinal imaging has 3.5-μm lateral resolution over a 600-μm FOV, while a high-resolution version is available with 1-μm resolution over a 240-μm FOV [77]. The Mauna Kea fiber-bundle-based fluorescence confocal platform has been evaluated in several clinical areas, including in vivo clinical studies in the lung and gastrointestinal tract [78, 79]. Independent research groups have also designed and built fiber-bundle-based point-scanning fluorescence confocal systems, such as that described by Lane et al., which uses a 561-nm excitation source to enable imaging of cresyl violet-stained tissue [80]. These authors applied this system to the bronchial epithelium, with a clinical focus on evaluating tissue to study the efficacy of chemopreventive agents without biopsy removal, which itself can induce spontaneous lesion regression.

These point-scanning confocal systems require a focused beam to be raster scanned across the sample along one axis at several kHz, which is usually accomplished with a resonant scanner or polygon mirror. Scanning along the "slow" axis is performed with a conventional galvo mirror at a much slower rate of 10 s of Hz. The frame rate of the system is often limited by the speed of the fast scanner, but this component can actually be eliminated by scanning a focused line along only one axis, with a single row of CCD camera pixels, or a linear array detector for detection. Gmitro et al. developed a confocal fluorescence microendoscope which uses a fiber-optic bundle and galvo-based line scanning at the proximal end. A custom designed 6-element, 3-mm-diameter, NA 0.46 miniature objective was also used at the distal tip [48, 81]. Gmitro's group has carried out extensive development of this platform, which has also incorporated spectral detection capabilities [82] and recently entered into in vivo pilot clinical studies [83].

The second distinct approach for beam scanning at the distal tip of a microendoscope involves directly translating the tip of the single fiber used for light delivery and collection. No separate scanning mirrors are involved and the beam-focusing

optics remains stationary. Harris et al. introduced a scanner based on an optical fiber mounted on a tuning fork which is then vibrated by an electromagnetic field [84]. This approach was commercialized by Optiscan, who developed several confocal fluorescence imaging platforms based on this principle for imaging the oral cavity, the skin, and the cervix, all of which were evaluated in pilot clinical studies [85–87]. In each organ site, confocal endomicroscopy demonstrated the ability to visualize cellular level detail and identify alterations due to neoplasia. The next step in all these studies are large-scale, randomized, blinded clinical trials where the diagnostic performance of these instruments can be evaluated and important factors such as clinician's learning curve can be assessed. In partnership with Optiscan, Pentax developed upper and lower GI endoscopes which integrated this type of single-fiber scanner at the distal tip of the scope, enabling conventional white light endoscopy and confocal endomicroscopy to be performed with a single instrument. Polglase et al. presented remarkably striking images from the esophagus and colon of patients using this system in 2005, highlighting the characteristic tissue features that are apparent with the technique (see table 8.2 top figures) [12]. Since then, these endoscopes have been evaluated in large, multicenter studies which are ongoing, but nevertheless have shown considerable promise in the area of biopsy guidance and surveillance [88, 89].

Seibel et al. have described an alternative approach to scanning a single optical fiber using piezoelectric tube actuators with quartered electrodes to displace the tip of an attached fiber. By driving the actuator along orthogonal axes with amplitude-modulated waveforms, 90-degrees out of phase, at the horizontal and vertical resonant frequencies of the fiber, a spiral scan pattern is achieved [19, 90]. As with any point-scanning method, linear or spiral, the digitized signal has to be remapped accordingly to generate an image of the true tissue structure. This type of actuator has been integrated in several endomicroscopy systems, as described in the following sections.

Another novel endomicroscopy approach which also uses a single optical fiber for beam delivery and collection is termed spectrally encoded confocal microscopy (SECM). SECM eliminates the need for a fast axis scan at the distal tip of a probe by using a broadband light source and dispersive optical element to generate a one-dimensional focused line of light at the sample, with different points along the line illuminated with a different wavelength [31, 91]. This way, light returning from each point is "encoded" by its wavelength and can be measured with a spectrometer; no point scan is required. The dispersed line does have to be scanned in the orthogonal direction, however, to sweep out an image. This approach has been successfully evaluated for its ability to identify the microscopic features of disease, including in the esophagus [92], where the characteristic features of normal squamous epithelium, gastric cardia, polyps, specialized intestinal metaplasia, and Barrett's esophagus were identified in SECM images. Progress has since been made in developing a compact SECM probe which enabled imaging within the swine small intestine, ex vivo, and an even smaller probe that can be used in human patients is under development [93].

8.3.4 Nonlinear Endomicroscopy

The endomicroscopy platforms described thus far are all based on imaging of single-photon fluorescence or backscattered light. Nonlinear microscopy techniques which have been successfully implemented in benchtop systems have also begun to be transitioned into compact and miniaturized packages compatible with endomicroscopy. These techniques all achieve optical sectioning, not through the use of a pinhole or slit mask, but through a quadratic dependence on illumination intensity which all but confines the generation of nonlinear signals to the focal plane [21]. Similar to the use of single rigid GRIN lens assemblies for confocal fluorescence described above, Jung and Schnitzer presented two-photon fluorescence images of fluorescently labeled neurons in brain slices, acquired with submillimeter diameter triplet GRIN objectives [94]. The short length GRIN objective eliminated the need to prechirp the excitation pulses to compensate for dispersive pulse broadening within the optical path to the specimen. The same group extended this work to in vivo animal models in 2004 [50]. Kim et al. described a benchtop microscope built in-house with a 1-mm-diameter, 15-mm-long GRIN lens which permits imaging at NA 0.45 in confocal fluorescence, multiphoton fluorescence, and second-harmonic modes [22].

Development of endomicroscope systems for nonlinear microscopy with fiber-optic instead of free-space beam delivery is made more difficult by broadening of the excitation pulse within the fiber itself. Gobel et al. presented a fiber-optic two-photon imaging system using a coherent fiber bundle and GRIN lens objective [55]. The 100 fs pulses from the Ti:Sapphire laser source were prechirped by a grating pair to compensate for group velocity dispersion within the fiber bundle; this approach was successful in restoring the original pulse width for average output powers below 5 mW. However, at the higher intensities typically used in multiphoton microscopy, severe pulse broadening remained which led to suboptimal fluorescence excitation at these intensities. Lelek et al. described an alternative method to both temporally and spectrally shaped femtosecond pulses prior to delivery through a fiber bundle [30]. This approach provided improved compensation for dispersive effects arising from nonlinear processes such as self-phase modulation, which are increasingly present at higher pulse energies but cannot be compensated with a grating or prism pair to introduce negative prechirp before launching.

As with the confocal fluorescence endomicroscopy systems described earlier, the use of a fiber-optic bundle inherently results in images with the discrete core pattern superimposed. This effect can be mitigated by image post-processing methods, but an underlying loss of information cannot be avoided. Again, application of single optical fibers with distal tip scanning enables a continuous image to be formed. Double-clad fibers offer improved efficiency in collection of the nonlinear signal generated at the sample by using a small single-mode core surrounded by a larger inner cladding to deliver and collect light, respectively. Myaing et al. used a double-clad fiber with 3.6-μm core, 90-μm inner cladding, and 125-μm outer cladding mounted within a piezoelectric tube actuator to generate a spiral scan pattern at 2.6

frames per second over a 220-micron-diameter FOV [39]. A NA 0.46/0.7× GRIN lens was used to image fluorescent beads and fluorescently labeled cells in culture. Later, Bao et al. described a handheld two-photon microscope again using dual-clad fiber, but mounted in a compact raster scanner similar to that developed by Optiscan for confocal endomicroscopy. This device produced images over a 475 μm^2 FOV at 1.7 frames per second, with images shown of intact (thick) rat kidney following staining with fluorescein [14].

Distinct from fiber-optic bundles and double-clad fibers with conventional single-mode cores, several novel types of optical fiber have been developed which can eliminate or compensate for spectral pulse broadening (see Sect. 8.2), each of which has been integrated into nonlinear endomicroscopy systems. In 2008, two-photon imaging systems were demonstrated with hollow-core photonic crystal fiber for excitation pulse delivery by both Engelbrecht et al. and Le Harzic et al. [28, 29]. Piezoelectric tube scanners translated the PCF tip in spiral or raster scan patterns, with a GRIN lens assembly as the objective. A miniature dichroic beamsplitter directed emitted fluorescence to a multimode fiber for delivery to a photomultiplier tube or avalanche photodiode. Both groups demonstrated imaging in biological tissues [28] and in cultured cells [29], with the former using a 25-Hz frame rate over a 200-micron-diameter FOV to observe dynamic fluorescent intensity fluctuations in the rat cerebellum following labeling with a fluorescent calcium indicator. Le Harzic et al. demonstrated imaging over a larger FOV (420 × 420 um), albeit at a lower frame rate of 0.8 Hz.

In addition to multiphoton fluorescence imaging, second- and third-harmonic imaging had been demonstrated with compact devices compatible with endomicroscopy. Second-harmonic generation (SHG) can be detected in regularly ordered tissues, such as collagen, using the same femtosecond Ti:Sapphire laser source as used for two-photon imaging. Researchers who had previously demonstrated two-photon endomicroscopy also reported second-harmonic imaging with similar optical setups; no fundamental modifications to the endomicroscopy probe itself are required, although a narrow band-pass filter centered at the SHG wavelength is added in front of the detector to block residual excitation light. Wu et al. [54] and Bao et al. [27] both used miniaturized systems based upon double-clad fiber to image second-harmonic emission from rodent tail tendon. The former used a piezo tube spiral scanner with GRIN lens, while the latter used the electromagnetically driven raster scanner with a miniature multielement objective lens developed by Optiscan. Both groups demonstrated combined SHG/two-photon imaging using a single platform, highlighting the feasibility of imaging in both these nonlinear modes. Less work has been reported on third-harmonic endomicroscopy, but Chia et al. reported a handheld probe with large mode area fiber (35-um core diameter) for beam delivery, multimode fiber for THG collection, MEMS scanner, and macroscopic optics [95]. To generate THG signals in the visible wavelength range, where many detectors have optimum sensitivity, it is necessary to use a femtosecond source emitting in the farther into the near infrared. These authors used a Cr:forsterite laser emitting in the 1,200–1,300-nm range and demonstrated its use in recording THG images from the skin of normal human volunteers.

As even more advanced modes of nonlinear microscopy such as coherent anti-Stokes Raman scattering (CARS) and stimulated Raman scattering (SRS) are demonstrated in benchtop platforms, there are research groups working on endoscopic implementations to facilitate clinical applications. With these, and other coherent Raman scattering (CRS) techniques, some elements of previous endomicroscopy systems including scanners and micro-optics are directly compatible, but other unique challenges remain. CRS uses two tunable laser beams to illuminate a sample at "pump" and "Stokes" frequencies; when the frequency difference is adjusted to match the vibrational mode of an intrinsic biological component, nonlinear interactions can generate light at new frequencies or transfer intensity between source frequencies. A significant feature of CRS is its use of picosecond, rather than femtosecond excitation pulses which incur far less broadening on delivery through conventional optical fiber than the femtosecond pulses used for multiphoton and harmonic imaging [96]. However, four-wave mixing in the fiber itself can produce an unwanted background contribution to the measured signal, which can be removed through use of separate fibers for illumination and collection [97]. A second key issue in developing CRS endomicroscopy is the need to direct both illuminating beams onto the sample with tightly overlapping foci. GRIN lenses tend to exhibit relatively large axial chromatic aberrations which can reduce the efficiency of nonlinear signal generation. Murugkar et al. designed and assembled a miniature lens system for CARS microscopy which comprised multiple lenses, each 1.8 mm in diameter, to compensate for chromatic aberration at the source wavelengths (800 and 1,040 nm) [98]. Saar et al. also designed a custom miniature objective for CRS imaging, this time by using two separate GRIN lenses separated by a diffractive optic, to create an imaging system with zero axial chromatic aberration at the illuminating pulse wavelengths [99]. This system also used the piezoelectric tube scanners used for other nonlinear endomicroscopy studies (described above) to translate the delivery fiber in a spiral scan pattern. In order to increase the collection efficiency of the signal photons, these authors used a photodiode positioned around the illumination optics, directly at the probe's tip. Numerical simulations indicated that this approach can more efficiently collect multiple-scattered CRS light from within thick samples, compared to methods which attempt to couple signal light back into an optical fiber.

8.3.5 Optical Coherence Tomography

Originally demonstrated in the early 1990s, optical coherence tomography (OCT) imaging generates cross-sectional images of tissue microstructure using interferometric detection of backscattered light. Analogous to ultrasound, OCT typically achieves spatial resolution of around 2–15 microns. After initial application to ophthalmology and dermatology, the development of fiber-optic probes and catheters in the mid-1990s led to new applications in cardiology and gastroenterology [100]. OCT probes are almost exclusively based on conventional single-mode fiber, with

most incorporating fixed optical elements at the distal tip and a proximal mechanism to scan the entire length of the fiber, either linearly or circumferentially [101–103]. Beam focusing at the distal tip is usually achieved with a spacer and GRIN lens bonded to the fiber tip, followed by a microprism to deflect the converging beam through 90 degrees, exiting the probe perpendicular to the axis of the fiber. Early studies established the characteristic image features of normal and neoplastic tissue in the esophagus [104, 105], the appearance of atherosclerotic plaques, and vascular response to stenting in the coronary arteries [106, 107].

The shift from time-domain OCT to the much faster Fourier-domain platforms in the mid-2000s revolutionized the field and also presented new challenges for endoscopic implementations. The ability to acquire and process several tens of thousands of A-lines per second required the development of probes which could scan much faster than those used in time-domain platforms [24]. Optical frequency-domain imaging (OFDI) has become the predominant form of OCT for endoscopic and catheter-based imaging; the use of rotary probes spinning at over 100 revolutions per second with linear pullback at several millimeters per second enables several-centimeter-long segments to be mapped at microscopic resolution (7-μm-axial, 30-μm-transverse). Tearney et al. demonstrated the ability of high-speed OFDI with a 2.6-F catheter to image a range of features, including thin-capped fibroatheromas, calcium, stent struts, and intimal hyperplasia within the coronary arteries of living patients [25]. Cardiovascular imaging requires a brief saline purge to displace blood from the imaging field, but the high speed of OFDI still enables several-centimeter segments to be imaged per flush. The same research group implemented OFDI in the gastrointestinal tract of human patients, where due to the much larger lumen compared the coronary vessels, the imaging probe was contained within an inflatable balloon catheter [108]. Once in position, the balloon was inflated to a diameter of 25 mm, which served to dilate the esophageal lumen and center the rotating probe. When rotated and translated to create a spiral scan path, the probe visualized tissue within a 6.5-cm-long window in the balloon. This enabled the characteristic image features of normal squamous mucosa, cardia, specialized intestinal metaplasia (SIM), and high-grade dysplasia/intramucosal carcinoma. Similar high-speed OCT systems are also under investigation in the esophagus for monitoring response to therapy, with the subsurface imaging capability of OCT potentially used to detect residual or missed areas of concern, even when hidden beneath normal epithelium [109].

8.4 Summary

Endomicroscopy – a microscopy at the tip of the endoscope is a reach and emerging area encompassing several imaging modalities starting from wide-field imaging, confocal imaging, nonlinear imaging, optical coherence tomography, and others. It serves as a complement to the macroscopic views obtained either by classical endoscopy or visual observation. To accomplish its goal it applies several modern

technologies spanning from new detectors and sources, fiber optics, integrated micromechanical systems, new fabrication technologies, and biochemical contrasts. It consequently increases its presence in clinical studies and applications. At the same time still leaves numerous challenges and research opportunities across multiple fields between basic sciences, engineering, and clinical implementations. Considering that classical microscopy is a gold standard for pathological assessment, endomicroscopy has a bright future in all new methods of development, multidisciplinary research, and finally technology translation to everyday use.

Acknowledgements I would like to thank Dr. Mark Pierce and Dr. Michal Pawlowski for a tremendous help, many suggestions, and discussions over the course of work to write this chapter.

References

1. J. Bailley, The endoscope. Gastrointest. Endosc. **65**, 886–893 (2007)
2. D. Panescu, Emerging Technologies: an imaging pill for gastrointestinal endoscopy. IEEE Eng. Med. Biol. Mag. July/August, 12–14 (2005)
3. M.A. Kara, J.J. Bergman, Autofluorescence imaging and narrow-band imaging for the detection of early neoplasia in patients with Barrett's esophagus. Endoscopy **38**(6), 627–631 (2006)
4. H. Inoue, K. Sasajima, M. Kaga, S. Sugaya, Y. Sato, Y. Wada, M. Inui, H. Satodate, S.E. Kudo, S. Kimura, S. Hamatani, A. Shiokawa, Endoscopic in vivo evaluation of tissue atypia in the esophagus using a newly designed integrated endocytoscope: a pilot trial. Endoscopy **38**, 891–895 (2006)
5. R.T. Bryan, L.J. Billingham, D.M.A. Wallace, Narrow-band imaging flexible cystoscopy in the detection of recurrent urothelial cancer of the bladder. BJU Int. **101**(6), 702–705 (2008)
6. E.V. Cauberg, D.M. de Bruin, D.J. Faber, T.G. van Leeuwen, J.J.M.C.H. de la Rosette, T.M. de Reijke, A new generation of optical diagnostics for bladder cancer: technology, diagnostic accuracy, and future applications. Eur. Urol. **56**, 287–297 (2009)
7. A.L. Clark, A.M. Gillenwater, T.G. Collier, R. Alizadeh-Naderi, A.K. El-Naggar, R.R. Richards-Kortum, Confocal microscopy for real-time detection of oral cavity neoplasia. Clin. Cancer Res. **9**, 4714–4721 (2003)
8. F. Helmchen, W. Denk, Deep tissue two-photon microscopy. Nat. Methods **2**, 932–940 (2005)
9. V. Becker, T. Vercauteren, C.H. von Weyhern, C. Prinz, R.M. Schmid, A. Meining, High-resolution miniprobe-based confocal microscopy in combination with video mosaicing. Gastrointest. Endosc. **66**(5), 1001–1007 (2007)
10. B.E. Bouma, S.H. Yun, B.J. Vakoc, M.J. Suter, G.J. Tearney, Fourier-domain optical coherence tomography: recent advances toward clinical utility. Curr. Opin. Biotechnol. **20**, 111–118 (2009)
11. J. Pawley, *Handbook of Biological Confocal Microscopy*, 3rd edn. (Springer, New York, 2006)
12. A.L. Polglase, W.J. McLaren, S.A. Skinner, R. Kiesslich, M.F. Neurath, P.M. Delaney, A fluorescence confocal endomicroscope for in vivo microscopy of the upper- and the lower-GI tract. Gastrointest. Endosc. **62**, 686–695 (2005)
13. K.C. Maitland, A.M. Gillenwater, M.D. Williams, A.K. El-Naggar, M.R. Descour, R.R. Richards-Kortum, In vivo imaging of oral neoplasia using a miniaturized fiber optic confocal reflectance microscope. Oral Oncol. **44**, 1059–1066 (2008)
14. H. Bao, J. Allen, R. Pattie, R. Vance, M. Gu, Fast handheld two-photon fluorescence microendoscope with a 475 x 475micron field of view for in vivo imaging. Opt. Lett. **33**, 1333–1335 (2008)

15. R.H. Webb, Confocal optical microscopy. Rep. Prog. Phys. **59**, 427–471 (1996)
16. W.R. Zipfel, R.N. Williams, W.W. Webb, Nonlinear magic: multiphoton microscopy in the biosciences. Nat. Biotechnol. **21**, 1369–1377 (2003)
17. T.J. Muldoon, N. Thekkek, D. Roblyer, D. Maru, N. Harpaz, J. Potack, S. Anandasabapathy, R.R. Richards-Kortum, Evaluation of quantitative image analysis criteria for the high-resolution microendoscopic detection of neoplasia in Barrett's esophagus. J. Biomed. Opt. **15**, 026027 (2010)
18. D. Kobat, M.E. Durst, N. Nishimura, A.W. Wong, C.B. Schaffer, C. Xu, Deep tissue multiphoton microscopy using longer wavelength excitation. Opt. Express **17**, 13354–13364 (2009)
19. C.M. Brown, P.G. Reinhall, S. Karasawa, E.J. Seibel, Optomechanical design and fabrication of resonant microscanners for a scanning fiber endoscope. Opt. Eng. **45**, 043001 (2006)
20. M.D. Chidley, K.D. Carlson, R.R. Richards-Kortum, M.R. Descour, Design, assembly, and optical bench testing of a high-numerical-aperture miniature injection-molded objective for fiber-optic confocal reflectance microscopy. Appl. Opt. **45**, 2545–2554 (2006)
21. L. Fu, M. Gu, Fibre-optic nonlinear optical microscopy and endoscopy. J. Microsc. **226**, 195–206 (2007)
22. P. Kim, M. Puoris'haag, D. Côté, C.P. Lin, S.H. Yun, In vivo confocal and multiphoton microendoscopy. J. Biomed. Opt. **13**, 010501 (2008)
23. H.J. Shin, M.C. Pierce, D. Lee, H. Ra, O. Solgaard, R. Richards-Kortum, Fiber-optic confocal microscope using a MEMS scanner and miniature objective lens. Opt. Express **15**, 9113–9122 (2007)
24. S.H. Yun, G.J. Tearney, B.J. Vakoc, M. Shishkov, R. Yelin, W.Y.Oh, A. Desjardins, R.C. Chan, D. Yelin, J.A. Evans, I.K. Jang, N.S. Nishioka, J.F. de Boer, B.E. Bouma, Comprehensive volumetric optical microscopy in vivo. Nat, Med. **12**, 1429–1433 (2006)
25. G.J. Tearney, S. Waxman, M. Shishkov, B.J. Vakoc, M.J. Suter, M.I. Freilich, A.E. Desjardins, W.Y. Oh, L.A. Bartlett, M. Rosenberg, B.E. Bouma, Three-dimensional coronary artery microscopy by intracoronary optical frequency domain imaging. J. Am. Coll. Cardiol. Img. **1**, 752–761 (2008)
26. E. Laemmel, M. Genet, G. Le Goualher, A. Perchant, J.-F. Le Gargasson, E. Vicaut, Fibered confocal fluorescence microscopy (Cell-viZio^{TM}) facilitates extended imaging in the field of microcirculation. J. Vasc. Res. **41**, 400 (2004)
27. H. Bao, A. Boussioutas, R. Jeremy, S. Russell, M. Gu, Second harmonic generation imaging via nonlinear endomicroscopy. Opt. Express **18**, 1255–1260 (2010)
28. C.J. Engelbrecht, R.S. Johnston, E.J. Seibel, F. Helmchen, Ultra-compact fiber-optic two-photon microscope for functional fluorescence imaging in vivo. Opt. Express **16**, 5556–5564 (2008)
29. R. Le Harzic, M. Weinigel, I. Riemann, K. König, B. Messerschmidt, Nonlinear optical endoscope based on a compact two axes piezo scanner and a miniature objective lens. Opt. Express **16**, 20588–20596 (2008)
30. M. Lelek, E. Suran, F. Louradour, A. Barthelemy, B. Viellerobe, F. Lacombe, Coherent femtosecond pulse shaping for the optimization of a non-linear micro-endoscope. Opt. Express **15**, 10154–10162 (2007)
31. G.J. Tearney, R.H. Webb, B.E. Bouma, Spectrally encoded confocal microscopy. Opt. Lett. **23**, 1152–1154 (1998)
32. F & T Fibers 1: Web product resources of F & T Fibers and Technology GmbH: http://www.fibersandtechnology.com/ (December 2011)
33. Fujikura 1: Web product resources of Fujikura America Inc.: http://www.fujikura.com/ (April 2011)
34. R.T. Kester, T. Christenson, R. Richards Kortum, T.S. Tkaczyk, Low cost, high performance, self-aligning miniature optical systems. Appl. Opt. **48**, 3375–3384 (2009)
35. J.A. Udovich, N.D. Kirkpatrick, A. Kano, A. Tanbakuchi, U. Utzinger, A. F. Gmitro, Spectral background and transmission characteristics of fiber optic imaging bundles. Appl. Opt. **47**, 4560–4568 (2008)

36. B.A. Flusberg, E.D. Cocker, W. Piyawattanametha, J.C. Jung, E.L.M. Cheung, M.J. Schnitzer, Fiber-optic fluorescence imaging. Nat. Methods **2**, 941–950 (2005)
37. B.E.A. Saleh, M.C. Teich, *Fundamentals of Photonics* (Wiley, New York, 1991)
38. X. Liu, M.J. Cobb, Y. Chen, M.B. Kimmey, X. Li, Rapid-scanning forward-imaging miniature endoscope for real-time optical coherence tomography. Opt. Lett. **29**, 1763–1765 (2004)
39. M.T. Myaing, D.J. MacDonald, X. Li, Fiber-optic scanning two-photon fluorescence endoscope. Opt. Lett. **31**, 1076–1078 (2006)
40. L.E. Kinsler, A.R. Frey, A.B. Coppens, J.V. Sanders, *Fundamentals of Acoustics*, 3rd edn. (Wiley, New York, 1982)
41. H. Miyajima, K. Murakami, M. Katashiro, MEMS optical scanners for microscopes. IEEE J. Sel. Top. Quantum Electron. **10**, 514 (2004)
42. D.L. Dickensheets, G.S. Kino, Micromachined scanning confocal optical microscope. Opt. Lett. **21**, 764–766 (1996)
43. D. Lee, O. Solgaard, Two-axis gimbaled microscanner in double SOI layers actuated by self-aligned vertical electrostatic combdrive, in *Proceedings of the Solid-State Sensors, Actuators and Microsystems Workshop*, pp. 352–355 (2004)
44. A.D. Aguirre, P.R. Herz, Y. Chen, J.G. Fujimoto, W. Piyawattanametha, L. Fan, M.C. Wu, Two-axis MEMS scanning catheter for ultrahigh resolution three-dimensional and En Face imaging. Opt. Express **15**, 2445–2453 (2007)
45. J.T.C. Liu, M.J. Mandella, H. Ra, L.K. Wong, O. Solgaard, G.S. Kino, W. Piyawattanametha, C.H. Contag, T.D. Wang, Miniature near-infrared dual-axes confocal microscope utilizing a two-dimensional microelectromechanical systems scanner. Opt. Lett. **32**, 256–258 (2007)
46. W. Jung, D.T. McCormick, J. Zhang, L. Wang, N.C. Tien, Z. Chen, Three-dimensional endoscopic optical coherence tomography by use of a two-axis microelectromechanical scanning mirror. Appl. Phys. Lett. **88**, 163901 (2006)
47. M. Kanai, US Patent 7,914,447: Confocal scanning endoscope system and image display area adjustment method thereof (2011)
48. A.R. Rouse, A. Kano, J.A. Udovich, S.M. Kroto, A.F. Gmitro, Design and demonstration of a miniature catheter for a confocal microendoscope. Appl. Opt. **43**, 5763–5771 (2004)
49. S. Sinzinger, J. Jahns, *Microoptics* (Wiley-VCH GmbH & Co. KGaA, Weinheim, 2003)
50. J.C. Jung, A.D. Mehta, E. Aksay, R. Stepnoski, M.J. Schnitzer, In vivo mammalian brain imaging using one- and two-photon fluorescence microendoscopy. J. Neurophysiol. **92**, 3121–3133 (2004)
51. R.S. Pillai, D. Lorenser, D.D. Sampson, Deep-tissue access with confocal fluorescence microendoscopy through hypodermic needles. Opt. Express **19**, 7213–7221 (2011)
52. R.P.J. Barretto, B. Messerschmidt, M.J. Schnitzer, In vivo fluorescence imaging with high resolution microlenses. Nat. Methods **6**, 511–515 (2009)
53. J. Knittel, L. Schnieder, G. Buess, B. Messerschmidt, T. Possner, Endoscope-compatible confocal microscope using a gradient index-lens system. Opt. Commun. **188**, 267–273 (2001)
54. Y. Wu, Y. Leng, J. Xi, X. Li, Scanning all-fiber-optic endomicroscopy system for 3D nonlinear optical imaging of biological tissues. Opt. Express **17**, 7907–7915 (2009)
55. W. Göbel, J.N.D. Kerr, A. Nimmerjahn, F. Helmchen, Miniaturized two-photon microscope based on a flexible coherent fiber bundle and a gradient-index lens objective. Opt. Lett. **29**, 2521–2523 (2004)
56. Grintech 1: www.grintech.de product specification for High-NA Endomicroscopic Imaging Objective for Fluorescence Microscopy: GT-MO-080-018-488 and GT-MO-080-0415-488 (October 2011)
57. Grintech 2: www.grintech.de product specification for High-NA Endomicroscopic Imaging Objective for 2-Photon Microscopy: GT-MO-080-018-810 and GT-MO-080-0415-810 (October 2011)
58. M. Bass, Editor-in-chief, *Handbook of Optics*, vol. 1, 3rd edn. (McGraw Hill, New York, 2010)
59. C. Liang, K.B. Sung, R.R. Richards-Kortum, M.R. Descour, Design of a high-numerical-aperture miniature microscope objective for an endoscopic fiber confocal reflectance microscope. Appl. Opt. **41**, 4603–4610 (2002)

60. M. Kyrish, U. Utzinger, M.R. Descour, B.K. Baggett, T.S. Tkaczyk, Ultra-slim plastic endomicroscope objective for non-linear microscopy. Opt. Express **19**, 7603–7615 (2011)
61. R.S. Kwon, D.G. Adler, B. Chand, J.D. Conway, D.L. Diehl, S.V. Kantsevoy, P. Mamula, S.A. Rodriguez, R.J. Shah, L.M.W.K. Song, W.M. Tierney, High-resolution and high-magnification endoscopes. Gastrointest. Endosc. **69**, 399–407 (2009)
62. R.S. Kwon, L. Wong Kee Song, D.G. Adler, J.D. Conway, D.L. Diehl, F.A. Farraye, S.V. Kantsevoy, V. Kaul, S.R. Kethu, P. Mamula, M.C. Pedrosa, S.A. Rodriguez, W.M. Tierney, Endocytoscopy. Gastrointest. Endosc. **70**, 610–613 (2009)
63. H. Pohl, M. Koch, A. Khalifa, I.S. Papanikolaou, K. Scheiner, B. Wiedenmann, T. Rösch, Evaluation of endocytoscopy in the surveillance of patients with Barrett's esophagus. Endoscopy **39**, 492–496 (2007)
64. T. Dromard, V. Ravaine, S. Ravaine, J. Lévêque, N. Sojic, Remote in vivo imaging of human skin corneocytes by means of an optical fiber bundle. Rev. Sci. Inst. **78**, 053709 (2007)
65. T.J. Muldoon, S. Anandasabapathy, D. Maru, R. Richards-Kortum, High-resolution imaging in Barrett's esophagus: a novel, low-cost endoscopic microscope. Gastrointest. Endosc. **68**, 737–744 (2008)
66. T.J. Muldoon, D. Roblyer, M.D. Williams, V.M.T. Stepanek, R. Richards–Kortum, A.M. Gillenwater, Noninvasive imaging of oral neoplasia with a high-resolution microendoscope. Head Neck **34**(3), 305–312 (2012). doi: 10.1002/hed.21735. Epub 2011 Mar 16.
67. M.C. Pierce, D. Yu, R. Richards-Kortum, High-resolution fiber-optic microendoscopy for in situ cellular imaging. JOVE **47**, e2306 (2011)
68. M.C. Pierce, P.M. Vila, A. Polydorides, R. Richards-Kortum, S. Anandasabapathy, Low-cost endomicroscopy in the esophagus and colon. Am. J. Gastroenterol. **106**, 1722–1724 (2011)
69. W. Zhong, J.P. Celli, I. Rizvi, Z. Mai, B.Q. Spring, S.H. Yun, T. Hasan, In vivo high-resolution fluorescence microendoscopy for ovarian cancer detection and treatment monitoring. Br. J. Cancer **101**, 2015–2022 (2009)
70. N. Mufti, Y. Kong, J.D. Cirillo, K.C. Maitland, Fiber optic microendoscopy for preclinical study of bacterial infection dynamics. Biomed. Opt. Express **2**, 1121–1134 (2011)
71. K.J. Rosbach, D. Shin, T.J. Muldoon, M.A. Quraishi, L.P. Middleton, K.K. Hunt, F. Meric-Bernstam, T.K. Yu, R.R. Richards-Kortum, W. Yang, High-resolution fiber optic microscopy with fluorescent contrast enhancement for the identification of axillary lymph node metastases in breast cancer: a pilot study. Biomed. Opt. Express **1**, 911–922 (2010)
72. B.A. Flusberg, A. Nimmerjahn, E.D. Cocker, E.A. Mukamel, R.P.J. Barretto, T.H. Ko, L.D. Burns, J.C. Jung, M.J. Schnitzer, High-speed, miniaturized fluorescence microscopy in freely moving mice. Nat. Methods **5**, 935–938 (2008)
73. A.F. Gmitro, D Aziz, Confocal microscopy through a fiber-optic imaging bundle. Opt. Lett. **18**, 565–567 (1993)
74. K.B. Sung, C. Liang, M. Descour, T. Collier, M. Follen, R. Richards-Kortum, Fiber-optic confocal reflectance microscope with miniature objective for in vivo imaging of human tissues. IEEE Trans. Biomed. Eng. **49**, 1168–1172 (2002)
75. K.B. Sung, R. Richards-Kortum, M. Follen, A. Malpica, C. Liang, M. Descour, Fiber optic confocal reflectance microscopy: a new real-time technique to view nuclear morphology in cervical squamous epithelium in vivo. Opt. Express **11**, 3171 (2003)
76. F. Jean, G. Bourg-Heckly, B. Viellerobe, Fibered confocal spectroscopy and multicolor imaging system for in vivo fluorescence analysis. Opt. Express **15**, 4008–4017 (2007)
77. K.B. Dunbar, M.I. Canto, "Confocal endomicroscopy." Tech. Gastrointest. Endosc. **12**, 90–99 (2010)
78. L. Thiberville, S. Moreno-Swirc, T. Vercauteren, E. Peltier, Charlotte Cavé, G. Bourg-Heckly, In vivo imaging of the bronchial wall microstructure using fibered confocal fluorescence microscopy. Am. J. Respir. Crit. Care Med. **175**, 22–31 (2007)
79. M.B. Wallace, P. Sharma, C. Lightdale, et al., Preliminary accuracy and interobserver agreement for the detection of intraepithelial neoplasia in Barrett's esophagus with probe-based confocal laser endomicroscopy. Gastrointest. Endosc. **72**, 19–24 (2010)

80. P.M. Lane, S. Lam, A. McWilliams, J.C. leRiche, M.W. Anderson, C.E. MacAulay, Confocal fluorescence microendoscopy of bronchial epithelium. J. Biomed. Opt. **14**, 024008 (2009)
81. Y.S. Sabharwal, A.R. Rouse, L. Donaldson, M.F. Hopkins, A.F. Gmitro, Slit-scanning confocal microendoscope for high-resolution in vivo imaging. Appl. Opt. **38**, 7133 (1999)
82. A.R. Rouse, A.F. Gmitro, Multispectral imaging with a confocal microendoscope. Opt. Lett. **25**, 1708–1710 (2000)
83. A.A. Tanbakuchi, J.A. Udovich, A.R. Rouse, K.D. Hatch, A.F. Gmitro, In vivo imaging of ovarian tissue using a novel confocal microlaparoscope. Am. J. Obstet. Gynecol. **202**, 90.e1–9 (2010)
84. M.R. Harris, Scanning microscope with a miniature head. U.K. patent GB 2340332 B (2001)
85. P.S. Thong, M. Olivo, K. Kho, W. Zheng, K. Mancer, M. Harris, K. Soo, Laser confocal endomicroscopy as a novel technique for fluorescence diagnostic imaging of the oral cavity. J. Biomed. Opt. **12**, 014007 (2007)
86. S. Astner, S. Dietterle, N. Otberg, H. Rowert-Huber, E. Stockfleth, J. Lademann, Clinical applicability of in vivo fluorescence confocal microscopy for noninvasive diagnosis and therapeutic monitoring of nonmelanoma skin cancer. J. Biomed. Opt. **13**, 014003 (2008)
87. J. Tan, M.A. Quinn, J.M. Pyman, P.M. Delaney, W.J. McLaren, Detection of cervical intraepithelial neoplasia in vivo using confocal endomicroscopy. BJOG **116**, 1663–1670 (2009)
88. M. Goetz, R. Kiesslich, Advances of endomicroscopy for gastrointestinal physiology and diseases. Am. J. Physiol. Gastrointest. Liver Physiol. **298**, G797–806 (2010)
89. K.B. Dunbar, P. Okolo, E. Montgomery, Confocal laser endomicroscopy in Barrett's esophagus and endoscopically inapparent Barrett's neoplasia: a prospective, randomized, double-blinded, controlled, crossover trial. Gastrointest. Endosc. **70**, 645–54 (2009)
90. E.J. Seibel, Q.Y.J. Smithwick, Unique features of optical scanning, single fiber endoscopy. Lasers Surg. Med. **30**, 177 (2002)
91. D. Yelin, I. Rizvi, W.M. White, J.T. Motz, T. Hasan, B.E. Bouma, G.J. Tearney, Three-dimensional miniature endoscopy. Nature **443**, 765 (2006)
92. D. Kang, M.J. Suter, C. Boudoux, H. Yoo, P.S. Yachimski, W.P. Puricelli, N.S. Nishioka, M. Mino-Kenudson, G.Y. Lauwers, B.E. Bouma, G.J. Tearney, Comprehensive imaging of gastroesophageal biopsy samples by spectrally encoded confocal microscopy. Gastrointest. Endosc. **71**, 35–43 (2010)
93. D. Kang, H. Yoo, P. Jillella, B.E. Bouma, G.J. Tearney, Comprehensive volumetric confocal microscopy with adaptive focusing. Biomed. Opt. Express **2**, 1412–1422 (2011)
94. J.C. Jung, M.J. Schnitzer, Multiphoton endoscopy. Opt. Lett. **28**, 902–904 (2003)
95. S. Chia, C. Yu, C. Lin, N. Cheng, T. Liu, M. Chan, I. Chen, C. Sun, Miniaturized video-rate epi-third-harmonic-generation fiber-microscope. Opt. Express **18**, 17382–17391 (2010)
96. F. Légaré, C.L. Evans, F. Ganikhanov, X.S. Xie, Towards CARS endoscopy. Opt. Express **14**, 4427–4432 (2006)
97. M. Balu, G. Liu, Z. Chen, B.J. Tromberg, E.O. Potma, Fiber delivered probe for efficient CARS imaging of tissues. Opt. Express **18**, 2380–2388 (2010)
98. S. Murugkar, B. Smith, P. Srivastava, A. Moica, M. Naji, C. Brideau, P. K. Stys, H. Anis, Miniaturized multimodal CARS microscope based on MEMS scanning and a single laser source. Opt. Express **18**, 23796–23804 (2010)
99. B.G. Saar, R.S. Johnston, C.W. Freudiger, X.S. Xie, E.J. Seibel, Coherent Raman scanning fiber endoscopy. Opt. Lett. **36**, 2396–2398 (2011)
100. B.E. Bouma, G.J. Tearney, Clinical imaging with optical coherence tomography. Acad. Radiol. **9**, 942–953 (2002)
101. G.J. Tearney, S.A. Boppart, B.E. Bouma, M.E. Brezinski, N.J. Weissman, J.F. Southern, J.G. Fujimoto, Scanning single-mode fiber optic catheter-endoscope for optical coherence tomography. Opt. Lett. **21**, 543–545 (1996)
102. B.E. Bouma, G.J. Tearney, Power-efficient nonreciprocal interferometer and linear-scanning fiber-optic catheter for optical coherence tomography. Opt. Lett. **24**, 531–533 (1999)

103. A.M. Rollins, R. Ung-arunyawee, A. Chak, R.C.K. Wong, K. Kobayashi, M.V. Sivak, J.A. Izatt, Real-time in vivo imaging of human gastrointestinal ultrastructure by use of endoscopic optical coherence tomography with a novel efficient interferometer design. Opt. Lett. **24**, 1358–1360 (1999)
104. B.E. Bouma, G.J. Tearney, C.C. Compton, N.S. Nishioka, High resolution imaging of the human esophagus and stomach in vivo using optical coherence tomography. Gastrointest. Endosc. **51**, 467–474 (2000)
105. J.M.V. Sivak, K. Kobayashi, J.A. Izatt, A.M. Rollins, R. Ung-runyawee, A. Chak, R.C.K. Wong, G.A. Isenberg, J. Willis, High-resolution endoscopic imaging of the GI tract using optical coherence tomography. Gastrointest. Endosc. **51**, 474–479 (2000)
106. I.K. Jang, G.J. Tearney, B.M. MacNeill, M. Takano, F. Moselewski, N. Iftimia, M. Shishkov, S.L. Houser, H.T. Aretz, E.F. Halpern, et al., In vivo characterization of coronary atherosclerotic plaque using optical coherence tomography. Circulation **111**, 1551–1555 (2005)
107. G. Guagliumi, V. Sirbu, Optical coherence tomography: high resolution intravascular imaging to evaluate vascular healing after coronary stenting. Catheter Cardiovasc. Interv. **72**, 237–247 (2008)
108. M.J. Suter, B.J. Vakoc, P.S. Yachimski, M. Shishkov, G.Y. Lauwers, M. Mino-Kenudson, B.E. Bouma, N.S. Nishioka, G.J. Tearney, Comprehensive microscopy of the esophagus in human patients with optical frequency domain imaging. Gastrointest. Endosc. **68**, 745–753 (2008)
109. D.C. Adler, C. Zhou, T.H. Tsai, et al., Three-dimensional optical coherence tomography of Barrett's esophagus and buried glands beneath neosquamous epithelium following radiofrequency ablation. Endoscopy **41**, 773–776 (2009)

Chapter 9
Multimodal Biomedical Imaging Systems

Rongguang Liang

Optical imaging technologies can provide real-time images of tissues in vivo and have the potential to reveal biochemical and/or molecular information; therefore, they can significantly improve identification of malignancy at early stages. The ability to obtain tissue architectural morphology and molecular information in vivo, without the need for tissue excision, offers advancement in disease diagnostics and therapy. Multimodal imaging systems combining multiple imaging modalities for complementary tissue information offer a number of advantages compared with a single imaging modality and improve the diagnosis and treatment of diseases using distinct imaging techniques.

There is a need to develop an imaging technology with high sensitivity and specificity in disease detection and with translational potential to clinical applications. Due to the limitation of individual imaging techniques, a new paradigm in biomedical imaging is to combine multiple imaging modalities for complementary tissue information. Recently, a number of multimodal imaging systems have been developed with different imaging techniques. Such combinations offer a number of advantages compared with a single imaging modality and improve the diagnosis and treatment of diseases using distinct imaging techniques.

This chapter will first discuss major biomedical imaging techniques and their advantages and limitations and then review selected multimodal imaging systems. Following this, various design principles and examples will be described.

R. Liang (✉)
College of Optical Sciences, University of Arizona, Tucson, AZ 85721, USA
e-mail: rliang@optics.arizona.edu

R. Liang (ed.), *Biomedical Optical Imaging Technologies*, Biological and Medical Physics, Biomedical Engineering, DOI 10.1007/978-3-642-28391-8_9,

9.1 Biomedical Optical Imaging Techniques: Advantages and Limitations

A number of biomedical optical imaging and spectroscopic techniques have been developed and commercialized for fundamental research and clinical applications. Each of these utilizes different contrast mechanisms and has unique features with encouraging results, but each also has some limitations. Assessment of image data is often complicated by the fact that a number of factors are involved in disease progression, each of which may affect the optical properties of tissue and influence the measured signal.

9.1.1 Transillumination Imaging

Transillumination imaging utilizes spatial variation of absorption and scattering in tissue. It is often used in wide field of view (FOV) mode and can be very effective to detect a target deep inside the tissue, which may be difficult to be detected using other methods.

While transillumination imaging is effective in detecting internal structures and features, such as lesions, deep inside the tissue, there are several drawbacks to this method. First, the transmitted image cannot provide depth information; secondly, the transmitted image does not provide detailed information on tissue surface; and thirdly, image resolution is often low because the light-carrying information comes from inside the tissue and undergoes some scattering. In addition, it is not always possible to apply transillumination imaging methods when the tissue of interest is relatively thick.

9.1.2 Reflectance Imaging

Reflectance imaging collects and analyzes both backscattered and specularly reflected photons without filtering. It is routinely used in the clinic for direct visual inspection, usually in lowresolution, large FOV mode. Reflectance imaging can also be used in highresolution, small FOV mode and can provide detailed information about the tissue surface.

Reflectance images generally show surface texture well; however, reflectance imaging is limited to detecting lesions based on gross morphological changes and has relatively low sensitivity in detecting changes in tissue. In addition, the detected light often contains light that is specularly reflected from the tissue surface. Unfortunately, specularly reflected light often saturates the detector and obscures tissue surface. With reflectance imaging, it can be difficult to determine the margin of disease with precision when the tumor extends into the submucosa because most of the photons collected by the imaging system come from the superficial layers of tissue.

9.1.3 Polarization Imaging

A polarization-gated imaging system uses polarized illumination, with an analyzer in the detection path to separate transmitted or backscattered photons with different polarization states, therefore providing improved structural and depth information.

A number of imaging methods based on polarization-gating techniques have been developed for biomedical applications, such as conventional polarization imaging, orthogonal polarized spectral imaging, and polarization ratio imaging. Polarization imaging techniques are simple and low cost and can provide a powerful tool for functional diagnostics and for the imaging of diseased fragments of tissues, as well as for the detection of tumor borders that are not visible to the naked eye. This offers the opportunity for a number of useful applications in clinical practice. However, a limitation of this technique is that it does not provide adequate biochemical and structural information.

9.1.4 Fluorescence Imaging

Fluorescence imaging locates diseased tissue either using autofluorescence from endogenous fluorophores or using the fluorescence signal from a fluorescent dye. This technique provides comprehensive and detailed probing of the structure and dynamics of biological specimens of widely varying dimensions.

While fluorescence imaging provides a highly sensitive technique for detection of biochemical and structural changes, it does not demonstrate a great degree of specificity due to the presence of bacteria, blood, food particles and various other changes that are not necessarily related to malignant transformation of tissue. False positive detection can result from the presence of bacteria or food particles, from detection geometry, from varying degrees of vascularization, from distribution of fluorophores, and due to other changes not necessarily related to malignant transformation of tissue. In addition, fluorescence imaging, by itself, lacks sufficient surface and depth information.

9.1.5 Confocal Imaging

By placing a small aperture in front of the detector to reject scattered photons outside of the focal point, confocal imaging increases the contrast of microscopic images, particularly in thick specimens, and provides depth discrimination in reflectance and fluorescence imaging. Confocal imaging utilizes the fact that scattered photons that undergo multiple scattering can be widely spread out from the focal point. Advantages of confocal imaging over conventional reflectance imaging include its controllable depth of field, improved image quality, and the ability to obtain optical sections of relatively thick specimens.

Confocal imaging uses point scanning. A scanning system scans a focused spot across the object of interest to obtain a two-dimensional image. Imaging speed is limited by the scanning system. Imaging speed is also limited by the numerical aperture (NA) of the objective lens since only a small fraction of the light from the focal point is collected by the objective lens. Another limitation of the confocal imaging technique is its limited imaging depth due to light scattering.

9.1.6 Optical Coherence Tomography

Optical coherence tomography (OCT) is based on a low-coherence interferometric technique. In OCT, the image contrast originates from scattering, birefringence, absorption, and difference in refractive index. Backscattered light is measured as a function of axial range and transverse position through coherence gating. Cross-sectional, tomographic images are generated by scanning the focused point across the tissue.

The interference between the sample and reference signals can be measured using either time-domain or frequency-domain techniques. In time-domain OCT, the reference mirror is scanned back and forth, and the interference signal is measured by a photodiode detector. In frequency-domain OCT, the optical path length of the reference arm is fixed and the interference signal is acquired by encoding the optical frequency in time with a spectrally scanning source (swept-source OCT) or is acquired with a dispersive detector (spectral-domain OCT). Frequency-domain OCT has a much higher sensitivity and imaging speed. In spectral OCT, a diffraction grating, and a line-scan CCD array are used in the detection arm to record the interference spectrum in parallel. In swept-source OCT, a wavelength-swept laser is used as the light source and a photodetector in the detection arm is employed to record the interference spectrum as the wavelength is swept.

OCT is capable of imaging the layer-to-layer architectonics of healthy tissues that have different optical characteristics. OCT can also reveal structural changes in tissues caused by pathologic conditions, such as inflammation and tumors.

While OCT can provide detailed information on underlying tissue structure, it has some potential drawbacks, such as small FOV, lack of tissue surface detail, and absence of information on biochemical and molecular compositions. Another shortcoming of OCT is its relatively slow imaging speed because it usually works as point scanning system. Some multiple point scanning systems and en face systems have been developed to address this shortcoming. In evaluating OCT image results, it may also be difficult to distinguish between different tissues, such as between normal and pathological tissues, because these tissues may have similar variations in optical properties, such as scattering, absorption, and refractive index. Another problem with OCT imaging is that soft tissue is compliant, moving both involuntarily and voluntarily. When the imaging device contacts the tissue, it can cause folds, stretching, and other deformations in the tissue that can make the tissue structure obtained from OCT difficult to interpret.

9.1.7 Multiphoton Imaging

Multiphoton imaging uses pulsed long-wavelength light to excite fluorescence at shorter wavelengths. A fluorophore absorbs the energy from two or more photons with long wavelength simultaneously; the summed energies of long wavelength exciting photons will produce an emission wavelength shorter than the excitation wavelength. The fluorescence signal can be generated from exogenous probes applied to the tissue or endogenous molecules that are inherently expressed.

Multiphoton imaging has attractive advantages over confocal imaging for live cells and for tissues with three-dimensionally resolved fluorescence imaging. Multiphoton excitation occurs only at the focal point of the objective lens, therefore minimizing the photobleaching and photodamage that are limiting factors in imaging live cells. Also, because the excitation wavelength is longer, multiphoton imaging provides superior optical sectioning at greater depths in thick specimens than is possible by other methods. Long wavelength and low-energy excitation lasers also cause less damage than short-wavelength lasers so that cells may be observed for longer periods with fewer toxic effects.

Similar to confocal imaging, multiphoton imaging has the limitations of small FOV and low image acquisition speed. Another drawback is the cost of ultrafast lasers used in multiphoton imaging.

9.1.8 Spectroscopy

Spectroscopy obtains detailed information about wavelength-dependent optical properties of tissue through the emitted or absorbed spectrum. Depending on the nature of the light and tissue interaction, several spectroscopy systems, such as scattering spectroscopy, fluorescence spectroscopy, and Raman spectroscopy, have been developed.

Scattering spectroscopy measures the amount of light that a substance scatters at certain wavelengths, incident angles, and polarization angles. There are several scattering spectroscopic technologies, such as diffuse reflectance spectroscopy (DRS), elastic scattering spectroscopy (ESS), light scattering spectroscopy (LSS), backscattering spectroscopy, and Raman spectroscopy.

Fluorescence spectroscopy measures autofluorescence or the exogenous fluorescence spectrum of the tissue. It can probe tissue to depths of up to several hundreds of microns and reveal intrinsic signatures that can be correlated to microstructures and biochemical composition of epithelial tissues.

Raman spectroscopy is a powerful method for molecular detection and characterization; it is particularly attractive for biological and biomedicine applications because it provides molecular-level information without the need to use exogenous fluorescent labels or the need to perturb the sample using stains or chemical fixatives. It can provide valuable information on chemical and structural changes due to disease as well as mechanical deformation induced by aging or a prosthetic implant.

While the spectroscopic method probes the tissue noninvasively and provides information on tissue morphology, function, and biochemical composition, it also has some potential shortcomings. First, the spectroscopic method is a point measurement, which means it does not provide surface detail. Second, spectra may be difficult to interpret because they may be influenced by unknown subsurface structures. Without depth-resolved anatomical information, it may be difficult to determine whether variation is due to changes in tissue function, biochemical differences, or thickness variation. For example, the loss of the fluorescence signal either can be a true loss of the fluorescence emission or can be caused by a thickening of overlying tissue layers. The Raman signal, typically much weaker than the tissue's autofluorescence, is often obscured by background signal, such as tissue autofluorescence and fluorescence from components in the light path.

9.2 Multimodal Optical Imaging Systems and Applications

Each individual optical imaging modality is typically sensitive only to a certain change in optical response. For instance, optical coherence tomography measures the backward scattered light from tissue to generate a morphological structural image. Fluorescence imaging measures fluorescence emission from the different biochemical constituents of tissue and generates maps of the tissue biochemistry. All imaging techniques provide valuable information of the light and tissue interaction, yet they are not all capable of comprehensive measurement of optical responses. The sensitivity and specificity of each single imaging modality, considered separately, is often low for detection and diagnosis of diseases.

In order to increase the sensitivity and specificity of optical imaging techniques, an emerging paradigm is to combine two or more optical imaging modalities, originating from independent contrast mechanisms, for a more comprehensive, non-destructive, and minimally invasive tissue characterization. By combining imaging modalities with complimentary contrast mechanisms, such as coherent backscattering for OCT and incoherent fluorescence excitation for fluorescence imaging, the multimodal imaging system can be more sensitive to tissue function and pathology and can have more specificity in detecting abnormal tissues. Multimodal images can be fused together to increase image contrast or can be registered together to reveal structural and function information.

The effectiveness of a multimodal system relies on the combination of the various imaging techniques but not on the extreme diagnostic capabilities of each technique. While multiple imaging modalities can provide complementary information, one modality can also guide another high-resolution, small FOV imaging modality to obtain detailed tissue information or to identify tissue margin.

In this subsection, only a few of the promising multimodal imaging systems will be discussed in detail.

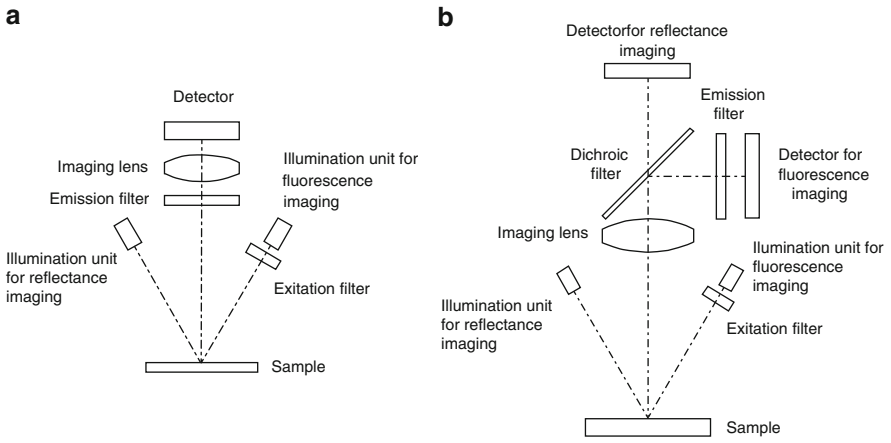

Fig. 9.1 Multimodal area imaging systems. (**a**) Sequential imaging with one detector and (**b**) parallel imaging with two detectors

9.2.1 Multimodal Area Imaging Systems

There are two commonly used area imaging techniques: reflectance imaging and fluorescence imaging. Other area imaging techniques, such as spectral imaging, narrowband reflectance imaging, and polarization imaging, are basically variations of reflectance imaging. Reflectance imaging generally provides a very useful image of surface texture but is limited to detecting lesions based on gross morphological changes, and its sensitivity in detecting change within the tissue is generally low. Fluorescence imaging provides biochemical and structural information of biological specimens. It is very sensitive to early tissue transformation and offers additional information about tissues that is not visible under conventional reflectance imaging. However, its specificity is usually low because it is sensitive to bacteria, food, blood, and other factors.

Because they are based on different contrast mechanisms and are sensitive to independent morphological and/or functional markers of diseases, the combination of fluorescence and reflectance imaging produces images that can better reveal biochemical and morphologic alterations that characterize early neoplasia. Fluorescence images and reflectance images can either be captured simultaneously or sequentially, depending on the system configurations.

Figure 9.1a is a configuration for sequential imaging with two imaging modalities sharing the same imaging path. Typically, only one detector is needed; the fluorescence image and reflectance image are captured by turning on the light source for each mode sequentially. When the wavelength for reflectance imaging is longer than the excitation wavelength for fluorescence imaging, the emission filter for fluorescence imaging can remain in the detection path. However, in some situations,

the emission filter may need to be moved out of the detection path when capturing reflectance image. This is the case, for example, when the excitation spectrum is wide and within the spectrum for reflectance imaging. While the illumination paths for two modalities are separated in Fig. 9.1a, they can share the same illumination path if a dichroic mirror is used to combine the light from two different light sources or if a filter array is used to select the illumination spectrum from the same light source.

Figure 9.1b is a configuration for parallel imaging. Typically, two detectors are necessary to take two images simultaneously. The reflectance signal and fluorescence signal are separated by the dichroic beamsplitter, and an emission filter is needed in the detection path of the fluorescence signal to block the excitation light. One challenge of parallel imaging lies in the choice of the spectra for both imaging modalities. The dichroic mirror separates and directs the fluorescence signal and the reflectance signal to their corresponding detectors. When there is overlap between the excitation light and light for reflectance imaging, or where the excitation light is used for reflectance imaging, a neutral filter may be needed in the reflectance imaging path to attenuate the excitation light which is usually very intense in order to excite sufficient fluorescence response.

Douplik et al. combined autofluorescence imaging and reflectance imaging to improve detection of dysplastic colonic lesions by capturing reflectance and fluorescence images sequentially [1]. The multimodal endoscope increased the detection rate of dysplastic and nondysplastic lesions by 26 and 13 %, respectively, compared to the white light endoscope.

To remove specular reflection in the reflectance image, a multimodal imaging system combining autofluorescence, white light reflectance, and orthogonal polarization reflectance imaging modalities was demonstrated for early detection of oral cancer [2]. The orthogonal polarization imaging removes specular reflection and increases contrast associated with subsurface vasculature, which is often increased in neoplastic lesions.

In order to reduce the false-positive rate, a narrowband reflectance imaging (NBI) was integrated into an autofluorescence endoscope [3]. Autofluorescence imaging scans large tissue surface quickly to identify possible suspicious lesions with high sensitivity, and then NBI is used to characterize the tissue properties in detail because NBI can provide detailed inspection of mucosal patterns for the detection of dysplasia.

Salomatina et al. combined reflectance and fluorescence polarization imaging with spectroscopic analysis of reflectance images for facilitating intraoperative delineation of basal cell carcinoma (BCC) [4]. Two images were captured sequentially, with one light source providing illumination for both imaging modalities and with both imaging modalities sharing the same detection system. Reflectance polarization imaging provides detailed information on skin morphology, and fluorescence polarization imaging exhibits high contrast of cancerous tissue. The optical densities and their wavelength derivatives for tumor and normal tissues can be used for intraoperative cancer delineation.

9.2.2 *Multimodal Imaging Systems Combining Area Imaging and Scanning Imaging Modalities*

Point- or line-scan imaging systems, such as OCT and confocal imaging, provide a microscopic view of tissue but are impractical for screening a large area of interest without a guidance technique. On the other hand, area imaging techniques, such as fluorescence imaging, can screen a large area quickly and may identify a suspected region with reasonable sensitivity. However, the resolution of area imaging is usually low, and it does not provide depth information; therefore, the specificity is usually not sufficient. To obtain the high-resolution depth information quickly and obtain biochemical information about the tissue as well, one solution is to combine a scanning imaging method with an area imaging modality so that the image from area imaging modality can guide a point or line scan.

The combination of OCT and fluorescence imaging is more sensitive to tissue function and pathology than either modality separately because of the complementary nature of contrast mechanisms of coherent backscattering for OCT imaging and incoherent fluorescence excitation for fluorescence imaging. The high-resolution tissue morphology revealed by OCT and the biochemical and metabolic information provided by fluorescence can provide complementary diagnostic information and can enhance the sensitivity and specificity in disease detection and diagnosis, therefore enhancing the ability to detect premalignant and malignant changes during their early stages.

Area imaging and point scanning imaging modalities have different requirements on the imaging optics. For point scanning systems, such as OCT, the imaging lens typically has a large NA and small FOV and is telecentric in tissue space. For area imaging, such as fluorescence imaging, the NA of the imaging lens is usually small, the FOV is relatively large, and telecentricity is generally not required.

For micro-area imaging systems, for example, fluorescence microscopy, the point scanning and area imaging modalities can share the same objective lens, as shown in Fig. 9.2a. A dichroic mirror is employed to combine the two imaging modalities. Typically, the dichroic mirror is designed to reflect shorter wavelengths and transmit longer wavelengths. Because the objective lens focuses two wavelength bands on the tissue, one for area imaging and the other for point scanning imaging, the correction of chromatic aberration presents a potential challenge.

When the FOV for area imaging is large, it is generally difficult for two imaging modalities to share the objective lens. The common configuration is to integrate two independent systems with a dichroic mirror or a relay lens or to simply combine them side by side without any additional component. Figure 9.2b integrates two systems through a dichroic mirror. This configuration is suitable when the working distance of one imaging modality is long enough. One advantage is that two imaging systems share the same optical axis, simplifying image registration.

The multimodal imaging system will generally offer better sensitivity and specificity than either modality alone. The false-positive detection in fluorescence imaging due to presence of bacteria, food particles, and other changes that are

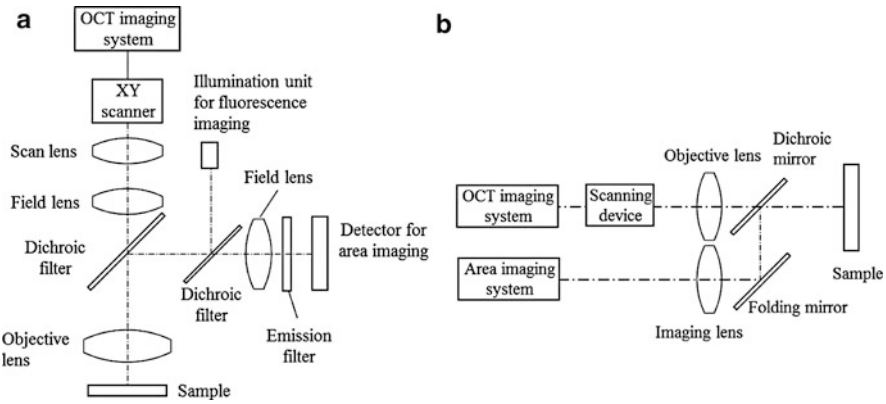

Fig. 9.2 Multimodal imaging system combining area imaging and scanning imaging modalities through dichroic mirrors, (**a**) sharing the objective lens, and (**b**) without common component

not necessarily related to malignant transformation of tissue can be reduced with OCT imaging. McNichols et al. developed a fluorescence-guided OCT endoscope to detect oral cancer with potentially higher sensitivity and specificity [5]. This multimodal imaging system allows rapid identification of suspected regions over a large area using fluorescence imaging and obtains coregistered high-resolution morphological features of the tissue using OCT. The abnormally increased fluorescence due to inflammatory reactions can be clearly differentiated from cancer by OCT imaging; on the other hand, the atypical structure of a mature scar in OCT image could be clarified with a fluorescence image. Pan et al. demonstrated that the specificity of fluorescence detection of transitional cell carcinoma was significantly enhanced by fluorescence-guided OCT (53 % versus 93 %), and the sensitivity of fluorescence detection was improved by combining it with OCT (79 % versus 100 %) [6, 7].

9.2.3 Multimodal Point Scanning Systems

Several imaging techniques discussed in Sect. 9.1 are point scanning techniques, such as OCT, spectroscopy, and confocal imaging. Each of those point scanning systems utilizes a different contrast mechanism and provides distinct information of the tissue under investigation. However, each technique has its limitations.

OCT can provide detailed morphological information of the tissue in real time, but it is sometimes difficult to interpret OCT images because contact of the device with tissue can cause folds, stretching, or other localized tissue deformations. Another issue with OCT imaging is that OCT images are simple maps of variations in reflectivity and do not directly reveal the molecular composition of the tissue.

While spectroscopic techniques in general can extract tissue biochemical or morphological information relevant to disease progression and diagnosis, each of these techniques has its own limitations. For example, the spectra in fluorescence

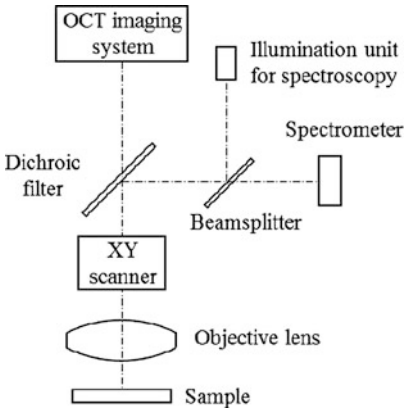

Fig. 9.3 Multimodal imaging system combining OCT and spectroscopic modalities

spectroscopy may be affected by the presence of bacteria, food particles, and other unknown subsurface structures, as well as the depth location of the fluorophores; Raman spectroscopy cannot provide microstructural information even though it can reveal tissue biochemical composition. Without depth-resolved anatomical information, it may be difficult to determine the cause of the variation in spectra.

In order to detect a diseased region with higher sensitivity and specificity, it is useful to combine OCT and spectroscopic techniques into one system for complementary information because of the complementary nature of contrast mechanisms. Spectroscopic data can be spatially and temporally correlated with the tissue structure in OCT images so that the two sets of data can confirm to each other.

Depending on the configuration, the imaging points for two modalities can be either overlapped using a dichroic mirror or separated without any combining component. Tumlinson et al. developed a combined OCT and laser-induced fluorescence (LIF) spectroscopic endoscope for in vivo mouse colon imaging [8,9]. Two systems run in parallel fibers down to the tip of an endoscopic probe and collect the signals from two different points simultaneously. The data can be correlated because the relative imaging points for two modalities are fixed.

In free space, the two imaging modalities are commonly combined with a dichroic mirror located in front of the scan mirror, as shown in Fig. 9.3. Therefore, the two modalities share the same objective lens and can obtain automatically registered, complementary tissue images simultaneously. One challenge is that the objective lens should have good correction of chromatic aberration over the spectrum for both modalities. Barton et al. developed a free-space combined OCT/LIF system to collect simultaneous OCT/LIF data from ex vivo tissues using the same objective lens [10]. A longpass dichroic mirror was employed to transmit the near-IR light for OCT imaging and reflect the UV or blue excitation light for fluorescence spectroscopy.

The configuration in Fig. 9.3 is also applicable for endoscopy when a special fiber, such as double-cladding fiber, is used [11]. The OCT channel uses the core of the double-cladding fiber, while the fluorescence spectroscopy channel delivers excitation light and collects the fluorescence signal through the large-area inner

cladding of the same double-cladding fiber. The OCT signal and fluorescence signal are separated by a double-cladding fiber coupler. This multimodal imaging system has the advantage that the two different signals are collected simultaneously and images are automatically registered.

Yuan et al. demonstrated a coregistered OCT and fluorescence molecular imaging system to obtain molecular information by measuring fluorescence intensity of fluorescent biomarkers which target specific molecules and tissue morphology at high resolution over 2–3-mm FOV [12]. The experimental results from mouse intestinal tissues show that this system has potential applications in small-animal imaging and clinical imaging. The same group also demonstrated a coregistered OCT and line-scan fluorescence laminar optical tomography system to measure depth-resolved tissue structural and molecular information at millimeter imaging scale [13].

Typically, the light sources for two modalities are different. However, in certain situations, the same light source can be used for both modalities. Podoleanu et al. developed a multimodal imaging system using the same light source, a 793-nm superluminescent diode, to produce simultaneous ICG fluorescence and OCT images of the eye fundus [14, 15]. The configuration is the same as Fig. 9.3 except that only one light source is used. This multimodal imaging system enables the user to visualize OCT slices and corresponding ICG angiograms of the ocular fundus simultaneously. The pixel-to-pixel correspondence between the OCT and angiography images enables precisely capturing OCT B-scans at selected points on the ICG fluorescence images.

Using the same configuration in Fig. 9.3, OCT and Raman spectroscopy have been integrated together to collect OCT volumetric data and biochemical Raman spectral maps simultaneously [16, 17]. The addition of Raman spectrometry to OCT allows similar physical structures of the tissue to be distinguished based on their chemical composition. The unique molecular signatures provided by the Raman spectrum allow the intrinsic biochemical composition of a tissue to be identified so that more information can be obtained on disease progression at both tissue and cellular levels.

9.2.4 Multimodal Spectroscopy

Several spectroscopic techniques have been developed to extract biochemical and morphological tissue information that is relevant to disease progression and diagnosis. While each technique alone can detect normal, dysplastic, and cancerous tissues with some degree of sensitivity and specificity, however, due to the complex nature of the disease progression, one type of spectroscopy is often not sufficient to accurately distinguish between normal and diseased tissues.

Because each of these spectroscopic techniques measures a different and complementary tissue parameter, the combination of two or more techniques in a single system provides more complete biochemical and morphological information that can be used in making a more accurate diagnosis. In addition, the multimodal system

also provides depth-sensitive information because each modality usually operates over a different spectrum. The typical wavelength for fluorescence spectroscopy is in the UV region, diffuse reflectance spectroscopy is in the visible region, and Raman spectroscopy is in the near-IR region. The penetration depth of light in tissues increases with wavelength. Therefore, fluorescence spectroscopy measures information at the most superficial level, diffuse reflectance spectroscopy provides information at an intermediate depth, and Raman spectroscopy gathers information from deeper within the tissue.

Typically, one light source, or a broadband light source with wavelength selection filters, is needed for each spectroscopic technique. In free space, the light from each light source is combined together with a dichroic mirror and is focused onto the tissue through the objective lens. The light from the tissue is collected through the same objective lens and is directed to the detector for each modality. In fiber-optic multimodal spectroscopy, the light from each light source is coupled into a multimode illumination fiber, and the light from the tissue is collected by the detection fibers. Each spectroscopic technique has a set of fibers to collect the light from the tissue and direct the light to the corresponding detector. Typically, an imaging lens is used to focus the light from the illumination fiber to the tissue and to couple the light from the tissue to the detection fibers. As an example, Fig. 9.4 shows a multimodal spectroscopy approach developed by Feld et al. to acquire reflectance, fluorescence, and Raman spectra through a fiber-optic probe for a more complete biochemical and morphological information that can be used in detecting and diagnosing disease more accurately [18–20]. This system contains three light sources: a Xe flash lamp with a wavelength selection filter for diffuse reflectance spectroscopy, a 377-nm N_2 laser for fluorescence spectroscopy, and an 830-nm diode laser for Raman spectroscopy. All three light sources are configured to be externally triggerable for data collection. The light from three light sources is coupled into a multimode fiber for illumination and then focused onto the tissue through the imaging lens. A set of fibers collect and send Raman light to a spectrograph after passing an 830-nm notch filter; the rest of the fibers collect reflectance or fluorescence light from the tissue and couple them to a spectrometer. This system demonstrated the ability to detect several morphologic features of vulnerable atherosclerotic plaques, including a thin fibrous cap, a large necrotic core, and an accumulation of superficial foam cells. It has the potential to serve as a robust, catheter-based clinical diagnostic technique.

Various combinations of spectroscopic techniques have been explored. Tunnel et al. developed a reflectance spectrofluorometer for clinical studies in the oral cavity, the uterine cervix, and the gastrointestinal tract. This approach combines diffuse reflectance spectroscopy, light scattering spectroscopy, and intrinsic fluorescence spectroscopy to provide biochemical, structural, and morphological information [21]. Rajaram et al. combined two modalities, namely, diffuse reflectance and intrinsic fluorescence spectroscopy, to obtain complementary information on tissue morphology, function, and biochemical composition for the spectral diagnosis of melanoma and nonmelanoma skin cancers [22]. Volynskaya demonstrated the combination of diffuse reflectance spectroscopy and intrinsic fluorescence spectroscopy

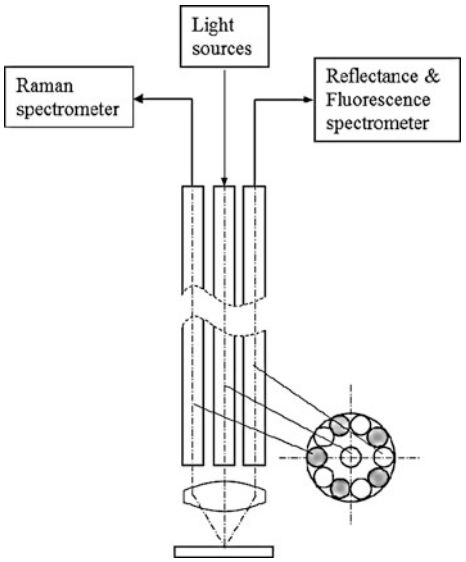

Fig. 9.4 Configuration of multimodal spectroscopy. The illumination light for each modality is coupled into the central fiber, and the signals are captured by surrounding fibers

to obtain promising results for discriminating breast cancer from benign breast lesions [23].

9.2.5 Multimodal Multiphoton Imaging Systems

Both multiphoton microscopy (MPM) and OCT are capable of noninvasive, high-resolution imaging in thick, scattering biological tissues. The contrast mechanisms for these two techniques are intrinsically different in that the former is based on the detection of fluorescence light through multiple photon absorption, whereas the latter detects backscattered light through coherent gating. The combination of OCT and multiphoton imaging offers complementary structural and functional information about tissues and is a powerful imaging tool that has both the sensitivity and specificity necessary to detect precancerous and cancerous lesions on both tissue and cellular levels [24]. It also has the potential to identify a particular area of interest through OCT and obtain high-resolution stack of multiphoton image of this particular region.

Typically, OCT and multiphoton imaging require different light sources in order to achieve optimal performance. Multiphoton imaging requires an ultrashort pulse laser for efficient excitation, and OCT needs a light source with broad bandwidth for high-resolution imaging. This is because multiphoton efficiency is proportional to the inverse of the laser pulse duration and the axial resolution of OCT is inversely proportional to the spectral bandwidth. While it is ideal to use different light source for each modality, one light source is also possible for both modalities [25].

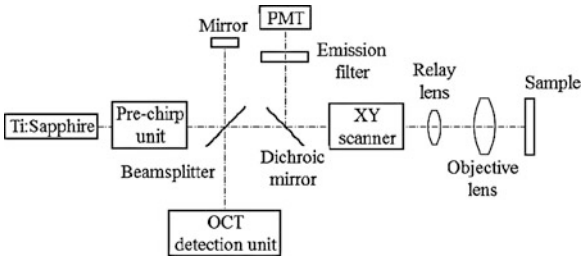

Fig. 9.5 Schematics of the combined multiphoton and optical coherence microscopy system

Figure 9.5 is a multimodal imaging system using one light source, a Ti:sapphire laser, that provides efficient multiphoton excitation and the broad bandwidth required for high-resolution OCT. Pulse duration and bandwidth are selected based on OCT resolution requirements and efficient fluorescence excitation. In the illumination path, no excitation filter is needed because the excitation spectrum is relatively monochromatic and is distinct from the emission spectrum. The prechirp unit, consisting of prisms or a grating, precompensates the dispersion later accumulated from the objective lens and from other optical components in the beam delivery path. The beam is then split by a beamsplitter into two arms, the sample arm and the OCT reference arm. The laser beam in the sample arm is raster scanned by two galvanometer mirrors and relayed by the relay lens to the entrance pupil of the objective lens. Then, the laser beam is focused onto the sample. The fluorescence signal and backscattered signal are collected by the same objective lens; the two signals are separated by the dichroic mirror after being descanned. The fluorescence signal is directed to the photomultiplier tube (PMT) to construct a multiphoton image, and the backscattered light is sent to the OCT detection path for interference with the reference beam. The dichroic mirror in the detection path can also be placed between the objective lens and the scan mirror for higher throughput. Without being descanned, the emission light is not motionless at the detector plane as the excitation beam is scanned across the sample. Therefore, the photosensitive surface of the detector must be sufficiently large and the quantum efficiency should be uniform. With simultaneous acquisition, perfect image registration is achieved, providing spatiotemporal relationships between tissue structure and function.

Because both OCT and multiphoton imaging have high resolution, it is important that the multimodal images be acquired from the same sampling volume. It is also desirable that two modalities have matched transverse and axial resolutions. The transverse and axial resolutions of MPM are determined by the NA of the objective lens. The NA is usually large in order to focus the laser beam to a small volume for high efficiency of nonlinear excitation. In OCT imaging, the transverse resolution is similarly determined by the NA of the objective lens, but its axial resolution comes from the coherence length of the light source, independent of the NA. Therefore, the coherence length of the light source should be selected to match the axial resolutions of multiphoton and OCT imaging. Tang et al. demonstrate that MPM and OCT channels can be coregistered with lateral resolution of approximately 0.5 μm and axial resolution of approximately 1.5 μm, utilizing an objective with 0.95 NA and

a 12-fs Ti:sapphire laser with a wavelength of 800 nm and a spectral bandwidth of 100 nm to provide short pulses necessary for efficient multiphoton excitation and the wide bandwidth for high-resolution OCT [26]. Vinegoni et al. combined optical coherence microscopy (OCM), MPM, and second harmonic generation (SHG) microscopy using a frequency-doubled Nd:YVO4-pumped Ti:sapphire laser with a center wavelength of 800 nm, a bandwidth of 60 nm, and an 80-MHz pulse repetition rate [27]. It was demonstrated that this system allows for the simultaneous acquisition of both anatomical (structural) and functional imaging information for applications in the fields of tissue engineering and cell biology.

9.2.6 System Combining Optical and X-Ray Imaging Techniques

Animal models are commonly used to study morphological changes of the diseased tissues in traditional research on disease mechanisms. This requires the excision and pathological study of the tissue of interest. Usually, it takes a long time period for measurable changes to occur and requires a large number of animal subjects because a number of animals are often sacrificed at each time point for histological evaluation.

Optical molecular imaging has been developed to study the disease process at the molecular level within living animals using fluorescence imaging contrast agents. This method has the potential in detecting specific molecular and metabolic changes within target tissues long before morphological changes can be detected. One advantage of fluorescence optical imaging is that the molecular changes can be monitored in vivo without sacrificing the animal. It has been routinely used in preclinical research and drug development.

While optical molecular imaging provides good sensitivity and specificity to molecular targets, it does not provide the appropriate contextual anatomical data for accurate localization of the molecular imaging signals within the animal. On the other hand, as a nonoptical imaging technique, X-ray imaging can provide accurate anatomical information and even 3-D anatomical information through computed tomography (CT).

Combining optical molecular imaging with X-ray imaging can provide both anatomical and functional information, with X-ray images providing the detailed penetrating anatomical guideposts to enhance the localization of the optical molecular imaging agent [28]. This approach can enhance the localization of molecular signals in live animals, with the anatomical information from X-ray imaging and the molecular signals from optical imaging. X-ray images are typically overlaid with optical images, allowing functional quantitative fluorescence data to be spatially/anatomically defined against the skeletal structure.

To combine an optical molecular imaging system and an X-ray imaging system, usually one high-sensitivity cooled CCD camera is needed to take both the fluorescence image and X-ray image through the scintillator plate, as shown in

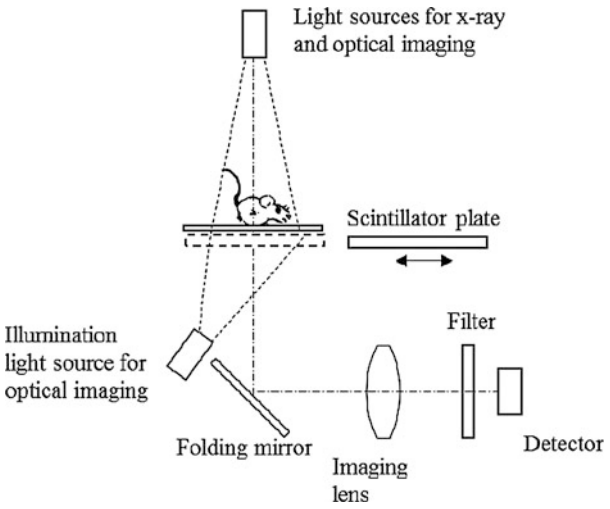

Fig. 9.6 Multimodal imaging system combining optical and X-ray imaging. The scintillator plate is moved into the detection path for X-ray imaging

Fig. 9.6 [29]. When taking X-ray images, the moveable CsI scintillator plate is moved into the imaging path and the X-ray irradiates the animal from above. The X-rays are differentially absorbed by bone and soft tissue, creating a projection of the animal's anatomical structure onto the phosphor screen. The phosphor plate then converts the X-ray signal to visible light, and the light is captured by the CCD camera at very high resolution. As both optical and radiographic images are captured at the same plane, they can be easily and precisely overlaid into one coregistered multimodal image.

9.2.7 Other Multimodal Imaging Systems

9.2.7.1 Multimodal Confocal Imaging Systems

Confocal imaging is an established optical imaging technique used for high-resolution imaging of cells and tissues. It can be performed in either reflectance or fluorescence mode, and both modes provide valuable and complementary information about disease processes. The combination of reflectance and fluorescence modes allows investigation of morphological change as well as molecular change in tissue, providing valuable and complementary information about the tissue. The multimodal system may have higher sensitivity and specificity in detecting precancerous lesions at earlier stages of neoplastic progression by imaging the molecular changes using molecular-specific contrast agents as well as the morphological changes [30–32].

The configuration is the same as that used for confocal fluorescence imaging. When the emission filter is moved out of the detection path, the captured image is a reflectance image from the excitation light. When two detectors are used, the two images can be obtained simultaneously, with a dichroic mirror separating light with different wavelengths.

9.2.7.2 Multimodal Photoacoustic Systems

Photoacoustic microscopy is an optical absorption-based imaging technique that detects laser-induced photoacoustic waves as a result of specific optical absorption. Three-dimensional photoacoustic images of tissue are acquired with scanning of optical illumination and ultrasonic detection. In addition to high-resolution structural information, OCT can also provide functional information about blood flow by measuring the Doppler shift. However, imaging hemoglobin oxygen saturation is still beyond the capability of conventional OCT.

Jiao et al. developed a multimodal imaging technique by integrating photoacoustic microscopy and spectral-domain OCT to acquire simultaneous volumetric microscopic images of both optical absorption and scattering contrasts in tissue [33]. The multimodal system provides 3-D microscopic imaging of biological tissues with complementary contrast mechanisms (optical absorption and scattering). In the integrated system, the illumination light for two modalities is combined with a dichroic mirror and then focused onto the same point inside the tissue through the scan mirror and the objective lens. The backscattered light is collected by the same objective lens and sent to the OCT detector. The photoacoustic wave generated from the focused point is detected directly by the ultrasound detector.

The multimodal system can potentially provide comprehensive information about biological tissues, including tissue anatomy, blood flow, and hemoglobin oxygen saturation, all from a single instrument.

9.3 Development of Multimodal Imaging Systems

The fundamental requirement in developing an efficient multimodal imaging system is that each imaging modality should have a different contrast mechanism. Otherwise, the additional information gained from different imaging modalities has limited value. The choice of modalities is driven by the contrast mechanism of each imaging system, the tissue being studied, the depth-resolved capability, and the working condition, such as whether the diagnosis is to be performed in vivo or ex vivo.

Multiple imaging modalities are typically combined through spatial, spectral, or temporal integration. In spatial integration, the imaging systems are combined without a common component; the respective optical axes are not overlapped, but partial or entire FOVs are overlapped. The images can be captured simultaneously

or sequentially, while each modality works independently. In spectral integration, different imaging modalities are integrated through the dichroic combiner. The optical axes may or may not overlap, and different modalities may share some components, such as the objective lens and scanner. One requirement for this configuration is that the each modality should have a distinct working spectrum with minimal overlap. For example, fluorescence imaging and optical coherence tomography can be spectrally incorporated because most endogenous components do not absorb or emit within the OCT spectral range. In temporal integration, each modality is basically independent without common component. Multimodal images are captured by moving the sample to the object plane of each modality or moving each modality to the sample sequentially. This configuration is time-consuming and the sample or the system should be stable enough so that multimodal images can be correlated accurately. Therefore, temporal integration is typically used to demonstrate the concept and is not commonly used in clinical applications.

Multimodal images can be acquired either sequentially or simultaneously. If the spectra of different modalities overlap, the system should be time multiplexed, which means that images are captured sequentially. When the spectra do not overlap, it is preferable to capture images simultaneously for better registration and faster image capture. Sometimes, it is difficult to image biological events that occur over a short interval by using a multimodal imaging system which requires switching between light sources and associated optical paths. For such applications, it is necessary to image all the details contained in the specimen at the same time.

In certain situations, spectral overlap is advantageous because more than one image can be captured with only one illumination beam. One example is dual-channel optical coherence tomography and indocyanine green dye (OCT–ICG) fluorescence system for investigation of the eye fundus [14]. The same superluminescent diode is used to simultaneously generate the OCT image and excite the ICG fluorescence. Pixel-to-pixel correspondence between the OCT and fluorescence images allows the user to obtain OCT B-scans precisely at selected points on the ICG images.

The effectiveness of a multimodal system relies on the combination of the various imaging techniques but not on the extreme diagnostic capabilities of each technique. It is always challenging to integrate different imaging techniques into one system because specific hardware is typically required for various imaging modalities. The clinical environment also does not allow for very complex instrumentation. Therefore, short-scale, simple, and reliable configurations must be considered for a multimodal system.

To develop an effective multimodal imaging system, one needs to understand the different types of information needed to obtain, principles and design considerations for each imaging modality, photon paths in the tissue, depth-resolved requirements, and signal separation. The design also needs to consider the resolution, material constraints, FOV, light source, illumination system design, and imaging system design.

9.3.1 Multimodal Imaging System Combining Polarized Reflectance, Fluorescence, and OCT Imaging

To improve sensitivity and specificity in rapid screening and diagnosis of disease, one potential approach is a multimodal imaging system combining polarized reflectance, fluorescence, and OCT imaging modalities. Polarized reflectance imaging provides a true-color surface image without specular reflection, fluorescence imaging detects biochemical changes, and OCT imaging investigates subsurface features of suspicious regions. The information provided by these three imaging modalities is complementary and can increase sensitivity and specificity in detection and diagnosis of diseases.

Fluorescence imaging is sensitive to early tissue transformation and is suitable for rapid screening of a large area, but it is sensitive to the environment and it can be difficult to quantify the data obtained. OCT imaging can provide a high-resolution depth image, but its FOV is typically small. With this multimodal system, one can use sensitive fluorescence imaging to locate suspicious regions rapidly, then guide OCT imaging to investigate the subsurface feature of suspicious regions.

Figure 9.7 shows two configurations of multimodal systems combining polarized reflectance, fluorescence, and OCT imaging modalities. In Fig. 9.7a, three modalities share the same objective lens through the dichroic mirror, which transmits visible light and reflects near-infrared light. The light for reflectance and fluorescence imaging is combined by another dichroic mirror. The polarizer or excitation filter is placed in front of the light source for the corresponding modalities, respectively. An analyzer and emission filter can either be moved in/out of the imaging path when taking the corresponding images or stay in the detection path. The three-dimensional OCT image is obtained by scanning the focused beam across the object through the scan mirror and scan lens. This configuration is suitable when the FOV is small and high resolution is required. The requirement for the objective lens is more demanding, considering the special needs for each modality. For example, both depolarization effects and autofluorescence in the objective lens should be minimized.

The configuration in Fig. 9.7b shows an approach for large-imaging FOV. Polarized reflectance imaging and fluorescence imaging share the same imaging lens, and OCT imaging has its own objective lens. The polarized light and excitation light illuminate the object directly without a dichroic mirror. The achievable resolution is typically lower than that in Fig. 9.7a because of the longer working distance. Because the analyzer and emission filter can be placed in front of the imaging lens, depolarization and autofluorescence in the imaging path will not degrade image quality; therefore, conventional optical materials can be used in the imaging path.

To design such a multimodal imaging system, we need to understand how to design each subsystem. This section will focus on the design of fluorescence imaging and polarization imaging. The design of OCT system is discussed in Chap. 5.

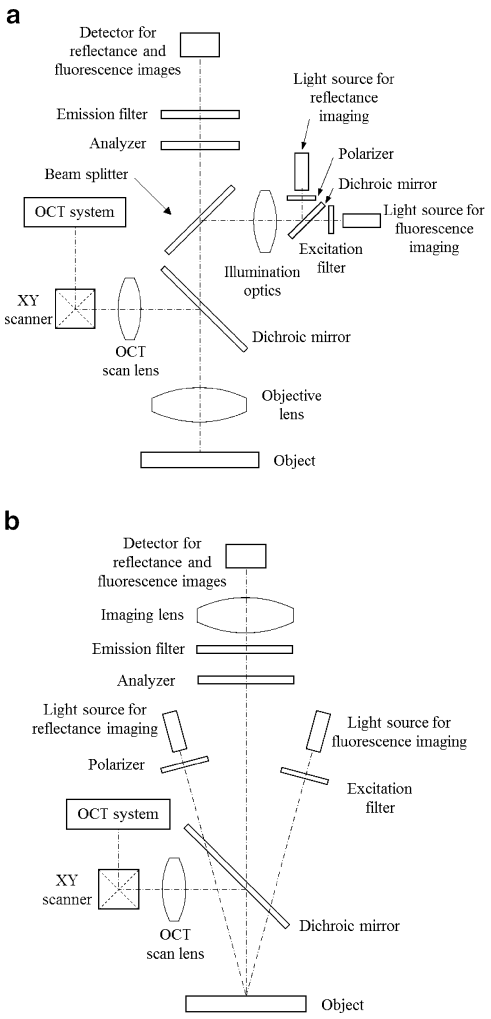

Fig. 9.7 Configurations of multimodal imaging system combining polarized reflectance, fluorescence, and OCT imaging modalities. (**a**) Three modalities share the objective lens, and (**b**) only polarized reflectance and fluorescence imaging use the same imaging lens

9.3.2 Fluorescence Imaging

As shown in Fig. 9.8, most fluorescence imaging systems have the following key elements: light source to excite fluorescence, illumination optics to deliver the excitation light, light collection or imaging optics to collect the fluorescence signal, fluorescence filters, and a detector to capture the fluorescence signal. Fluorescence filters generally include excitation filter, emission filter, and dichroic beamsplitter.

An effective fluorescence imaging system requires careful consideration of the illuminating light source, excitation/emission filters, and detector, as well as the illumination and detection optics because the fluorescence signal is typically very weak. In this section, these components will be discussed in detail.

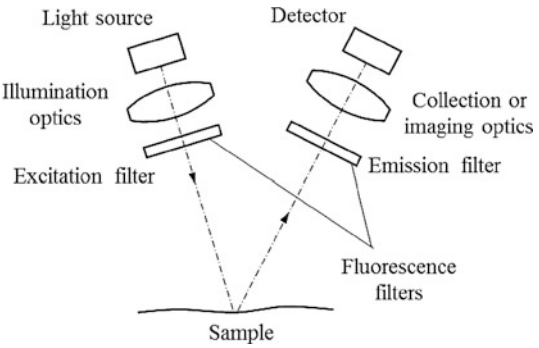

Fig. 9.8 Configuration of a typical fluorescence imaging system

9.3.2.1 Light Sources

The most important requirement of the light source in fluorescence imaging is a close match of the spectrum to the excitation wavelength of the fluorochrome to achieve high brightness and high contrast images. The wavelength of the light source determines which type of fluorophore can be excited and how well that fluorophore can be excited. The wavelength away from the peak of the excitation spectrum may produce background noise that can overshadow the fluorescence signal of interest. The wavelength is also the major factor in determining the probed depth, given that the penetration depth of light in tissue strongly depends on the wavelength.

Light source intensity is the other major factor in fluorescence imaging. Most fluorophores have low quantum yields; therefore, powerful light sources are needed to excite enough fluorescent light to be detected by the eye or other detectors.

There are two types of light sources used in fluorescence imaging: noncoherent and coherent sources. Noncoherent light sources are usually broadband; these are typically used in spectroscopy and area imaging systems. The most common noncoherent light sources are mercury, xenon, and metal halide arc lamps.

The light intensity of a mercury (HBO) lamp is not uniform from UV to near-IR light, with peaks of intensity at 313, 334, 365, 406, 435, 546, and 578 nm; in between the peaks, the energy of the light source is very low. HBO lamps are suitable for the applications that need blue or UV light to excite fluorescence.

Xenon arc (XBO) lamps have a relatively flat emission spectrum without emission peaks across the visible spectrum. The uniform emission levels and lower fluctuations make XBO lamps better suited to applications in ratio imaging and other quantitative applications. XBO lamps also have the advantage that they exhibit stable emission intensity over time.

Mercury–xenon arc lamps have the best characteristics of both xenon and mercury lamps. The spectral distribution of a mercury–xenon lamp includes a continuous spectrum from the ultraviolet to infrared and a strong mercury line spectrum. It has a bluish-white spectrum and extremely high UV output.

Metal halide (HXP) lamps have a similar emission spectrum to mercury lamps. In addition to higher radiation levels in the continuous regions between lines, HXP lamps have an emission output featuring pressure-broadened versions of the prominent mercury arc spectral lines.

One advantage of arc lamps is that one light source can be used for either broadband illumination for reflectance imaging or narrowband illumination for fluorescence and reflectance imaging. The disadvantages are that they are bulky, and one or more filters are required to select the spectrum for optimal fluorescence excitation.

With recent advances in efficiency and thermal management, light-emitting diodes (LEDs) are finding more and more applications in biomedical imaging. LEDs produce an output with a spectrum bandwidth wider than the laser but much narrower than the arc lamp. The diverse spectra afforded by LEDs make it possible to select an individual LED to supply the optimum illumination wavelength for a specific application. Although LEDs are regarded as narrowband light sources, there are still tails outside of the LED spectrum. These tails must be blocked when LEDs are used as the excitation light source in fluorescence imaging system.

LEDs have several advantages over the other noncoherent light sources, including compact size, low power consumption, low heat generation, fast switching, high emission stability, and extremely long life span. LEDs can instantly illuminate at full intensity as soon as electrical current is applied. The controllable stability of LED intensity is a key benefit for biomedical imaging when consistent and repeatable measurement is required for quantitative analysis.

A laser, the only coherent light source, is monochromatic. Lasers produce a highly coherent light, which can be collimated, expanded, and focused to a diffraction-limited spot. The laser beam can be easily coupled into an optical fiber and delivered to a remote site. Many fluorescence-scanning devices for biomedical applications use lasers as their excitation light sources, given that the combination of focused energy and a narrow spectrum width contributes to excellent sensitivity and resolution.

There are a number of commonly used lasers in fluorescence imaging. Argon lasers generate a variety of wavelengths from UV to visible light, for example, 364, 457, 488, and 514 nm. They are often used as the excitation source for many common fluorophores, such as fluorescein isothiocyanate (FITC) and Cy2. Neodymium:yttrium aluminum garnet (Nd:YAG) solid-state lasers can generate a strong line at 532 nm using a frequency-doubling method and can be used to excite Cy3. The helium–neon (HeNe) laser at 633 nm is usually used to excite Cy5. HeNe lasers with other wavelengths have also become available.

9.3.2.2 Illumination Path

The basic requirement of the illumination system for fluorescence imaging is to closely match the excitation peak of the fluorophore to excite the fluorescence effectively. Other considerations include illumination efficiency, intensity, and

uniformity. The fluorescence signal is usually very weak; therefore, the efficiency of the light delivery system becomes much more important in fluorescence imaging system compared to other imaging systems. The intensity must be sufficient to excite fluorescence from the object. The fluorescence emission is generally less sensitive to the angle of illumination than the irradiance. Therefore, there is no special requirement for uniformity of angular distribution. However, good spatial uniformity is required in order to achieve high-contrast fluorescence images within the FOV because the fluorescence signal at each point is proportional to the level of illumination at that location.

For simple fluorescence imaging systems, excitation light can be delivered to the sample from a light source directly without any additional optics. For some applications, an array of light sources, typically LEDs, provide enough excitation light with reasonable uniformity. For many fluorescence imaging systems, illumination optics are required in order to deliver excitation light to the sample more efficiently and uniformly. In conventional fluorescence microscopes, Köhler illumination is generally employed. When there is no beam-shaping element for improving the spatial distribution of the light from the light source, the arc of the light source, or the emitting surface, should be imaged onto the entrance pupil of the objective lens for better illumination uniformity. For other fluorescence imaging systems, such as macro imaging systems, beam-shaping elements (such as a lenslet array, light pipe, or aspheric elements) are usually used to provide spatially uniform excitation light to the sample.

When illumination and imaging paths share the same objective lens, the transmission of both the excitation and emission light should be as high as possible. Optical glasses are typically optimized for excellent transmittance throughout the total visible spectrum from 400 to 800 nm and usually do not transmit near-UV light well enough, especially dense flint glasses. For example, N-SF6, commonly used in negative optical element for chromatic aberration correction, has an internal transmittance of 0.04 at 365 nm for a 10-mm slab. BK7, fused silica, CaF2, FK5 HT, LLF1 HT, and LF5 HT are glasses with excellent homogeneity and UV transmittance and are often used in fluorescence imaging systems. For example, FK5 HT has a transmittance of 99 % at 365 nm, and the transmittance of fused silica at 193 nm is 98 %.

Another consideration of optical materials for fluorescence imaging is autofluorescence. Autofluorescence of optical components is considered an isotropic generation of the secondary stray light inside the system. This is undesirable and should be minimized because it is a major source of unwanted light in fluorescence imaging systems. Ideally, the optical materials used in the illumination path should not emit autofluorescence, although the negative effect of autofluorescence can be minimized by placing an excitation filter as the last element in the illumination path.

One more requirement on illumination is sample protection, especially in live-cell imaging applications. The sample must be protected from overexposure either by attenuating the light intensity or by limiting the duration of the illumination to the exposure time of the sensor.

9.3.2.3 Fluorescence Filters

The goal in developing fluorescence imaging systems is to excite the fluorophore as efficiently as possible and to collect as much emitted fluorescent light as possible while blocking as much excitation light as possible in the detection channel. Fluorescence filters are the key components to achieving this goal. Generally, one or more of the following filters are necessary in a fluorescence imaging system:

1. Excitation filter to select the optimal excitation wavelength from a light source
2. Emission filter to specifically transmit the emission wavelength of the light emitted from the sample and to block the excitation light
3. Dichroic beamsplitter to separate the excitation and emission light

Properties of Fluorescence Filters

There are four types of filters commonly used in fluorescence imaging: shortpass filter, bandpass filter, longpass filter, and dichroic beamsplitter. Dichroic beamsplitters, also called dichroic mirrors, are usually designed for a 45° angle of incidence to separate beams of two different spectral ranges. The dichroic beamsplitter can be either a flat plate or a cube. The advantage of a beamsplitter cube is that there is no spatial shift for the transmitted beam.

A fluorescence filter is composed of a substrate onto which a stack of thin layers of different dielectric materials, with alternating high and low refractive indices, are deposited. The specifications of thin film filters include performance specifications, such as center wavelength, average passband transmission, bandwidth, edge sharpness, cut-on/cut-off wavelengths, and optical quality specifications, such as surface flatness, wedge, transmitted wavefront distortion, scratches and digs, pinholes, and clear aperture. The center wavelength of a bandpass filter is the mean of the wavelengths at 50 % of peak transmission. The bandwidth is defined as the full width half maximum (FWHM) of the passband. The average passband transmission is the average transmission of light passing through the filter within the passband or transmission band. Wavelengths with 50 % peak transmission in the transition region are commonly called cut-on and cut-off wavelengths. Surface flatness, typically specified in fractions or multiples of a wavelength, is a measure of the deviation of the surface from a perfect flat plane. Wedge, measured in arc minutes or arc seconds, defines how parallel the two outer surfaces of a thin film filter are. Transmitted wavefront distortion, measured in fractions or multiples of a wavelength, is the distortion of a plane wave when transmitted through a filter. Scratches and digs specify the surface quality of a thin film filter. A comprehensive surface quality specification is typically stated as a scratch–dig combination, such as 60–40. Pinholes are small breaks in the coating of a thin film filter.

As shown in Fig. 9.9, thin film filters have several performance limitations when the angle of incidence differs from the nominal value: blue shift of cut-on and cut-off wavelengths, polarization splitting, distortion of the transmitted profiles, and

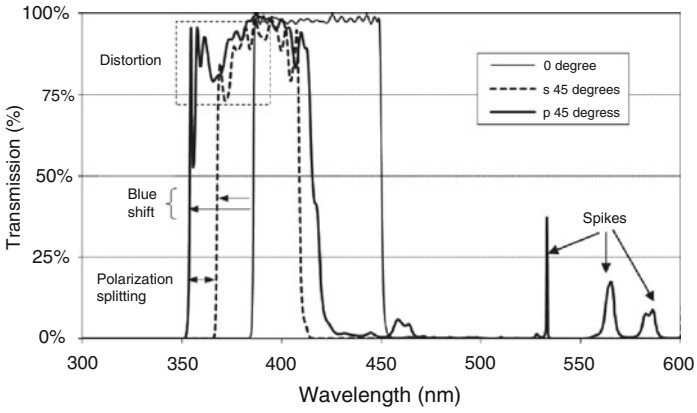

Fig. 9.9 Filter performance and angle of incidence

spikes in the blocking band. Those undesired effects become more pronounced as the deviation in angle of incidence increases.

Selection of Fluorescence Filters

It is crucial that optical filters be chosen to give the best performance, both in brightness and contrast, for a given fluorophore. The ratio of the emitted fluorescence intensity to the excitation light intensity in a typical application is between 10^{-4} (for very highly fluorescent samples) and 10^{-6}. Therefore, the system must attenuate the excitation light by as much as 10^{-7} (weak fluorescence) without diminishing the fluorescence signal. A good combination of optical filters can reduce excitation light noise and stray light from the excitation source and other components, as well as instrument autofluorescence outside the emission band.

When choosing an excitation filter, both the light source spectrum and the excitation spectrum have to be considered because the range and overall shape of the emission profile are the same for any wavelength inside the excitation spectrum. It is advantageous to use as much light within the excitation spectrum as possible from the light source, provided that all the excitation light can be blocked by the longpass or bandpass filter in the detection path. However, allowing a wide range of wavelengths away from the peak of the excitation wavelengths further increases the background noise and may damage the object. Therefore, a bandpass filter is usually preferred because the shortpass filter also passes UV light, which can cause photobleaching and autofluorescence noise.

Because the observed background autofluorescence roughly increases in proportion to the bandwidth of the excitation spectrum, narrowing the bandwidth of the excitation filter can reduce the background noise and enhance image contrast. However, this reduces image brightness as well. Therefore, a balance should be

chosen between the level of contrast and brightness for a given application. For many applications, the optimal bandwidth of an excitation filter is approximately 40 nm and is centered on the absorption maximum of the fluorophore.

The illumination system in fluorescence imaging is designed for uniform illumination on the tissue with high efficiency and minimal flare, not desired for the true imaging of the light source. The industry standard for commercial quality is sufficient for excitation filters. Specifically, the wedge is less than ± 3 arc minutes, the scratch–dig is 80–50, the thickness tolerance is ± 0.15 mm, and the transmitted wavefront error is less than 5 λ/inch.

Emission filters can be either longpass or bandpass filters. A longpass filter may be preferred when the application requires a maximum emission signal and when spectral discrimination is not necessary. It transmits fluorescence from all fluorophores with an emission spectrum longer than its cut-on wavelength. Bandpass filters should be selected to maximize the signal-to-noise ratio (SNR) for applications where discrimination of signal components is more important than overall image brightness. For a high-resolution fluorescence imaging system, a bandpass filter that transmits a band at or near the emission peak of the fluorophore generally minimizes the background noise and improves the sensitivity and linear range of the measurement.

The bandwidth of the emission filter has a major impact on the brightness and contrast of the fluorescence image. Brightness increases with increasing bandwidth of the emission filter, while contrast is higher when the bandwidth is narrower. The narrower the bandwidth of the emission filter, the more selectively it transmits the desired fluorescence signal and further reduces background noise, resulting in higher contrast. But if the bandwidth of the emission filter is too narrow, the signal itself becomes too weak for detection. Bandpass filters with a bandwidth of 20–40 nm are optimal for most fluorescence imaging applications. Filters with a bandwidth greater than 40 nm allow for the collection of light at a wider spectral range and give a higher total signal; however, it is more difficult to discriminate between closely spaced, overlapping emission spectra. Filters with bandwidths narrower than 20 nm transmit fewer signals and are most useful with fluorophores with very narrow emission spectra.

The dichroic mirror is typically mounted at a 45° angle to the optical axis of the objective lens to reflect light in the excitation band and to transmit light in the emission band. The transmission cutoff of the dichroic mirror lies between the fluorophore's excitation spectrum and its emission spectrum such that the excitation and emission wavelengths are separated effectively. To collect as much fluorescence signal as possible, a shorter cutoff wavelength is usually chosen when the excitation spectrum and emission spectrum are close and Stokes shift is small. In addition, both coating and substrate materials of the dichroic beamsplitter should have minimal autofluorescence.

The emission filter and dichroic beamsplitter in the detection path generally require an industry standard for precision quality where the wedge is less than ± 1 arc min, the scratch–dig is 60–40, the thickness tolerance is ± 0.05 mm, and the transmitted wavefront error is less than 1 λ/inch.

Brightness and contrast are two important aspects in evaluating a selected set of fluorescence filters. Ideally, the selection of fluorescence filters should maximize both brightness and contrast. However, a trade-off has to be made because brightness and contrast are usually contradictory. As a general rule, excitation filters are chosen to maximize blocking in the emission filter transmission passband, while emission filters are chosen to maximize blocking in the corresponding excitation filter passband. The dichroic beamsplitter is selected to maximize both the excitation and emission light intensities. Also, it is preferable to block out-of-band light with an excitation filter instead of with an emission filter.

The optimal position of the excitation filter is where the range of the ray angle is small and away from the light source to reduce the angular effect of the optical coatings and autofluorescence of the components in the illumination path. To reduce autofluorescence from the components in the detection path, the emission filter should be placed in front of other optical components in the detection path. However, in many applications, it is not practical to place the emission filter as the first element. For example, in a fluorescence microscope, there is not enough space for the emission filter in front of the objective lens. The next optimal location for the emission filter is where the range of ray angles is small.

9.3.2.4 Imaging Path

The basic requirements for the detection system in a fluorescence imaging system include high-resolution, high fluorescence signal collection and transmission. When the excitation and detection paths share the same objective lens, a high transmission of the excitation light is an additional requirement.

Generally, high-resolution and high light-collection efficiency are related through the NA: the larger the NA, the higher the resolution and light-collection efficiency. In cases where the fluorescence signal is more critical than the resolution, it is often a better choice to design the imaging lens with a large NA but with lower aberration correction using fewer optical elements.

One critical optical property of optical materials in fluorescence imaging is autofluorescence. Autofluorescence of optical components is considered an isotropic generation of the secondary stray light inside the system. This is undesirable and should be minimized because it is the major source of unwanted light in fluorescence imaging systems. Autofluorescence in optical glass is generated by color centers, which are originated by rare earth elements and other critical impurities in optical glasses. The autofluorescence of plastic optics is significantly higher than that of optical glass, especially in the short wavelengths. At a short wavelength near 400 nm, the autofluorescence of plastic optics is about 5 to 10 times higher than the Borofloat glass.

It is difficult to prevent autofluorescence from the optical materials from reaching the detector. Therefore, it is critical to select optical materials with low autofluorescence coefficients in order to obtain high-contrast fluorescence images.

9.3.2.5 Detectors

The detector is one of the key components in biomedical imaging because it determines at what level the signal can be detected, what relevant structures can be resolved, and the dynamics of the process that is visualized and recorded. Through the detector, the optical signal is converted into electrical energy, thereby producing a measurable signal that is proportional to the number of photons detected. The measured, continuous analog signal is then converted to a discrete digital signal. Given that there are a limited number of intensity conversion levels, 8, 10, 12 or 16 bit, it is unavoidable that this conversion process introduces a certain amount of error.

Three commonly used light detectors are photodiode, PMT, and solid-state imaging sensors. The first two employ a photosensitive surface that detects incident photons and generates an integrated electronic signal, but these devices lack spatial discrimination. PMTs can be used to detect the incoming photons at high speed because they do not store a charge and can respond to changes of the input light within a few nanoseconds. PMTs typically generate a low noise signal and have a large dynamic range to accurately reflect the photon flux. PMTs also have large gain without sacrificing bandwidth.

Silicon photodiode and avalanche photodiode devices (APDs) also respond very quickly to incoming light but without large gain. Compared to PMTs, the spectral sensitivity of photodiodes is relatively flat and the quantum efficiency (QE) is relatively high over the entire visible spectrum. The major drawback with photodiodes is that they produce a considerable amount of noise, resulting in a low SNR under photon-limited conditions, which is the case for fluorescence imaging. Another disadvantage, compared to PMTs, is that the photosensitive surface is smaller than the PMT.

Solid-state imaging sensors consist of a dense matrix of photodiodes incorporating charge storage regions. CCD and CMOS detectors are two commonly used solid-state detectors in biomedical imaging. Solid-state sensors can be characterized by a number of parameters including QE, dynamic range, uniformity, SNR, response speed, and spatial resolution.

The CCD is the most widely used imaging sensor in biomedical imaging. While a CCD sensor is usually operated at room temperature, the performance can be significantly enhanced by cooling the sensor to reduce the dark current. Although the CCD consists of silicon photodiodes, its spectral sensitivity is different from that of a simple silicon photodiode detector because the CCD surface has channels used for charge transfer, which are shielded by polysilicon gate electrodes. These structures absorb the shorter wavelengths, resulting in a lower blue sensitivity of the device. These losses can be eliminated in the back-illuminated CCD where light falls onto the back of the CCD in a thinned and transparent region.

There are a number of new CCDs developed for some special applications, such as slow scan CCD, intensified CCD (ICCD), and electron multiplying charge coupled devices (EMCCD). Slow scan CCDs are designed specifically for low

light applications. They have very low background and low noise, allowing for long image acquisition time. The readout and thermal noise are minimized through slow readout rates and cooling. Slow scan CCD cameras are generally limited in their frame rates, and the SNR is poor when exposure times are short, unless the specimen has extremely bright fluorescence. ICCD uses an image intensifier that is fiber-optically coupled to the CCD chip to increase the sensitivity down to a single photon level. The image intensifier converts incoming photons into electrons at the photocathode, multiplies the electrons with high-voltage acceleration through a microchannel plate, and then reconverts the multiplied electrons back to photons through a phosphor-coated window. The photons emitted at the phosphor-coated window are then projected onto a CCD through a fiber-optic plate. ICCD cameras have very fast response times and the CCD camera readout is the slowest step in the image acquisition. ICCD cameras are frequently used in studying dynamic events and for ratio imaging of ion-sensitive fluorochromes. EMCCD is developed for applications that demand rapid frame-rate capture at extremely low light levels. EMCCDs employ an on-chip amplification mechanism to multiply the photoelectrons that are generated in the silicon; therefore, the signal from a single photon event can be amplified above the read noise floor at fast readout speeds.

A CMOS sensor is a low-cost, compact, versatile detector with the virtues of silicon detection but without the problems of charge transfer. Rapid developments in CMOS sensors give them a potentially important future role in fluorescence imaging. CMOS sensors have an amplifier and digitizer associated with each photodiode in an integrated on-chip format, which allows manipulation of individual photodiodes, user-selectable ROI readout, high-speed sampling, electronic shuttering, and exposure control.

The key parameters to consider when selecting the optimal detector for a specific application include QE, internal gain, dynamic range, response speed, and noise. The selection of detector also depends on the temporal resolution required to study specific biological processes. For a process with picosecond or nanosecond time resolution, for example, fluorescence decay, high-speed detectors are required.

No single detector will meet all requirements of fluorescence imaging; some trade-offs between requirements are necessary. For example, when time is available for image integration, a slow scan CCD usually outperforms an intensified camera in all areas because of its higher QE and lower noise. However, when time is a critical parameter, an intensified CCD is often the only choice. With future development, CMOS sensors may replace the CCD in many fluorescence imaging systems.

9.3.2.6 System Considerations

The design considerations for a fluorescence imaging system include the power and homogeneity of the excitation light, the FOV and NA of the detection system, the sensitivity and noise characteristics of the detector, and the transmission and blocking capabilities of the fluorescence filters.

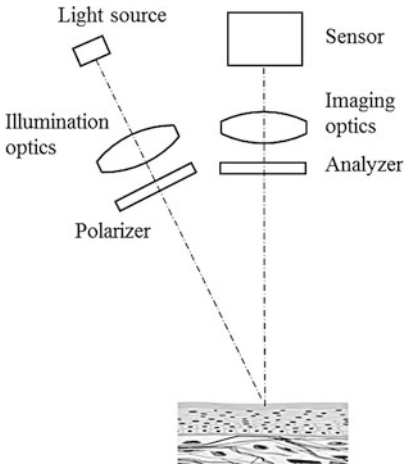

Fig. 9.10 Basic diagram of a polarization imaging system

The design of an optical system for fluorescence analysis must consider the entire optical path because fluorescence signals are usually very weak. The low fluorescence signal level requires a highly efficient optical system to improve light-capturing abilities for higher throughput and to provide a higher dynamic range to accommodate vast differences in fluorophore concentrations across the tissue. To optimize fluorescence signal detection, excitation filters should be designed to maximize blocking in the transmission passband of the emission filter in the illumination path and to maximize blocking in the corresponding transmission passband of the excitation filter in the detection path. In general, it is preferable to block out-of-band light with an excitation filter instead of an emission filter so that the sample will be exposed to less radiation. For systems whose excitation and emission paths share common optical elements, such as a microscope objective lens, and for systems whose excitation and emission paths do not share the same elements but it is not appropriate to place the emission filter in front of the detection path, special attention should be paid to the autofluorescence properties of optical materials.

As a general guideline, the detection path should have as few optical elements as possible to increase light transmission and minimize the autofluorescence of the optical components. The same requirement is also desired for the excitation path.

9.3.3 Polarization Imaging

Figure 9.10 is a basic diagram of a conventional polarization imaging system. A linear polarizer is placed in the illumination path to ensure a linear polarization of illumination, and a second polarizer, with an orthogonal transmission axis, is used as an analyzer, positioned between the sensor and the tissue. The specularly

reflected light is blocked by the analyzer, thus, only the cross-polarized component of the scattered light contributes to image formation. This technique is an effective tool for functional diagnostics and for imaging subcutaneous tissue layers. It has been also applied extensively in biomedical imaging to eliminate specular reflection. To design a polarization imaging system, we need to understand the properties of different polarizers and polarization effects in optical systems [34].

9.3.3.1 Polarizer

Polarizers are essential in polarization imaging systems to precondition the illumination light and to filter the light from the tissue. A polarizer usually converts unpolarized or mixed-polarization light into light with a single polarization state or transforms light between polarization states. There are two types of polarizers: absorptive polarizers and beamsplitting polarizers. An absorptive polarizer absorbs light with the unwanted polarization state and transmits light polarized along its transmission axis. A beamsplitting polarizer splits the incident beam into two beams having orthogonal polarization states.

Polarizers are generally specified by the following parameters: transmission, contrast ratio, acceptance angle, wavefront quality, beam deviation, laser damage threshold, temperature range, surface quality, and geometric specifications. Transmission is the percentage of light that passes through the polarizer, and the contrast ratio is the ratio between the transmission of the desired polarization and the undesired orthogonal polarization. The acceptance angle is the range of incidence angles over which the polarizer has acceptable performance. Wavefront quality is the measure of distortion when a plane wave passes through the polarizer. Beam deviation is an angular measure of how much the light direction changes when passing through the polarizer. The laser damage threshold is the amount of laser power that the polarizer can handle. Surface quality defines the level of defects to be allowed on the surface. Geometrical specifications include thickness, outside diameter, and the clear aperture of the polarizer.

The sheet polarizer is the most common, inexpensive absorptive polarizer. It consists of a matrix of oriented dye molecules or crystals on a polymer substrate. A sheet polarizer works throughout the visible spectrum but deteriorates in IR light, and it is totally ineffective in UV light because polyvinyl alcohol (PVA) absorbs strongly in the 200–400-nm region. A sheet polarizer has 45–90 % transmission for polarized light and a contrast ratio ranging from 100:1 to 1,000:1. Its acceptance angle is relatively large, up to 20°. The transmitted wavefront is poor, on the order of few waves. The advantages of a sheet polarizer include a large angular acceptance and extreme flexibility for custom shapes and sizes. However, the sheet polarizer can only be used in low irradiance applications. The typical power limit is 1 W/cm^2. Other limitations include low working temperature range and low transmission in short wavelengths. Another type of absorptive polarizer is made of elongated silver nanoparticles embedded near the surface of a glass. It is more durable and can polarize light much better than a sheet polarizer. Other advantages include more

resistance to UV radiation and chemicals, better resistance to temperatures (up to +400°C), and a large acceptance angle, as high as 20°.

Beamsplitting polarizers split the incident light into two beams with orthogonal polarization states by one of the following mechanisms: reflection, birefringence, thin film coating, or wire-grid metal coating. The thin film beamsplitting polarizer is based on interference effects. A thin film stack of alternating high- and low-index materials of appropriate thickness is coated onto one surface of a plate polarizer or onto the hypotenuse of a right angle prism that is then cemented to a second right angle prism to form a cube. The thin film polarization beamsplitter can tolerate relatively high light levels of 500 W/cm^2. One major limitation of thin film polarizers is that their performance has a strong dependence on wavelength and angle of incidence.

Birefringent polarizers exploit the birefringent properties of crystals such as calcite and quartz. When the unpolarized ray strikes the surface of the crystal, it is split by refraction into two linearly polarized rays with orthogonal polarization states: an ordinary ray (*o*-ray) and an extraordinary ray (*e*-ray). There are several types of birefringent polarizers, such as the Nicol prism, Glan–Thompson prism, Glan–Foucault prism, Glan–Taylor prism, and Wollaston prism. The angle of incidence in birefringent polarizers is limited, and the aperture is smaller than 30 mm in diameter due to the limited availability of large crystals.

A wire-grid polarizer consists of an array of fine parallel metallic wires deposited on one surface or imbedded into a glass substrate. The transmitted wave has an electric field purely perpendicular to the wires and is, therefore, linearly polarized. The direction of polarization is defined by the wire direction, not by the plane of incidence. The performance changes very little with angle of incidence; it can be used at acceptance angles of 20° without depolarization of the skew rays. The transmitted wavefront error of a wire-grid polarizer is small and suitable for most imaging applications. However, astigmatism and coma introduced by the titled polarization beamsplitter are a concern for the transmitted beam in some optical systems. Because it is made from metal wire and glass, a wire-grid polarizer can withstand temperatures as high as 200°C and power densities greater than 50 kW/cm^2. One limitation of the wire-grid polarizer is its surface quality. Its scratch–dig is around 80–50, which is relatively poor due to current manufacturing methods.

Choosing the right polarization element is one of the key steps in designing a polarization imaging system. Each polarization element has its own niche in polarization imaging with applications that it best serves. By understanding the requirements of an imaging system and the key requirements of the polarization elements, one can identify the polarization elements that best fit the specific application. One of the first parameters to consider is wavelength range [34]. This can easily limit the types of polarizers to be considered. For example, for UV light with wavelengths between 270 and 400 nm, only a few polarizers, such as wire-grid and crystal polarizers, are available. Other factors to consider include acceptance angle, size, working temperature, and the transmission/reflection wavefront.

9.3.3.2 Polarization Effects in Optical Systems

When light propagates through an optical system, the transmission, reflection, and optical path length are polarization dependent because all optical components in the system change the polarization state to some extent due to refraction, reflection, coating, and birefringence.

At nonzero angles of incidence, the *s* and *p* components of the light have different transmission and reflection characteristics for refractive and reflective surfaces. Generally, for a nonflat lens surface and noncollimated light, the angle of incidence varies across the lens surface; therefore, the lens surface acts as a weak, spatially varying partial polarizer. Large variations in the angle of incidence could be an indication that polarization effects should be considered [34].

Most coatings in optical systems are designed to improve light throughput, either to reduce reflection on refractive surfaces or to enhance the reflection on reflective surfaces, without considering phase retardance. Generally, all coatings have polarization effects to some extent. A coating on the lens surface may result in either more or less polarization effect compared to an uncoated surface. Maximizing light throughput and minimizing phase shift may work against each other. To optimize light throughput with minimum phase shift requires some trade-offs.

Another consideration is birefringence which is the difference in refractive indices of an optical material between two orthogonal polarization states. When unpolarized light is incident onto a birefringent material, it is split into two paths with orthogonal polarization states, and the phase of each path accumulates at a different rate. This results in different optical path lengths and different focal lengths for light with different polarization states, thus degrading imaging performance.

Most optical glass elements are isotropic and have no natural birefringence. However, because optical elements are usually mounted using mechanical parts, the interface between the optical element and the mechanical element can produce stress. Stress can introduce anisotropic material birefringence, resulting in a change in the optical path. Birefringence is an inherent property of plastic optical materials and can be categorized into orientational birefringence and stress birefringence. In addition to birefringence generated from mechanical loads during standard operation, birefringence can also be generated in optical components by a change in temperature. Due to the mismatch of coefficients in thermal expansion of cemented elements and thermal mismatch between the optical element and the mounting material, uniform temperature changes can produce mechanical stress in optical components.

9.3.3.3 Design Considerations of Polarization Imaging Systems

Optical designs consist of lens and coating designs. Typically, lens designs optimize wavefront performance and image quality without considering coating effects; coating designs only maximize transmittance or reflection within the working spectrum

and the angle of incidence without consideration of diattenuation and retardance. In many situations, even for polarization imaging systems, this decoupled process, where the lens and the coating are designed independently, works well. However, for some polarizationsensitive imaging systems, it is necessary to analyze the polarization effects from optical coatings.

During the optical design phase, we need to determine the forms of polarization effects (diattenuation or retardance or both) and identify surfaces with large polarization effects. Low polarization design requires that the optical system designer consider surface geometries, optical materials, and coatings that can cause polarization aberrations and end-to-end polarization aberration analysis of the entire optical system. We also need to understand how the polarization aberrations add or cancel between surfaces. Measurements of coatings or dielectric samples during the design phase allow models to better simulate system performance.

A general guide in designing a polarization imaging system is to place the polarizer as the last element in the illumination path and to place the analyzer as the first element in the imaging path. With the polarizer as the last element in the illumination path, undesired polarization effects induced by elements in the illumination path are minimized. Similarly, with the polarizer as the first element, no special consideration is necessary for optical elements in the imaging path. However, this guideline is not suitable for some applications, for example, when the illumination path and imaging path share some common components.

9.3.4 Design of OCT Imaging Systems

Chapter 5 discusses the different configurations of OCT systems. Three different OCT techniques have been developed: time-domain, spectrometer-based Fourier-domain, and swept-source Fourier-domain techniques. While the configurations for the sample arm are the same, each technique has different configurations in reference arm and signal detection. For time-domain OCT (TD-OCT), a high-speed scanning optical delay line (ODL) is needed for real-time imaging. The most commonly used optical delay line for real-time time-domain OCT is Fourier-domain rapid-scanning ODL (RSOD) [35]. In spectrometer-based Fourier-domain OCT (FD-OCT), a spectrometer based on a linear detector array samples the spectrum from the reference arm and sample arm. The design of the spectrometer should consider the frequency resolution, the spectral response, and the spot size of the beam. These parameters determine the falloff characteristic and axial resolution of the image. Considering the limited number of pixels in the detector array, a trade-off is required between the imaging range and the axial resolution in the spectrometer design. In swept-source OCT (SS-OCT), both the reference arm and detection arm are relatively simple. The optical path length in the reference arm is fixed, and the light from the reference arm and sample arm is delivered to the photodiode directly without additional optics.

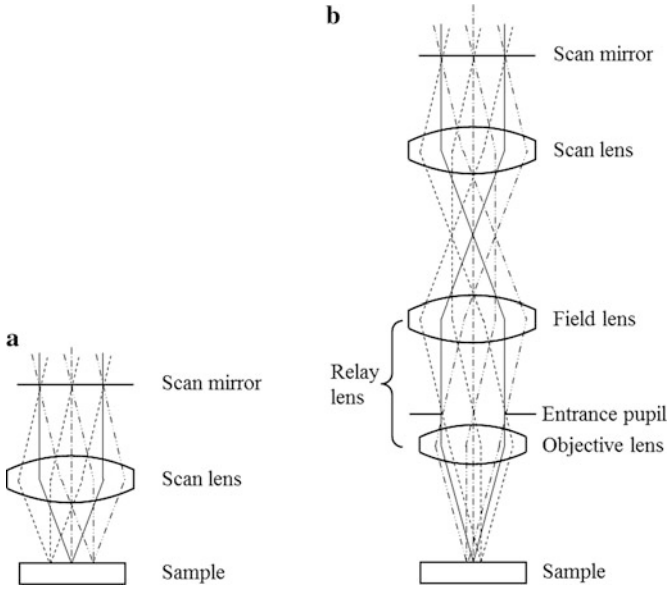

Fig. 9.11 OCT scan lens (**a**) without and (**b**) with relay lens

This section will only discuss the optical design of the sample arm which is the same for all three types of OCT technique.

9.3.4.1 Scan Lens

Because the OCT system is typically a point scanning system, a scan lens is needed to scan the focused spot across the sample. Figure 9.11 shows two scan lens configurations. In Fig. 9.11a, the scan mirror scans the collimated beam at the pupil plane, or its conjugated plane, of the scan lens. Ideally, the scan lens should be an F-theta lens and should be telecentric in the tissue side. The F-theta lens has a linear relationship between the scan length and the scan angle at the pupil plane. Good telecentricity is needed for uniform light-collection efficiency and to reduce post-image processing to correct images at different depths.

Figure 9.11b is another configuration of the sample arm. A relay lens is used to relay the focused spot from the scan lens to the sample. This relay lens can also be treated as the combination of an objective lens and a field lens. The advantage of this configuration is that the scanning system can be spaced apart from the sample. It is generally preferable that the OCT system share the same objective lens with other imaging modalities. The requirement of the scan lens is same as the scan lens in Fig. 9.11a.

9.3.4.2 Scanning Systems

An efficient beam-scanning system with scan mirrors should have the following characteristics: good duty cycle, stationary pivot point, high scan speed, and the capability of scan rotation. A good duty cycle requires that all nonuseful scanning be minimized. A stationary pivot point is required, and it should be at the entrance pupil or imaged at the entrance pupil plane of the objective lens so that the beam at the entrance pupil remains constantly in position and purely rotates, achieving the smallest focused spot it can achieve and maintaining a constant illumination. When the beam scans at the pupil plane, the objective lens works in a telecentric mode and converts the change of the scan angle at the pupil plane to the movement of the focused spot in the object plane. A high scanning speed is another essential requirement for OCT imaging, especially for in vivo applications. It is desired that the scanning direction be rotatable to obtain the best possible image quality and time resolution with respect to the specimen shape or other characteristics [34].

A typical scanning system utilizes two high-speed scan mirrors driven by galvanometer motors or a combination of a galvanometer scanner and an acousto-optical deflector or a polygon scanner. The two scanners mounted on mutually perpendicular axes are either close-coupled or optical-coupled through a relay system and scan in orthogonal directions, producing a rectilinear raster scan. In a close-coupled scanning system, the two scan mirrors are positioned as closely as possible, with the entrance pupil of the objective lens or its conjugate plane located at the midpoint between them. This configuration is relatively simple and compact. However, this arrangement only achieves approximate telecentricity, the closer the two mirrors, the smaller the telecentric error. Another problem with close-coupled mirrors is the beam shift on the second mirror. When the mirrors scan, the beam moves around the pupil plane, instead of being stationary. Therefore, the intensity of the image may vary across the field; the resolution and contrast may be reduced because it is possible that only part of the pupil is effectively used for illumination and detection during scanning [34]. In an optical-coupled scanning system, a relay system is employed to image one mirror onto the other so that both mirrors can be exactly at the conjugate planes of the entrance pupil of the objective lens. The beam position is always fixed at both scanning planes because of the conjugate condition; therefore, there is no beam movement at the entrance pupil during the scanning process. This configuration meets all of the requirements of a good scanning system: good duty cycle, stationary pivot point, high speed, and rotatable scanning direction.

The microelectromechanical system (MEMS) scanner is a device that has emerged in recent years to provide the beam scan in OCT imaging [36, 37]. A MEMS scanner is a silicon device where the mirror is connected to small flexures, allowing it to oscillate. One-dimensional and two-dimensional MEMS mirrors have been developed and used in OCT imaging. The MEMS scanner offers a number of advantages: small size, fast speed, high accuracy, and repeatability. However, the

high-speed MEMS mirror typically has a small mirror and it can only be used for a small beam, possibly limiting the NA, therefore the resolution.

9.4 Multimodal Imaging System for Dental Application

The multimodal imaging system has a great potential in detecting early tooth decay with high sensitivity and specificity. The polarized, true-color tooth image enables dentists to examine tooth condition without specular reflection. With the help of a polarized reflectance image, fluorescence imaging can screen the large region and identify an abnormal region quickly. OCT imaging can then further investigate the structural changes in the abnormal region [38].

For reflectance and fluorescence imaging, the FOV should be large enough to cover at least one tooth so that the abnormal region can be detected quickly, and the depth of field should be sufficient to obtain a good image of the entire tooth surface. Therefore, the configuration in Fig. 9.7b is a better option. Polarized reflectance imaging and fluorescence imaging share the same imaging path. A Fourier-domain OCT system based on a swept laser source is used for higher imaging speed and lower noise. In order to combine the three imaging modalities with reasonable working distance, the optical configuration in Fig. 9.11a is advantaged for OCT scanning. This section will discuss the detailed design of this multimodal imaging system [39].

9.4.1 Introduction to Detection of Dental Caries

Dental caries is an infectious, communicable disease resulting in destruction of tooth structure by acid-forming bacteria found in dental plaque, an intraoral biofilm, in the presence of sugar. The infection results in the loss of tooth minerals that begins with the outer surface of the tooth and can progress through the dentin to the pulp, ultimately compromising the vitality of the tooth. The early detection and characterization of caries lesions is very important because surgical restorative procedures can be reduced. If detected at an early stage, the dental practitioner can implement measures to reverse and control caries, such as identifying patients in need of preventive care, implementing fluoride treatments, implementing plaque control measures, and identifying patients that are at high risk of developing dental caries.

Many optical technologies have been developed to characterize the changes of optical properties of tooth structure related to demineralization. Those technologies include reflectance, fluorescence, transillumination [40], confocal [41], OCT

[42], photothermal radiometry [43], Raman spectroscopy [44], and multiphoton microscopy [45]. All of these methods characterize one or more property changes of the tooth structure. However, none of them can detect dental caries in early stage with high sensitivity and specificity.

Reflectance imaging is the most widely used method in caries detection. Dentists commonly examine the teeth visually or through an intraoral camera by capturing the backscattered light from the tooth surface. One problem with conventional reflectance imaging is the specular reflection on the tooth surface. This specular reflection can cause some false positives and obscure surface features.

The fluorescence of teeth was discovered by Stubell in 1911 with UV excitation. In the early 1980s, Alfano and Yao reported the first systematic investigation of tooth fluorescence with different light excitations [46, 47]. It was discovered that by using light of wavelengths 350, 410, and 530 nm, the emission wavelength peaks obtained for teeth were, respectively, 427, 480, and 580 nm. The peaks of the emission spectra of carious regions were shifted to the red portion of the spectrum. Also, Alfano and Yao reported that the relative intensity of light in the red portion was greater for a carious region than for a sound region. Two fluorescence techniques have been developed to detect dental caries. The first technology uses blue light excitation [48]. When teeth are illuminated with high-intensity blue light, namely, 400 nm, they emit light through the visible spectrum. Sound, healthy enamel shows a higher fluorescence than demineralized enamel; demineralized areas appear relatively darker under light that excites the fluorescence. The amount of mineral loss in surface lesions correlates strongly with the loss of fluorescence signal. Another technology developed by Hibst and Gall in 1998 uses red light excitation [49]. When teeth are illuminated with red light, the fluorescence radiation from healthy tooth regions is strongly reduced so that the fluorescence radiation from carious regions is superposed with autofluorescence of the healthy tooth tissue. Clean, healthy tooth structure exhibits little or no fluorescence. Red fluorescence is proportional to the severity of tooth decay.

Dental OCT imaging was first reported in 1995 [42]. Preliminary work focused on correlating optical scattering signatures with tissue structures in the periodontium region of the oral cavity. Since then, several groups have investigated OCT imaging for dental applications [50–52]. Amaechi et al. observed a linear correlation between the mineral loss in enamel and dentine measured by transverse microradiography (TMR) and the reflectivity loss measured by OCT. In 2005, Fried et al. demonstrated that the increase in the integrated reflectivity in the PS-OCT perpendicular polarization axis correlated well with increasing mineral loss/severity caused by natural demineralization, by comparing with digital microradiographs (DM) and polarized light microscopy (PLM).

While fluorescence imaging has good sensitivity in the detection of dental caries, it doesn't provide information on lesion depth and suffers from low specificity attributed to the presence of plaque, calculus, and stains on the tooth surface. In addition, ambient light and hydration of tooth tissue also degrade the quality of the fluorescence image. OCT imaging can provide high-resolution tooth images with

depth, size, and boundary information. However, the OCT system has a small FOV and is not practical for large-scale imaging for in vivo dental applications. The common limitation of fluorescence imaging and OCT imaging is that both techniques cannot identify calculus and stains with enough sensitivity and specificity.

In order to quickly detect dental decay with high sensitivity and specificity, it is advantageous to combine polarized reflectance, fluorescence, and OCT imaging techniques. Fluorescence and OCT images are distinct and complementary, with fluorescence providing information about biochemical composition and OCT providing information about tooth structural information. The polarized illumination method is used in reflectance imaging to remove specular reflection. With the help of reflectance imaging, calculus, stain, and amalgam can be clearly identified. Another advantage of this multimodal imaging system is that fluorescence and reflectance imaging can quickly screen an entire tooth and identify the suspicious regions, then OCT imaging can be performed to obtain detailed structural information. Thus, this multimodal imaging system may achieve higher sensitivity and specificity in dental caries detection than any single modality alone.

9.4.2 Light Source

To design an effective fluorescence imaging system, it is necessary to select the spectrum matching the peak of the fluorescence excitation spectrum of the tooth. Figure 9.12a is the excitation spectrum of a carious region with fluorescence detected at 700 nm. The most efficient fluorescence excitation is around 400 nm [53]. The fluorescence emission spectrum of the tooth with excitation light at 400 nm is shown in Fig. 9.12b. It is very clear that there is a significant decrease of fluorescence as tooth decay develops. Therefore, a light source with peak wavelength of around 400 nm or a broadband light source with a bandpass filter whose central wavelength is around 400 nm is the choice for fluorescence imaging for caries detection. The UV LED with peak wavelength around 400 nm is optimal to excite tooth fluorescence. This source has narrow spectrum bandwidth, light weight, instant on and off, small footprint, and long lifetime. However, there are tails in the emitted spectrum and those tails may be inside the emission spectrum of the sample. Therefore, a bandpass or shortpass filter is often needed to block the tails within the emission spectrum.

The main function of polarized reflectance imaging is to provide the dental practitioner with a clinical view of the tooth surface, as well as white spots of early decay. A true color rendition of the tooth is important in examining tooth condition. Therefore, a visible spectrum light source is needed. White LEDs are excellent for this application because they are compact and can be turned on/off instantly so that the reflectance imaging mode and fluorescence imaging mode can be switched quickly.

For OCT imaging, it is necessary to select a wavelength that can penetrate as deep into the enamel as possible, which helps to map the depth of tooth decay. As

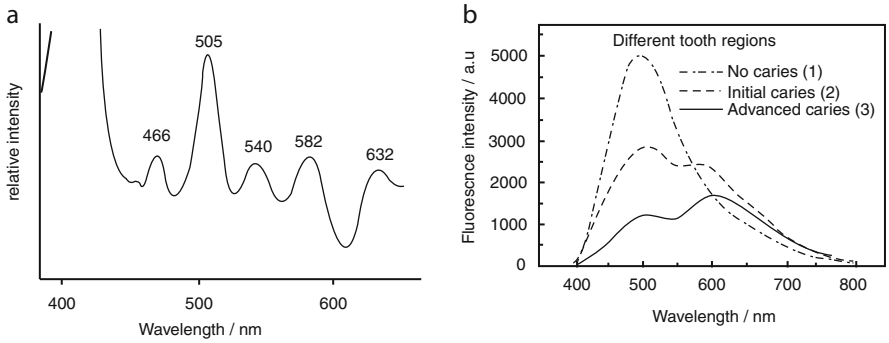

Fig. 9.12 (**a**) Fluorescence excitation spectrum of a strong fluorescent carious region. Fluorescence was detected at 700 nm. (**b**) Emission spectra at different region with excitation wavelength of 400 nm [53]

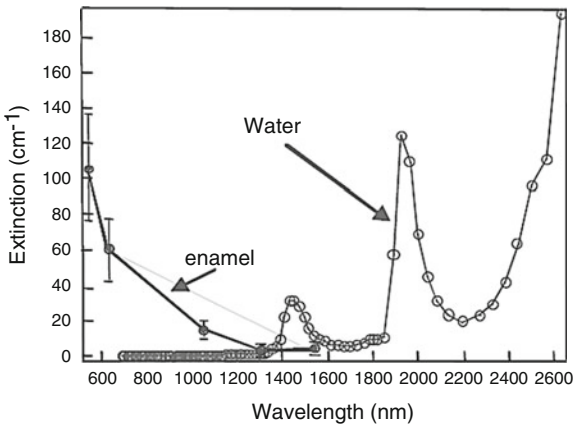

Fig. 9.13 The attenuation coefficient of dental enamel [54]

shown in Fig. 9.13, the magnitude of scattering decreases exponentially at longer wavelengths and reaches minimum around 1,300 nm [54]. At longer wavelengths past 1,550 nm, the attenuation coefficient is not expected to decrease further due to the increasing absorption coefficient of water which is ~12 % by volume in dental enamel. Therefore, a swept-source laser with a central wavelength of 1,325 nm and a bandwidth of 100 nm is used in this multimodal imaging system.

9.4.3 Detector

Because it is an area imaging system, an area detector, namely, CCD or CMOS, is needed. Ideally, a cooled CCD is the best choice for fluorescence imaging because

the fluorescence signal is usually very weak. For a handheld device, a color CMOS detector is commonly used because of its compactness and low cost. One problem with the use of CMOS in fluorescence imaging is low signal-to-noise ratio. To remedy this effect, stronger UV light excitation is necessary. For OCT, an InGaAs photodetector is selected; this device has high responsivity at 1,310 nm (0.95 A/W), low DC offset, and low noise.

9.4.4 Illumination Path

One basic requirement of an illumination system for fluorescence imaging and polarized reflectance imaging is illumination uniformity. With LEDs as the light sources, there are several approaches to achieve uniform illumination. The first approach is using lenslet array. The light from the LED is collimated and then divided into subsections by the lenslet array, and then a field lens overlaps the light from each lenslet onto its focal plane. The second approach uses a light pipe to uniformize the light from LEDs, and then the uniformized output is relayed to the tissue surface. The third approach uses a freeform lens to redistribute the light from the LED to generate uniform illumination. The fourth option uses LEDs directly, without any additional optical element.

For this multimodal imaging system, the last approach is used. The drawback of this approach is that uniformity is not as good as the other three methods. Because there is no additional optical component to generate uniform illumination, the divergent angles of LEDs should be optimally selected and the positions and orientations of the LEDs should be optimized to maximize light efficiency and illumination uniformity.

Even UV LEDs can be regarded as monochrome light sources, but there are some very weak tails in the emission spectrum. Therefore, a bandpass filter, whose transmission is shown in Fig. 9.14a, is used to block the LED light in the emission spectrum. A polarizer is placed in front of the white LEDs to provide polarized light illumination. Since it is in the illumination path and there is no special requirement on transmitted wavefront, a sheet polarizer is a good candidate because it has a flexible shape, large acceptance angle, and low cost.

The OCT subsystem in this multimodal system is a point scanning system; it is necessary to raster scan the focused point across the tissue to generate 3-D images. Even two optically coupled scan mirrors are a better solution; two close-coupled mirrors are used because the scan angle is not large and they occupy less space. To combine OCT imaging and area imaging modalities, a dichroic mirror is employed. The transmission of this dichroic mirror is plotted in Fig. 9.14b. This mirror has very high reflectivity from 1,200 to 1,400 nm and high transmission from 460 to 1,150 nm. This dichroic mirror also has reasonable transmission from 320 to 410 nm and a second reflection band from 430 to 455 nm. Therefore, it reflects

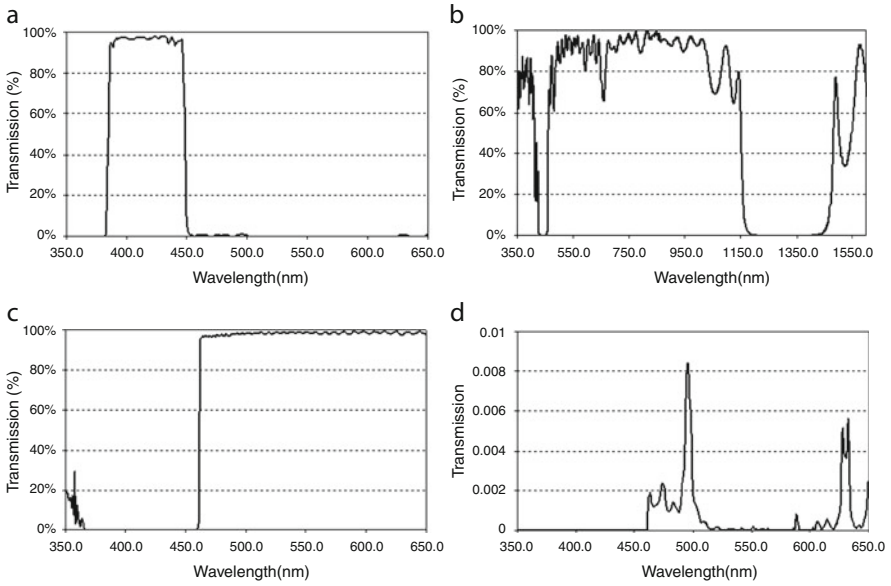

Fig. 9.14 Transmission plots of (**a**) bandpass filter, (**b**) dichroic mirror, and (**c**) longpass filter. (**d**) The transmission of the light from the UV LED after passing through the bandpass filter, dichroic mirror twice, and longpass filter (assuming the reflectivity of the sample is 1)

illumination light and signal for OCT and transmits the illumination light and signal for reflectance and fluorescence imaging.

9.4.5 Detection Path

Fluorescence imaging and polarized reflectance imaging share the same detection path, including imaging lens and detector, without any moving element. For polarization imaging, a polarizer with orthogonal axis relative to the polarizer in front of the white LEDs is placed as the first element in the imaging path. To block the excitation light, a longpass filter, instead of a bandpass filter, is placed after the polarizer in the detection path in order to capture visible light for polarized reflectance imaging. Ideally, the cut-on wavelength of this emission filter should be low enough so that enough blue light can be transmitted, but not too low, to pass the excitation light. Figure 9.14c is the transmission plot of the longpass filter.

Assuming the reflectivity of the sample is 1, Fig. 9.14d plots the transmission of light from the UV LED after passing through the bandpass filter, dichroic mirror twice, and longpass filter. There are some very weak leakages after 460 nm.

Considering the spectrum bandwidth of UV LEDs, the effect of excitation UV LEDs on the fluorescence signal is negligible.

Because the polarizer and the emission filter are the first and second elements in the detection path, there is no any special requirement on material, coating, and mounting for optical elements in the imaging path. One shortfall with this configuration is that half of the fluorescence signal is blocked by the polarizer. To overcome this limitation, multiple UV LEDs are needed for fluorescence imaging.

Key parameters for designing an area imaging system are NA and FOV. For fluorescence imaging, the NA should be as large as possible to maximize light-collection efficiency because the fluorescence signal is very weak. However, large NA means shallow depth of field. Therefore, a trade-off must be made when determining the NA. The large FOV will help screen large areas faster, but the resolution is lower given the fixed number of pixels in the detector. Also, the large FOV means the probe will be larger, which is not desirable because the probe will be inserted into the oral cavity. In order to quickly screen teeth without missing regions, the minimal FOV should be larger than a tooth.

NA and FOV are also two key parameters when designing OCT imaging optics. The larger the NA is, the higher the resolution. However, large NA means shorter working distance and/or a larger scan lens, which should be avoided in handheld devices. Similarly, large FOV requires a larger scan lens because the scan lens is typically designed as telecentric on the tissue side.

With the above considerations, the FOV of the imaging lens for fluorescence and polarized reflectance imaging is determined as 18×13.5 mm, and the NA is 0.02. The system can cover one full tooth and two half adjacent teeth and can obtain a sharp image of the occlusal surface of the molar, which has a couple of millimeters between the cusp and pit. The selected NA of the OCT scan lens is 0.09 and the FOV is 5×5 mm. The lateral resolution of the OCT scan lens is 10 μ m, determined by the wavelength and NA, and the axial resolution is 12 μ m in air, determined by the coherence length of the light source.

9.4.6 Optical Design

Generally, special attention must be paid to the selection of optical materials, coatings, lens shapes, and lens mounting methods for fluorescence and polarized imaging systems. For this multimodal system, the analyzer and the emission filter are the first and second element in the detection path, therefore, conventional materials can be used and coatings can be designed without consideration of phase shift.

Because the imaging system for fluorescence imaging and reflectance imaging has a relatively small FOV and low NA, a triplet lens format with three singlets

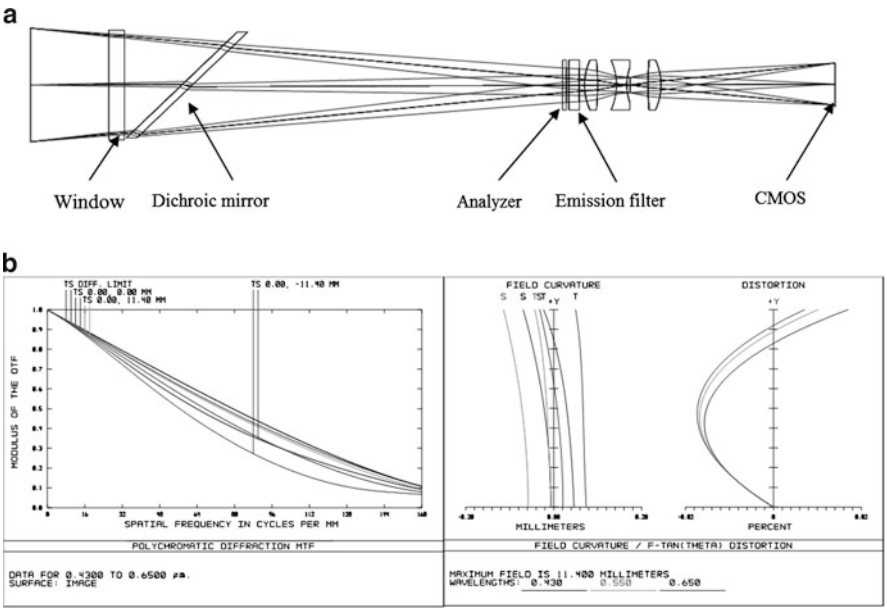

Fig. 9.15 Imaging lens for polarization reflectance and fluorescence imaging. (**a**) Layout and (**b**) performance plots

works perfectly. Figure 9.15a shows the layout of this imaging lens; the two positive singlets on each side are identical. The design also considers the effect of the polarizer, window, emission, and tilted dichroic filters. The performance of this imaging lens is plotted in Fig. 9.15b. It is a well-corrected system with some remaining spherical aberration, coma, astigmatism, and lateral color. Distortion is quite small, only 0.02 %, because of the symmetrical configuration.

Figure 9.16a is the layout of the OCT scan lens. The designed aperture is located between the two galvo mirrors. MTF in Fig. 9.16b shows that this lens has a very good performance with a small amount of spherical aberration. Telecentricity when the first scan mirror and second scan mirror scan is plotted in Fig. 9.16c. The largest chief ray angle is about 1.2 degrees when the first scan mirror scans.

Figure 9.17 shows a diagram of the multimodal imaging system. Inside the box is the schematic diagram of the OCT imaging system [55, 56]. The light source is a high-speed frequency-swept external cavity laser (Thorlabs SL1325-P16) with average output power of 12 mW and 3-dB spectral bandwidth of approximately 100 nm. The light from the laser is split by a 99:1 fiber coupler; 1 % of the light is coupled to the Mach–Zehnder interferometer (MZI) as the frequency clock of the laser. The rest of light goes to a fiber-based Michelson interferometer and is further split to the reference arm and sample arm. In the reference arm, the light from the

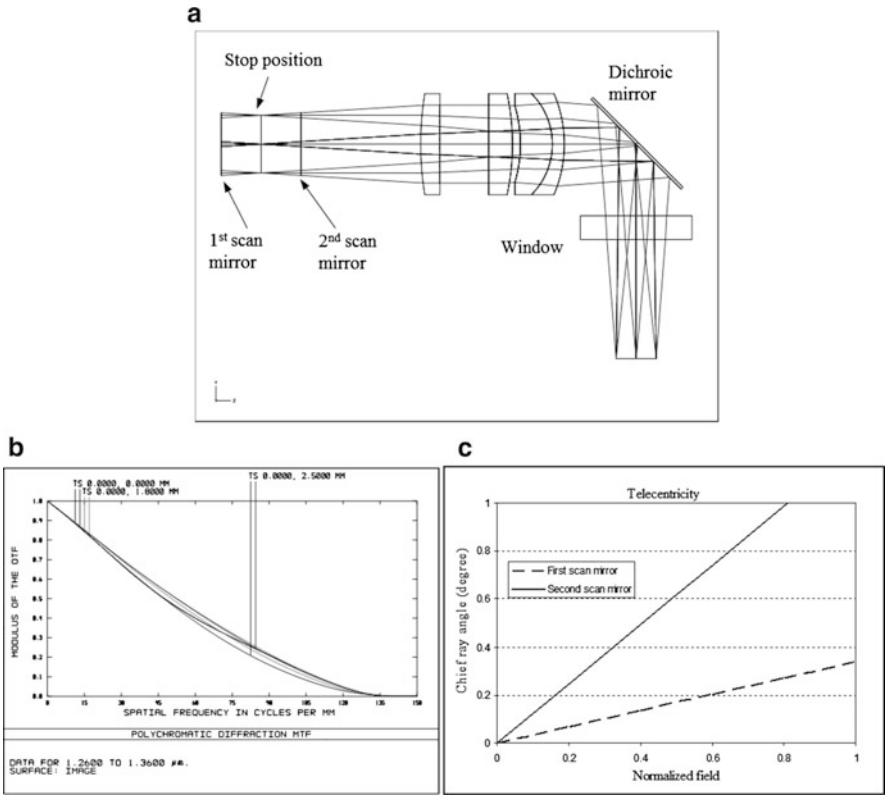

Fig. 9.16 OCT scan lens. (**a**) Lens layout, (**b**) MTF of the lens, and (**c**) chief ray angles when the first scan mirror and second scan mirror scan separately

fiber is collimated and reflected by a mirror which is movable to match the optical path lengths between the sample arm and reference arm. In the sample arm, the light is collimated and is directed by the XY galvo scan mirrors toward the sample for transverse scans (B-scans). The axial scans (A-scans) are performed at 16 kHz, same as the frequency-swept speed of the laser. An aiming laser with the wavelength of 632 nm is coupled into the reference and sample arms to indicate the focused spot position. The interference signal between the light from the reference arm and from the sample arm is detected by a balanced detector (Thorlabs PDB120C, 75 MHz) and is sampled by a 14-bit high-speed digitizer capable of 100 MS/s. The depth-dependent reflectivity profiles of the sample are generated through the Fourier transform of the OCT interference signals. The configuration of area imaging system is same as Fig. 9.7b. The dichroic mirror shown in Fig. 9.14b combines OCT path and area imaging path.

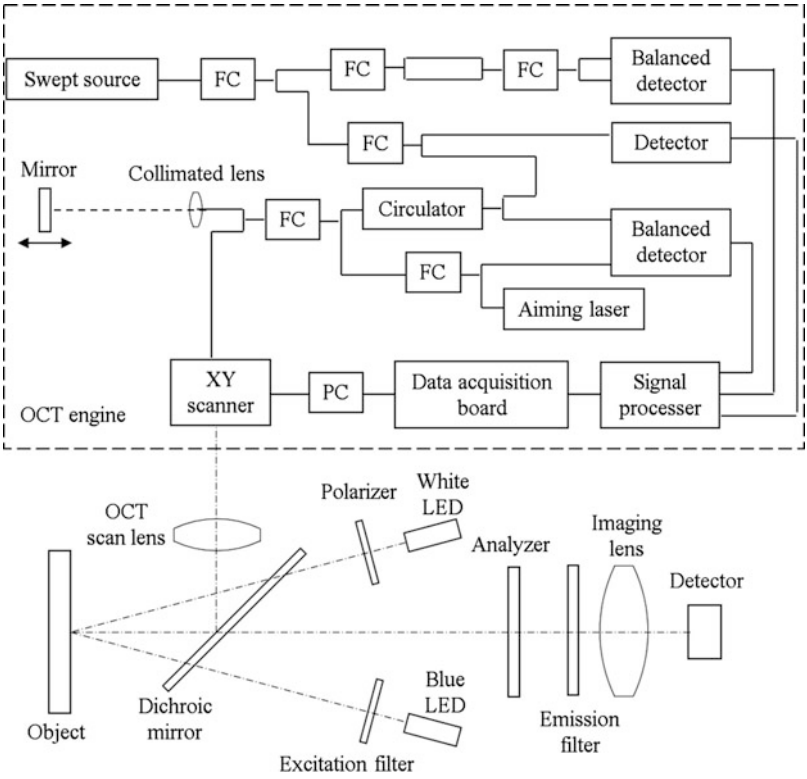

Fig. 9.17 Diagram of multimodal imaging system. *OCT* engine is inside the dashed box. *FC* fiber coupler

9.4.7 Applications in Caries Detection

This multimodal imaging system has the advantage that the user can screen the tooth or oral cavity with visible polarized light to obtain a visible reflectance image, just as a conventional intraoral camera, or screen the tooth with blue excitation light to view the fluorescence image. With polarized white light reflectance image and fluorescence image and possibly with further image processing, the user can identify healthy, carious, and suspicious regions quickly. Once the carious and suspicious regions are located, OCT imaging can then be used to scan those regions. For carious regions, OCT images can provide more detailed information, such as decay depth, size, and boundary. For suspicious regions, OCT images can verify whether the regions are indeed carious lesions, and if so, how deep the lesions are. All three images, reflectance, fluorescence, and OCT, can be saved for progression monitoring.

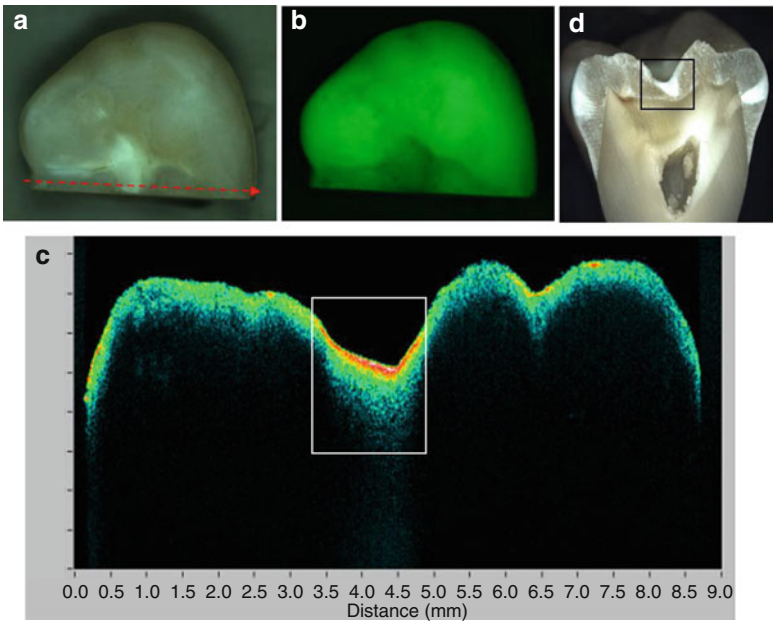

Fig. 9.18 Visible reflectance (**a**), fluorescence (**b**), and OCT (**d**) images of the occlusal surface of a sectioned tooth. (**c**) The image of the tooth section. The dotted arrow shows the OCT scan line and direction. The caries captured by OCT (*white box* in (**d**)) correlates well with that in the section image (*black box* in (**c**)). The *dot arrow* indicates the OCT scanning position and direction

Extracted tooth samples were used to demonstrate the performance of the multimodal imaging system for dental caries detection. After the teeth were extracted, they were placed in a fresh solution of chloramine T 0.5 % for 3 days for sterilization. Some tooth samples were sectioned to correlate OCT images with tooth structural information beneath the tooth surface. For each tooth sample, the imaging system captured and saved all three images: visible polarized reflectance, fluorescence, and OCT.

Figure 9.18 shows the three images obtained with the multimodal system on the occlusal surface of a sectioned tooth, along with an image of the tooth section. All three images clearly show that there is a carious region: a white spot in the reflectance image (Fig. 9.18a), a dark area in the fluorescence image (Fig. 9.18b), and the large depth of the scattering profile in the center of OCT image (Fig. 9.18c). The carious region is also verified by the tooth section (black box in Fig. 9.18d).

Figure 9.19 demonstrates a case in which OCT is able to identify false positives in the reflectance and fluorescence images. The white spot in the visible reflectance image (Fig. 9.19a) and the dark region in the fluorescence image (Fig. 9.19b) both indicate the presence of caries. However, the OCT image in Fig. 9.19c only shows small variation in the shallow depth of scattering profile across the scan line, which

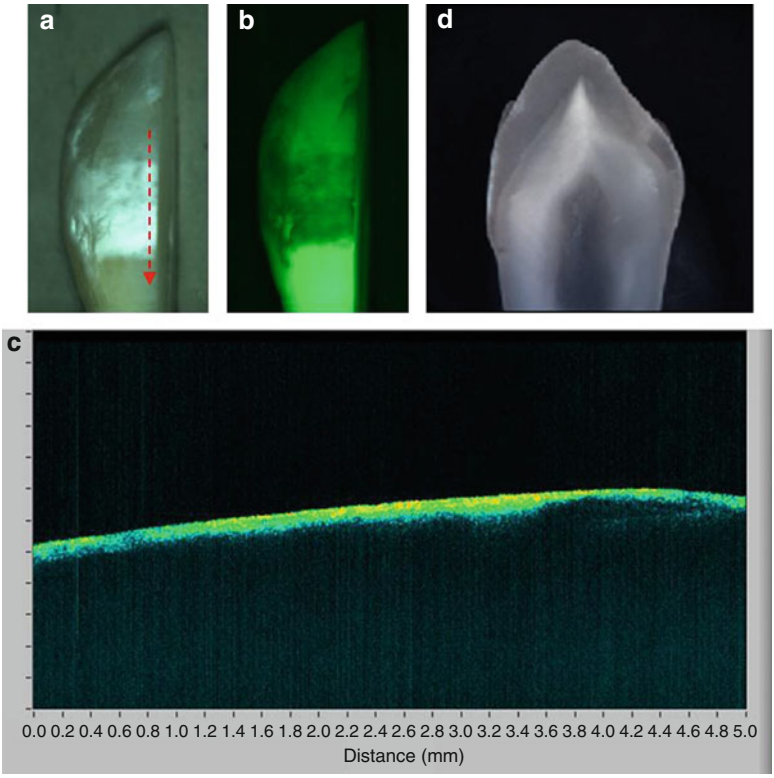

Fig. 9.19 Reflection (**a**), fluorescence (**b**), and OCT images (**d**) of a sectioned tooth. The image of the tooth section is displayed in (**c**). The *dot arrow* indicates the OCT scanning position and direction

means there is very little decalcification. This finding is validated by the digital image of the tooth section (white box in Fig. 9.19d), which shows just the beginning stage of decalcification. The OCT image in Fig. 9.19c also shows the difference between the white spot (stronger signal due to higher reflection) and the healthy region even when the decalcification is very shallow.

Unfortunately, stain, calculus, and other debris on the tooth surface can impair the specificity of fluorescence imaging in caries detection. Figure 9.20 shows that stain causes false positives in the fluorescence image because the stain appears darker in the fluorescence image as shown in Fig. 9.20b. If only a fluorescence image is available, these darker regions in the fluorescence image could be misinterpreted as caries. With the polarized reflectance image in Fig. 9.20a and OCT image in Fig. 9.20c, the false positive caused by stain in fluorescence image can be avoided.

The above ex vivo experimental results demonstrate that the multimodal imaging system incorporating polarized reflectance, fluorescence, and OCT imaging

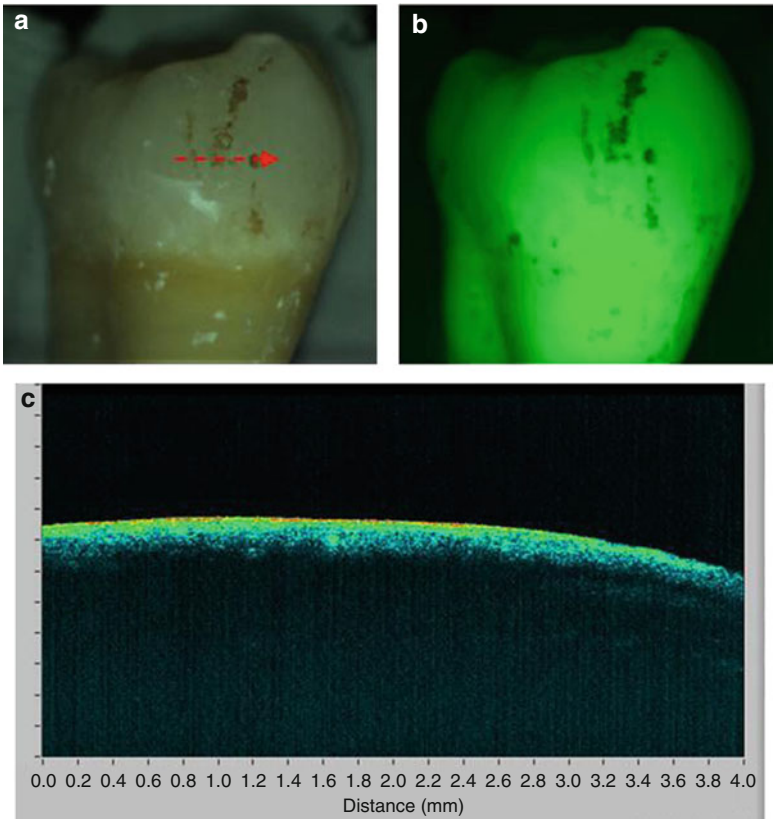

Fig. 9.20 Reflection (**a**), fluorescence (**b**), and OCT images (**c**) of a tooth with stain. The *dot arrow* indicates the OCT scanning position and direction

modalities has a great potential for early detection of dental caries with high sensitivity and specificity. The three imaging modalities correlate with each other and/or complement each other in detecting caries, stain, calculus, and other property changes of tooth structure.

References

1. A. Douplik, S. Zanati, N. Marcon, M. Cirocco, B. Wilson, J. Boehm, S. Rychel, J. Fengler, Combined autofluorescence and white-light endoscopy for improved detection of dysplastic colonic lesions, in *Biomedical Optics*, Technical Digest (CD) (Optical Society of America), paper ME63 (2006)
2. M. Rahman, P. Chaturvedi, A.M. Gillenwater, R.Richards-Kortum, Low-cost, multimodal, portable screening system for early detection of oral cancer. J. Biomed. Opt. **13**, 030502 (2008)

3. M.A. Kara, et al., Endoscopic video-autofluorescence imaging followed by narrow band imaging for detecting early neoplasia in Barrett's esophagus. Gastrointest. Endosc. **64**, 176–185 (2006)
4. E. Salomatina, A. Muzikansky, V. Neel, A.N. Yaroslavsky, Multimodal optical imaging and spectroscopy for the intraoperative mapping of nonmelanoma skin cancer. J. Appl. Phys. **105**, 102010 (2009)
5. R.J. McNichols, A. Gowda, B.A. Bell, R.M. Johnigan, K.H. Calhoun, M. Motamedi, Development of an endoscopic fluorescence image guided OCT probe for oral cancer detection. in *Biomedical Diagnostic, Guidance, and Surgical-Assist Systems III*, ed. by T. Vo-Dinh, W.S. Grundfest, D.A. Benaron. Proc. SPIE **4254**, 23–30 (2001)
6. Y.T. Pan, T.Q. Xie, C.W. Du, S. Bastacky, S. Meyers, M.L. Zeidel, Enhancing early bladder cancer detection with fluorescence-guided endoscopic optical coherent tomography. Opt. Lett. **28**, 2485–2487 (2003)
7. Z.G. Wang, D.B. Durand, M. Schoenberg, Y.T. Pan, Fluorescence guided optical coherence tomography for the diagnosis of early bladder cancer in a rat model. J. Urol. **174**(6), 2376–2381 (2005)
8. A.R. Tumlinson, L.P. Hariri, U. Utzinger, J.K. Barton, Miniature endoscope for simultaneous optical coherence tomography and laser-induced fluorescence measurement. Appl. Opt. **43**, 113–121 (2004)
9. L.P. Hariri, A.R. Tumlinson, D.G. Besselsen, U. Utzinger, E. Gernere, J.K. Barton, Endoscopic optical coherence tomography and laser induced fluorescence spectroscopy in murine colon cancer model. Lasers Surg. Med. **38**(4), 305–313 (2006)
10. J. Barton, F. Guzman, A. Tumlinson, Dual modality instrument for simultaneous optical coherence tomography imaging and fluorescence spectroscopy. J. Biomed. Opt. **9**(3), 618–623 (2004)
11. S.Y. Ryu, H.Y. Choi, J. Na, E.S. Choi, B.H. Lee, Combined system of optical coherence tomography and fluorescence spectroscopy based on double-cladding fiber. Opt. Lett. **33**, 2347–2349 (2008)
12. S. Yuan, C.A. Roney, J. Wierwille, C.W. Chen, B. Xu, G. Griffiths, J. Jiang, H. Ma, A. Cable, R.M. Summers, Y. Chen, Co-registered optical coherence tomography and fluorescence molecular imaging for simultaneous morphological and molecular imaging. Phys. Med. Biol. **55**, 191–206 (2010)
13. Y. Chen, S. Yuan, Q. Li, R. Naphas, J. Wierwille, T.R. Blackwell, P.T. Winnard, V. Raman, K. Glunde, Integrated optical coherence tomography (OCT) and fluorescence laminar optical tomography (FLOT). IEEE J. Sel. Top. Quantum Electron. **16**(4), 755–766 (2010)
14. G.M. Dobre, A.Gh. Podoleanu, R.B. Rosen, Simultaneous optical coherence tomography-indocyanine green dye fluorescence imaging system for investigations of the eye's fundus. Opt. Lett. **30**, 58–60 (2005)
15. A.G. Podoleanu, G.M. Dobre, R. Cernat, J.A. Rogers, J. Pedro, R.B. Rosen, P. Garcia, Investigations of the eye fundus using a simultaneous optical coherence tomography/indocyanine green fluorescence imaging system. J. Biomed. Opt. **12**(1), 014019 (2007)
16. C.A. Patil, N. Bosschaart, M.D. Keller, T.G. van Leeuwen, A. Mahadevan-Jansen, Combined Raman spectroscopy and optical coherence tomography device for tissue characterization. Opt. Lett. **33**, 1135–1137 (2008)
17. J.W. Evans, R.J. Zawadzki, R. Liu, J.W. Chan, S.M. Lane, J.S. Werner, Optical coherence tomography and Raman spectroscopy of the ex-vivo retina. J. Biophoton. **2**(6–7), 398–406 (2009)
18. O.R. Sepanovi, Z. Volynskaya, C.R. Kong, L.H. Galindo, R.R. Dasari, M.S. Feld, A multimodal spectroscopy system for real-time disease diagnosis. Rev. Sci. Instrum. **80**, 043103 (2009)
19. O.R. Scepanovic, M. Fitzmaurice, A. Miller, C.R. Kong, Z. Volynskaya, R.R. Dasari, J.R. Kramer, M.S. Feld, Multimodal spectroscopy detects features of vulnerable atherosclerotic plaque. J. Biomed. Opt. **16**(1), 011009 (2011)

20. O.R. Scepanovic, M. Fitzmaurice, J.A. Gardecki, G. Angheloiu, S. Awasthi, J.T. Motz, J.R., Kramer, R.R. Dasari, M.S. Feld, Detection of morphological markers of vulnerable atherosclerotic plaque using multimodal spectroscopy. J. Biomed. Opt. **11**(2), 021007 (2006)
21. J.W. Tunnell, A.E. Desjardins, L. Galindo, I. Georgakoudi, S.A. McGee, J. Mirkovic, M.G. Mueller, J. Nazemi, F.T. Nguyen, A. Wax, Q. Zhang, R.R. Dasari, M.S. Feld, Instrumentation for multi-modal spectroscopic diagnosis of epithelial dysplasia. Technol. Cancer Res. Treat. **2**, 505–514 (2003)
22. N. Rajaram, T.J. Aramil, K. Lee, J.S. Reichenberg, T.H. Nguyen, J.W. Tunnell, Design and validation of a clinical instrument for spectral diagnosis of cutaneous malignancy. Appl. Opt. **49**, 142–152 (2010)
23. Z. Volynskaya, A.S. Haka, K.L. Bechtel, M. Fitzmaurice, R. Shenk, N. Wang, J. Nazemi, R.R. Dasari, M.S. Feld, Diagnosing breast cancer using diffuse reflectance spectroscopy and intrinsic fluorescence spectroscopy. J. Biomed. Opt. **13**(2), 024012 (2008)
24. E. Beaurepaire, L. Moreaux, F. Amblard, J. Mertz, Combined scanning optical coherence and two-photon-excited fluorescence microscopy. Opt. Lett. **24**, 969–971 (1999)
25. B.W. Graf, Z. Jiang, H. Tu, S.A. Boppart, Dual-spectrum laser source based on fiber continuum generation for integrated optical coherence and multiphoton microscopy. J. Biomed. Opt. **14**(3), 034019 (2009)
26. S. Tang, T.B. Krasieva, Z. Chen, B.J. Tromberg, Combined multiphoton microscopy and optical coherence tomography using a 12-fs broadband source. J. Biomed. Opt. **11**, 020502 (2006)
27. C. Vinegoni, T.S. Ralston, W. Tan, W. Luo, D.L. Marks, S.A. Boppart, Integrated structural and functional optical imaging combining spectral-domain optical coherence and multiphoton microscopy. Appl. Phys. Lett. **88**, 053901 (2006)
28. M. Autiero, L. Celentano, R. Cozzolino, P. Laccetti, M. Marotta, G. Mettivier, M.C. Montesi, P. Riccio, G. Roberti, P. Russo, Multimodal system for in vivo tumor imaging in mice. Proc. SPIE **6191**, 340–352 (2006)
29. W. McLaughlin, D. Vizard, *Kodak In Vivo Imaging System: Precise Coregistration of Molecular Imaging with Anatomical X-Ray Imaging in Animals* (Application Notes Eastman Kodak Co., Rochester, 2006)
30. A.L. Carlson, L.G. Coghlan, A.M. Gillenwater, R.R. Richards-Kortum, Dual-mode reflectance and fluorescence near-video-rate confocal microscope for architectural, morphological and molecular imaging of tissue. J. Microsc. **228**, 11–24 (2007)
31. J. Park, P. Mroz, M.R. Hamblin, A.N. Yaroslavsky, Dye-enhanced multimodal confocal microscopy for noninvasive detection of skin cancers in mouse models. J. Biomed. Opt. **15**, 026023 (2010)
32. M.Y. Al-Arashi, E. Salomatina, A.N. Yaroslavsky, Multimodal confocal microscopy for diagnosing nonmelanoma skin cancers. Lasers Surg. Med. **39**, 696–705 (2007)
33. S. Jiao, Z. Xie, H.F. Zhang, C.A. Puliafito, Simultaneous multimodal imaging with integrated photoacoustic microscopy and optical coherence tomography. Opt. Lett. **34**, 2961–2963 (2009)
34. R. Liang, *Optical Design for Biomedical Imaging* (SPIE, Washington, 2011)
35. K.F. Kwong, D. Yankelevich, K.C. Chu, J.P. Heritage, A. Dienes, 400-Hz mechanical scanning optical delay line. Opt. Lett. **18**, 558–560 (1993)
36. J. Sun, S. Guo, L. Wu, L. Liu, S.W. Choe, B.S. Sorg, H. Xie, 3D in vivo optical coherence tomography based on a low-voltage, large-scan-range 2D MEMS mirror. Opt. Express **18**, 12065–12075 (2010)
37. A.D. Aguirre, P.R. Hertz, Y. Chen, J.G. Fujimoto, W. Piyawattanametha, L. Fan, M.C. Wu, Two-axis MEMS scanning catheter for ultrahigh resolution three-dimensional and En Face imaging. Opt. Express **15**, 2445–2453 (2007)
38. R. Liang, V. Wong, M. Marcus, P. Burns, P. McLaughlin, Multimodal imaging system for dental caries detection. Proc. SPIE **6425**, 642502 (2007)
39. R. Liang, V. Wong, P. McLaughlin, Optical design of a multimodal imaging system. Proc. SPIE **6849**, 684908 (2008)

40. A. Schneiderman, M. Elbaum, T. Shultz, S. Keem, M. Greenebaum, J. Driller, Assessment of dental caries with Digital Imaging Fiber-Optic TransIllumination (DIFOTI): in vitro study. Caries Res. **31**(2), 103–110 (1997)
41. C. Rousseau, S. Poland, J.M. Girkin, A.F. Hall, C.J. Whitters., Development of fibre-optic confocal microscopy for detection and diagnosis of dental caries. Caries Res. **41**(4), 245–251 (2007)
42. B.W. Colston, Dental OCT. Opt. Express **3**, 230–238 (1998)
43. R.J. Jeon, A. Mandelis, S.H. Abrams, Depth profilometric case studies in caries diagnostics of human teeth using modulated laser radiometry and luminescence. Rev. Sci. Instrum. **74**(1), 380–383 (2003)
44. A.C.-T. Ko, L.P. Choo-Smith, M. Hewko, M.G. Sowa, C.C.S. Dong, B. Cleghorn, Detection of early dental caries using polarized Raman spectroscopy. Opt. Express **14**, 203–215 (2006)
45. P. Lin, H. Lyu, C.S. Hsu, C. Chang, F. Kao, Imaging carious dental tissues with multiphoton fluorescence lifetime imaging microscopy. Biomed. Opt. Express **2**, 149–158 (2011)
46. R.R. Alfano, S.S. Yao, Human teeth with and without dental caries, studied by visible luminescent spectroscopy. J. Dent. Res. **60**(2), 120–122 (1981)
47. R.R. Alfano, S.S. Yao, Human teeth with and without caries studied by laser scattering, fluorescence and absorption spectroscopy. IEEE J. Quantum Electron **20**, 1512–1516 (1984)
48. H. Bjelkhagen, F. Sundstrom, B Angmar-Manson, H Ryden, Early detection of enamel caries by luminescence excited by visible laser light. J. Swed. Dent. **6**, 1–7 (1982)
49. R. Hibst, R. Gall, Development of a diode laser-based fluorescence caries detector. Caries Res. **32**, 294, (1998)
50. B.T. Amaechi, Optical coherence tomography for dental caries detection and analysis. Proc. SPIE **4610**, 100–108 (2002)
51. D. Fried, Imaging caries lesions and lesion progression with polarization sensitive optical coherence tomography. J. Biomed. Opt. **7**(4), 618–627 (2002)
52. B. Amaechi, Correlation of quantitative light-induced fluorescence and optical coherence tomography applied for detection and quantification of early dental caries. J. Biomed. Opt. **8**(4), 642–647 (2003)
53. K. Konig, G. Flemming, R. Hibst, Laser-induced autofluorescence spectroscopy of dental caries**.** Cell Mol. Biol. **44**, 1293–1300 (1998)
54. R. Jones, G. Huynh, G. Jones, D. Fried, Near-infrared transillumination at 1310-nm for the imaging of early dental decay. Opt. Express **11**, 2259–2265 (2003)
55. R. Huber, M. Wojtkowski, J.G. Fujimoto, J.Y. Jiang, A.E. Cable, Three-dimensional and C-mode OCT imaging with a compact, frequency swept laser source at 1300 nm. Opt. Express **13**, 10523–10538 (2005)
56. Thorlabs OCS1300SS Swept Source OCT System User Guide, Newton, NJ 07860 (2011)

Chapter 10
Multimodal Diffuse Optical Imaging

Xavier Intes, Vivek Venugopal, Jin Chen, and Fred S. Azar

Diffuse optical imaging, particularly diffuse optical tomography (DOT), is an emerging clinical modality capable of providing unique functional information, at a relatively low cost, and with nonionizing radiation. Multimodal diffuse optical imaging has enabled a synergistic combination of functional and anatomical information: the quality of DOT reconstructions has been significantly improved by incorporating the structural information derived by the combined anatomical modality. In this chapter, we will review the basic principles of diffuse optical imaging, including instrumentation and reconstruction algorithm design. We will also discuss the approaches for multimodal imaging strategies that integrate DOI with clinically established modalities. The merit of the multimodal imaging approaches is demonstrated in the context of optical mammography, but the techniques described herein can be translated to other clinical scenarios such as brain functional imaging or muscle functional imaging.

10.1 Introduction

Advances in clinical imaging are being made through the combination of imaging techniques and multimodal imaging platforms, such as PET/CT, PET/MRI, and MRI/US. More recently, optical imaging methods have been used in multimodal imaging platforms such as MRI/DOT (diffuse optical tomography),

X. Intes (✉) · V. Venugopal · J. Chen
Biomedical Engineering Department, Rensselaer Polytechnic Institute, Troy, NY 12180, USA
e-mail: intesx@rpi.edu

F.S. Azar
Clinical Data Solutions, Office of Medical & Health Affairs, Philips Healthcare, Ramsey, NJ 07446-2709, USA

R. Liang (ed.), *Biomedical Optical Imaging Technologies*, Biological and Medical Physics, Biomedical Engineering, DOI 10.1007/978-3-642-28391-8_10,

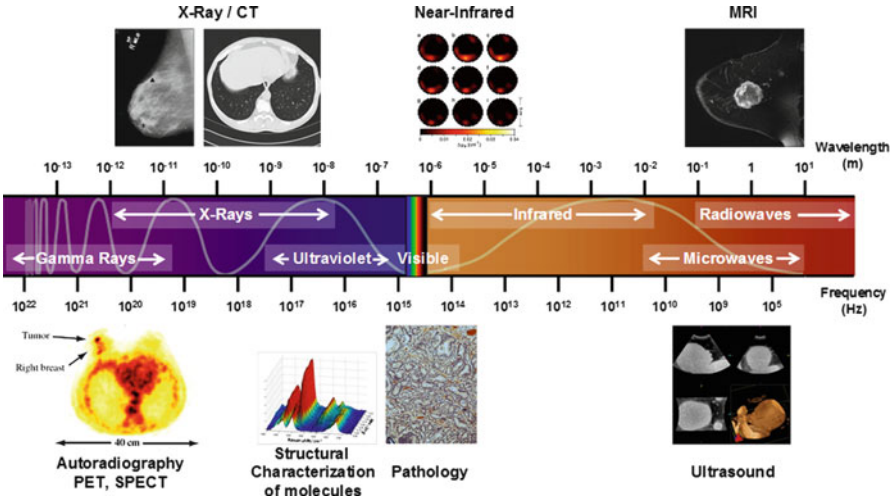

Fig. 10.1 Electromagnetic spectrum and associated imaging modalities

PET/DOT, MRI/DOS (diffuse optical spectroscopy), X-ray/DOT, US/DOS, and other combinations using optical methods as a complementary imaging modality. Each imaging technique relies on different physical tissue interaction principles and in some cases on the use of different molecular probes (cf. Fig. 10.1). As a result, multimodal imaging methods may provide a unique combined set of structural, functional, molecular, and/or metabolic information. The complexities of integrating different methods are offset by the potential for increased performance in both sensitivity and specificity (by reducing false-positive and false-negative results) in screening, diagnosis, staging, treatment monitoring, or image-guided intervention.

In this chapter, we will review the basic principles of diffuse optical imaging, including instrumentation and reconstruction algorithm design. We will also discuss the approaches for multimodal imaging strategies that integrate DOI with clinically established modalities. The merit of the multimodal imaging approaches is demonstrated in the context of optical mammography, but the techniques described herein can be translated to other clinical scenarios such as brain functional imaging or muscle functional imaging.

10.2 Tissue Optics for Diffuse Optical Imaging

Light propagation in biological samples is highly dependent on the probing wavelength. Due to the strong light absorption properties of hemoglobin and water, optical techniques that are based on ultraviolet or visible spectra are restricted to interrogating shallow tissue. Thus, to probe tissue deeper than half a centimeter

(thick tissue), optical instruments should operate in the near-infrared (NIR) spectral window in which biological tissues exhibit relatively weak absorption. This spectral range, also known as the "therapeutic" window (wavelengths between $\lambda \in$ [700 and 1,000] nm), allows in vivo imaging through several centimeters of tissue (up to $\sim$15 cm in breast tissue). Then the tissue properties of interest can be limited to three main parameters: scattering, absorption, and fluorescence.

The first major phenomenon that rules light propagation is elastic scattering. On a microscopic scale, the sharp transitions of the refraction index induce a change in the direction of light propagation. The overall effect of these light redirections occurring at different scales partially characterizes the propagating medium. Light scattering is a wavelength-dependent phenomenon conveying significant information about tissue structure. In particular, scattering depends on the sizes, indices of refraction, and structures of the denser subcellular components. Experimental evidence demonstrates that nuclear size [1], cell membranes [2], and mitochondria [3] are the major contributors to scattering in vivo. The cell nuclei (5–10 μ m) are appreciably larger than the probing optical wavelength (0.01–1 μ m). They predominantly scatter light in the forward direction, and there is also appreciable scattering in the backward direction (Mie scattering). Mitochondria are oblong scatterers with a 1–4 $-$ μ m length and a 0.2–0.5 $-$ μ m diameter and are responsible for scattering at larger angles (Rayleigh scattering). Contrasts in the size, density, distribution, and refraction index of these organelles generate optical signatures that may be disease specific [4].

The second main phenomenon that rules light propagation is absorption. Absorption corresponds to a loss on energy associated with molecular electronic transitions. The absorbed energy is then transformed into heat through nonradiative decay or, less frequently, light of lower energy (fluorescence). The main molecules exhibiting strong absorption characteristics, or chromophores, are oxy- and deoxyhemoglobin, melanin, water, lipids, porphyrins, NADH, flavins, and other structural components. However, when imaging thick tissue, due to the large volume probed by the photons, the predominant light-absorbing molecules can be further reduced to hemoglobin, water, and lipid. Other molecules contribute negligibly to the overall absorption due to their relatively smaller absorption cross section, low concentration, and/or their confined biodistribution. The main chromophores exhibit spectrally dependent absorbing properties that permit to distinguish between them and quantify their concentration in vivo when optical data is collected at multiple wavelengths. Especially, the ability to quantify independently oxy- and deoxyhemoglobin is unique among clinical imaging modalities, making optical techniques a desirable functional imaging modality in numerous clinical scenarios.

Fluorescence is an absorption-mediated phenomenon. It is related to an electronic transition from the excited state to the ground state of a molecule. In some cases, this relaxation may generate a photon of lower energy. Such photon generation will be specific to a molecular species and can be characterized by two intrinsic molecular parameters: the quantum yield and the lifetime. The quantum yield is defined by the ratio of the number of fluorescent photons emitted versus the number of

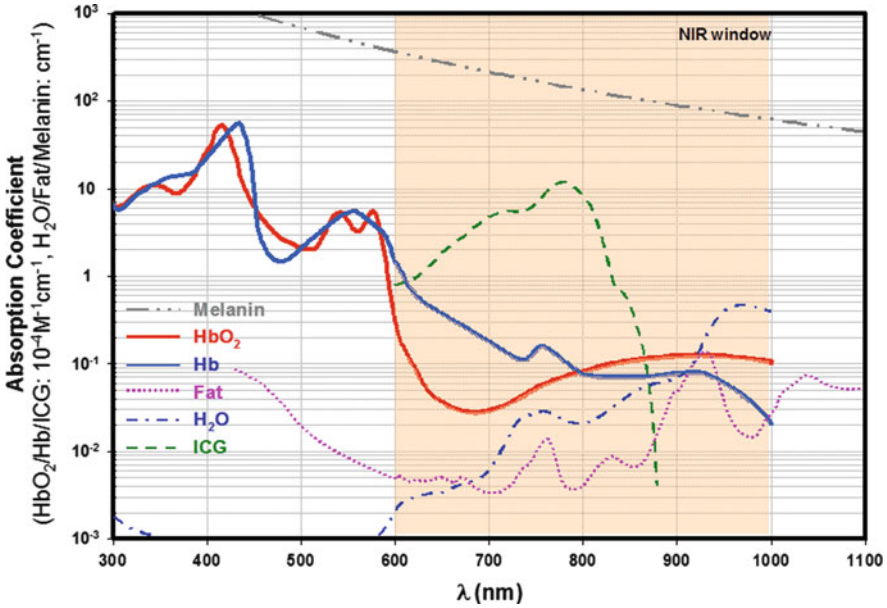

Fig. 10.2 Absorption coefficient of major chromophores vs. optical wavelength

photons emitted. The lifetime is defined as the average amount of time the molecule spends in the excited state following absorption of photons. Both parameters are dependent (however weakly) on environmental factors such as temperature, solvent, pH, etc. [5]. Numerous endogenous molecules fluoresce in the UV and visible spectral range [6]. However, the NIR range is relatively free from background autofluorescence and fluorescence applications for thick tissue imaging focus mainly on exogenous fluorophores. Numerous fluorescent compounds have been synthesized with appropriate spectral features for optical applications. Historically, the first dye of interest was synthesized in 1871 by von Baeyer and is still the most dominant fluorophore for clinical uses: fluorescein. Fluorescein is characterized by a relatively high absorptivity (also known as extinction coefficient) and high quantum yield. The dye exhibits a fluorescence peak around 520 nm. Thus, fluorescein has found few applications in imaging deep-seated tissue. To overcome the limitation of fluorescein, many fluorescent dyes with spectral features falling in the NIR window have been synthesized with excellent fluorescent properties [87]. However, to date, indocyanine green (ICG) is the only fluorescent contrast agent approved by the FDA with optimal NIR spectral features. It is commonly used clinically for diagnostic purposes [7–9] and has been used in optical mammography. The absorption spectra of the main chromophores and ICG are provided in Fig. 10.2.

10.3 Instrumentation

Optical examination of thick tissue based on transmitted light through large organs has been documented as far back as the early nineteenth century [11]. However, the diagnostic potential of diffuse optical imaging was systematically investigated only in the 1970s thanks to the introduction of NIR sources and detectors developed for optical telecommunications. Following the work of Gros et al. [12] which demonstrated that optical contrasts in the breast are spectrally dependent [13], many technical improvements were achieved in the development of multispectral systems [14] in the 1970s.

However, in the 1980s and early 1990s, numerous efforts have been produced to design new instrumental techniques that offer high resolution (on the millimeter scale or below) [15]. This focus has changed since the recognition that diffuse optical imaging techniques do not compete with other clinical anatomical imaging modalities in terms of spatial resolution. The current efforts of the diffuse optical imaging community center on designing instruments that are sensitive to functional changes, that are relatively cost-effective, and that can be deployed on the bedside or in the primary care physician office [16].

Three major experimental techniques exist in the NIR diffuse optical imaging field. These three techniques are categorized by the time dependence of the source intensity impinging on the tissues and are referred to as continuous wave (CW), frequency domain (FD), and time domain (TD) photon migration. In this section, we review these alternative technological approaches and discuss their relative merits and disadvantages.

10.3.1 Continuous Mode

Uses of light sources that continuously shine (or CW) on the specimen have been the first historically to be employed [11,17,18]. CW systems encompass instruments based on a light source that emits at a constant intensity but also systems in which sources are modulated at low frequency (∼kHz). The latter are the most common instruments as phase-locked detection techniques allow source multiplexing with high sensitivity. CW techniques are attractive techniques due to the availability of high-power (up to watts) and spectrally narrow sources over a broad range of NIR wavelengths and at a low cost. Also very sensitive affordable detectors with high quantum yield (number of electron pairs generated per absorbed photon) are available in this spectral range. The two main detectors commonly employed are avalanche photodiodes (APD) and photomultipliers (PMT) [19]. PMTs are the most sensitive detectors with the drawback of reduced dynamic range and higher costs compared to APDs.

To probe deep tissue such as in optical mammography, source-detector separation spans from a couple of centimeters to a dozen of centimeters, depending on the configuration selected. Due to the strong attenuation of the signal over such propagation distances, the spectral information is acquired sequentially by time multiplexing the wavelengths as hyperspectral source power is limited by ANSI standard and offers limited signal to noise ratio. The optical signal must then be integrated over a second or more to acquire robust data. Thus, acquisition time can be rather lengthy and fast hemodynamic monitoring becomes extremely challenging.

If the majority of diffuse optical imaging systems developed are based on CW techniques, they suffer from intrinsic disadvantages. First, monochromatic CW techniques are unable to distinguish between the effects of absorption and scattering [20]. Only recently has it been demonstrated that by using multiple wavelengths, absorption and scattering contributions could be unmixed [21]. Though in practical cases, such approach requires accurate estimation of background optical properties, which is not attainable with a CW data set alone but circumvented by implementing a few time-dependent channels [42, 61].

Second, intensity data are extremely sensitive to the surface tissues comparatively to deeper regions. As a consequence, CW techniques are highly dependent on the tissue-probe coupling. If such drawback can be attenuated in the case of static systems with numerous optode measurements [22, 23], it renders optical examination based on handheld probe highly operator dependent and sensitive to hemodynamic changes in the dermal capillaries.

10.3.2 Frequency Domain

To alleviate some of the drawbacks associated with CW techniques, numerous efforts have been put forward to integrate systems using time-dependent source amplitude. Technically, two distinct approaches using time-dependent sources are feasible: frequency domain (FD) and time domain (TD). Frequency domain refers to techniques based on a source whose amplitude is modulated in the MHz range (up to 1 GHz) and detection performed at the same frequency. Such a technique provides a set of two measurements: modulation amplitude attenuation and phase shift due to light propagation. In turn, these data allow to effectively separate the contributions of absorption and scattering [24, 25]. A comprehensive review of the frequency domain technology has been performed by Chance et al. [26].

The development of FD imagers for thick tissue has been strongly influenced with the efforts of Carl Zeiss [27, 28] and Siemens Medical Engineering [29] in the mid-90s. The prototypes built by these companies were dedicated to the topographical examination of the soft compressed breast. The breast was gently compressed between two clear windows, and a multiwavelength source-detector

pair, in transmittance configuration, was raster scanned over the compressed breast area. However, the implementation of reconstruction methods was crucial to provide information that was clinically useful [30, 31].

A tomographic system based on six laser diodes operating at wavelengths from 660 to 836 nm modulated at 100 MHz has been developed at Dartmouth College [32]. Light delivery and collection is performed via fiber bundles that are rigidly coupled to a 2D circular ring which rotates such that one of the 16 fiber bundles in the measured plane is aligned with the light source coupler while the other 15 fiber bundles are each connected to a photomultiplier tube (PMT) detector. The fibers are directly in contact with the pendulant breast, and light pressure is applied to ensure proper contact. The system does not require matching liquid. Acquisition is performed in the same plane, but multiple planes can be investigated for 3D imaging.

FD instrumentation is also used to supplement CW techniques. A hybrid CW frequency domain device for optical tomography has been developed at the University of Pennsylvania [33]. The system combines four amplitude-modulated laser diodes (690, 750, 786, and 830 nm) which are rapidly switched between 45 optical fibers on a 9×5 array and detected in reflectance, whereas transmitted light is detected by a CW CCD camera. The information obtained by the FD channels supplement the spatially dense CW information for enhanced functional tomography [34].

10.3.3 Time Domain

The first implementations of time-resolved techniques for diffuse optical imaging were motivated by the notion that minimally scattered photons (ballistic photons) enabled the rendering of images similarly to X-ray computed tomography (CT) with a relatively good resolution [35]. However, such photons can be reliably detected only for a few millimeter-thick samples, and the idea was abandoned. Time domain refers to techniques based on a source that produces a short pulse of light (typically less than 200 ps) and detectors recording the time of flight of photons exiting the sampled volume with a temporal resolution in the tenth of picoseconds or less. The temporal distribution of photons detected after propagation is known as the temporal point spread function (TPSF). Such data set is the richest in terms of information content and provides an unmatched set of data type: amplitude, mean time of flight, variance, skew, and Laplace transform [36]. Such data types provide enhanced separation between absorption and scattering contributions over the frequency domain. However, such benefits come at the cost of more expensive instrumentation and greater difficulty to implement in clinical prototypes. Also, TD optical imaging is a photon-starved technique that requires relatively long integration time (a few seconds compared to subsecond for CW and FD systems) to obtain TPSF with good statistical distributions.

The majority of time domain optical imaging systems are based on time-correlated single-photon counting (TCSPC) hardware, single-photon counting PMTs, and pulsed laser diodes. Significant technological advances have been made in these three areas in the last decade, leading to a widespread acceptance of time-resolved techniques in various biophotonics fields. Recently, with the advent of fast-gated CCD, time-gating techniques have been also employed. The benefit of the time-gating CCD is the high spatial density offered by this detector. However, the current CCD do not have an optimal quantum yield in the NIR window, and the necessity to acquire multiple gates sequentially to reconstruct a TPSF can lead to lengthy acquisition time.

Similarly to the Carl Zeiss and Siemens Medical Engineering system, prototypes based on soft compression of the breast between two planar plates and raster scan of multiwavelength source-detector pair in transmittance geometry have been developed by the Physikalisch-Technische Bundesanstalt group in Berlin [37] and Politecnico di Milano groups [38]. Both systems have implemented off-axis detection channels to provide depth information necessary for tomographic imaging. Advanced Research Technologies (ART) Inc., Montreal, developed a commercial system based on the same technology and principles: SoftScan®. The main difference between this commercial system and the academic system is that in the ART system, the examination is performed in the prone position with the breast gently compressed in a chamber filled with matching liquid and in the academic system, the patient is in a supine position similarly to mammographic systems. ART's system employs four pulsed laser diodes, a coaxial detection channel with 4 off-axis channels [39].

Tomographic systems that do not employ mechanical scans of the optodes but rather sequential point excitation of the tissue based on source fiber multiplexing and parallel detection with fiber bundles have been developed at the University College of London (UCL) and at the University of Pennsylvania. The UCL system is a two-wavelength (780 and 815 nm), 32-detection/excitation channel system [40], whereas the UPenn system is a six-wavelength (690, 750, 780, 800, 830, and 840 nm) system spatially multiplexed to 64 fiber positions and 16 detection channels acquiring the signal in parallel [41] and has been designed for concurrent MRI examination. These systems acquire data from multiple projections, allowing accurate tomographic reconstructions.

10.3.4 Ad Hoc Instrument Design Optimization

Volumetric diffuse optical imaging is a model-based imaging technique whose performance is significantly dependent on the accuracy of the light propagation model, the reconstruction strategies, and the data sets collected. It is well established that quantitative accuracy and image resolution are dependent on the number of source-detector pairs employed but also on the number of wavelengths used to probe the medium. To offer superior quantitative performances and to increase

resolution, dense optode measurements are necessary. Whereas to distinguish efficiently different biological chromophores, acquisition of dense multispectral data is crucial. The implementation of dense spatial and spectral data sets comes at an increased cost in terms of both acquisition time and instrument complexity.

The acquisition of high-resolution spatial information is essential for improved resolution and quantitative accuracy [42]. However, due to time constraints, confined space in the imaging chambers, and/or hardware memory restrictions for reconstructions, the spatial measurement density that can be acquired/employed is realistically limited. The number of measurements becomes then the limiting factor for quantitative high-resolution imaging. Within these restrictions, it then becomes essential to identify the best possible spatial sampling strategy. To guide the design of the instrument and/or develop practical imaging protocols, optimization strategies can be used a priori to determine the optimal acquisition parameters.

One objective criterion to determine the optimal spatial sampling, consist in simulating different acquisition scenarios, is to compute the associated forward models and perform a singular value analysis (SVA) of the Jacobians [43, 44]. The distribution of the eigenvalues obtained through singular value decomposition (SVD) provides an insight on the number of usable eigenmodes in the measurement space after truncation. The optimal set of parameters is the one providing the maximum usable measurement eigenmodes. The approach can be used to estimate the optimal number of sources, number of detectors, number of projections, number of frequencies, etc. However, it is important to note that this technique provides the general optimal set of parameters to design instrument and imaging protocols, but specimen-specific optimization strategies may still be required.

Similarly, the choice of the optimal sets of wavelength for functional imaging is paramount in designing the most effective imaging platform. The choice of wavelengths to perform diffuse optical imaging has been historically dictated by the limited offer of sources in the NIR spectral range. However, with recent advances in laser diode technology, a much greater choice of wavelengths is available nowadays. Therefore, objective strategies identifying the optimal set of wavelengths for NIR imaging should be employed a priori to design the instrument. For functional imaging studies, the main molecules of interest are oxy-, deoxyhemoglobin, water, and lipids. The absorption spectra of these chromophores do not have preeminent features in the NIR spectral window. Thus, when employing a limited number of spectral information, quantitative estimation of the concentration suffers from cross talk between the absorbers investigated.

Corlu et al. [45] proposed an objective strategy to select the optimal set of wavelengths, given a fixed number of wavelengths available and given the a priori knowledge of the absorption spectra of the chromophores. Based on simulations, they identified the best set of 4 wavelengths that provided minimal cross talk between oxy-, deoxyhemoglobin, and water by maximizing the uniqueness with which the chromophores can be distinguished. Recently, Brendel et al. [46] have extended the formulation of Corlu in the case of uncertainty in the extinction coefficient of the chromophores. Available absorption spectra from the literature show significant deviations, and thus this uncertainty should be taken into account

to avoid systematic bias. They demonstrated superior results in terms of minimized interparameter cross talk based on their approach compared to techniques not taking into account spectra uncertainties.

10.3.5 Safety/Regulatory Considerations

The diffuse optical imaging field is maturing, and various optical imaging systems are commercially available to the clinicians. Optical imaging instruments provide diagnostic information impacting patient health and are therefore subject to governmental regulatory oversight. Thus, it is critical to identify the regulatory issues that impact the design of optical clinical products. As stated by the first requirement of the "essential Principles of Safety and Performances of Medical devices" [47]:

> *Medical devices should be designed and manufactured in such a way that, when used under the conditions and for the purposes intended and, where applicable, by virtue of the technical knowledge, experience, education or training of intended users, they will not compromise the clinical condition or the safety of patients, or the safety and health of users or, where applicable, other persons, provided that any risks which may be associated with their use constitute acceptable risks when weighted against the benefits to the patient and are compatible with a high level of protection of health and safety.*

Therefore, patient protection concerns are essential in the design of clinical optical imager.

The different safety hazards of interest during the design of the optical imaging platform include tissue trauma, electrical shock, material toxicity, disease transmission, electromagnetic compatibility, and software malfunction. These considerations are common to a large variety of medical devices. In addition, optical imaging devices need to consider the potential hazard originating from the interaction of light with biological tissue. The recommended exposure limits for protecting patients and device operators from these safety risks are listed in international standards.

Optical hazards can be divided in three main categories: photochemical, photothermal, and photomechanical [48]. Diffuse optical imaging techniques are operating in the NIR window, and thus, the primary optical hazard of concern is the photothermal damage. The absorption of light by the tissue leads to local increase of temperature to levels that may injure the tissue. Therefore, diffuse optical instruments should be designed to shine light below the maximum permissible exposure (MPE) limit for the skin. The MPE is the highest power or energy density (in W/cm^2 or J/cm^2) of a light source that is considered safe, i.e., that has a negligible probability for creating damage. It is usually about 10 % of the dose that has a 50 % chance of creating damage [49] under worst-case conditions. The MPE is organ and wavelength dependent. However, thanks to the increase in detector sensitivity, numerous optical imaging systems are based on class I or class II light sources that are safe for the patient, even in the case of starved photon techniques such as time domain approaches.

10.4 Diffuse Optical Tomography

Three-dimensional imaging of thick tissues based on optical measurements is known as diffuse optical tomography (DOT). DOT falls in the class of nonlinear ill-posed inverse-scattering problem which presents many challenges. Three processes are required to perform DOT. First, light propagation in the tissue imaged must be modeled. Second, a sensitivity matrix is constructed based on the light propagation model, a matrix that relates the surface measurements to the internal distribution of the optical properties imaged. Third, the inverse problem is solved by inverting the sensitivity matrix to retrieve the three-dimensional distribution of the optical properties of the tissue imaged. All three steps significantly impact the fidelity of DOT.

10.4.1 Theory

Different theoretical models are used to compute the forward model. In the case of multiscattering regime, the three different techniques commonly employed are the Monte Carlo method, the radiative transport equation (RTE) and its approximation, and the diffusion equation. The Monte Carlo method is considered as the "gold standard" to simulate light propagation through tissues. The Monte Carlo method uses a statistical approach to calculate the light energy fluence rate at any location in the tissue. This model follows one photon at a time and calculates the probability of scattering or absorption of this photon. In each interaction point, the scattering direction, the absorption, and the distance to the next interaction point are modeled as random variables on the basis of the optical properties of the tissue. This process is repeated for a certain predetermined number of photons. The Monte Carlo method is seldom used in DOT due to the computational burden associated with simulating large packets of photons. Only recently, Monte Carlo has been demonstrated to be a viable forward model for diffuse optical tomography [10]. With the advent of massively parallel systems based on graphics processor units (GPU), Monte Carlo-based reconstructions may become computationally efficient in the near future [50].

The RTE allows modeling light in a relatively more computationally efficient framework than MC methods. The RTE is an integrodifferential equation describing the energy flow per unit normal area per unit solid angle per unit time. It can be derived via conservation of energy [51]. Analytical solutions to the RTE are difficult to derive, and generally, the equation is solved numerically with finite element or finite difference solvers. The RTE offers the same advantages as the MC method: flexible, proven to be accurate over a large span of optical properties, and accurate for small interrogated finite volumes but more complex to implement. The RTE has been successfully employed as the forward model to perform optical tomography. However, it is generally used only when certain conditions are met: small source-detector separations [52, 53], tissue with low-absorbing/scattering regions (i.e.,

cerebrospinal fluid, synovial fluid in joints) [54, 55]. In other cases, approximations to the RTE are introduced to provide more computationally efficient methods.

In the case of predominant scattering, the diffusion equation that is an approximation of the radiative transport equation is preferred due to its simpler mathematical expression. Its mathematical expression both in the frequency domain and the time domain can be easily solved analytically for planar geometries [56,57] (the CW case corresponds to a null frequency). In the case of heterogeneous media, the diffusion equation can be also solved analytically by using perturbative approaches such as the Born or the Rytov approximation [58]. However, for complex boundary conditions, numerical methods or more refined analytical algorithms [59] are necessary to model accurately the light propagation, leading to increase in the computational burden. Even though the diffusion equation is less accurate than MC methods or the RTE, it is the most commonly used forward model in dynamically diffuse optical tomography. It has been employed successfully to provide 3D functional maps of tissue activities in the brain [60, 61], breast [62–64], and muscle [65, 66].

10.4.2 Use of A Priori Information

Even though considerable advances have been performed in modeling and reconstruction techniques, due to the diffuse nature of the light collected, diffuse optical tomography remains an ill-posed, poorly conditioned inverse problem that can suffer from nonuniqueness and low spatial resolution. One way to improve the performance of optical tomography is to incorporate a priori information in the image formation process. Lately, the incorporation of two different kinds of priors has been demonstrated to significantly improve the performance of functional optical properties: spectral and spatial priors.

Incorporating spectral priors in the optical inverse formulation consists in utilizing all the multispectral information collected in one inverse problem to estimate directly the functional and structural parameters of interest conversely to classical methods that derive these parameters from optical reconstructions of absorption and scattering performed at each individual wavelength. In this formulation, the absorption coefficient is modeled as the linear sum of all the individual chromophores in the tissue:

$$\mu_{\mathrm{a}}\left(\lambda_j\right) = \sum_i \varepsilon\left(\lambda_j\right) C_i \tag{10.1}$$

where $\varepsilon(\lambda_j)$ is the wavelength-dependent extinction coefficient, known a priori, of the ith chromophore with a concentration C_i (Hb, HbO_2, H_2O, and lipids in the case of the breast). The scattering coefficient is modeled with a spectral power law derived from a simplified Mie scattering theory [44, 45]:

$$\mu_{s'}\left(\lambda_j\right) = A\lambda_j^{-b} \tag{10.2}$$

where A, the scattering prefactor, depends on the number and size of the scatterers and b, the scattering exponent, depends on the size of the scatterers. Incorporating these models in the multispectral reconstructions allows to directly map functional and structural parameters simultaneously. The method has been demonstrated to improve robustness and accuracy in quantitative functional imaging of the breast [21, 67].

Similarly, the use of anatomical priors from auxiliary clinical imaging modality can dramatically increase the spatial and quantitative accuracy of optical imaging. The incorporation of structural priors in optical imaging can be traced back to the work of Chang et al. [68]. Based on simulations, they demonstrated that by using an anatomically accurate optical (AAO) model derived from a segmented MRI data, optical reconstructions were able to retrieve the pathology accurately. Since, the introduction of spatially localized anatomical areas in the optical image formation flow has become a significant area of research for the optical tomography community. The many different methods devised to include anatomical priors can be clustered in two main categories, hard and soft priors.

Hard priors represent the most straightforward method in implementing the anatomical priors. In these approaches, the volume to be imaged is segmented in different structures based on the anatomical modality data. Hard prior methods enforce the anatomical boundaries onto the optical imaging reconstructions. All voxels belonging to the same spatial domain are then correlated in the optical reconstructions, reducing dramatically the number of unknowns to estimate. The implementation of hard priors varies from assuming that all segmented tissues have homogenous optical properties [69], that some segmented tissues are homogenous, and that compromised tissues are heterogeneous [70] or utilize homogenous tissue-dependent optical properties obtained in a first step as initial guesses for higher-resolution optical reconstructions in a second step [71]. All these methods have been proven to be robust even in the case of noisy optical data [57].

However, hard priors imply that the anatomical structure of the probed tissue is known and that there is a spatial correlation between the anatomical and optical edges. In realistic scenarios, structural or physiological correlation between the true optical solution and a prior image from a different medical imaging modality cannot be guaranteed. This can be due to the different contrast mechanisms revealed by each modality and/or geometrical deformation occurring during the different examination protocols. Then, it is expected that enforcing incorrect priors can lead to nontrustworthy optical reconstructions. To alleviate this issue, methods incorporating soft priors have been proposed.

Conversely to hard priors, reconstruction techniques based on soft priors do not force the anatomical boundaries to coincide with the optical domains. Thus, changes of the optical parameters across boundaries are allowed, reducing the impact of imperfect/incomplete anatomical information on the optical reconstructions. Guven et al. [72] proposed a Bayesian formulation minimizing the incorrect bias from the prior anatomical data but preserving the prior information leading toward the true solution. Intes et al. [67] extended this method to functional imaging of the breast

and incorporated spectral priors as well. Optical-property recovery in simulation was accurate within 15 %, even when anatomical data did not specify a tumor region of interest.

10.5 Combining Diffuse Optical Imaging with Other Modalities

10.5.1 Magnetic Resonance Imaging

Fusion of optical imaging techniques with MRI is an active field of research. Thanks to its high soft tissue contrast and three-dimensional imaging capabilities, MRI is the perfect candidate for optical multimodal integration. To date, the focus of optical/MRI fusion has been mainly limited to derive high-resolution structural information to guide the optical inverse problem or to validate the nature and localization of the information collected by one of the stand-alone systems.

The chief difficulty in performing MRI-optical hardware fusion resides in designing an optical instrument delivering and collecting light without interference from the high magnetic field. Thus, typically, the optical instruments are designed around long optical fibers (up to 10 m) to operate in a shielded environment outside the MRI examination room. The fibers are delivered to the examination chamber through a magnetically shielded conduit. The fibers need to be void of any magnetic material for safety reasons and to avoid artifacts in the MRI data. Similarly, the fiber holder should be compatible with MRI requirements but still provide high-precision positioning of the optical fibers ($\sim$ tenth of a millimeter). Such holder also holds the MR coil, limiting the space available for optimal optode positioning. Moreover, due to the MR bore size and the nature of clinical MR coils, the physical space available to bring in the fibers is limited, leading to a reduced number of fibers that can be efficiently coupled with the MR systems. This is especially limiting with the detection fibers that are generally fiber bundles of 3–5-mm diameter for clinical applications. Thus, current optical systems that are integrated with clinical MRI are typically limited to 16 detection fibers (cf. Fig. 10.3). Then 3D optical imaging becomes difficult, and great care should be taken to position the optodes close to the pathology to be imaged. This can be very challenging in clinical settings in which the imaging session time is restricted, constraining the time allocated to position the pathology within the plane of the optical fibers.

MRI-optical fusion has been first developed to benefit from the high-resolution MR anatomical maps. Such anatomical images are typically acquired with T1-weighted or T2-weighted spin-echo sequences and registration with optical images performed via static fiduciary markers. The MR image structure can be further segmented into the different types of tissues investigated. In the case of optical mammography, MR allows to segment the main structure of the breast (adipose and fibroglandular tissue) and potentially the lesion. Spatial correlation

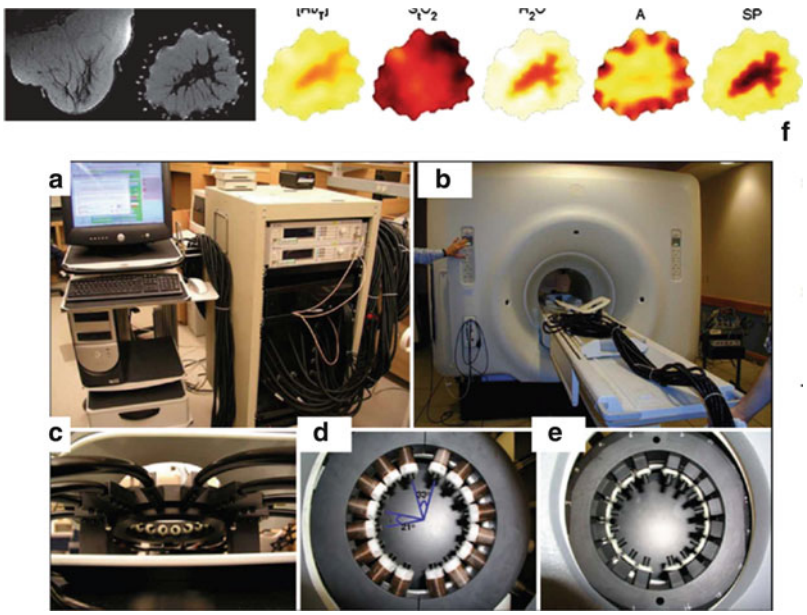

Fig. 10.3 The Dartmouth NIR/MRI systems. (**a**) Photograph of the portable NIR instrumentation and control console. (**b**) Optical fibers extend from the system into the MRI. (**c**) Open architecture breast array coil houses the optical fiber-positioning system. (**d**) The first- and (**e**) second-generation MR-compatible fiber-positioning mechanisms. (**f**) One set of breast MRI/NIR images (Used with permission from [75])

between MR structural contrast and optical contrast (hemoglobin and water) has been demonstrated [73] supporting the rationale of using MR-derived structural priors in the optical inverse problem.

However, the current focus of MRI-optical fusion lies beyond the need to improve optical imaging performances. Especially, the field of MR is very dynamic with constant progress toward in vivo high-resolution functional imaging. Therefore, present efforts from the optical imaging community focus on identifying the complementary information that optical imaging can offer to MR imaging. In the context of breast oncology, MRI is an efficient modality to detect lesions but suffers from a lack of specificity (around 67 %) [74]. Conversely, optical imaging techniques demonstrate promises in providing diagnostic functional information to characterize the suspicious lesion. Stand-alone systems have been shown to provide up to 88 % specificity [75], and the integration of multispectral optical imaging with MRI may lead to increased optical specificity [76].

Similarly, functional MRI (fMRI) may benefit greatly from concurrent optical acquisition. Especially, fMRI studies based on BOLD are limited at mapping relative changes in tissue oxygen saturation, whereas optical imaging techniques are able to quantitatively map both oxygenated and deoxygenated blood at high frame rates (up to a few Hz). Therefore, optical imaging can provide complementary

quantitative functional information to calibrate BOLD signals and to monitor accurately the oxygenation state of the tissue. To date, the clinical integration of optical imaging with fMRI has been limited to brain imaging. Numerous studies have demonstrated the good correlation both spatially and temporally between the BOLD MRI and optical imaging [77–79]. Application of this approach to other clinical scenarios such as functional imaging of tumors is ongoing [80].

10.5.2 Computer Tomography

Application of optical techniques to breast oncology has been one of the main driving forces behind development in the field of diffuse optical imaging. While some breast lesions are still discovered by palpation, the majority of breast cancer diagnoses are made with X-ray mammography [81]. Therefore, the combination of optical imaging with X-ray imaging is a logical step toward clinical acceptance of optical imaging.

Hardware fusion of both techniques is not as challenging as MRI-optical fusion. X-ray mammographers offer an open architecture that provides more flexibility to couple optical hardware. However, in the case of breast examination, the acquisition for both modalities should not be performed simultaneously but sequentially. Thus, the challenge in the hardware fusion of both techniques resides in designing an optical probe that can be mounted/unmounted on the X-ray compression plates in minimal time but still with great precision for accurate registration and without displacement of the breast.

The hardware fusion of X-ray and optical imaging is still very limited for clinical applications. Figure 10.4 provides an overview of the system built at Massachusetts General Hospital (MGH). In this implementation, an optical system based on both CW and FD laser modules was integrated with a digital breast tomosynthesis (DBT) imager [82]. The optical probes are embedded in anodized aluminum covers that can be securely attached to an optically transparent cassette that is fastened to the DBT system. The source and detector aluminum probes can be easily inserted in the cassette and released prior to the X-ray scans without movement of the imaged specimen. Such approach allows for true coregistration between the two modalities. Then, spatial priors derived from the X-ray scans can be used to guide the inverse optical problem. An example of a clinical examination performed with this dual-modality system is provided in Fig. 10.4.

10.5.3 Ultrasound

Ultrasound (US) is a well-established clinical modality in breast oncology used as an adjunct to mammography to discriminate cyst from solid lesions. Ultrasound is also a useful imaging modality to guide minimally invasive procedures such as core needle biopsy [83]. Ultrasound imaging systems are based on a handheld

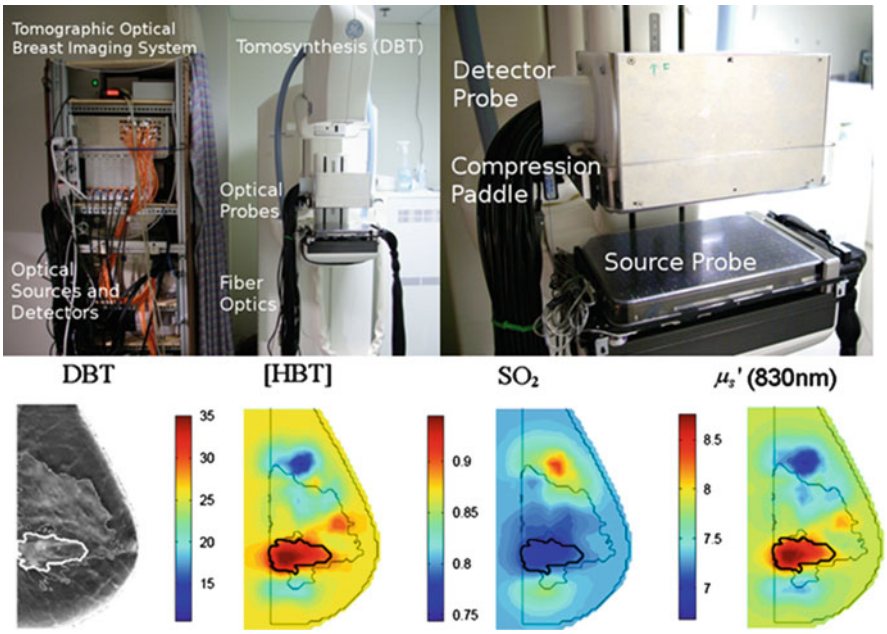

Fig. 10.4 Optical imager integrated with digital breast tomosynthesis. Example of DBT and optical functional parameters Reconstructed image sections for the right breast in 45-year-old woman. The breast contains a 2.5-cm invasive ductal carcinoma (highlighted by the thick black margin).

probe that is mechanically scanned by the operator over the region of interest. The small dimension and flexibility of the US probes allow for an easy optical-US coupling without modifying the standard US operating procedures, though optical interrogation of tissue is then performed in the reflectance geometry which is not optimal to probe deep tissue and which is very sensitive to tissue/optode coupling.

A typical implementation of DOI integrated with ultrasound is depicted in Fig. 10.5. This system developed at the University of Connecticut is based on a commercial US transducer that is mounted on the center of a custom handheld probe with the optodes distributed at the periphery. The light delivery and light collection is performed via optical fibers to allow for a small footprint and easy cleaning. The optodes are distributed over the surface of the probe to offer multiple distance measurements required to image deep-seated tissue (a couple of centimeters). The probe is holding 12 optical source fibers, 4 optical detector fibers, and 20 piezoelectric crystals comprising the US array. The optical and US systems can operate simultaneously for coregistration without interference.

The structural information provided by the US imaging system is used to guide the optical imaging reconstruction process. The lesion is localized on the US image, and the lesion volume is segmented in a refined mesh whereas the nonlesion

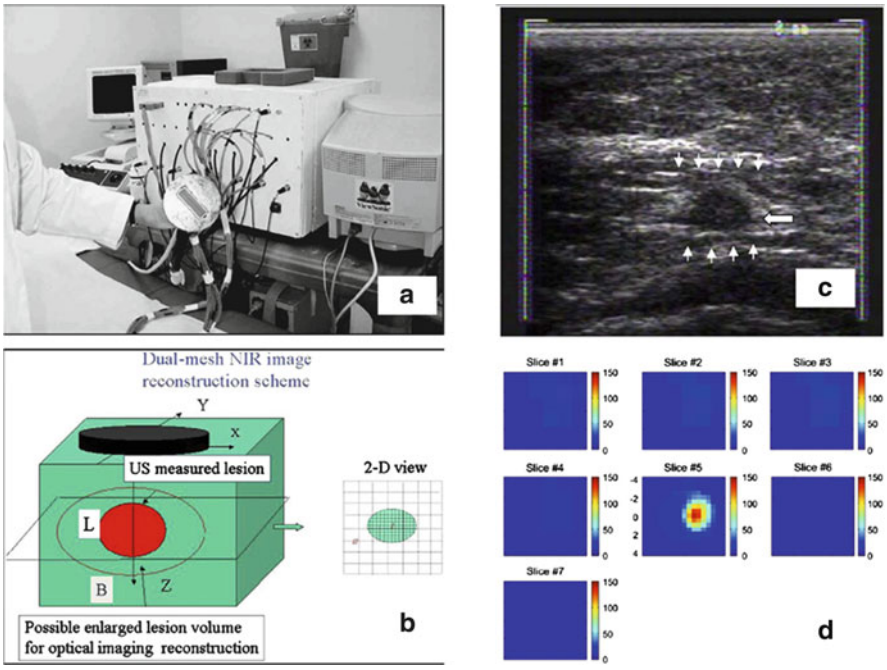

Fig. 10.5 (**a**) Prototype of the handheld combined NIR/US imager developed in the University of Connecticut. (**b**) The entire imaging volume is segmented into lesion (L) and background (B) regions. The fine imaging grid is used for the lesion region, and the coarse grid is used for the background. (**c**) NIR/US images of a nonpalpable lesion in a 55-year-old woman. US showed a nodular mass with internal echoes, and the lesion was considered suspicious. The maps of total hemoglobin concentration distribution correspond to slices from 0.7 cm underneath the skin surface to the chest wall, with 0.5-cm spacing. The lesion is well resolved in slice 5 (Used with permission from [70])

tissues are segmented in a coarser grid. An example of a clinical dual-modality examination is provided in Fig. 10.5. An 8-mm suspicious lesion identified on the US was showing a significant increase in total hemoglobin concentration (∼10-fold) compared to the background tissue. The lesion was diagnosed as an infiltrating ductal carcinoma which was supporting the finding of the optical readings.

10.5.4 Positron Emission Tomography (PET)

The primary goal of combining diffuse optical imaging with other clinical modalities is to benefit from the structural information provided by the high-resolution imaging modalities in order to improve upon functional potential of DOI. In particular, the structural details acquired using MRI, US, and X-ray imaging are used as a priori information to guide the optical reconstructions that suffers from

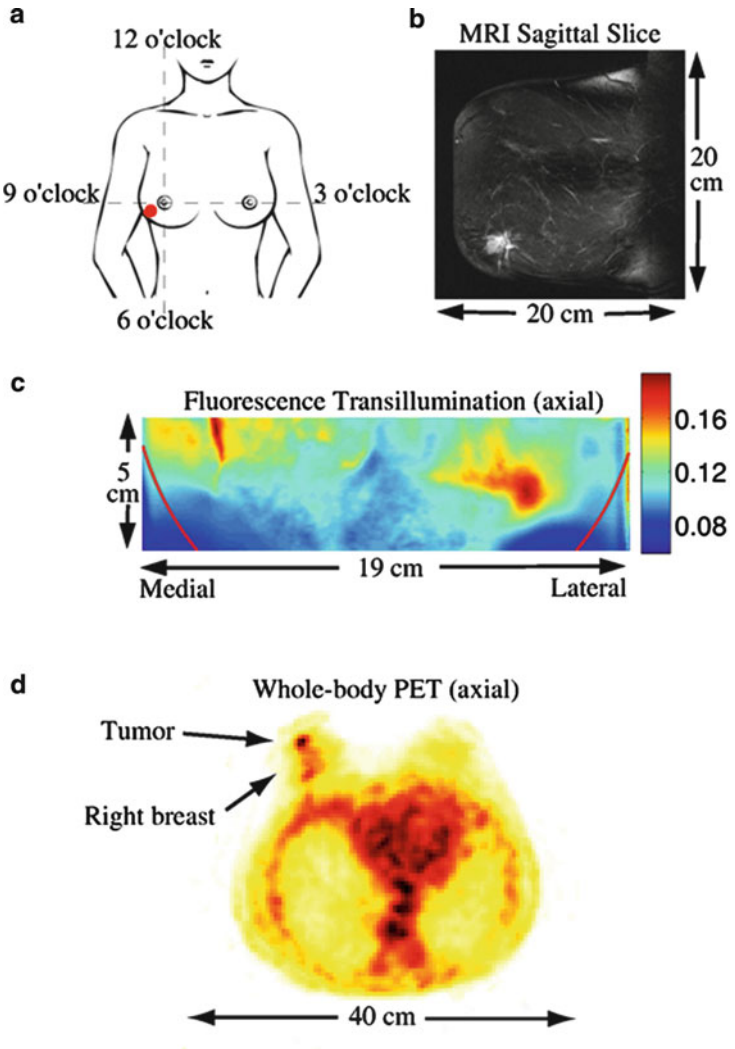

Fig. 10.6 (**a**) Illustration of the tumor location. (**b**) Gadolinium-enhanced sagittal MR image slice showing the tumor in the lower *left corner*. (**c**) Fluorescent transillumination image (explained in text). (**d**) Axial slice from 18F-FDG whole body PET image. The view is from the patient's feet (i.e., the right breast appears on the *left side*) (Figures (**a**–**c**) reprinted with permission from [64,88]. © 2007, Optical Society of America

low-resolution and partial volume effects. Only recently, the combination of optical imaging with other clinical functional imaging modalities has been considered. Especially, the combination of PET with DOI is currently being pursued. However, to date, the combination of both techniques is done nonconcurrently and relies on software registration.

PET is a clinically established modality that relies on exogenous contrast agents to measure noninvasively physiological processes in vivo with ^{18}F-fluorodeoxyglucose (^{18}F-FDG) being the main tracer used clinically. This tracer accumulates in metabolically active tissue over time providing functional information of the state of the tissue. Clinical PET imaging session are generally performed with whole body system, but recently dedicated PET breast imagers have been developed [84, 85]. Such dedicated systems allow for efficient coregistration and thus comparison of specific regions between the two stand-alone modalities. Current work performed at the University of Pennsylvania demonstrated spatial congruence between PET and optical contrast from patient with tumors [86] (cf. Fig. 10.6). Hardware fusion of these dedicated imagers with optical imaging system is poised to occur in the near future.

10.6 Conclusion

Diffuse optical imaging, particularly diffuse optical tomography, is an emerging clinical modality capable of providing unique functional information, at a relatively low cost, and with nonionizing radiation. However, DOT suffers from low spatial resolution and associated contrast dilution. To overcome this limitation, DOT has been combined with established anatomical clinical modalities such as MRI, CT, or US. Multimodal diffuse optical imaging has enabled a synergistic combination of functional and anatomical information: the quality of DOT reconstructions have been significantly improved by incorporating the structural information derived by the combined anatomical modality. Current multimodal DOT implementations are being designed to optimize and facilitate their use in the clinical environment and to provide functional information of added diagnostic value to the radiologist.

References

1. V. Backman, R. Gurjar, K. Badizadegan, I. Itzkan, R.R. Dasari, L.T. Perelman, M.S. Feld, Polarized light scattering spectroscopy for quantitative measurement of epithelial structures *in situ*. IEEE J. Sel. Top. Quantum Electron. 5, 1019–1026 (1999)
2. J. Beuthan, O. Minet, J. Helfman, G. Muller, The spatial variation of the refractive index in biological cells. Phys. Med. Biol. **41**, 369–382 (1996)
3. B. Beauvoit, S.M. Evans, T.W. Jenkins, E.E. Miller, B. Chance, Correlation between the light scattering and the mitochondrial content of normal tissues and transplantable rodent tumors. Anal. Biochem. **226**, 167–174 (1995)
4. V. Backman, M.B. Wallace, L.T. Perelman, J.T. Arendt, R. Gurjar, M.G. Muller, Detection of pre-invasive cancer cells. Nature **406**, 35–36 (2000)
5. J.R. Lackowicz, *Principles of Fluorescence Spectroscopy* (Kluwer Academic-Plenum Publ., New York, 1999)
6. M.A. Mycek, B.W. Pogue, *Handbook of Biomedical Fluorescence* (CRC Press LLC, Boca Raton, 2003)

7. R. Benson, H. Kues, Fluorescence properties of indocyanine green as related to angiography. Phys. Med. Biol. **23**, 159–163 (1978)
8. R. Branch, J. James, A. Read, The clearance of antipyrine and indocyanine green in normal subjects and in patients with chronic liver disease. Clin. Pharmacol. Ther. **20**, 81–89 (1976)
9. C. Niemann, T. Henthorn, T. Krejcie, C. Shanks, C. Enders-Klein, M. Avram, Indocyanine green kinetics characterize blood volume and flow distribution and their alteration by propanolol. Clin. Pharm. Ther. **67**, 342–350 (2000)
10. J. Chen and X. Intes, Comparison of Monte Carlo Methods for Fluorescence Molecular Tomography - Computational Efficiency. Medical Physics **38**(10), 5788–5798 (2011)
11. M. Cutler, Transillumination as an aid in the diagnosis of breast lesions. Surg. Gynecol. Obstet. **48**, 721–728 (1929)
12. C.M. Gros, Y. Quenneville, Y. Hummel, Diaphanologic mammaire. J. Radiol. Electrol. Med. Nucl. **53**, 297 (1972)
13. A.E. Profio, O.W. Sartorius, G.A. Navarro, Scientific basis of breast diaphanography. Med. Phys. **16**, 60–65 (1989)
14. E. Carlsen, *Diagnostic Imaging* (Spectrascan, S. Windsor, 1982)
15. J.C. Hebden, S.R. Arridge, D.T. Delpy, Optical imaging in medicine: I. Experimental techniques. Phys. Med. Biol. **42**, 825–840 (1997)
16. A.P. Gibson, J.C. Hebden, S.R. Arridge, Recent advances in diffuse optical imaging. Phys. Med. Biol. **50**, R1–R43 (2005)
17. R. Bright, in *Disease of the Brain and Nervous System*. vol. 2431 (Longman, London, 1831)
18. T.B. Curling, A practical treatise on the diseases of the testis and the spermatic cord and Scrotum (Samule Hihgley, London, 1843), pp. 125–181
19. G.F. Knoll, *Radiation Detection and Measurements*, 3rd edn. (Wiley Text Books, Wiley, New York, 1999)
20. S.R. Arridge, W.R.B. Lionheart, Nonuniqueness in diffusion-based optical tomography. Opt. Lett. **23**, 882–884 (1998)
21. A. Corlu, T. Durduran, R. Choe, M. Schweiger, E.M.C. Hillman, S.R. Arridge, A.G. Yodh, Uniqueness and wavelength optimization in continuous-wave multispectral diffuse optical tomography. Opt. Lett. **28**, 2339–2431 (2003)
22. D.A. Boas, T. Gaudette, S.R. Arridge, Simultaneous imaging and optode calibration with diffuse optical tomography. Opt. Express **8**, 263–273 (2001)
23. X. Intes, J. Ripoll, T. Kitai, Y. Chen, S. Nioka, A.G. Yodh, B. Chance, CW-optical breast imaging enhanced with Indocyanine green. Med. Phys. **30**, 1039–1047 (2003)
24. Y. Yao, Y. Wang, Y. Pei, W. Zhu, R.L. Barbour, Frequency domain optical imaging of absorption and scattering distributions by a Born iterative method. JOSA A **14**, 325–342 (1997)
25. X. Intes, B. Chance, Multi-frequency diffuse optical tomography. J. Modern Opt. **52**, 2139–2159 (2005)
26. B. Chance, M. Cope, E. Gratton, N. Ramirez, B.J. Tromberg, Phase measurement of light absorption and scatter in human tissue. Rev. Sci. Instrum. **69**, 3457–3481 (1998)
27. M. Kaschke, H. Jess, G. Gaida, J.M. Kaltenbach, W. Wrobel, Transillumination imaging of tissue by phase modulation techniques. Proc. OSA Adv. Opt. Imaging Photon Migration **21**, 88–92 (1994)
28. K.T. Moesta, H. Kaisers, S. Fantini, M. Tonnies, M. Kaschke, P.M. Schlag, Lasermammografie der Brustdruse-Sensitivitatssteigerung durch Hochfrequenzmodulation. Langenbecks Arch. Chir. Suppl. **1**, 543–548 (1996)
29. L. Gotz, S.H. Heywang-Kobrunner, O. Schutz, H. Siebold, Optische mammographie an praoperativen patientinnen. Akt. Radiol. **8**, 31–33 (1998)
30. M.A. Franceschini, K.T. Moesta, S. Fantini, G. Gaida, E. Gratton, H. Jess, W.W. Mantulin, M. Seeber, P.M. Schlag, M. Kaschke, Frequency-domain techniques enhance optical mammography: initial clinical results. Proc. Natl. Acad. Sci. USA **94**, 6468–6473 (1997)
31. S. Fantini, S.A. Walker, M.A. Franceschini, M. Kaschke, P.M. Schlag, K.T. Moesta, Assessment of the size, position and optical properties of breast tumors in vivo by noninvasive optical

methods. Appl. Opt. **37**, 1982–1989 (1998)
32. T.O. Mcbride, B.W. Pogue, S. Jiang, U.L. Osterberg, K.D. Paulsen, A parallel-detection frequency-domain near-infrared tomography system for hemoglobin imaging of the breast in vivo. Rev. Sci. Instrum. **72**, 1817–1824 (2001)
33. J.P. Culver, R. Choe, M.J. Holboke, L. Zubkov, T. Durduran, A. Slemp, V. Ntziachristos, B. Chance, A.G. Yodh, Three-dimensional diffuse optical tomography in the parallel plane transmission geometry: evaluation of a hybrid frequency domain/continuous wave clinical system for breast imaging. Med. Phys. **30**, 235–247 (2003)
34. A. Corlu, R. Choe, T. Durduran, K. Lee, M. Schweiger, S.R. Arridge, E.M. C. Hillman, A.G. Yodh, Diffuse optical tomography with spectral constraints and wavelength optimization. Appl. Opt. **44**, 2082–2093 (2005)
35. J.C. Hebden, S.R. Arridge, D.T. Delpy, Optical imaging in medicine: I. Experimental techniques. Phys. Med. Biol. **42**, 825–840 (1997)
36. M. Schweiger, S.R. Arridge, Application of temporal filters to time-resolved data in optical tomography. Phys. Med. Biol. **44**, 1699–1717 (1999)
37. D. Grosenick, H. Wabnitz, H.H. Rinneberg, K.T. Moesta, P.M. Schlag, Development of a time-domain optical mammograph and first in vivo applications. Appl. Opt. **38**, 2927–2943 (1999)
38. A. Pifferi, P. Taroni, A. Torricelli, F. Messina, R. Cubeddu, Four-wavelength time-resolved optical mammography in the 680–980 nm range. Opt. Lett. **28**, 1138–1140 (2003)
39. X. Intes, Time-domain optical mammography initial results. Acad. Radiol. **12**, 934–947 (2005)
40. F.E.W. Schmidt, M.E. Fry, E.M.C. Hillman, J.C. Hebden, D.T. Delpy, A 32-channel time-resolved instrument for medical optical tomography. Rev. Sci. Instrum. **71**, 256–265 (2000)
41. X. Intes, J. Yu, A.G. Yodh, B. Chance, Development and evaluation of a multi wavelength – multi channel time resolved optical instrument for NIR/MRI mammography co-registration, in *IEEE – EMBS NEBE 2002: Defining the Future for Biomedical Engineering*, Philadelphia (2002)
42. S.D. Konecky, G.Y. Panasyuk, K. Lee, V. Markel, A.G. Yodh, J.C. Schotland, Imaging complex structures with diffuse light. Opt. Express **16**, 5048–5060 (2008)
43. J.P. Culver, V. Ntziachristos, M. Holboke, A.G. Yodh, Optimization of optode arrangements for diffuse optical tomography: a singular value analysis. Opt. Lett. **26**, 701–703 (2004)
44. X. Intes, B. Chance, Multi-frequency diffuse optical tomography. J. Modern Opt. **52**, 2139–2159 (2005)
45. A. Corlu, R. Choe, T. Durduran, K. Lee, M. Schweiger, S.R. Arridge, E.M. C. Hillman, A.G. Yodh, Diffuse optical tomography with spectral constraints and wavelength optimization. Appl. Opt. **44**, 2082–2093 (2005)
46. B. Brendel, T. Nielsen, Selection of optimal wavelengths for spectral reconstructions in diffuse optical tomography. J. Biomed. Opt. **14**, 034041 (2009)
47. M. Cheng, *Medical Device Regulations: Global Overview and Guiding Principles* (World Health Organization, Geneva, 2003)
48. J.T. Pfefer, B.A. Drum, Regulation and regulatory science for optical imaging, in *Translational Multimodality Optical Imaging*, ed. by F. Azar, X. Intes, Ch. 15 (Artech House, Norwood, 2008)
49. K. Schröder, *Handbook on Industrial Laser Safety* (Technical University of Vienna, 2000)
50. E. Alerstam, T. Svensson, S. Andersson-Engels, Parallel computing with graphics processing units for high speed Monte Carlo simulation of photon migration. J. Biomed. Opt. **13**, 060504 (2008)
51. S. Chandrasekhar, *Radiative Transfer* (Dover, New York, 1960)
52. R. Aronson, R.L. Barbour, J. Lubowsky, H. Graber, Application of transport theory to infra-red medical imaging. Modern Math. Methods Transport Theory, 64–67 (NA, 1991)
53. G.S. Abdoulaev, A.H. Hielscher, Three-dimensional optical tomography with the equation of radiative transfer. J. Electron. Imaging **12**(4), 594–601 (2004)
54. M. Firbank, S.R. Arridge, M. Schweiger, D.T. Delpy, An investigation of light transport through scattering bodies with non-scattering regions. Phys. Med. Biol. **41**, 767–783 (1998)

55. A.K. Scheel, M. Backhaus, A.D. Klose, B. Moa-Anderson, U. Netz, K.G. Hermann, First clinical evaluation of sagittal laser optical tomography for detection of synovitis in arthritic finger joints. Ann. Rheumatic Dis. **64**, 239–245 (2005)
56. N. Patterson, B. Chance, B.C. Wilson, Time resolved reflectance and transmittance for the non-invasive measurement of tissue optical properties. Appl. Opt. **28**, 2331–2336 (1989)
57. R.C. Haskell, L.O. Svaasand, T. Tsay, T. Feng, M.S. McAdams, T.J. Tromberg, Boundary conditions for the diffusion equation in radiative transfer. JOSA A **11**, 2727–2741 (1994)
58. M. O'Leary, Imaging with diffuse photon density waves, PhD Dissertation, University of Pennsylvania (1996)
59. J. Ripoll, V. Ntziachristos, Iterative boundary method for diffuse optical tomography. JOSA A **20**, 1103–1110 (2003)
60. J. Hebden, A. Gibson, R. Yusof, N. Everdell, E. Hillman, E. Delpy, Three-d dimensional optical tomography of the premature infant brain. Phys. Med. Biol. **47**, 4155–4166 (2002)
61. Y. Chen, D. Tailor, X. Intes, B. Chance, Correlation between Near-Infrared spectroscopy (NIRS) and magnetic resonance imaging (MRI) on rat brain oxygenation modulation. Phys. Med. Biol. **48**, 417–427 (2003)
62. D.R. Leff, O.J. Warren, L.C. Enfield, A. Gibson, T. Athanasiou, D.K. Patten, Diffuse optical imaging of the healthy and diseased breast: a systematic review. Breast Cancer Res. Treatment **108**(1), 9–22 (2008)
63. X. Intes, S. Djeziri, Z. Ichalalene, N. Mincu, Y. Wang, P. St-Jean, Time-domain optical mammography SoftScan?: initial results. Acad. Radiol. **12**, 934–947 (2005)
64. X. Intes, J. Ripoll, Y. Chen, S. Nioka, A. Yodh, B. Chance, In vivo continuous-wave optical breast imaging enhanced with Indocyanine Green. Med. Phys. **30**, 1039–1047 (2003)
65. T. Hamaoka, K.K. McCully, V. Quaresima, K. Yamamoto, B. Chance, Near-infrared spectroscopy/imaging for monitoring muscle oxygenation and oxidative metabolism in healthy and diseased humans. J. Biomed. Opt. **12**(6), 1–16 (2007)
66. Y. Lin, G. Lech, S. Nioka, X. Intes, B. Chance, Noninvasive, low-noise, fast imaging of blood volume and deoxygenation changes in muscles using light-emitting diode continuous-wave imager. Rev. Sci. Instrum. **73**, 3065–3074 (2002)
67. X. Intes, C. Maloux, M. Guven, B. Yazici, B. Chance, Diffuse Optical Tomography with physiological and spatial a-priori constraints. Phys. Med. Biol. **49**, N155–164 (2004)
68. J. Chang, H.L. Graber, P.C. Koo, R. Aronson, S.L. Barbour, R.L. Barbour, Optical imaging of anatomical maps derived from magnetic resonance images using time-independent optical sources. IEEE Trans. Med. Imaging **16**, 68–77 (1997)
69. B.W. Pogue, K.D. Paulsen, High resolution near-infrared tomographic imaging simulations of the rat cranium by use of a priori magnetic resonance imaging structural information. Opt. Lett. **23**, 1716–1718 (1998)
70. B. Brooksby, H. Dehghani, B.W. Pogue, K.D. Paulsen, Near infrared tomography breast image reconstruction with a priori structural information fromMRI: algorithm development forreconstructing heterogeneities. IEEE J. STQE **9**, 199–209 (2003)
71. M. Schweiger, S.R. Arridge, Optical tomographic reconstruction in a complex head model using a priori boundary information. Phys. Med. Biol. **44**, 2703–2721 (1998)
72. M. Guven, B. Yazici, X. Intes, B. Chance, Diffuse optical tomography with a priori anatomical information. Phys. Med. Biol. **50**, 2837–2858 (2005)
73. T. Hupper, R.D. Hoge, A.M. Dale, M.A. Franceschini, D.A. Boas, Quantitative spatial comparison of diffuse optical imaging with blood oxygen level dependent and arterial spin labeling-based functional magnetic resonance imaging. J. Biomed. Opt. **11**, 064018 (2006)
74. C. Kuhl, The current status of breast MR imaging Part I: choice of technqine, image interpretation, diagnostic accuracy, and transfer to clinical practice. Radiology **244**, 672–691 (2007)
75. M. Khayat, Clinical studies in optical imaging: an industry perspective, in *Translational Multimodality Optical Imaging*, Ch. 14, ed. by F. Azar, X. Intes (Artech House, Norwood, 2008)

76. C.M. Carpenter, B.W. Pogue, S. Jiang, H. Dehghani, X. Wang, K.D. Paulsen, W.A. Wells, J. Forero, C. Kogel, J.B. Weaver, S.P. Poplack, P.A. Kaufman, Image-guided optical spectroscopy provides molecular-specific information in vivo: MRI-guided spectroscopy of breast cancer hemoglobin, water, and scatterer size. Opt. Lett. **32**, 933–935 (2007)
77. V. Toronov, X. Zhang, A. Webb, A spatial and temporal comparison of hemodynamic signals measured using optical and functional magnetic resonance imaging during activation in the human primary visual cortex. NeuroImage **34**, 1136–1148 (2001)
78. X.V. Zhang, V. Torornov, A. Webb, Simultaneous integrated diffuse optical tomography and functional magnetic resonance imaging of the human brain. Opt. Express **13**, 55135521 (2005)
79. Y. Chen, D. Tailor, X. Intes, B. Chance, Quantitative correlation between Near-Infrared spectroscopy (NIRS) and magnetic resonance imaging (MRI) on rat brain oxygenation modulation. Phys. Med. Biol. **48**, 417–427 (2003)
80. F.A. Howe, S.P. Robinson, D.J.O. McIntyre, M. Stubbs, J.R. Griffiths, Issues in flow and oxygenation dependent contrast (FLOOD) imaging of tumours. NMR Biomed. **14**, 497–506 (2001)
81. S.E. Singletary, Multidisciplinary frontiers in breast cancer mamangenetm: a surgeon's perspective. Cancer **109**, 1019–1029 (2007)
82. Q. Zhang, T.J. Brukilacchio, A. Li, J.J. Stott, T. Chaves, E. Hillman, T. Wu, M. Chorlton, E. Rafferty, R.H. Moore, D.B. Kopans, David A. Boas, Coregistered tomographic x-ray and optical breast imaging: initial results. J. Biomed. Opt. **10**, 024033 (2005)
83. Q. Zhu, S. Tannenbaum, S.H. Kurtzman, Optical tomography with ultrasound localization for breast cancer diagnosis and treatment monitoring. Surg. Oncol. Clin. **16**, 307–321 (2007)
84. S. Surti, J.S. Karp, Imaging characteristics of a 3-D GSO whole body PET camera. J. Nucl. Med. **45**, 1040–1049 (2004)
85. R. Freifelder, J.S. Karp, Dedicated PET scanners for breast imaging. Phys. Med. Biol. **42**, 2453–2480 (1997)
86. S.D. Konecky, R. Choe, A. Corlu, K. Lee, R. Wiener, S.M. Srinivas, J.R. Saffer, R. Freifelder, J.S. Karp, N. Hajjioui, F. Azar, A.G. Yodh, Comparison of diffuse optical tomography of human breast with whole body and breast only positron emission tomography. Med. Phys. **35**, 446–455 (2008)
87. K. Licha, C. Olbrich, Optical imaging in drug discovery and diagnostic applications. Adv. Drug Deliv. Rev. **57**(8), 1087–108 (2005)
88. A. Corlu, et al., Opt. Express **15**, 6696 (2007)

Index

R. Liang (ed.), *Biomedical Optical Imaging Technologies*, Biological and Medical Physics, Biomedical Engineering, DOI 10.1007/978-3-642-28391-8,